

TUNL LIII
PROGRESS REPORT

1 DECEMBER 2014 – 30 NOVEMBER 2015

TRIANGLE UNIVERSITIES NUCLEAR LABORATORY

DUKE UNIVERSITY
NORTH CAROLINA STATE UNIVERSITY
UNIVERSITY OF NORTH CAROLINA AT CHAPEL HILL
Box 90308, DURHAM, NORTH CAROLINA 27708-0308, USA

Work described in this Progress Report is supported by the United States Department of Energy, Office of Science (Low Energy and Medium Energy Nuclear Physics Programs), under:

Grant No. DE-FG02-97ER41033 (Duke University),

Grant No. DE-FG02-97ER41042 (North Carolina State University), and

Grant No. DE-FG02-97ER41041 (University of North Carolina).

Contents

Introduction	vii
Personnel	xv
1 Hadron Structure and Few-Nucleon Systems	1
1.1 Low-Energy Description of Hadron Structure	2
1.1.1 ^4He Compton Scattering at 60 MeV and Commissioning of a New Cryogenic Target	2
1.1.2 A Cryogenic Target for Compton-Scattering Experiments at HI γ S	4
1.1.3 The Gerasimov-Drell-Hearn Sum Rule Experiment at HI γ S: Progress on the HI γ S Frozen-Spin Target	6
1.1.4 Neutron Polarization from Deuteron Photodisintegration	8
1.2 Few-Nucleon Systems	10
1.2.1 Neutron-Neutron Quasifree Scattering in Neutron-Deuteron Breakup	10
1.2.2 Testing the TUNL Shielded Neutron Source	12
1.2.3 Three- and Two-Body Photodisintegration of ^3He with Double Polarizations	14
1.2.4 Three-Body Photodisintegration of ^3H and ^3He	16
1.2.5 Tritium Gas Target System for Photodisintegration Experiments	18
1.2.6 Evaluation of Silicon Strip Detectors with Low-Energy Protons	20
1.2.7 Evaluation of a Prototype Wire Chamber	22
1.2.8 Monte-Carlo Simulations of $^3\text{H}(\gamma, pn)n$ and $^3\text{He}(\gamma, pp)n$ Experiments at HI γ S	24
2 Nuclear Astrophysics	27
2.1 Nucleosynthesis in Hydrostatic and Explosive Environments	28
2.1.1 New Recommended $\omega\gamma$ for the $E_r^{\text{cm}} = 458$ keV Resonance in $^{22}\text{Ne}(p, \gamma)^{23}\text{Na}$	28
2.1.2 High Beam-Intensity Study of $^{17}\text{O}(p, \gamma)^{18}\text{F}$ and Thermonuclear Reaction Rates for $^{17}\text{O}+p$	30
2.1.3 Thermonuclear Reaction Rate Evaluation for $^{18}\text{Ne}(\alpha, p)^{21}\text{Na}$	32
2.1.4 Evaluation of $^{29}\text{Si}(p, \gamma)^{30}\text{P}$ and Its Relevance to Classical Nova Presolar Grains	34
2.1.5 Photo-Induced Depopulation of the ^{180m}Ta Isomer	36
2.2 Thermonuclear Reaction Rates	38
2.2.1 The Impact of Reaction Rate Variations on Nucleosynthesis	38
2.2.2 Statistical Methods for Thermonuclear Reaction Rates and Nucleosynthesis Simulations	40
3 Nuclear Structure	43
3.1 Study of Many-Body Systems	44
3.1.1 The Role of Deformation on the Dipole Strength Distribution of the Pygmy Dipole Resonance: ^{154}Sm Isotope	44
3.1.2 The energy dependence of Fission Product Yields from neutron-induced fission of ^{235}U , ^{238}U and ^{239}Pu	46
3.1.3 Fission Product Yields Using Mono-Energetic Photon Beams at 13 MeV	48
3.1.4 γ -Ray Induced Fission-Product Yield of ^{239}Pu at 11 MeV	50

3.1.5	Mono-Energetic Photon-Induced $^{235}\text{U}/^{239}\text{Pu}$ Fission Cross-Section Ratio Measurements at 8 to 17 MeV	52
3.1.6	Neutron-Capture Experiments	53
4	Fundamental Symmetries in the Nucleus	56
4.1	The Neutron Electric Dipole Moment	57
4.1.1	Search for the Electric Dipole Moment of the Neutron	57
4.1.2	Development of a Systematic-Studies Apparatus for the nEDM Experiment	59
4.1.3	Development of the PULSTAR Vestibule Including Cryogenic UCN Windows	61
4.1.4	PULSTAR Charcoal Pump System: The Double Valve	63
4.1.5	Measurements of Superfluid Helium Film Flow for the PULSTAR Project	65
4.1.6	Heat Switches for the PULSTAR Test Facility	67
4.1.7	Ultra-Cold Neutron Storage Cells for the SNS nEDM Collaboration	69
4.1.8	Design and Testing of Neutron Windows and Seals for the nEDM Project	71
4.1.9	Commissioning of the Ultracold-Neutron-Source Facility at the NC State PULSTAR Reactor	73
4.2	Fundamental Coupling Constants	75
4.2.1	The UCNA experiment	75
4.2.2	The Nab Experiment	77
4.2.3	A New Determination of the ^{19}Ne β Asymmetry	79
4.2.4	Neutron Interferometric Search for Dark Energy	81
4.2.5	Oklo Reactors and Implications for Nuclear Science	83
4.2.6	CALIOPE: A Search for CP Violation in Positronium	85
4.2.7	Electromagnet Design for an Experimental Search for CP -violation in Positronium Decay	87
5	Neutrino Physics	90
5.1	$\beta\beta$ -Decay Experiments	91
5.1.1	Construction and Commissioning of the MAJORANA DEMONSTRATOR Project	91
5.1.2	Monte Carlo Waveform Fitting for the MAJORANA DEMONSTRATOR	93
5.1.3	Simulations of Surface α -Particle Contamination for the MAJORANA DEMONSTRATOR	95
5.1.4	Identifying MAJORANA DEMONSTRATOR Backgrounds by Single-Site Time Correlation	97
5.1.5	Underground Low-Background Assay at KURF	99
5.1.6	Development of a Beamline and Target Chamber for Measuring $(^3\text{He},n)$ Reaction Cross Sections	101
5.1.7	The Neutron Capture Cross Section on $^{63,65}\text{Cu}$ Between 0.4 and 7.5 MeV	103
5.1.8	The $^{76}\text{Ge}(n,2n)^{75}\text{Ge}$ Cross Section between 10 and 15 MeV	105
5.1.9	The $^{76}\text{Ge}(n,p)^{76}\text{Ga}$ Reaction and the Search for $0\nu\beta\beta$ Decay in ^{76}Ge	107
5.1.10	Determination of the Differential Cross Section of $^{76}\text{Ge}(n,n'\gamma)$ at $E_n = 5$ and 8 MeV	109
5.1.11	The $^{76}\text{Ge}(n,n'\gamma)^{76}\text{Ge}$ Reaction and the Search for the $0\nu\beta\beta$ Decay of ^{76}Ge	111
5.1.12	The $^{134}\text{Xe}(n,n'\gamma)^{134}\text{Xe}$ reaction at 5 MeV	113
5.1.13	Partial Cross Sections of Neutron-Induced Reactions on ^{136}Xe at $E_n = 5$ MeV for $0\nu\beta\beta$ Background Studies	115
5.1.14	Final Results from $2\nu\beta\beta$ Decay of ^{96}Zr to Excited States	117
5.1.15	New Limits on the β Decay of ^{96}Zr	119
5.1.16	Final Results from Search for Resonant Double-Electron Capture of ^{156}Dy	121
5.1.17	A Brief Exploration of Low-Threshold Detectors	123
5.1.18	TUNL's KamLAND Effort	125
5.1.19	Effective Operators for Double-Beta Decay	127

6 Applications of Nuclear Physics and Nuclear Data Evaluation	130
6.1 Homeland and National Nuclear Security	131
6.1.1 Measurements of the $^{238}\text{U}(n,2n)$ Cross Section of from 6 to 15 MeV	131
6.1.2 Dipole Transitions in ^{240}Pu	133
6.1.3 Sub-barrier Photofission of ^{232}Th and ^{238}U	135
6.1.4 Upgrade to the Inventory-Sample Neutron Detector	137
6.2 National Ignition Facility Activities	139
6.2.1 Measurement of the $^{80}\text{Kr}(n,2n)^{79}\text{Kr}$ Cross Section at 14.8 MeV	139
6.2.2 Exploratory Measurement of the $^{209}\text{Bi}(n,4n)^{206}\text{Bi}$ Cross Section at 28 MeV	141
6.2.3 Measurement of the $^{169}\text{Tm}(n,3n)^{167}\text{Tm}$ cross section	143
6.3 Public Health Research	145
6.3.1 Rutherford Backscattering Spectrometry of Small Molecules in Water Purification Membranes	145
6.3.2 Nuclear Resonance Fluorescence Measurements on Light Nuclei	147
6.4 Plant Physiology Research	149
6.4.1 Development of a Modular Plant Imaging PET System and Its Use in Evaluating Corn Plant Root Systems	149
6.5 Nuclear Data Evaluation	151
6.5.1 Nuclear Data Evaluation Activities	151
6.5.2 A Systematic Evaluation of β -Decay Half-Life Values in the Light Nuclei	153
6.5.3 Nuclear Data Compilation for Beta Decay Isotopes	155
7 Accelerator Physics	158
7.1 The High-Intensity γ -Ray Source (HI γ S)	159
7.1.1 Operation of the HI γ S Facility—FY 2014	159
7.1.2 Operation of the HI γ S Facility—FY 2015	161
7.1.3 Developing an Injection Mode with 100 ns Electron Beam Pulses	163
7.1.4 Extending OK-5 Wiggler Operations at the Duke Storage Ring	165
7.1.5 Characterizing the Betatron Tune Knobs at the Duke Storage Ring	167
7.1.6 Measuring the Storage Ring Lattice Using a Tune-Based Technique	169
7.1.7 Improved Pulsed Mode Operation for the Duke Storage-Ring-Based FEL	171
7.1.8 A Two-Color Storage Ring FEL	173
7.2 The FN Tandem Accelerator and Ion Sources	175
7.2.1 Tandem Accelerator Operation	175
7.2.2 A ^3He Gas-Recirculation System for the Helium Ion Source	177
7.3 The LENA Accelerator and Ion Sources	179
7.3.1 LENA’s New ECRIS Acceleration Column: Overview	179
7.3.2 New ECRIS Acceleration Column: Electrostatic Design	181
7.3.3 New ECRIS Acceleration Column: Secondary Electron Issues	183
7.3.4 ECRIS Upgrade: The Plasma Extraction System	185
7.3.5 The LENA ECR Ion Source: Beam Pulsing	187
8 Nuclear Instrumentation and Methods	190
8.1 Detector Development and Characterization	191
8.1.1 Characterizing TUNL’s Surface Barrier Silicon Detectors	191
8.1.2 Commissioning the Enge Focal Plane Detector	193
8.1.3 The Characterization of a ^{10}B -Doped Capture-Gated Liquid Scintillator	195
8.1.4 Simulation of Proposed New HPGe Clover Detector for LENA	197
8.2 Data Acquisition Hardware and Software Development	199
8.2.1 Development of the DAQLINK Package for Live DAQ Monitoring	199
8.2.2 Toward an EPICS Slow Control System for the Enge Spectrograph	201
8.2.3 γ -Ray Spectroscopy Using the Binned Likelihood Method	203
8.2.4 Timing Reconstruction Algorithm for γ -Ray Detections	205
8.2.5 Status of the ORCA Data Acquisition Software	207

A Appendices	210
A.1 Graduate Degrees Awarded	211
A.2 Publications	212
A.3 Invited Talks, Seminars, and Colloquia	227
A.4 Professional Service Activities	232
Glossary of Acronyms	235
Index	237

Introduction

Who We Are

The Triangle Universities Nuclear Laboratory (TUNL) is a consortium of three major universities in the North Carolina Triangle area: Duke University (Duke), North Carolina State University (NCSU) and the University of North Carolina at Chapel Hill (UNC). The primary mission of TUNL is to advance the frontiers of nuclear physics and to educate students and young scientists in an environment that provides experiences at the forefront of the field. The TUNL is a Department of Energy (DOE) Center of Excellence funded by the Low-Energy Program (LEP) in the Office of Nuclear Physics (ONP). The Center is supported primarily through three grants from the ONP/LEP, one to each consortium university. The grant numbers are listed at the beginning of this report. The grants to NCSU and UNC support the experimental nuclear physics research groups at these institutions. The budgets for these awards include student and postdoc support, senior investigator and research scientist salaries, travel, and modest funding for research instrumentation and laboratory materials and supplies. The Duke grant has two components: (1) support for the shared research infrastructure at TUNL (including operation of accelerator facilities, technical and administrative support staff, support for special research facilities, materials, supplies and equipment), and (2) support for the experimental low-energy nuclear physics research group at Duke. In addition, the Nuclear Data Program in the ONP supports efforts at NCSU and Duke.

This year the TUNL consortium included 22 faculty members, 58 graduate students, 13 postdoctoral fellows and 5 research scientists. About 30 undergraduate students participated in research at TUNL through research assistantships at the consortium universities, the TUNL REU program, and international exchange programs. The activities of this research community are supported by the TUNL staff which includes administrative personnel, technicians, engineers, and research scientists. The consortium conducts research over a wide range of topics in nuclear physics that broadly include fundamental symmetries, neutrino physics, nuclear astrophysics, and strong interaction physics (hadron structure, light nuclei, and many-body systems). Complimentary to advancing these basic scientific areas, TUNL groups are conducting R&D on particle detectors, signal processing electronics, data acquisition systems, production and evaluation of ultra-low-radioactivity materials, and particle accelerator systems with emphasis on high-intensity laser Compton gamma-ray sources. Also, groups at TUNL are applying nuclear-physics techniques to areas of national nuclear security, homeland security, and interdisciplinary science research areas, e.g., plant physiology, municipal water purification, and medical physics.

In addition to consortium members, long-term collaborators contribute substantially to the research and education activities at TUNL. These collaborators participate in and lead research projects at the laboratory, thus significantly expanding the opportunities for undergraduate students and students from under-represented ethnic groups to participate in nuclear research. The collaborators include groups from two local historically black universities (North Carolina Central University and North Carolina A&T State University) plus several primarily undergraduate-serving institutions (James Madison University, the University of North Georgia, University of Connecticut at Avery Point, and Tennessee Technological University). In addition, there are long-term international collaborations with groups from the Istituto Nazionale di Fisica Nucleare (Pisa), Jagiellonian University (Cracow), the Joint Institute for Nuclear Research (Dubna), the Technische Universität Darmstadt, the University of Cologne, and the University of Mainz. In our applications and interdisciplinary research programs, we collaborate with scientists from several national laboratories, including Jefferson Laboratory, Lawrence Livermore National Laboratory, Los Alamos National Lab-

oratory, and Pacific Northwest National Laboratory.

Our Research Program

The groups at TUNL conduct research over a broad range of topics in strong and weak interactions nuclear physics. The main areas in the strong-interactions program are low-energy QCD, nuclear astrophysics, and many-body nuclear structure and reactions. The low-energy QCD research includes studies of hadron structure and few-nucleon reaction dynamics. This research is enabled by the unique and world-leading capabilities of the accelerator facilities at TUNL and is supported by accelerator physics R&D conducted in concert. The central thrust of the weak-interactions research is the search for physics beyond the Standard Model. The techniques applied in this pursuit include precision tests of fundamental symmetries, determinations of the properties of neutrinos, and high-precision measurements of weak coupling constants. In this research area TUNL groups have major responsibilities on two DOE-funded large-scale collaborative projects: (1) the nEDM experiment at the Spallation Neutron Source (SNS) at Oak Ridge National Laboratory (ORNL), which is a test of violation of time-reversal invariance via the measurement of the neutron electric dipole moment, and (2) the MAJORANA DEMONSTRATOR, which is an R&D effort aimed at developing the technique and technology for searching for neutrinoless double- β -decay using enriched ^{76}Ge as the sample and detector. The MAJORANA DEMONSTRATOR is sited at the Sanford Underground Research Facility (SURF) in Lead, SD. Both projects are managed by ORNL, which has well established collaborations with the three TUNL universities.

Our Facilities and Support Staff

TUNL operates three accelerator facilities: the High Intensity Gamma-Ray Source (HI γ S), the Laboratory for Experimental Nuclear Astrophysics (LENA) and the tandem Van de Graaff accelerator laboratory.

Of the three facilities, HI γ S has the largest user community and supports the broadest research program. HI γ S is a Compton-backscattering γ -ray source that produces γ -ray beams by colliding photons inside the optical cavity of a free-electron laser with electrons circulating in a storage ring. This source delivers nearly mono-energetic and highly polarized γ -ray beams to targets with the highest spectral intensity of all accelerator-driven γ -ray beam sources worldwide. The capabilities of HI γ S are in large part due to its intrinsic design advantages over other sources along with the work of the accelerator physics group that is focused on advancing the γ -ray beam capabilities of this unique facility.

LENA is a light-ion, low-energy accelerator facility with beam capabilities optimized for nuclear astrophysics experiments. This laboratory has two low-energy electrostatic accelerators capable of delivering high-current charged-particle beams to experiments. One is an electron-cyclotron-resonance source on a 200-kV isolated potential platform; the other is a 1-MV JN Van de Graaff accelerator.

The main accelerator in the tandem laboratory is an FN tandem Van de Graaff that has a maximum terminal voltage of 10 MV. The beams at this facility support a nuclear physics research program that uses light-ions and neutron beams to study nuclear structure and the strong interaction at low energies. The special beam capabilities include nearly mono-energetic unpolarized and polarized fast neutron beams and polarized proton and deuteron beams. The pulsed beam capabilities in the tandem lab enable measurements of neutron velocities via time-of-flight techniques.

The accelerators at LENA and the tandem laboratory are operated by research groups, i.e., faculty, students and postdocs, and are maintained by the technical staff. R&D to create new capabilities is carried out by the research groups in collaboration with the technical staff.

In addition to the accelerator facilities, the TUNL research infrastructure includes non-accelerator research facilities, e.g., R&D laboratories at Duke, NCSU and UNC; a low-background counting facility at Duke; and a low-radioactivity fabrication and assembly facility at UNC. TUNL also has several research laboratories at the Kimballton Underground Research Facility (KURF) in Kimballton, VA, which is a regional facility operated by Virginia Tech in an active limestone mine.

The technical and administrative staffs at TUNL are vital to carrying out the research program. The technical staff provides research support, maintains the accelerators and research facilities, and supports accelerator operations. In addition, TUNL research groups have access to laboratory materials, supplies, and a pool of research equipment. The expertise of the technical staff includes mechanical systems, high vacuum systems, cryogenics, optical systems, electronics, data acquisition, accelerator controls systems, high-power electrical systems, ion sources, electron guns, and RF and electrostatic accelerator systems. The accelerator physicists work with TUNL faculty to advance beam capabilities at the local accelerator facilities.

Our Education Program

The graduate education mission of TUNL shapes the style and environment for conducting research. TUNL faculty continue to attract some of the most talented students in the physics departments at the three consortium universities into nuclear physics. The intellectual energy in the university environment, the commitment of the TUNL faculty to physics education, and the hands-on philosophy of the TUNL faculty all contribute to an environment that fosters scientific creativity, technological innovation, and leadership. For almost five decades, TUNL has been a major contributor to the training of experimental nuclear physicists in the U.S., educating about 8% of the nations Ph.D.s in this field.

Research Experience for Undergraduates

The research activities at TUNL also provide opportunities for undergraduate students to participate in forefront basic and applied research during the academic year and the summer. Faculty with students from several primarily undergraduate-serving institutions, e.g., the University of North Georgia and James Madison University, are conducting research in collaboration with TUNL groups. Among these institutions are two local historically black universities, NC A&T State University in Greensboro, NC and NC Central University in Durham, NC.

Furthermore, since 2000 TUNL has run a NSF-supported REU program. Beginning in 2012, the REU program expanded to include high-energy particle physics and is operated in collaboration with the Duke high-energy physics (HEP) group. The NSF funding supports twelve participants each summer, of which eight conduct research with TUNL groups. The four students conducting research in high-energy physics spend the last six weeks of the program at CERN with the Duke HEP group. Including the REU students, about 30 undergraduates conducted research with TUNL groups this year.

Seminars

The TUNL seminar program continues with characteristic vigor, with 15 invited speakers. A full list of the titles and speakers from this year's seminars is given in the appendix to the progress report. The seminar series is augmented by the TUNL Informal Lunch Talks (TILTs), where graduate students and postdoctoral fellows present their research projects. A related series of talks, the Triangle Nuclear Theory Colloquia, are also beneficial to TUNL faculty and students.

Orientation and Training Classes

Another component to our educational effort is a special lecture series given by local speakers on Advances in Physics as part of the REU program during the summer. These are supplemented by classes on some of the basic experimental and theoretical techniques used in nuclear physics as well as classes on scientific writing. These are primarily for the REU students and entering graduate students.

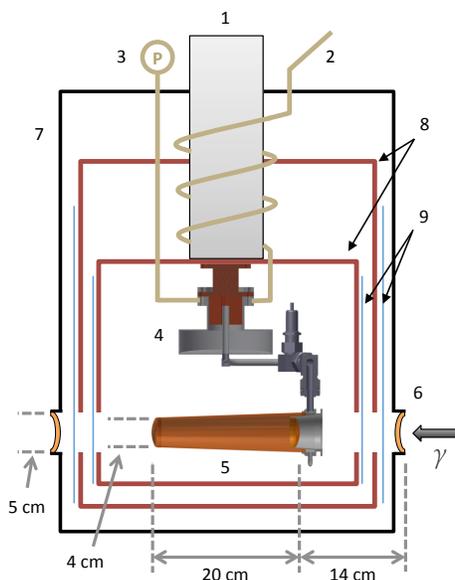
Research Highlights

Some highlights of research accomplishments during this reporting period are presented here. A more comprehensive description of individual projects constitutes the body of this Progress Report.

1. Cryogenic Target for Compton-Scattering Experiments at HI γ S Commissioned

Construction of the cryogenic target for Compton-scattering experiments at HI γ S was completed this year, and the target was used in a commissioning experiment that measured the cross section for Compton scattering from ^4He at 61 MeV. The target has the capability of liquefying hydrogen, deuterium and helium-4. The cooling device is a Sumitomo Model RDK-415D Gifford-McMahon cryocooler. It has a cooling power of 1.5 W at 4.2 K and a base temperature of around 3 K. The standard-pressure boiling points of LHe, LD $_2$ and LH $_2$ are 4.2 K, 24 K and 20 K, respectively. The apparatus is equipped with a heater for running at 20 to 24 K when liquefying D $_2$ or H $_2$. A schematic of the target cryostat is shown in Fig. 1. A paper describing the technical details and performance of the target has been submitted to Nuclear Instruments and Methods in Physics Research A.

Figure 1: A schematic of the target cryostat. The target cell is a 0.25 L truncated cone made of 0.125-mm thick Kapton foil. The cell is 20 cm long with 4-cm-diameter end caps. The main parts of the cryotarget are numbered in the diagram: the cryocooler (1), gas inlet (2), vent line (3), condenser (4), Kapton cell (5), beam windows (6), vacuum can (7), heat shields (8), and superinsulation (9).



2. New Method for Resonance Strength Determination Applied to the $E_{cm} = 458$ keV Resonance in $^{22}\text{Ne}(p,\gamma)^{23}\text{Na}$

In preparation for LENA measurements to better understand abundance anomalies in globular clusters, an entirely new method to analyze singles and coincidence γ -ray pulse-height spectra has been developed. The method is based on two novelties: (i) a decomposition of the entire measured spectrum, including Compton background, escape peaks, etc., into different components (for different primary transitions, room background, etc.), and (ii) performing the fitting in a Bayesian parameter estimation framework. A manuscript by UNC graduate student Jack Dermigny, has been completed and will be submitted for publication shortly (Dermigny, Iliadis, Buckner, and Kelly, to be submitted to NIM A). This technique has been applied to the $^{22}\text{Ne}(p,\gamma)$ reaction - a critical reaction in understanding the origin of the Na-O anticorrelation in globular clusters.

New branching ratios have been derived, including a newly discovered branch to the 7082-keV state in ^{23}Na and a decrease of 1013% in the ground-state branching ratio relative to previous results. The resonance strength of $\omega\gamma$ (458 keV) = 0.583(43) eV based on these results is recommended. Also, this work reduces the uncertainty in the resonance strength from 9.7% to 7.3%. Details of the

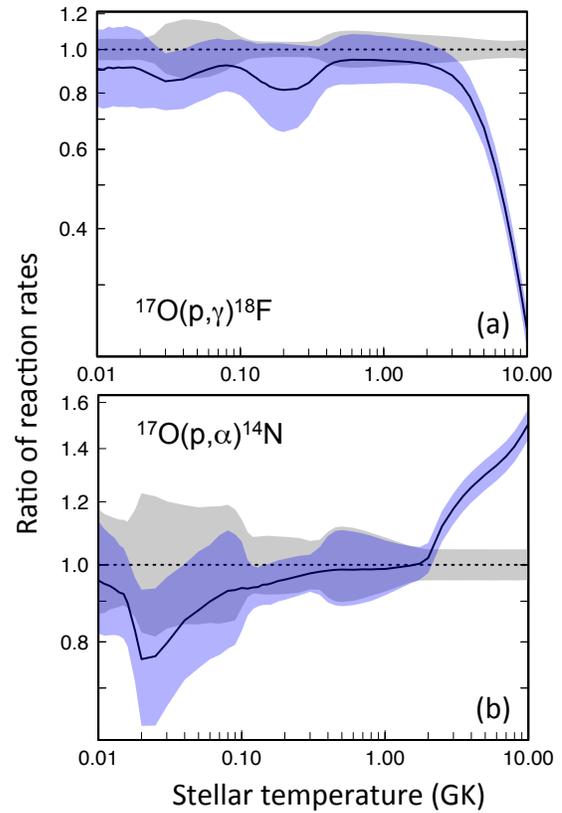


Figure 2: Reaction rate comparison as a function of temperature of present results with a recent evaluation. All rates are normalized to the new recommended rate. The solid curve shows the ratio of previous and present recommended rates. The grey shaded area represents the one-sigma (1σ) uncertainties in the present rates, and the blue shaded area denotes the 1σ uncertainties of the previous evaluated rates.

new measurements and analysis are reported by K.J. Kelly *et al.*, Phys. Rev. C **92**, 035805 (2015).

3. New Determination of Thermonuclear Reaction Rates for $^{17}\text{O}+\text{p}$

Hydrogen burning of the oxygen isotopes takes place in several stellar environments. New measurements of the $^{17}\text{O}(\text{p},\gamma)^{18}\text{F}$ reaction at incident energies of 170 to 530 keV were performed at LENA. Improvements over previous work include significantly higher beam intensities, the use of a γ -ray coincidence spectrometer, and a novel data analysis technique made possible by the spectrometer. New thermonuclear rates for the $^{17}\text{O}+\text{p}$ reactions have been determined by combining these new data with all consistent results from previous measurements. The new rates are plotted in Fig. 2 in comparison with previous evaluated rates. This work is reported by M.Q. Buckner *et al.*, Phys. Rev. C **91**, 015812 (2015).

4. Measurement of the Neutron-Capture Cross Section of ^{76}Ge and ^{74}Ge

Gamma-rays from neutron-induced reactions in materials used in neutrinoless double beta decay searches are potentially a significant source of background in these ultra-low background counting experiments. A program for measuring cross sections for neutron induced reactions on isotopes used in $0\nu\beta\beta$ searches is underway at TUNL. Here we report new cross-section measurements for neutron capture on ^{76}Ge and ^{74}Ge at neutron energies below 15 MeV. These measurements were carried out in the tandem laboratory using the neutron activation technique. High-resolution γ -ray spectroscopy was used to determine the γ -ray activity of the daughter nuclei of interest. Prior to this work data only existed at thermal energies and at 14 MeV. As shown in Fig. 3, our ^{76}Ge total capture cross-section data are in good agreement with the TENDL-2013 model calculations and the ENDF/B-VII.1 evaluations. However, our $^{74}\text{Ge}(\text{n},\gamma)^{75}\text{Ge}$ cross sections are about a factor of

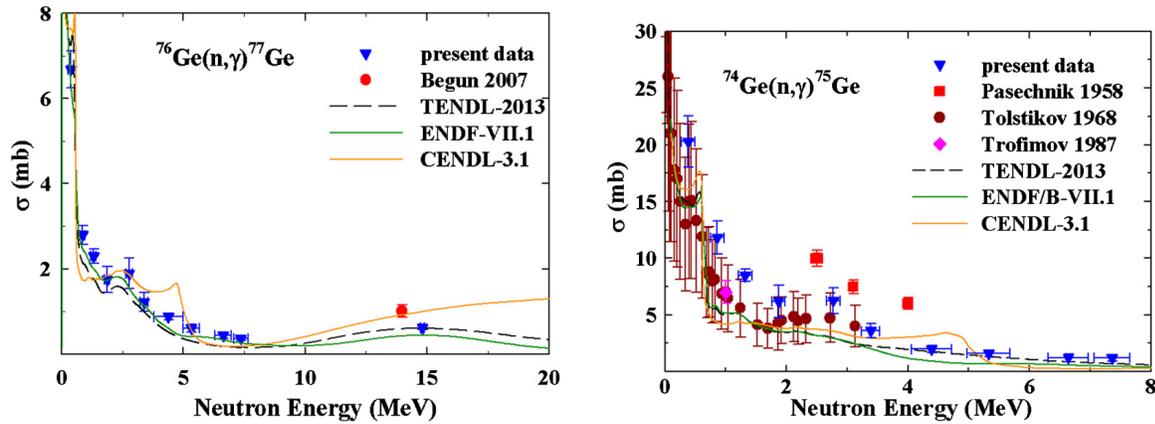


Figure 3: Neutron capture cross sections on ^{76}Ge (left) and ^{74}Ge (right) as a function of the incident neutron energy. The data are in comparison to evaluations and the model prediction TENDL-2013. The ENDF/B-VII.1 and JENDL-4.0 evaluations overlap substantial over the entire energy range of these data.

two larger than predicted and about 3.5 times larger than the $^{76}\text{Ge}(n,\gamma)^{77}\text{Ge}$ cross sections. This observation should be considered in the optimization of the relative masses of enriched ^{76}Ge to natural Ge used in a large-scale $0\nu\beta\beta$ detector. These results are reported by Megha Bhike, B. Fallin, Krishichayan and W. Tornow, Phys. Lett. B **741**, 150 (2015).

5. MAJORANA DEMONSTRATOR Highlights

There has been substantial progress on construction and commissioning of the MAJORANA DEMONSTRATOR (MJD), an array high purity Ge detectors, enriched to 87% ^{76}Ge underground at the Sanford Underground Research Facility (SURF) in Lead, SD. The Demonstrator will search for neutrinoless double-beta decay and examine the viability of a future larger scale Ge experiment. Progress this past year includes:

- Based on the completed set of assays of all materials used in construction and assembly of the DEMONSTRATOR, our simulations project a total background of 3.5 counts/t-y in the region of interest (ROI) centered at the double beta decay end-point energy. This is close to our specified goal of 3.0 counts/ROI-t-y, and exceeds the key performance parameter goal of ≤ 10 counts/ROI-t-y.
- We completed assembly of the first ultra-clean array module (Module 1), which contains seven strings of detectors mounted in an electroformed vacuum cryostat mounted on its transportable monolith. There are a total of twenty (16.8 kg) ^{enr}Ge detectors and (5.7 kg) ^{nat}Ge detectors. A successful in-house repair at the TUNL vacuum shop allowed us to install and operate its thermosyphon dewar which had failed during its initial testing. The first in-shield commissioning run was started on June 26 and was completed on October 7. The run was stopped to allow us to install the inner electroformed copper shielding and implement several additional improvements to the module. Background data from this run are currently being analyzed.
- A total of 35 detectors with a mass of 29.7 kg were produced from our 87% enriched ^{76}Ge material. Initially ORTEC produced 30 detectors with a mass of 25.3 kg, providing a yield of 64.4%, comparable to all previous experiments. However, we were able to successfully recover and reprocess material captured from the detector manufacturers “waste stream” that provided us with an additional 4.4 kg of detectors and resulted in a final yield of 74.5%, the best ever achieved.
- Underground electroforming at the Temporary Clean Room (TCR) located at the Ross Campus at SURF was completed in April 2015. We produced a total of 2474 kg of electroformed Cu.



Figure 4: Installation of Module 1 strings being conducted inside the glovebox. During the reporting period, commissioning of Module 1 was started and the first low-background in-shield data were collected. Also construction on Module 2 was started.

Machining of the inner Cu shielding plates was completed in October, and they were installed in November 2015.

6. Neutron EDM Experiment Highlights

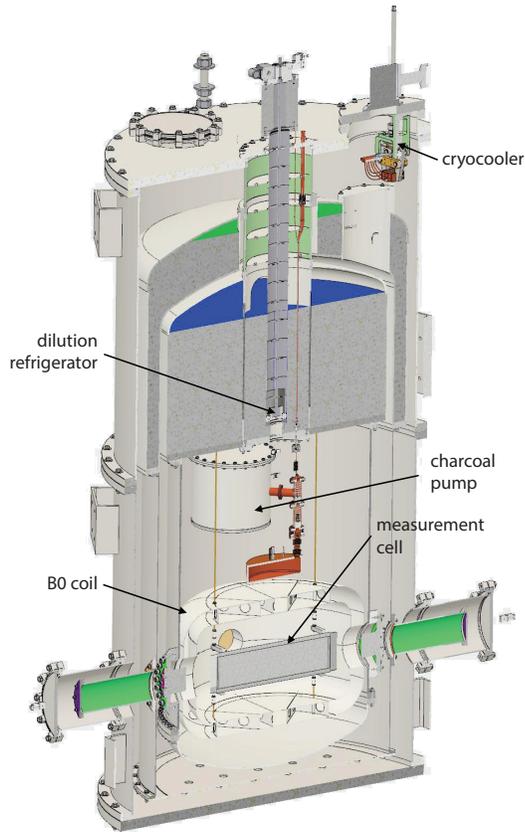
The nEDM collaboration is in its critical component demonstration phase, focusing on the development of the key components of the large-scale nEDM apparatus. TUNL's primary activity is the development of a small-scale test apparatus for use at the PULSTAR ultracold neutron (UCN) source that will allow one to explore UCN– ^3He interactions. During the past year, we have finalized and ordered this apparatus in addition to constructing and testing many of individual design components. TUNL is also playing a leading role in the measurements of UCN storage times in the nEDM measurement cells. This work is being performed at Los Alamos National Laboratory. Concurrent with the nEDM work, the construction of the UCN source at the PULSTAR reactor at NCSU is proceeding with full-scale cryogenic tests using flammable gasses occurring in 2015. The NC State group has also built and tested a second general purpose cryogen-free testing facility that is presently being used to test seals and composite materials for the larger nEDM experiment. An engineering diagram of the test apparatus is shown in Fig. 5.

Summary of Research Results

The main body of this progress report is a compilation of status reports of research projects conducted by TUNL groups during the period **December 1, 2014 to November 30, 2015**, which covers part of the first year of the current three-year grants (March 1, 2015 to February 28, 2018) to the three consortium universities from the DOE ONP Low-Energy Program.

During this reporting period research groups at TUNL published 62 papers in refereed journals of which 11 were letters and in other high-impact journals. Consortium members delivered more than 55 invited talks at APS meetings, conferences, and workshops, plus department colloquia and seminars. In addition, the consortium groups published 35 papers in conference proceedings. About 50% of the journal papers were based on work done at the on-site accelerator and research facilities. This report summarizes accomplishments made during this reporting period in nuclear and accelerator physics research. Selected instrumentation and equipment R&D activities associated with research projects at TUNL are reported as well.

Figure 5: Engineering vertical cross-sectional schematic of the nEDM systematic studies apparatus. For scale, the Dewar is approximately 1 m in diameter. The apparatus will enable the collaboration to conduct tests in five key scientific areas identified as essential for the larger nEDM project. Initially the apparatus will be used to measure the neutron and/or ^3He storage lifetimes in a full-size measurement cell. The measurement cell will be filled with liquid ^4He at a temperature of about 450 mK and placed within a uniform magnetic field generated by the B_0 coil. Cryogenic conventional and superconducting magnetic shields surround this geometry, as will thermal-radiation shields and, finally, a series of additional external conventional magnetic shields. UCNs from the PULSTAR source will be transported to the cell through a series of guides and will enter the cell through a high-transmission port. Polarized ^3He will be produced externally and introduced into the cell alongside the polarized UCNs through the same port.



Personnel

Department of Physics, Box 90308, Duke University,
Durham, NC 27708-0308

Department of Physics, Box 8202, North Carolina State University,
Raleigh, NC 27695-8202

Department of Physics and Astronomy, University of North Carolina,
Chapel Hill, NC 27599-3255

Faculty

Ahmed, M. W. (Adjunct Associate Professor)	NCCU/Duke
Barbeau, P. S. (Assistant Professor)	Duke
Champagne, A. E. (Professor)	UNC
Clegg, T. B. (Professor)	UNC
Gao, H. (Professor)	Duke
Golub, R. (Professor)	NCSU
Gould, C. R. (Professor)	NCSU
Green, M. P. ¹ (Assistant Professor)	NCSU
Haase, D. G. (Professor)	NCSU
Henning, R. (Assistant Professor)	UNC
Howell, C. R. (Director, Professor)	Duke
Huffman, P. R. (Associate Director, Professor)	NCSU
Iliadis, C. (Professor)	UNC
Karwowski, H. J. (Professor)	UNC
Kelley, J. H. (Research Associate Professor)	NCSU
Longland, R. (Assistant Professor)	NCSU
Ludwig, E. J. (Professor Emeritus)	UNC
Mitchell, G. E. (Professor Emeritus)	NCSU
Roberson, N. R. (Professor Emeritus)	Duke
Tilley, D. R. (Professor Emeritus)	NCSU
Tonchev, A. P. (Adjunct Associate Professor)	LLNL/Duke
Tornow, W. (Professor Emeritus)	Duke
Walter, R. L. (Professor Emeritus)	Duke
Weller, H. R. (Assoc. Dir. for Nuclear Physics at HI γ S, Professor Emeritus)	Duke
Wilkerson, J. F. (Associate Director, Professor)	UNC
Wu, Y. K. (Associate Director for Light Sources, Associate Professor)	Duke
Young, A. R. (Professor)	NCSU

¹As of 8/15

TUNL Advisory Committee

Aprahamian, A.	University of Notre Dame
McGovern, J.	University of Manchester
McKeown, R.	Thomas Jefferson National Laboratory
Schatz, H.	Michigan State University and NSCL
Tribble, R.	Brookhaven National Laboratory
Vigdor, S. E. (Chair)	Indiana University Bloomington

HI γ S Program Advisory Committee

Beise, E. J.	University of Maryland
Chen, J. P.	Thomas Jefferson National Laboratory
Donnelly, T. W.	Massachusetts Institute of Technology
Garvey, G. T. (Chair)	Los Alamos National Laboratory
Griesshammer, H.	George Washington University
Rehm, K. E.	Argonne National Laboratory
Sherrill, B. M.	Michigan State University and NSCL

Associated Faculty

Crawford, B. E.	Gettysburg College
Crowe, B. J.	North Carolina Central University
Dutta, D.	Mississippi State University
Engel, J.	University of North Carolina
Gai, M.	University of Connecticut at Avery Point
Keeter, K. J.	Idaho State University
Korobkina, E.	North Carolina State University
Markoff, D. M.	North Carolina Central University
McLaughlin, G. C.	North Carolina State University
Norum, B.	University of Virginia
Pedroni, R. S.	North Carolina A&T State University
Prior, R. M.	North Georgia College and State University
Purcell, J. E.	Georgia State University
Shriner, J. F.	Tennessee Technological University
Spraker, M. C.	North Georgia College and State University
Stephenson, S. L.	Gettysburg College
Weisel, G. J.	Penn State Altoona

Accelerator Physics Staff for Operations

Hao, H.	Research Scientist (at HI γ S)
Mikhailov, S. F.	Senior Research Scientist (at HI γ S)
Popov, V. G.	Senior Research Scientist (at HI γ S)
Westerfeldt, C. R.	Research Scientist (low energy accel.) & Rad. Safety Manager

Research Staff

Bhike, M. (Research Associate)	Duke
Caldwell, T. (Research Associate) ¹	UNC
Chyzh, A. ² (Research Associate)	NCSU
Crowell, A. S. (Research Scientist)	Duke
Esterline, J. H. (Research Associate)	Duke
Howe, M. A. (Senior Research Scientist)	UNC
Kalbach Walker, C. (Senior Research Scientist)	Duke
Kendellen, D. P. (Research Associate)	Duke
Krishichayan (Research Associate)	Duke
Leung, K. (Research Associate)	NCSU
Liu, T. ³ (Research Associate)	Duke
Meziane, M. ⁴ (Research Associate)	Duke
O'Shaughnessy, C. (Research Associate)	UNC
Seo, P.-N. (Research Associate)	UVA
Sikora, M. H. (Research Associate)	GWU
Wexler, J. (Research Associate)	NCSU
Xu, W. (Research Associate)	UNC
Ye, Z. ⁶ (Research Associate)	Duke
Zhao, Z. W. ⁷ (Research Scientist)	Duke

Technical and Nuclear Data Support Staff

Busch, M.	Mechanical Engineer
Carlin, B. P.	Electronics Supervisor
Dunham, J. D.	Accelerator Technician
Emamian, M.	Mechanical Engineer (at HI γ S)
Faircloth, J.	Project and Building Maint. Coordinator (at HI γ S)
Johnson, M.	Vacuum Technician (at HI γ S)
O'Quinn, R. M.	Accelerator Supervisor
Pentico, M.	Accelerator Technician (at HI γ S)
Rathbone, V.	Accelerator Technician (at HI γ S)
Sheu, G.	Project Coordinator, Nuclear Data
Swift, G. ⁸	Vacuum Engineer (at HI γ S)
Thomas, B. ⁹	Associate in Research
Wallace, P. ⁸	Electrical Engineer and Safety Manager (at HI γ S)
Walsh, B. ^{4,8}	Accelerator Technician
Wang, P.	RF Engineer (at HI γ S)

¹As of 11/15²Supported by NNSA/DOE³As of 9/15⁴Departed 5/15⁵As of 10/15⁶Departed 9/15⁷As of 4/15⁸Supported by DHS⁹Part time, as of 3/15

Graduate Students

Awe, C.	Duke	Marshall, C.	NCSU
Bartram, C.	UNC	Medlin, G.	NCSU
Combs, D. ¹	NCSU	Meijer, S.	UNC
Cooper, A.L.	UNC	Othman, G.	UNC
Cude-Woods, C.	NCSU	Peng, C.	Duke
Cumberbatch, L. C.	Duke	Portillo, F.	NCSU
Dees, E. ²	NCSU	Powell, J.	UNC
Dermigny, J.	UNC	Rager, J.	UNC
Downen, L. N.	UNC	Raybern, J.	Duke
Fallin, B. A.	Duke	Reid, A. ⁵	NCSU
Finch, S. W. ³	Duke	Rich, G.	UNC
Friesen, F. Q.	Duke	Sahbaee, P. ⁶	NCSU
Gillis, T.	UNC	Shanks, B.	UNC
Giovanetti, G. K. ³	UNC	Silano, J.	UNC
Heacock, B.	NCSU	Sosothikul, S.	NCSU
Hedges, S.	Duke	Strain MacMullin, J. ³	UNC
Huang, M.	Duke	Snavely, K.	UNC
Hunt, S.	UNC	Swindell, A. G.	U. Conn
Huffer, C.	NCSU	Ticehurst, D. R.	UNC
Kelly, K.	UNC	Trimble, J.	UNC
Laskaris, G. ³	Duke	Vorren, K.	UNC
Li, B. ⁴	Duke	VornDick, B. ³	NCSU
Li, L.	Duke	White, C.	NCSU
Li, W. ⁴	Duke	Wierman, K.	UNC
Li, X.	Duke	Witchger, A.	NCSU
Lin, L.	UNC	Xiong, W.	Duke
Lipman, A.	NCSU	Yan, J.	Duke
Little, D.	UNC	Yan, X.	Duke
Liu, P.	Duke	Zeck, B. ⁷	NCSU
Malone, C.	Duke	Zhang, Y.	Duke
Malone, R.	Duke	Zhou, W.	Duke

Visiting Scientists

Davis, E. D.	7/15 - 8/15	Kuwait University, Kuwait City, Kuwait
Witala, H.	8/15 - 9/15	Jagiellonian University, Cracow, Poland

Administrative Support Personnel

Adair, S. ⁸	Research Assistant (at UNC)
Cox, J. ⁹	Research Assistant (at UNC)
Paul, M. ¹⁰	Staff Assistant
West, B. ⁸	Staff Assistant

¹Supported by NNSA/DOE²Supported by NSF/DOE³Graduated with Ph.D. Degree between 9/14 and 11/15⁴Exchange student from USTC, China⁵Supported by DOE/Office for Science & Technology at the Embassy of France in the US⁶Supported by Duke University School of Medicine⁷Supported in part by LANL⁸Departed 5/15⁹As of 9/15¹⁰Partially supported by the Duke University Physics Department

Undergraduates

<i>Student</i>	<i>Institution</i>	<i>Faculty Advisor</i>
Amram O. ¹	Carnegie Mellon U.	A. T. Goshaw (Duke)
Billings, F.	NCCU	M. W. Ahmed
Brandt, A.	NCSU	A. R. Young
Bray I. ¹	Clarkson University	W. Tornow
Bullard, R.	NCSU	P. R. Huffman
Calderado, C.	UNC	T. B. Clegg
Elofson D. ¹	Bridgewater State U.	A. T. Arce (Duke)
Fedeler, S.	NCSU	P. R. Huffman
Flower, C.	Duke University	H. Gao
He, T.	Duke University	Y. Wu
Kowal K. ¹	Lewis & Clark College	R. Longland
Lambert, A.	NCSU	R. Golub
Leadbetter, C.	UNC	P. S. Barbeau
Lindeman C. ¹	Haverford College	M. C. Kruse and A. T. Arce (Duke)
Liu, B.	NCSU	A. R. Young
Liu, H. ²	Duke University	Y. Wu
Lively, K.	NCSU	D. G. Haase and C. R. Gould
Martin, J.	UNC	T. B. Clegg
Masood K. ¹	University of Florida	P. S. Barbeau
Miller K.	Duke University	P. S. Barbeau
Nance, J.	UNC	J. F. Wilkerson
Niazi R. ¹	University of Oklahoma	J. Engel (UNC)
Nibbs K. ¹	Vassar College	R. Henning
Olmsted S. ¹	East Tennessee State U.	J. H. Kelley
Peibo A.	William and Mary	P. S. Barbeau
Perreau, N. ¹	UNC	C. Walter (Duke)
Riggin D. ¹	Duke University	K. Scholberg (Duke)
Runge, J.	NCSU	R. Longland
Smith A. ¹	Baylor University	M. C. Kruse and A. T. Arce (Duke)
Suh B.	Duke University	P. S. Barbeau
Surbrook, J.	UNC	J. F. Wilkerson
Torre A.	Duke University	P. S. Barbeau
Underwood, D.	NCSU	R. Longland
Valdillez, R.	NCSU	P. R. Huffman
Wu, B.	Duke University	P. S. Barbeau
Yates, S.	Duke University	C. R. Howell

¹Supported by the TUNL NSF REU Program²Exchange student from Shandong University, China

Hadron Structure and Few-Nucleon Systems

Chapter 1

- **Low-Energy Description of Hadron Structure**
- **Few-Nucleon Systems**

This segment of the TUNL program is designed to perform measurements that will help guide theoretical work connecting QCD with nuclear constituents and nuclei, *e.g.*, chiral effective field theories and lattice QCD. The aim is to provide data that are important for testing the nuclear force models used in ab-initio few-nucleon calculations and for developing low-energy QCD theories of nuclear interactions and structure.

The focus of experiments relating to the low-energy description of hadrons is on measurements that will reduce the uncertainties in the electric and magnetic polarizabilities of the proton and neutron. These experiments probe the internal degrees of freedom of nucleons using Compton scattering from unpolarized and polarized targets at HI γ S. In addition, the circularly polarized beam and frozen spin target at HI γ S will be used to measure the spin-dependent cross section for photodisintegration of the deuteron. These data will provide integrand values for the Gerasimov-Drell-Hearn (GDH) sum rule.

During this reporting period, a new cryogenic target was built and commissioned for use in high-precision measurements of the electric and magnetic polarizabilities of the neutron. The target was also used to measure the Compton scattering cross section from ^4He at 60 MeV. A phenomenological model to assess the sensitivity of the measured angular distribution to the polarizabilities is being developed.

Work on commissioning the HI γ S Frozen-Spin-Target (HIFROST) system for GDH measurements involved optimizing the ^3He to ^4He mixture ratio for the dilution refrigerator and installing a new inner vacuum chamber and magnetic-field-holding coil. A temperature of about 190 mK was reached, with ongoing work designed to go below 100 mK.

Data were also collected on double-differential cross-sections from two- and three-body photodisintegration of polarized ^3He using circularly polarized photon beams with energies of 16.5 MeV (three-body) and 29 MeV (two-body). These data, when combined with data above pion threshold from other laboratories, will directly test the ^3He GDH sum rule prediction.

The three-nucleon (3N) system provides a theoretically solid platform for examining the nuclear Hamiltonian in an environment where both nucleon-nucleon and 3N interactions are important. Ongoing work includes measurements of the neutron-neutron quasifree-scattering cross section in neutron-deuteron breakup, and finalizing the design concept for the first phase of ^3H photodisintegration measurements. Measurements of the $^3\text{H}(\gamma, pn)n$ and $^3\text{He}(\gamma, pn)p$ reactions at HI γ S will determine the scattering lengths a_{nn} and a_{np} . Significant progress was made in developing the tritium gas-cell for these measurements.

1.1 Low-Energy Description of Hadron Structure

1.1.1 ^4He Compton Scattering at 60 MeV and Commissioning of a New Cryogenic Target

M.H. SIKORA, M.W. AHMED, D.P. KENDELLEN, H.R. WELLER, *TUNL*

A new cryogenic target has been built to facilitate high-precision measurements of the electric and magnetic polarizabilities of the neutron. It has been used to measure the Compton scattering cross section from ^4He at an incident energy of 60 MeV. A phenomenological model to assess the sensitivity of the measured angular distribution to the polarizabilities is being developed. These data, along with future planned experiments using liquid deuterium and hydrogen, will provide stringent constraints on chiral-effective-field-theory calculations.

One of the main goals of the Compton@HI γ S program is to obtain data that will enable high-precision extractions of the electric and magnetic polarizabilities of the neutron, α_n and β_n , by measuring the Compton-scattering angular distribution of low- Z elements. These angular distributions constrain calculations of α_n and β_n using chiral effective field theory (χEFT). Precise knowledge of these fundamental properties of the neutron provide valuable insight into the structure and properties (such as their masses) of nucleons.

Experimentally, the challenge in measuring these angular distributions follows from the fact that the Compton-scattering cross section scales with Z^2 and thus is very small for very light elements. The need for high statistical accuracy requires maximizing the target density. For hydrogen, deuterium, and helium targets, this necessitates the use of liquid rather than gas targets. A system has been designed and built to cool these gases cryogenically to temperatures ranging from 4 to 24 K. As a first step towards measurements using liquid hydrogen and deuterium, a commissioning run of the new apparatus was conducted using liquid ^4He . This provided an opportunity to assess the performance and stability of the cryogenic target and of a new digitizer-based data acquisition system. In addition to benchmarking the performance of the new hardware, the sensitivity of the measured angular distribution to the isoscalar ($\alpha_n \pm \beta_n$) polarizabilities will be determined using a phenomenological model [Mye12].

This experiment was performed at an incident beam energy of $E_\gamma = 60$ MeV over a total beam time of approximately 50 hours, with an average intensity of $1.9 \times 10^7 \gamma/\text{s}$. Scattered γ -rays from the target were observed with the HINDA array of NaI detectors shown in Fig. 1.1. The detectors were located at angles ranging from 40° to 159° . Each core NaI detector is surrounded by an additional shield of eight thin NaI detectors. These were used to veto the large cosmic-ray background by rejecting events that deposited energy above a certain threshold in the shields. This restriction, along with an additional timing cut on beam-related events, suppressed more

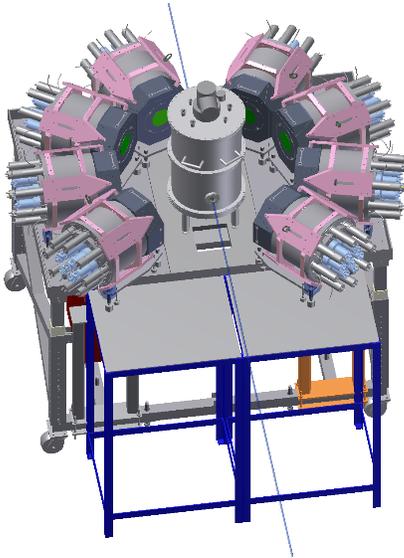


Figure 1.1: Drawing of the HINDA array and cryogenic target. The beam goes from top to bottom in the figure, following the thin blue line.

than 99.9% of the cosmic-ray background. Representative spectra at forward and backward angles are shown in Fig. 1.2.

Spectra at forward angles contain an exponential background arising from various atomic processes, and this background must be subtracted. A GEANT4 simulation of the Compton scattering process was used to obtain the response function of each HINDA core. The simulated spectra were then convolved with a Gaussian to fit the scattering data. At forward angles an additional exponential function was subtracted from the scattering spectrum. Sample fit results are shown in Fig. 1.2. Yields could then be extracted by integrating the subtracted spectra over the region of interest. The convolved response function was used to determine the fraction of the line shape lying within this region.

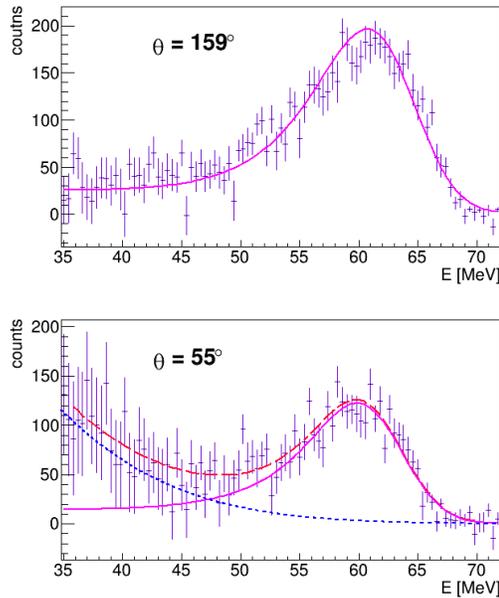


Figure 1.2: Sample spectra from forward- and backward-angle HINDA core elements, shown with fits. The forward angle detectors show an exponential background from atomic scattering processes, while the backward angle spectra are clean.

The differential cross section was then computed using

$$\frac{d\sigma}{d\Omega} = \frac{Y}{f_{abs} \cdot N_{\gamma} \cdot t \cdot \Omega_{eff}} \quad (1.1)$$

where Y is the extracted yield, f_{abs} is the average attenuation of the beam over the length of the target, N_{γ} is the total number of incident γ

rays, t is the target thickness, and Ω_{eff} is the effective solid angle of each detector. The average attenuation of the beam can be calculated using known photoabsorption data [Ber15]. The target thickness is determined by monitoring the pressure and temperature of the target throughout the irradiation. The quantity N_{γ} was determined via the five-paddle flux monitoring system [Pyw], and the effective solid angle was obtained from the GEANT4 simulation by randomly generating events from within the entire target volume and recording the number of γ rays subsequently observed in each detector. Preliminary results are shown in Fig. 1.3.

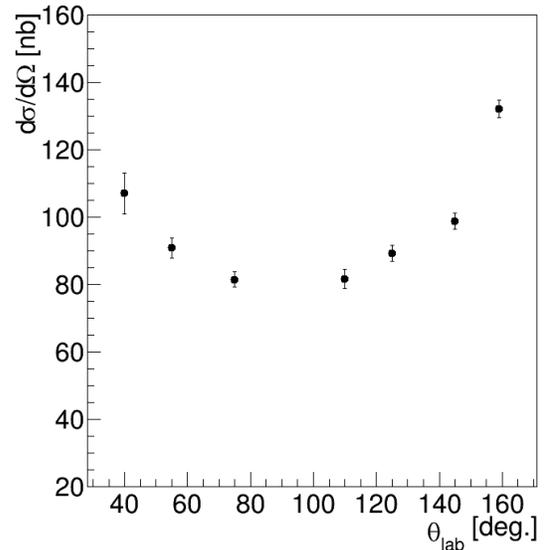


Figure 1.3: Preliminary angular distribution of the ${}^4\text{He}(\gamma,\gamma)$ reaction.

An assessment of the overall systematic uncertainty is currently in progress, as is the application of the aforementioned phenomenological model to determine the sensitivity to the polarizabilities. The results of this commissioning run have demonstrated the reliability of the new apparatus and the feasibility of obtaining high quality data.

-
- [Ber98] M. Berger *et al.*, *XCOM: Photon Cross Sections Database*, www.nist.gov/pml/data/xcom/index.cfm, 1998.
- [Mye12] L. Myers *et al.*, *Phys. Rev. C*, **86**, 044614 (2012).
- [Pyw] R. Pywell, www.kanga.usak.ca/nucleus.

1.1.2 A Cryogenic Target for Compton-Scattering Experiments at HI γ S

D.P. KENDELLEN, M.W. AHMED, H.R. WELLER, *TUNL*; G. FELDMAN, *George Washington University, Washington, DC*

We have developed a cryogenic target for Compton scattering experiments at HI γ S. It is able to liquify deuterium, hydrogen, or helium to fill a 0.25 L target cell.

A 0.25 L Kapton-cell cryogenic target has been designed and built to liquify deuterium (LD₂), hydrogen (LH₂), or ⁴He (LHe). It will be used in Compton scattering experiments at HI γ S to measure nuclear and nucleon polarizabilities. In the case of deuterium, the electromagnetic polarizabilities of the neutron, α_n and β_n , can be probed by scattering a γ -ray beam on an unpolarized LD₂ target. Scattered photons will be detected by the HI γ S NaI Detector Array (HINDA). The LH₂ target will be used to perform model-independent measurements of the proton polarizabilities, α_p and β_p . See Ref. [Gri12] for a review of nucleon polarizability measurements.

A schematic of the cryostat is shown in Fig. 1.4. The main components are: a cryocooler and condenser to liquify the incoming gas, a Kapton target cell, and a vacuum can with thermal radiation shields to isolate the components from room temperature.

The cooling device is a Sumitomo Model RDK-415D Gifford-McMahon cryocooler. It has 1.5 W of cooling power at 4.2 K and a base temperature of around 3 K. Low temperatures are produced through compression and expansion of high-purity helium gas in a closed loop between an external compressor and the cold head. See Ref. [Rad09] for more on the cooling cycle. The normal boiling points of LHe, LD₂, and LH₂, are 4.2 K, 24 K, and 20 K, respectively. The apparatus is equipped with a heater for running at 20 to 24 K when liquefying D₂ or H₂. Heating is also necessary to avoid freezing D₂ or H₂ in the fill and pressure relief lines.

The liquefaction process begins as room temperature gas enters through a fill line at the top of the cryostat (Item 2 in Fig. 1.4). From there the fill line wraps around the cold head and the gas is cooled inside copper heat exchangers. Next the precooled gas enters the condenser where it

collects on a series of copper fins, drips downward, and flows through a tube to the bottom of the Kapton cell. Boiloff vapor exits the cell through a vent line at the top and returns to the condenser to be reliquefied.

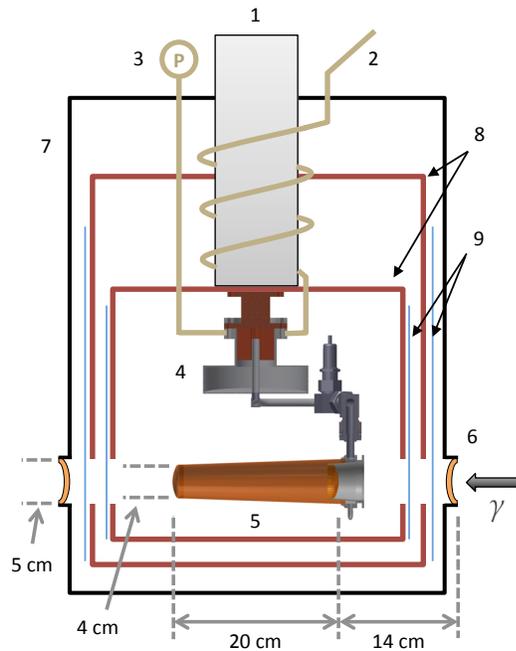


Figure 1.4: Schematic of the cryotarget with its cryocooler (1), gas inlet (2), vent line (3), condenser (4), Kapton cell (5), beam windows (6), vacuum can (7), heat shields (8), and superinsulation (9).

The cell is 20 cm long with 4-cm-diameter end caps. We formed it using 0.125-mm-thick Kapton film. The wall is the frustum of a cone to encourage bubbles to flow to the vent line. A valve on the vent line may be closed to build pressure and force the liquid back into a reservoir below the condenser. This greatly reduces the turnaround time for “empty” target runs, as in Ref. [Mac95].

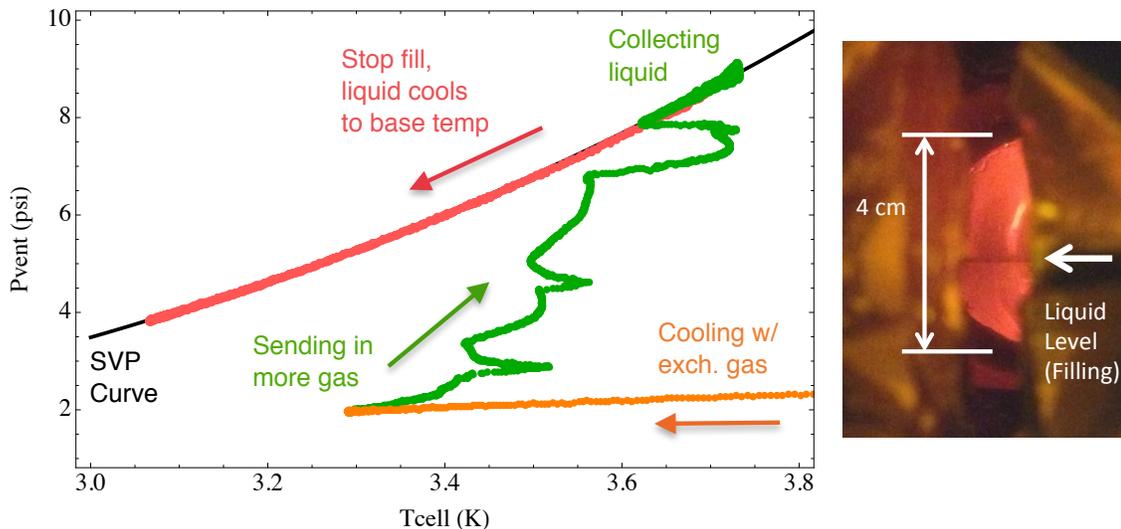


Figure 1.5: Measured vent line pressures and liquid temperatures during a fill, along with a photo of the LHe. The black curve is the saturated vapor pressure of liquid helium as a function of temperature.

When filled with LD_2 at 24 K, the target thickness is $9.80 \times 10^{23} \text{ D/cm}^2$.

Initial testing of the target was carried out with helium, rather than flammable D_2 gas. Liquefying helium also pushes the limits of the refrigerator in cooling power and base temperature. We have liquefied helium and filled the target cell at temperatures ranging from 3–4 K during several test runs. The liquid level was observed through the beam windows and slits in the superinsulation, as shown in Fig. 1.5. There was a factory-calibrated thermometer inserted directly into the liquid (T_{cell}) and a pressure gauge atop the vacuum can (P_{cell}). It is important to measure the liquid temperature accurately, since it determines the density and target thickness. Uncertainties in target thickness contribute to the uncertainties in the measured cross sections.

To cross-check the thermometer’s calibration, we monitored the pressures and temperatures in the cell and compared them to the saturated vapor pressure (SVP) of liquid helium. Fig. 1.5 displays the measured pressures and temperatures. The SVP as a function of temperature is from Ref. [Don15]. First the cell was cooled with a small amount of helium gas inside. This gas facilitates heat transfer between the cell and copper condenser fins. As the cell cooled below 4 K, we added more gas through a needle valve. The pressure settled near 8 to 9 psi as the cell began to fill with liquid. Finally the helium supply was closed off, removing the heat load from incoming gas, and the liquid cooled to

the cryocooler’s base temperature of $T_{\text{cell}} \approx 3.1$ K (where $P_{\text{SVP}} = 4$ psi). With liquid in the cell, there is excellent agreement between the (T, P) pairs and the SVP curve.

Bubbling in the cryogenic liquid represents another source of uncertainty in density and target thickness. Throughout the fill, the background heating was low enough that there were no visible bubbles in the bulk liquid. When the liquid reached the very top of the cell, the invisible bubbles began to collect, form small visible bubbles, and drift toward the outlet. The liquid below remained clear. Bubbling should be further reduced in LD_2 due to its larger latent heat of vaporization.

We have installed the cryotarget in the experimental hall and are preparing for a commissioning run with the γ -ray beam and LHe target. After that we will install safety measures for flammable gases, then proceed to LD_2 testing and production running.

[Don15] R. Donnelly, *Tables of Helium Properties*, darkwing.uoregon.edu/~rjd, 2015.

[Gri12] H. Griebhammer *et al.*, Prog. Part. Nucl. Phys., **67**, 841 (2012).

[Mac95] B. MacGibbon, Ph.D. thesis, University of Illinois, 1995.

[Rad09] R. Radebaugh, J. Phys.: Condens. Matter, **21**, 164219 (2009).

1.1.3 The Gerasimov-Drell-Hearn Sum Rule Experiment at HI γ S: Progress on the HI γ S Frozen-Spin Target

P.-N. SEO, H. CHEN, D.G. CRABB, R. DUVE, B. NORUM, C. ZOBEL, *University of Virginia, Charlottesville, VA*; C.R. HOWELL, D. KENDELLEN, G. SWIFT, H.R. WELLER, *TUNL*

The HI γ S Frozen-Spin-Target system was tested at HI γ S and University of Virginia to optimize the ^3He and ^4He gas mixture ratio for the dilution refrigerator. The goal is to enable the target to reach temperatures below 100 mK, the desired range for the GDH experiment. A new inner vacuum chamber was installed and was mounted with a newly wound horizontal magnetic-field-holding coil. The lowest temperature reached in the dilution refrigerator during these tests was about 190 mK. We describe the challenges encountered during the tests and the steps taken to resolve them.

A program is being commissioned at HI γ S to measure the Gerasimov-Drell-Hearn (GDH) sum-rule integrand for the deuteron below pion production threshold. To facilitate this measurement, the HI γ S frozen-spin target system (HIFROST) has been under development at HI γ S and University of Virginia (UVa) by a collaboration between the UVa group and TUNL scientists. The desired operating target temperature is about 50 mK. This system is currently being installed and tested at HI γ S. We present the status of the commissioning of the target.

The dilution refrigerator for HIFROST, which is described in detail in Ref. [Nii76], was designed to reach temperatures lower than 50 mK and was successfully operated at CERN and later at Helmholtz-Zentrum-Geesthacht at these conditions. The refrigerator was relocated from Germany to UVa in the summer of 2012. Soon thereafter, the target was tested by cooling it to about 270 mK without an optimized ^3He and ^4He gas mixture ratio. The results of these tests were reported in 2013. Once the infrastructure to support the operation of the refrigerator was complete at HI γ S, the refrigerator was tested there by cooling it. A minimum temperature of about 200 mK was reached in October 2014, without optimizing the gas mixture ratio. During these tests, a CH_2 dummy target was placed in the mixing chamber to mimic the eventual heat load. Different types of thermal sensors, covering different temperature ranges, were positioned in the target area to monitor its temperature.

The result of the October test indicated that dilution conditions were achieved with a circu-

lated gas mixture of ^3He and ^4He and that a temperature of about 200 mK was reached for a few hours. The test also successfully demonstrated our ability to recover the gas mixture and return it to the designated storage tanks. Following this test, the target was left in an idle standby mode overnight. After recovering the target from standby mode, an attempt to repeat the test by reproducing the temperature achieved earlier was unsuccessful. This unusual behavior led to an evaluation of several factors: the cooling process for dilution, the mixing ratio of the gases, and potential leaks developing in a ^3He circulation line during the cold phase.

Prior to the next test of the target, a residual gas analyzer was added to the ^3He -circulation loop to sample the gases. The inner vacuum chamber (IVC) with a broken holding coil was replaced with a new IVC with a newly-wound and tested holding coil. A new bypass capillary to deliver liquid helium directly from a 4 K pot into the holding coil area, outside of the IVC, was soldered onto the IVC. The purpose of the bypass is to help in the cooling of the holding coil and to help cool/maintain a 1 K pot.

In March 2015, several tests were performed at HI γ S to establish the stability of cooling the ^4He section effectively before introducing a mixture of gases into the refrigerator and optimizing the ^3He -to- ^4He ratio for dilution. These modifications resulted in reaching a lower temperature limit of about 190 mK. This higher-than-expected lowest temperature limit was attributed to possible heat load on the cryostat due to thermal contact between various layers of the

cryostat. Upon investigation, electrical conduction was discovered between the radiation copper shields. To mitigate this problem, thin Teflon spacers were installed on the shields and no further measurable electrical contact was found between them.

In addition to the installation of the spacers on the shields, super insulation around the outer vacuum chamber (OVC) was also installed. A broken O-ring on the ^3He back flange was also replaced. Following these repairs and modification, the target was tested at UVa in June 2015. A stable initial cooling of the ^4He section of the refrigerator with low cooling power was achieved. The initial ^4He cold-vapor flow rate was 85 standard liters per minute (SLPM) over 60 minutes and then gradually decreased to 25 SLPM over 40 minutes while the 4 K pot remained at 4 K and the 1 K pot had superfluid helium.

While cooling down the ^4He section of the refrigerator, we monitored the resistance of the holding coil. During the cool-down, the resistance dropped from 587 ohm at room temperature to 9 ohm. However, the coil never reached a superconducting state. The coil is intended to be cooled by the superfluid film from the 1 K pot creeping along the outer wall of the IVC, but we did not have a thermal sensor near the coil on the IVC to confirm these conditions. Multiple subsequent tests, in which the coil was isolated from the OVC by wrapping it with a layer of Teflon tape, confirmed that the inner wall of the OVC was in thermal contact with the coil. This find-

ing led to the production of a new IVC and the holding coil to increase the spacing between the IVC and the OVC. The new/recycled IVC has a slightly smaller outer diameter (3.93cm) than the current one (4.0cm).

In October 2015, a new holding coil was wet wound at UVa. It has the same configuration of three layers with trim coils on the ends and uses a NbTi superconducting wire in a Cu matrix [Sup]. The coil was tested in November 2015 at HI γ S. The linearity of the magnetic field as a function of current and field strength over the length of the coil were measured. The results of these measurements are consistent with the properties of the previously wound coils. The new IVC and coil are now thermally and electrically isolated from the inner wall of the OVC. We plan to test the coil in the refrigerator in December 2015. We plan on resuming the tests with the goal of optimizing the dilution conditions after the test of the holding coil. The near-term objective is to reach a temperature in the target area of the refrigerator that would allow the GDH experiment to be run. These tests will be performed at UVa. Upon successful tests of dilution at UVa, we plan on bringing the target back to the HI γ S facility.

[Nii76] T. O. Niinikoski and F. Udo, Nucl. Instrum. Methods, **134**, 219 (1976).

[Sup] <http://www.supercon-wire.com/content/nbti-superconducting-wires/>.

1.1.4 Neutron Polarization from Deuteron Photodisintegration

R.E. PYWELL, *University of Saskatchewan, Saskatoon, SK, Canada*; B.E. NORUM, S. TKACHENKO, P.-N. SEO, *University of Virginia, Charlottesville, VA*; B. SAWATZKY, *Thomas Jefferson National Accelerator Facility, Newport News, VA and Temple University, Philadelphia, PA*

The HI γ S facility was used to test a design for a helium analyzer to be used for a measurement of neutron recoil polarization in the low-energy photodisintegration of deuterium. Results on the gas analyzer showed the need for a more effective interior reflective coating. However, simultaneous measurements by neutron detector cells surrounding the heavy-water target were used to verify theoretical calculations of the angular distribution of neutrons from deuteron photodisintegration.

The polarization of the neutrons emerging from deuteron photodisintegration is a puzzle which has not been well explained by current theoretical calculations. Nath *et al.* [Nat72] observed that the polarization of the emerging neutrons undergoes a sudden change as the photon energy is increased between 10 and 15 MeV. The magnitude of this change is not reproduced by any calculation.

An upcoming experiment, approved by the 2012 Program Advisory Committee, plans to measure the neutron polarization from $d(\gamma, n)p$ at several angles over the photon energy range from 8 to 16 MeV. The polarization will be measured by scattering the neutrons off a high-pressure, active ^4He gas analyzer cell. The scattered neutrons will be detected by BC-505 neutron detector cells borrowed from the Blowfish array. A run was conducted in June 2015 to test a prototype analyzer cell constructed at the University of Virginia using technology derived from Tornow's experience at TUNL, with some adjustments in the dimensions.

Experimental Setup

We used the upstream target room for this run and employed a circularly polarized beam of 9 MeV photons. The target was a Lucite container, 20 cm long and filled with D_2O . We placed the single gas analyzer 1.5 m away from the target at an angle of 45° from the target center. Six neutron-detector cells were placed in the horizontal plane around the analyzer cell at a distance of 34 cm from the its center. The detectors were placed on either side of the analyzer cell at the

angles of 35° , 65° , and 115° relative to a line from the D_2O target to the analyzer cell.

The analyzer cell was filled with a helium/xenon mixture to a pressure of about 1900 psi. The 65-mm-diameter pressure cell was viewed on either end by two photomultiplier tubes (PMTs). The interior wall of the cell was coated with a material to reflect the UV light created by a recoiling α -particle in the gas mixture. The entry window to the PMTs has a wavelength-shifting coating to allow detection of the light by the PMTs. The analyzer PMTs and all the neutron detector cells are connected to charge integrating analog-to-digital converters (ADCs) and time-to-digital converters (TDCs) through constant fraction discriminators.

As a monitor for the experiment, six additional neutron detector cells were placed around the D_2O target, 1.0 m away from its center. One was placed at a forward angle, one at a backward angle, and four at 90° in the center-of-mass frame. In the laboratory frame these were at the angles of 52° , 87° , and 122° .

There were two separate data-acquisition triggers for the experiment. One was an "OR" of the neutron cells around the analyzer cell. When an event from these cells was received, we would look for a signal from the analyzer PMTs at the appropriate time. The second event was an OR of the cells around the target. Thus we effectively had two experiments running in parallel.

The Gas Analyzer

The results from the gas analyzer were disappointing. We were unable to see signals from the

analyzer PMTs that were time correlated with the beam in the set-up described above. We were able to see such signals when we moved the analyzer cell to a distance of 52 cm from the target, but it was not clear that these signals were, in fact, due to neutrons.

Further analysis plus comparison with a GEANT4 simulation showed that the efficiency of the analyzer cell for detecting neutrons, was very far below what was expected. This was completely inconsistent with an existing cell built at TUNL. Eventually it was found that the efficiency of the reflective coating on the inside wall of the gas cell was far below the specifications claimed by the manufacturer. A new cell with better characteristics is under construction at University of Virginia and TUNL.

Deuteron Photodisintegration Angular Distribution

We were able to use the neutron cells around the D₂O target to verify the deuteron photodisintegration calculations of Arenhövel *et al.* [Sch91] [Are91]. We have analyzed this data using techniques similar to those used for analyzing Blowfish data. This served as a useful test of methods that will be applied to the analysis of the upcoming measurement of the Gerasimov-Drell-Hearn (GDH) sum rule for the deuteron.

Each cell signal is recorded by two charge-integrating ADCs, each with a different gate width. This allows the calculation of a pulse shape discrimination (PSD) parameter that can be used to separate signals from photons and neutrons. Along the lines of a method first employed by Pridham [Pri14] we have modified the PSD calculation method to improve the applicable range of light output to which the PSD can be employed and, more importantly, to make it possible to reliably calculate the number of neutrons missed by a PSD cut.

The neutron time-of-flight can also be employed to remove the photons contaminating our neutron spectra. After appropriate cuts, a comparison to a GEANT4 simulation shows excellent agreement for the shape of the light output spectrum, as shown in Fig. 1.6.

A particular difficulty encountered in this analysis is the existence of “out-of-time” photons. These are photons from the accelerator produced by electrons in RF buckets outside the main one. These photons, while small in number compared

to the main beam bunch, can arrive at the same time as neutrons from the target. Since no PSD cut is ever perfect, these photons can mimic neutrons. Therefore we have to be particularly aggressive in applying a PSD cut to remove these photons. This, in turn, means that some neutrons are missed due to such a cut. We have therefore developed better methods for making a correction to the neutron yield for the neutrons missed by a PSD cut. Since this introduces an additional uncertainty in the neutron yield it would be better for future measurements, to avoid, if possible, beam tunings where the number of out-of-time photons is large.

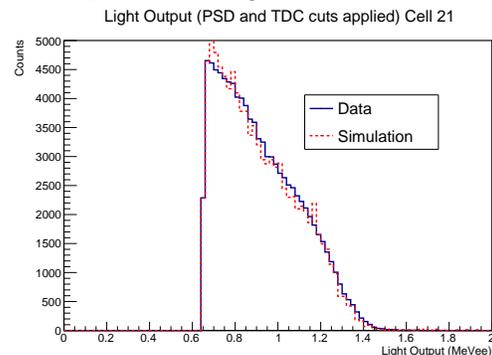


Figure 1.6: Comparison of the measured light output spectrum and the spectrum predicted by the GEANT4 simulation.

Preliminary analysis of our data seems to indicate the neutron yield in each of our six cells is in agreement with the yield predicted by the GEANT4 simulation using the angular distribution parameters from Arenhövel *et al.* However only a small subset of the data that was taken has been analyzed. The analysis is continuing.

-
- [Are91] H. Arenhövel and M. Sanzone, *Photodisintegration of the deuteron: a review of theory and experiment*, volume 3, Springer, 1991.
- [Nat72] R. Nath, F. Firk, and H. Schultz, Nucl. Phys., **A194**, 49 (1972).
- [Pri14] G. Pridham, Master’s thesis, University of Saskatchewan, 2014.
- [Sch91] K.-M. Schmitt, P. Wilhelm, and H. Arenhövel, Few-Body Systems, **10**, 105 (1991).

1.2 Few-Nucleon Systems

1.2.1 Neutron-Neutron Quasifree Scattering in Neutron-Deuteron Breakup

R.C. MALONE, A.S. CROWELL, J.H. ESTERLINE, B.A. FALLIN, F.Q.L. FRIESEN, Z. HAN, C.R. HOWELL, C.R. MALONE, D. TICEHURST, W. TORNOW, *TUNL*; B. CROWE, D. MARKOFF, *North Carolina Central University, Durham, NC*; H. WITALA, *Jagiellonian University, Kraków, Poland*

Measurement of the neutron-neutron quasifree scattering cross section in neutron-deuteron breakup is of interest for models of three-nucleon interactions. Recent measurements of this cross section are larger than theoretical predictions by approximately 20 percent. We have conducted a measurement of this cross section at 10 MeV to verify this discrepancy. Further measurements at several angles and other energies below 20 MeV are planned.

Advances in rigorous ab-initio three-nucleon ($3N$) calculations have produced accurate predictions of most experimental $3N$ scattering data. However, some discrepancies remain, such as the cross-section for neutron-neutron quasifree scattering (nn QFS) in neutron-deuteron (nd) breakup. In this breakup configuration, the proton remains at rest in the laboratory frame. Recent measurements of this cross section at 26 and 25 MeV are larger than theoretical predictions by almost 20% [Sie02, Rua07] (see Fig. 1.7).

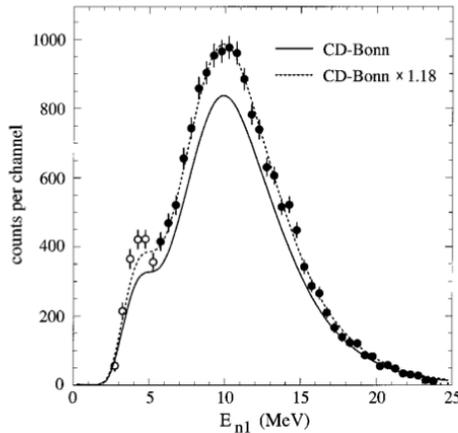


Figure 1.7: Experimental data for nn QFS in nd breakup at 26 MeV. The solid curve is the theoretical prediction from a Monte-Carlo simulation using cross sections calculated with the CD-Bonn nucleon-nucleon potential; the dashed curve represents the simulation scaled by a factor of 1.18 [Sie02].

The theoretical prediction can be brought

into agreement with the data by scaling the 1S_0 nn matrix element by a factor of 1.08. This results in either a change of the sign of the 1S_0 scattering length, suggesting the existence of a bound di-neutron state, or it decreases the effective range parameter by 10%, which is a large charge-symmetry and charge-independence breaking effect [Wit11]. Because of the significant implications of this discrepancy, we have undertaken an independent measurement of this cross section at TUNL.

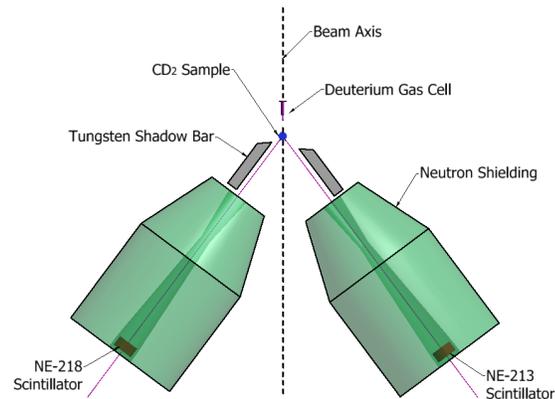


Figure 1.8: Schematic diagram of the experimental setup used at TUNL to measure the nn QFS cross section in nd breakup (not to scale). The detectors are at equal angles of 36.7° on either side of the beam and are approximately 2.6 m from the sample. The sample is about 10 cm from the gas cell. The two unshielded detectors used to monitor neutron flux are not shown.

The TUNL measurement of the nn QFS cross section in nd breakup was conducted using time-of-flight techniques. A pulsed neutron beam with a period of 400 ns and pulse width of about 2 ns FWHM was used. Neutrons were produced with an energy of 10 MeV via the ${}^2\text{H}(d,n){}^3\text{He}$ reaction. The neutrons scattered from a cylindrical deuterated polyethylene sample with a diameter of 28.3 mm, a height of 36.4 mm, and its axis oriented perpendicular to the incident beam axis. Scattered neutrons were detected using two shielded liquid scintillators placed at equal angles of 36.7° on either side of the beam axis (see Fig. 1.8). Two additional liquid scintillators were used to monitor the incident neutron flux.

A pulse height threshold of 238.5 keVee (half the cesium edge) was used to eliminate low-energy background events, and pulse-shape discrimination reduced γ -ray events. Neutron-deuteron breakup events were selected via a coincidence requirement. A typical two-dimensional coincidence spectrum is shown in Fig. 1.9. Although there are backgrounds due to accidental coincidences, the kinematic locus is clearly visible, and the quasifree region is well separated from backgrounds. Accidental coincidences were measured by selecting coincidences that were triggered by neutrons scattering from separate beam pulses. (Such coincidences cannot be true nd breakup events.) The accidental counts were subtracted from the raw coincidence spectrum.

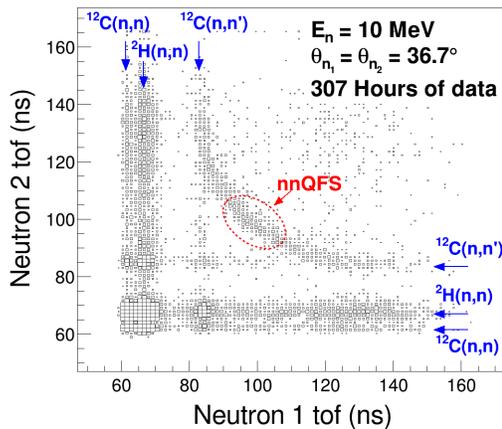


Figure 1.9: A plot of the two-dimensional TOF coincidence spectrum. The red, dashed circle marks the quasifree region and the blue arrows indicate accidental coincidences due to scattering from carbon and deuterium.

After subtracting background counts, events in the region of interest were selected with a two-dimensional gate and projected onto the kinematic locus. The breakup cross section was de-

termined by normalizing the net counts to the nd elastic scattering cross section. Neutron attenuation in the sample and detector efficiencies were also included in computing the cross section from the yields.

Our preliminary result is shown in Fig. 1.10. The error bars represent the statistical error only. The data also have a systematic uncertainty of about $\pm 7\%$. The measured cross section is in agreement with the theoretical point-geometry calculation. A Monte Carlo simulation is under development to average the theoretical calculation over the finite geometry of the experiment to allow a direct comparison of theory to our data.

Work is underway to develop a setup for measuring nn QFS at several angles simultaneously. These measurements will be performed using the shielded neutron source at TUNL. The results of early testing suggest that the signal-to-noise ratio at the shielded neutron source is acceptable for conducting these measurements (see Sect. 1.2.2).

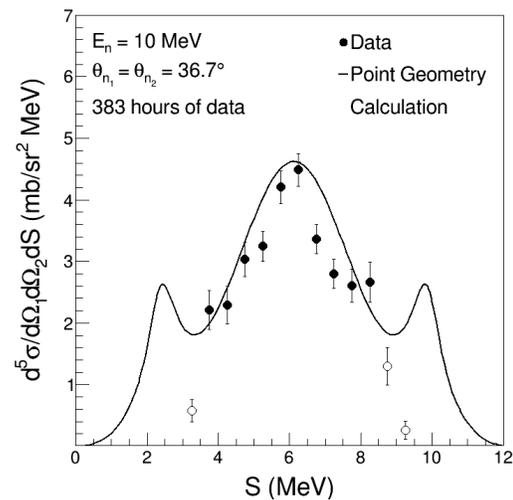


Figure 1.10: Preliminary results showing the measured nn QFS cross section as a function of S , the arclength along the kinematic locus. The open circles represent points near the detector energy threshold. The theoretical point-geometry cross section was calculated using the CD-Bonn potential [Wit11].

[Rua07] X. C. Ruan *et al.*, Phys. Rev. C, **75**, 057001 (2007).

[Sie02] A. Siepe *et al.*, Phys. Rev. C, **65**, 034010 (2002).

[Wit11] H. Witała and W. Glöckle, Phys. Rev. C, **83**, 034004 (2011).

1.2.2 Testing the TUNL Shielded Neutron Source

R.C. MALONE, A.S. CROWELL, B.A. FALLIN, F.Q.L. FRIESEN, Z. HAN, C.R. HOWELL, *TUNL*;

A new shielded neutron source has been constructed at TUNL. Preliminary tests have been conducted to determine whether the signal-to-noise ratio is good enough to conduct measurements of the neutron-neutron quasifree scattering cross section in neutron-deuteron breakup.

The TUNL shielded source area was upgraded in 2014 to improve its performance as a neutron beam facility. A schematic of the source and experiment area is shown in Fig. 1.11. A new housing for the copper beam collimator was designed with a large copper annulus around its center. Copper and steel blocks were stacked around the beam collimator to shield fast neutrons, while paraffin blocks doped with lithium and boron compounds were stacked farther from the collimator to moderate and capture slow neutrons. The exterior layer of the wall is four-inch-thick lead to attenuate γ rays produced by neutron interactions in the wall (see Fig. 1.11).

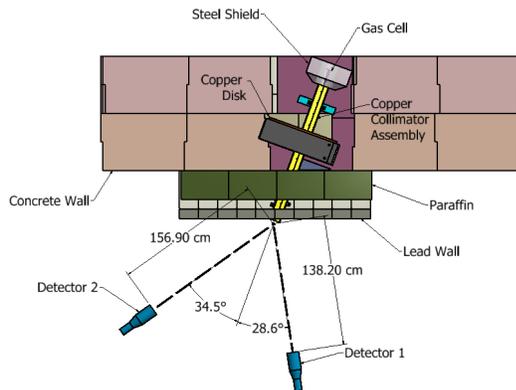


Figure 1.11: Schematic diagram of the TUNL shielded source area and the detectors used for this measurement. Copper and steel blocks stacked around the collimator are not shown.

Tests were conducted in early 2015 to characterize the neutron beam and to examine the signal-to-noise ratio for the measurement of neutron-neutron quasifree scattering (nn QFS) in neutron-deuteron (nd) breakup. Deuterons

with an energy of 7.3 MeV were incident on a deuterium gas cell at 5 atm of pressure, producing 10 MeV neutrons via the ${}^2\text{H}(d,n){}^3\text{He}$ reaction. The neutrons were collimated by a long copper collimator (see Fig. 1.11). The neutron flux cross-sectional profile, normalized to the integrated beam current, was measured across the face of the beam at distances of 164.2 and 260.8 cm from the gas cell. The resulting horizontal and vertical beam profiles are shown in Fig. 1.12.

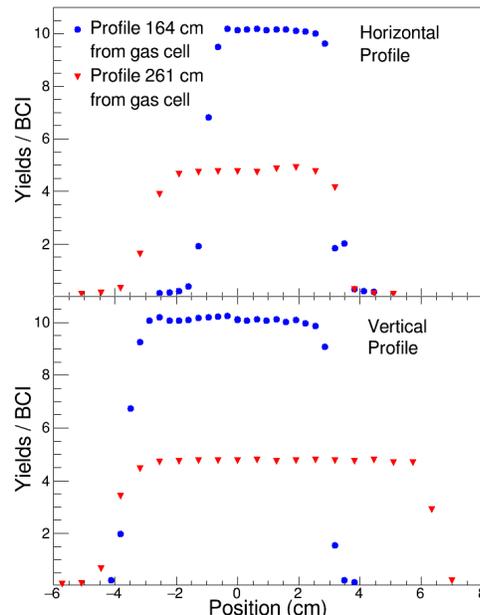


Figure 1.12: Neutron yields across the profile of the beam, normalized to the integrated beam current. In all plots, the zero position represents the center of the copper collimator, not necessarily the center of the beam. All error bars are smaller than the data points.

Time-of-flight (TOF) spectra of neutrons

scattering from cylindrical samples of polyethylene (3.389 g of CH_2 , 14.18 mm in diameter and 22.70 mm high) and deuterated polyethylene (25.17 g of CD_2 , 28 mm in diameter and 35.1 mm high) were measured to assess the signal-to-noise ratio. For each measurement, the sample was oriented with its axis perpendicular to the beam axis. Two liquid BC-501A scintillator detectors were placed at angles of 28.6° and 34.5° relative to the beam axis. Both detectors were approximately 1.5 meters from the scattering sample (see Fig. 1.11). A minimum detector threshold corresponding to a pulse-height of 238.5 keVee (half the cesium edge) was used to reduce backgrounds from low-energy neutrons, and pulse shape discrimination techniques were applied to reduce background events from γ rays.

The TOF spectrum for scattering from CH_2 measured by detector 1 in Fig. 1.11 is shown in Fig. 1.13. At this flight path, the peaks due to elastic scattering from carbon and hydrogen overlap significantly. A peak due to inelastic scattering from carbon sits just below the elastic peaks. Also visible are a peak near channel 880 and a smaller peak near channel 1120.

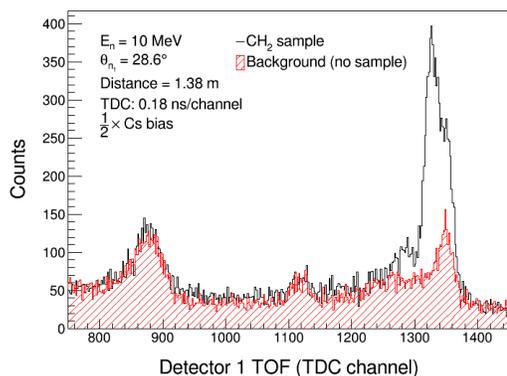


Figure 1.13: A TOF spectrum in detector 1 for scattering from CH_2 and a background spectrum.

The large peak near channel 880 is due to neutrons scattering from a survey telescope located 3.1 meters downstream from the scattering sample at zero degrees. The smaller peak near channel 1120 is due to neutrons that scattered elastically from the sample or air into the right detector and subsequently scattered into

the left detector. The spectra for detector 2 are similar, except that the TOF resolution is better due to the longer neutron flight path.

In order to shield detector 1 from neutrons scattering from air and the survey telescope, paraffin blocks were placed at beam height downstream of the CD_2 target, between the beamline and the detector. Tungsten shadow bars were also placed upstream of detector 1 at an angle of about 30° to further reduce background events. Figure 1.14 shows the resulting TOF spectrum for scattering from the CD_2 target. The shielding was effective; close study reveals that elastic scattering from air was reduced by about 40%, and the peak due to scattering from the survey telescope is eliminated. Furthermore, the peak due to neutrons scattering from the right detector into the left detector is reduced by about 25% (an effect not visible in Fig. 1.14). Spectra for detector 2 are similar except that TOF resolution is better and there is no change due to the shielding, since this detector remained unshielded in both tests.

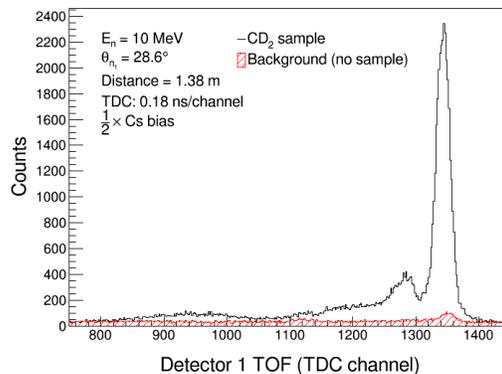


Figure 1.14: A TOF spectrum in detector 1 for scattering from CD_2 and a background spectrum. This is after setting up paraffin shielding and tungsten shadow bars.

These measurements demonstrate that the signal-to-noise at the SSA was improved by the upgrade. Another test is scheduled for the fall of 2015 to measure the signal-to-noise ratio for nd breakup events. If the signal-to-noise ratio is acceptable, measurements of the nn QFS cross section in nd breakup will proceed at energies of 10 and 16 MeV (see Sect. 1.2.1).

1.2.3 Three- and Two-Body Photodisintegration of ^3He with Double Polarizations

H. GAO, M.W. AHMED, P. CHU, C. FLOWER, J.N. HEIDEMAN, H.J. KARWOWSKI, D. KENDELLEN, G. LASKARIS, M. MEZIANE, J.M. MUELLER, C. PENG, H.R. WELLER, Y.K. WU, W. XIONG, X. YAN, Y. ZHANG, W. ZIMMERMAN, *TUNL*; T. AVERETT, *College of William and Mary, Williamsburg, VA*; D. DUTTA, *Mississippi State University, Starkville, MS*; B. TSANG, J. MANFREDI, *Michigan State University, East Lansing, MI*; A. DELTUVA, *Institute of Theoretical Physics and Astronomy, Vilnius University, Vilnius, Lithuania*; A.C. FONSECA, *Universidade de Lisboa, Lisboa, Portugal*; J. GOLAK, R. SKIBIŃSKI, H. WITAŁA, *Jagiellonian University, Kraków, Poland*; P.U. SAUER, *Leibniz Universität Hannover, Hannover, Germany*.

We present double-differential cross-sections from an experiment on three-body photodisintegration of polarized ^3He using a circularly polarized photon beam at and incident energy of 16.5 MeV. We also present progress on the experiment on two-body photodisintegration of ^3He with double polarizations at 29 MeV.

An important window for the study of QCD is through the investigation of the structure and particularly the spin structure of the nucleon and few-body nuclei. Therefore sum rules involving the spin structure of the nucleon or nuclei are currently at the forefront of intensive experimental and theoretical efforts. Among spin sum rules, the GDH sum rule [Dre66, Ger66] is particularly interesting. There have been efforts worldwide to test the GDH sum rule on the proton and neutron [Dut04, Dut05]. More recently, experimental investigations of the GDH sum rule on nuclei such as the deuteron [Sli08, Ahm08, Ahr09] and ^3He [Las13, Las15, Bar13, Cos14] have begun.

The determination of the GDH sum rule on ^3He at energies between the two-body photodisintegration around 5.5 MeV and the pion production threshold around 140 MeV is important for testing state-of-the-art three-body calculations, which predict a large contribution to the integral. Such calculations are also important to experiments utilizing polarized ^3He as an effective polarized neutron target to probe the structure of the neutron. The GDH integral below pion threshold based on three-body calculations [Del09, Ski05] was predicted to be about $140 \mu\text{b}$ [Las15], which comes from the sum of three-body and two-body contributions. The estimates of Deltuva (Skibinski) are about $170 \mu\text{b}$ ($130 \mu\text{b}$) for three-body and $-30 \mu\text{b}$ ($10 \mu\text{b}$) for two-body. The HI γ S facility provides a unique ability to investigate the GDH integral below the pion pro-

duction threshold using the photodisintegration of ^3He with double polarizations.

The first experiment [Las13, Las15] on the three-body photodisintegration of ^3He using a longitudinally polarized ^3He target and a circularly polarized γ -ray beam took place at HI γ S [Wel09] at incident photon energies of 12.8 and 14.7 MeV. The calculations by Deltuva *et al.* [Del09] provide a good description of the results. They include single-baryon and meson-exchange electromagnetic currents, relativistic single-nucleon charge corrections, and the proton-proton Coulomb force. The calculations of Skibinski *et al.* [Ski05], which are less successful in describing the data, are based on solving the three-body Faddeev equations with a three-body force and several models for the electromagnetic currents.

To see whether such agreement continues at higher energies and to resolve the discrepancy between the past unpolarized cross-section measurements above 15 MeV [Las13], a new measurement of $^3\vec{H}e(\vec{\gamma}, n)pp$ was performed at a photon energy of 16.5 MeV. The spin-dependent double-differential, single-differential, and total cross sections and the contribution from the three-body channel to the GDH integrand were extracted and compared with state-of-the-art three-body calculations [Las15]. Fig. 1.15 shows the contributions from the three-body photodisintegration of ^3He to the GDH integrand, together with the theoretical predictions, as a function

of photon energy. The calculations which include the Coulomb interaction are in good agreement with the results of previous measurements at 12.8 and 14.7 MeV but can no longer describe the results at 16.5 MeV. The GDH integrand was found to be about one standard deviation larger than the maximum value predicted by the theories [Las13, Las15]. To investigate whether the larger-than-expected GDH integrand value at 16.5 MeV is due to statistics, future measurements at higher energies are needed.

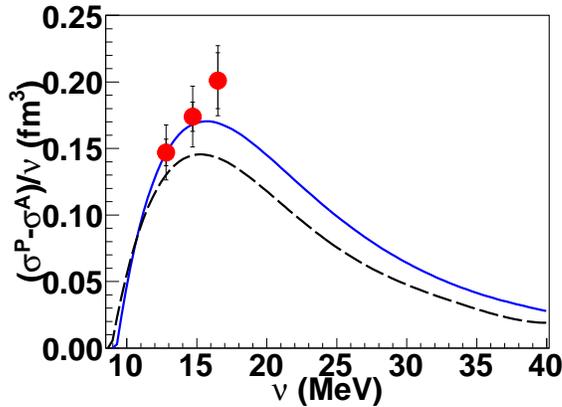


Figure 1.15: The GDH integrand results compared with the theoretical predictions of Ref. [Del09] (solid-blue curve) and Ref. [Ski05] (dashed-black curve). The inner error bars represent the statistical uncertainties while the outer include the statistical and systematic uncertainties added in quadrature.

The first measurement of the two-body photodisintegration of ${}^3\text{He}$ with double polarizations at a photon energy of 29.0 MeV was performed in May 2014. The protons from the two-body photodisintegration were detected by 72 fully depleted silicon detectors placed every 25° at proton scattering angles between 45° and 120° (eighteen detectors at each angle). Six aluminium hemispheres were used to place the detectors about 10 cm from the center of the ${}^3\text{He}$ target chamber. Each hemisphere housed up to twelve detectors and allowed us to maximize the number of detectors around the ${}^3\text{He}$ cell.

The data analysis is currently in progress and quantities such as spin-dependent single-differential and total cross sections and the ${}^3\text{He}$ GDH integrand value from the two-body break-

up at 29.0 MeV will be extracted. The extension of these measurements to higher photon energies and measurements on the three-body breakup channel above 16.5 MeV will provide crucial tests of the differential cross sections, the energy dependence of the predictions, and whether the contribution to the GDH integral below the pion threshold is indeed dominated by the three-body channel. These measurements, when combined with data above pion threshold from other laboratories, will directly test the ${}^3\text{He}$ GDH sum rule prediction.

-
- [Ahm08] M. Ahmed *et al.*, Phys. Rev. C, **77**, 044005 (2008).
- [Ahr09] J. Ahrens *et al.*, Phys. Lett., **B672**, 328 (2009).
- [Bar13] P. A. Bartolomé *et al.*, Phys. Lett., **B723**, 71 (2013).
- [Cos14] S. Costanza *et al.*, Euro. Phys. J. A, **50** (2014).
- [Del09] A. Deltuva, A. Fonseca, and P. Sauer, Phys. Rev. C, **80**, 064004 (2009), and references therein.
- [Dre66] S. D. Drell and A. C. Hearn, Phys. Rev. Lett., **16**, 908 (1966).
- [Dut04] H. Dutz *et al.*, Phys. Rev. Lett., **93**, 032003 (2004).
- [Dut05] H. Dutz *et al.*, Phys. Rev. Lett., **94**, 162001 (2005).
- [Ger66] S. Gerasimov, Sov. J. Nucl. Phys., **2**, 430 (1966).
- [Las13] G. Laskaris *et al.*, Phys. Rev. Lett., **110**, 202501 (2013).
- [Las15] G. Laskaris, Ph.D. Thesis, Duke University, NC, USA, 2015.
- [Ski05] R. R. Skibiński *et al.*, Phys. Rev. C, **72**, 044002 (2005), and references therein.
- [Sli08] K. Slifer *et al.*, Phys. Rev. Lett., **101**, 022303 (2008).
- [Wel09] H. R. Weller *et al.*, Prog. Part. Nucl. Phys., **62**, 257 (2009).

1.2.4 Three-Body Photodisintegration of ${}^3\text{H}$ and ${}^3\text{He}$

F.Q.L. FRIESEN, M.W. AHMED, A.S. CROWELL, L.C. CUMBERBATCH, B. FALLIN, C.R. HOWELL, D. TICEHURST, W. TORNOW, *TUNL*; B.J. CROWE, D.M. MARKOFF, *North Carolina Central University, Durham, NC*; H. WITALA, *Jagiellonian University, Krakow, Poland*

We are developing an apparatus to measure the differential cross section for ${}^3\text{H}(\gamma, pn)n$ and ${}^3\text{He}(\gamma, pn)p$ at HI γ S using a linearly polarized γ -ray beam at 15 and 25 MeV. The goal is to determine the scattering lengths a_{nn} and a_{np} . The initial apparatus will consist of gas targets, collimators for selecting protons in the kinematic area of interest, silicon detectors for charged-particle calorimetry, and neutron detectors. The design concept for the first phase of these measurements was finalized during this reporting period.

The three-nucleon (3N) system provides a theoretically solid platform for examining the nuclear Hamiltonian in an environment where both nucleon-nucleon and 3N interactions are important. The substantial agreement between ab-initio 3N calculations and data gives confidence in the theoretical treatment, but remaining discrepancies imply that there might be features in the reaction dynamics that are not well understood. For example, the measured cross section for neutron-neutron (nn) quasi-free scattering (QFS) and the space-star configuration in neutron-deuteron (nd) breakup are about 20% larger than predicted by theory [Cou12, Sie02, Rua07, Set05].

Such discrepancies suggest that the ${}^1\text{S}_0$ nn force might be stronger than would be expected from charge symmetry. We are conducting two complementary measurements at TUNL to gain insight into this dilemma. A cross-section measurement of nn QFS in nd breakup is conducted in the tandem laboratory, and the ${}^3\text{H}(\gamma, pn)n$ reaction will be studied at HI γ S. These experiments will have enough accuracy to resolve discrepancies in existing data for the total cross section and determine the ${}^1\text{S}_0$ nn scattering length a_{nn} to an accuracy of ± 1 fm. The system for the HI γ S experiment will be commissioned with ${}^3\text{He}$ gas targets with the goal of determining the ${}^1\text{S}_0$ neutron-proton (np) scattering length a_{np} with the same accuracy.

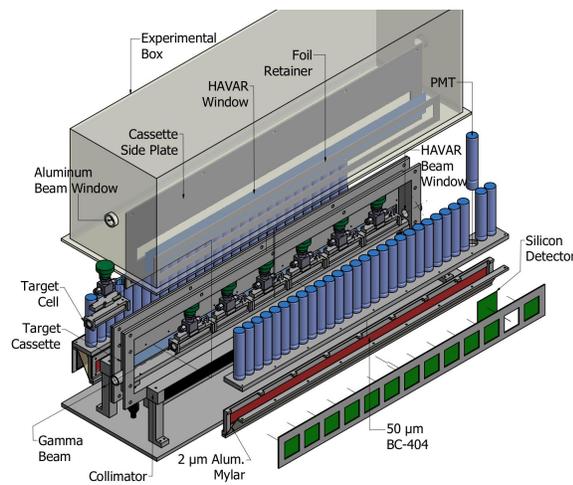


Figure 1.16: Exploded schematic view of the experimental setup, minus the neutron detectors. The thin scintillator method of particle ID is depicted.

The experimental setup for our measurements is shown in Fig. 1.16. While we plan eventually to use a tracking-based setup, the initial measurements will be made using an array of collimators to select the angle of emitted charged-particles. The targets will be mounted to a central rail. On both sides of the targets are a set of collimators and silicon detectors. The box enclosing the targets and detectors will be roughly 80 cm long and 30 cm in the other dimensions. Neutron detectors (not shown) will be located about 1 m away from the beam axis. By using a horizontally polarized beam, most of the protons from the reaction will be directed through the collimators. The collimator system is being designed to detect the charged-particles for both exclusive and inclusive measurements of the nn final-state interaction (FSI) for tritium and the np FSI for ${}^3\text{He}$.

The performance goals of the system are: (1)

a charged-particle energy resolution of ≤ 250 keV FWHM for particles with energies around 4.5 MeV, including a 1.5% spread in the γ -ray beam energy; (2) use of segmented neutron detectors with pulse-shape-discrimination capability in coincidence with detection of a charged particle; (3) identification of deuterons from 2-body photodisintegration events; and (4) multiple layers of containment of the tritium gas (see Fig. 1.16 and Sect. 1.2.5). The third feature could possibly be accomplished through charged-particle identification using a combination of thin scintillator and silicon detectors. An alternative is using time-of-flight information from the neutron plus the charged particle energy to isolate the two-body events kinematically.

Background events would be identified with combined cuts on the charged-particle energy, $\Delta E/E$ particle identification, and time of flight. Fig. 1.17 shows the expected number of counts after 150 hours of run time at a γ -ray energy of 15.2 MeV for two values of a_{nn} , assuming an exclusive measurement as described. This includes a Gaussian approximation for the energy spread of the beam with 225 keV FWHM, and the measured resolution profile of the silicon strip detectors to be used in the experiment.

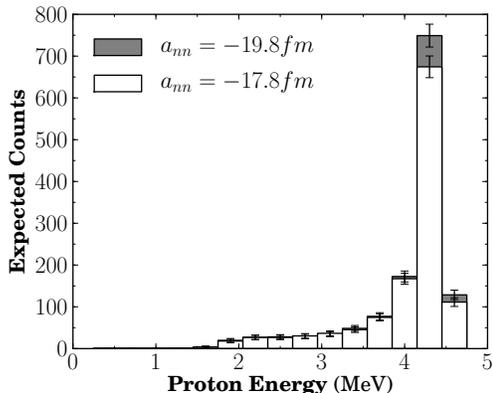


Figure 1.17: Simulated spectrum with statistical errors after 150 hours of beam time at 15.2 MeV. Neutron detector efficiency is not included.

A prototype wire chamber of the type originally planned for the experiment was constructed and tested with sources and proton beams in the tandem accelerator lab. It was found that the necessarily thin mylar windows deflected under slight pressure changes, introducing large non-uniformities in gain across the face of the chamber (see Sect. 1.2.7). A windowless time-projection-chamber-based system is being investigated as an upgrade to replace the collimators once the initial runs are complete, instead of wire

chambers.

Over the past year, we investigated the feasibility of using freely available 500- μ m-thick silicon strip detectors produced for the CMS collaboration by ST Microelectronics and obtained from Fermilab [Poo10]. The energy resolution of the detectors using the original CMS configuration was about 1 MeV for 5 MeV protons. Testing with the detectors reconfigured for use with standard preamplifiers greatly improved the measured proton energy resolution to around 175 keV FWHM for 4.5 MeV protons, though this is still larger than the 50 keV that is typical of large-area surface-barrier detectors. The resolution profile as a function of energy was measured, and included in the simulation of the experiment (see Sect. 1.2.6 for details). It is adequate for our application, in which the kinematic region of interest spans around 250 keV for the proton.

Development of a GEANT4 simulation of the experiment is ongoing (see Sect. 1.2.8). The simulation has demonstrated that an exclusive measurement will provide the greatest sensitivity to the scattering lengths in both ${}^3\text{H}(\gamma, pn)n$ and ${}^3\text{He}(\gamma, pn)p$. The collimator geometry is currently being optimized to maximize sensitivity to a_{nn} in the ${}^3\text{H}(\gamma, pn)n$ experiment.

A 50- μ m-thick rectangle of BC-404 coupled to phototubes as shown in Fig. 1.16 and used in combination with a 400 μ m silicon surface barrier detector was recently tested in the tandem lab to evaluate the efficacy of this configuration for performing $\Delta E/E$ particle identification. An 8-MeV deuteron beam incident on a nickel foil target provided a broad energy range of protons and scattered deuterons at 90° . It was found that the energy resolution of the scintillator was not adequate for distinguishing protons from deuterons, despite the relatively large amount of energy deposited.

- [Cou12] A. H. Couture *et al.*, Phys. Rev. C, **85**, 054004 (2012).
- [Poo10] O. Pooth, *The CMS Silicon Strip Tracker: Concept, Production and Commissioning*, p. 49, Vieweg+Teubner Verlag, Fachmedien Wiesbaden GmbH, Wiesbaden, 1 edition, 2010.
- [Rua07] X. C. Ruan *et al.*, Phys. Rev. C, **75**, 057001 (2007).
- [Set05] H. R. Setze *et al.*, Phys. Rev. C, **71**, 034006 (2005).
- [Sie02] A. Siepe *et al.*, Phys. Rev. C, **65**, 034010 (2002).

1.2.5 Tritium Gas Target System for Photodisintegration Experiments

F.Q.L. FRIESEN, C.R. HOWELL, *TUNL*

Tritium gas targets will be used for measurements of the ${}^3\text{H}(\gamma, pn)n$ at the high intensity gamma-ray source. We report developments in the design of the target cells and the systems for handling and storing the tritium gas. The cell design and containment systems have been updated following recommendations from external reviewers.

The experiment to study the ${}^3\text{H}(\gamma, pn)n$ reaction will use approximately 300 Ci of gaseous ${}^3\text{H}$, which will be contained in seven target cells constructed using thin HAVAR windows to minimize proton energy loss. The thickness has been increased from 2.54 to 6.35 μm . Dividing the target into separate gas volumes limits the maximum tritium loss in the event of a leak. The modified cell design eliminates the need for epoxy. All seals between the windows and target body made with micro welds or indium gaskets. Prototypes are being constructed using both methods. The target body is machined from a solid piece of 316 stainless steel, rather than aluminum as in the original design. This change was made to improve structural strength and weldability, and because 316 stainless is a thoroughly vetted material for primary containment of tritium. To further improve structural stability and ease of fabrication, all windows are now flat (see Fig. 1.18). The cells will be pressurized with tritium gas to slightly above atmospheric pressure and will be refilled once a year to remove the ${}^3\text{He}$ decay products and avoid pressure buildup.

The key design goals are to prevent release of tritium, and capture material in the event of a leak or foil rupture. Our three techniques are containment, monitoring, and use of scrubber systems. Three independent tritium scrubbing systems will be constructed.

At the recommendation of the external reviewers, we are obtaining a tritium glovebox with a dedicated tritium scrubber system capable of operating in ambient atmosphere. All procedures involving the transfer of tritium between components will take place in this space. The volume surrounding the glovebox will be further enclosed by a set of plastic barriers and connected to the high speed exhaust system. When the ${}^3\text{H}$ targets are mounted in the apparatus, the enclos-

ing leak-tight box may only be opened inside the glovebox. To reduce proton energy loss and the presence of oxygen and water [Pap82], the air in the box will be displaced with helium. The helium atmosphere will be continuously monitored for tritium.

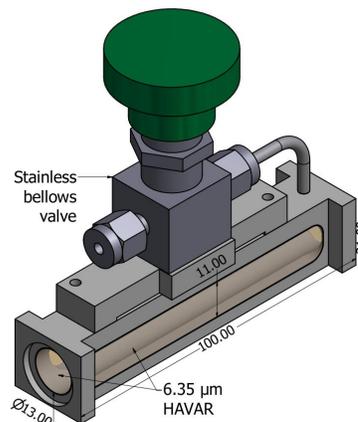


Figure 1.18: A schematic of the updated target-cell design. The γ -ray beam will be collimated to 1 cm diameter at the target furthest downstream. Targets are held to the mounting rail with bolts in the bottom of the cell. Lengths are in mm.

The first of the three scrubbing systems is a recovery system dedicated to cleaning the volume of the target cassette (see Fig. 1.19). It is capable of recovering elemental tritium for re-use but must be operated in an inert environment. It uses a molecular sieve dryer to remove water [Uni04], then a nickel bed to capture oxygen and crack organics, followed by a ZrFe bed to capture and store tritium.

The second scrubbing system is dedicated to the tritium glovebox (see Fig. 1.20). It uses a heated palladium catalyst to combine tritium

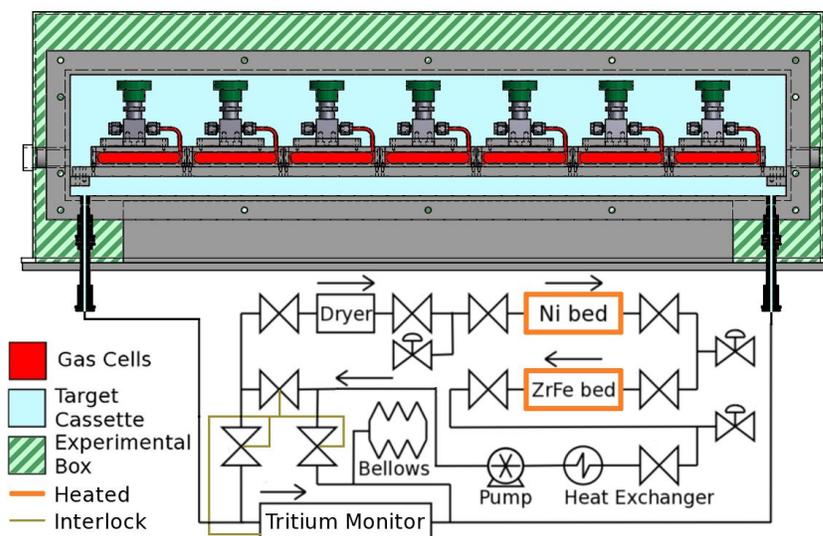


Figure 1.19: Diagram showing the target cassette with its recovery system and the enclosing experimental box. Cassette walls, collimators, and detectors are not shown for clarity. The monitor continuously samples the cassette volume, and can engage the scrubber system if needed.

with ambient oxygen to make water, which is subsequently captured by a molecular sieve dryer. Captured tritium cannot be re-used, but the system has a large throughput and can operate in atmosphere.

Finally there is a backup scrubber for the cassette recovery system, using the same method as the glovebox scrubber, but having a smaller capacity.

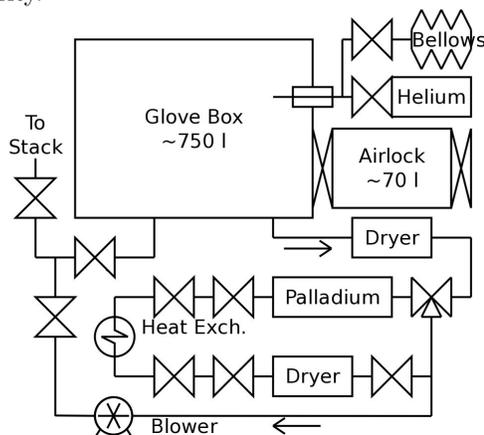


Figure 1.20: Diagram of the glovebox and associated scrubber system.

The tritium will be stored and purified using a temperature-controlled uranium bed. The bed will also be used to recover excess tritium gas left in the manifold after a filling operation. When the bed is at room temperature, tritium is stored as UT_3 , and impurities such as 3He can be safely pumped out [RCT]. The 3H detector to be used

in the chamber for the interlock is a modified solid-state detector capable of directly detecting β particles from the decay [Wam94]. With this design, the interlock functions over a wide range of the pressures in the chamber.

Once filled, the targets will be kept in the target cassette, a closed volume that provides an additional layer of containment and can be easily removed from the experimental setup. Targets not in use will be stored in the cassette with stainless steel sides bolted on, and with the reclamation system connected. This assembly is stored in the glovebox.

The experimental setup will be commissioned using 3He and 2H -filled targets (see Sect. 1.2.4). This approach will provide verification of the readiness of the tritium targets and the experimental apparatus for experiments with the Γ -ray beam measurement.

[Pap82] P. J. Papagiannakopoulos and C. E. Easterly, *Int. J. Chem. Kinetics*, **14**, 77 (1982).

[RCT] RCTRITEC, *Uranium Beds*, www.rctritec.com.

[Uni04] University of Rochester, *Cryogenic Target Handling System Operations Manual*, 2004.

[Wam94] W. Wampler, *Nucl. Instrum. Methods A*, **349**, 473 (1994).

1.2.6 Evaluation of Silicon Strip Detectors with Low-Energy Protons

F.Q.L. FRIESEN, M.W. AHMED, A.S. CROWELL, L.C. CUMBERBATCH, B. FALLIN, C.R. HOWELL, D. TICEHURST, W. TORNOW, *TUNL*; B.J. CROWE, D. MARKOFF, *North Carolina Central University, Durham, NC*; H. WITALA, *Jagiellonian University, Krakow, Poland*

In support of the ${}^3\text{H}(\gamma, pn)n$ and ${}^3\text{He}(\gamma, pn)p$ experiments to be carried out at HI γ S, 500- μm -thick silicon strip detectors originally destined for the CMS experiment were tested with low-energy protons in the tandem laboratory. The silicon detectors are needed to make accurate measurements of the kinetic energy of charged particles emitted in the reactions.

Section 1.2.4 of this report describes the experiments to study the ${}^3\text{H}(\gamma, pn)n$ and ${}^3\text{He}(\gamma, pn)p$ reactions at HI γ S. During this reporting period, we investigated the feasibility of using 500- μm -thick silicon strip detectors for measuring the energy of charged particles in the experiments. The strip detectors were produced for the Compact Muon Solenoid (CMS) collaboration by ST Microelectronics. A strong factor in considering these detectors is that they were donated to our experiment by Fermilab. In this investigation, protons from the tandem accelerator at TUNL were scattered off of a thin gold target foil to 90° . They then exited the chamber through a 6.35 μm HAVAR foil and were incident on the detectors being tested. Monte-Carlo calculations done with the code TRIM were used to account for energy-loss effects.

The detectors themselves have a 94 x 92 mm active area and a strip pitch of 122 μm , for a total of 768 strips per detector [Poo10]. These detectors are appealing because they cover a large area, are thick enough to fully stop 7 MeV protons, and are available at no cost. They were originally intended for use with the APV25 readout ASIC (application-specific integrated circuit). Several detectors and readout chips were obtained and wire-bonded at Fermilab.

The APV25 chips are versatile, and can support readout of a variety of silicon strip detectors, but they were designed for tracking rather than for spectroscopy of low-energy charged particles. The detectors were first tested with the APV25 units, as this would allow for individual strip readout. Each APV chip connects to 128 strips and amplifies signals from the strips with an array of 128 adjustable folded cascode preamps followed by 50-ns CR-RC shapers. The

chip is clocked at 20 MHz and continuously stores these analog signals in a capacitor-based analog pipeline. When a trigger signal is received by the chip, it retrieves stored charge from the pipeline a set time in the past, and outputs it serially with some digitally-encoded information over a set of differential lines. The chips are individually configurable over I²C (inter-integrated circuit) connections. A single strip detector has six associated APVs, multiplexed onto three differential output lines at 40 MHz.

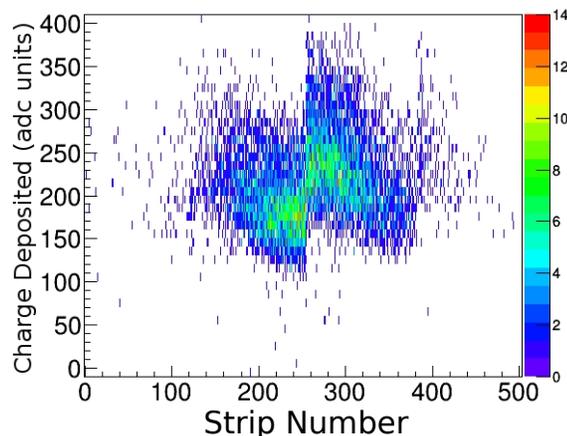


Figure 1.21: Pedestal-subtracted detector response to a proton beam centered on strip 256. The boundaries between APV chips occur every 128 strips.

The DAQ used a field-programmable gate array in a VME module to generate the clock signal for the APV chips. This same line also carried triggers and other control signals. The clock signal was digitized alongside the outputs from the APV board, and the four signals were later pro-

cessed with a python-based code. Trigger signals were typically provided by a small 50- μm -thick silicon transmission detector positioned in front of the detector being tested. When a particle passed through the transmission detector, the system would trigger the APV chips twice: once to access the measurement from just before the particle hit, and a second time to measure the energy deposited by the particle. This provided compensation for drifting pedestals.

The tracking performance was very good, with signals at normal incidence confined to three strips. However, the energy resolution of individual channels was relatively poor. Figure 1.21 shows the accumulated detector response across 512 strips, with the scattered proton beam centered on strip 256. In total, the proton energy resolution of the strip detector when read out through the APV chips was found to be about 1 MeV for 5 MeV protons.

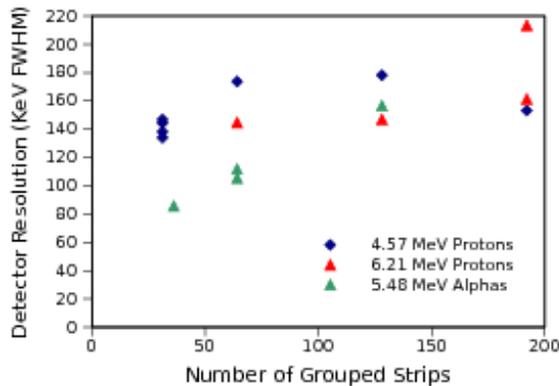


Figure 1.22: Measured silicon detector resolution as a function of the number of strips grouped together when read out through Ortec 142.

In an effort to improve the energy resolution of the silicon detectors, they were modified for use with traditional silicon preamplifiers by combining multiple strips together to reduce the number of channels needed to read out the detector. These are AC-coupled strips, with a thin oxide layer between each p-type implant and with the overlying aluminized layer creating the coupling capacitors. The detector backplane receives the bias, and the strips sit near ground.

Channels were combined by using silver epoxy to precisely bridge across connections on the glass pitch adapter between the aluminized strips on the detector and the APV chips. These combined signals were routed to sub-miniature version-A connectors and amplified by Ortec 142 preamplifiers. Different groupings of strips were also in-

vestigated as shown in Fig. 1.22. Groupings of 64 strips were used to measure the resolution profile shown in Fig. 1.23, as well as the linearity shown in Fig. 1.24.

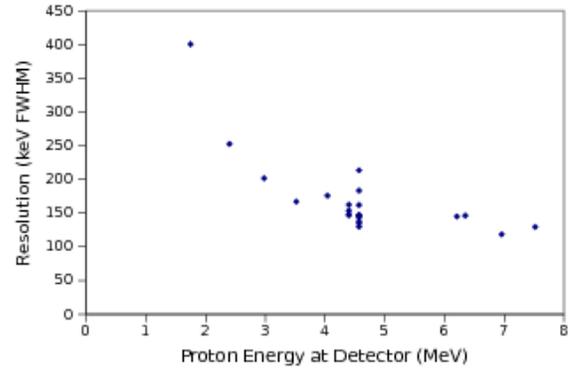


Figure 1.23: Measured silicon detector resolution as a function of incident proton energy. Each point is an independent trial.

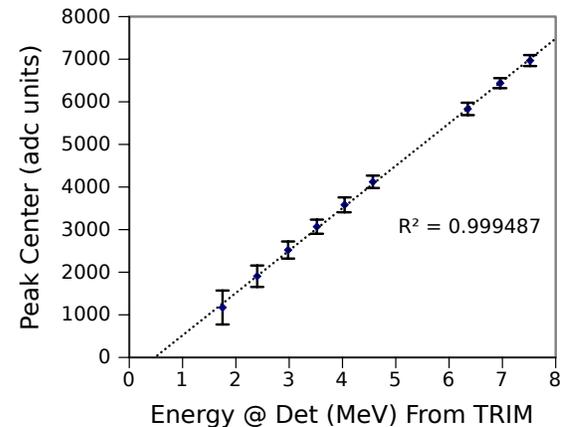


Figure 1.24: Linearity and resolution of silicon strip detector with 64 strips combined together

Despite the relatively poor energy resolution compared to small-area surface-barrier detectors, the scattering length measurement can still be carried out with the modified strip detectors. However, it may be necessary to upgrade them prior to more general differential cross section measurements to be made with a tracking-based setup at a later stage of the experiment.

[Poo10] O. Pooth, *The CMS Silicon Strip Tracker: Concept, Production and Commissioning*, p. 49, Vieweg+Teubner Verlag, Fachmedien Wiesbaden GmbH, Wiesbaden, 1 edition, 2010.

1.2.7 Evaluation of a Prototype Wire Chamber

F.Q.L. FRIESEN, M.W. AHMED, A.S. CROWELL, L.C. CUMBERBATCH, B. FALLIN, C.R. HOWELL, D. TICEHURST, W. TORNOW, *TUNL*; B.J. CROWE, D. MARKOFF, *North Carolina Central University, Durham, NC*; H. WITALA, *Jagiellonian University, Krakow, Poland*

A prototype wire chamber of the type originally planned as part of a tracking system for the ${}^3\text{H}(\gamma, pn)n$ and ${}^3\text{He}(\gamma, pn)p$ experiments (see Sect. 1.2.4) was constructed and tested with radioactive sources and proton beams in the tandem laboratory. It was found that the necessarily thin Mylar windows deflected under slight pressure changes, introducing large and unpredictable non-uniformities in gain.

A prototype wire chamber with anode wire and cathode strip readout for use with low energy charged particles was designed, constructed, and tested. The windows were made from 2- μm -thick aluminized Mylar, electrically etched with a CNC milling machine to create isolated strips 8 mm wide. The anode planes consist of gold-plated tungsten wires, 20 μm in diameter with a 2 mm spacing. The cathode planes were held 8 mm on either side of the anode plane. The frame was machined from bulk FR4. Printed circuit boards were designed in-house and fabricated by an outside vendor.

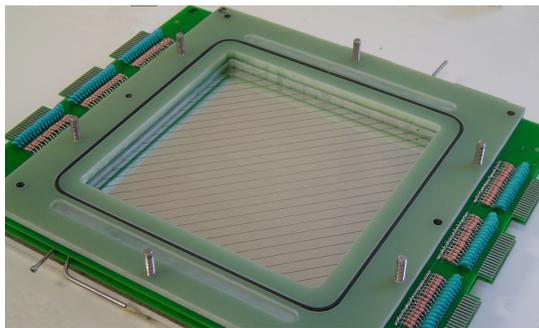


Figure 1.25: Partially disassembled wire chamber. Cathode edge-card connectors are located at the top of the chamber and not visible.

The chamber with the top cathode board removed is shown in Fig. 1.25. The lower cathode strips are visible under the anode wires. The anode bias resistors and coupling capacitors are visible on the left and right sides of the anode board. Discriminator cards (2735PC) connect to the 96 independent anode channels via the anode

board edge-card connectors. The discriminators produce ECL (emitter-coupled logic) signals processed by an FPGA (field programmable gate array) based trigger system implemented in a Caen 1495 module. Each cathode board supports 32 independent strips, which connect to preamplifier cards, and then into FERA (Fast Encoding and Readout ADC) modules.

The Mylar windows were chosen to be 2 μm thick, as part of our strategy for minimizing energy loss of low-energy charged particles traversing the apparatus. The original design of the tracking detector required two wire chambers followed by silicon detectors. Therefore, before being measured, particles would have had to pass through four Mylar windows, in addition to exiting the foil surrounding the gas target cell (see Sect. 1.2.5). The working gas was chosen to be helium, again to reduce energy loss.

The chamber was tested with a ${}^{90}\text{Sr}$ electron source and with protons from the tandem accelerator (typically less than 100 nA on target) scattered off of a thin gold target foil at a scattering angle of 90° . Protons from the tandem were usually tagged using a 50- μm -thick silicon transmission detector and/or a plastic scintillator paddle in coincidence. Coincidence testing showed consistently low efficiency for protons throughout most of the chamber, but with a clear response to the presence of a beam or source. A small area, usually near an edge, would often exhibit a much higher gain than other portions of the chamber, and preventing breakdown/excessive current in this region was a limiting factor in increasing the chamber voltage.

The chamber was first used with an argon/isobutane mixture because it is a well-

understood combination [Blu08] and is similar to helium/isobutane. Figure 1.26 shows that the count rate reaches a plateau as the voltage increases, and that, as expected, the plateau position is modulated by the fraction of quenching gas. Increasing the voltage increases the size of the amplification region around the anodes, which subsequently increases the number of ions recombining at the cathodes and emitting photons which can potentially scatter electrons from the cathode and create unwanted feedback. Introducing more quenching gas causes more of these photons to be absorbed before reaching the cathode [Apr06]. This effect also causes the chamber to be photosensitive.

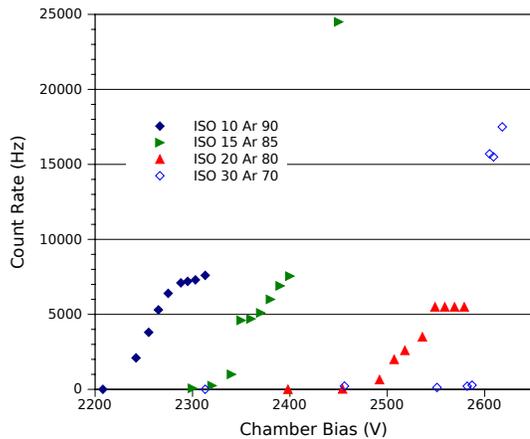


Figure 1.26: Count rate of a single cathode strip in response to a ^{90}Sr source for different gas mixtures as a function of applied voltage.

Gas was delivered to the chamber via two mass-flow controllers feeding into a manifold. The gas exiting the chamber was originally planned to flow through a bubbler, but the pressure required to displace the mineral oil from the tube caused deflection of the Mylar by over 3 mm at the center, which was far too much, given the 8 mm anode-cathode spacing. The bubbler was replaced with a 2 m length of 3.5 mm diameter tubing with an open end. Flow rates were kept as low as the flow controllers would allow without sacrificing too much accuracy. They were typically 20 to 100 cc/minute. Even at these flow rates, deflection of the cathodes was detectable via the slightly distorted image reflected by the Mylar. The air in the experimental area was kept as still as possible, and the chamber was covered with a protective layer of cardboard during bench-top testing with sources, but it is nevertheless possible that very small time-varying pres-

sure fluctuations harmed the repeatability of the measurements.

The cathode preamplifier cards had a tendency to enter parasitic oscillation caused by a small fraction of the output coupling back into the input. The anode discriminator electronics would then easily pick up this feedback. This became more pronounced as signals from the chamber increased in amplitude. Capacitors were added between the cathode strips and ground to mimic the capacitance between cathodes and the grounded aluminized layer usually present on the side of the Mylar facing outside the chamber, thereby creating a filter which suppresses oscillation on the timescale of the feedback. Much effort was also put into ensuring the soundness of the grounding system and power supplies. This yielded some improvements, but the lack of a second aluminized layer on the outsides of the cathodes likely deprived the sensitive elements of some electromagnetic shielding.

One of the key functions of the wire chambers in the tracking-based design was to provide a measurement of energy deposited by particles traversing the apparatus as part of $\Delta E/E$ particle identification. This measurement must be highly self-consistent over time across the sensitive areas of all the detectors. This is further complicated by the radiation safety requirement (adopted after work on the prototype chamber began) that the full apparatus be sealed in a box with the tritium targets, rendering it physically inaccessible at HI γ S, where the experiments were to be run. The need to flow-count gas going into and out of this sealed volume while maintaining precise pressure equilibrium across the Mylar windows would also have posed a significant challenge.

For these reasons, we decided against a tracking detector using wire chambers. The first iteration of the experiment will instead use collimators to select the kinematic region of interest, even though this means we will be unable to collect differential cross section angular dependencies. A windowless time projection chamber using pure helium gas and gas electron multipliers is being investigated as an alternative for particle tracking.

[Apr06] E. Aprile *et al.*, *Noble Gas Detectors*, Wiley-VCH Verlag GmbH, Weinheim, 2006.

[Blu08] W. Blum *et al.*, *Particle Detection with Drift Chambers*, Springer, Berlin, second edition, 2008.

1.2.8 Monte-Carlo Simulations of ${}^3\text{H}(\gamma, pn)n$ and ${}^3\text{He}(\gamma, pp)n$ Experiments at HI γ S

Z. HAN, F.Q.L. FRIESEN, M.W. AHMED, A.S. CROWELL, L.C. CUMBERBATCH, B. FALLIN, C. R. HOWELL, D. TICEHURST, W. TORNOW, *TUNL*; B.J. CROWE, *North Carolina Central University, Durham, NC*; I.J. GRAY, *University of Minnesota Twin Cities, Minneapolis, MN*; H. WITALA, *Jagiellonian University, Krakow, Poland*

We are developing an experiment to measure the two- and three-body differential cross sections for photodisintegration of ${}^3\text{H}$ and ${}^3\text{He}$. These data will be used to determine the ${}^1\text{S}_0$ nn scattering length (a_{nn}) and np scattering length (a_{np}), respectively. Influences of long-range three-nucleon interactions are studied by comparing the experimental nucleon-nucleon scattering lengths obtained from two-body and three-body final states. The Monte-Carlo simulations will aid in optimizing the experiment's design and data analysis approach. We describe the features of the simulations for the three-body case and summarize progress made during the reporting period in developing the simulations-software.

Experiments to measure the differential cross sections for photodisintegration of ${}^3\text{H}$ and ${}^3\text{He}$ are being developed at the Triangle Universities Nuclear Laboratory. The goal is to provide data for assessing the theoretical treatment of meson-exchange currents in the photodisintegration of nuclei and to investigate long-range features of three-nucleon interactions. Measurements will be performed using a linearly polarized γ -ray beam at the High Intensity γ -Ray Source, HI γ S. The apparatus being developed should allow us to perform photodisintegration measurements with a variety of particle coincidence configurations.

The proton energy spectrum will be measured at several polar angles in the range from 45° to 135° . The sensitivity of this reaction to meson-exchange currents and nucleon-nucleon scattering lengths will be used to investigate long-range three-nucleon interactions. The first measurements will be performed with an incident γ -ray energy of 15 MeV. Higher energies will be considered in subsequent studies. In the preliminary conceptual experiment design, the trajectories and energies of the emitted protons will be determined with wire chambers and silicon detectors located on either side of thin-walled gas targets.

We are currently working to develop software to perform Monte-Carlo simulations of the three-body photodisintegration of ${}^3\text{H}$ and ${}^3\text{He}$, based on the GEANT4 toolkit. Using cross-section calculations by Witala and Skibinski [Wit11, Ski03],

photodisintegration events are generated inside the gas targets, and the emitted protons are propagated from the reaction site through the detection apparatus. The simulations of the proton energy spectra will allow direct comparison between measurements and theory. Count-rate and background estimations will be performed with the simulations and will be used in the planning, design optimization, and data analysis of the experiment.

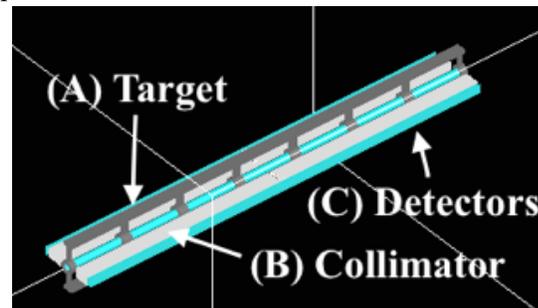


Figure 1.27: Preliminary GEANT4 geometry design for the Monte-Carlo simulation of the three-body photodisintegration experiment. The label (A) denotes the target set; (B) is the collimator with square-packing circular holes; and (C) shows the ideal detector assemblies, which will be replaced by BC404 detectors.

The performance goals of the simulations are:

- To aid in comparing the measurements to

theory;

- To analyze systematic uncertainties;
- To estimate the count rates of the reactions of interest, as well as the background count rates, so that we can project the statistical accuracy for our determination of a_{nn} ;
- To evaluate the use of $\Delta E/E$ detectors for charged particle identification; and
- To use the results as a tool in the development of data-analysis software.

The simulations first generate proton events from a predicted distribution by sampling with respect to E_γ plus θ_p , θ_n , ϕ_p , and ϕ_n (the four relevant detection angles), and the γ -ray interaction position in the target for each event. The simulations then propagate protons through the apparatus while recording their energy and position at different stages in the process as they move from the target to the liquid scintillators.

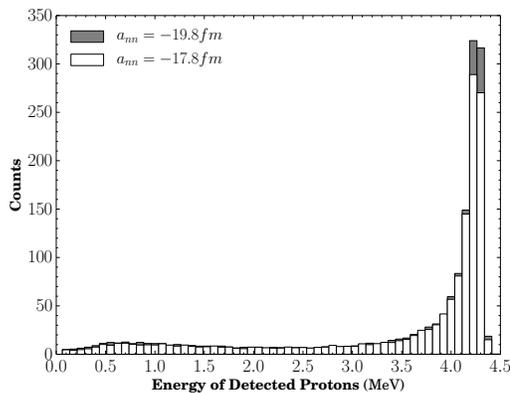


Figure 1.28: Preliminary count estimation for $E_\gamma = 15.2$ MeV for ${}^3\text{H}(\gamma, pn)n$ assuming two different scattering lengths and using 75-keV energy bins. The simulations were implemented with the preliminary geometry.

Previous simulations were based on the wire-chamber experimental setup design. To reduce the experimental complexity and improve the sensitivity of the $\Delta E/E$ method for particle identification, the current design is a collimator-based setup, as shown in Fig. 1.27.

The system consists of symmetric sets of collimators on both sides of the targets, with plastic scintillators and silicon strip detectors behind the collimators. The collimators will select a certain angular acceptance, while the scintillator and silicon detectors will provide measurements of particle energy and $\Delta E/E$ particle identification. Neutron detectors are also added for kinematically complete measurements of the configurations of particular interest.

Preliminary simulations for ${}^3\text{H}(\gamma, pn)n$ at $E_\gamma = 15.2$ MeV assuming scattering lengths a_{nn} equal to -17.8 fm and -19.8 fm are shown in Fig. 1.28. The proton and neutron were constrained by setting $\theta_p = \theta_n = 85.5 \pm 7^\circ$ and $\Delta\phi = 173 \pm 7^\circ$. The simulated proton energy spectra in Fig. 1.28 shows that the difference in the counts in the region of interest for the two values of a_{nn} is about 10%. This simulation includes finite-geometry effects and collimator angular acceptance. The energy spread in the γ -ray beam is not included.

The GEANT4 simulation for the collimator-based design was written during this reporting period. The main purpose of the simulation was to optimize the design of the collimator. The simulated data may be also used to develop and test the data-analysis software. They will also be employed for optimizing the experiment geometry. The simulations will eventually be extended to two-body photodisintegration.

[Ski03] R. Skibinski *et al.*, Phys. Rev. C, **67**, 054002 (2003).

[Wit11] H. Witała and W. Glöckle, Phys. Rev. C, **83**, 034004 (2011).



THE TUNL NUCLEAR ASTROPHYSICS GROUP. FROM LEFT TO RIGHT: (FRONT ROW) KEEGAN KELLY, ANDREW COOPER, JACK DERMIGNY, DAVID LITTLE; (MIDDLE ROW) JOHN KELLEY, RICHARD LONGLAND, TOM CLEGG, SEAN HUNT; (BACK ROW) LORI DOWNEN, FEDERICO PORTILLO, CHRISTIAN ILIADIS, ART CHAMPAGNE

Nuclear Astrophysics

Chapter 2

- **Nucleosynthesis in Hydrostatic and Explosive Environments**
- **Thermonuclear Reaction Rates**

Almost all questions in astrophysics ultimately require a detailed understanding of stars and stellar properties, thus challenging stellar models to become more sophisticated, quantitative, and realistic in their predictive power. This, in turn, requires more detailed input physics, such as thermonuclear reaction rates and opacities, plus a concerted effort to validate models through systematic observations. Consequently, the study of nuclear reactions in the universe remains the focus of nuclear astrophysics research at TUNL.

Our accomplishments during this reporting period include: (1) the lowest energy in-beam measurement to date of the $^{17}\text{O}(p,\gamma)^{18}\text{F}$ reaction important for classical nova nucleosynthesis; (2) the design of a new method to analyze singles and coincidence γ -ray pulse-height spectra, which has been applied to both the $^{17}\text{O}(p,\gamma)^{18}\text{F}$ and $^{22}\text{Ne}(p,\gamma)^{23}\text{Na}$ reactions; (3) the discovery of a low-energy resonance in the $^{29}\text{Si}(p,\gamma)^{30}\text{S}$ reaction important for explosive stellar hydrogen burning; (4) the completion and submission of a review article of classical nova nucleosynthesis and an evaluation of the $^{18}\text{Ne}(\alpha,p)^{21}\text{Na}$ reaction; (5) continued work on correlations and uncertainties in reaction networks so that the specific reactions that are linked to astrophysical observables can be determined.

2.1 Nucleosynthesis in Hydrostatic and Explosive Environments

2.1.1 New Recommended $\omega\gamma$ for the $E_r^{\text{cm}} = 458$ keV Resonance in $^{22}\text{Ne}(p,\gamma)^{23}\text{Na}$

K.J. KELLY, A.E. CHAMPAGNE, R. LONGLAND, M.Q. BUCKNER *TUNL*

A new measurement of the resonance strength of the $E_r^{\text{cm}} = 458$ keV resonance in $^{22}\text{Ne}(p,\gamma)^{23}\text{Na}$ is based on precise primary branching ratio determinations using the `TFRACTIONFITTER` class of `ROOT`. The recommended strength is $\omega\gamma(458 \text{ keV}) = 0.583(43)$ eV, more than one standard deviation above a recent result based on literature branching ratios. This change affects all resonance strengths and cross sections measured relative the 458-keV resonance.

Stellar winds from massive asymptotic giant branch (AGB) stars are believed to contribute to the observed sodium-oxygen anti-correlation in globular clusters [D’A83, Ren08]. The most uncertain nuclear reactions involved in the production and destruction of ^{23}Na in massive AGB stars are [Ces13] the $^{20}\text{Ne}(p,\gamma)^{21}\text{Na}$, $^{22}\text{Ne}(p,\gamma)^{23}\text{Na}$, and $^{23}\text{Na}(p,\alpha)^{20}\text{Ne}$ reactions. Accurate measurements of these reaction rates at astrophysically relevant energies will improve the accuracy of stellar AGB models. However, a well-known reference resonance that can provide an absolute cross-section scale is required for accurate measurements of these reactions. The $^{22}\text{Ne}(p,\gamma)^{23}\text{Na}$ resonance at $E_r^{\text{cm}} = 458$ keV ($E_x = 9252.1(10)$ keV, $S_p = 8794.11(2)$ keV [Fir07]) is an ideal reference resonance for p -capture reactions on Ne isotopes. A careful measurement of this resonance strength has recently been performed [Lon10]. However, the calculation of their strength was inversely proportional to a weighted average of the ground-state branching ratios reported in Refs. [Pii71, Mey73], which were measured with lower efficiency detectors.

A high-statistics measurement of the 458-keV resonance in $^{22}\text{Ne}(p,\gamma)^{23}\text{Na}$ was recently performed as a check on the $\omega\gamma(458 \text{ keV})$ value reported in Ref. [Lon10]. Targets for this work were fabricated using the Eaton Ion Implanter at UNC Chapel Hill by implanting singly ionized ^{22}Ne atoms into a tantalum target-backing at an implantation energy of 100 keV, and the JN accelerator at LENA provided about 0.01 C of protons on target at $E_p = 494$ keV. The resulting

γ -ray spectrum was measured with a 135% relative efficiency high-purity germanium detector.

The branching ratios from this resonance were determined using `GEANT` [Ago03] simulations of each possible decay cascade from the 9252-keV resonant state coupled to the `TFRACTIONFITTER` [Bar93] class of `ROOT` [Bru97]. Version 4.9.6 of `GEANT` was used for all simulations. Branching ratios derived from this analysis are shown in Table 1 with a comparison to those from previous work. Note that a new primary branch from the resonant state to the 7082-keV excited state in ^{23}Na was identified for the first time in this work.

Table 2.1: Branching ratios (in %) for primary transitions from the 458-keV resonance in $^{22}\text{Ne}(p,\gamma)^{23}\text{Na}$.

Transition	Present	[Mey73]	[Pii71]
$R \rightarrow 0$	41.77(67)	46.0	48.0
$R \rightarrow 2391$	4.05(12)	3.7	5.0
$R \rightarrow 2640$	8.27(18)	8.5	6.0
$R \rightarrow 2982$	31.73(52)	32.0	39.0
$R \rightarrow 3678$	4.85(16)	4.1	-
$R \rightarrow 3848$	-	-	2.0
$R \rightarrow 3914$	0.37(9)	0.7	-
$R \rightarrow 4430$	1.69(9)	1.8	-
$R \rightarrow 5766$	2.78(9)	2.4	-
$R \rightarrow 6921$	2.43(9)	0.8	-
$R \rightarrow 7082$	2.06(9)	-	-

The accuracy of the present branching ratios was verified via the calculation of the experimental yield, Y , as determined from each observed

primary transition, j , according to

$$Y_j = \left[\frac{N_\gamma f_{SC}}{N_B B \eta_p W} \right]_j, \quad (2.1)$$

where N_γ , η_p , B , and W are the observed number of γ -ray counts, the detector full-energy peak efficiency, the branching ratio, and angular correlation factor associated with a particular transition, respectively. All primary γ -rays were emitted isotropically from the target because the resonant state has $J(9252 \text{ keV}) = 1/2$. Angular correlations for all secondary transitions were included in our GEANT simulations. The parameter N_B is the number of bombarding particles collected during data acquisition and was constant for all Y_j . The parameter f_{SC} corrects the observed γ -ray peak for coincidence-summing effects. The calculation of f_{SC} factors is expanded upon in Ref. [Kel15].

Values of Y_j were calculated assuming the branching ratios of Refs. [Pii71, Mey73], and of the present work separately. Given that the same experimental yield should be obtained independent of the transition being analyzed, we chose to probe the accuracy of the literature and present branching ratios by analyzing the variation in the corresponding Y_j . This variation was quantified via the geometric standard deviation, σ^{geo} , of each set of Y_j . This is defined as

$$\sigma^{geo} = \exp \left\{ \left[\frac{1}{N} \sum_j \ln \left(\frac{Y_j}{\mu_g} \right)^2 \right]^{\frac{1}{2}} \right\}, \quad (2.2)$$

where N and μ_g are the total number of data points and the geometric mean of the set of Y_j .

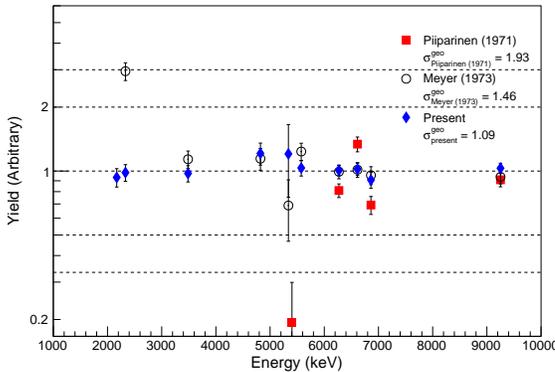


Figure 2.1: The experimental yield from the 458-keV resonance in $^{22}\text{Ne}(p,\gamma)^{23}\text{Na}$ calculated from Eq. 2.1.

The Y_j resulting from this analysis are shown in Fig. 1. The σ^{geo} obtained using the branching ratios of Refs. [Pii71, Mey73] are, respectively, 77% and 34% higher than that obtained using

the present branching ratios. Additionally, the Y_j calculated using the newly identified transition to the 7082-keV excited state in ^{23}Na , seen at 2170 keV in Fig. 1, is in good agreement with the Y_j of the same data set.

The ground-state-transition branching ratio measured in this work is 10 to 13% lower than those of Ref. [Mey73] and Ref. [Pii71]. This result increases the strength measurement of Ref. [Lon10] by about 11.3%, or about 1.2 σ . Given that the technique used in Ref. [Lon10] was independent of effects associated with the charge integration, absolute detector efficiency, or assumed target stoichiometry, we chose to correct their result by replacing their assumed ground-state branching ratio with the value reported here. Therefore, we recommend $\omega\gamma(458 \text{ keV}) = 0.583(43) \text{ eV}$. The uncertainty in this strength has also been reduced from 9.7% [Lon10] to 7.3%. It should be noted that this strength is consistent with our measured yield and assumed stoichiometry. The revision of this resonance strength affects all resonance strengths and cross sections measured relative to this resonance. Further details on this work can be found in Ref. [Kel15], which was recently accepted by Phys. Rev. C.

- [Ago03] S. Agostinelli *et al.*, Nucl. Instrum. Methods A, **506**, 250 (2003).
- [Bar93] R. Barlow and C. Beeston, Comp. Phys. Commun., **77**, 219 (1993).
- [Bru97] R. Brun and F. Rademakers, Nucl. Instrum. Methods A, **81**, 389 (1997).
- [Ces13] J. M. Cesaratto *et al.*, Phys. Rev. C, **88**, 065806 (2013).
- [D'A83] F. D'Antona, R. Gratton, and A. Chieffi, Mem. Soc. Astron. Italiana, **54**, 17 (1983).
- [Fir07] R. B. Firestone, Nucl. Data Sheets, **108**, 1 (2007).
- [Kel15] K. J. Kelly *et al.*, Phys. Rev. C, (2015), Accepted for publication.
- [Lon10] R. Longland *et al.*, Phys. Rev. C, **81**, 055804 (2010).
- [Mey73] M. A. Meyer and J. J. A. Smit, Nucl. Phys. A, **205**, 177 (1973).
- [Pii71] M. Piiparinen, A. Anttila, and M. Viitasalo, Z. Phys., **247**, 400 (1971).
- [Ren08] A. Renzini, Mon. Not. R. Astron. Soc., **391**, 354 (2008).

2.1.2 High Beam-Intensity Study of $^{17}\text{O}(p,\gamma)^{18}\text{F}$ and Thermonuclear Reaction Rates for $^{17}\text{O}+p$

M. BUCKNER, C. ILIADIS, K.J. KELLY, L.N. DOWNEN, A.E. CHAMPAGNE, J.M. CESARATTO, C. HOWARD, R. LONGLAND, *TUNL*;

Hydrogen burning of the oxygen isotopes takes place in several stellar environments. We made a new measurement of the $^{17}\text{O}(p,\gamma)^{18}\text{F}$ reaction at incident energies of 170 to 530 keV. Improvements over previous work include significantly higher beam intensities, the use of a sophisticated γ -ray coincidence spectrometer, and a novel data analysis technique made possible by the spectrometer. We present new thermonuclear rates for the $^{17}\text{O}+p$ reactions, taking all consistent results from previous measurements into account.

Hydrogen burning of the oxygen isotopes takes place in a variety of sites, including low-mass stars during hydrogen core and shell burning, AGB stars during hydrogen shell burning, intermediate-mass AGB stars during hot-bottom burning, and both CO and ONe classical novae during the explosion. Observations of oxygen elemental and isotopic abundances in stellar spectra [Tsu08] or in presolar grains [Mey08] can provide strong constraints for stellar model simulations if reliable thermonuclear reaction rates for the hydrogen burning of oxygen are available over a wide region of stellar temperatures.

Because of the astrophysical importance of the $^{17}\text{O}+p$ reaction rates, we performed a new measurement of the (p,γ) channel at bombarding energies between 170 keV and 530 keV. We measured the cross section at much lower energies than those used in previous in-beam experiments. Given that the sensitivity in a nuclear counting experiment is *directly* proportional to the signal count rate, increasing the proton beam current is of utmost importance. Our maximum beam current was about 2 mA, representing an order of magnitude improvement over Ref. [DL14]. In addition, the sensitivity is approximately inversely proportional to the *square root* of the background count rate. Thus, for the first time in this reaction, we performed the measurement using a sophisticated γ -ray coincidence spectrometer, consisting of a large-volume HPGe detector and a NaI(Tl) annulus, which not only allowed for a significant reduction in background, but also provided valuable experimental information for the interpretation of the ^{18}F decay scheme at each measured bombarding energy.

The substantial increase in detection sensitivity also allowed for a novel data analysis method that relies on a decomposition of the complete HPGe coincidence spectrum into different components arising from various primary decays in $^{17}\text{O}(p,\gamma)^{18}\text{F}$. We demonstrated that our method gives consistent results for the strengths of the low-energy resonances at bombarding energies of 193 keV and 518 keV compared to the most sensitive previous measurements. With regard to the low-energy S-factor, our data, unlike previous prompt γ -ray studies, contain almost the entire decay strength in $^{17}\text{O}+p$. Thus our S-factor data points scatter much less than previous results.

Based on the present measurement and all consistent previous studies, we calculated new thermonuclear reaction rates for the $^{17}\text{O}(p,\gamma)^{18}\text{F}$ and $^{17}\text{O}(p,\alpha)^{14}\text{N}$ reactions that will allow for more reliable simulations of low-mass stars and classical novae.

Our results are compared to the 2010 reaction rate evaluation [Ili10] in Fig. 2.2. The ratios of previous and present *recommended* rates are shown as solid black lines.

For the $^{17}\text{O}(p,\gamma)^{18}\text{F}$ reaction, our rates are higher by up to 20% for temperatures below 3 GK. Our much higher rates at elevated temperatures (a factor of four at 10 GK) arise because the direct capture rate was artificially cut off by Ref. [Ili10] at an energy of 1.2 MeV, whereas here we take the full direct capture S-factor into account. Except at $T = 40$ to 60 MK, our rate uncertainties (grey shaded area, representing a 68% coverage) are smaller than those of Ref. [Ili10] (blue shaded area) at almost all temperatures. Our (p,γ) rates are in overall agreement with the

recent results of Di Leva *et al.* [DL14], with a maximum deviation of about 20% near 30 MK.

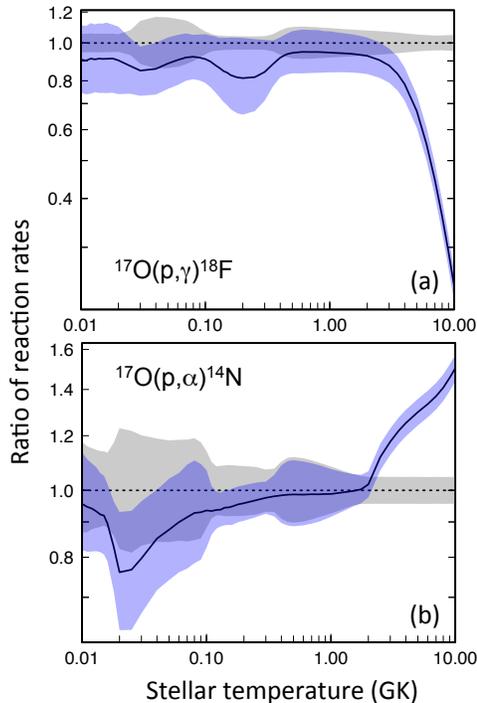


Figure 2.2: Reaction rate comparison of present results with a recent evaluation [Ili10]. All rates are normalized to the new recommended rate. The shaded areas are described in the text. The solid line shows the ratio of previous and present recommended rates.

For the $^{17}\text{O}(p,\alpha)^{14}\text{N}$ reaction, the present and previous [Ili10] rate uncertainties are similar. The recommended rates deviate by about 30% near 20 MK and by about 50% at 10 GK. The deviation at low temperatures is caused by the higher adopted upper limit for the spectroscopic factor of the -2 keV subthreshold resonance, while the deviation at the highest temperatures is caused by the fact that we use a different Hauser-Feshbach prescription (TALYS versus NON-SMOKER) compared to Ref. [Ili10]. The change was made in order to account for missing resonance contributions.

This work has now been published [Buc15].

-
- [Buc15] M. Q. Buckner *et al.*, Phys. Rev. C, **91**, 015812 (2015).
- [DL14] A. Di Leva *et al.*, Phys. Rev. C, **90**, 019902 (2014).
- [Ili10] C. Iliadis *et al.*, Nucl. Phys., **A841**, 31 (2010).
- [Mey08] B. S. Meyer *et al.*, Rev. Mineral. Geochem., **68**, 31 (2008).
- [Tsu08] T. Tsuji, Astron. Astrophys., **489**, 1271 (2008).

2.1.3 Thermonuclear Reaction Rate Evaluation for $^{18}\text{Ne}(\alpha,p)^{21}\text{Na}$

R. LONGLAND, C. ILIADIS, *TUNL*; P. MOHR, *Diakonie-Klinikum, D-74523 Schwäbisch Hall, Germany*;

The $^{18}\text{Ne}(\alpha,p)^{21}\text{Na}$ reaction is a key reaction for CNO-cycle breakout during explosive hydrogen burning in X-ray bursts. Here, we report on a new evaluation of this rate using a Monte Carlo method for uncertainty propagation. Our results are consistent with other evaluations, but are the first to present statistically meaningful, temperature-dependent uncertainties.

During their explosions, X-ray bursts burn hydrogen at high temperatures to create isotopes far from the valley of stability. The start of this nucleosynthesis begins with breakout from the CNO cycle, which is strongly influenced by the $^{18}\text{Ne}(\alpha,p)^{21}\text{Na}$ reaction. This reaction's cross section has not been well measured directly because it involves a radioactive target, ^{18}Ne . As a result, the uncertainty in its rate is large and has a significant impact on X-ray burst nucleosynthesis.

The $^{18}\text{Ne}(\alpha,p)^{21}\text{Na}$ reaction proceeds through excited states in ^{22}Mg . Previously, studies have been performed to identify the particular states in ^{22}Mg that strongly contribute to the rate at 1 to 2 GK, the temperature range important in X-ray bursts. Nuclear properties of those states have also been determined, although there are disagreements between experiments that make them challenging to interpret. An overview is presented in Ref. [Moh14].

In this study, we re-evaluated the rate of the $^{18}\text{Ne}(\alpha,p)^{21}\text{Na}$ reaction using the Monte Carlo reaction rate formalism first presented in Ref. [Lon10]. However, an extra source of uncertainty stems from quantum number assignments for the intermediate states in ^{22}Mg . We extended the RATESMC code, allowing us to investigate the impact of those ambiguities on the reaction rate.

In order to evaluate the rate for this reaction, we must first assess uncertainties in the input parameters. The reaction rate per particle-pair is given by

$$\langle\sigma v\rangle = \left(\frac{2\pi}{\mu kT}\right)^{3/2} \hbar^2 \sum_i \omega\gamma_i e^{-E_{r,i}/kT}, \quad (2.3)$$

where T is the temperature, and $E_{r,i}$ and $\omega\gamma_i$ are the energy and strength of the i th resonance,

respectively. The resonance strength depends on the partial widths Γ_α of the α particle and Γ_p of the proton and on the total width, Γ , through the relation

$$\omega\gamma_{\alpha p} = (2J + 1) \frac{\Gamma_\alpha \Gamma_p}{\Gamma}. \quad (2.4)$$

For most low energy resonances, $\Gamma_\alpha \ll \Gamma_p$, so $\Gamma_p \approx \Gamma$, so the resonance strength can be approximated as

$$\omega\gamma_{\alpha p} \approx (2J + 1)\Gamma_\alpha. \quad (2.5)$$

The quantity J is the spin of the state.

The dominant uncertainties for calculating the rate of the $^{18}\text{Ne}(\alpha,p)^{21}\text{Na}$ reaction are, therefore, in the resonance spins and α -particle partial widths of the states in ^{22}Mg . The latter can be divided into four broad groups: (i) those with well-determined mirror states in ^{22}Ne , (ii) those for which the approximation in Eq. (2.5) is no longer appropriate. This group does not affect the rate at astrophysical energies; (iii) states for which widths in the mirror nucleus have been measured but whose determination is strongly model dependent; and (iv) states for which no spectroscopic information is known. Uncertainties in the α -particle partial widths for the first three groups are factors of two, three, and three, respectively. For the last group, only upper limits to the widths can be assigned upper. These were adopted from Ref. [Pog13]. See Ref. [Moh14] for more detail.

To include the ambiguities in the quantum number assignments in group (iv), we extended our Monte Carlo reaction-rate-uncertainty method by sampling over possibilities according to their experimental likelihoods. Tentative assignments from Ref. [Mat09] were assigned a 50% probability, with the remaining probability

being spread evenly over other possible assignments given the available data.

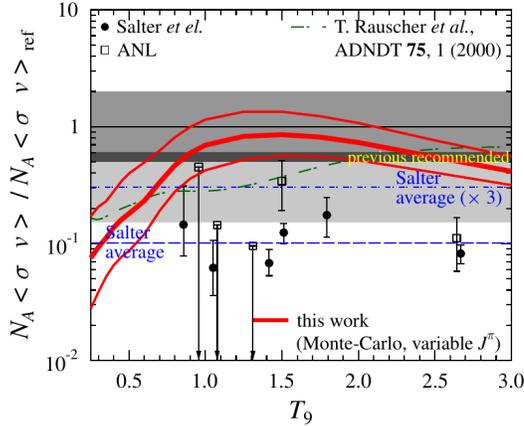


Figure 2.3: The reaction rate compared to literature estimations. Note that here, the present rate in red depicts the $1\text{-}\sigma$ uncertainties. The other estimations show estimates for the rate’s upper and lower bounds.

The resulting reaction rate is shown as red lines in Fig. 2.3. These rates are normalized to the reference rate presented by Ref. [Moh13], so that, for example, at 0.3 GK the present rate is approximately 10 times smaller than the reference rate. The upper and lower red lines represent the $1\text{-}\sigma$ uncertainties in the rate, whereas the grey regions represent the “upper” and “lower” limits of previous rates. Our new rate agrees well with that presented previously, and supports the proposal that reverse-reaction rates (the “Salter average”), should be multiplied by three to correct for excited state contributions. Our rate is, however, about three times greater than that adjusted average rate at 1.5 GK.

The Monte Carlo method also allows us to calculate the fractional contributions of different resonances to a reaction rate. This is useful for identifying those resonances which should be measured if we want to have the largest impact on reducing nucleosynthesis uncertainties. A fractional-contribution plot for the $^{18}\text{Ne}(\alpha, p)^{21}\text{Na}$ reaction is shown in Fig. 2.4.

Between 0.5 and 2.0 GK—the temperatures most important for X-ray burst nucleosynthesis—we see that only a handful of resonances contribute significantly to the reac-

tion rate. At 0.5 GK, the resonance at $E_r = 938$ keV dominates the reaction rate. At higher temperatures, however, the picture becomes less clear as resonances associated with poorly measured mirror states begin to dominate the rate. Those identified here as being the most critical are the one at $E_r = 1401$ keV, the broad resonance at $E_r = 1567$ keV, and the resonance at $E_r = 1610$ keV.

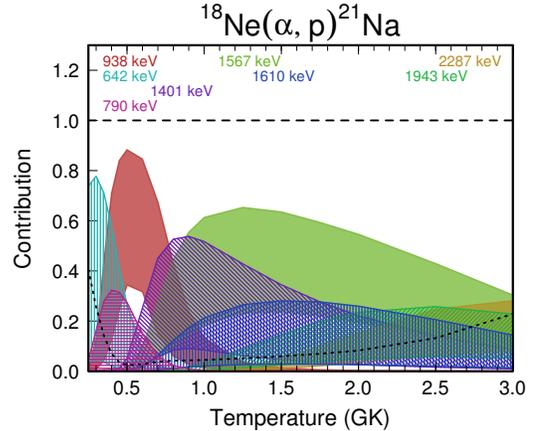


Figure 2.4: Fractional contributions of individual resonances to the total rate. Each curve is labeled at the top of the figure. The bands in these contributions correspond to the uncertainties in each resonance. For example, at 1.0 GK, the resonance at $E_r = 1567$ keV (green) contributes between 15% and 60% of the total rate while the $E_r = 1401$ keV resonance (red) contributes between 2% and 50% of the total rate.

-
- [Lon10] R. Longland *et al.*, Nucl. Phys., **A841**, 1 (2010).
- [Mat09] A. Matic *et al.*, Phys. Rev. C, **80**, 055804 (2009).
- [Moh13] P. Mohr and A. Matic, Phys. Rev. C, **87**, 035801 (2013).
- [Moh14] P. Mohr, R. Longland, and C. Iliadis, Phys. Rev. C, **90**, 065806 (2014).
- [Pog13] I. Pogrebnyak *et al.*, Phys. Rev. C, **88**, 015808 (2013).

2.1.4 Evaluation of $^{29}\text{Si}(p,\gamma)^{30}\text{P}$ and Its Relevance to Classical Nova Presolar Grains

L.N. DOWNEN, C. ILIADIS, *TUNL*

Classical novae are of great interest to the nuclear astrophysics community, and nova presolar grains provide another avenue to study these explosions. Silicon isotopic ratios in grains can be used to understand classical novae but can only be interpreted correctly if the reactions that create and destroy these species are well known. We show that uncertainties in the $^{29}\text{Si}(p,\gamma)^{30}\text{P}$ reaction rate uncertainties to discrepancies between the expected and observed silicon isotopic ratios. The ongoing study of the 220.9 keV, 312 keV, and 324.1 keV resonances in this reaction is discussed.

Classical novae are thermonuclear explosions that occur in binary systems of main sequence and white dwarf stars that are thought to contribute significantly to the galactic abundance of rare species [Jos06]. Novae involving white dwarf stars of oxygen and neon (ONe) composition are unusually interesting due to their higher burning temperatures. While the elemental evolution of these events can be understood using telescopic techniques, no information about the isotopic distributions can be ascertained with them. Thus, the study of presolar grains can aid in understanding nova events. ONe nova grains are distinguished by above-solar values of $\delta(^{30}\text{Si}/^{28}\text{Si})$ and close-to-solar values of $\delta(^{29}\text{Si}/^{28}\text{Si})$, where $\delta(^i\text{Si}/^{28}\text{Si})$ is defined as $[(^i\text{Si}/^{28}\text{Si})/(^i\text{Si}/^{28}\text{Si})_{\odot} - 1] \times 1000$ [Ama01]. Therefore, accurate reaction rates governing the abundance of ^{29}Si are critical when comparing grain isotopic ratios to those predicted by reaction network calculations.

Pioneering work [Jos07] has already shown that such comparisons, while promising, are fraught with unforeseen problems. The most notable discrepancy is that isotopic ratios measured in presolar grains only match nova model predictions if the ejected nova material mixes with 90–95% close-to-solar material before grain formation [Ama01]. However, these studies have not taken into account the often large effect that reaction rate uncertainties can have on predicted abundances. In fact, if reaction rate uncertainties are taken into account in nucleosynthesis models, this extreme pre-condensation mixing is not necessarily required. A comparison of silicon isotopic ratios illustrates this effect. The red line in Fig. 2.5 shows silicon abundances from

the ONe classical-nova nucleosynthesis model assuming a mass of 1.15–1.35 M_{\odot} . They differ significantly from the presolar grain abundances [Jos07], given by the markers. However, if one assumes a factor of five uncertainty in the $^{29}\text{Si}(p,\gamma)^{30}\text{P}$ rate, the uncertainty bounds of the silicon abundances, given by the dashed black lines, intersect with several of the presolar grain measurements. Clearly, the large effect that uncertainties in the $^{29}\text{Si}(p,\gamma)^{30}\text{P}$ reaction rate have on $\delta(^{29}\text{Si}/^{28}\text{Si})$ indicates that this reaction warrants further study. Therefore, the effect of reaction rate uncertainties on classical nova nucleosynthesis models must be explored, and this also motivates the exploration of other reactions where rate uncertainties could be reduced by new nuclear physics experiments.

To identify important contributions to the reaction rate uncertainty, a Monte Carlo procedure [Lon10] was used to determine that the strength uncertainties of the $E_r^{\text{lab}} = 220.9$ keV, 312 keV, and 324.1 keV resonances have a large impact on the overall $^{29}\text{Si}(p,\gamma)^{30}\text{P}$ rate in temperatures relevant to classical nova nucleosynthesis — roughly 0.1 to 0.5 GK. The $E_r^{\text{lab}} = 220.9$ keV and 312 keV resonances have not been observed to date, and the $E_r^{\text{lab}} = 324.1$ keV resonance strength uncertainty of 30% [Rei85] warrants remeasurement with higher precision. The $E_r^{\text{lab}} = 416.7$ keV resonance was very carefully measured previously [Rii79] and can be used as the basis for relative measurements of other resonance strengths.

To undertake this experiment, first a natural tantalum backing was produced and cleaned at TUNL using chemical etching and resistive heating. It was then sent to collaborators at the Cen-

ture of Nuclear Spectrometry & Mass Spectrometry in Orsay, France for ^{29}Si ion implantation using their Source of Negative Ions by Cesium Sputtering system and natural silicon metal. The target was then characterized using the 1 MV JN Van de Graff ion source at LENA and a 135% efficiency high-purity germanium (HPGe) detector, orientated at 0° relative to the target chamber. There was minimal lead shielding. We used the $E_r^{\text{lab}} = 416.7$ keV resonance for the characterization.

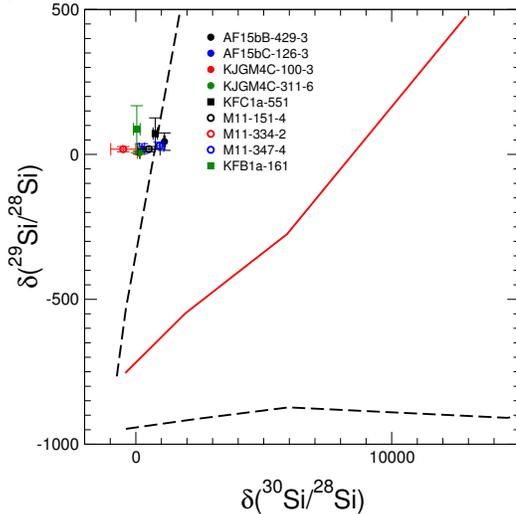


Figure 2.5: Comparison of silicon abundances from classical-nova nucleosynthesis models and presolar grain measurements.

The first stage of data collection involved the study of the $E_r^{\text{lab}} = 312$ keV and 324.1 keV resonances in $^{29}\text{Si}(p,\gamma)^{30}\text{P}$ and was completed in Fall 2014. Thus far, data have been accumulated with 15 C of protons from the 1 MV JN Van de Graff ion source. The detector system consists of the 135% efficiency HPGe detector at 0° surrounded by a NaI(Tl) annulus, 2.5-cm-thick lead shielding, and a 5-cm-thick anti-coincidence scintillator shield. A detailed yield curve of this energy region is given in Fig. 2.6. The analysis of these data is currently underway and is expected to conclude in Fall 2015.

The second stage of data collection consists solely of the $E_r^{\text{lab}} = 220.9$ keV resonance study. Because the strength of this resonance is significantly lower than those measured with the JN in the first stage of data collection, the likelihood of detection of this resonance could be greatly improved if a higher proton fluence could be used

to improve signal strength and quickly accumulate large amounts of data. Unfortunately, the current electron-cyclotron-resonance (ECR) ion source, while capable of roughly ten times the current of the JN, cannot reach energies above 200 keV. However, the improved ECR system [Coo14] was designed to accelerate protons to a maximum energy of 240 keV. Therefore, the improved system will be used to measure this resonance. This stage of the experiment is scheduled for Fall 2015.

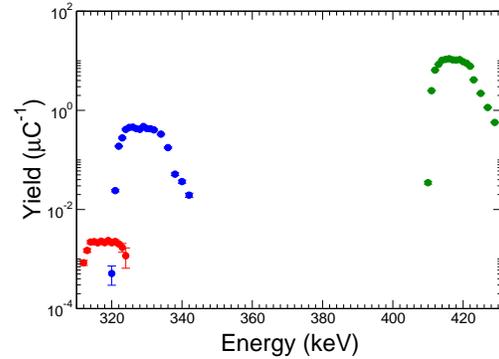


Figure 2.6: The experimental excitation energy range explored at present. Transition yields indicating the 312 keV, 324.1 keV, and 416.7 keV resonances are given by the red, blue, and green markers, respectively.

-
- [Ama01] S. Amari *et al.*, *Astrophys. J.*, **551**, 1065 (2001).
 - [Coo14] A. L. Cooper *et al.*, In *APS Meeting Abstracts*, p. 14009, 2014.
 - [Jos06] J. José, M. Hernanz, and C. Iliadis, *Nucl. Phys.*, **A777**, 550 (2006).
 - [Jos07] J. José and M. Hernanz, *Meteoritics Planet. Sci.*, **42**, 1135 (2007).
 - [Lon10] R. Longland *et al.*, *Nucl. Phys.*, **A841**, 1 (2010).
 - [Rei85] J. P. L. Reinecke, F. B. Waanders, and P. Oberholzer, *Nucl. Phys.*, **A435**, 333 (1985).
 - [Rii79] M. Riihonen, J. Keinonen, and A. Anttila, *Nucl. Phys.*, **A313**, 251 (1979).

2.1.5 Photo-Induced Depopulation of the ^{180m}Ta Isomer

M. BHIKE, KRISHICHAYAN, W. TORNOW *TUNL*

To help resolve the mysteries surrounding the nucleosynthesis of ^{180}Ta , we have measured the cross section for the depopulation of its isomer, ^{180m}Ta . This work was carried out at the HI γ S facility with monoenergetic photon beams at energies from 2.5 to 3.1 MeV. The irradiated foils of natural tantalum, containing 14.4 mg of ^{180m}Ta , were γ -ray counted at TUNL's low-background counting facility.

The exotic odd-odd nucleus ^{180m}Ta is famous for being the only naturally occurring isomer and, at the same time, for being nature's rarest isotope. Only 0.012% of natural tantalum is ^{180m}Ta ; the remainder is ^{181}Ta . The isomer owes its existence to the highly K-forbidden transition between the $J^\pi = 9^-$ ($E_x = 77.1$ keV) isomeric state and the $J^\pi = 1^+$ ground state. The half-life of ^{180m}Ta is more than 1.2×10^{15} years, while the ground state has a half-life of only 8.154 hours, decaying either by electron capture to ^{180}Hf or by β^- to ^{180}W [Col85], as shown in Fig. 2.7.

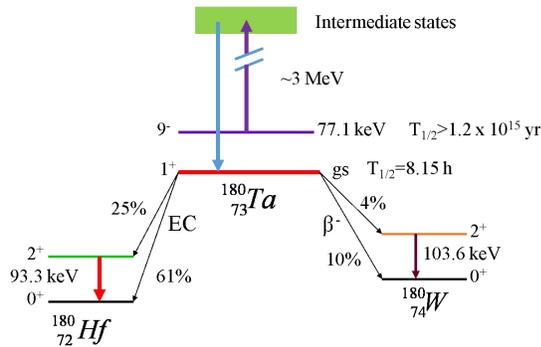


Figure 2.7: Schematic energy-level diagram of ^{180}Ta and its daughters.

In spite of considerable experimental and theoretical efforts, the nucleosynthesis of ^{180}Ta has been a challenging astrophysical problem. Surprisingly, the puzzle is not in the rarity of the isotope but rather in the mechanism producing sufficient amounts of it. The problem lies in the fact that it is bypassed in the normal nucleosynthesis processes for heavy nuclei. It lies outside the main path of the s-process, which proceeds through the stable Hf isotopes directly to ^{181}Ta . It is also shielded against the r-process by its stable isobar ^{180}Hf . A number of possible pro-

duction processes for ^{180m}Ta have been pursued with no conclusive results. These include the p-process, neutrino nucleosynthesis, spallation reactions in the interstellar medium, photodisintegration reactions, and certain complex paths within the regular s-process [Ton00, Bel99]. The photodisintegration reaction on ^{180m}Ta and neutron capture on ^{179}Ta leading to ^{180m}Ta are experimentally unverified aspects of possible s- and p-process explanations for the origin and abundance of this isomer. They thus rely on theoretical model calculations. The steps towards measuring the neutron-capture cross section on radioactive ^{179}Ta were to produce it through the $^{180}\text{Hf}(p,2n)^{179}\text{W}$ reaction, radiochemically separate it, and use it to measure the thermal-neutron-capture cross section.

The photo-activation of ^{180m}Ta was conducted using TUNL's High-Intensity Gamma-Ray Source (HI γ S). Monoenergetic γ rays with energies of 2.3 and 3.1 MeV passed through a 1.0-inch-diameter lead collimator, and impinged on the targets. The corresponding electron beam energies were 382 and 426 MeV, respectively, and the electron current was kept constant at 90 mA. The γ -ray energy spread was approximately 300 keV FWHM. Natural tantalum and indium targets 2.5 cm in diameter with a mass of about 1.2 g were irradiated for approximately ten hours. The indium target was included to measure the $^{115}\text{In}(\gamma,\gamma')^{115m}\text{In}$ cross section, which can be used as an independent photon-flux monitor in other photo-activation experiments. The target assembly was positioned 4 m behind the lead collimator. The absolute photon flux was obtained using an 8 inch \times 12 inch NaI detector in combination with the HI γ S scintillator paddle system. The average γ -ray flux at the target position was about 2×10^7 $\gamma/(\text{cm}^2\text{s})$.

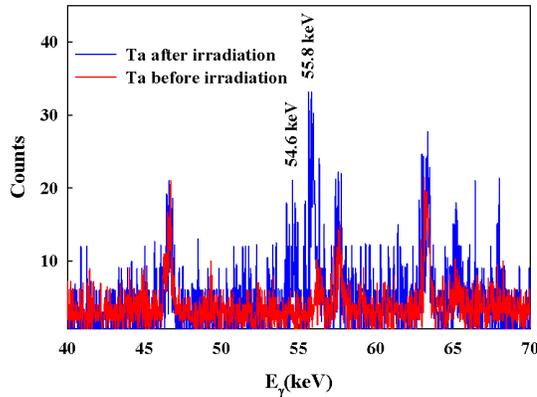


Figure 2.8: Characteristic ^{180}Hf x-ray spectrum from photoactivation of the natural tantalum sample at 3.11 MeV. The spectrum measured with the unirradiated Ta target is shown for comparison.

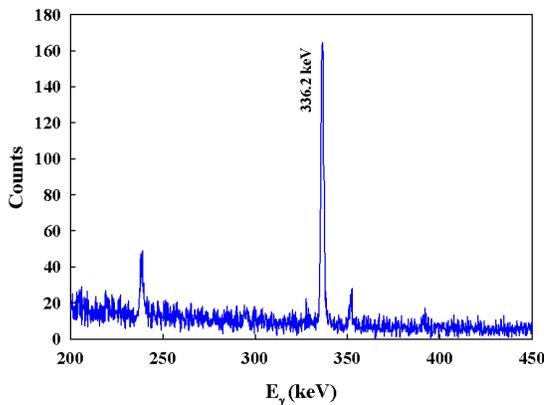


Figure 2.9: Observed γ -ray spectrum of the indium sample irradiated at 3.11 MeV.

After the irradiation, the activated Ta sample was counted off-line in TUNL’s low-background counting facility using a 13% planar HPGe detector in close geometry. The excellent energy resolution of about 0.5 keV at 55 keV enabled

the separation of the $K_{\alpha 1}$ (55.79 keV) and $K_{\alpha 2}$ (54.61 keV) x-ray lines of ^{180}Hf produced by the electron-capture process of the ^{180}Ta ground state, as shown in Fig. 2.8. Prior to the exposure to the beam, a γ -ray background spectrum was obtained and is also shown. The relative efficiency of the detector was determined using a ^{241}Am source.

For the ^{115}In activation experiment, the planar detector was replaced by a standard HPGe detector for the detection of the 336.2 keV γ -ray transition depopulating the 4.49 h isomer in ^{115}In . Results are shown in Fig. 2.9. In this case the relative efficiency of the detector was determined using a mixed γ -ray source containing isotopes with energies ranging from 59.5 keV (^{241}Am) to 1836.1 keV (^{88}Y). The distance between the sample and the front face of the detector was 5 cm.

Table 2.2: Cross-section data

E_{γ} (MeV)	^{180}Ta (mb)	^{115}In (mb)
2.50	12.21 ± 1.31	0.0037 ± 0.0004
3.11	11.47 ± 1.06	0.0081 ± 0.0007

Our values for the $^{115}\text{In}(\gamma, \gamma')^{115m}\text{In}$ and $^{180}\text{Ta}(\gamma, \gamma')^{180m}\text{Ta}$ reactions are given in Table 2.1.5. They are the first ^{180m}Ta depopulation data measured with monoenergetic γ -ray beams obtained from accelerators. The previous experiments all involved bremsstrahlung beams [Bel99]. In the future we will extend our measurements to lower energies, which are more relevant to astrophysical conditions.

[Bel99] D. Belic *et al.*, Phys. Rev. Lett., **83**, 5242(R) (1999).

[Col85] C. B. Collins *et al.*, Phys. Rev. C, **42**, 1813 (1985).

[Ton00] A. P. Tonchev and J. Harmon, Appl. Rad. Isotopes, **52**, 873 (2000).

2.2 Thermonuclear Reaction Rates

2.2.1 The Impact of Reaction Rate Variations on Nucleosynthesis

K.J. KELLY, R. LONGLAND, C. ILIADIS *TUNL*

Nuclear reaction cross sections are crucial for understanding the synthesis of the elements in stars. Identifying those reactions whose cross-section uncertainties lead to ambiguities in nucleosynthesis is crucial for nuclear astrophysics. Various methods of identifying these nuclear reactions are discussed, along with their successes and drawbacks.

The goal of the experimental nuclear astrophysicist is to improve our understanding of the universe by measuring nuclear reactions that are crucial to various stellar evolution sites but are poorly known at the relevant temperatures. Perfecting a fast, reliable method for identifying these key reactions is of utmost importance.

The work of Refs. [Lon10, Ili10, Ili0b] describe a method for determining nuclear reaction-rate probability-density functions (PDFs) that vary smoothly with temperature and are typically lognormally distributed. These PDFs can then be incorporated into Monte Carlo nucleosynthesis calculations such as those described in Refs. [Lon12, Kel13, Ili15]. The rate of a reaction x at a temperature T encountered during a nucleosynthesis calculation i is written as

$$\begin{aligned} x_i(T) &= e^{\mu(T)} \times e^{\sigma(T) * p_i} \\ &= x_{med}(T) \times (f.u.(T))^{p_i}. \end{aligned} \quad (2.6)$$

The terms $x_{med}(T)$ and $f.u.(T)$ are the median rate and the factor uncertainty for a reaction and are related to the lognormal shape parameters $\mu(T)$ and $\sigma(T)$. The parameter p_i , referred as the rate variation factor, is the power to which $f.u.(T)$ is raised during a calculation. It is sampled randomly according to a normal distribution and independently for all reactions prior to each nucleosynthesis calculation. Note that p_i is constant during a calculation. The reciprocity relation between forward and reverse reaction rates is enforced in the choice of p_i 's.

The final abundances of all isotopes and the p_i values chosen for all reactions are recorded after each nucleosynthesis calculation, so that they can be plotted against one another to reveal trends between abundances and rate variations. An example of this type of plot for the Si/H elemen-

tal ratio relative to the rate variation factor for the $^{30}\text{P}(p,\gamma)^{31}\text{S}$ reaction from a calculation of a classical nova is shown in Fig. 2.10 [Kel13]. If a systematic change in a final abundance is observed with respect to the change in p_i value for a certain reaction, such as that shown in Fig. 2.10, then the uncertainty in this reaction has a strong influence on the abundance, and the reaction may need to be measured. It is important that here the reaction rate is varied within its estimated uncertainties, so that an important distinction is made between reactions that are well measured and those that are not.

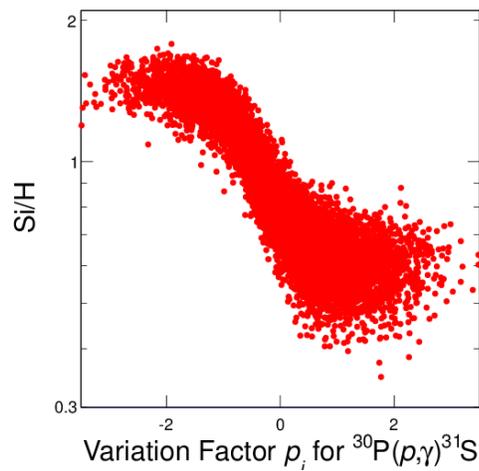


Figure 2.10: Correlation of the Si/H elemental abundance ratio to the $^{30}\text{P}(p,\gamma)^{31}\text{S}$ rate variation factor from a nucleosynthesis network calculation of a classical nova containing a $1.35 M_{\odot}$ white dwarf.

The nucleosynthesis networks used for these calculations can require hundreds of isotopic abundances and thousands of reactions, so we

cannot examine every possible correlation by hand, seeking the important ones. Therefore we have worked hard over the past several years to develop methods of identifying important abundance-reaction correlations, typically through filtering the correlation data through an algorithm to calculate a correlation coefficient indicative of the importance of the correlation.

The work of Ref. [Ili15] summarized two of the primary correlation coefficients that have been used. The Pearson coefficient r returns a number from 0 to ± 1 , indicating how well the correlation data are described by a monotonically increasing ($r > 0$) or decreasing ($r < 0$) function. For a set of k data points of the form (x, y) , this parameter is given by

$$r = \frac{\sum_k (x_k - \bar{x})(y_k - \bar{y})}{\sqrt{\sum_k (x_k - \bar{x})^2} \sqrt{\sum_k (y_k - \bar{y})^2}}. \quad (2.7)$$

The Pearson coefficient is useful for identifying linear abundance-reaction correlations, but nonlinear correlations are also common. The Spearman coefficient, r_s , is more useful in such cases. It is expressed by an equation identical in form to Eq. 2.7, but with the *rank* of x and y in place of x and y . The rank tends to linearize data and identifies most nonlinear correlations. The correlation shown in Fig. 2.10 is has $r_s = -0.86$.

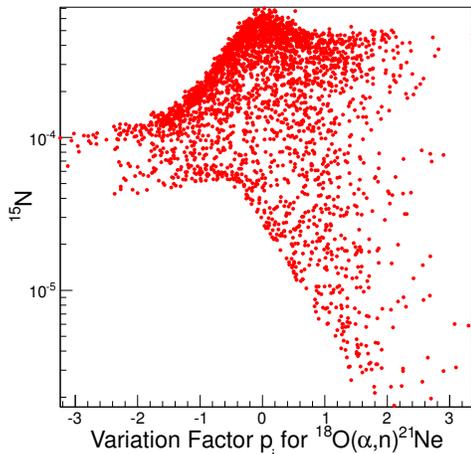


Figure 2.11: Correlation of the ^{15}N abundance from a network calculation of supernova shock-induced nucleosynthesis to the $^{18}\text{O}(p,\gamma)^{21}\text{Ne}$ rate variation factor.

Some correlations are also nonlinear in rank. For example, the correlation of the ^{15}N abundance and the rate variation factor for the $^{18}\text{O}(p,\gamma)^{21}\text{Ne}$ reaction shown in Fig. 2.11 has a $r_s = 0.05$ and is, therefore, not identified as a significant correlation even though it is clearly interesting. The most successful alternative method we have investigated is the mutual information or I

method. Mutual information is a measure of the similarity between the product of the individual x and y probability distributions, $p(x)$ and $p(y)$, and their joint distribution, $p(x, y)$. This coefficient is given by

$$I = \frac{1}{\sqrt{H(x)H(y)}} \sum_x \sum_y p(x, y) \log \frac{p(x, y)}{p(x)p(y)}, \quad (2.8)$$

where $0 < I < 1$. The H are the marginal entropies of x and y . The correlation shown in Fig. 2.11 was calculated to have $I = 0.223$, which is an indication of a significant correlation.

Nonlinear correlations can also be fairly successfully identified by simply fitting the correlation rank data to linear and polynomial trends. The ratio of their χ^2 values is another potential means of identifying important correlations that are nonlinear in rank and is given by

$$Q = \frac{\chi^2(\text{Linear Fit})}{\chi^2(\text{Polynomial Fit})}. \quad (2.9)$$

If a correlation is nonlinear, then the polynomial fit has a smaller χ^2 and Q is large. If there is no observable correlation, then both the linear and polynomial fits return equally poor χ^2 values and Q is about 1. The correlation of Fig. 2.11 was calculated to have $Q = 1.45$ and was determined as the most important correlation for ^{15}N in this calculation. A drawback of this method is that there is no maximum value for Q . All values of Q must be considered relative to one another, accepting only the largest values.

The Spearman coefficient appears to be an effective metric for finding the majority of important correlations while the Q and I correlation coefficients show potential for the identification of those that are more unique and unexpected. Further alternative methods of correlation identification are currently being investigated.

[Ili0b] C. Iliadis *et al.*, Nucl. Phys. A, **841**, 251 (2010b).

[Ili10] C. Iliadis *et al.*, Nucl. Phys. A, **841**, 31 (2010).

[Ili15] C. Iliadis *et al.*, J. Phys. G, **42**, 034007 (2015).

[Kel13] K. J. Kelly *et al.*, Astrophys. J., **777**, 130 (2013).

[Lon10] R. Longland *et al.*, Nucl. Phys. A, **841**, 1 (2010).

[Lon12] R. Longland, Astron. Astrophys., **548**, A30 (2012).

2.2.2 Statistical Methods for Thermonuclear Reaction Rates and Nucleosynthesis Simulations

C. ILIADIS, R. LONGLAND, A.E. CHAMPAGNE, *TUNL*;

Rigorous statistical methods for estimating thermonuclear reaction rates and nucleosynthesis are becoming increasingly established in nuclear astrophysics. We discuss the application of the Monte Carlo method to two related questions. First, given a set of measured nuclear parameters, how can one best estimate the resulting thermonuclear reaction rates and associated uncertainties? Second, given a set of appropriate reaction rates, how can one best estimate the abundances from nucleosynthesis calculations? The result is probability density functions for use in deriving statistically meaningful reaction rates and final abundances

Many forefront questions in astrophysics ultimately require a detailed knowledge of stellar properties, thus challenging stellar models to become more sophisticated, quantitative, and realistic in their predictive power. This requires more detailed physics input, such as thermonuclear reaction rates and opacities, plus a concerted effort to validate models through systematic observations. The study of nuclear reactions in the observable universe remains at the forefront of nuclear physics and astrophysics research.

Thermonuclear reaction rates are at the heart of every astrophysical model. Statistical methods are necessary to improve estimates of both thermonuclear reaction rates and nucleosynthesis predicted by nuclear reaction networks. Experimental reaction rates can be estimated by using a Monte Carlo method, once appropriate probability density functions are adopted for each nuclear physics input quantity [Lon10]. For example, resonance energies are best described by a Gaussian probability density, while for resonance strengths a lognormal probability density is more appropriate. Unobserved resonances of unknown strength can be easily incorporated into this framework by assuming a Porter-Thomas probability density [Pog13]. The random sampling over all nuclear input parameters produces in most cases a lognormal (output) reaction rate probability density. This function provides statistically rigorous recommended (median) reaction rates and factor uncertainties [Ili10]. The calculations are ultimately important for the design of experiments at stable beam and radioactive-ion beam facilities.

These results led directly to the construc-

tion of a next-generation nuclear reaction library, STARLIB [Sal13], containing reaction rates, uncertainties, and rate probability densities for easy implementation into reaction networks for stellar models. STARLIB contains the necessary nuclear physics information to perform Monte Carlo nucleosynthesis simulations. All reaction rates can be sampled simultaneously, except for reverse reactions, since these are related to the corresponding forward reaction rates via the reciprocity theorem. For the sampling of reaction rates, which are described by lognormal probability densities, we introduce a Gaussian random variable p_i for each reaction i . In the simplest case, it can be assumed that this *rate variation factor* is independent of temperature [Lon12]. The random factor by which a given sampled rate is modified from its median value is given by $(f.u.)^{p_i}$, which is temperature-dependent in any case through the factor uncertainty $f.u.$

The impact of reaction rate uncertainties on the abundance of a given nuclide can be assessed as follows. Scatter plots displaying the final abundance, X_f , versus the rate variation factor p_i of reaction i are useful for quantifying correlations. To illustrate these points, we will apply in the following the Monte Carlo method to Big Bang nucleosynthesis. Observations of primordial ^4He , ^2H and ^7Li abundances have reached an unprecedented level of precision. Therefore, reliable predicted abundances are needed before the observations can be confronted with theory. Such studies have interesting implications for testing standard or non-standard Big Bang models, since Big Bang nucleosynthesis represents the earliest milestone of known physics when we look back

in time. Numerous studies have shown that the predicted Big Bang abundances of the light elements, for example, ^2H and ^4He , agree with the observations. The sole exception is ^7Li , which is overproduced by a factor of three relative to observations. The ^7Li problem represents the central unsolved puzzle of nucleosynthesis in the early universe.

Results from the Monte Carlo procedure are shown in Fig. 2.12. For this network, the rates of all reactions, except for reverse reactions, are independently sampled. In other words, each rate is multiplied by a temperature-independent random variation factor p_i and thus is sampled according to a temperature-dependent lognormal probability density function. The sampling is repeated for 30,000 reaction network runs. The histogram of all 30,000 final number-abundance ratios $^7\text{Li}/\text{H}$ is displayed in the left panel of Fig. 2.12. The dashed lines represent the 16th, 50th, and 84th percentiles, which amount to $^7\text{Li}/\text{H} = 4.56 \times 10^{-10}$, 4.94×10^{-10} , and 5.34×10^{-10} , respectively. These values are based on our best estimates for the probability density functions of all reaction rates in the network. As already noted, the observations result in a factor of three smaller $^7\text{Li}/\text{H}$ ratio, indicated by the black bar in the lower part of the left panel. Thus it is unlikely that the solution of the ^7Li problem will be found in uncertain nuclear physics.

The next question is: which reaction rates have the strongest impact on the predicted $^7\text{Li}/\text{H}$ ratio? Once identified, these reactions can be subjected to further scrutiny and the experimental data can be inspected for previously unaccounted systematic effects. The Monte Carlo results presented above contain an answer to this question since the p_i value of each reaction is recorded for each of the 30,000 network calculations. The middle panel of Fig. 2.12 displays the final $^7\text{Li}/\text{H}$ ratios of all 30,000 network runs versus the sampled rate variation factors p_i , of $^3\text{H}(\alpha,\gamma)^7\text{Li}$, and the left panel shows the comparable results of $^3\text{He}(\alpha,\gamma)^7\text{Be}$. The projection of either of these scatter plots onto the ordinate results in the same histogram we just discussed. Again, the spread along the y-direction is caused by the combined uncertainties of all reaction rates in the network. The impact of a given

reaction rate on the final abundance of a given nuclide, X_f , is apparent in the scatter plot: if the variation in p_i results in a flat distribution of X_f , we can conclude that the given rate and the given abundance are uncorrelated. This is the case depicted in the middle panel. On the other hand, if the variation in p_i results in a systematic change of X_f , the given rate and the given abundance are correlated. This is the situation shown in the right panel.

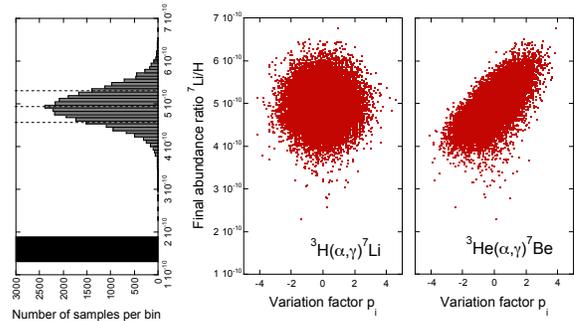


Figure 2.12: Results of a Monte Carlo study of Big Bang nucleosynthesis. (Left) Histogram of final $^7\text{Li}/\text{H}$ number abundance ratio. The observed range is indicated by the black bar. (Middle) Final $^7\text{Li}/\text{H}$ number abundance ratio versus variation factor of the $^3\text{H}(\alpha,\gamma)^7\text{Li}$ rate. (Right) Final $^7\text{Li}/\text{H}$ number abundance ratio versus variation factor of the $^3\text{He}(\alpha,\gamma)^7\text{Be}$ rate.

This work has now been published [Ili15].

- [Ili10] C. Iliadis *et al.*, Nucl. Phys., **A841**, 31 (2010).
- [Ili15] C. Iliadis *et al.*, J. Phys. G, **42**, 034007 (2015).
- [Lon10] R. Longland *et al.*, Nucl. Phys., **A841**, 1 (2010).
- [Lon12] R. Longland, Astron. Astrophys., **548**, A30 (2012).
- [Pog13] I. Pogrebnyak *et al.*, Phys. Rev. C, **88**, 015808 (2013).
- [Sal13] A. L. Sallaska *et al.*, Astrophys. J. Suppl. Ser., **207**, 18 (2013).

Nuclear Structure

• Study of Many-Body Systems

Studies of collective modes of excitation can provide information about short-ranged correlations between nucleons in nuclei and can reveal features of the nuclear equation of state. The observed dipole excitation strength in excess of the tail of the giant dipole resonance is referred to as the “pygmy dipole resonance” or PDR. The generally accepted mechanism for the PDR is the vibration of a neutron skin relative to an isoscalar core. If this picture is correct, a study of its strength as a function of isospin and target mass number should provide information about the density dependence of the symmetry energy term in the nuclear equation of state. While most of the PDR experiments at HI γ S are led by groups from Darmstadt, GSI, Dresden, Frankfurt, and Cologne, the local group has been focusing on fission research.

Although nuclear fission was discovered more than three-quarters of a century ago, research in this field is currently experiencing a renaissance. The predictive power of computer codes aimed at describing the complicated many-body physics governing the fission process has reached new levels of precision. In parallel, new neutron-induced fission experiments at TUNL are revealing unexpected phenomena. We are now also performing studies of photofission fission-product yields at HI γ S to look at the influence of the probe initiating the fission process.

The photon strength function is an important piece of information needed in nuclear science computer codes aimed at predicting neutron capture cross sections. Work on neutron-capture experiments using the DANCE detector array at LANL is ongoing.

3.1 Study of Many-Body Systems

3.1.1 The Role of Deformation on the Dipole Strength Distribution of the Pygmy Dipole Resonance: ^{154}Sm Isotope

KRISHICHAYAN, M. BHIKE, W. TORNOW, J. H. KELLEY, *TUNL*; A.P. TONCHEV, *Lawrence Livermore National Laboratory, Livermore, CA*; G. RUSEV, M. GOODEN, *Los Alamos National Laboratory, Los Alamos, NM*; D. SAVRAN, B. LÖHER, *GSI Helmholtzzentrum für Schwerionenforschung, Darmstadt, Germany*; V. DERYA, *Universität zu Köln, Köln, Germany*; N. TSONEVA, *Institut für Theoretical Physik, Germany and INRNE, Bulgaria*

The photo-response of ^{154}Sm has been investigated in the energy range below 8.0 MeV using photon scattering at the HI γ S facility. The aim is to look at the role of deformation on the dipole strength distribution of the pygmy dipole resonance. Our detector configuration, consisting of four LaBr $_3$ (Ce) detectors in addition to four HPGe detectors, enables us to distinguish between E1, M1, and E2 strength. Detailed efficiency measurements for the LaBr $_3$ (Ce) detectors were carried out and compared with Monte Carlo simulations

In stable and closed-shell nuclei, a resonance-like concentration of dipole strength is observed at excitation energies below the neutron separation energy. This clustering of strong dipole transitions has been named the pygmy dipole resonance (PDR). These excitations manifest themselves as a pronounced concentration of dipole strength on the tail of the giant dipole resonance (GDR).

In hydrodynamic and collective approaches, it was suggested that an oscillation of a small portion of neutron-rich nuclear matter relative to the rest of the nucleus is responsible for the generation of pygmy resonances. From the analysis of transition densities, the unique behavior of the PDR mode is revealed, making it distinct from the well-known GDR. Systematic studies of the PDR over isotonic and isotopic chains of nuclei indicate a correlation between the observed total $B(\text{E1})$ strength of the PDR and the neutron-to-proton ratio N/Z in the nucleus [Tso08].

The existence of the PDR mode below the neutron threshold also has important astrophysical implications. For example, the rates of the (γ, n) and (n, γ) reactions in the explosive nucleosynthesis of certain neutron-deficient heavy nuclei may be significantly enhanced by the PDR [Arn03].

Furthermore, for very neutron-rich exotic nuclei, the PDR is an important topic of study at the new generation of radioactive ion beam fa-

ilities. Up to now, however, this nuclear structure phenomenon has only been observed in semi-magic nuclei with closed, spherical neutron shells (the $N = 82$ and $N = 50$ isotones) or close to such shells. In the present work, we extended our investigation to examine the PDR in nuclei that have constant deformation in their ground states in order to understand the role of deformation on the fragmentation of the PDR strength and its evolution when ones moves away from the closed shell. The samarium isotopes with atomic numbers 144, and 154 are the main targets of interest.

The samarium chain provides a long series of isotopes with varying properties. The nuclide ^{144}Sm has 82 neutrons and is a good example of a spherical nucleus. Its GDR is fit well with a single Lorentz line. On the other hand, ^{154}Sm has two peaks, which is characteristics of a deformed nucleus, where the deformation splits the GDR into two bumps [Ton98]. The nuclei in between have giant resonances that display various undulations and bumps, with the giant resonance becoming wider as the nuclear surface is softened by the addition of neutrons. Calculations using the quasi-particle random-phase approximation (QRPA) [Dan07] have predicted that deformed nuclei display an enhanced E1 strength at lower energies compared to the corresponding strength distribution in spherically shaped nuclei. In these calculations, whose results are shown in Fig. 3.1,

the nuclear shape was considered as an extra parameter in addition to the size of the neutron skin.

During our previous measurements with a ^{144}Sm target, we faced two experimental challenges. First, no discrete transitions “survived” when the photon excitation energy exceeded 5.5 MeV, and second, unresolved strength at high excitation energy was difficult to measure due to the relatively low-efficiency of the HPGe detectors.

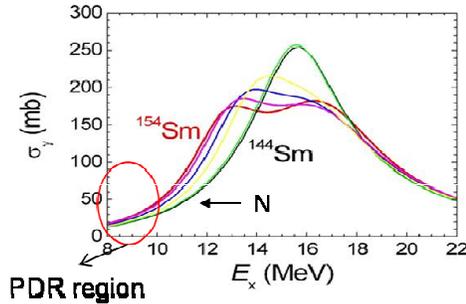


Figure 3.1: Evolution of the GDR for all samarium isotopes calculated using the QRPA model.

Therefore we employed a new experimental approach in our nuclear-resonance-fluorescence measurement on ^{154}Sm . In addition to the four 60% HPGe detectors used in the past, the experimental setup includes four lanthanum bromide, $\text{LaBr}_3(\text{Ce})$, detectors, which have high efficiency at higher energies. These detectors were mounted at three different angles with respect to the linearly polarized photon beam, at horizontal, vertical, and backward angles. This configuration allows us to distinguish between E1, M1, and E2 strength. Quasi-monochromatic and 100% linearly polarized photon beams were provided by

the HI γ S facility at TUNL. A 123% efficient (relative to a standard 3” \times 3” NaI detector) coaxial HPGe detector was placed downstream of the target position in order to measure the energy distribution of the beam. During beam-profile measurements, the beam was attenuated by a series of copper absorbers mounted upstream.

Detailed efficiency measurements for the $\text{LaBr}_3(\text{Ce})$ detectors were performed and compared with Monte Carlo simulations. Fig. 3.2 depicts the efficiency plot for one of these detectors.

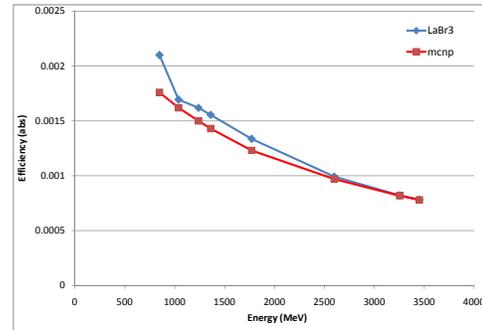


Figure 3.2: Measured efficiency data for one of our $\text{LaBr}_3(\text{Ce})$ detectors, compared with MCNP simulations.

-
- [Arn03] M. Arnould and S. Goriely, Phys. Rep., **384**, 1 (2003).
- [Dan07] F. Danau *et al.*, Phys. Rev. C, **76**, 014317 (2007).
- [Ton98] A. P. Tonchev *et al.*, Phys. Rev. C, **58**, 2851 (1998).
- [Tso08] N. Tsoneva and H. Lenske, Phys. Rev. C, **77**, 024321 (2008).

3.1.2 The energy dependence of Fission Product Yields from neutron-induced fission of ^{235}U , ^{238}U and ^{239}Pu

W. TORNOW, M. BHIKE, B.F. FALLIN, S.W. FINCH, C.R. HOWELL, KRISHICHAYAN, *TUNL*; M.E. GOODEN, M.M. FOWLER, D.J. VIEIRA, J.B. WILHELMY, *Los Alamos National Laboratory, Los Alamos, NM*; M.A. STOYER, A.P. TONCHEV, *Lawrence Livermore National Laboratory, Livermore, CA*

Data acquisition and analysis on the fission product yields of ^{235}U , ^{238}U , and ^{239}Pu have continued in this reporting period. After completion of the first phase of measurements, focusing on incident neutron energies below 4 MeV, measurements of the second phase have been carried out at 4.6 MeV and 5.5 MeV, and measurements at 7.5 MeV are planned for 2016. The goal is to learn more about the energy dependence of the fission product yields when the second chance fission threshold is approached and exceeded.

Fission studies relate the yields and kinetic energies of fission products to the potential energy surface of the compound nuclear system. The evolution of the fissioning system from the initial particle impact, through intermediate saddle points to scission, and finally to separated fission fragments is governed by a series of complicated phenomena. At low excitation energies, shell and pairing effects influence both the mass and energy distributions. As a result, detailed nuclear structure information is needed to describe fission data in this energy range. At excitation energies well above the fission barrier, shell and pairing effects are washed out and the liquid drop model is well suited to describe experimental data. The second chance fission process ($n, n'f$), which provides an increase in the total fission cross section, plays a crucial role, because it is governed by a combination of both scenarios. Therefore, there is considerable interest from the theory communities at LANL and LLNL to investigate fission in the 5 to 8 MeV neutron energy range in order to fine-tune their fission codes.

The energy dependence of the fission product yields (FPYs) has considerable impact on both fundamental and applied physics. Although our ongoing FPY studies are primarily performed and supported with a focus on applied physics, it has been our goal from the very beginning to also provide data for fundamental physics applications, ranging from r -process nucleosynthesis in astrophysics to the so-called reactor anti-

neutrino anomaly.

The $^2\text{H}(d, n)^3\text{He}$ reaction has been used to produce monoenergetic neutrons at 4.6 and 5.5 MeV. Our standard dual fission chambers [Bha14], each dedicated for one of the three actinide isotopes, were used. After irradiation for approximately five days, the γ rays from the actinides samples were counted for six to eight weeks to identify and measure the yield of the fission products of interest.

Typical γ -ray spectra obtained from a ^{239}Pu sample before and after irradiation are shown in Fig. 3.3 where some of the fission products of interest are indicated. Note the high background for this actinide. In comparison, the background yield is much smaller for ^{235}U and is almost negligible for ^{238}U .

Figure 3.4 shows our results for the FPY of ^{147}Nd produced in neutron-induced fission of ^{239}Pu in the energy range between 0.5 and 14.8 MeV. Unlike ^{235}U and ^{238}U , for which the FPY is independent of incident neutron energy or exhibits a small negative slope at low energies, the important fission fragment ^{147}Nd shows a currently unexplained positive slope up to 3.5 MeV, before the slope turns negative at higher energies. Analysis of the ^{235}U and ^{238}U data obtained at 5.5 MeV is ongoing.

[Bha14] C. Bhatia *et al.*, Nucl. Instrum. Methods A, **757**, 7 (2014).

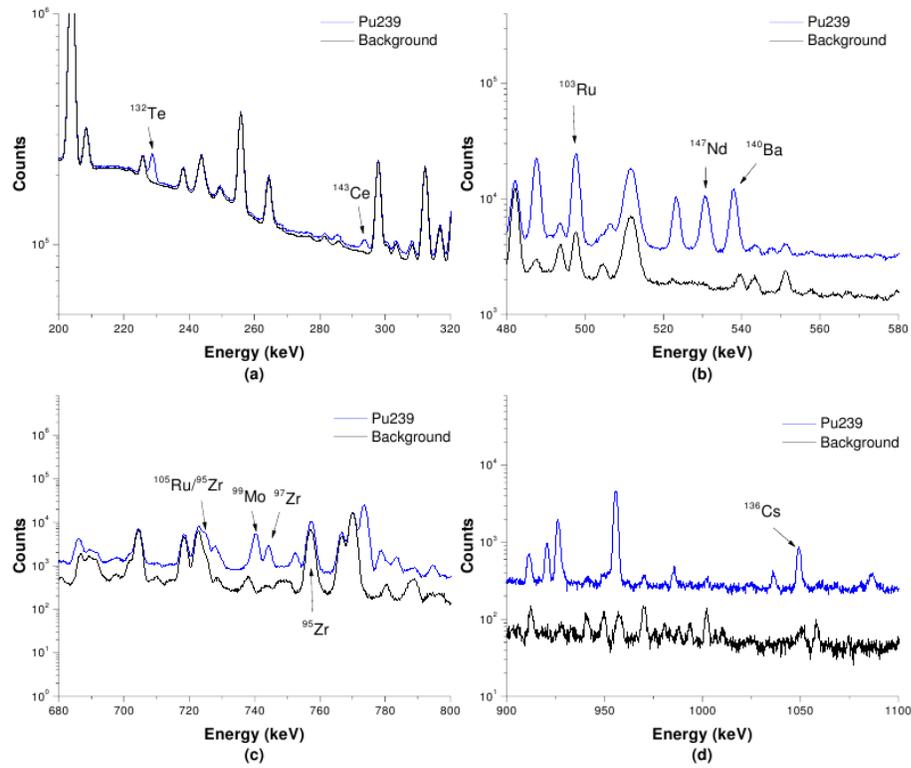


Figure 3.3: Various energy regions of the γ -ray spectrum from ^{239}Pu approximately four days after irradiation. The corresponding live-time-normalized background data, taken prior to irradiation, are also shown. Relevant fission products in each region are labeled.

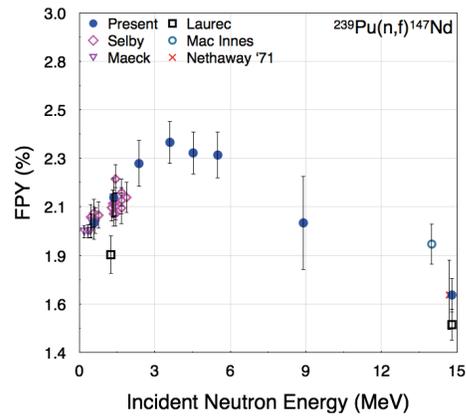


Figure 3.4: Present data along with existing literature data for ^{147}Nd from the fission of ^{239}Pu

3.1.3 Fission Product Yields Using Mono-Energetic Photon Beams at 13 MeV

KRISHICHAYAN, M. BHIKE, W. TORNOW, *TUNL*; A.P. TONCHEV, *LANL*

Fission product yields (FPYs) of ^{239}Pu , ^{235}U , and ^{238}U were measured for the first time using monoenergetic photon beams. The targets were irradiated for sixty hours at $E_\gamma = 13.0$ MeV, and the FPYs were determined by measuring and analyzing their γ -ray spectra. The data will provide a unique comparison with the results of neutron-induced FPY measurements. They hopefully will yield an important understanding of this fundamental process.

Nuclear fission is a complex process in which the collective motion of nucleons results in a large change in the shape of the nucleus, the formation of nucleon configurations, and the redistribution of internal energy between the different degrees of freedom. Of special interest are measurements of the yields of the fission products. These measurements are an important source of information on the evolution and break-up of the nucleus during the fission process.

the absence of a binding energy and Coulomb barrier. Consequently, the nuclear excitation energy corresponds to the energy of the absorbed photon. This gives rise to the unique possibility of studying nuclear fission at low excitation energies, just above the fission barrier but below the neutron binding energy.

Figure 3.5 shows the fission cross sections for ^{239}Pu , ^{235}U and ^{238}U obtained from the NNDC database [Nat]. The cross sections peak at around 14 MeV. We plan to carry out fission-product-yield measurements on ^{239}Pu , ^{235}U and ^{238}U using mono-energetic photon beams from TUNL's HI γ S facility at incident energies of 9, 11, and 13 MeV to compare to existing TUNL data for neutron-induced fission in the same excitation-energy range.

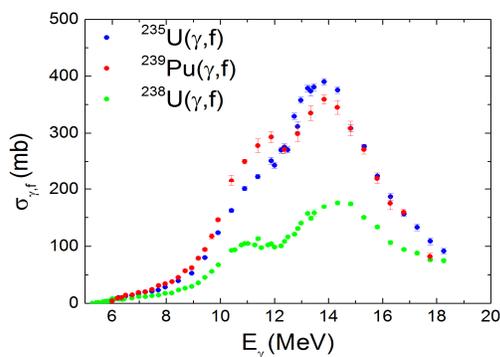


Figure 3.5: Plot of the experimental photo-fission cross section of ^{239}Pu , ^{235}U and ^{238}U as a function of incident photon energy.

The use of the well understood electromagnetic probe to study fission offers significant advantages over hadron-based reactions. First, unlike reactions with neutrons and charged particles, the same angular momentum (one or, with much smaller probability, two units) is transferred to the nucleus over a wide range of photon energies. Another property of photon probes is

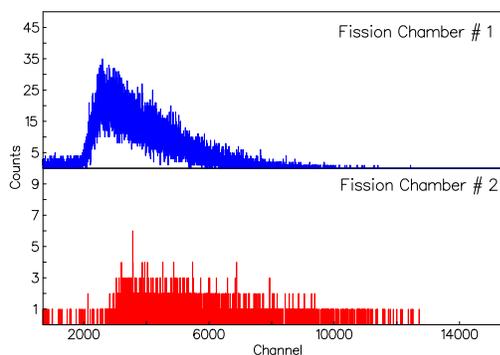


Figure 3.6: Fission spectra measured with a dual-fission chamber for monitor foils of ^{235}U (upper panel) and ^{239}Pu (lower panel).

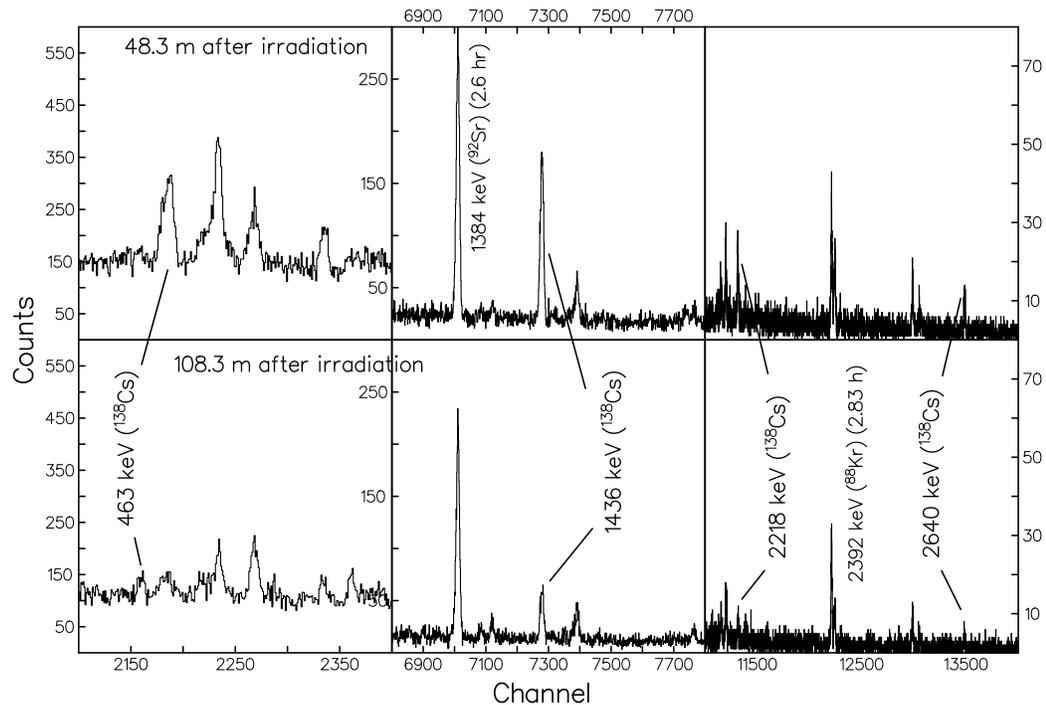


Figure 3.7: Spectra showing γ -ray lines from the decay of the fission fragment ^{138}Cs , with a half-life = 33.41 minutes. The upper panels show the data collected 48.3 minutes after the end of irradiation of the ^{238}U target; the lower panels give the data taken 108.3 minutes after the end of irradiation.

In order to quantify the number of fissions that occur during irradiation of the target samples, a specially fabricated dual-fission ionization chamber [Bha14] was used. A thin monitor foil of ^{235}U was placed in chamber 1, with a similar foil of ^{239}Pu in chamber 2. Figure 3.6 shows online the spectra obtained with the dual-fission chamber. The accumulated data will be used to quantify the total number of fission events occurring during irradiation. After sixty hours of irradiation, γ rays from the three target samples (^{235}U , ^{238}U , and ^{239}Pu) were counted at TUNL's low-background counting facility. A typical γ -ray

spectrum for the ^{238}U target is shown in Fig. 3.7, where decay lines from ^{138}Cs fission fragments are clearly seen, having a half-life of 33.41 minutes.

Data analysis for over twenty fission products is in progress.

[Bha14] C. Bhatia *et al.*, Nucl. Instrum. Methods A, **757**, 7 (2014).

[Nat] National Nuclear Data Center, <http://www.nndc.bnl.gov>.

3.1.4 γ -Ray Induced Fission-Product Yield of ^{239}Pu at 11 MeV

M. BHIKE, KRISHICHAYAN, W. TORNOW, *TUNL*; A. P. TONCHEV *Lawrence Livermore National Laboratory, Livermore, CA*

The yield of important fission products from neutron-induced fission of ^{239}Pu were previously found to vary with the incident neutron energy. This surprising result motivated a study of the photo-fission of ^{239}Pu at the same range of excitation energies. The cumulative fission yields of eight fission products from photo-fission of ^{239}Pu at 11 MeV have now been obtained using the activation technique and a mono-energetic γ -ray beam from the HI γ S facility. These fission-product yield data are the first ever obtained with mono-energetic γ rays.

Owing to the difficulty of performing photo-fission experiments, especially with monoenergetic photons, very little detailed and systematic data have been reported in the literature. Following the unexpected observation of a neutron energy dependence of important high-yield fission products obtained from neutron-induced fission of ^{239}Pu between 0.6 and 14 MeV [Goo15], a program was initiated to study photo-fission in the same excitation energy range in the corresponding intermediate nuclei ^{240}Pu for $^{239}\text{Pu}(n,f)$ and ^{239}Pu for $^{239}\text{Pu}(\gamma,f)$.

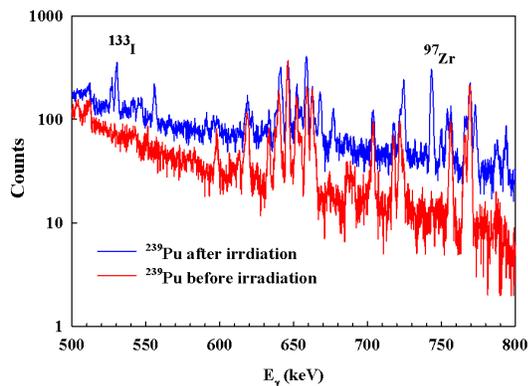


Figure 3.8: Portion of a typical γ -ray spectrum at $E_\gamma = 11$ MeV.

The photo-activation of ^{239}Pu was conducted using TUNL's High Intensity Gamma-Ray Source (HI γ S). The ^{239}Pu target was provided by Los Alamos National Laboratory. The target was 1.24 cm in diameter with a mass of 0.238 g. It was sandwiched between gold foils with the same diameter and a thickness of 0.01 cm. The gold foils served for γ -ray flux determi-

nation based on the $^{197}\text{Au}(\gamma,n)^{196}\text{Au}$ reaction of known cross section. The target assembly was irradiated for about nine hours with approximately 10^7 $\gamma/\text{cm}^2\text{s}$. The energy spread of the 11.0 MeV γ -ray beam was approximately 150 keV FWHM. A 1/2 inch lead collimator six inches long was used.

After activation, the induced γ -ray activity from the fission products in the ^{239}Pu was counted over a period of two months using a number of different counting cycles, ranging from minutes to days. HPGe detectors in TUNL's low-background counting facility were used for the activated ^{239}Pu target and the gold monitor foils. Both the plutonium and gold samples were counted in acrylic holders at 5 cm distance from the front faces of the detectors. To reduce the high dead time from the inherent radioactivity of the Pu sample, 1.1 mm of Cd was placed inside of the acrylic holder facing the HPGe detector. The cadmium helped to reduce the rate of low energy γ rays while leaving the higher energy lines of interest basically unaffected.

An energy slice of a typical HPGe detector spectrum containing the fission products ^{133}I and ^{97}Zr is shown in Fig. 3.8. Here the lower curve was obtained before irradiation and the upper curve after irradiation. The curves have been normalized to the same counting time. The γ -ray spectra were processed using the peak-fitting program TV [The93]. Extensive background γ -ray spectra were measured in the same counting geometry to check for interferences in the region of interest.

The decay curve for each fission fragment was plotted to ensure that there were no interfering transitions. The decay curve for ^{97}Zr is shown in

Fig. 3.9.

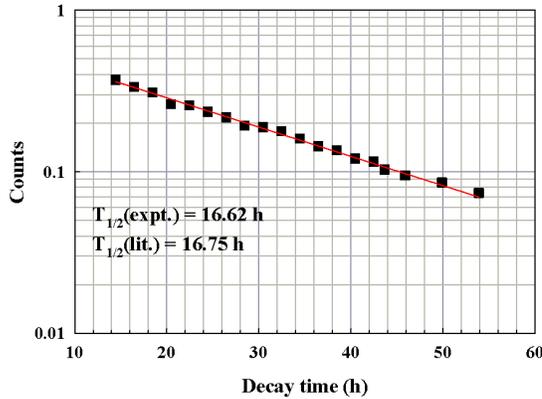


Figure 3.9: Measured decay curve for ^{97}Zr obtained from fission of ^{239}Pu at $E_\gamma=11$ MeV.

In this exploratory experiment, we have identified eight fission fragments: ^{91}Sr , ^{94}Y , ^{97}Zr , ^{99}Mo , ^{133}I , ^{136}Cs , ^{142}La , and ^{143}Ce . The cumulative fission-product yields have been determined for these fission fragments and are given in Table 3.1.4. In general, these yields agree fairly well with those obtained from neutron-induced fission of ^{239}Pu . A detailed comparison is in progress.

Table 3.1: Fission product yields (FPY) from 11 MeV γ -ray induced fission on ^{239}Pu .

Fission Product	FPY (%)
^{91}Sr	4.15 ± 0.51
^{94}Y	4.54 ± 0.57
^{97}Zr	7.97 ± 0.92
^{99}Mo	5.13 ± 0.61
^{133}I	9.89 ± 1.17
^{142}La	3.88 ± 0.33
^{143}Ce	2.61 ± 0.30

In the future, data will be obtained at lower and higher γ -ray energies with considerably improved statistical accuracy. Irradiation times of one hundred hours are planned. In the near future, data will be obtained simultaneously for the three actinides ^{235}U , ^{238}U and ^{239}Pu at 13 MeV, followed by a run at 9 MeV γ -ray energy.

[Goo15] M. Gooden *et al.*, submitted to Nucl. Data Sheets, (2015).

[The93] J. Theuerkauf, In *Program TV, Institute for Nuclear Physics, University of Cologne (unpublished)*, 1993.

3.1.5 Mono-Energetic Photon-Induced $^{235}\text{U}/^{239}\text{Pu}$ Fission Cross-Section Ratio Measurements at 8 to 17 MeV

KRISHICHAYAN, S. FINCH, C.R. HOWELL, W. TORNOW, *TUNL*; A.P. TONCHEV, *Los Alamos National Laboratory, Los Alamos, NM*

We have performed the first measurements of the photofission cross-section ratio of $^{235}\text{U}/^{239}\text{Pu}$ that uses mono-energetic photons and a specially fabricated dual-fission ionization chamber. Preliminary results are compared with previous measurements and evaluations.

Nuclear fission is a complex process in which the collective motion of nucleons results in a large change in the shape of the nucleus, the formation of nucleon configurations, and the multiple redistribution of internal energy between the different degrees of freedom. Of special interest in fission studies are measurements of the fission cross sections. The advantages of photon-induced fission over neutron-induced fission are discussed in Sect. 3.1.3.

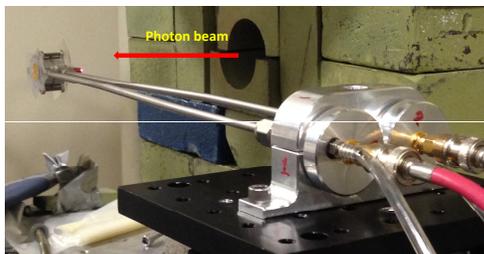


Figure 3.10: The dual-fission ionization chamber used in the present experiment.

Cross-section measurements for photon-induced fission of the actinides have been one of the priorities of several laboratories during the last sixty to seventy years. These measurements used a variety of γ -ray sources, including bremsstrahlung sources, annihilation in flight of positrons, and neutron capture γ rays. Each source had its own limitations. In the present work, we have utilized mono-energetic and circularly polarized photon beams provided by the HI γ S facility at TUNL. The principal component

in obtaining accurate fission cross-section data is the quantitative determination of the number of fissions which occur in the target. To accomplish this, a specially fabricated dual-fission ionization chamber (DFC) [Bha14] was used. It is shown in Fig. 3.10. In its original form, this DFC contains a thick activation target and two thin reference foils of the same isotope. It has been used to measure fission-product yields with incident neutrons. In the present investigation, the thick target was not used, and reference foils of ^{235}U and ^{239}Pu were placed in fission chambers 1 and 2, respectively. By taking the ratio of the number of fission events in each chamber, we do not need to know the γ -ray flux, as the two chambers see the same flux. Typical pulse height fission spectra produced by the two reference foils are shown in Fig. 3.6 in Sect. 3.1.3.

From the number of fission events, for each beam energy, the fission cross-section ratio for $^{235}\text{U}/^{239}\text{Pu}$ was deduced, and the results are shown in Fig. 3.11. Also shown in this figure are the cross-section ratios determined from the measurements of Caldwell [Cal80] and Bowman [Bow64] on ^{235}U and of Berman [Ber86] on ^{239}Pu , using different experimental techniques.

[Ber86] B. Berman *et al.*, Phys. Rev. C, **34**, 2201 (1986).

[Bha14] C. Bhatia *et al.*, Nucl. Instrum. Methods A, **757**, 7 (2014).

[Bow64] C. Bowman, G. Auchampaugh, and S. Fultz, Phys. Rev. C, **133**, B676 (1964).

[Cal80] J. Caldwell *et al.*, Phys. Rev. C, **21**, 1215 (1980).

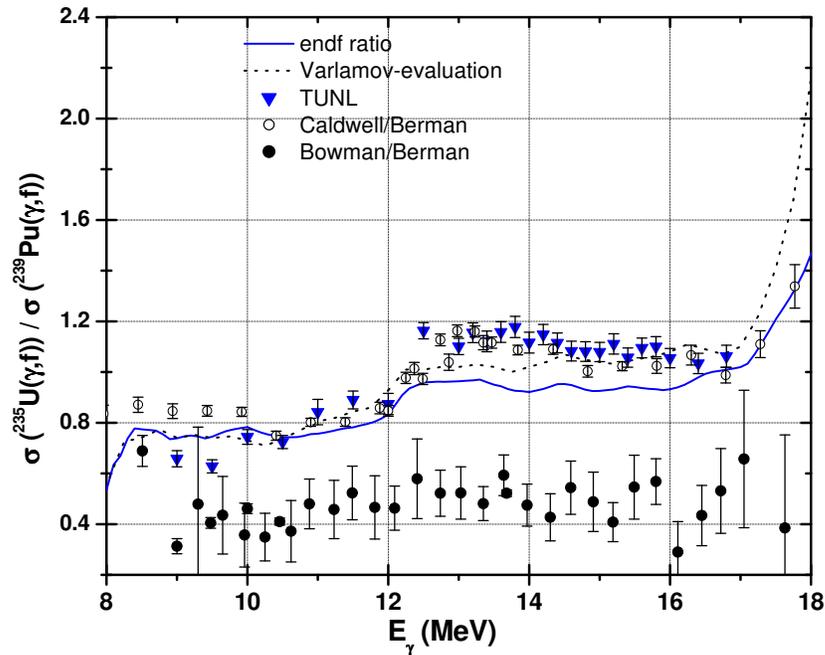


Figure 3.11: The $^{235}\text{U}/^{239}\text{Pu}$ fission cross section ratio values compared with the literature data.

3.1.6 Neutron-Capture Experiments

G.E. MITCHELL, B. BARAMSAI, A. CHYZH, C.L. WALKER, *TUNL*; OTHERS, *Charles University, Prague and Rez Institute of Nuclear Physics, Rez, Czech Republic; Los Alamos National Laboratory, Los Alamos, NM; Lawrence Livermore National Laboratory, Livermore, CA*

Our measurements of neutron-capture reactions are performed with the DANCE detector array—a highly efficient calorimeter consisting of 160 BaF₂ detectors. The high degree of segmentation is used to perform neutron resonance spectroscopy. Several new methods have been developed to determine resonance spins from the multiplicity distributions. The study of the statistical γ -ray cascade from different resonances and for different multiplicities provides unique opportunities to test models of the photon strength function.

Our primary research efforts emphasize neutron-capture reactions measured with the Detector for Advanced Neutron Capture Experiments (DANCE) located at the Los Alamos Neutron Science Center (LANSCE) at LANL. We focus on nuclei that are important for applied science as well as for nuclear structure. Much of the support for this work comes from an NNSA Academic Alliances grant.

DANCE is an array of 160 barium fluoride crystals. This calorimeter identifies capture by the total γ -ray energy. The high efficiency of

the calorimeter means that measurements can be made with very small targets. The capture cross sections for specific nuclei are valuable for stewardship science, for advanced-fuel-cycle calculations, and for nuclear astrophysics. The primary nuclear structure interest is in the photon low-energy collective excitations, namely the scissors mode and pygmy resonances. Specifically, we use the properties of the γ -ray cascade from isolated neutron resonances to determine resonance quantum numbers and properties of the photon strength function.

We use the computer program DICEBOX, developed by our Prague collaborators, to model the γ -ray spectrum for all multiplicities. We vary the photon strength functions in order to obtain the best agreement with experiment. Thus our approach is a trial-and-error method, not a unique best fit approach.

Thus far we have measured ^{89}Y , $^{94,95,97}\text{Mo}$, $^{117,119}\text{Sn}$, $^{151,153}\text{Eu}$, $^{152,154,155,156,157,158}\text{Gd}$, and $^{161,163}\text{Dy}$. Our immediate project for late 2015 is the measurement of ^{166}Er . We have collaborated on measurements of ^{87}Sr both with the DANCE array and with the neutron time-of-flight (nTOF) system at CERN. We have finished the analysis of ^{89}Y , $^{94,95}\text{Mo}$, and the europium and gadolinium isotopes. Preliminary analysis of the $^{161,163}\text{Dy}$ and the $^{117,119}\text{Sn}$ data has been completed; final analysis is in progress. A paper on the ^{97}Mo data has been accepted by Phys. Rev. C. A proposed experiment on ^{166}Er has been submitted for the next WNR run cycle.

Detailed agreement with the extreme statistical model was obtained for neutron capture on ^{95}Mo . This was verified by a separate measurement of the two-step cascade at the Institute of Nuclear Physics, Rez, Czech Republic. Of particular interest is the behavior of the scissors-mode resonance as a function of mass and deformation in the gadolinium isotopes. Analysis of the γ -cascade data in the gadolinium isotopes led to the clear conclusion that scissors-mode resonances are built not only on the ground state, but also on excited levels in all product nuclei studied, thus confirming the Brink hypothesis. Also there appears to be evidence for an odd-even effect of the strength of the scissors mode. Study of the ^{166}Er is an attempt to clarify this situation.

We have also collaborated with the nTOF group at CERN. They have used their nTOF

calorimeter to study the same strontium target that was used for the DANCE measurement. In addition to providing detailed spectroscopic information, this measurement will enable a direct comparison of the relative merits of the two most advanced calorimeters for neutron-capture measurements.

Analysis of the particle strength functions (PSFs) in the rare earth mass region has led to conflicting results between experiments at Oslo, Dresden and Los Alamos. The status of the PSFs in this region is still in a state of flux.

Our work on the resonance parameters has been much more clear-cut. In favorable cases, the average multiplicity of the γ -ray decay is sufficient to determine the spin of an s -wave resonance. In general, however, it is necessary to perform a detailed analysis of the multiplicity distribution. One method that we have developed [Bar12] involves pattern recognition theory. This method works for well-isolated resonances but is inconclusive for doublets. In collaboration with our colleagues from Prague, we have developed an alternate method that adopts prototype multiplicity distributions for resonances with known spin, and decomposes the experimental cross section into cross sections for the separate spins. This approach is basically a generalization of early empirical methods. This method [Bec11] works well even for doublets, but provides no quantitative measure of the assignment's correctness. In practice we utilize a combination of the two methods.

[Bar12] B. Baramsai *et al.*, Phys. Rev. C, **85**, 024622 (2012).

[Bec11] F. Becvar *et al.*, Nucl. Instrum. Methods, **647**, 73 (2011).



CHRISTIAN WHITE, A GRADUATE STUDENT AT NC STATE, IS ATTACHING THERMOMETRY IN PREPARATION FOR A 3 K TEST OF A CRYOGENIC GAS-GAP HEAT SWITCH FOR THE NEUTRON EDM EXPERIMENT.

Fundamental Symmetries in the Nucleus

Chapter 4

- The Neutron Electric Dipole Moment
- Fundamental Coupling Constants

The Fundamental Symmetries and Neutrinos chapter of the 2015 Long Range Plan for Nuclear Science focuses on four key questions, “for which nuclear science brings a unique arsenal of experimental and theoretical expertise and tools: *What are the absolute masses of neutrinos, and how have they shaped the evolution of the universe?; Are neutrinos their own antiparticles?; Why is there more matter than antimatter in the present universe?; and What are the unseen forces that disappeared from view as the universe expanded and cooled?*.” TUNL’s major initiatives directed towards addressing these questions are discussed in this and the following chapter.

In fundamental symmetries, a major TUNL effort has been in the U.S.-led search for a neutron EDM. It will be located at the Spallation Neutron Source at Oak Ridge National Laboratory and aims for a hundred-fold improvement in sensitivity, potentially opening a path towards major discoveries in the 10–50 TeV range. This effort will address the questions of the origin of matter and the nature of new forces in the early universe. Over the past year, work has continued in a number of areas necessary for the transition from R&D work to construction of the apparatus.

Smaller-scale precision-measurement experiments also probe electroweak interactions. These measurements are important for example in astrophysics, where uncertainties in the axial-vector coupling (G_A) influence predictions of the p - p solar neutrino flux, and in beyond-the-Standard-Model physics, where new scalar or tensor interactions could be revealed through β -decay correlation studies. In Big Bang nucleosynthesis, the neutron-to-proton conversion rate set by the neutron lifetime competes with the Hubble rate to determine the primordial ${}^4\text{He}$ abundance. Finally, fundamental symmetry violations in the lepton sector would have implications on our current understanding of particle interactions. TUNL has active programs probing many of these areas of physics.

4.1 The Neutron Electric Dipole Moment

4.1.1 Search for the Electric Dipole Moment of the Neutron

M.W. AHMED, R.E. BULLARD, H. GAO, R. GOLUB, D.K. FRAME, D.G. HAASE, P.R. HUFFMAN, E. KOROBKINA, K. LEUNG, K.M. LIVELY, A.R. REID, J.R. ROWLAND, S. SOSOTHIKUL, C.M. SWANK, C.R. WHITE, A.J. WITCHGER, A.R. YOUNG, *TUNL*; THE nEDM COLLABORATION

TUNL plays a major role in the development of an experiment to measure the neutron electric dipole moment. As part of this experimental program, we are helping develop a new technique that holds the promise of improving the sensitivity by up to two orders of magnitude over existing measurements. During the past year, TUNL researchers have measured the UCN storage times in full-sized measurement cells; continued efforts on geometric-phase-effect studies; developed components such as a heat switch and cryogenic clamp for the PULSTAR systematic studies apparatus; developed components for the larger nEDM experiment such as cryogenic neutron entrance windows; and collaborated on efforts to optimize light collection in the nEDM apparatus.

The nEDM experiment aims to set an upper limit on the static electric dipole moment of the neutron that is two orders of magnitude below the current limit of 3×10^{-26} e cm. Such a limit would place strong constraints on possible physics beyond the Standard Model and could shed new light on the origin of the matter/antimatter asymmetry in the universe. As such, it has been stated to be of “highest priority” by the Nuclear Science Advisory Committee (NSAC), in both the 2007 Long Range Plan and in the 2014 NSAC neutron physics subcommittee. A noted strength of the nEDM experiment is the control of systematic effects and the ability to make two systematically independent measurements using the precession and dressed spin modes.

The current conceptual design is shown in Figs. 4.1 and 4.2. A value (or limit) for the neutron EDM will be extracted from the difference between neutron spin-precession frequencies for parallel and anti-parallel magnetic fields of about 30 mGauss and electric fields of about 75 kV/cm. This experiment, based on the proposal by Golub and Lamoreaux [Gol94], uses a polarized ^3He comagnetometer and will detect the neutron precession via spin-dependent neutron capture on ^3He . A high density of trapped ultracold neutrons is produced via phonon production in superfluid ^4He , which can also support large electric fields.

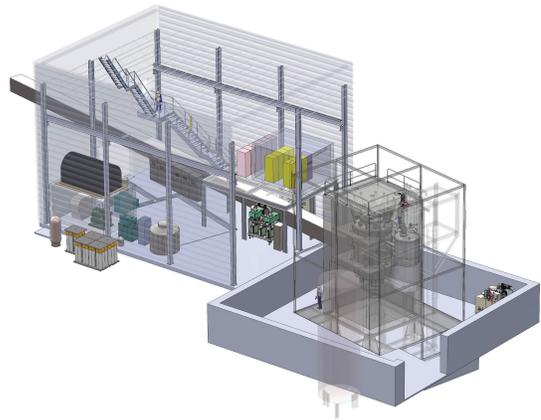


Figure 4.1: Engineering design of the nEDM apparatus when located in the external buildings at the Spallation Neutron Source at Oak Ridge National Laboratory.

TUNL researchers continue to play an active role in all aspects of the nEDM experiment. Crucial to the initial development of this project was our involvement in the continued research and development work of key components of the overall experiment. Much of this work will continue, with our primary effort now focused on addressing a number of outstanding issues related to maximizing the sensitivity of the measurement. The key component is the development of an apparatus that will enable smaller-scale tests of

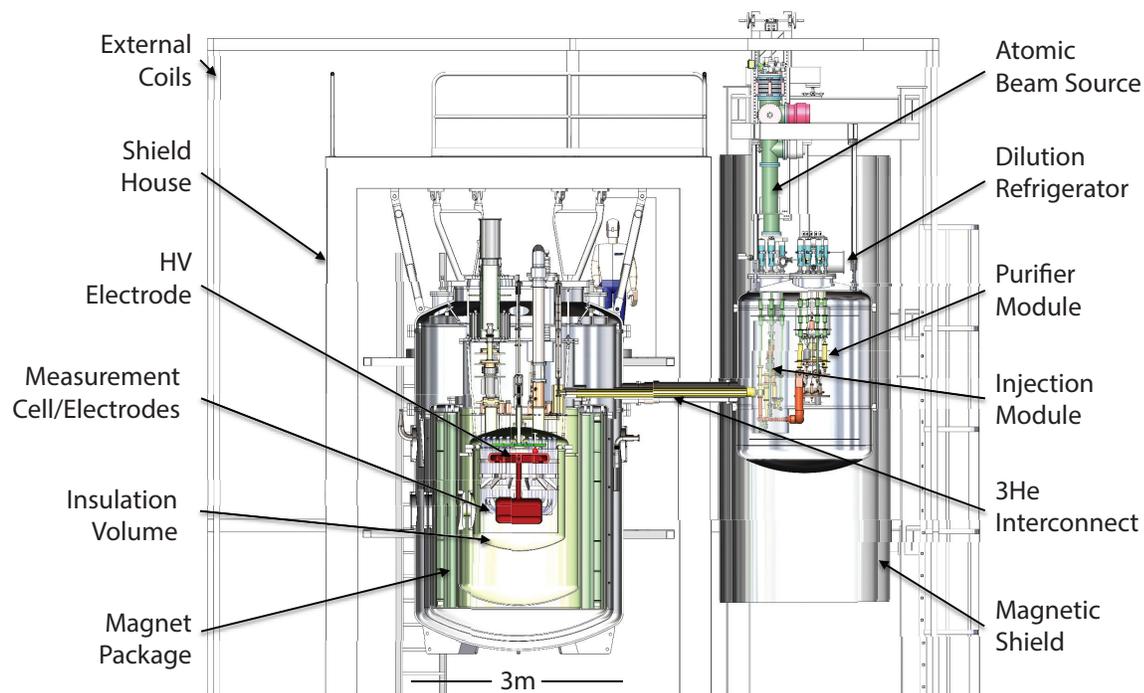


Figure 4.2: Cross sectional view of the nEDM apparatus. The neutron beam enters from the left and is down-scattered in liquid helium to produce ultracold neutrons that are confined within the measurement cells. The cells are positioned within a strong electric field and weak magnetic field. The cells are surrounded by about 1,500 l of liquid helium housed in a composite vessel. The ^3He system and central volume are cooled to below 500 mK with a $^3\text{He}/^4\text{He}$ dilution refrigerator.

key systematic effects using both polarized ultracold neutrons (UCNs) and polarized ^3He . These measurements will utilize the PULSTAR UCN source, located on the campus of NC State University and soon come online, as well as the existing polarized ^3He capabilities at TUNL.

The upcoming sections provide additional details on many of the scientific aspects of TUNL's involvement in nEDM. Sect. 4.1.2 overviews the design and development of the systematic studies apparatus while Sects. 4.1.3, 4.1.4, 4.1.5, and 4.1.6 provide details on testing and development of specific cryogenic components for this apparatus. Sect. 4.1.7 describes the UCN storage lifetime measurements made in collaboration with Los Alamos National Laboratory and Sect. 4.1.5 overviews development activities for the larger-scale nEDM effort. Sect. 4.1.9 describes the development of the UCN source at the PULSTAR

reactor facility on the campus of N.C. State.

In addition to the research outlined above, several TUNL faculty serve in leadership roles in the project. Golub serves as a principal scientist; Golub and Huffman co-chair the internal technical committee and serve on the project's executive committee; Haase, Korobkina and Huffman serve as subsystem managers for the construction of the cryovessel, the systematic studies apparatus, and for the assembly and commissioning of the subsystems, respectively; and Huffman serves on the federal project team as the project's technical coordinator and deputy project manager. Several others serve as work-package managers for components of the subsystems.

[Gol94] R. Golub and S. K. Lamoreaux, *Phys. Rep.*, **237**, 1 (1994).

4.1.2 Development of a Systematic-Studies Apparatus for the nEDM Experiment

H. GAO, R. GOLUB, D.G. HAASE, P.R. HUFFMAN, E. KOROBKINA, K. LEUNG, A.R. REID, S. SOSOTHIKUL, C.M. SWANK, C.R. WHITE, A.J. WITCGER, *TUNL*; A. HAWARI, *North Carolina State University, Raleigh, NC*; THE nEDM COLLABORATION

An apparatus is being constructed to allow key systematic effects in the neutron electric-dipole-moment (nEDM) experiment to be explored. The apparatus will initially allow measurement of the neutron and/or ^3He storage lifetimes in a full-size measurement cell. The ultimate goal is to permit the testing of five key scientific areas identified as essential for the larger nEDM project.

The nEDM project team has identified a new opportunity that will significantly reduce the risk to the nEDM project while shortening the time to a physics measurement. The PULSTAR ultracold-neutron (UCN) source (see Sect. 4.1.9) will soon come online and become a world-class source of UCNs, comparable in intensity to existing sources at both the Institut Laue Langevin and Los Alamos National Laboratory. This source, coupled with the existing polarized ^3He capabilities at TUNL, is enabling development of a setup for investigating many polarized-UCN/polarized- ^3He interactions at cryogenic temperatures.

During the past year, we have focused on completing the design and ordering the dewar for the apparatus, along with the cryogenic design and testing of several components. This section will focus on the overall design of the apparatus. Sects. 4.1.6, 4.1.4, and 4.1.3 provide specifics on the design and testing of individual components.

A schematic of the apparatus is shown in Fig. 4.3. A measurement cell filled with liquid ^4He at a temperature of about 450 mK will be placed within a uniform magnetic field generated by the B_0 coil. Cryogenic conventional and superconducting magnetic shields surround this geometry, as will thermal-radiation shields and, finally, a series of additional external conventional magnetic shields. UCNs from the PULSTAR source will be transported to the cell through a series of guides and will enter the cell through the vestibule region shown in Fig. 4.4. Polarized ^3He will be produced externally and introduced into the cell alongside the polarized UCNs through the vestibule.

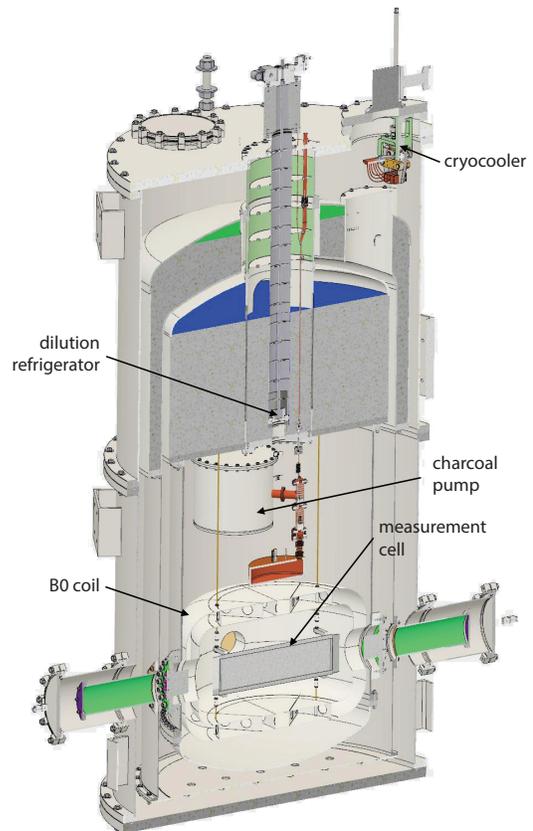


Figure 4.3: Engineering vertical cross-sectional schematic of the nEDM systematic-studies apparatus. For scale, the Dewar is approximately 1 m diameter.

Interactions of the UCNs with the ^3He will be monitored using the spin-dependent neutron-capture rate. Light from neutron capture pro-

duces scintillations in the liquid helium and will be wavelength shifted to visible wavelengths using deuterated fluors. It will then be transported away from the cell through acrylic light-guides for detection by photomultiplier tubes. Pulses will be digitized and analyzed offline. At the end of a measurement cycle, the unpolarized ^3He will be removed from the liquid using a charcoal pumping system.

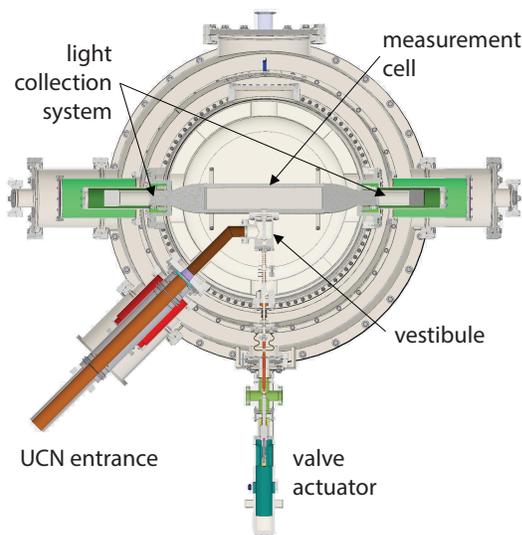


Figure 4.4: Engineering horizontal cross-sectional schematic of the nEDM systematic-studies apparatus showing the measurement cell, vestibule, UCN guide, and valve actuators.

The areas where studies at TUNL will provide significant advances to the development and implementation of the nEDM project are as follows:

- *Measurement of scintillations due to the relative UCN and ^3He precession and demonstration of the critical-dressing technique.* The motion of a spin under the application of static and non-resonant oscillating magnetic fields is quite complicated. Without the new apparatus, the measurements necessary to establish working parameters for the double resonance of UCNs and ^3He must occur on the project's critical path during the commissioning phase. The proposed apparatus will allow the critical-dressing parameters to be established and the techniques for providing the critical dressing to be experimentally vetted in parallel with the construction and commissioning of the main apparatus. This will reduce both the time to data collection and the overall risk to the project.

- *Measurement of the trajectory correlation function for systematic-error quantification.* Differences between the actual trajectory correlation function in the measurement cells and those predicted by theory may result in a mishandling of the geometric-phase systematic error, leading to a false nEDM result. The proposed apparatus will allow these functions to be measured prior to performing measurements in the main apparatus, in order to establish, for example, the effect of wall collisions on the correlation function.

- *Detection of the ^3He pseudomagnetic field in search of possible double-resonance effects.* This field results from the spin-dependent coherent-scattering cross section, which leads to an energy shift for the UCNs that is spin-dependent and thus appears as a magnetic field. The pseudomagnetic field is not directly affected by the application of an electric field, but can be the source of fluctuations in the precession frequency and hence extra noise in the system. The magnitude of the pseudomagnetic field can be reduced by ensuring that the ^3He spins have no component along the static magnetic field. This is possible by careful control of the spin-flip pulses.

- *Development of techniques for NMR imaging of ^3He .* Inhomogeneities in the ^3He distribution can couple with field gradients and/or detection non-uniformities to produce a false nEDM signal. The proposed apparatus will enable us to develop imaging techniques to map the uniformity of the ^3He distribution and to study inhomogeneities that might arise as a result of polarity-dependent heat currents, for example, that drive the ^3He distribution in different directions.

- *Study techniques for reversing $\sigma_{^3\text{He}}$, σ_{UCN} and B_0 .* Establishing the experimental parameters for reversing the spins and magnetic fields will take a considerable length of time during the commissioning phase of the apparatus. Developing these techniques in parallel in the new apparatus will provide an environment where a more complete study of these reversals can be performed without the external time constraints imposed by the critical path. This will reduce both the risk to the project and the time to data collection.

This program of studies will occur in parallel with the construction and commissioning of the main nEDM apparatus. We estimate that the entire program will last four to five years.

4.1.3 Development of the PULSTAR Vestibule Including Cryogenic UCN Windows

P.R. HUFFMAN, E. KOROBKINA, K. LEUNG, A.R. REID, C.R. WHITE, A.J. WITCHGER, *TUNL*

The PULSTAR systematic-studies apparatus is designed to carry out a series of tests using a full-sized nEDM measurement cell. This cell has one side entrance, so our systematic-studies apparatus is designed to accommodate both the UCNs and polarized ^3He entering through this hole. The design and initial testing of this entrance vestibule, including a cryogenic window for the UCN guide and Kapton bellows are described.

The systematic studies vestibule component serves two primary functions. First, it must allow both polarized ultracold neutrons (UCNs) and polarized ^3He to be introduced into an nEDM measurement cell. This requires a UCN window that will allow UCNs from the PULSTAR UCN source to enter into the liquid-helium-filled volume. Secondly, the thermal heat link from the mixing chamber of the dilution refrigerator is a cylinder of liquid helium that passes through the vestibule. Thirdly, it needs a three-position-valve arrangement that can (a) shield depolarizing regions when filling the cell with UCNs and ^3He ; (b) provide a good thermal link to the cell when cooling the cell; and (c) also seal off the measurement cell once it is full and measurements begin. The engineering design and prototype vestibule are shown in Fig. 4.5.

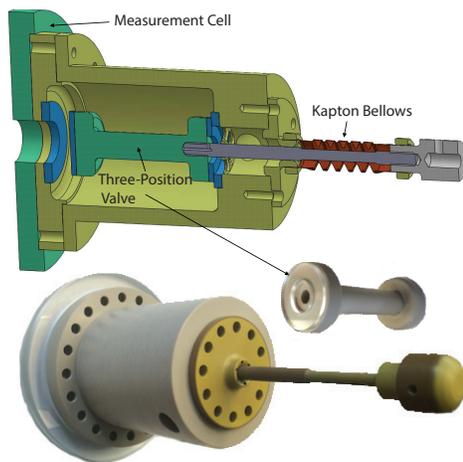


Figure 4.5: An engineering schematic (above) and photograph of the vestibule. Individual components are described in the text.

The physics design requirements allow only plastic and UCN/ ^3He -friendly materials to be used in this area. Thus significant development, prototyping, and testing of these components are required. The vestibule and UCN window components were tested separately.

A full-sized vestibule assembly has been manufactured from a combination of PEEK and Torlon. A Kapton bellows is used to seal the valve actuator from the surrounding vacuum. The test setup has been fully assembled and tested for mechanical movement with mock parts for the three-position valve.

The valve sealing surfaces are made from deuterated PMMA. This material is being custom manufactured by a chemist from the University of Tennessee. Testing of the prototype will occur once these pieces are available.

As reported previously, we developed a method of folding a seamless Kapton tube into a flexible bellows shape. This bellows is capable of repeated leak-tight cryogenic actuation in a superfluid helium bath; a sample bellows has withstood 500 cryogenic cycles of compression by 5 mm (14 % $\Delta L/L$). This folded bellows is both RF transparent and nonmagnetic. A photograph of a prototype bellows is shown in Fig. 4.6.

UCNs from the PULSTAR UCN source will be directed from the source to the apparatus using neutron guides. Once they enter the cryostat, the UCNs will travel through Kapton tubes to the vestibule region. In order to minimize UCN loss from interactions with the Kapton, we showed that a polystyrene coating on Kapton foils stays on and does not crack after repeated thermal cycling to liquid nitrogen temperature (77 K). At the UCN entrance to the vestibule, the UCNs must pass through a low-loss window

that separates the liquid helium in the vestibule from the UCN guide.



Figure 4.6: Photograph of a folded Kapton bellows.

The UCN window (see Fig. 4.7) will be constructed from a thin plastic film that will serve both as the UCN window and the nominal gasket-sealing material for the window. The material of choice is 0.033-mm-thick biaxially oriented polypropylene (BOPP) film from ViAM Films. BOPP has strong mechanical properties, even at cryogenic temperatures.

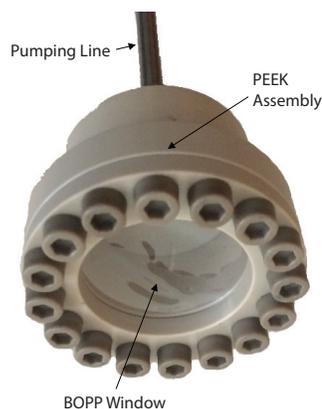


Figure 4.7: The UCN window test assembly. The window was shown to be leak-tight at 1.7 K while surrounded by liquid helium.

Real-dimensioned UCN windows and PEEK assembly have been manufactured. The BOPP film acts as the window and superfluid-tight gasket material. The BOPP-to-PEEK sealing geometry is the same as that developed for kapton gaskets previously. Superfluid-tight tests of the UCN window have been conducted in a LHe bucket-Dewar down to 1.7 K (see Fig. 4.8). An overpressure burst test at room temperature, shows that the window can withstand up to 70 psig.

In addition to the component development described above, we have constructed an all-metal residual-gas-analyzer (RGA) setup to test

materials for out-gassing. Any hydrogenous (i.e. water) materials absorbed in the plastics could significantly degrade the UCN storage times in the system. This also has implications for the larger-scale nEDM experiment.

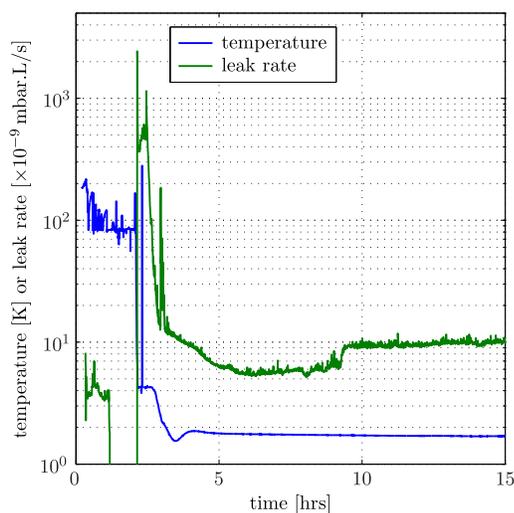


Figure 4.8: Temperature and leak rate during the UCN window cold leak test. Results show that the UCN window is leak tight to $< 10^{-8}$ mbarL/s in 1.7 K superfluid helium.

With this new setup shown in Fig. 4.9, a program is underway to test materials to determine their out-gassing properties. Materials that show significant water out-gassing, for example, will be studied under varied conditions such as treating them with heavy (deuterated) water or only exposing the material to an inert atmosphere, to see the level to which the out-gassing can be minimized.

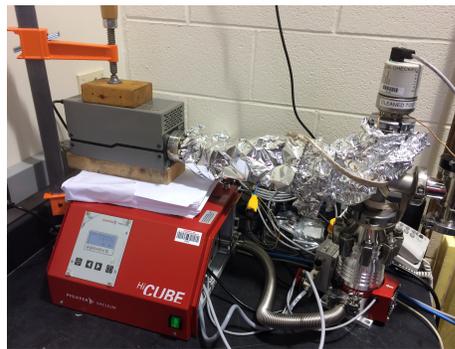


Figure 4.9: Photograph of the RGA system for studying out-gassing of materials used in the nEDM experiment.

4.1.4 PULSTAR Charcoal Pump System: The Double Valve

K.K.H. LEUNG, E. KOROBKINA, D. HAASE, *TUNL*

The PULSTAR Systematics Study Apparatus contains a charcoal pump. A double-valve system is being developed to reduce the gas conductive heat load between the pump and the 0.5 K buffer volume when the pump is heated and outgassed. The valve is nominally closed by a compressed spring and opened when pulled on by a wire. The material of the valve system has to be non-magnetic due to its proximity to the measurement cell.

Depolarized ^3He will be removed from the measurement cell in the Systematics Study Apparatus using a charcoal pump (Fig. 4.10). The charcoal needs to be regularly heated to about 10 K and purged before it becomes saturated. During this process, a high gas pressure will be created from the charcoal. The double valve will thermally separate the charcoal pump and the buffer volume, which is at 0.4 K, by sealing off an intervening volume with low vacuum before the charcoal is heated.

the slack in the lower wire, the top valve is opened first and then the bottom valve. After sufficient removal of ^3He , the wire is lowered to a position such that only the bottom valve is closed, and then we wait some time for the pressure to drop, since the supply of ^4He and ^3He is now removed. Then the wire is lowered further, so that the top valve is also closed, creating a sealed-off volume with low vacuum. Now the charcoal can be heated and outgassed without gas conduction of heat to the superfluid.

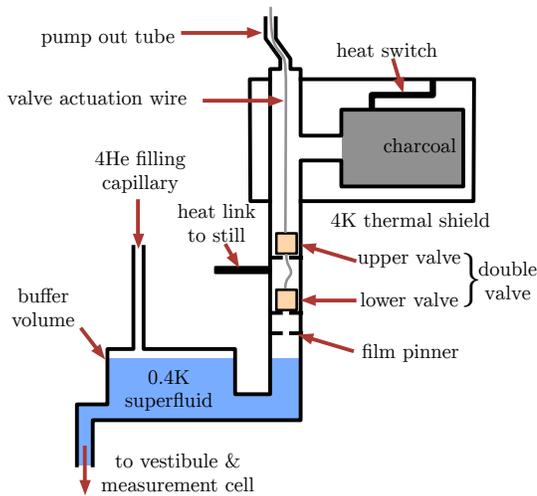


Figure 4.10: Schematic of the ^3He removal system.

In the double-valve system (Fig. 4.11), compressed springs are used to create a sufficiently good seal between the valve body and valve seat when there is no pulling force by the wires. When removing depolarized ^3He from the measurement cell is required, the upper wire is pulled by an actuation mechanism at room temperature. Due to

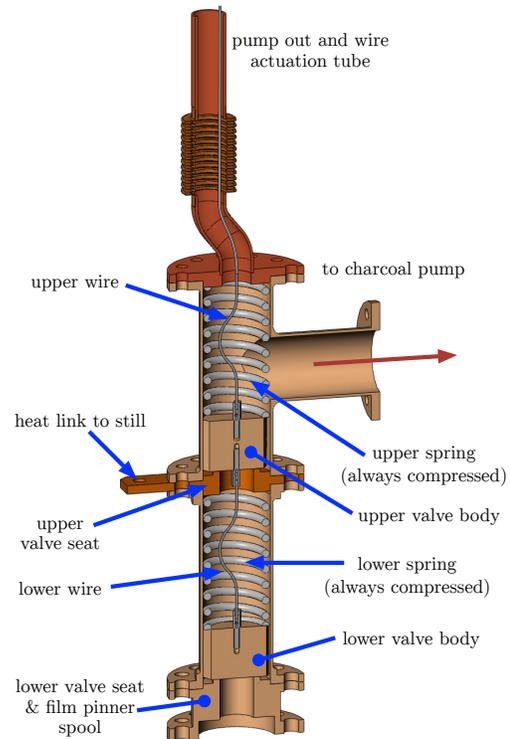


Figure 4.11: Schematic of the double-valve system. The static seals between the bolted flanges will be made with Kapton gaskets.

The bottom of the double valve is only 26 cm from the measurement cell, so non-magnetic materials having low thermal conductivity are required for the valve tubing, the valve seat and body, and the spring. The spring must also provide sufficient force to the valve body to create a superfluid-tight seal at the lower valve. This requirement can be reduced by having highly flat and polished sealing surfaces. The spring-loaded, pull-wire-actuated valve is inspired by a design [Sal89] that demonstrated a $< 1 \times 10^{-5}$ mbar L s $^{-1}$ leak rate at 4.2 K with a 10 mbar pressure difference and 20 lbf.

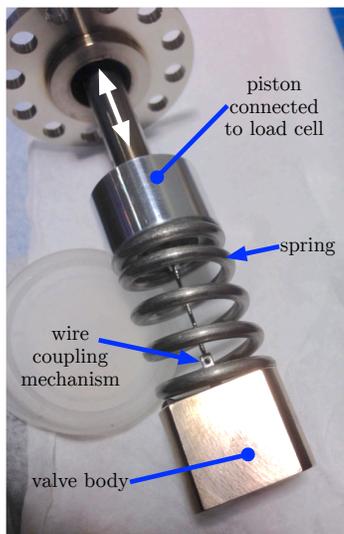


Figure 4.12: Inside of the 1.7 K leak rate testing insert. A movable piston presses the valve body against a valve seat (not shown) via a spring. A load cell at room temperature is used to measure the force on the piston. The spring can also be removed for tests.

Our current candidate materials for the spring are phosphor bronze or beryllium copper; for the valve tubing, valve body, and seat they are Cu-Ni 90-10 or SS 316LN. A test system that can be cooled to 1.7 K in a LHe bucket Dewar has been designed and built to measure the force on the seal versus the leak rate. A movable piston connected to a load cell is used with a test spring to press a valve body onto a valve seat

(Fig. 4.12).

The lowest room-temperature helium leak rate (1 bar difference) reached with the spring test is 1.5×10^{-4} mbar L s $^{-1}$ with 70 lbf and a 0.002" thick Kapton gasket. When the spring is removed and the piston is pressing directly onto the valve body, a leak rate of 2.3×10^{-5} mbar L s $^{-1}$ is reached with 70 lbf, indicating an uneven force on the valve body due to the spring. This latter leak rate is two orders of magnitude better than in Ref. [Sal89], since we have 1 bar difference, but it was done at room temperature and with a greater force. However, this leak rate is still higher than the requirement of $< 3 \times 10^{-8}$ mbar L s $^{-1}$.

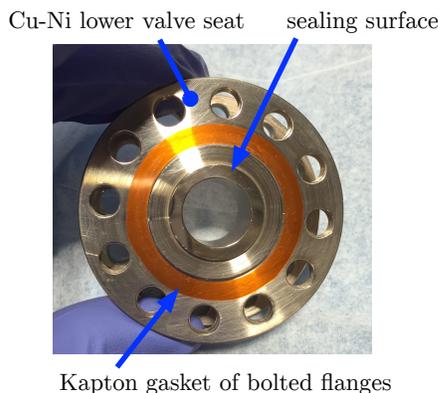


Figure 4.13: The lower valve seat. This surface was commercially lap polished with a #9 microgrit finish, but scratches are still visible.

We are currently working with lap-polishing companies to improve the polishing of the valve surfaces (Fig. 4.13), and we are seeking to improve the transfer of force from the spring to the valve body. We also need to acquire suitable material for the final double-valve pieces, since the commercial Cu-Ni 90-10 we initially tried to use has a 1.8% iron content, causing it to be magnetic.

[Sal89] R. Salmelin *et al.*, J. Low Temp. Phys., **76**, 83 (1989).

4.1.5 Measurements of Superfluid Helium Film Flow for the PULSTAR Project

D.G. HAASE, D.K. FRAME, J.R. ROWLAND, *TUNL*

We have measured the thermal responses of resistive bolometers suspended above or immersed in superfluid helium. These results bear on the testing and application of etched silicon wafers to suppress superfluid helium film flow in the nEDM PULSTAR experiment.

The tests at the PULSTAR Test Facility will include the injection of polarized ^3He into the test cell filled with superfluid ^4He , and the subsequent removal of the depolarized ^3He after the measurement cycles. We propose to remove the depolarized ^3He by evaporation, taking advantage of the much higher vapor pressure of ^3He relative to ^4He [Dub09]. We have designed a ^3He removal system that includes a charcoal gas adsorption pump to remove the ^3He - ^4He vapor, a gas-gap heat switch to control the operation of the adsorption pump, a valve system to select the removal of the ^3He and the regeneration of the adsorption pump, and an etched silicon “film pinner” to reduce the flow of superfluid ^4He , which would reduce the effectiveness of the charcoal pump.

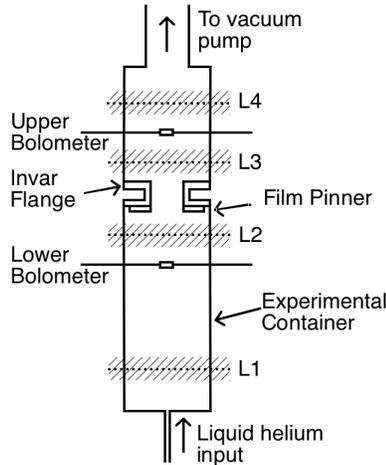


Figure 4.14: Cross sectional view of the film-pinner test volume, showing locations of the film pinner and the lower and upper bolometers. The hatched areas show the approximate liquid levels L1 to L4.

get cell a superfluid ^4He film can crawl up the pumping tube and evaporate. This additional gas flow would rapidly fill up the charcoal adsorption pump and require more frequent heating/desorption cycles. We have included in our design an etched silicon film pinner with atomically sharp edges. As the film crosses such an edge the surface tension causes the film to become so thin that it cannot maintain a superfluid flow [Shi98].

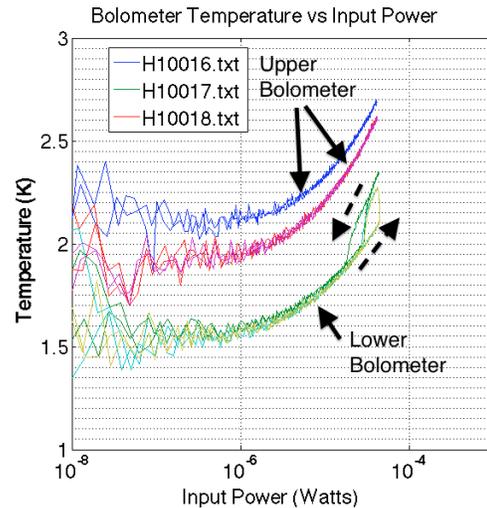


Figure 4.15: Three bolometer power curves measured with the liquid at level L1. The upper and lower bolometers were measured simultaneously. The upper bolometer has not cooled to its minimum temperature. The lower bolometer displays hysteresis upon heating and cooling. The dotted arrows indicate the paths of increasing and decreasing input power.

In the removal of the ^3He vapor from the tar-

The film-pinner test volume is shown in Fig. 4.14. A cylindrical copper volume, 2.54 cm

in inside diameter (ID) and 16.5 cm high, was filled with liquid helium through a 0.010-in ID tube at the bottom and the vapor was removed through a 1.27-cm diameter tube at the top. A silicon film pinner with an orifice 8 mm in diameter is epoxied to an Invar flange located 10.7 cm above the bottom of the test volume. Two temperature-sensitive RuO bolometers are suspended above and below the film pinner from #36 phosphor bronze wires. We measured the response of the bolometers while the measurement cell was filled with liquid over a period of several hours at near constant temperature. The level of the liquid at any time was inferred by the amount of gas condensed into the system.

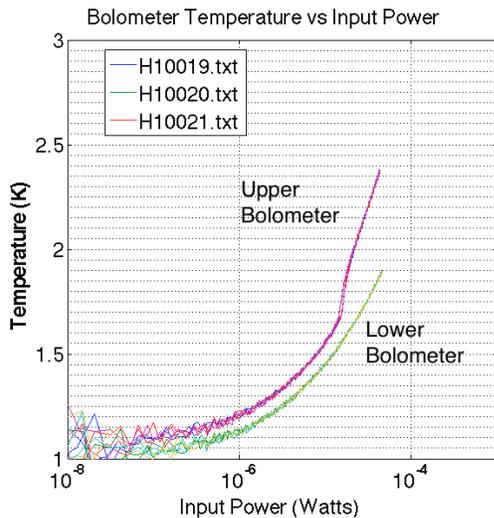


Figure 4.16: Measurements with the liquid at level L2. The lower bolometer appears to be completely in the liquid phase. The upper bolometer displays a kink at an input power of about 20 microwatts, but there is little or no hysteresis upon heating and cooling.

The bolometers were measured by using a voltage that increased from 0 to V_{\max} and then back to zero over a period of 30 seconds. From the measured current and voltage across the bolometer, the bolometer resistance and applied power were calculated. Preliminary temperatures were calculated from the relation $R = a \exp(bT^{1/2})$ [Li86]. When the liquid level is at level L1 on the diagram, both bolometers should be above the liquid meniscus (see Fig. 4.15). If a superfluid film crawls up the walls of the con-

tainer it should show effects on both bolometers. With liquid at level L2, the lower bolometer would be covered by the liquid (see Fig. 4.16). At level L3, there should be film flow into the upper part because the pinner is immersed (see Fig. 4.17). At level L4, which was not reached in this measurement, both bolometers would be immersed in the liquid phase. Our preliminary results display hystereses in the upper bolometer that do not appear until the liquid level is above the film pinner. We associate this with the evaporation of a flowing superfluid helium film. Therefore it would appear that the pinner retards superfluid film flow. However, at levels L1 and L2, there is a kink in the T vs. P curve. This may be the result of a static adsorbed helium film. [Fok66]

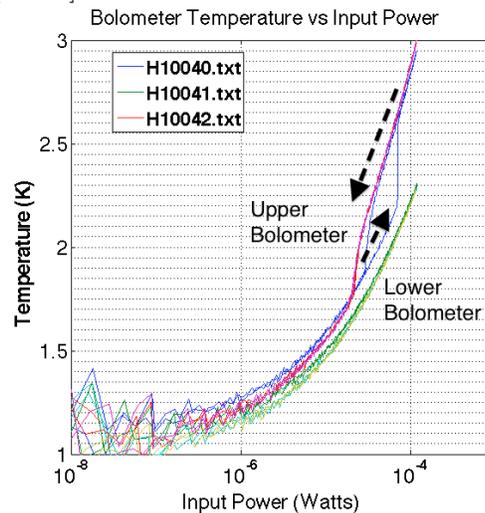


Figure 4.17: Bolometer curves with the liquid at level L3. The upper bolometer displays hysteresis upon heating and cooling. The dotted arrows indicate the directions of increasing and decreasing input power.

-
- [Dub09] F. Dubose, Ph.D. thesis, North Carolina State University, 2009.
 - [Fok66] K. Fokkens, K. W. Taconis, and R. D. B. Ouboter, *Physica*, **32**, 2129 (1966).
 - [Li86] Q. Li *et al.*, *Cryogenics*, **26**, 46 (1986).
 - [Shi98] P. J. Shirron and M. J. DiPirro, *Adv. Cryo. Eng.*, **43**, 949 (1998).

4.1.6 Heat Switches for the PULSTAR Test Facility

C.R. WHITE, D.G. HAASE, P.R. HUFFMAN, *TUNL*

The cryostat for the PULSTAR Test Facility requires two heat switches. A gas-gap heat switch will control the removal of ^3He from the experimental cell. A mechanical heat switch will connect a 4 K cryocooler to the helium bath of the PULSTAR dewar. This will reduce liquid helium consumption and allow longer unattended operation. We have tested and are modifying both heat switches.

Gas-gap Heat Switch

In the PULSTAR EDM experiment a charcoal pump will be used to selectively remove ^3He from the measurement cell. The pump will be cooled by a thermal link to a liquid helium bath. When the charcoal is saturated it must be regenerated by heating to 20 K, in order to out-gas the helium. During this process, the thermal link to the helium bath must be severed in order to reduce helium boil off in the bath. A helium gas-gap heat switch for controlling the cooling of the charcoal has been designed and tested [Mar10, DeP04, Fra86]. Full saturation of the charcoal by helium will generate about 1 KJ of heat. Since the pumping time is on the order of hours, the switch should be able to remove as much as 0.5 W of heat in its ON state, while keeping the charcoal end below 7 K. When the switch is turned off, the heat load should, at minimum, be less than 0.5 W, despite the larger temperature difference.

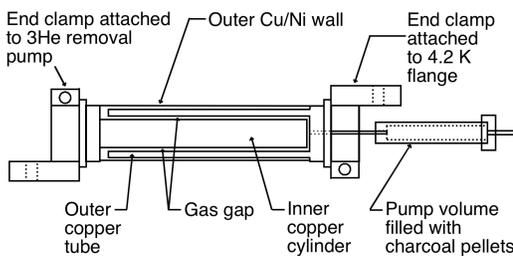


Figure 4.18: Diagram of gas-gap heat switch. The actual gap between the inner cylinder and the outer copper tube is 0.020 inches.

The cylindrical body of the switch consists of three parts: an inner copper cylinder, an outer copper tube, and a 90/10 Cu/Ni outer

wall (see Fig. 4.18). A small stainless steel tube passes through one of the copper ends into the gap in between. On the other end of this tube is a small copper cylinder containing charcoal, through which the heat switch is filled with helium gas to 10,000 Pa at room temperature and then closed off. When the charcoal temperature drops below a certain point, it adsorbs the helium, removing the gas conduction and making the Cu-Ni wall the main contributor to the thermal conduction.

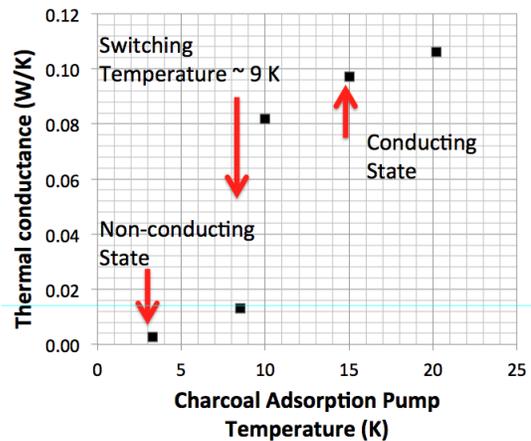


Figure 4.19: Measured thermal conductance of the gas gap heat switch as a function of the temperature of the charcoal adsorption pump. When the adsorption pump is at a temperature above about 9 K, the gas gap is filled with helium and the heat switch conducts heat.

The switch was assembled and filled. Then one end was clamped onto an RDK-415D cryocooler, which cools as low as 3 K. Two heaters were attached, one to the free end of the heat switch, and one to the small charcoal container.

For cooling of the charcoal pump, a thin strip of copper connected the charcoal to the cryocooler. The charcoal was heated to various values between 3 K and 20 K, and at each temperature, the temperatures across the switch were measured as a function of heat input. The average thermal conductance at each charcoal pump temperature is shown in Fig. 4.19, which indicates a switching point of around 9.5 K and a difference in conduction of almost two orders of magnitude between fully ON and fully OFF. The value of the thermal conductance through the switch at $T_{\text{hot}} = 7$ K was 0.074 W/K as compared to the goal of 0.179 W/K. When the switch is off and $T_{\text{hot}} = 20$ K, the heat flow is reduced to 0.02 W, which is in the acceptable range. A new switch has been machined with a gap that is smaller by a factor of five, which should increase the thermal conductance by a similar factor.

Mechanical Thermal Clamp

In the PULSTAR EDM experiment, a mechanical heat switch will be used to thermally link the liquid helium bath to an RDK-415D cryocooler. The cryocooler can be used to remove heat from the liquid helium bath and reduce helium loss. However, it must be turned off during neutron measurements, because the moving piston would induce magnetic effects in the measurement cell. When the cryocooler is off, a large heat load would be placed on the helium bath, and thus the cryocooler should be mechanically and thermally disconnected from the bath. When connected to the bath, the target thermal resistance for the heat switch is 1 K/W including the connections from the clamp to the cryocooler.

The heat switch is a mechanical clamp (see Fig. 4.20) that is closed onto an aluminum rod extending into the liquid helium volume. The contact with the aluminum is made by two copper pieces which are thermally isolated from the rest of the clamp by two pieces of G10. From these copper pieces, two copper braids extend to the cryocooler and are attached to it. The clamp may be opened and closed by a large threaded screw running through its body. A stainless steel rod can be inserted into this screw in order to open and close the clamp while under vacuum.

The heat switch was tested by closing it onto a small aluminum rod with a 25 W heater in its end. This assembly was then attached to the cryocooler and cooled. RuO resistance temperature sensors were placed along the assembly to determine the thermal resistance of various com-

ponents. The heat load was varied until the rod was at 4.2 K. At this temperature, the heat flow across the switch was 100 mW. The total thermal resistance was 11 K/W, with 6 K/W coming from the clamp connection to the rod, 4 K/W from the copper braids, and 1 K/W from the connection to the cryocooler. The resistance from the braids can be easily reduced, and the clamp connection can be gold-plated. However, grease cannot be used on clamping surface. Currently, the setup is being modified so that the clamp can be closed onto the rod after the assembly has cooled, as will be the case in the PULSTAR Dewar. If thermal contraction has a role in lessening the clamping force, then this strategy could lead to lower resistance values. The current measured resistance values are, however, outside of the useful range needed for this experiment.



Figure 4.20: Diagram of the thermal clamp showing clamped aluminum bar.

-
- [DeP04] M. J. DePirro *et al.*, AIP Conference Proceedings, **710**, 463 (2004).
 - [Fra86] D. J. Frank and T. C. Nast, Adv. Cryo. Eng., **31**, 933 (1986).
 - [Mar10] D. Martins *et al.*, AIP Conference Proceedings, **1218**, 1652 (2010).

4.1.7 Ultra-Cold Neutron Storage Cells for the SNS nEDM Collaboration

K.K.H. LEUNG, R.E. BULLARD, R. GOLUB, P.R. HUFFMAN, E. KOROBKINA, *TUNL*; THE SNS NEDM COLLABORATION

The measurement cells of the SNS nEDM experiment have to satisfy many stringent conditions. Research on the cell coating and production is currently performed at NCSU. This year, UCN storage measurements performed at LANL with our new cells indicate that the “weak patch” problem plaguing previous versions of the cells appears to have been resolved.

At the heart of the SNS nEDM experiment are the $7 \times 10 \times 40 \text{ cm}^3$ measurement cells, which will be filled with superfluid ^4He at around 0.4 K containing a 10^{-10} concentration of polarized ^3He . Polarized ultra-cold neutrons (UCNs) are produced in the cells via super-thermal down-conversion with a polarized cold neutron beam. The ^3He and UCN spins are manipulated by RF-fields (up to 1 G and 3 kHz) in the presence of a highly homogenous magnetic field (around 10 mG with gradients less than 10^{-8} G/cm) and a strong electric field of about 50 kV/cm. Scintillation light at 80 nm is produced in the helium after spin-dependent $n + ^3\text{He} \rightarrow p + ^3\text{H} + 764 \text{ keV}$ captures. This XUV light will be wavelength shifted at the cell walls and then guided out to detectors in a warmer region of the experiment. Therefore the cells are required to be non-magnetic, non-conductive, cryogenically friendly, and able to withstand strong electric field gradients. They also need excellent polarized UCN and ^3He storage properties, a high XUV down-conversion efficiency, and good light transport properties.

Measurement cell production is currently done inside the NCSU Education and Research Laboratory’s class 1000 clean room, equipped with photoresist, low-UV lighting. UV-transparent PMMA plates are cleaned and annealed in a vacuum oven to relieve stresses that can cause crazing when cooling to cryogenic temperatures. The inner surfaces are then swing-coated with a solution of deuterated polystyrene, which has good UCN reflection properties, and deuterated tetraphenyl butadiene, a wavelength shifter, dissolved in deuterated toluene. This coating technique, developed at Duke University [Ye09, Ye08] is known to produce optically clear, smooth coatings. An atomic-force-microscopy

image made at our facility shows our coatings to be flat to within about 20 nm. This has been shown to be good for ^3He polarization and desirable if guiding the light inside the plates is required.

Six PMMA plates are then glued together using a deuterated version of a methylene-chloride-based PMMA cement to form a measurement cell (see Fig. 4.21). The glue is dispensed in a controlled manner using a microscopic guided robotic dispenser from Asymtek. A groove is cut into the plates to break the flow of the glue before it reaches the inside of the cell to reduce risk of it affecting the coating.



Figure 4.21: An NCSU measurement cell under a UV-lamp. The top opening is for ^3He transport in the final experiment. In the storage experiments, it is used for UCNs, while the visible groove and holes are for thermometry wiring.

UCN storage measurements are performed at Los Alamos National Laboratory. In 2014, we installed a new outer vacuum vessel to improve vacuum cleanliness and a new LN-cooled heat shield to more easily cool the cells to 20 K (see Fig. 4.22). The storage of UCNs is performed using a fill-and-empty mode. With the UCN guide-switcher connecting the source to the cell and

the cell valve open, UCNs are loaded into the cell from the LANSCE sD₂ UCN source. The cell valve is then closed and the guide-switcher is changed to connect the cell to the detector. After different holding times, the survivors are emptied to the detector.

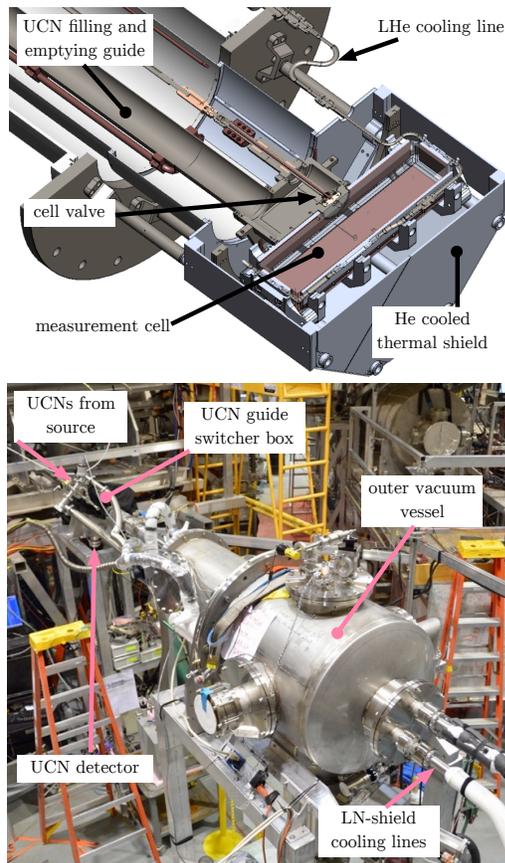


Figure 4.22: The UCN storage apparatus at the LANSCE UCN source. **Top:** Interior of the apparatus. **Bottom:** The apparatus with the new outer vacuum vessel and LN-cooled shield installed at the UCN beam line in 2015.

In December 2014, measurements on a cell produced at LANL were re-made with the upgraded apparatus at a new beam-line location to verify the previous results and to check aging effects of the cells. The data showed the same behavior: when a small, 0.1 to 0.4 cm² patch of bad-quality coating (a neutron optical potential of 50 to 90 neV) is exposed to UCNs, the higher energy UCNs are quickly lost due to more frequent reflection off the patch and a larger reflection-loss-probability from the patch. This causes a strong, quickly-decaying component in the surviving UCN counts. Fitting the data with the weak-patch model included gives $\chi^2_\nu = 0.9$, while fitting without it gives $\chi^2_\nu = 6.2$.

In January 2015, the first NCSU cell was produced. UCN storage measurements exhibit no loss of UCNs due to a weak patch, as seen in Fig. 4.23, allowing a best fit with $\chi^2_\nu = 0.9$. The initial UCN spectrum required for the data analysis was modeled by Monte-Carlo UCN-tracking calculations and was further varied to check for systematic effects. These were found to be small. Effects of the UCNs not exploring the cell ergotically (i.e. break down of UCN gas theory) were also tested with Monte Carlo calculations. The conclusion that the weak-patch problem has been solved appears robust.

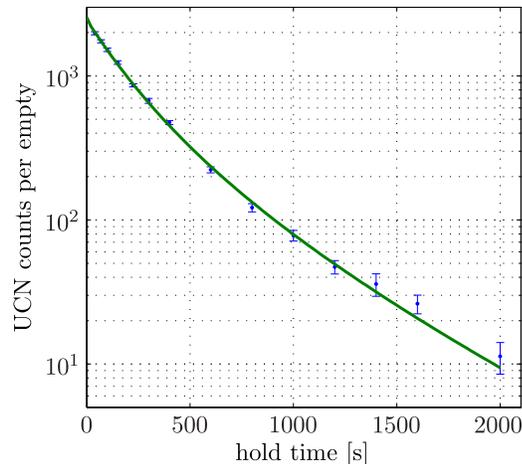


Figure 4.23: Results of the UCN storage measurements made with the NCSU cell at 30 K. The fitted line is made without the weak-patch model.

Efforts over the past two years at setting up cell-production facilities at NCSU and developing fabrication techniques have been highly successful. UCN storage measurements have demonstrated our cells to be free of the previous weak patch problem. This has come from a combination of better cell-wall geometries, an improved swing-coating jig, cell production in a clean room, and controlled glue deposition with a robotic dispenser. The next work will involve further reducing UCN losses on the coated surfaces (e.g. through removal of hydrogen contaminants on the surface), exploring alternative coatings that may allow us to store a higher numbers of UCNs, and optimizing the XUV-to-optical light conversion efficiency.

[Ye08] Q. Ye, Ph.D. thesis, Duke University, 2008.

[Ye09] Q. Ye *et al.*, Phys. Rev. A, **80**, 023403 (2009).

4.1.8 Design and Testing of Neutron Windows and Seals for the nEDM Project

K.M. LIVELY, A.J. WITCHGER, D.G. HAASE, *TUNL*

Neutrons from the ORNL Spallation Neutron Source will enter the measurement volume of the nEDM experiment through windows that must meet strict requirements as to mechanical, electromagnetic and nuclear properties. Through simulations and experiments we have investigated materials and mounting designs for the windows.

The nEDM neutron collection-and-measurement cell will be enclosed in a 1 m³ volume made of a wound composite material. The volume will contain superfluid liquid helium at a pressure of 1 bar and a temperature of about 0.35 K. Neutrons from the spallation neutron source will enter the experimental volumes after traversing eight windows. The windows and window mounts must be non-conducting, non-metallic, non-superconducting, and non-activated by the neutron flux. In addition, the last two windows—one on the inner magnet vessel and the other on the insulation volume—must be able to maintain a 2 bar pressure difference.

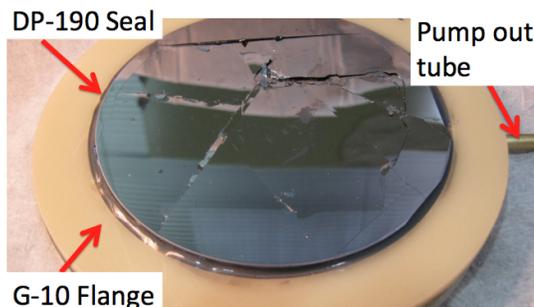


Figure 4.24: Result of a pressure and cooling test of a 100 mm diam. x 3 mm. thick Si $\langle 111 \rangle$ wafer directly bonded to a G-10 collar with Scotchweld DP-190 gray epoxy. It fractured upon cooling to 77 K and application of an external pressure differential of 1 bar.

We have identified single crystal silicon or single crystal quartz as the most suitable materials for the windows. Each of these materials is available in the required 15 cm diameter size. Each material is brittle and has an extremely small coefficient of thermal expansion, making it a chal-

lenge to mount the windows to the experimental volume. Silicon fails through cracking along a crystal plane. The cracking could be seeded by defects, scratches or uneven strains caused by the mount or, for thick samples, by rapid cooling. Surface defects which could seed cracks should be removed by etching [Pet82].

We have tested mounts and selected epoxies to mount silicon windows and have tested them at both room temperature and liquid nitrogen temperature (see Fig. 4.24) We have also performed discrete-element simulations to model the response of the windows and the mounts to pressure gradients and cooling.

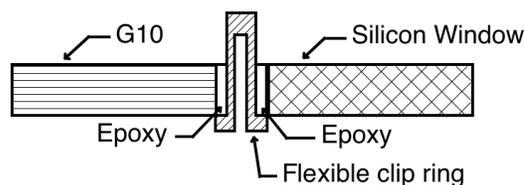


Figure 4.25: Cross section diagram of the clip-ring seal configuration. The intent is to reduce the stress of the differential contraction of the G-10 onto the silicon by the flexing of the clip arms.

Finite element models (FEM) of several initial mount designs were tested using Autodesk Simulation Mechanical. Initially, 2-D axisymmetric wireframe models were used to guide the selection of second round, 3-D models, which are more computationally expensive. A promising model which emerged from these wireframes is the one shown in Fig. 4.25, in which the silicon and the G-10 mount are connected by a slotted ring (a “clip”) that may flex slightly as the G-10 con-

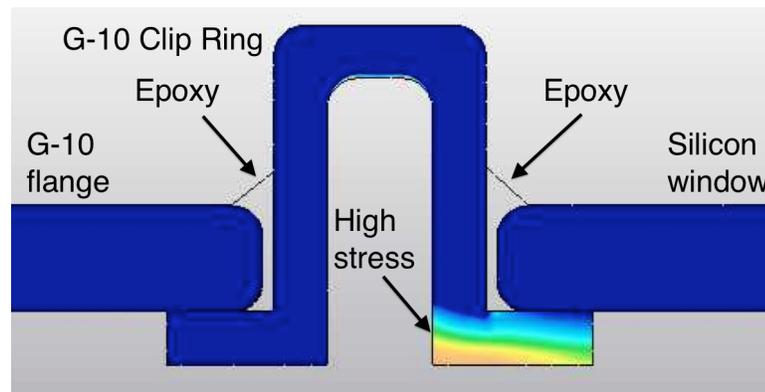


Figure 4.26: Simulation of the cross section for the clip-ring seal configuration.

tracts around the silicon. On the right of these cross-section images is the silicon window, 1 cm in thickness and with a radius of 7.5 cm; the middle is the G-10 clip; and the left is an outer G-10 flange. For each of these 2-D models, the temperature was uniformly controlled across the entire assembly to cool down over one simulated hour from 293 K to 77 K, and the subsequent stress response due to contraction was simulated.

Autodesk's Safety Factor (SF) calculation, which describes the ratio of yield strength to Von Mises stress at each element, was used as a diagnostic of the model. Yield strengths of 300 MPa were chosen for G-10 and silicon, a conservative value in the case of silicon, but one consistent with the fracturing failure mode described in the literature. Figure 4.26 shows a 5 mm thick clip with an inner clip edge 1.2 cm above the silicon top face. Of several designs, this displayed

the lowest SF of 2.13, and was advanced to 3-D modeling.

Our most recent 3-D calculations have investigated a clip ring made of Torlon, which is preferable to G-10 because of its isotropic properties. The fully rendered Torlon clip model used a 1 mm layer of epoxy between the lateral and horizontal faces of the Torlon and silicon, as well as a 1.5 atm pressure applied across the bottom faces of the assembly. The lowest safety factor present in this model was 2.9, indicating the best response yet for an assembly. The next step is to investigate the relationship between epoxy and Torlon, to see whether it thermally cycles well and what the shear strength is for silicon to Torlon bonds.

[Pet82] K. E. Peterson, *Proc. of IEEE*, **70**, 420 (1982).

4.1.9 Commissioning of the Ultracold-Neutron-Source Facility at the NC State PULSTAR Reactor

R. GOLUB, P.R. HUFFMAN, E. KOROBKINA, G.L. MEDLIN, A.R. YOUNG, *TUNL*; A.T. COOK, A.I. HAWARI, B.W. WEHRING, *North Carolina State University, Raleigh, NC*

We have finished construction and have begun commissioning of an ultracold-neutron source facility at the PULSTAR reactor on the campus of North Carolina State University. Detailed evaluation of the source’s performance will allow optimization of UCN production. In the near future, the source will be utilized for systematic studies related to nEDM measurements.

The ultracold-neutron (UCN) source facility being commissioned at the PULSTAR reactor on the campus of North Carolina State University will provide a competitive UCN flux for measurements including the neutron electric dipole moment (nEDM), β decay, and material scattering [Kor07]. In addition, it will serve as a platform for improving UCN source technology. In particular, the nEDM collaboration is finalizing plans for a smaller test apparatus that will be operated at the PULSTAR source to study systematic effects related to the nEDM measurement. There is also the possibility that the source will be used for other neutron β -decay experiments such as the Los-Alamos-based neutron lifetime experiment.

The source utilizes the high leakage of epithermal and thermal neutrons from the under-moderated reactor core. The 1-MW-thermal PULSTAR reactor cooling system has been upgraded to run at 2 MW, and a license amendment for a new fuel arrangement is currently being processed.

One liter of solid ortho-deuterium at a temperature below 5 K serves as the UCN converter material and is surrounded by a solid methane cold moderator in a cup-shaped container. The cold moderator temperature can be tuned between 30 K and 60 K to optimize the neutron-flux-peak tuned for down-scattering in the UCN converter. The source sits inside a heavy-water thermal moderator. Construction of the heavy-water tank and the cryostat that houses the cryogenic methane and deuterium containers has been completed, and the helium liquefier that provides cooling has been tested [Kor14].

Unlike traditional reactor-based UCN sources, the PULSTAR source was designed to be

placed in the former thermal-column facility outside of the reactor pool. A unique graphite-lined port was built to efficiently transport neutrons away from the core. This delivers a majority of the neutron flux to the source, while minimizing heating of the source by reactor γ rays. The performance of this neutron transport system was measured directly using activation of cadmium-covered gold foils and a heavy-water tank approximating the source tank. This setup has been modeled using the MCNP code, and the measurement is currently being used to benchmark the MCNP model of the final source design. Fig. 4.27 shows an MCNP plot of the reactor and UCN source geometry.

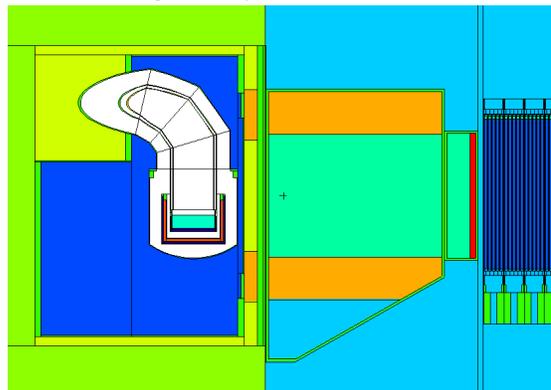


Figure 4.27: MCNP input geometry of the reactor and UCN source.

The source is mounted to the thermal-column shield door, allowing it to be easily rolled out of the reactor biological shield, as shown in Fig. 4.28. A replacement shield door that will allow the source to be serviced and tested in situ without an extended shutdown of the reactor has been constructed.

A guide system to transport UCNs from the source out of the biological shield has been constructed. The guides are ^{58}Ni -coated quartz tubes that are 15.2 cm in diameter and coated using a custom-built e-beam vacuum chamber at Virginia Polytechnic and State University.



Figure 4.28: Partially assembled heavy-water tank and cryostat on the thermal column door, rolled out of the reactor thermal column void.

To manage and condense methane and deuterium gas, a gas-handling system was constructed and tested. The helium liquefier and parallel cooling loops were used to condense methane and deuterium, which are controlled by the gas handling system, into the cryogenic containers. The UCN density is limited by the neutron lifetime in the deuterium, so the all-metal gas-handling system was built completely out of VCR stainless steel components that should prepare and maintain very clean deuterium over many operational cycles. The gas-handling system is shown in Fig. 4.29.

As the lifetime is also dependent on hydrogen and para-deuterium contamination, systems were built both to prepare deuterium in a very high ortho-fraction and to monitor the para-deuterium and hydrogen content to high precision, based on the previous work of Liu [Liu03]. A para-to-ortho spin converter utilizes the paramagnetism of a catalyst material (tested with both commercial Oxisorb and iron hydroxide) to induce spin flips and quickly reach equilibrium near the triple point of deuterium. A Raman spectrometer built for the purpose is then used to determine the ortho/para ratio of a deuterium

sample and place an upper limit on the presence of hydrogen and HD species [Kor14].

Part of the strategy for optimizing the source for UCN production is detailed modeling and evaluation of its performance. The source design allows the energy of the cold neutrons at peak flux to be tuned between 30 K and 60 K to optimize UCN production in the deuterium. It also permits the solid methane moderator to be switched out for a different moderator, such as mesitylene or triphenylmethane. Neutron-scattering kernels for methane at temperatures above 22 K were produced for modeling using our MCNP geometry.



Figure 4.29: Methane and deuterium gas handling systems.

UCN production in $s\text{D}_2$ has been shown to vary depending on the crystal's growth and treatment. A system is currently under construction to examine the crystal both visually and with embedded temperature sensors, as well as simulate warmer blackbody loads. A detailed study of the UCN converter in situ will be conducted while waiting for final safety approval for its installation into the reactor's former thermal column.

[Kor07] E. Korobkina *et al.*, Nucl. Instrum. Methods A, **579**, 530 (2007), Proceedings of the 11th Symposium on Radiation Measurements and Applications.

[Kor14] E. Korobkina *et al.*, Nucl. Instrum. Methods A, **767**, 169 (2014).

[Liu03] C.-Y. Liu *et al.*, Nucl. Instrum. Methods A, **508**, 257 (2003).

4.2 Fundamental Coupling Constants

4.2.1 The UCNA experiment

E. B. DEES, J. WEXLER, A. R. YOUNG, *TUNL*; THE UCNA COLLABORATION

The UCNA experiment has provided precise values for the axial form factor ($\lambda = g_A/g_V$) of the neutron from measurements of the β -asymmetry, A_o , using ultracold neutrons. The most recent published value for A_o came from the LANSCE 2010 run-cycle. Progress in the past year was toward understanding the systematic error budget for the 2011–2012 dataset, currently under analysis.

UCNA is an experiment which specifically attacks the need to determine angular correlations with a distinct approach to systematic errors that is complementary to traditional angular correlation measurements performed with cold neutron beams. Instead of cold neutrons, UCNA utilizes ultracold neutrons, which offer a distinct approach to the key neutron-related sources of systematic error in measuring the β -asymmetry. These are the neutron polarization and neutron-produced backgrounds. The UCNA experiment is described in detail in Plaster *et al.* [Pla12], and all of the articles and theses produced by the LANL UCN project are available at <http://neutron.physics.ncsu.edu/UCNA>.

UCNA’s most recent published value of the β -asymmetry is $A_o = -0.11954(55)_{\text{stat}}(98)_{\text{sys}}$ and was determined from data taken during the 2010 run cycle at LANSCE [Men13]. Data from 2011 and 2012 are currently being analyzed. Figure 4.30A shows the UCNA experiment at present. Ultracold neutrons are provided by the UCN source in Area B of LANSCE. A detailed characterization of this source can be found in Ref. [Sau13]. The guides for the polarized UCNs are coated with diamond-like-carbon (DLC) and pass through the “polarizer/AFP” magnet, a shutter required for polarimetry, and then into the spectrometer where β decays are measured for the UCNs in the decay volume of about 30 l. The detector packages at either end of the spectrometer consist of a multiwire proportional counter (MWPC), to provide position information, in front of a plastic scintillator for timing and energy reconstruction. A number of improvements were implemented after the 2010 run, including the addition of the polarimetry

shutter, ultrathin beryllium-coated end-cap foils for the decay volume, and an LED-pulsar system to provide linearity and gain-monitoring data for the β -detectors.

Table 4.1: The most important sources of uncertainty for the 2010 dataset with their projected values for the 2011–2012 dataset and a “final” future run assuming minimal improvement of the LANL UCN source.

Uncertainty	2011–2012 (in analysis)	Final Run (projected)
Statistics	± 0.40	± 0.28
Depolarization	$(0.7) \pm 0.1$	$(0.7) \pm 0.1$
Energy Recon.	± 0.08	± 0.08
Backscatter	0.56 ± 0.15	0.56 ± 0.15
Angle Effect	-0.8 ± 0.2	-0.8 ± 0.1
Total Systematic	0.46 ± 0.28	0.46 ± 0.22
Total	0.46 ± 0.49	0.46 ± 0.36

Our analysis of the 2012–2013 UCNA data is currently focused on the systematic corrections and uncertainties due to the neutron polarization and β -energy reconstruction. The angular distribution for the detection of decay β -particles alone from polarized neutrons is $\Gamma = 1 + (v/c) \langle P \rangle A(E) \cos \theta$, where v is the β -particle’s speed, $\langle P \rangle$ is the average polarization of the neutron populations, and $A(E)$ is the β -asymmetry correlation parameter. Therefore, we need to know the average neutron polarization in order to determine $A(E)$. Our target uncertainty for the polarization is 0.1%. Because UCNs can be polarized to essentially 100% using a “high” field, 7 T, polarizer [Hol12], we determine the absolute polarization by a relatively crude, 10% measure-

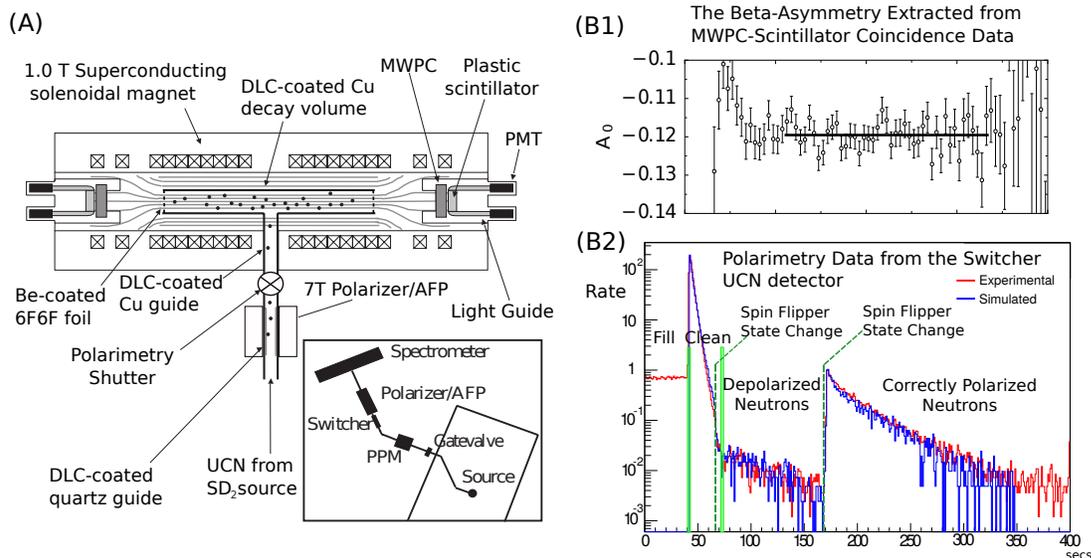


Figure 4.30: A) The current UCNA experimental geometry. B1) The value of A_0 extracted from the 2010 UCNA data set showing the expected energy-independent behavior, and B2) the switcher detector during a depolarization measurement showing a comparison between experimental and Monte-Carlo data. The vertical green bars indicate when the shutter closes and then reopens, and the dashed vertical lines show when the spin-flipper changes state.

ment of the equilibrium fraction of depolarized UCNs.

The polarimetry shutter implemented after the 2010 measurements greatly enhanced our ability to measure depolarization. The statistical precision for the depolarized population is now about 0.1% (with improvements expected after the LANL source upgrade), and our goal to eliminate the need for Monte-Carlo-based corrections now seems achievable.

The depolarization measurements involve changing the state of the switcher, a device which permits UCNs to flow either from the source into the decay volume or, if the switcher state is changed, to flow from the decay volume into a monitor detector mounted below the switcher. This procedure involves using the polarizer/spin-flipper system as a spin analyzer and measuring both the signal due to depolarized neutrons and the much more numerous neutrons which maintain their correct polarization. The experimental signal in the switcher-detector for UCNs loaded with the spin-flipper off is shown as the red curve in part B2 of Fig. 4.30.

We confirm our understanding of the technique through an absolute calibration procedure, which involves loading known depolarized fractions into the trap, measuring them with our method, and assessing our dependence on our assumptions concerning depolarization mechanisms using a Monte Carlo model of the depolarization process. As one can see from the blue curve in the figure, our model currently repro-

duces the experimentally measured signal at all relevant phases of the depolarization measurement at the 15% level or better, using a set of guide parameters consistent with guide characterization measurements.

The asymmetry is extracted from the rate measured in the detector packages (see part B1 of Fig. 4.30). During the 2011–2012 run period, the number of sources used to determine our energy calibration was increased from three to six, and we increased the number of calibration runs in order to track variations in the calibration. We also implemented an LED pulser system which allowed us to obtain linearity and gain-monitoring data on a β -run by β -run basis. Our ongoing efforts involve implementing the data from our linearity scans to correct for drift in our calibration between source measurements. The LED system and calibration analysis effort is being led by the Caltech group, with contributions from the Kentucky and NCSU groups.

- [Hol12] A. T. Holley *et al.*, Rev. Sci. Instrum., **83**, (2012).
 [Men13] M. P. Mendenhall *et al.*, Phys. Rev. C, **87**, 032501 (2013).
 [Pla12] B. Plaster *et al.*, Phys. Rev. C, **86**, 055501 (2012).
 [Sau13] A. Saunders *et al.*, Rev. Sci. Instrum., **84**, 013304 (2013).

4.2.2 The Nab Experiment

J. WEXLER, A. R. YOUNG, B. A. ZECK *TUNL*; THE NAB/UCNB COLLABORATION

The Nab experiment seeks to determine the β - ν correlation parameter in neutron decay with a relative precision at least ten times better than the current value. The decay particles will be measured in silicon detectors that are each segmented into 128 pixels. Over the past year, our team, together with the fundamental neutron physics group at LANL, has established that these detectors have the performance needed for the Nab experiment. This was done using the front-end and data-acquisition electronics needed for the final experiment.

The Nab experiment is designed to determine the electron-neutrino correlation parameter $a(E)$ through time-of-flight (TOF) measurements of decay protons tagged in coincidence with β particles [Poč09]. To leading order, $a(E) \approx a_0 = (1 - \lambda^2)/(1 + \lambda^2)$, where $\lambda = g_A/g_V$ is the axial form factor of the nucleon. The primary motivation for this measurement is to determine λ at the 0.025% level, providing essentially an order of magnitude improvement over the current precision. Furthermore, since the most precise values of λ are derived at present from measurements of the β -asymmetry using a very different approach, Nab provides a powerful cross-check of our understanding of the systematic errors in the global dataset for λ .

In the Nab experiment, a cold neutron beam on the Fundamental Neutron Physics Beam Line passes through the Nab magnetic spectrometer at right angles to its symmetry axis, as shown in Fig. 4.31. When measuring the a coefficient, protons are only detected in the TOF arm (upward in Fig. 4.31), but β -particle events are reconstructed from “hits” in both detectors to form a prompt “start” to the proton TOF measurement. (We discuss proton detection below.) Decay protons and β 's are filtered before they enter the TOF drift region by a region of strong, roughly magnetic field with $B_f = 4$ T. Inside that region, the adiabatic invariance of the flux through the charged-particle orbits results in reflecting all particles whose pitch angle with respect to the magnetic field exceeds $\theta_m = \arccos(\sqrt{B_f/B_0}) \approx 26^\circ$ [Jac98]. The field is then reduced dramatically to 0.12 T, so that the same adiabatic invariance results in charged particle trajectories almost parallel to the magnetic field lines in the TOF arm of the spectrometer.

The charged particles then traverse the TOF region, with the TOF of the protons very strongly correlated with their initial decay speed. At the end of this region, the magnetic field is increased to values near 1 T, ensuring the decay region maps to a reasonable area of the silicon detector.

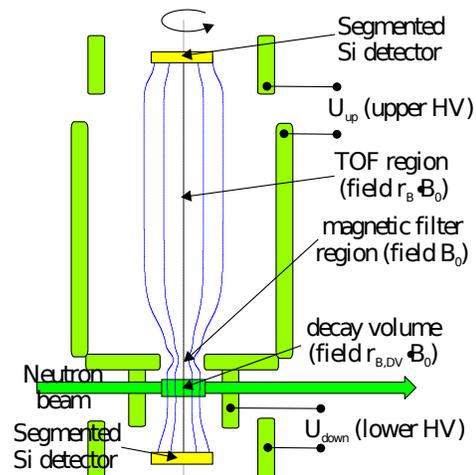


Figure 4.31: Schematic diagram (not to scale) of the Nab experiment. The electric and magnetic fields have cylindrical symmetry around the vertical axis. The electrodes are in light green; the magnetic coils are not shown.

Proton detection is accomplished in the Si detector in the TOF arm of the spectrometer by applying a very well-defined -30 kV potential step at the end of the TOF region. The $a(E)$ parameter is extracted from the proton TOF data by performing a cut (nominally 50 keV) on the energy of the decay β and then histogramming the decay probability *vs.* $1/t_p^2$, where t_p is the proton

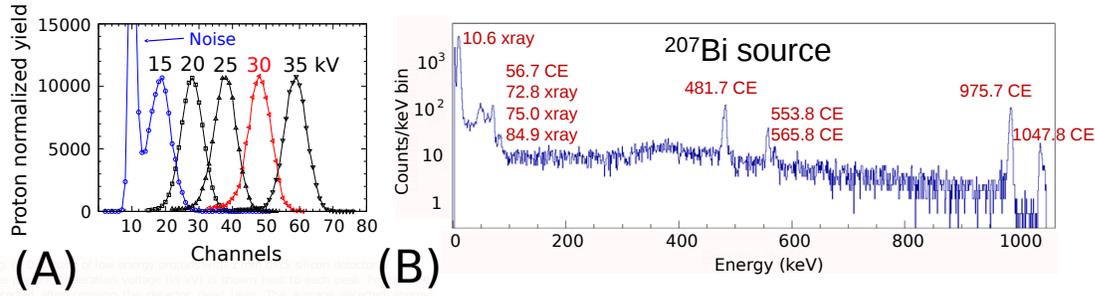


Figure 4.32: (A) Single-pixel proton response for the Nab detectors as a function of proton energy, as measured at the TUNL low energy proton facility. (B) Recent ^{207}Bi source spectrum showing atomic X-ray lines, down to the 10 keV l-shell lines, and conversion lines.

TOF. Given the very low energy of the proton, the proton TOF is $p_p \propto 1/t_p$ and the probability distribution is given by:

$$\varphi(1/t_p^2) = \begin{cases} 1 + a(E)\beta \frac{p_p^2 - p_e^2 - p_\nu^2}{p_e p_\nu} & \text{for } \left| \frac{p_p^2 - p_e^2 - p_\nu^2}{p_e p_\nu} \right| < 1, \\ 0 & \text{otherwise,} \end{cases} \quad (4.1)$$

where $\beta = v/c$ and p_e , p_ν , and p_p are the decay electron, neutrino and proton momenta respectively. From Eq. (4.1), the slope of the decay probability plotted against $1/t_p^2$ provides the value for the electron-neutrino correlation at electron energy E_e .

Some key results of the detector development program are depicted in Fig. 4.32. The silicon PIN-diode detectors are nominally 11.5 cm diameter and 2 mm thick, segmented into 128 hexagonal pixels via conductive pads on the back face of each detector. Protons are detected by biasing the detector at -30 kV relative to the TOF region held at ground potential and detecting the resultant mono-energetic pulse to tag protons. Using variable energy, collimated beams of protons and deuterons, we determined the dead-layer on our detectors to be about 100 nm and measured the response to protons from 15 to 35 keV [SB14], thus clearly demonstrating excellent signal-to-background for the planned acceleration potential, as seen in Fig. 4.32(A).

The energy calibration for the proton beam studies was carried out using Monte-Carlo modeling with the pescelope code [Sem97]. This yielded the energy deposition in the thin films encapsulating the source and the detector dead-layer, and allowed us, by analyzing the peak lo-

cation and spectral shape for both X-ray and conversion electron lines, to isolate the effects of the encapsulating foils on the sources. Studies of sealed γ -ray and conversion-electron sources have served to subsequently establish the calibration, resolution, and threshold of all active pixels on a set of 24 pixels instrumented using the front-end electronics boards planned for the final experiment. Recent results, demonstrating the detection of 10 keV X-ray lines from a ^{207}Bi source are depicted in Fig. 4.32(B), with the active pixels having thresholds below 5 keV and an energy resolution FWHM less than 5 keV at 10 keV electron energies. This essentially establishes the performance required for Nab.

We have also detected proton-electron coincidence events from β -decay and established a very powerful approach to data acquisition from our detectors. The NI PXIe-5171R digitizer system permits us to establish the existence of an electron-proton coincidence (where both the electron and the proton create triggers with our low-threshold trigger filter, separated typically by tens of microseconds) and then process and store all relevant waveforms for the hit and neighboring pixels.

-
- [Jac98] J. Jackson, *Classical Electrodynamics*, John Wiley & Sons, Inc., 3rd Ed., 1998.
- [Poč09] D. Počanić *et al.*, Nucl. Instrum. Methods A, **611**, 211 (2009).
- [SB14] A. Salas-Bacci *et al.*, Nucl. Instrum and Methods A, **735**, 054512 (2014).
- [Sem97] J. Sempau *et al.*, Nucl. Instrum. Methods B, **132**, 377 (1997).

4.2.3 A New Determination of the ^{19}Ne β Asymmetry

D.C. COMBS, A.R. YOUNG, *TUNL*

Data from the 1996 Princeton ^{19}Ne β asymmetry experiment was reanalyzed in an effort to correct for positrons scattering off the detector faces. The experiment was simulated using the Monte Carlo package PENELOPE, and the resulting correction was applied to the data, yielding a zero-energy intercept of the asymmetry $A_0 = -0.0378^{+0.0007}_{-0.0004}(\text{sys}) \pm 0.0003(\text{stat})$. Using this asymmetry value, the element V_{ud} in the CKM matrix is found to be $0.9760(10)$, the most precise value from a mirror decay (including the neutron).

In 1996, an experiment to determine the β asymmetry in the decay of ^{19}Ne was performed at Princeton [Jon96]. Due to inconsistencies in the simulated and measured spectra of scattered positrons, the results were never published. We have performed a new simulation and analysis of that experiment using the Monte Carlo software PENELOPE v2002 [Bar95].

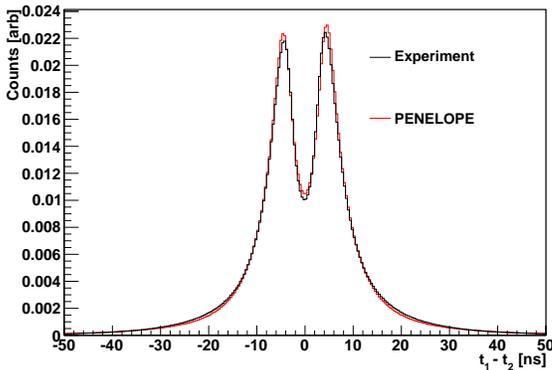


Figure 4.33: Timing spectrum from the data and the best-fit timing spectrum from the simulation.

The analysis uses five parameters: the detector threshold, the electronic noise and three “walk” correction parameters. The timing of the β signals was measured using leading-edge discrimination, with the timing-walk correction specified as a function of energy and given by [Jon96]

$$w(E) = p_1 + \frac{p_2}{p_3 + E}. \quad (4.2)$$

The three parameters are allowed to vary in order to simultaneously fit the ^{60}Co data and the coincident timing spectrum from the experiment.

The ^{60}Co was used for timing calibration and to determine the energy dependence of the threshold crossing time for the β timing signals. The timing spectrum is filled using the difference in threshold crossing time of pulses from coincident events (events leaving energy in both detectors). Approximately 30% of all events scatter from one detector into the other, leaving some amount of energy in both detectors. The sign of the timing difference is used to identify the hit detector. The simulation also records the z -component of momentum of each primary particle. Figure 4.33 shows the best-fit timing spectrum from the simulation and the spectrum from the data.

Table 4.2 lists the corrections to the asymmetry and their associated systematic uncertainties. The first portion of the table shows the corrections calculated using the results of the simulation. The events from the simulation are sorted into one of three categories based on whether the event left enough energy to be above threshold in one detector, both detectors, or neither detector. For the classes of events that were above threshold there are two types of correction. The backscatter correction accounts for events in which the experimental data would have indicated the wrong initial direction of the positron. The energy correction accounts for energy loss due to scattering. A single correction accounts for the events that went undetected. The sign of the correction is relative to the magnitude of the asymmetry, so that a positive correction indicates an increased asymmetry and vice versa for a negative correction. A global systematic uncertainty of 25% is applied to each Monte Carlo correction based on a conservative assessment of agreement with a set of benchmark observables. The final two entries in the table represent uncertainties

Table 4.2: List of corrections to the asymmetry and their uncertainties. The sign is relative to the magnitude of the uncorrected asymmetry. All values are multiples of 10^{-4} .

Systematic	Correction (10^{-4})	Uncertainty (10^{-4})
Monte Carlo Corrections:		
Above threshold in both detectors:		
Backscatter correction	+14.5	± 3.6
Energy loss correction	-2.0	± 0.5
Above threshold in a single detector:		
Backscatter correction	+3.0	± 0.8
Energy loss correction	-0.9	± 0.2
Below threshold in both detectors:		
Energy non-linearity	-	± 0.9
Polarization	-	+5.7 -0.0
Total	+13.6	+6.9 -3.8

without corrections. The energy calibration uncertainty is determined by varying the detected energy by 2% and looking at the resulting change in the asymmetry. The worst performing detector had a maximum non-linearity of about 1% at 1500 keV. The uncertainty in the asymmetry due to polarization is found assuming a polarization of $100_{-1.5}^{+0}\%$ [Jon96].

The resulting value of the asymmetry is $A_0 = -0.0378_{-0.0004}^{+0.0007}(\text{sys}) \pm 0.0003(\text{stat})$. This value and the global average of measurements of the lifetime are used to determine a value for the element V_{ud} in the CKM matrix, which describes quark mixing. The result is $V_{ud} = 0.9760(10)$. This is 1.7σ from the most precise determination of V_{ud} derived from $0^+ \rightarrow 0^+$ decays, which is $0.97425(22)$ [Har09]. Table 4.3 lists the leading contributions to the uncertainty in V_{ud} . The largest contribution comes from the uncertainty in the β asymmetry followed by the nuclear-independent correction, the radiative corrections and the uncertainty in the lifetime. The other sources of uncertainty are less significant than

any of those listed in the table by at least an order of magnitude.

Table 4.3: Primary contributions to the uncertainty in V_{ud} .

Parameter	Uncertainty
A_0	0.0009
Δ_R^V	0.0002
$\delta_C^V - \delta_{NS}^V$	0.0002
$t_{1/2}$	0.0001
δ'_R	0.00006
Total	0.0010

[Bar95] J. Baro *et al.*, Nucl. Instrum. Methods B, **100**, 31 (1995).

[Har09] J. C. Hardy and I. S. Towner, Phys. Rev. C, **79**, 055502 (2009).

[Jon96] G. Jones, Ph.D. thesis, Princeton University, Princeton, NJ, 1996.

4.2.4 Neutron Interferometric Search for Dark Energy

A.R. YOUNG, B.J. HEACOCK, *TUNL*; M. SNOW, K. LI, *Indiana University, Bloomington, IN*; D. PUSHIN, *University of Waterloo, Waterloo, ON, Canada*; M. HUBER, M. ARIF, *National Institute of Standards and Technology, Gaithersburg, MD*; *The INDEX Collaboration*

A laboratory search for dark energy using neutron interferometry is now underway at the National Institute of Standards and Technology’s Center for Neutron Research. Specifically, we are constraining the chameleon field, a scalar field that may be driving the dark-energy expansion of the universe. We are now working to further constrain the chameleon field as well as search for other fifth forces using two-blade neutron interferometry.

The chameleon scalar field was first proposed by J. Khoury and A. Whelton as a candidate for the dark-energy expansion of the universe [Kho04a, Kho04b]. The field takes its name from a coupling to matter which causes the chameleon field’s effects to be extinguished in regions of space where the local matter density is too large. Hence, the field can drive the universe’s expansion in low density regions of space through a self-interaction, yet remain elusive elsewhere. Remarkably, however, for a coupling to matter that is sufficiently strong, laboratory experiments are sensitive to the chameleon field [Bra13]. The theory is constrained by setting an upper limit on the chameleon-matter coupling, β , defined within the interaction potential as:

$$V[\phi] = \Lambda^4 + \frac{\Lambda^{4+n}}{\phi^n} + \frac{\beta}{M_{\text{Pl}}} \rho \phi, \quad (4.3)$$

where n is the Ratra-Peebles index and a positive integer, M_{Pl} is the Plank mass, ρ is the matter density, and $\Lambda \simeq 2.4$ meV is scaled by the dark energy expansion of the universe [Bra13].

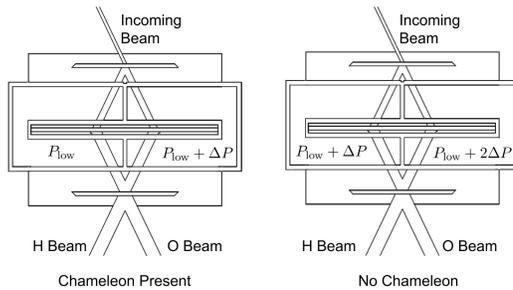


Figure 4.34: Schematic of the experimental setup shown in the chameleon-present and chameleon-attenuated pressure configurations.

We are currently finishing an experiment which constrains the chameleon-matter coupling using a neutron interferometer. In this experiment the interferometer is in the Mach-Zehnder geometry shown in Fig. 4.34. To produce a phase shift from the chameleon field, one of the beam paths goes through a gas chamber with a pressure ranging from 2.5×10^{-5} torr to 0.015 torr (P_{low} in Fig. 4.34), while the other beam path experiences higher pressures ($P_{\text{low}} + \Delta P$). This is shown in the left half of Fig. 4.34. Two sets of runs were completed, with ΔP set to 0.1 torr and 1 torr. Results are shown in Fig. 4.35.

To isolate the chameleon phase, the difference between the phases of the two configurations shown in Fig. 4.34 is taken. To account for drifts in the phase of the interferometer, the data was filtered as prescribed in Ref. [Swa10]. The residuals of the measured and predicted phases as a function of β were then used to solve for the limiting value of β for a 95% one-sided confidence interval. Our preliminary result ranges from 4.0×10^6 for $n = 1$ to 2.7×10^7 for $n = 6$.

Greater sensitivity to the chameleon field should be possible using two-blade interferometry. This technique may also be sensitive to other fifth-force theories, such as those described in Ref. [Les14]. We are currently in the pre-design phase of constructing a large interferometer (see Fig. 4.36) that will be operated in vacuum. A chameleon field would then deflect neutrons toward the deflecting plate. This would cause a shift in the rocking curve generated by tilting a prism which slightly deflects neutrons in the direction perpendicular to the Bragg planes of the crystal. Figure 4.37 was generated using an already-existing interferometry crystal at NIST.

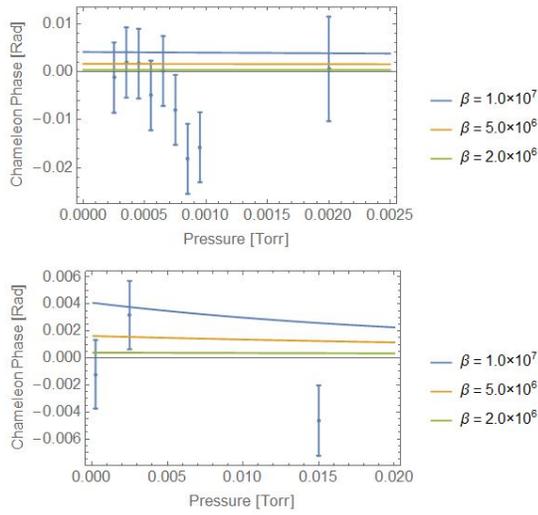


Figure 4.35: Phase shift versus the low-pressure setpoint. Theoretical phase shifts for a few values of the chameleon-matter coupling values, β , are also shown. The top graph corresponds to a differential pressure of 0.1 torr, while for the bottom graph, the value is 1 torr.

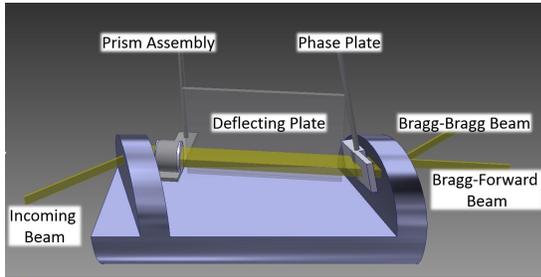


Figure 4.36: Concept for a large two-blade interferometer designed to be sensitive to the chameleon field and other fifth force searches.

The FWHM of the central interference peak in Fig. 4.37 is inversely proportional to the thickness of the diffracting crystals [Rau15]. Therefore, the two blade interferometer being designed will have thick diffracting blades (1 to 3 cm), rendering it more sensitive to very small deflections of the neutron beam path.

The Neutron Interferometric Dark Energy

eXperiment (INDEX) collaboration intends to continue our search for dark energy by developing neutron interferometric experimental techniques specifically designed for the detection of dark energy. Our strategy may involve additional running with the current gas-cell geometry, but development of a two blade interferometer, because of its possible application to other short-range-force searches, is a high priority activity for the next few years.

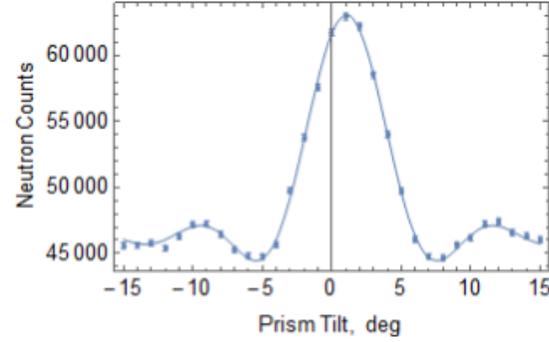


Figure 4.37: Rocking-curve data recently taken at NIST with an existing crystal with 2.5-mm-thick diffracting blades.

-
- [Bra13] P. Brax, G. Pignol, and D. Roulier, *Phys. Rev. D*, **88**, 083004 (2013).
 - [Kho04a] J. Khoury and A. Weltman, *Phys. Rev. D*, **69**, 044026 (2004).
 - [Kho04b] J. Khoury and A. Weltman, *Phys. Rev. Lett.*, **93**, 171104 (2004).
 - [Les14] T. Leslie *et al.*, *Phys. Rev. D*, **89**, 114022 (2014).
 - [Rau15] H. Rauch and S. A. Werner, *Neutron Interferometry: Lessons in Experimental Quantum Mechanics, Wave-particle Duality, and Entanglement*, volume 12, Oxford University Press, 2015.
 - [Swa10] H. E. Swanson and S. Schlamminger, *Measurement Sci. Tech.*, **21**, 115104 (2010).

4.2.5 Oklo Reactors and Implications for Nuclear Science

E.D. DAVIS, *Department of Physics, Kuwait University, Kuwait*; C.R. GOULD, *TUNL*; E.I. SHARAPOV, *Joint Institute for Nuclear Research, Dubna, Russia*

We recently reviewed the nuclear physics interests in the Oklo natural nuclear reactors, focusing particularly on the sensitivity of neutron resonance energy shifts to changes over time in the fine structure constant α and in X_q , the ratio of the average quark mass and to the QCD mass scale. We suggested a new formula for the combined sensitivity to α and X_q that exhibits the dependence on Z and A , allowing QED and QCD effects to be disentangled if more data are available.

The Oklo natural nuclear reactors in Gabon, West Africa were discovered in 1972 and have continued to generate scientific interest across many disciplines to this day. The basic facts are well established: two billion years ago the natural percentage of ^{235}U was 3.7%, comparable to today's power reactors and sufficient to allow a cycling chain reaction to proceed in ordinary water over hundreds of thousands of years. The fission products also remained in place, allowing present-day isotopic abundance data to be used as constraints on neutron resonance energy shifts over time.

Time varying fundamental constants are a feature of many new theories seeking to understand the smallness of the cosmological constant and the nature of dark energy. Shlyakhter was the first to recognize the potential of Oklo data to constrain changes in fundamental constants [Shl76], noting that if the energy of a ^{149}Sm resonance shifts down from its present day value of $E_r(\text{now}) = 97.3\text{ meV}$, then more ^{149}Sm will be burned in the neutron flux, and less ^{149}Sm will be found in the isotopic remains of the reactor. Conversely, if the resonance shifts up, less will be burned, and the remains will be richer in ^{149}Sm . In practice, the temperature of the neutron spectrum must be taken into account, other resonances may contribute, and details of the results can change when the epithermal component of the flux is included from MCNP Monte Carlo modeling.

In our review [Dav14] we noted that the water content and the temperatures of the reactors have been uncertain parameters for many years, and we summarized recent work pointing to lower temperatures than earlier assumed. Nuclear cross sections are input to all Oklo model-

ing and we also discussed a parameter, the ^{175}Lu ground state cross section for thermal neutron capture leading to the isomer $^{176\text{m}}\text{Lu}$, that warranted further investigation.

Damour and Dyson initiated the modern era of Oklo fundamental constant studies with a landmark 1996 analysis [Dam96] which approximated the neutron capture resonance energy E_r as a difference in expectation values of the nuclear Hamiltonian \hat{H} :

$$E_r = \langle r | \hat{H} | r \rangle - \langle g | \hat{H} | g \rangle, \quad (4.4)$$

where $|g\rangle$ denotes the eigenket of the ground state of the target nucleus and $|r\rangle$ denotes the eigenket of the compound nucleus state formed by the capture of the neutron. This difference is then related to a difference in Coulomb energies, resulting in their widely-used estimate

$$\frac{\Delta\alpha}{\alpha} = -\frac{\Delta_r}{M} \quad (4.5)$$

with $M = 1.1\text{ MeV}$.

In reviewing this estimate we identified some corrections and improvements that could be made, based on better nuclear structure data. We recently incorporated this work in a follow up publication [Dav15].

We also reviewed analyses of how Oklo data place constraints on the time variation of the dimensionless ratio $X_q = m_q/\Lambda$, where $m_q = \frac{1}{2}(m_u + m_d)$ is an average quark mass and Λ is the QCD mass scale. The most complete analysis to date has been that of Flambaum and Wiringa in Ref. [Fla09]. Combining their work with that of Damour and Dyson led us to propose a more general resonance shift expression $\Delta_r \equiv E_r(\text{Oklo}) - E_r(\text{now})$ due to the (small)

changes $\Delta X_q \equiv X_q(\text{Oklo}) - X_q(\text{now})$ and $\Delta\alpha \equiv \alpha(\text{Oklo}) - \alpha(\text{now})$. Specifically:

$$\Delta_r = a \frac{\Delta X_q}{X_q} + b \frac{Z^2}{A^{4/3}} \frac{\Delta\alpha}{\alpha}, \quad (4.6)$$

where the coefficients a and b are independent of A and Z . At present there are insufficient data on multiple isotopes to allow a test of this expression. Nevertheless, even with only ^{149}Sm data, Oklo continues to provide a very tight constraint on time variation of the fine structure constant over the last two billion years:

$$\left| \frac{\Delta\alpha}{\alpha} \right| < 1.1 \times 10^{-8}, \quad (4.7)$$

at a 95% confidence limit [Dav15].

- [Dam96] T. Damour and F. J. Dyson, Nucl. Phys., **B480**, 37 (1996).
- [Dav14] E. D. Davis, C. R. Gould, and E. I. Sharapov, Int. J. Mod. Phys. E, **23**, 1430007 (2014).
- [Dav15] E. D. Davis and L. Hamdan, Phys. Rev. C, **92**, 014319 (2015).
- [Fla09] V. V. Flambaum and R. B. Wiringa, Phys. Rev. C, **79**, 034302 (2009).
- [Shl76] A. I. Shlyakhter, Nature, **264**, 340 (1976).

4.2.6 CALIOPE: A Search for CP Violation in Positronium

R. HENNING, A.E. CHAMPAGNE, C.L. BARTRAM, J. OTHMAN, K. NIBBS, *TUNL*

CALIOPE is a new experiment looking for CP -violation through correlations between the directions of the three photons emitted in ortho-positronium (o-Ps) decay and the spin of the o-Ps. It will detect γ rays using the APEX NaI array and will have a tagged source and a novel, conventional electromagnet to reduce systematic uncertainties. The high angular acceptance of APEX will provide about twenty-five times the statistics of previous experiments.

CALIOPE, or CP Aberrant Leptons in Ortho-Positronium Experiment, will search for CP -violating angular correlations in positronium (Ps) decay. Recent interest in searches for fundamental symmetry violations in the lepton sector, including long-baseline neutrino experiments [LBN] and attempts to measure electric dipole moments [Han08], provide motivation for our research. If discovered, CP -violation in the lepton sector would have profound implications on our current understanding of particle interactions and would require modifications to the Standard Model in the form of new physics. CALIOPE will increase the angular coverage over the previous experiment [Yam10] by a factor of twenty-five and will enable us to obtain higher statistics. Additionally, CALIOPE will implement a large, reversible electromagnet, capable of generating a field of about 0.5 T with a field inhomogeneity of less than 2%. This magnet as well as sophisticated data-analysis techniques will further improve our sensitivity over previous experiments. Figure 4.38 shows a cross sectional diagram of the CALIOPE apparatus.

Positronium, a bound state of an electron and a positron, is inherently unstable. The triplet state, o-Ps, decays into three γ rays, whereas p-Ps, the singlet state, decays into two γ rays. CALIOPE uses the existing APEX detector to detect these γ rays. APEX is a cylindrical array of twenty-four sodium iodide bars with PMTs on either end. CALIOPE uses ^{22}Na deposited on Kapton foil at the center of the APEX array as a source of positrons. The foil is sandwiched between two pieces of scintillator, which tag the positron emitted in the β decay of ^{22}Na . The scintillator light is piped via optical fiber to a nearby PMT, which serves as our start signal. The positron migrates into a disk of Aerogel,

where it interacts with an electron in the SiO_2 to form positronium. The resulting decay γ rays are detected by the sodium iodide bars. An ambient magnetic field can alter the lifetimes of the $m = 0$ magnetic spin states. The CALIOPE experiment uses a large electromagnet because we need to be able to separate out these spin states in order to measure our observable.

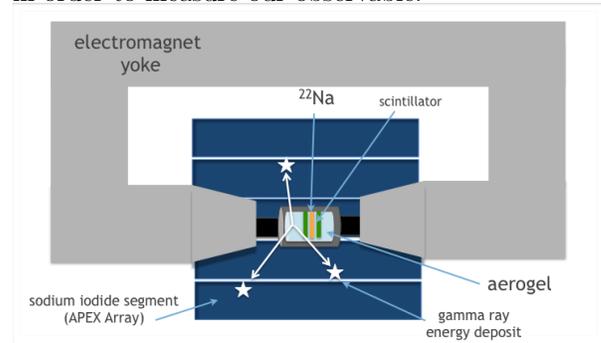


Figure 4.38: Diagram of the CALIOPE apparatus.

The orientation of the γ rays with respect to the spin allows us to measure the following CP -violating observable:

$$(\vec{S} \cdot \vec{k}_1)(\vec{S} \cdot \vec{k}_1 \times \vec{k}_2) = P_2 \cos \phi \sin \psi \sin 2\theta \quad (4.8)$$

A visualization of the decay, including the angles in Eq. 4.8, is shown in Fig. 4.39. The arrow labeled S is the spin-quantization axis, n is the normal to the decay plane, and k_1 and k_2 are the highest and second highest energy γ rays, respectively. The quantity P_2 in Eq. (4.8) is the tensor polarization term, which can be expressed as

$$P_2 = \frac{N_{+1} - 2N_0 + N_{-1}}{N_{+1} + N_0 + N_{-1}}. \quad (4.9)$$

where N_i is the population of the $m_s = i$ positronium state. The presence of a magnetic field breaks the degeneracy in the N_i states and provides us with a nonzero value of P_2 . The observable in Eq. (4.8) is CP -violating and, importantly, also CPT conserving. This means that our experiment will exclusively search for CP -violation.

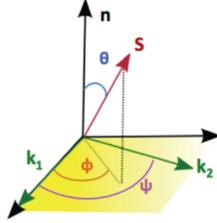


Figure 4.39: Schematic diagram of o-Ps Decay

Angular correlations in ordinary, CP -conserving positronium decays exist and have been calculated by Bernreuther [Ber81]. These have been incorporated into our simulation. Using GEANT4 [Gea], we have tested multiple designs for the source-holder configuration and have gained an understanding of how the surrounding materials affect our ability to measure the asymmetry. We are developing a table of systematic uncertainties based on Monte Carlo simulations. Figures 4.40 and 4.41 show our observable as a function of the measured angles in o-Ps decay both without and with CP -violation, respectively.

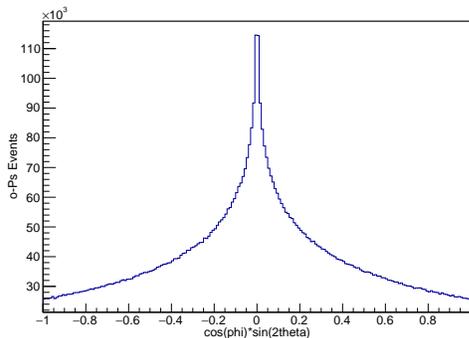


Figure 4.40: Monte Carlo simulation of the computed asymmetry $\sin(2\theta) \cos(\phi)$ for normal o-Ps decays.

The design of our electromagnet was developed using the simulation software RADIA [Rad]. RADIA enabled us to test the effectiveness of iron shielding to isolate PMTs from strong magnetic fields. Progress involving the DAQ has entailed testing various digitizers, including CAEN V1730

and Struck SIS3301 cards. We believe we can achieve high timing resolution for hits in our detector using a method tested by an REU student last summer (see Sect. 8.2.4). Figure 4.42 is a picture of our collaboration.

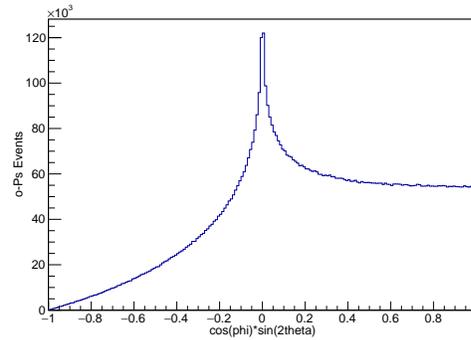


Figure 4.41: Same as Fig. 4.40 but for CP -violating o-Ps decays.



Figure 4.42: The CALIOPE Collaboration

-
- [Ber81] W. Bernreuther and O. Nachtmann, *Z. Phys. C*, **11**, 235 (1981).
- [Gea] *Geant4*, <http://geant4.cern.ch/>, Accessed: 2015-03-25.
- [Han08] D. Hanneke, S. Fogwell, and G. Gabrielse, *Phys. Rev. Lett.*, **100**, 120801 (2008).
- [LBN] *Deep Underground Neutrino Experiment*, <http://www.dunescience.org/>, Accessed: 2015-12-22.
- [Rad] *Radia*, <http://www.esrf.eu/Accelerators/Groups/InsertionDevices/Software/Radia>, Accessed: 2015-12-22.
- [Yam10] T. Yamazaki *et al.*, *Phys. Rev. Lett.*, **104**, 083401 (2010).

4.2.7 Electromagnet Design for an Experimental Search for CP -violation in Positronium Decay

R. PETERSBURG, C.L. BARTRAM, R. HENNING; *TUNL*

The CALIOPE experiment, a search for CP -violating angular asymmetries in the γ rays emitted in the decay of ortho-positronium, requires a magnetic field to align the spins of the positronium atoms before they decay. This field is to be generated with an electromagnet that allows the field direction to be reversed in order to reduce systematic uncertainties in the asymmetry measurement. We calculate that a magnetic field of about 0.5 T is needed and propose an optimized design for the experiment.

The CALIOPE experiment, described in Sect. 4.2.6, will search for CP -violation in the decay of ortho-positronium (o-Ps) by calculating the following term:

$$(\vec{S} \cdot \vec{k}_1)(\vec{S} \cdot \vec{k}_1 \times \vec{k}_2) = P_2 \cos \phi \sin \psi \sin 2\theta \quad (4.10)$$

In this equation, k_1 and k_2 are the momenta of the highest and second highest energy γ rays, respectively; ϕ is the angle between the projection of the spin onto the decay plane and k_1 ; θ is the angle between the normal to the decay plane and the spin axis; and ψ is the angle between k_1 and k_2 . The quantity P_2 in the observable above is the tensor polarization term, which can be expressed as follows:

$$P_2 = \frac{N_{+1} - 2N_0 + N_{-1}}{N_{+1} + N_0 + N_{-1}} \quad (4.11)$$

N_i is the population of the $m_s = i$ o-Ps state. In the absence of a magnetic field, the three populations are equal and P_2 is zero. The effect of a magnetic field on positronium can be described in terms of perturbation theory. In what is essentially the Zeeman effect for positronium, the $m = 0$ o-Ps and parapositronium (p-Ps) states mix and form perturbed states with altered lifetimes. The magnetic field creates a tensor polarization and provides us with a non-zero value for P_2 . In this report we present studies that led to the baseline design for the CALIOPE magnet.

The electromagnet yoke will be made of iron, with copper coils wrapped close to the pole tips of the magnet. Cooling will be achieved with a water jacket or through the use of water-cooled copper coils. A diagram is shown in Fig. 4.43.

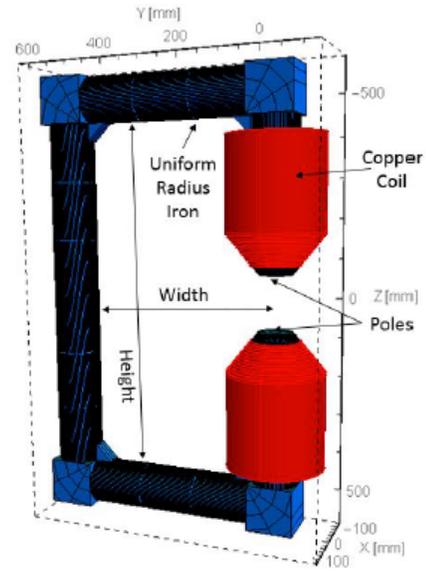


Figure 4.43: Schematic diagram of the CALIOPE electromagnet.

The electromagnet was developed with the intention of creating a magnetic field of 0.5 T, or 5 kGauss, to achieve optimal polarization. We designed the magnet using the RADIA software [Rad], which runs in Mathematica. Two goals were to maximize magnetic homogeneity and minimize longitudinal magnetic fields in the photomultiplier tubes. An important concept in this optimization process is a “non-functional field”, which describes components of the magnetic field perpendicular to the “functional field”. The “functional field” refers to the field localized near the positronium source and pointing down

the length of the APEX detector array (the z -direction). An optimization process, which minimized the ratio of the non-functional fields to the functional fields, was used to select various features of the magnet. Minimizing the non-functional fields reduces the magnetic field close to the photomultiplier tubes. The optimization process yielded a maximum field strength of 300 Gauss near the photomultiplier tubes. Consequently, studies are underway to understand and reduce the effects of such a magnetic field on the photomultiplier tubes. We have already shown that a steel pipe of about 0.25-inch wall thickness wrapped around the photomultiplier tube holder reduces the magnetic field by about an order of magnitude to acceptable levels, as shown in Fig. 4.44.

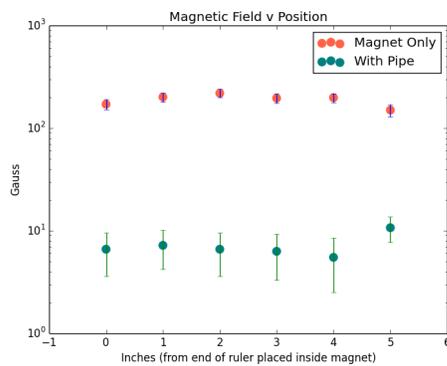


Figure 4.44: Reduction in the magnetic field at the PMTs due to shielding.

Other constraints, such as the dimensions of the APEX array, were taken into consideration. The final electromagnet design has a height of 900 mm, a width of 500 mm, a radius of 58 mm, and a pole radius of 42 mm. Between fifteen and twenty coil layers will be used, corresponding to a power dissipation of between 1500 and 1400 (± 200) watts and a current between 48 and 39 (± 2) amps. Figures 4.45 through 4.47 show results of some of the RADIA calculations. The optimal design which resulted from the RADIA simulation has been incorporated into our Monte Carlo simulation using GEANT4 [Gea].

The electromagnet will enable us to change the polarity of the field, which will help us cancel out systematic effects. It will also be easier to assemble than a permanent magnet and will provide some level of adjustability to the magnetic field. Our simulations also yield an inhomogeneity in the field of less than 2%, whereas previous experiments only achieved less than 10% [Yam10]. We believe that these and other improvements will enable us to achieve a higher sensitivity to CP -violation than past experiments.

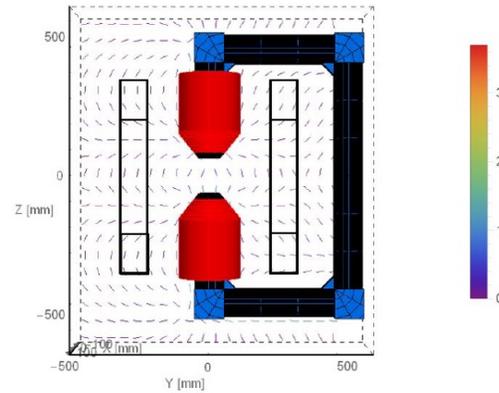


Figure 4.45: Cross Section of the magnet showing the magnetic field directions.

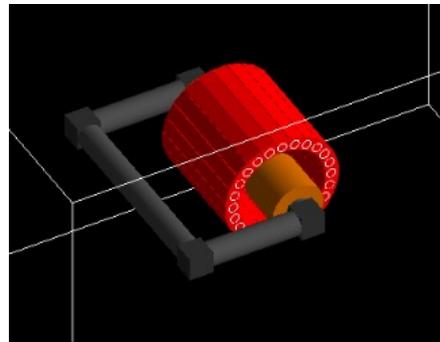


Figure 4.46: GEANT4 diagram of the detector array with the magnet.

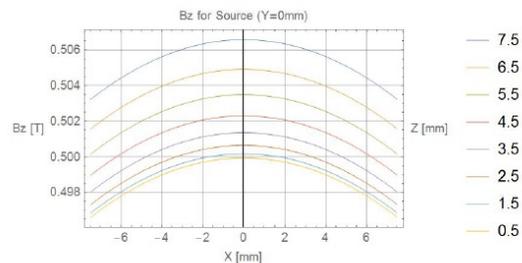


Figure 4.47: The z -component of the magnetic field.

[Gea] *Geant4*, <http://geant4.cern.ch/>, Accessed: 2015-03-25.

[Rad] *Radia*, <http://www.esrf.eu/Accelerators/Groups/InsertionDevices/Software/Radia>, Accessed: 2015-12-22.

[Yam10] T. Yamazaki *et al.*, *Phys. Rev. Lett.*, **104**, 083401 (2010).

Neutrino Physics

Chapter 5

- $\beta\beta$ -Decay Experiments

5.1 $\beta\beta$ -Decay Experiments

5.1.1 Construction and Commissioning of the MAJORANA DEMONSTRATOR Project

M. BUSCH, T.S. CALDWELL, T. GILLIS, G.K. GIOVANETTI, M.P. GREEN, R. HENNING, M.A. HOWE, J.M. MACMULLIN, S.J. MELJER, C.M. O'SHAUGHNESSY, J. RAGER, B.E. SHANKS, J.E. TRIMBLE, K. VORREN, J.F. WILKERSON, W. XU, *TUNL*

We report recent progress on the construction and commissioning of the MAJORANA DEMONSTRATOR at the 4850-foot level of the Sanford Underground Research Facility. TUNL has played a leading role in many of these activities and has provided a significant on-site workforce. During the reporting period, we have started the commissioning of Module 1 and collected our first low-background in-shield data. We have also started construction on Module 2.

We have made substantial progress in the construction and commissioning of the MAJORANA DEMONSTRATOR (MJD), an array of high purity germanium detectors, enriched to 87% in ^{76}Ge . MJD is being constructed underground at the Sanford Underground Research Facility (SURF) in Lead, SD. The DEMONSTRATOR will search for neutrinoless double-beta decay and examine the viability of a future, larger scale germanium experiment. In this report we highlight the accomplishments of the last year in which TUNL has taken a leading or significant role.

We completed data-taking with the prototype module in the shield and it has been decommissioned. The components of its vacuum system were repurposed for the Module 2 vacuum system, which was assembled on-site by TUNL staff and collaborators. A TUNL graduate student has used data from the prototype to develop analysis techniques that determine the physical location of background sources using the full detector spectra [Mac15]. This work helped identify the thermometry components and lead solder as the dominant contributors of background in the prototype. These components were for diagnostic purposes and are not used in Modules 1 and 2.

Based on the completed assays of all materials used in construction and assembly of the DEMONSTRATOR, our simulations project a total background of ≤ 3.5 counts/t-y in the region of interest centered at the end-point energy for double-beta decay for Modules 1 and 2. This is close to our specified goal of ≤ 3.0 counts/t-y and exceeds the key performance parameter goal

of < 10 counts/t-y.



Figure 5.1: Installation of Module 1 strings being conducted inside the glovebox.

We completed assembly of the first ultra-clean array module (Module 1), which contains seven strings of detectors mounted in an electroformed vacuum cryostat mounted on its transportable monolith (see Fig. 5.1). There are a total of twenty detectors containing 16.8 kg of ^{76}Ge in $^{\text{enr}}\text{Ge}$ detectors and 5.7 kg in $^{\text{nat}}\text{Ge}$ detectors. A successful repair on the module's thermosyphon Dewar at the TUNL vacuum shop allowed us to

install and operate the Dewar, which had failed during its initial testing. The first in-shield commissioning run was started on June 26 and was completed on October 7. The run was stopped to allow us to install the inner electroformed copper shielding and implement several additional improvements to the module internals. Background data from this run are currently being analyzed (see Fig. 5.2). We are also using the data to study the low energy performance of MJD and to assess its ability to search for different dark-matter candidates. During this time, a TUNL engineer has continued to coordinate the on-site fabrication of parts for Module 2 and its shield (see Fig. 5.3).

High Rn: No Cuts

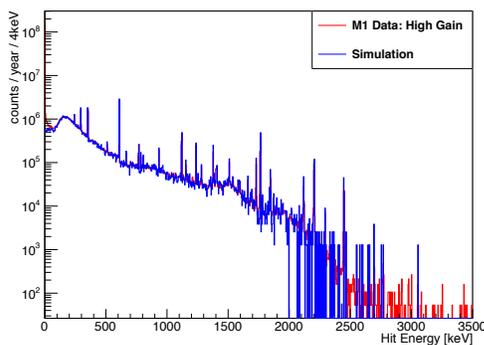


Figure 5.2: (Shown in red is the single spectrum for the Module 1 array in the shield but with the cavity filled with room air, which is high in radon. Overlaid in blue is a simulated spectrum for Module 1 in the same configuration.

During the reporting period, MJD transitioned into production data-taking. We tested the data pipeline from SURF to the National Energy Research Science Computing Center in Oakland, CA. Our online and offline analysis tools were also commissioned, and the collaboration is currently running with fully automated data-processing. A sophisticated and comprehensive on-line monitoring system that provides real-time updates on the status of all underground systems was implemented and is described in Sect. 8.2.5. TUNL post-docs and graduate students are contributing significant effort to the development of analysis software and the analysis of the data itself.

A total of 35 detectors with a mass of 29.7 kg were produced from our 87% enriched ^{76}Ge ma-

terial. Initially ORTEC produced 30 detectors with a mass of 25.3 kg, providing a yield of 64.4%, comparable to all previous experiments. However, we were able to successfully recover and reprocess material captured from the detector manufacturer’s “waste stream.” This provided us with an additional 4.4 kg of detectors and resulted in a final yield of 74.5%, the best ever achieved.

Underground electroforming at the Temporary Clean Room (TCR) located at the Ross Campus at SURF was completed in April 2015. We produced a total of 2474 kg of electroformed Cu. Machining of the inner Cu shielding plates was completed in October, and they were installed in November 2015.

Finally, we recommissioned the KURF low-background assay system and performed several critical assays for MJD. We are also designing a world-class ultra-low background γ -ray-assay system that is based on MJD technology.



Figure 5.3: Checking the alignment of the inner copper shield installation table.

[Mac15] J. S. MacMullin, Ph.D. thesis, University of North Carolina at Chapel Hill, 2015.

5.1.2 Monte Carlo Waveform Fitting for the MAJORANA DEMONSTRATOR

B. SHANKS, C. O'SHAUGHNESSY, J. NANCE, J.F. WILKERSON, *TUNL*

We describe a Markov Chain Monte Carlo framework for fitting waveforms from germanium p-type point-contact detectors in the MAJORANA DEMONSTRATOR. Early results suggest it can reliably reconstruct the location of energy deposition inside the detector, but further validation work is needed.

The MAJORANA DEMONSTRATOR is an array of p-type point-contact (PPC) germanium detectors which will search for neutrinoless double-beta decay ($0\nu\beta\beta$) in ^{76}Ge (see Sect. 5.1.1). Because $0\nu\beta\beta$ is an extremely rare process, background reduction and rejection are critical to the sensitivity of the experiment. The DEMONSTRATOR will use pulse-shape analysis (PSA) to reject background events based on the waveform shape. Compared to simple filtering methods, fitting the entire digitized waveform increases the information that can be extracted from the pulse shape. The MAJORANA collaboration has developed a Bayesian Markov Chain Monte Carlo (MCMC) fitting routine [Gil95] to fit waveforms using a model of PPC detector response. This model depends sensitively on the characteristics of each unique detector crystal.

In a germanium detector, a signal is induced at the readout electrode as charge carriers drift through the detector volume. The amplitude of the induced charge Q is proportional to the change in the weighting potential the charge drifts over and to the charge of the carriers q according to the Shockley-Ramo Theorem [Kno10]

$$Q = q\Delta\varphi_0 \quad (5.1)$$

For a single-electrode detector, like a PPC, the weighting potential is identical to the normalized electric potential. The drift path and velocity of the carriers will likewise depend on the electric fields inside the detector. Therefore, an accurate model of waveform generation depends critically on an accurate calculation of fields within the detector.

This calculation is performed using the software package FIELDGEN [Coo11], developed at ORNL. Given the crystal geometry, the concentration of crystal impurities, and the detector operating voltage, FIELDGEN calculates the weight-

ing potential and electric fields within the crystal volume using a numerical relaxation routine. The MAJORANA collaboration uses a high precision optical measuring device from Starrett to measure crystal dimensions. Impurity concentrations are measured by the manufacturer, ORTEC, during fabrication using a Hall-effect technique, but the errors on this measurement can be as high as 30%. In order to improve the accuracy, it is possible to compare the calculated depletion voltage at a given impurity concentration to the observed depletion voltage of the detector. A golden-search algorithm has been implemented to find the correct impurity concentration given a depletion voltage. An example of a weighting potential calculated with FIELDGEN is shown in Fig. 5.4.

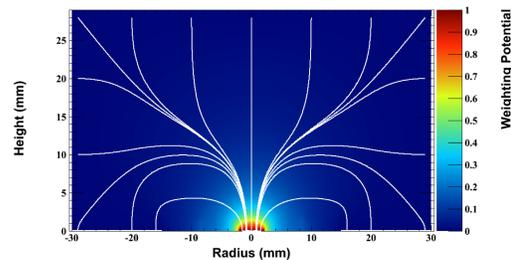


Figure 5.4: Weighting potential in a PPC germanium detector calculated using FIELDGEN. The white lines show charge-carrier drift paths. The point contact electrode is at bottom center.

Once the field calculations have been performed for a crystal, the signal from an energy deposition at a given location can be modeled by simulating the dynamics of the charge carrier motion while applying the Shockley-Ramo Theorem. A second ORNL package, named SIGGEN [Coo11], is used to perform this calculation and produce waveforms such as shown in Fig. 5.5.

The MAJORANA detectors are p-type, meaning the positively charged holes drift toward the electrode, and electrons drift toward the outside surface of the detector. Since the weighting potential in a PPC detector is strongly peaked near the electrode, as seen in Fig. 5.4, it is clear from Eq. 5.1 that holes are responsible for the majority of the signal. However, it is important to note that the total signal generated is the sum of the contributions from both holes and electrons. For an energy deposition in the crystal bulk, the carriers will drift in the region of low weighting potential for around 0.1 to 1 μs before the holes reach the electrode region. During this “drift time,” the electron contribution will be a sizable percentage of the overall signal. Once the holes reach the electrode, the signal sharply rises over a “collection time” of 10’s of ns.

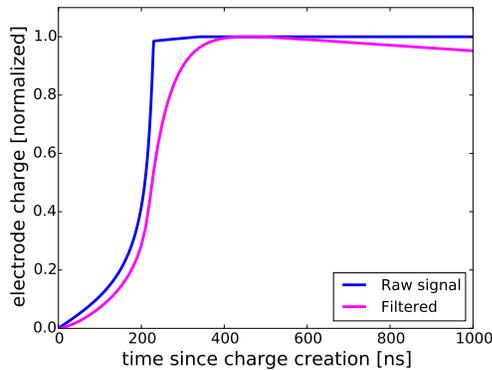


Figure 5.5: Example signal calculated in a PPC detector. The raw signal is the output from SIGGEN. The electronics readout introduces additional shaping to the signal. An exaggerated example is the “filtered” curve. The first 150 ns are the drift time; the holes are fully collected shortly after 200 ns.

The final contribution to the measured waveform is additional shaping caused by the electronics readout chain. A simple model of the MAJORANA electronics shaping is an RC filter with a short bandwidth (~ 50 ns) and a long decay time of about 70 μs . The exact values are determined for each detector using a pulser. The effect on signal shape is shown in Fig. 5.5.

Using this model, a signal can be generated for an energy deposition at any given location in the detector. It is possible, then, to use a fitting algorithm to estimate the location of a deposition event (within the crystal-axis symmetry of germanium). For non-linear and high-dimensional regression, Markov Chain Monte Carlo (MCMC) techniques are widely recognized as powerful fitting tools [Gil95]. Using a Bayesian framework, an MCMC algorithm will converge on the pos-

terior probability distribution function for each input variable, given the observed data. For this application, the Metropolis-Hastings sampling algorithm has been used to estimate the position within the detector, the energy deposition time, and the amplitude of a digitized waveform. Sample results are shown in Fig. 5.6.

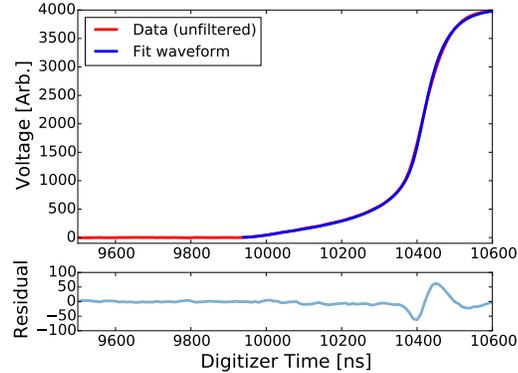


Figure 5.6: A MAJORANA waveform is shown in red, with the MCMC best fit in blue. Residuals are plotted below.

Early results from the MCMC fitting are promising. However, it is clear from the residuals in Fig. 5.6 that the modeled collection region of the signal does not reproduce the true waveform shape. It is suspected that this could be due to an overly simplified electronics shaping model. In the future, digitized pulser data could be used to construct a non-analytic electronics shaping transfer function, which could be used to apply the electronics shaping with greater fidelity.

Using the current model, the MCMC fit reconstructs the position of an energy deposition within a mm^3 uncertainty, within an eight-fold azimuthal degeneracy due to the crystal symmetry. These results have only been achieved on a small subset of detectors, and have not been validated using data with known location profiles. Dedicated data will soon be taken to determine whether the model has any systematic biases. After validation, this technique could be extended to use PSA for background rejection.

[Coo11] R. Cooper *et al.*, Nucl. Instrum. Methods A, **629**, 303 (2011).

[Gil95] W. Gilks, S. Richardson, and D. Spiegelhalter, *Markov Chain Monte Carlo in Practice*, Chapman & Hall/CRC Interdisciplinary Statistics. Taylor & Francis, 1995.

[Kno10] G. Knoll, *Radiation Detection and Measurement*, John Wiley & Sons, 2010.

5.1.3 Simulations of Surface α -Particle Contamination for the MAJORANA DEMONSTRATOR

J. RAGER, R. HENNING, J.F. WILKERSON, *TUNL*

We describe the ongoing work of simulating the surface and bulk α -particle component of the background spectrum for the MAJORANA DEMONSTRATOR.

The MAJORANA DEMONSTRATOR (MJD) is a neutrinoless double-beta decay ($0\nu\beta\beta$ decay) experiment located at the 4850 ft. level of Sanford Underground Research Facility. Its design incorporates modular arrays of natural and enriched (in ^{76}Ge) germanium detectors. These arrays are divided into two modules enclosed within ultra-pure, low-background electroformed copper (EFCu).

As with most low-energy experiments of its class, MJD faces a significant challenge in its ability to mitigate a sea of backgrounds. These backgrounds come from a variety of different sources, such as cosmogenic activation of impurities within the germanium detectors, inherent radioactivity of non-EFCu components close to the detectors, ambient radiation from the laboratory's surrounding rock walls, and cosmic muons penetrating the rock overburden.

In order to understand the contributions of these respective sources to the total energy spectrum, detailed and accurate simulations are needed for comparison against production data. Our goal is to conduct a simulation study of surface and bulk α -particle backgrounds inside the EFCu cryostat. These backgrounds arise from nuclides in the ^{238}U decay chain, with ^{210}Po and ^{222}Rn being of particular interest. The former emits a low energy α particle which, if attenuated by the dead layer of the detectors, can overlap the energy region of interest for $0\nu\beta\beta$ decay; the latter creates the long-lived radioactive daughter ^{210}Pb .

The software used in this work is MAGE, a Monte Carlo framework for the GEANT4 simulation toolkit [Bos11]. It is developed by the MAJORANA and GERDA collaborations, from whom the software derives its name. Concerns arose early in this study over compile-time issues in

MAGE with certain specific hadronic interactions, and also over inaccuracies resulting from the extrapolation of high-energy hadronic cascade models in GEANT4 to low energies. We were especially interested in α -capture mechanisms such as (α, n) and (α, γ) , but we have subsequently used cross-section calculations [Kon13] from the TALYS nuclear-reaction code plus range tables for α particles in germanium from the NIST ASTAR database [Ber15] to set upper bounds on the probability of α capture in germanium within the energy range of 5 to 10 MeV.

At 5.3 MeV, the probability of a single interaction between an incident α particle and ^{76}Ge or major contaminants such as ^{74}Ge and ^6Li in the germanium crystals is less than or equal to 5×10^{-11} and thus effectively negligible. From this, we conclude that there is no need to include hadronic models in our α -particle simulations at all. Since then, simulations of surface α particles has proceeded using the as-built MAJORANA DEMONSTRATOR geometry in MAGE. Figure 5.7 shows the results of simulating a point ^{210}Po source on the surface of a germanium crystal.

[Ber15] M. Berger *et al.*, *astar: stopping-power and range tables for helium ions*, <http://physics.nist.gov/PhysRefData/Star/Text/ASTAR.html>, 2015.

[Bos11] M. Boswell *et al.*, *IEEE Trans. Nucl. Sci.*, **58**, 1212 (2011).

[Kon13] A. Koning *et al.*, *TENDL-2012 Nuclear Data Library: Alpha sub-library for Ge ($Z=32$)*, ftp://ftp.nrg.eu/pub/www/talys/tendl2012/alpha_html/Ge/AlphaGe.html, 2013.

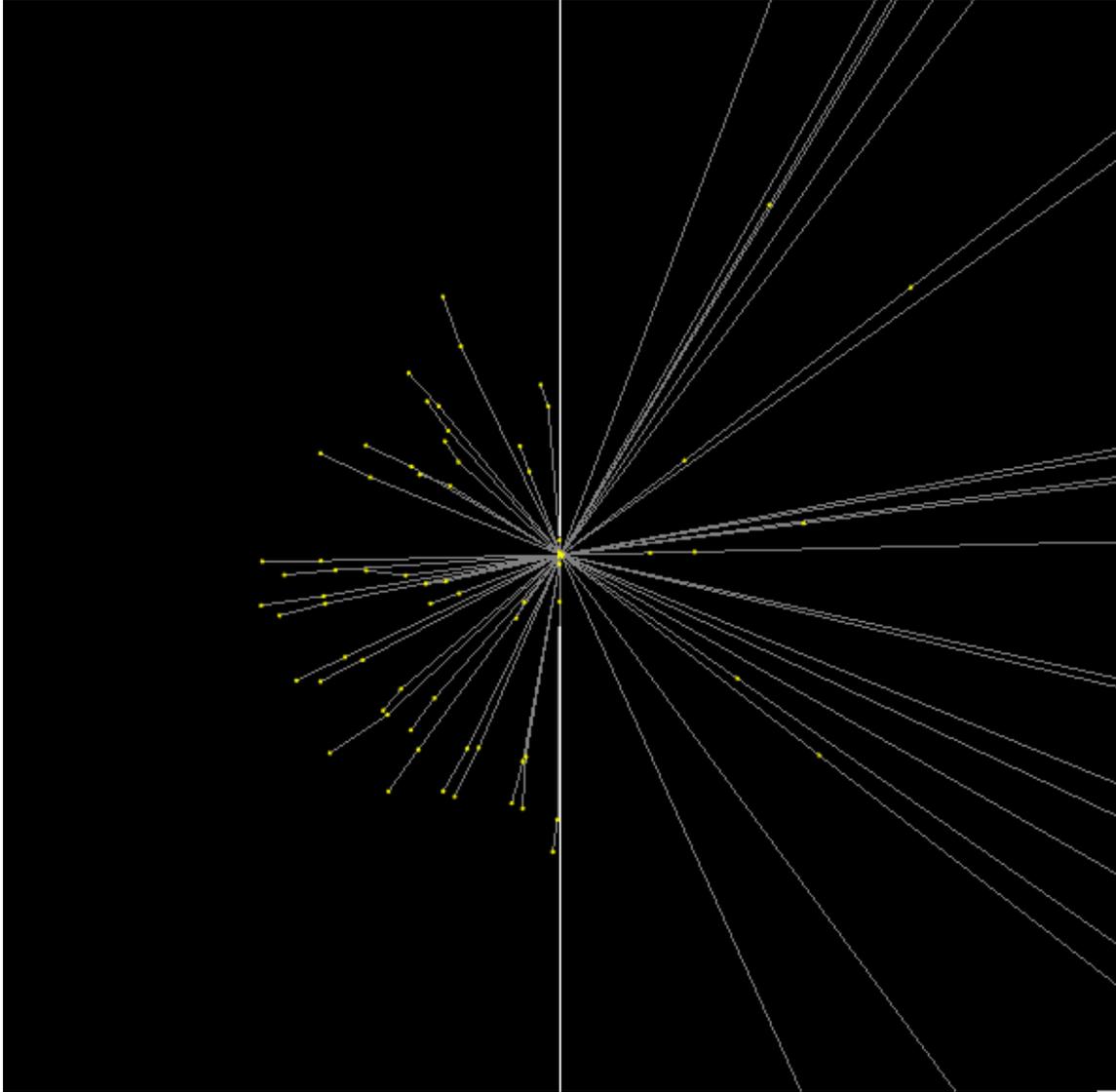


Figure 5.7: Preliminary Monte Carlo simulations of a ^{210}Po point source on the surface of a germanium crystal. The material to left of the white vertical line is germanium; the area to the right is air. The tracks and electromagnetic interactions of α particles are depicted. The ^{210}Po α particles in the germanium have track lengths of hundredths of a mm.

5.1.4 Identifying MAJORANA DEMONSTRATOR Backgrounds by Single-Site Time Correlation

T. GILLISS, R. HENNING, B. SHANKS, J.F. WILKERSON, *TUNL*; J.A. DETWILER, *University of Washington*

This report summarizes ongoing work to measure cosmogenically produced ^{68}Ge backgrounds in the MAJORANA DEMONSTRATOR neutrinoless double-beta decay experiment.

The MAJORANA DEMONSTRATOR is searching for the neutrinoless double-beta decay of ^{76}Ge using an array of HPGe detectors deployed in ultra-low background cryostats. It is currently undergoing commissioning at the Sanford Underground Research Facility in Lead, SD (see Sect. 5.1.1).

With the DEMONSTRATOR’s requirement of ultra-low backgrounds, it is essential to understand the spectral contributions of all materials present in the experiment, including radioactive impurities within the detectors themselves. One source of potential background is cosmogenically induced ^{68}Ge .

The isotope ^{68}Ge can be produced in germanium detectors by cosmic-ray spallation at the surface of the earth. As depicted in Fig. 5.8, this ^{68}Ge is accumulated during manufacturing and transport of germanium crystals and is mitigated by underground storage, shielded transportation containers, and minimized surface exposure. Accounting for ^{68}Ge concentrations is an essential task of the DEMONSTRATOR, because the decay of this isotope can contribute a background to the double-beta decay signal.

^{68}Ge decays via electron capture with a half-life of 270.95 days, yielding ^{68}Ga . For a K-shell electron capture, the subsequent relaxation of the ^{68}Ga orbitals yields an approximately 10 keV X-ray. ^{68}Ga is then unstable against decay and emits a positron with an endpoint energy of 1899.1 keV, an 87.94% branching ratio, and a 67.7 minute half-life. In the case that one or both annihilation γ rays sum with the positron within a detector, it is possible to observe energy depositions in the 2039 keV region of interest.

If left unchecked, the ^{68}Ge decay chain would constitute a dominant background contribution for the DEMONSTRATOR [FDR12]. Fortunately, in such background events, the summing energies

would be deposited in distinct locations within the DEMONSTRATOR’s detectors, thereby allowing many of these events to be vetoed using pulse shape analysis techniques or granularity cuts [Abr14, Sha13]. In addition, the low-energy thresholds and excellent energy resolution of germanium detectors allow for background mitigation via a single-site time-correlation (SSTC) cut. That is, by tagging an electron-capture X-ray, one can veto data from the subsequent positron decay by masking data from that detector for several half lives.

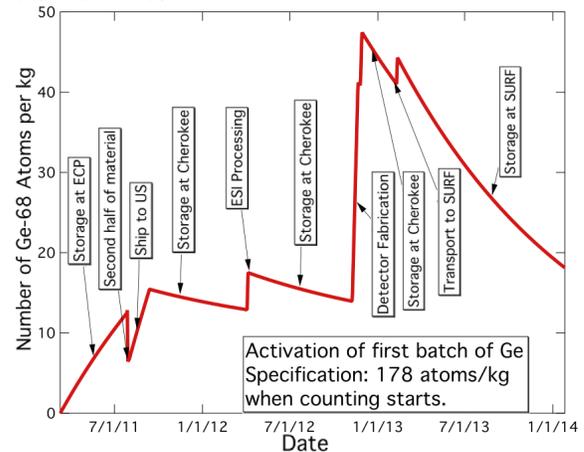


Figure 5.8: The calculated presence of ^{68}Ge throughout detector processing at the surface. In shielded storage, the concentration of ^{68}Ge impurities decays with a 270.95 day half-life [Whi14].

Fig. 5.9 presents preliminary energy spectra of events vetoed by the SSTC cut within the DEMONSTRATOR’s prototype detector module. These spectra are populated by events that have occurred within 67.7 min of a preceding 10-keV event and in the same detector as that event. A cut on maximum-waveform-current versus energy, known as “A/E”, was applied to

plot just those events with waveforms indicative of multiple sites of energy deposition, as in an event where both ^{68}Ga annihilation γ rays are captured within the same detector. While the beta-decay signature is obscured by more dominant backgrounds in the spectra seen here, these same methods can be used to observe the products of the ^{68}Ga decay and determine its contribution to the total background spectrum in the DEMONSTRATOR's lower-background enriched detector modules. From the activity of ^{68}Ga , one can also infer each detector's integrated cosmic ray exposure.

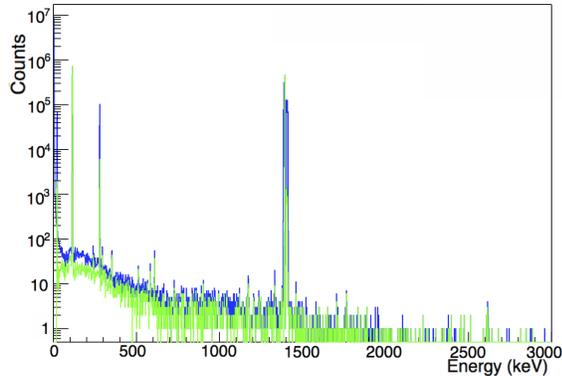


Figure 5.9: The blue energy spectrum shows candidate ^{68}Ga -decay events that fell within an SSTC time window for all working detectors in the DEMONSTRATOR's prototype module. The green spectrum includes only those events depositing energy in multiple locations, as determined by an A/E cut. The peak around 100 keV is populated by pulser events. Other prominent peaks can be seen close to their calibrated energies: ^{214}Pb at low energy, ^{40}K midway through the spectra, and ^{208}Tl just above 2600 keV.

The SSTC cut can be optimized to discount data in times surrounding positron events while minimizing the cost to live time. Such optimization preserves the experiment's sensitivity and depends on the rate of K-shell events, the rate of background events at the K-shell energy, and the efficiency of K-shell event identification [Det11]. Given sufficiently low energy thresholds, the tagging can also be extended to include L-shell electron captures around 1 keV. Current work explores these optimization parameters and faces the task of distinguishing prompt electron capture signals from the electronic noise and events of degraded energy that also populate the low-energy spectrum.

-
- [Abr14] N. Abgrall *et al.*, *Adv. High Energy Phys.*, **2014**, 365432 (2014).
- [Det11] J. A. Detwiler, *Single-Site Time Correlation Cut Optimization*, Technical report, Majorana Demonstrator, 2011.
- [FDR12] Majorana Collaboration, *Majorana Demonstrator Final Design Report*, Technical report, 2012.
- [Sha13] B. Shanks and C. O'Shaughnessy, TUNL Progress Report, **LII**, 28 (2013).
- [Whi14] B. White, *Production and Acceptance Testing of Enriched Ge Detectors for the Majorana Demonstrator*, Contribution to Neutrino 2014, 2014, <https://indico.fnal.gov/contributionDisplay.py?contribId=373&sessionId=30&confId=8022>.

5.1.5 Underground Low-Background Assay at KURF

J. TRIMBLE, R. HENNING, J.F. WILKERSON, M. GREEN, *TUNL*

Two HPGe detectors are in operation at the Kimballton Underground Research Facility, located within a mine near Ripplemead, VA. These detectors are used for materials assay in a low-background environment. A status update of the low-background counting facility and future plans for the facility are provided.

Facility Overview

The Kimballton Underground Research Facility (KURF) is located about 25 miles from Virginia Polytechnic and State University in the Kimballton mine owned by Lhoist North America. The low-background counting (LBC) facility has two HPGe detectors used exclusively for low-background assay work. The first detector, “MELISSA,” is a 1.1kg, 50% RE (relative efficiency compared to NaI) Canberra LB (low-background) detector. The other detector, “VT-1,” is a 0.956 kg, 35% RE ORTEC LLB Series detector in a J-type configuration. For more technical details regarding the facility and detector setup, see Ref. [Fin11].

Monitoring and data acquisition are controlled by ORCA [How], which is run on a Mac Pro computer in the Naval Research Laboratory trailer. With ORCA, it is possible to stop and start runs, control the liquid nitrogen (LN) levels in the detector Dewars, and monitor the data in real time. The slow controls and DAQ are regularly accessed remotely, since TUNL personnel are only present at KURF about once every two weeks.

Detector Rehabilitation

Both detectors were subjected to a thorough rehabilitation program with preventive maintenance while management of the facility was transferred from one graduate student to another. MELISSA and VT-1 were warmed up and brought back to UNC to repump the cryo-space vacuums on both detectors.

After pumping down VT-1, the detector was biased and tested prior to being returned to KURF. However, while attempting to reach the bias voltage, the test spectra all showed undesired noise, possibly from the electronics. The de-

tor was unbiased and ORTEC was contacted. The maintenance technician recommended that we open the HV filter to clean it, as there may have been residue buildup inside the housing. Upon opening the filter, residue was indeed discovered. The inside of the HV filter housing was cleaned three times using ethanol to achieve the level of cleanliness required to reach bias voltage. Even with the cleaning, however, great care was taken to bias the detector very slowly.

After both detectors were biased and tested at UNC, they were returned to KURF for installation. One drawback to the setup at KURF was the difference in shutdown logics for the two detectors. Since VT-1 is an ORTEC detector, it uses ORTEC inhibit logic in its shutdown circuit. MELISSA is from Canberra, so it uses TTL as its logic. The HV source that is used for MELISSA allows us to control the HV card via ORCA. However, it only accepts TTL logic. The computer electronics manager at TUNL was able to build an adapter which translates an ORTEC shutdown signal from VT-1 into a TTL signal that is accepted by the HV module.

Neutron Activation Analysis

Neutron activated samples of polytetrafluoroethylene (PTFE) and fluorinated ethylene propylene (FEP) tubing—candidate materials for the MAJORANA DEMONSTRATOR—were γ -assayed in the LBC facility at KURF. Neutron activation is utilized as a counting method when impurities in a sample may be at too low levels to detect with passive radio-assay techniques. Samples are placed in a high neutron flux environment, such as a nuclear reactor, to be bombarded with energetic neutrons. Impurities in the sample capture a neutron, converting them to an unstable isotope. This isotope in turn β -decays

Table 5.1: Isotopes observed in neutron activation of primordial radioactive isotopes and their most intense emitted γ -rays used in neutron activation analysis.

Impurity Isotope	Activation Isotope	Half-life (days)	Relevant γ ray (keV)	Intensity (%)
^{238}U	^{239}Np	2.356	106	25.34
^{232}Th	^{233}Pa	26.975	312	38.5

to another isotope, as shown in Table 5.1. The characteristic γ -ray energies of the decay products can be used to positively identify them and therefore to infer the original impurity. Similar reactions are used to identify ^{238}U and ^{232}Th impurities.

No uranium/thorium activation products were observed in any of the samples, and calculated initial activity limits (90% C.L.) of ^{238}U and ^{232}Th in the 0.002-in PTFE samples were 7.6 ppt and 5.1 ppt, respectively. The same limits in the FEP tubing sample were 150 ppt and 45 ppt, respectively. These levels are acceptable for use in the MAJORANA DEMONSTRATOR.

Future Plans

We are currently designing the next generation of low background counting at KURF, with plans for the MAJORANA Very-Low Background Radioassay Counting Facility at KURF (MAVRCK). The intent of the new system is to use techniques and procedures developed by the MAJORANA collaboration to significantly reduce the background rates seen in the two current detectors. We are currently in the simulation phase of the project. The simulations are being used to determine the most effective design of the MAVRCK system, such as the thickness of the outer lead shield, the shape of the cryostat, and the size of the crystal.

One of the key improvements relative to the current systems will be the integration of elec-

troformed copper (EFCu) into the design. We are currently working with MAJORANA on the best way to include this extremely low background material. However, we already have grown the cryostat that will eventually be used in the MAVRCK system. One effect that our simulation efforts have highlighted is the use of EFCu as the inner shield. Once the GEANT4 simulation was complete, we systematically modeled each copper piece in the system (except the cryostat) as EFCu as opposed to OFHC copper, to see the effect that each item had on the background. All simulations assumed that the cryostat was EFCu, because that piece has already been grown in the electroforming laboratory at SURF.

Conclusion

The LBC at KURF has been in operation for over six years. With sufficient notice, samples can be assayed fairly quickly. While most of the assayed samples come from the MAJORANA collaboration, samples from other institutions have also been assayed. At present both detectors are in operation, assaying samples.

[Fin11] P. Finnerty *et al.*, Nucl. Instrum. Methods A, **642**, 65 (2011).

[How] M. A. Howe, orca.physics.unc.edu/~markhowe/.

5.1.6 Development of a Beamline and Target Chamber for Measuring $({}^3\text{He},n)$ Reaction Cross Sections

D.R. TICEHURST, D. COMBS, C. MALONE, C.R. HOWELL, A.R. YOUNG, *TUNL*

Cross-section measurements of the $({}^3\text{He},n)$ reaction on several nuclei used in searches for neutrinoless double-beta decay will be carried out in the tandem laboratory at TUNL. These measurements require a pulsed ${}^3\text{He}$ beam, a target chamber with a thin window at forward angles to reduce attenuation of the emitted neutrons, and a long flight path so that key states in the residual nucleus can be resolved using time-of-flight. The beamline and target chamber have been installed and are being evaluated.

Cross-section measurements for the $({}^3\text{He},n)$ two-proton transfer reaction will be carried out on isotopes relevant to experiments that search for neutrinoless double-beta ($0\nu\beta\beta$) decay. The aim of these measurements is to test the BCS ground-state approximation in quasiparticle random-phase approximation (QRPA) calculations of the nuclear matrix element for $0\nu\beta\beta$ decay [Avi08]. The BCS picture neglects effects in the decay process such as the rearrangement of nucleons beyond the annihilation of two neutrons and the creation of two protons. A phenomenon called pairing vibrations, which are fluctuations about the BCS state, could cause such effects [Bri05]. For instance, in an even-even nucleus near the Fermi surface where the energy gap to the next available single-particle orbital is greater than the pairing energy, excited 0^+ states could be due to pairing vibrations [Fre12]. If this is the case, these excited 0^+ states should share a substantial fraction of the two-nucleon transfer strength with the ground state of the final nucleus.

In this work we evaluate the conjecture of using BCS ground states in QRPA calculations by determining the strength of two-proton transfer to 0^+ excited states relative to the strength for transitions to the 0^+ ground state of the residual nucleus.

The $({}^3\text{He},n)$ reaction measurements require a long neutron flight path for precise neutron energy determination via the time-of-flight method. The goal is to have a neutron energy resolution better than 0.5 MeV for neutron energies less than about 25 MeV. The time spread in the pulsed ${}^3\text{He}$ beam in the tandem lab was determined by measurements in 2015 to be about

1.5 ns FWHM. The targets will be about 2.5 mg/cm² thick. To achieve the desired energy resolution with these parameters, the neutron detectors have been installed 13 m from the target at angles from 0° to 18° relative to the beam.

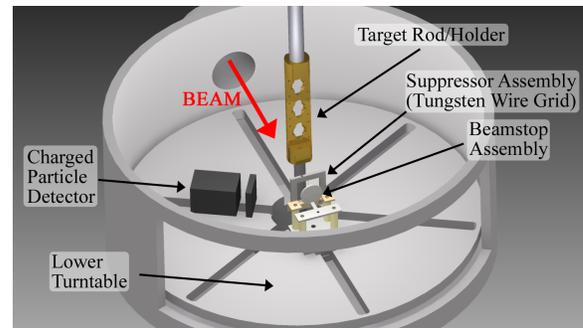


Figure 5.10: Schematic diagram of the target chamber. The charged particle detector and the suppressor/beamstop assembly are attached to the bottom plate. The top cover of the chamber and the steel neutron window have been removed from the diagram for clarity. All surfaces that could be exposed to scattered helium have been covered with a thin layer of lead.

An existing target chamber was modified for this experiment. The main modification was to remove a section of the chamber wall around 0° and replace it with a 0.5 mm thick piece of stainless steel to reduce the attenuation of the emitted neutrons. The steel was attached to the chamber with A-12 epoxy to form a vacuum-tight seal. The beam stop and suppressor grid were fabricated to sit just behind the target. The beam stop and limiting apertures along the beamline are lined with lead to reduce neutron

backgrounds in the detectors due to ($^3\text{He},n$) reactions.

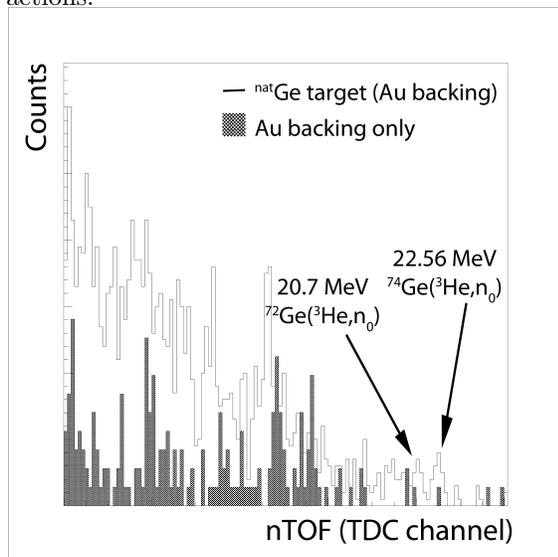


Figure 5.11: Measured time-of-flight spectrum from the $^{\text{nat}}\text{Ge}(^3\text{He},n)$ reaction at $\theta = 0^\circ$ and beam energy 15 MeV. The background spectrum is overlaid.

Measurements were conducted in 2013 to commission the new 70° beamline and to determine the magnitude and sources of neutron background. A pulsed beam of 21 MeV α particles of

50 pA was delivered to target. The repetition rate was 2.5 MHz. A 1.8 mg/cm^2 $^{\text{nat}}\text{Ni}$ target, similar to the germanium and tellurium targets that will be made, was used. With this target the foreground-to-background ratio was about 4:1, which is acceptable.

An experiment was conducted during this reporting period using a pulsed ^3He beam and a $^{\text{nat}}\text{Ge}$ target. A detector was placed at 0° at a distance of 13 m from the target. Data were accumulated for 6.7 hours with an average beam current of 15 pA . The time-of-flight spectra acquired in this measurement are shown in Fig. 5.11 for a 2.35 mg/cm^2 $^{\text{nat}}\text{Ge}$ sample on a gold backing and for the gold backing foil alone. Enhancements in the counts in the time-of-flight spectrum are indicated for the ($^3\text{He},n$) reaction corresponding to the most abundant isotopes, ^{72}Ge and ^{74}Ge .

[Avi08] F. T. A. III, S. R. Elliot, and J. Engel, *Rev. Mod. Phys.*, **80**, 481 (2008).

[Bri05] D. M. Brink and R. A. Broglia, *Nuclear Superfluidity*, Cambridge University Press, Cambridge, UK, 2005.

[Fre12] S. J. Freeman and J. P. Schiffer, *J. Phys. G.*, **39**, 124004 (2012).

5.1.7 The Neutron Capture Cross Section on $^{63,65}\text{Cu}$ Between 0.4 and 7.5 MeV

I. BRAY, *Clarkson University, Potsdam, NY*; M. BHIKE, KRISHICHAYAN, W. TORNOW, *TUNL*

Copper is being used as a cooling and shielding material in most searches for neutrinoless double-beta decay. In order to accurately interpret background events in such searches, the cross sections of neutron-induced reactions on copper must be known. We have measured the cross section of the $^{63,65}\text{Cu}(n,\gamma)^{64,66}\text{Cu}$ reactions using target activation at energies from 0.4 MeV to 7.5 MeV. Previous data were limited to energies below 3 MeV. Our results are compared to predictions from two nuclear data libraries.

Sophisticated experiments around the world are seeking to observe neutrinoless double-beta decay ($0\nu\beta\beta$). Two such collaborations are GERDA, at the Gran Sasso Laboratory in Italy, and EXO-200, at the Waste Isolation Pilot Plant in New Mexico [Tor14]. These experiments utilize different candidates for $0\nu\beta\beta$ decay— ^{76}Ge ($Q = 2039$ keV) and ^{136}Xe ($Q = 2457.8$ keV), respectively—but both rely on copper as a shielding and cooling material [Tor14]. The reduction of natural background is absolutely imperative in order to detect the signal from $0\nu\beta\beta$ decay. Therefore extensive knowledge of the sources of background in the experimental setups is needed, and both GERDA and EXO are vulnerable to background from neutron-induced reactions on copper. Current data on neutron capture on $^{63,65}\text{Cu}$ exists for neutron energies up to 3 MeV, with sparse data at higher energies. The goal of this experiment is to measure the cross section for neutron capture on these copper isotopes to aid in the reduction of background signals in $0\nu\beta\beta$ -decay searches.

The experiment was performed at TUNL via the neutron activation method [Bhi14]. The targets were copper disks 1.9 cm in diameter. The thicknesses of the ^{63}Cu targets varied between 1 and 1.25 mm, while the thickness of the ^{65}Cu target was 2.5 mm. To monitor the neutron flux, indium foils of the same area were attached to the front and back sides of the target. The target and monitor foils were surrounded by a cadmium cage to reduce the effect of thermal neutrons. Monoenergetic neutrons were produced at various energies through using two reactions. The $^3\text{H}(p,n)^3\text{He}$ reaction was employed to produce neutron beams at six different energies between

0.4 and 4 MeV. The $^2\text{H}(d,n)^3\text{He}$ reaction was utilized for four energies between 4 and 8 MeV. As shown in Fig. 5.12, the experimental setup for the measurements with $^2\text{H}(d,n)^3\text{He}$ consists of a 3 cm long gas cell pressurized to 4 atm with high-purity deuterium gas. A 6.5 mm Havar foil separates the gas from the accelerator vacuum. A liquid-scintillator-based neutron detector positioned at 0° relative to the incident proton or deuteron beam direction at a distance of about 3 m from the neutron production target was used to monitor the neutron flux.

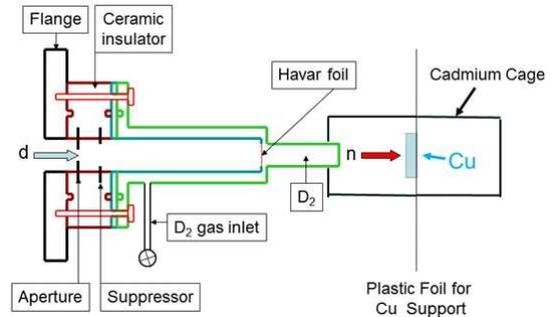


Figure 5.12: Schematic view of the experimental arrangement for the $^{63,65}\text{Cu}(n,\gamma)^{64,66}\text{Cu}$ cross-section measurements using the $^2\text{H}(d,n)^3\text{He}$ reaction.

After irradiation, off-line γ -ray spectroscopy was employed to count the induced activity in the targets using well-shielded and calibrated high-purity germanium (HPGe) detectors of 60% relative efficiency. Table 5.2 gives the properties of the γ -ray transitions we used.

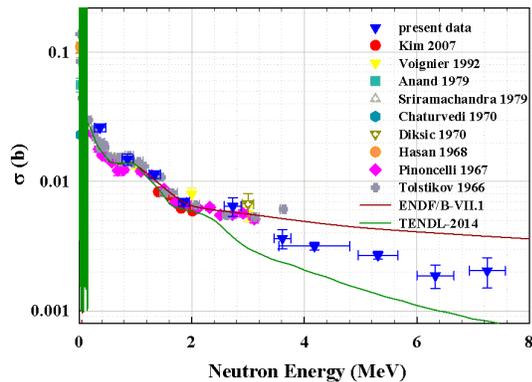
Due to the 5.12 min half-life of ^{66}Cu , a quick transfer from irradiation to measurement was necessary. Therefore, an HPGe detector

Table 5.2: Properties of the γ -ray transitions used for the $^{63,65}\text{Cu}(n,\gamma)^{64,66}\text{Cu}$ reactions and the indium monitor reactions

Nucleus	$T_{1/2}$	E_γ (keV)	I_γ (%)
$^{63}\text{Cu}(n,\gamma)^{64}\text{Cu}$	12.701(2) h	511.0	35.2
$^{65}\text{Cu}(n,\gamma)^{66}\text{Cu}$	5.120(14) m	1039.2	9.23
$^{115}\text{In}(n,n')^{115m}\text{In}$	4.486(4) h	336.24	45.8
$^{115}\text{In}(n,\gamma)^{116m1}\text{In}$	54.29(17) m	1293.56	84.8

and its data-acquisition system were mounted in the hallway directly outside the target room at TUNL. This system reduced transfer time to between 30 and 90 seconds and was used for all measurements of the $^{65}\text{Cu}(n,\gamma)^{66}\text{Cu}$ except at 4.5 MeV. All other measurements were taken in TUNL's low-background counting facility.

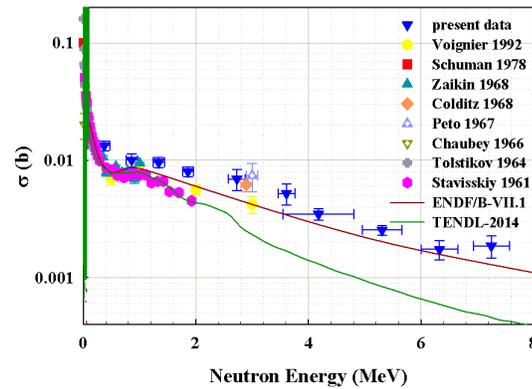
As has been described in Ref. [Bhi14], auxiliary measurements were performed with an untritiated “neutron production” target at neutron energies of 2.73 MeV and 3.61 MeV to account for so-called off-energy neutrons. Auxiliary measurements were also done at the energies of 6.33 MeV and 7.5 MeV with an empty deuterium cell to correct for off-energy neutrons.

**Figure 5.13: Comparison plot of the cross-section data for $^{63}\text{Cu}(n,\gamma)^{64}\text{Cu}$ with existing data and the evaluations ENDF/B-VII.1 and TENDL-2014.**

Our results for the $^{63}\text{Cu}(n,\gamma)^{64}\text{Cu}$ reaction are plotted in Fig. 5.13. The cross-section values are in the range of 30 to 1 mb for incident neutrons of 0.4 to 7.5 MeV. Our data agree well with the existing data from 0.37 to 2.73 MeV. From 3.6 to 7.5 MeV they are close to an average of the two evaluations shown, ENDF/B-VII.1 and TENDL-2014.

Our results for the $^{65}\text{Cu}(n,\gamma)^{66}\text{Cu}$ reaction are plotted in Fig. 5.14. The data from this

work are slightly higher than the existing data between 0.37 and 3.6 MeV, but agree well with the evaluation ENDF/B-VII.1 from 4.5 to 7.5 MeV. TENDL-2014 predicts lower values than the present data. It is worth noting that much of the existing data in the low-energy region are relatively old. Those experiments were performed with NaI scintillator detectors, whereas the present work used high-resolution HPGe detectors.

**Figure 5.14: Comparison plot of the cross section data for $^{65}\text{Cu}(n,\gamma)^{66}\text{Cu}$ with existing data and the evaluations ENDF/B-VII.1 and TENDL-2014.**

The present work provides the first neutron capture cross-section data on $^{63,65}\text{Cu}$ in the incident neutron energy range from 4 to 8 MeV and supplements existing data from 0.4 to 4 MeV. The data are important to improve evaluations such as ENDF/B-VII.1 and TENDL-2014 and to provide valuable knowledge of potential sources of background radiation in the ongoing searches for neutrinoless double-beta decay.

[Bhi14] M. Bhike and W. Tornow, Phys. Rev. C, **89**, 031602(R) (2014).

[Tor14] W. Tornow, (2014), arXiv:1412.0734v1 [nucl-ex].

5.1.8 The $^{76}\text{Ge}(n,2n)^{75}\text{Ge}$ Cross Section between 10 and 15 MeV

M. BHIKE, KRISHICHAYAN, W. TORNOW, *TUNL*

The cross section for the reaction $^{76}\text{Ge}(n,2n)^{75}\text{Ge}$ to both the isomeric and ground state have been measured with the activation method between 10 and 15 MeV to help resolve inconsistencies in the current database. The data are important to interpret potential neutron-induced backgrounds in currently running, large-scale experiments searching for the neutrinoless double-beta decay of ^{76}Ge .

The GERDA [Ago13] and MAJORANA [Abg14] collaborations use germanium-diode detectors in their searches for the neutrinoless double-beta decay ($0\nu\beta\beta$) of ^{76}Ge . The detectors, which are enriched to 86% in ^{76}Ge , serve as both source and detector. Common to all $0\nu\beta\beta$ -decay searches is the requirement that background events in the energy region of interest, a narrow energy band centered at the Q value for $0\nu\beta\beta$ decay, must be extremely small.

The $^{76}\text{Ge}(n,2n)^{75}\text{Ge}$ reaction is of special importance because its $(n,2n)$ cross section is typically hundreds of mb. This reaction either proceeds directly to the ground state of ^{75}Ge or populates the isomeric $7/2^+$ state at 139.7 keV, which, in turn, decays with a half-life of 47.7 s almost exclusively to the $1/2^-$ ground state. The ^{75}Ge ground state β -decays to ^{75}As with a half-life of 82.78 m.

The cross sections of the $^{76}\text{Ge}(n,2n)^{75}\text{Ge}$ and $^{76}\text{Ge}(n,2n)^{75m}\text{Ge}$ reactions have been measured at incident neutron energies from 10 to 14.8 MeV in small energy steps using the activation technique. The threshold energies for these reactions are 9.55 MeV and 9.69 MeV, respectively.

Monoenergetic neutron beams were produced at ten energies from 10.0 to 14.5 MeV via the $^2\text{H}(d,n)^3\text{He}$ reaction and at 14.8 MeV using the $^3\text{H}(d,n)^4\text{He}$ reaction. Typical deuteron beam currents on target were $1.5 \mu\text{A}$. The metallic germanium targets were 10 mm square, 2 mm thick, and contained about 1.5 g of germanium with the same isotopic composition as that of the enriched HPGe detectors used in GERDA and MAJORANA. For neutron flux determination, the germanium slab was sandwiched between gold foils with the same area as the target and with a thickness of 0.025 mm. The slab was supported by a thin plastic foil and was placed at a dis-

tance of 1.9 cm from the end of the neutron-production deuterium gas cell. The gas cell was sealed from the beamline vacuum by a $0.635 \mu\text{m}$, thin Havar foil. Due to the high thresholds of the $^{76}\text{Ge}(n,2n)^{75}\text{Ge}$ and $^{76}\text{Ge}(n,2n)^{75m}\text{Ge}$ reactions, breakup neutrons from the neutron source reaction do not have enough energy to contribute to the production of ^{75}Ge .

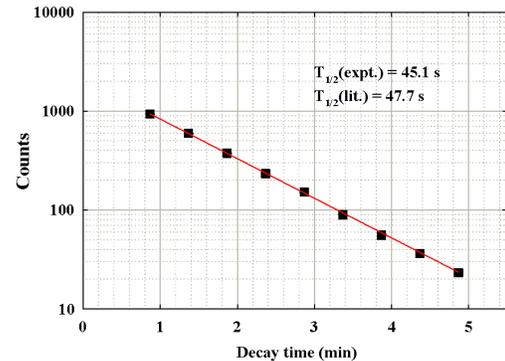


Figure 5.15: Decay curve for the 139.68 keV γ -ray line of ^{75m}Ge measured at $E_n = 14.5$ MeV

The pressure in the deuterium gas cell and the energy loss of the deuteron beam contributed to the energy spread of the neutron beam. The neutron flux was monitored using a 1.5 inch \times 1.5 inch BC-501A neutron detector of known absolute efficiency, placed at 0° relative to the incident beam and at a distance of 293.5 cm from the end of the deuterium gas cell. This neutron monitor was also essential in determining the mean neutron energy. For this purpose the incident charged-particle beam was pulsed at a repetition rate of 2.5 MHz with overall time resolution of 2.5 ns. The neutron energy was inferred from the measured time-of-flight.

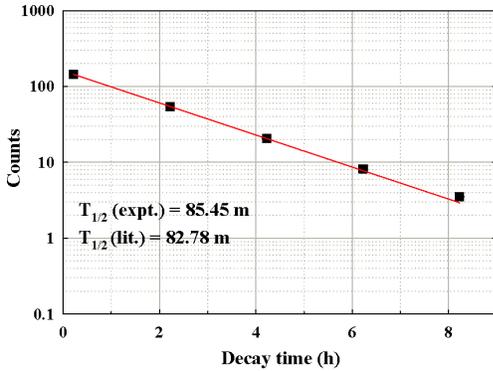


Figure 5.16: Decay curve for the 264.6 keV γ -ray line of ^{75}Ge measured at $E_n = 14.5$ MeV

The Ge target was irradiated for 3 minutes for measuring the $^{76}\text{Ge}(n,2n)^{75m}\text{Ge}$ reaction and for 1 hour for the $^{76}\text{Ge}(n,2n)^{75}\text{Ge}$ reaction. Well-shielded 60% HPGe detectors were used to record the yield of the 139.7 keV and 264.6 keV γ -ray lines corresponding to ^{75m}Ge and ^{75}Ge , respectively. The γ -ray spectra from the off-line measurements of the activated samples were analyzed using the software TV [The93] to identify the reaction products and their respective peak areas.

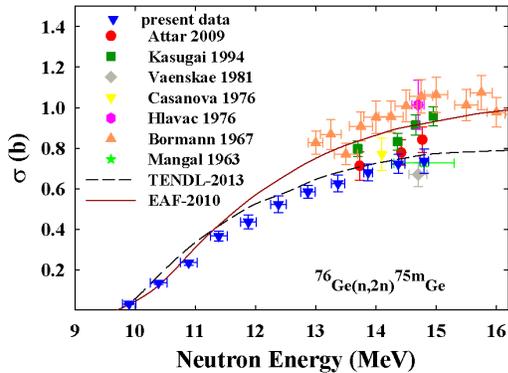


Figure 5.17: Measured cross-section data for the $^{76}\text{Ge}(n,2n)^{75m}\text{Ge}$ reaction compared to existing data and evaluations.

Figures 5.15 and 5.16 show decay curves for the 139.6 and 264.6 keV γ -ray lines obtained after irradiation with 14 MeV neutrons. There is good agreement between the measured and literature half-life values. The cross sections were determined relative to those from the gold monitor

foils measured simultaneously in the same geometry. The details of this method are discussed in Ref. [Bhi14].

Our measured cross-sections for the $^{76}\text{Ge}(n,2n)^{75m}\text{Ge}$ reaction are shown in Fig. 5.17 along with the existing data between 13 and 16 MeV and the TENDL-2013 and EAF-2010 evaluations. The EAF-2010 evaluation is in good agreement with our data between 10-12 MeV, but considerably over-predicts our measurements from 12 MeV onwards. The TALYS evaluation, TENDL-2013, over-predicts our data only slightly in the entire energy range investigated.

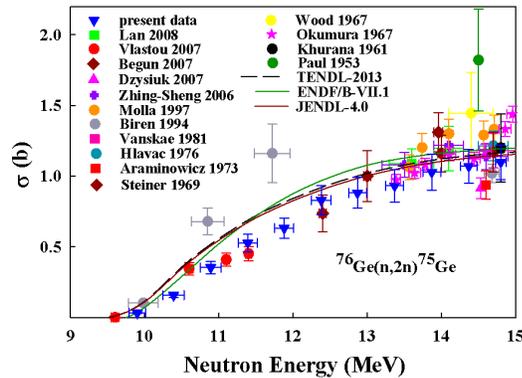


Figure 5.18: Measured cross-section data for the $^{76}\text{Ge}(n,2n)^{75}\text{Ge}$ reaction compared to existing data and evaluations.

Figure 5.18 shows our measured cross-section data for $^{76}\text{Ge}(n,2n)^{75}\text{Ge}$ compared to previous data. The three curves are the TENDL-2013, ENDF/B-VII.1, and JENDL-4.0 evaluations which all overestimate most of the measured cross-section data below 13 MeV. Not surprisingly, however, they describe the bulk of the data in the 14 MeV region fairly well.

[Abg14] N. Abgrall, *Adv. High Energy Phys.*, **2014**, 1 (2014).

[Ago13] M. Agostini, *Phys. Rev. Lett.*, **111**, 122503 (2013).

[Bhi14] M. Bhide and W. Tornow, *Phys. Rev. C*, **89**, 031602(R) (2014).

[The93] J. Theuerkauf, In *Program TV, Institute for Nuclear Physics, University of Cologne (unpublished)*, 1993.

5.1.9 The $^{76}\text{Ge}(n,p)^{76}\text{Ga}$ Reaction and the Search for $0\nu\beta\beta$ Decay in ^{76}Ge

W. TORNOW, M. BHIKE, KRISHICHAYAN, *TUNL*

The $^{76}\text{Ge}(n,p)^{76}\text{Ga}$ reaction and the subsequent β decay of ^{76}Ga back to ^{76}Ge has been used to excite the 3951.9 keV state of ^{76}Ge , which decays by emission of a 2040.7 keV γ ray. Using HPGe detectors, the associated pulse-height signal may be indistinguishable from the potential signal produced in neutrinoless double-beta decay of ^{76}Ge , with its Q value of 2039.0 keV. In the neutron energy range between 10 and 20 MeV the production cross section of the 2040.7 keV γ ray is approximately 0.1 mb.

According to current knowledge, neutrinoless double-beta ($0\nu\beta\beta$) decay, if it occurs in nature, is the only mechanism that would provide unambiguous information on the Majorana nature of the neutrino. As a second-order weak-interaction process, the expected half-life for $0\nu\beta\beta$ decay is $T_{1/2} > 10^{25}$ yr. Future large-scale experiments aim at the so-called inverted neutrino mass hierarchy regime ($\langle m_{\beta\beta} \rangle \sim 20$ meV), which corresponds to $T_{1/2} > \sim 5 \times 10^{26}$ yr. Reaching this goal will require background event rates not to exceed 1 count per tonne of the isotope of interest per keV in the region of interest (ROI) during one year of counting. Background events from neutron-induced reactions in the detector material itself or its surrounding shielding are one of the major concerns.

Here we focus on background processes induced by fast neutrons with energies greater than 10 MeV that could interfere with searches for $0\nu\beta\beta$ decay in ^{76}Ge performed with HPGe detectors enriched to 86% in ^{76}Ge , with 14% ^{74}Ge . In this case the ROI is centered at 2039.0 keV, with a width of ± 2.5 to 3 keV.

Difficulties in understanding earlier TUNL results for γ -ray spectra from the $^{74,76}\text{Ge}(n,n'\gamma)^{74,76}\text{Ge}$ reactions induced by neutrons with energies of 5 to 12 MeV [Est12] prompted us to revisit the $^{76}\text{Ge}(n,p)^{76}\text{Ga}$ reaction with a focus on the decay of the 3951.9 MeV state and its emission of a 2040.7 keV γ ray. A partial level scheme of ^{76}Ge is shown in Fig. 5.19, indicating the decay of the 3951.9 keV state with its associated branching ratios [Cam71].

The $^{76}\text{Ge}(n,p)^{76}\text{Ga}$ reaction has a threshold of 6215.4 keV. The fact that ^{76}Ga has a half-life of only 32.6 s necessitates a high neutron flux

in order to produce a sufficiently large ^{76}Ga activity for subsequent γ -ray counting. We used the $^2\text{H}(d,n)^3\text{He}$ reaction to produce 19 MeV neutrons. The target was a germanium slab, 10 mm square and 6 mm thick, with a mass of approximately 3.2 g. It consisted of 86% ^{76}Ge and 14% ^{74}Ge . It was irradiated for 120 s with neutrons produced by a 1.7 μA deuteron beam. After irradiation, the slab was positioned in front of a 60% relative efficiency HPGe detector located outside of the irradiation room. The germanium slab was counted for a total of 120 s in 30 s increments using the Canberra Multiport II hardware and the associated GENIE software. The total yield in the 3951.7 keV line was approximately 150 counts, and the yield for the γ -ray line at 2040.7 keV was more than a factor of ten lower.

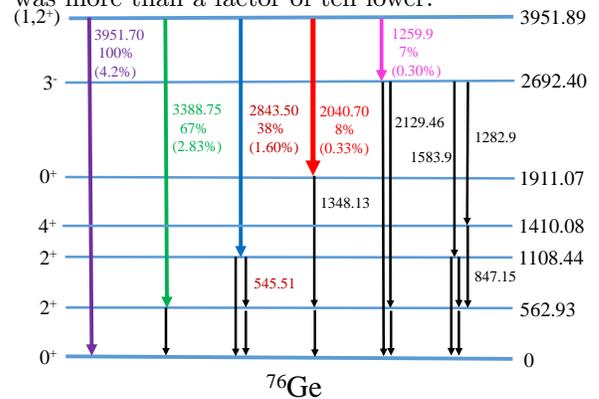


Figure 5.19: Partial level scheme of ^{76}Ge . The transitions of interest with their branching ratios are given by bold arrows. The branching ratios in parenthesis refer to the decay of ^{76}Ga . Energies are in keV.

A total of 110 individual irradiations were performed. The resulting spectra were added to

form a sum spectrum, after making sure no gain changes occurred during the course of the measurements. The γ -ray energy region containing the 2843.5 keV, 3388.75 keV, and 3951.7 keV transitions is shown in panel (a) of Fig. 5.20, while panel (b) focuses on the 2040.7 keV energy region. In addition to the energies quoted by Camp and Foster [Cam71], we provide in parenthesis the energy values found in the present work. Due to the smaller branching ratio of the 2040.7 keV transition, the peak-to-background ratio in Fig. 5.20(b) is considerably smaller than that of the more intense γ -ray lines in part (a) of the figure.

The energies of most of our observed peaks are very close to the literature values, thus providing confidence in our energy calibration. This is particularly true for the 1940.3 ± 0.14 keV and 2073.75 ± 0.07 keV lines. However we notice that the centroid of the nominal 2040.7 keV line in part (b) of the figure is not located at 2040.7 keV, but at 2039.4 keV, much closer to the Q value of $0\nu\beta\beta$ decay of ^{76}Ge at 2039.0 keV. In addition, the line is broader than expected from a single γ ray. It turned out that the neutron-capture γ ray of 2037.97 keV is responsible for the broader width and the lower centroid energy. This delayed transition originates from the decay of the ^{77}Ge ground and/or isomeric state after neutron capture on ^{76}Ge .

Using the predicted 10-mb cross section for the $^{76}\text{Ge}(n,p)^{76}\text{Ga}$ reaction at $E_n = 20$ MeV and the known probability of 9.6% for exciting the 3951.9 keV state in ^{76}Ge after β decay of ^{76}Ga , we find a cross section of approximately 1 mb. Taking the 8% branching ratio for the decay of this state via the emission of a 2040.7 keV γ ray into account, provides a production cross section of (0.08 ± 0.02) mb for the production of the 2040.7 keV γ ray at 20 MeV.

In addition to the $^{76}\text{Ge}(n,p)^{76}\text{Ga}$ reaction focused on in the present work, inelastic neutron

scattering, i.e., the $^{76}\text{Ge}(n,n'\gamma)^{76}\text{Ge}$ reaction, is also expected to produce the 2040.7 keV γ -ray line. As described in Sect. 5.1.11, the same reaction also produces a 2037.5 keV transition with a considerably larger cross section than that of the 2040.7 keV transition. Adding the delayed 2037.97 keV γ -ray line from neutron capture on ^{76}Ge , we note that $0\nu\beta\beta$ decay searches involving ^{76}Ge are susceptible to background γ -ray events produced by three different neutron-induced reactions on ^{76}Ge , two of them involving fast neutrons.

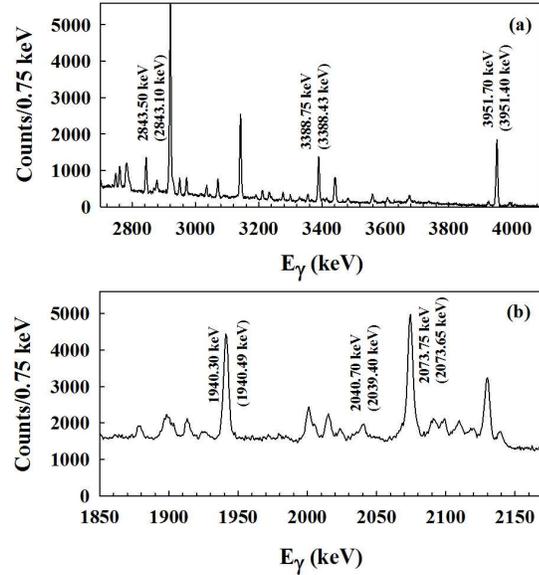


Figure 5.20: Two energy regions of the spectrum of γ rays obtained from the reaction $^{76}\text{Ge}(n,p)^{76}\text{Ga}$ following γ -ray decay of ^{76}Ga .

[Cam71] D. Camp and B. Foster, Nucl. Phys., **A177**, 401 (1971).

[Est12] J. Esterline *et al.*, private communication, (2012).

5.1.10 Determination of the Differential Cross Section of $^{76}\text{Ge}(n,n'\gamma)$ at $E_n = 5$ and 8 MeV

J.H. ESTERLINE, B.A. FALLIN, S.W. FINCH, M.E. GOODEN, C.R. HOWELL, J.H. KELLEY, W. TORNOW, *TUNL*

We have been continuing efforts to obtain differential cross sections for neutron activation of ^{76}Ge from data acquired at TUNL in 2011 and 2012. Numerous transitions have been tentatively identified, including some that may contribute to the background in searches for neutrinoless double-beta decay.

Pursuant to the work described in [Est12], we have expanded our examination of neutron-induced transitions in ^{76}Ge from the environs of 2039 keV, the Q -value of its neutrinoless double-beta ($0\nu\beta\beta$) decay, to a more general study of previously undetected, or at least unreported, transitions from relatively highly excited states of that isotope. This broader effort has been motivated by the discovery of such states [Toh13, Cri15]. It could lead to the observation of new energy levels that could directly contribute to backgrounds in the region of interest (ROI) for $0\nu\beta\beta$ searches through activation of ^{76}Ge by cosmogenic spallation neutrons. Some such neutrons are still present, despite the high overburdens generally employed for shielding. In addition, our efforts provide information on the nuclear structure of ^{76}Ge that could be of indirect value to determinations of nuclear matrix elements for $A = 76$. These matrix elements are an important factor in extracting the neutrino mass from any observed half-life. To this end, we extended our analysis to include data taken at a neutron energy of 5 MeV.

Our experimental apparatus for an incident energy of 8 MeV is described in Ref. [Est12]. The apparatus for 5 MeV differed in a few regards. First, only two 60% HPGe detectors were employed at 110° and 120° , and no measurements were taken with clover detectors. In addition, the deuterium gas cell was pressurized to 3 atm.

Analysis to this point has focused on precisely identifying the contribution of ^{76}Ge to the observed spectra. With 86% enrichment and the presence of iron and nickel foils for neutron-flux normalization, this involves the subtraction of spectra obtained both with a substitute sample of

natural germanium and without any sample but only the normalization foils. The natural germanium target approximates the ^{74}Ge contamination in our enriched sample, since ^{74}Ge is germanium's most abundant isotope at 37%.

The analysis process is illustrated in Fig. 5.21 for emission energies extending about 40 keV on either side of the $0\nu\beta\beta$ Q -value of 2039 keV. The spectra shown are (1) ^{76}Ge plus the monitor foils (red); (2) the monitor foils alone (green); (3) the natural germanium target with contributions from the monitor foils already subtracted (cyan); and (4) the ^{76}Ge spectrum with the natural germanium and monitor-foil contributions subtracted (black). Scaling factors have been applied to the two subtracted spectra so that the peak areas of transitions in ^{56}Fe and ^{74}Ge match wherever present.

Three reference energies of importance are also plotted as vertical lines. In order of increasing energy, they are a 2037.5 keV peak newly identified in Ref. [Cri15], the 2039 keV $0\nu\beta\beta$ Q -value, and a long-known (but presumed very weak) peak at 2040.7 keV.

The comprehensive identification of potential newly-observed or, in large part, recently-observed [Toh13, Cri15] peaks remains a work in progress, as does the ultimate determination of cross sections from the fully reduced spectra.

[Cri15] B. Crider *et al.*, Phys. Rev. C, **92**, 034310 (2015).

[Est12] J. Esterline *et al.*, TUNL Progress Report, **LI**, 41 (2012).

[Toh13] Y. Toh *et al.*, Phys. Rev. C, **87**, 041304 (2013).

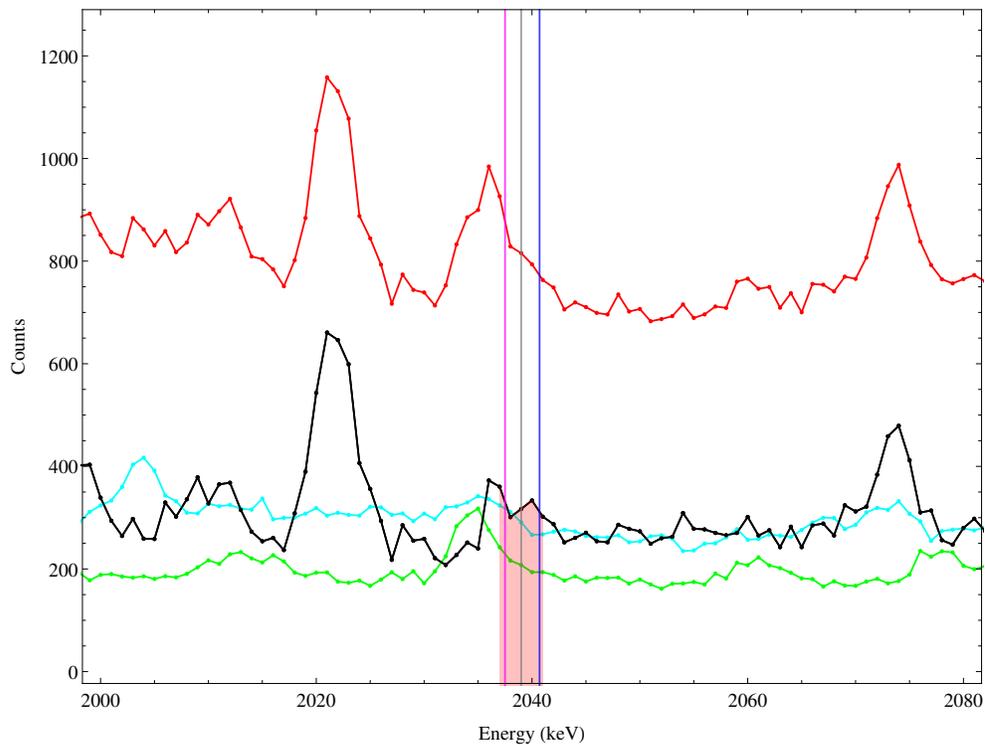


Figure 5.21: Spectra obtained at a neutron energy of 5 MeV, displayed for a subset of energies amply containing the ROI (± 2 keV in the case of the MAJORANA experiment, here highlighted) about the $0\nu\beta\beta$ Q -value of 2039 keV. The red curve is for ^{76}Ge + monitor foils; the green curve is for the monitor foils alone; the cyan curve is for the natural germanium target (monitor foil contributions subtracted), and the black curve shows the background-corrected spectrum for just ^{76}Ge .

5.1.11 The $^{76}\text{Ge}(n,n'\gamma)^{76}\text{Ge}$ Reaction and the Search for the $0\nu\beta\beta$ Decay of ^{76}Ge

W. TORNOW, S.W. FINCH, KRISHICHAYAN, *TUNL*

The upgraded shielded $^2\text{H}(d,n)^3\text{He}$ neutron source facility at TUNL was used to continue efforts to characterize neutron-induced backgrounds relevant to searches for $0\nu\beta\beta$ decay of ^{76}Ge with its Q value of 2039.0 keV. First results obtained at $E_n = 5.0$ MeV for the reaction $^{76}\text{Ge}(n,n'\gamma)^{76}\text{Ge}$ are presented. They support TUNL's earlier observation of a γ -ray transition at 2037.5 keV, which is much stronger than the predicted, but never clearly observed transition at 2040.7 keV from the decay of the 3951.9 keV state of ^{76}Ge excited in inelastic neutron scattering.

In continuation of our ongoing program [Est12] to identify potential neutron-induced backgrounds in searches for neutrinoless double-beta ($0\nu\beta\beta$) decay, we returned to the $^{76}\text{Ge}(n,n'\gamma)^{76}\text{Ge}$ reaction, now using the upgraded shielded neutron source (see Sect. 1.2.2) which utilizes the $^2\text{H}(d,n)^3\text{He}$ reaction in a heavily shielded configuration, providing a collimated neutron beam of adjustable cross sectional area. In our first measurement we used two 60% HPGe detectors inserted into passive shields made of lead and copper and positioned at 90° and 125° relative to the incoming 2.5-cm-diameter, pulsed neutron beam of $E_n = 5.0$ MeV with an energy spread of ± 0.4 MeV.

Figure 5.22 shows an overview of the experimental setup. The target was a disk of metallic germanium 3 cm in diameter, 4 mm thick, and enriched to 86% in ^{76}Ge , with a 14% contribution of ^{74}Ge . It was positioned at an angle of 45° relative to the neutron beam. The front face of the HPGe detector located at 90° was 6 cm from the center of the neutron beam, with its shield only 4 cm away. Even at such a short distance from the neutron beam its halo was not detectable; γ rays originating from lead and copper were not observed in the HPGe detector spectra.

The spectrum shown in Fig. 5.23 focuses on the region of interest in searches for $0\nu\beta\beta$ decay of ^{76}Ge . The γ -ray transition at 2037.5 keV previously observed in Ref. [Est12] at neutron energies between 5 and 12 MeV and recently confirmed by Ref. [Cri15] at energies below 5 MeV is clearly visible, centered between the al-

ready known transitions located at 2022.5 keV and 2074.4 keV. The right tail seen in Fig. 5.23 next to the 2037.5 keV γ -ray line may be due to the 2040.7 keV transition expected from the decay of the 3951.9 keV state in ^{76}Ge . This tail has been observed consistently at all energies studied in the work of Ref. [Est12]. Clearly, in the neutron energy range between 2.5 MeV and 25 MeV the 2037.5 ± 0.5 keV transition is more of a concern for $0\nu\beta\beta$ -decay searches using ^{76}Ge (Q value of 2039.0 keV) than is the 2040.7 keV transition. As in the work of Ref. [Est12], data were also taken with a natural germanium sample to identify γ -ray transitions originating from the $^{74}\text{Ge}(n,n'\gamma)^{74}\text{Ge}$ reaction. It should be noted that the spectrum of Fig. 5.23 was obtained without Compton suppression. Using an active BGO Compton suppression shield, we expect at least a factor-of-two increase in the peak-to-background ratio. Work is in progress on determining the cross section for all the transitions observed. With the upgraded shielded neutron source facility the number of newly observed transitions in ^{76}Ge has almost doubled, to approximately one hundred. It will be a great challenge to put all these levels into a consistent level scheme for the triaxially deformed ^{76}Ge nuclide.

[Cri15] B. P. Crider *et al.*, EPJ Web of Conferences, **93**, 05001 (2015).

[Est12] J. H. Esterline *et al.*, unpublished, (2012).

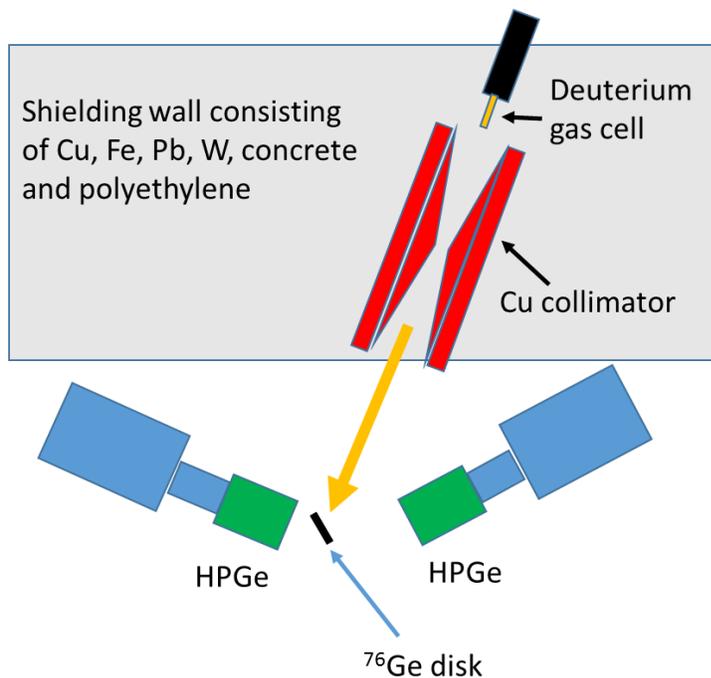


Figure 5.22: Schematic view of the experimental setup featuring the shielded $^2\text{H}(d,n)^3\text{He}$ neutron source, with two HPGe detectors inserted into passive shields and viewing a ^{76}Ge sample.

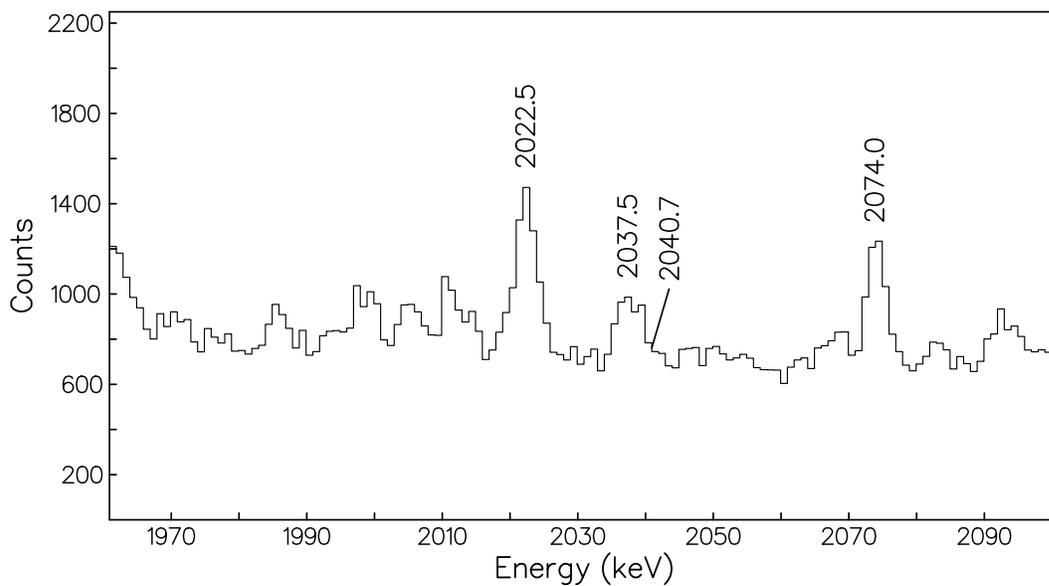


Figure 5.23: Partial γ -ray spectrum obtained with a 60% HPGe detector positioned at 90° for a 5 MeV neutron beam striking a germanium disk enriched to 86% in ^{76}Ge . The region of interest for $0\nu\beta\beta$ searches of ^{76}Ge is centered at 2039.0 keV, just between the newly discovered γ -ray transition of 2037.5 keV and the predicted transition at 2040.7 keV.

5.1.12 The $^{134}\text{Xe}(n,n'\gamma)^{134}\text{Xe}$ reaction at 5 MeV

KRISHICHAYAN, S. FINCH, W. TORNOW *TUNL*

Neutron inelastic scattering measurements on ^{134}Xe have been recently carried out at the upgraded shielded neutron source at TUNL. The isotope ^{134}Xe is a 10 to 20 % contamination in ongoing searches for the neutrinoless double-beta decay ($0\nu\beta\beta$) of ^{136}Xe , and its sensitivity to neutron-induced background is currently not well understood.

There exist R&D work, prototypes, and already operating detectors aimed at the detection of dark matter particles, neutrinos, and neutrinoless double-beta decay which utilize liquid xenon as the detector medium. Here we refer to the projects named EXO, LUX, XENON, XMASS, KamLAND-Zen, and ZEPLIN. Although the associated experiments are designed to operate deep underground in mines, the muon induced spallation neutrons and (α,n) neutrons from α -particle emitting impurities in detector components and to a lesser extent, from the surrounding rocks, are of special concern. They tend to create signals in the detectors which may mimic the signals of interest. As a result, neutron induced cross-section data are needed in order to estimate the probability of reactions given the neutron flux at the detector location. In principle, neutron energies up to a few GeV are involved, but in practice, only low-energy neutrons from about 1 to 20 MeV are of interest. Higher-energy neutron induced processes tend to be so violent that their signature in a detector can be distinguished from the signals of interest. Neutrons with energy below 1 MeV are eventually captured and the resulting de-excitation γ rays produce signatures which are often different from the pulses of interest.

In the following we focus on $0\nu\beta\beta$ searches. Liquid xenon is used as an active source and detector material for the EXO collaboration. It is enriched to approximately 80% in ^{136}Xe , while the remaining 20% is ^{134}Xe . The KamLAND-Zen collaboration uses a 90% ^{136}Xe and 10% ^{134}Xe gaseous mixture loaded into a liquid scintillator detector.

Given the rare nature of the $0\nu\beta\beta$ process, a detailed understanding of the backgrounds in the measurement is of utmost importance and much needed. While neutron-induced background studies have concentrated so far on ^{136}Xe , not much is known about ^{134}Xe .

Therefore, recently we performed a neutron inelastic scattering measurement on ^{134}Xe using a pulsed 5.0 MeV incident neutron beam, produced by the $^2\text{H}(d,n)^3\text{He}$ reaction. The experiment was carried out using upgraded shielded neutron source area. Two 60% HPGe detectors, surrounded by passive shielding were used to detect the de-excitation γ rays from a highly enriched high-pressure ^{134}Xe gas sphere. Data were also taken with an identical empty gas sphere, serving as a sample-out target.

Off-line gamma-ray analysis was done using the RADWARE analysis package [Rad95] to identify the reaction products and the respective peak areas. A part of the spectrum, in the range of interest, obtained in the present measurement is shown in Fig. 5.24. Taking the energy resolution of 1.67% of EXO-200 into account, the γ -ray energy region of interest includes the 2420 to 2500 keV energy range. For KamLAND-Zen the energy range of interest is considerably larger, ranging from 2350 to 2550 keV.

In order to understand and observe the population of excited states in ^{134}Xe in the energy range of the Q value of $0\nu\beta\beta$ at 2458 keV we are planning to take data at other incident neutron energies as well.

[Rad95] D. C. Radford, *Nuc. Instrum. Methods A*, **361**, 297 (1995).

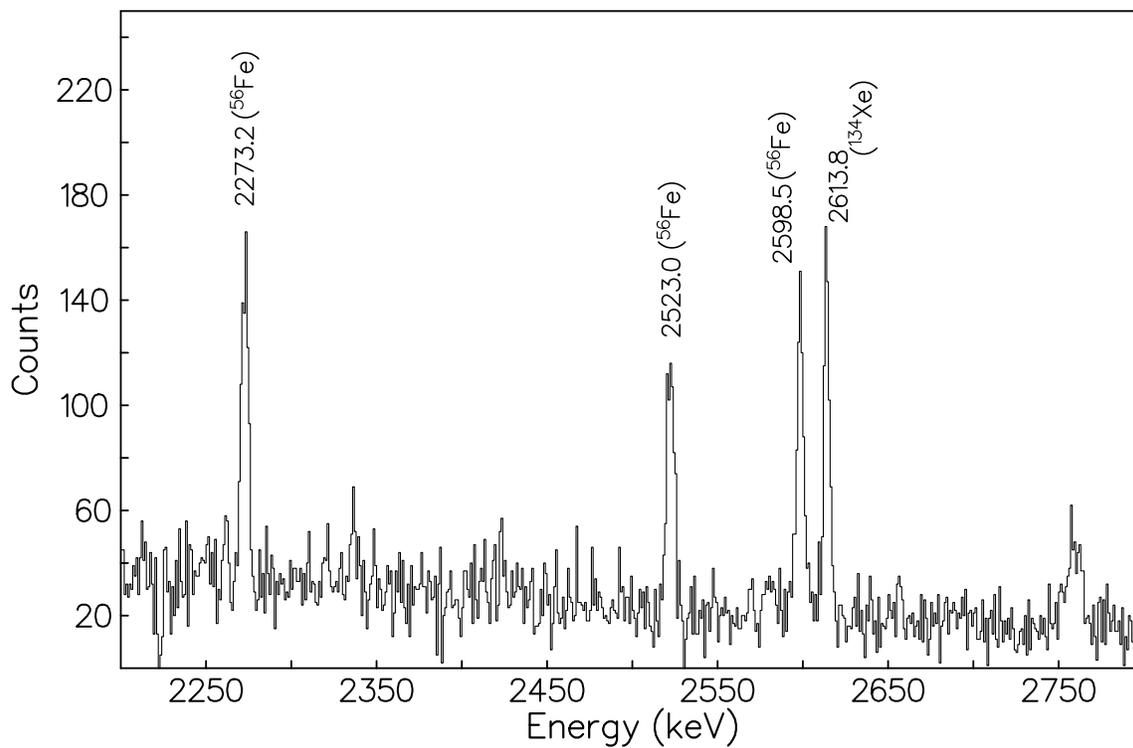


Figure 5.24: A part of the γ -ray spectrum as observed in the present measurements at an incident neutron energy of 5.0 MeV. The γ -ray energy region of interest for EXO-200 is from 2420 to 2500 keV, whereas for KamLAND-Zen, the region of interest is from 2350 to 2550 keV. Except for the γ -ray transition of 2613.8 keV, the other strong transitions originating from the stainless-steel sphere containing the ^{134}Xe gas.

5.1.13 Partial Cross Sections of Neutron-Induced Reactions on ^{136}Xe at $E_n = 5$ MeV for $0\nu\beta\beta$ Background Studies

M. BHIKE, J. BRADT, J. ESTERLINE, S.W. FINCH, M.E. GOODEN, B. FALLIN, W. TORNOW *TUNL*

Partial cross sections for neutron-induced reactions on ^{136}Xe were measured at TUNL using 5 MeV monoenergetic neutrons. These results are important for estimating potential neutron-induced backgrounds in the EXO and KamLAND-Zen neutrinoless double-beta decay searches. Pulsed neutron beams were used, and the deexcitation γ -rays from ^{136}Xe were detected with two 60% HPGe detectors.

The isotope ^{136}Xe has been considered as one of the most promising candidates for neutrinoless double-beta decay ($0\nu\beta\beta$) due to its large Q value and its ideal characteristics for use in large-scale experiments. The EXO [Aug12] and KamLAND-Zen [Gan13] collaborations use ^{136}Xe as both a target and a detector medium in their ongoing search for neutrinoless double-beta decay. Although these experiments operate underground to minimize cosmic-ray induced background events, spallation neutrons are a concern, because they could potentially produce γ -rays in the energy of interest for $0\nu\beta\beta$, which is 2458 keV for ^{136}Xe . Therefore, we are measuring the neutron-induced cross sections on ^{136}Xe in the energy range between 4 and 16 MeV. These data can then be used to guide theoretical calculations for these important reactions at lower and higher energies.

The experiment was carried out at the shielded-neutron-source area of the tandem facility. A gas cell filled with 3 atm of deuterium gas was bombarded with a deuteron beam pulsed at 2.5 MHz to produce a pulsed neutron beam with an energy of 5 MeV. The target consisted of 725 mg of xenon gas enriched to 99.9% in ^{136}Xe . It was contained in a titanium sphere with an inner diameter of 0.96 cm and a wall thickness of 0.2 mm. The sphere, pressurized to about 250 atm, was placed into the beam, along with 0.15 g of nickel foils at the front face of the titanium sphere. The nickel foils served as a neutron flux monitor using the $2^+ \rightarrow 0^+$ transition in ^{58}Ni .

The γ rays produced were measured using two 60% HPGe detectors positioned at 110° and 120° with respect to the incident neutron beam. The center-to-center distance between the neutron production gas cell and the xenon sphere

was 175 cm, and the distances between the xenon sphere and the front face of the HPGe detectors were 10 cm at 110° and 10.8 cm at 120° . The HPGe detectors were surrounded by an inner cylinder made of copper (2.8 mm wall thickness and 25 cm long) and an outer cylinder made of lead (20 mm wall thickness and 10 cm long). Approximately 32.4 hours of beam time was used for the sample-in measurement. Data were also taken with an empty cell and monitor foils with a similar configuration in order distinguish xenon transitions from background. The experimental setup is similar to the one shown in Bradt *et al.* [Bra12] with only the upper xenon sphere in place.

The data-acquisition system used was SpecTcl, which records event by event. When used with time-of-flight, it allowed us to remove accidental background and break-up neutron contributions, leaving only beam-correlated events. The software package tv [The93] was used to process the data and to perform background subtraction and peak integrations.

Most of the observed γ -ray lines have been identified as backgrounds due to inelastic neutron scattering from the $^{\text{nat}}\text{Ti}$ cell material. Unfortunately, the $2^+ \rightarrow 0^+$ transition energy in ^{136}Xe (1313.2 keV) overlaps almost entirely with the $4^+ \rightarrow 2^+$ transition energy in ^{48}Ti (1312.1 keV). Nevertheless cross section information for the $0^+ \rightarrow 2^+$ transition could be obtained because we had the data taken with an identical but empty titanium sphere. These background runs were also helpful to make sure that the results reported in the present work are only from ^{136}Xe -related γ -ray transitions, and not from misidentified peaks. A background-subtracted γ -ray spectrum is shown in Fig. 5.25. All the γ -ray

lines present in the xenon-sample data but not the empty-target runs have been identified. Table 5.1.13 shows the preliminary γ -ray production cross sections we have obtained for all twelve observed transitions in ^{136}Xe .

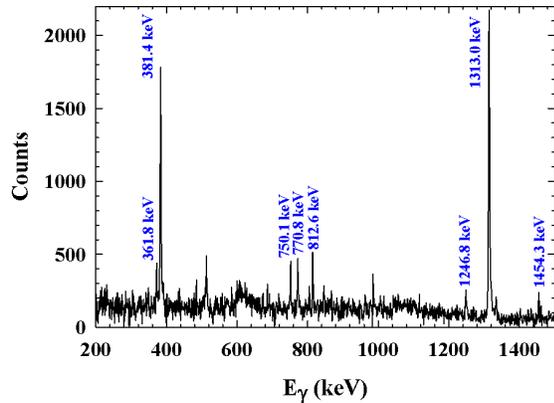


Figure 5.25: A portion of the γ -ray spectrum from detector 1. The spectrum shown is the difference spectrum obtained with the filled ^{136}Xe sphere and the empty sphere. Identified peaks from ^{136}Xe are labeled.

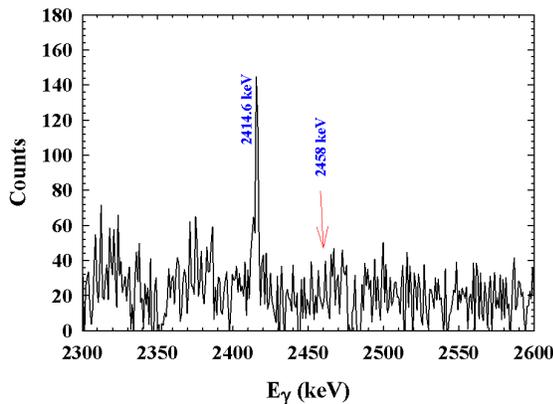


Figure 5.26: The portion of the γ -ray energy spectrum between 2300 and 2600 keV for detector 1. The expected $0\nu\beta\beta$ energy of 2458 keV is labeled with a red arrow. The spectrum shown is the difference spectrum of the filled ^{136}Xe sphere and the empty sphere.

Focusing on the energy region relevant to $0\nu\beta\beta$ of ^{136}Xe , we note that within the 1.67% energy resolution of the EXO detector, the known level scheme of ^{136}Xe does not show any γ -ray transitions, which could cause single-site events in the energy region centered at 2458 keV. The

closest level is at 2414.7 keV (see Fig. 5.26). As expected from the information in the literature, Fig. 5.26 does not show any indication of the two ^{136}Xe lines at 2444.4 keV and 2465.0 keV, because the associated states do not decay directly to the ground state. However, the γ -ray cascades associated with the decay of these states may be a potential problem for KamLAND-Zen, because the individual γ rays could be recorded as one single event in the KamLAND-Zen detector. Given the detector's 4.2% energy resolution, these events cannot be distinguished easily from the $0\nu\beta\beta$ signal-of-interest at 2458 keV. The EXO detector, however, would recognize them as multi-site events.

We will estimate the importance of the 2444.4 keV and 2465.0 keV states in the KamLAND-Zen experiment from the observed yield of the 2414.7 keV transition, once the analysis of the ^{58}Ni cross-section measurement is completed.

Table 5.3: Observed γ -ray transitions in ^{136}Xe and their associated cross sections. The results are normalized to the ^{58}Ni cross section.

E_γ (keV)	Transition	$\frac{\sigma(\text{Det1})}{\sigma(\text{Ni})}$	$\frac{\sigma(\text{Det2})}{\sigma(\text{Ni})}$
1313.02	$2^+ \rightarrow 0^+$	2.57 ± 0.19	2.31 ± 0.15
381.36	$4^+ \rightarrow 2^+$	0.58 ± 0.03	0.57 ± 0.04
812.63	$3^+, 4^+ \rightarrow 2^+$	0.28 ± 0.02	0.21 ± 0.02
369.81	$6^+ \rightarrow 6^+$	0.13 ± 0.01	0.08 ± 0.01
2289.60	$2^+ \rightarrow 0^+$	0.29 ± 0.03	0.22 ± 0.02
2414.60	$2^+ \rightarrow 0^+$	0.25 ± 0.03	0.19 ± 0.01
750.05	$5 \rightarrow 4^+$	0.17 ± 0.01	0.17 ± 0.01
770.75	$(4^+) \rightarrow 4^+$	0.18 ± 0.01	0.17 ± 0.01
1246.84	$4^+ \rightarrow 2^+$	0.19 ± 0.02	0.17 ± 0.01
2868.90	$2^{(+)} \rightarrow 0^+$	0.10 ± 0.01	0.10 ± 0.01
2979.10	$2^+ \rightarrow 0^+$	0.08 ± 0.01	0.09 ± 0.01
1962.20	$3^- \rightarrow 2^+$	0.25 ± 0.02	0.17 ± 0.01

[Aug12] M. Auger *et al.*, Phys. Rev. Lett., **109**, 032505 (2012).

[Bra12] J. Bradt *et al.*, TUNL progress report, **LI**, 39 (2012).

[Gan13] A. Gando *et al.*, Phys. Rev. Lett., **110**, 062502 (2013).

[The93] J. Theuerkauf, In *Program TV, Institute for Nuclear Physics, University of Cologne (unpublished)*, 1993.

5.1.14 Final Results from $2\nu\beta\beta$ Decay of ^{96}Zr to Excited States

S.W. FINCH, W. TORNOW, *TUNL*

A search for the double- β decay of ^{96}Zr to excited states of ^{96}Mo has recently concluded, resulting in the collection of 685.7 days of data at KURF. An isotopically enriched ^{96}Zr sample was placed between two germanium detectors in order to observe coincidence γ rays from the resulting cascade. The final half-life limits for this decay are presented.

Observation of neutrinoless double- β ($0\nu\beta\beta$) decay would identify the neutrino as a Majorana particle and allow for a measurement of the neutrino mass. The $0\nu\beta\beta$ decay rate is proportional to the neutrino mass and a nuclear matrix element (NME). Extracting the neutrino mass requires a theoretical evaluation of the NME, which is very difficult at present. The two-neutrino double- β ($2\nu\beta\beta$) decay rate is used to calibrate these calculations. By measuring $2\nu\beta\beta$ decay to an excited final state (see Fig. 5.27) we can provide additional information to help fine tune these NME calculations.

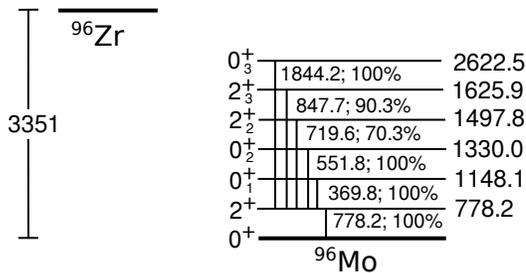


Figure 5.27: The excited states of ^{96}Mo following the double- β decay of ^{96}Zr . All energy values are given in keV.

The experimental apparatus consists of two coaxial high-purity germanium (HPGe) detectors, with the isotope of interest sandwiched between them. The detectors record the two coincident γ rays from the $0^+ \rightarrow 2^+ \rightarrow 0^+$ decay sequence. The detectors and sample are housed inside a NaI annulus, which is used as an active veto. Passive shielding includes 0.75 in. of copper, 6 in. of lead, and the 1450-meter-water-equivalent overburden at KURF. This apparatus has previously measured the $2\nu\beta\beta$ -decay half-life of ^{100}Mo and ^{150}Nd to their excited 0_1^+ states [Kid09, Kid14]. The original goal of this exper-

iment was to extend these successful measurements to include ^{96}Zr .

Our ^{96}Zr source consists of two ZrO_2 samples: one with 7.284 g enriched to 91.39% ^{96}Zr and the other with 26.969 g enriched to 64.15%, giving a total of 17.914 g ^{96}Zr . This sample was placed inside the detector apparatus from March 2012 to September 2014. Excluding detector downtime and runs which did not meet our data quality cuts, 685.7 days (1.877 yr) of data were produced, amounting to 74% detector live time.

Our analysis procedure requires a strict anti-coincidence in the NaI veto. The γ - γ coincidence is enforced in the HPGe detectors using an energy cut of $\pm 2\sigma$, where σ is the Gaussian detector resolution. For the 0_1^+ state, which produces a 369.8 + 778.2 keV coincidence, there are two candidate events matching this selection criteria at the conclusion of data collection, as shown in Fig. 5.30. This result is consistent with the experimental background. In fact, for all the excited states shown in Fig. 5.27, the region of interest was found to be consistent with background.

As no counts were seen above background, a limit on the half-life may be extracted using

$$T_{1/2} > \frac{\ln 2 t N_0 \epsilon_{\gamma\gamma}^{tot}}{N_d}, \quad (5.2)$$

where t is the counting time, N_0 is the number of nuclei present, $\epsilon_{\gamma\gamma}^{tot}$ is the coincidence efficiency, and N_d is a statistical factor indicating the upper limit of counts indistinguishable from background. The method of Feldman and Cousins was used for the statistical factor. In the event that fewer events were seen than predicted by the background model, the experimental sensitivity is given in addition to the confidence limit. These results are summarized in Table 5.4. These results include a 5.0% systematic uncertainty on the apparatus efficiency.

Table 5.4: The 90% half-life limits for the $2\nu\beta\beta$ decay of ^{96}Zr to excited states in ^{96}Mo extracted from the present experimental data. Previous best limits and a systematic estimate for the lifetime are also given.

J^π	E [keV]	$T_{1/2}$ [yr]			
		This work C.L.	This work Sensitivity	Previous work [Bar96]	Systematic law [Ren14]
0_1^+	1148.1	$> 3.2 \times 10^{20}$	$> 2.8 \times 10^{20}$	$> 6.8 \times 10^{19}$	2.59×10^{20}
0_2^+	1330.0	$> 1.4 \times 10^{20}$	-	-	4.29×10^{20}
2_2^+	1497.8	$> 1.0 \times 10^{20}$	-	$> 6.1 \times 10^{19}$	7.42×10^{20}
2_3^+	1625.9	$> 1.2 \times 10^{20}$	-	$> 5.4 \times 10^{19}$	1.21×10^{21}
0_3^+	2622.5	$> 1.1 \times 10^{20}$	$> 1.0 \times 10^{20}$	-	2.08×10^{25}

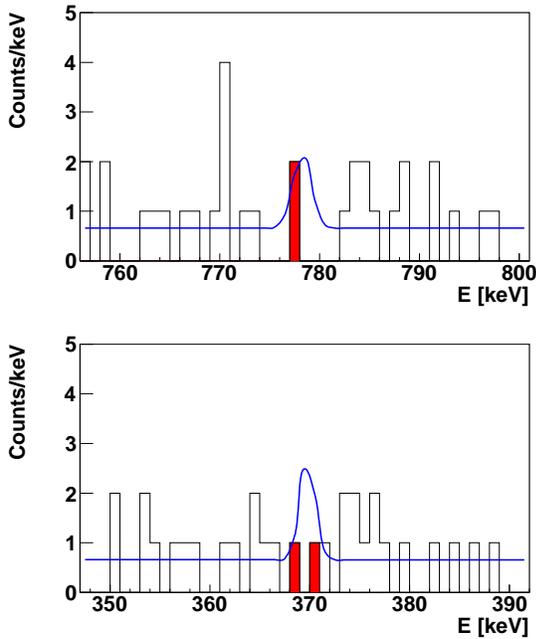


Figure 5.28: The $\beta\beta$ decay to the 0_1^+ state region of interest with the ^{96}Zr sample in place for 685.7 days. The top histogram shows events in coincidence with 369.8 keV and the bottom histogram shows events in coincidence with 778.2 keV. Events matching the γ - γ coincidence criteria are shaded in red. The minimum detectable signal above background at the 90% confidence level is shown by the blue curve.

As can be seen, our results represent an improvement over the previous experimental limits. A systematic law was proposed in Ref. [Ren14] to estimate $\beta\beta$ -decay half-lives. A formula was fit to experimental data for the ground state decays, but was found to have good agreement for

excited state decays as well. For the 0_1^+ state, our experimental limit exceeds the prediction of this systematic law by 25% and excludes the prediction at the 93% confidence level. Furthermore, we can use our experimental limits on the half-life to extract limits on the $2\nu\beta\beta$ nuclear matrix element. This has been done for the three nuclides studied by this apparatus and results are summarized in Table 5.5. A theoretical estimate of the NME using the interacting boson model [Bar13] gave $|M_{\text{eff}}^{2\nu}(0_1^+)| = 0.04$ for the decay to the 0_1^+ state of ^{96}Mo shown in Fig. 5.27. Unfortunately the present work was not strict enough to test this theoretical prediction, but the present work does hint at a small NME.

Table 5.5: Experimentally extracted nuclear matrix elements for $2\nu\beta\beta$ decay to the excited 0_1^+ state. The three searches performed by the present apparatus are summarized.

Nuclide	$ M_{\text{eff}}^{2\nu}(0_1^+) $
^{96}Zr	< 0.13
^{100}Mo	$0.172^{+0.019}_{-0.013}$ [Kid09]
^{150}Nd	$0.0465^{+0.0098}_{-0.0054}$ [Kid14]

[Bar96] A. S. Barabash *et al.*, J. Phys. G, **22**, 487 (1996).

[Bar13] J. Barea, J. Kotila, and F. Iachello, Phys. Rev. C, **87**, 014315 (2013).

[Kid09] M. F. Kidd, J. H. Esterline, and W. Tornow, Nucl. Phys., **A821**, 251 (2009).

[Kid14] M. F. Kidd *et al.*, Phys. Rev. C, **90**, 055501 (2014).

[Ren14] Y. Ren and Z. Ren, Phys. Rev. C, **89**, 064603 (2014).

5.1.15 New Limits on the β Decay of ^{96}Zr

S.W. FINCH, W. TORNOW, *TUNL*

As a by product of the search for the double- β decay of ^{96}Zr to excited states of ^{96}Mo (see Sect. 5.1.14), a measurement of the single- β decay of ^{96}Zr was performed. The use of the coincidence technique in the search for this decay allows for unambiguous distinction between the $\beta\beta$ decay to excited states and the β -decay modes. This is the first experiment able to make such a distinction.

^{96}Zr differs from other double- β -decay candidates in that single- β decay is energetically allowed, but only via a long-lived fourth-forbidden decay. The half-life has been theoretically estimated as 2.4×10^{20} yr [Hei07]. This half-life is ten times larger than the double- β decay half-life measured by the NEMO-3 collaboration: $T_{1/2}^{2\nu\beta\beta} = [2.35 \pm 0.14(\text{stat}) \pm 0.16(\text{syst})] \times 10^{19}$ yr [Arg10]. This estimate is, however, the same magnitude as estimates for double- β decay to excited final states.

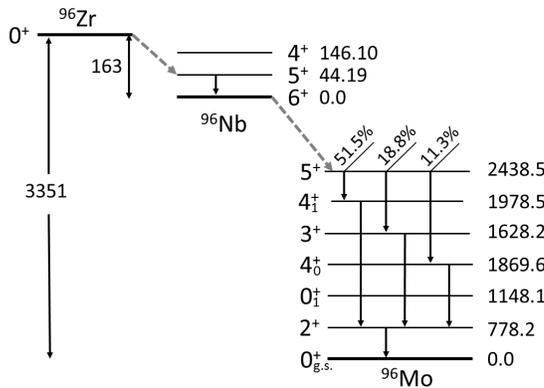


Figure 5.29: The β -decay scheme for ^{96}Zr and ^{96}Nb . Note that double- β to an excited state would likely proceed to the 0_1^+ state. All energy values are given in keV.

Although the β -decay of ^{96}Zr is below the detection threshold of the current experiment, the daughter nucleus, ^{96}Nb , decays to ^{96}Mo with a half-life of 23.35 hours and emits a cascade of γ rays as it de-excites to the ground state, as shown in Fig. 5.29. This cascade proceeds through the 2^+ level of interest for double- β decay to excited final states. Previous attempts to measure ^{96}Zr 's

$\beta\beta$ decay to an excited final state only searched for the single 778.2 keV γ ray from the $2^+ \rightarrow 0^+$ part of the decay. Because this γ ray also appears in the γ -ray cascade resulting from single- β decay, single-detection experiments are only sensitive to $T_{1/2}^{\beta+\beta\beta}$. With the detector apparatus discussed in Sect. 5.1.14, we can independently measure both the β and $\beta\beta$ -decay modes.

Noticeably, all single- β decay events contain three coincident γ rays. This is in contrast to $2\nu\beta\beta$ decays to an excited final state, which contain two coincident γ rays. For the present detection technique, there are multiple coincidences that may occur. Firstly, any two of the three γ rays may be detected in coincidence. This is referred to as a two- γ -ray event and gives rise to three separate regions of interest for each decay mode. The second method requires detection of all three γ rays, where two γ rays are detected in a single detector via coincident summing. This detection method is referred to as a three- γ -ray event and also results in three separate regions of interest for each decay mode. This method has a lower efficiency, but compensates with a lower experimental background due to the higher energy events.

In all, there are three decay sequences with six regions of interest for each decay sequence. The analysis procedure of Sect. 5.1.14 was used to investigate each individual region of interest. Three of these regions were found to be unfit for analysis and were not included. The decays proceeding through the 4_1^+ and 3_0^+ states each had one two- γ -ray event omitted due to the overlap of naturally occurring background lines. Additionally, a three- γ -ray event was omitted for the 3_0^+ decay mode because it is located near the cutoff energy, where nonlinearities in the energy calibration can occur. In the remaining regions

Table 5.6: Half-life limits for ^{96}Zr 's β decay from the combined statistical analysis at the 90% confidence level.

Decay sequence	Two- γ events [yr]	Three- γ events [yr]	Combined [yr]
$5_0^+ \rightarrow 4_1^+ \rightarrow 2_0^+ \rightarrow 0_0^+$	1.6×10^{19}	1.6×10^{19}	2.4×10^{19}
$5_0^+ \rightarrow 3_0^+ \rightarrow 2_0^+ \rightarrow 0_0^+$	1.1×10^{19}	0.18×10^{19}	1.0×10^{19}
$5_0^+ \rightarrow 4_0^+ \rightarrow 2_0^+ \rightarrow 0_0^+$	0.61×10^{19}	0.14×10^{19}	0.66×10^{19}
Combined	2.1×10^{19}	0.94×10^{19}	2.4×10^{19}

of interest, no events were observed above background, so limits were set in a method analogous to Sect. 5.1.14.

The coincidence efficiency was measured as a function of position using a ^{102}Rh source, which follows the same $0^+ \rightarrow 2^+ \rightarrow 0^+$ decay scheme as the double- β decay of ^{96}Zr to excited final states. Corrections are then applied to this efficiency measurement to adjust for the γ ray's energy, target attenuation, and sample geometry. For the three γ -ray cascades of this experiment, GEANT4 simulations normalized to the efficiency data were used to calculate the apparatus' efficiency. This procedure results in a combined systematic uncertainty on the efficiency of 7.5 to 7.7% for the different decay modes. This uncertainty is factored into the final limits at the 90% confidence level.

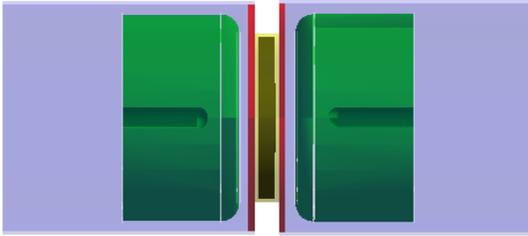


Figure 5.30: A geant4 model of the two coaxial HPGe detectors and surrounding the ^{96}Zr sample.

The results of the analysis for each individual region of interest may be combined to form one statistically significant result, as shown in Table 5.6. The final result is a combined limit of $T_{1/2}(\beta(^{96}\text{Zr})) > 2.4 \times 10^{19}$ yr. Noticeably, the same limit may be produced using only the most intense $5_0^+ \rightarrow 4_1^+ \rightarrow 2_0^+ \rightarrow 0_0^+$ transition. This is

because additional transitions increase the background, thus reducing the detector's total sensitivity, at the same rate at which they increase the total efficiency. The limit produced using only the search for two- γ -ray events is a very comparable 2.1×10^{19} yr.

Unfortunately, our limit is not sufficient to test the theoretical limit of 2.4×10^{20} yr by Ref. [Hei07]. Furthermore, the present limit is less than the previous limit of 3.8×10^{19} [Arp94]. The previous work used a single detector to search for the 778.2 keV γ ray. This results in a higher efficiency, but with an increased background. As the present experiment covers a larger solid angle, the coincidence summing of the three coincident γ rays becomes a large factor and noticeably decreases the efficiency compared to a single detector with half the solid angle. As has been previously stated, although the technique of Ref. [Arp94] is sufficient for limit setting, any observation would require detection of coincident γ rays to distinguish the β and $\beta\beta$ decay to excited states. The background reduction provided by the γ - γ coincidence has also been shown in the present work and will be necessary in any future searches. As such, the present experiment has a much higher discovery potential even though the produced limits may not be as competitive.

[Arg10] J. Argyriades *et al.*, Nucl. Phys., **A847**, 168 (2010).

[Arp94] C. Arpesella *et al.*, Europhys. Lett., **27**, 29 (1994).

[Hei07] H. Heiskanen *et al.*, J. Phys. G, **34**, 837 (2007).

5.1.16 Final Results from Search for Resonant Double-Electron Capture of ^{156}Dy

S.W. FINCH, W. TORNOW, *TUNL*

Resonant double-electron capture is a possible experimental alternative to neutrinoless double- β decay. The decay may be detected by observing the γ rays emitted as the excited-state daughter nucleus decays to the ground state. In this experiment, two clover HPGe detectors surround an enriched $^{156}\text{Dy}_2\text{O}_3$ target and search for the de-excitation γ rays. Final experimental results are presented.

In double electron capture (ECEC), the nucleus captures two atomic electrons, decreases its atomic number by two, and emits two neutrinos. As the only directly emitted particles are neutrinos, this process would be very hard to observe if not for atomic x-ray or nuclear γ -ray transitions in the daughter state. Double-electron capture can proceed through a zero-neutrino mode ($0\nu\text{ECEC}$), if the neutrino is a Majorana particle. If the Q value of the transition is degenerate with an excited state of the daughter nucleus, the decay rate may be resonantly enhanced [Kri11]. This resonant enhancement could decrease the half-life by up to a factor of 10^{10} for a complete degeneracy. In this case, the phase space available for neutrinos is so restricted that the neutrinoless mode dominates over the 2ν mode. This process is detectable by the γ -ray cascade from the excited state to the ground state in the daughter nucleus. Thus, detection of this cascade would be evidence for Majorana neutrinos. In the present experiment, this cascade is comprised of two coincident γ rays, which is the experimental signature.

In order search for $0\nu\text{ECEC}$, an apparatus was assembled at KURF using two HPGe clover detectors surrounding the target material, as shown in Fig. 5.31. A NaI annulus surrounds the sample and clover detectors to reduce background γ rays and serve as a Compton suppression shield. Six inches of lead surround the NaI annulus and serves as passive shielding. This apparatus mimics the design of the apparatus used in Sect. 5.1.14 and is designed for detecting coincident γ -ray cascades. Clover detectors are utilized because they have a larger total volume and higher efficiency than conventional coaxial HPGe detectors. Another advantage of clover detectors

is the higher coincidence efficiency. A large reduction in background is made by imposing a γ - γ coincidence and detecting the two separate γ rays in a cascade. In the two-clover apparatus we can search for coincidences between the two clover detectors (referred to as external coincidences) as well as within the four-fold segmentation of a single clover detector (referred to as internal coincidences).

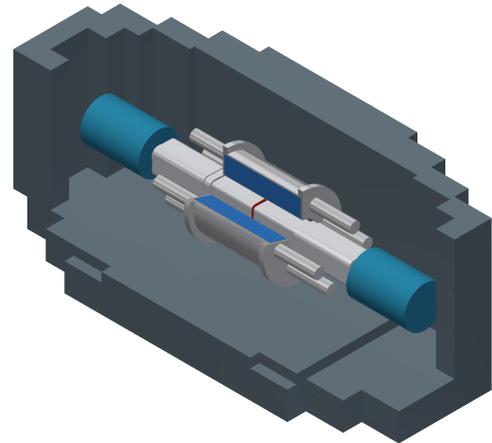


Figure 5.31: Schematic of the two clover detectors and NaI annulus as installed inside the lead shielding at KURF. The sample is shown in red, between the two detectors.

Reference [Eli11] used high precision Q -value measurements to show that ^{156}Dy is a promising candidate for $0\nu\text{ECEC}$ and identified four states with a possible resonant enhancement. ^{156}Dy , however, suffers from an extremely low natural abundance of 0.056%. For this experiment we acquired two enriched Dy_2O_3 samples: 803 mg en-

Table 5.7: The final half-life limits for the $ECEC$ decay of ^{156}Dy to excited states at the 90% confidence level. Both the confidence limit, the experimental sensitivity, and the previous measurement are given

J^π	E [keV]	Lim $T_{1/2}$ [yr] This work C.L.	Lim $T_{1/2}$ [yr] This work Sensitivity	Lim $T_{1/2}$ [yr] Previous limit [Bel12]
1^-	1946.4	1.0×10^{18}	2.8×10^{17}	9.6×10^{15}
0^-	1952.4	2.2×10^{17}	1.9×10^{17}	2.6×10^{16}
0_4^+	1988.5	9.5×10^{17}	5.0×10^{17}	1.9×10^{16}
2^+	2003.7	6.7×10^{16}	-	3.0×10^{14}

riched to 21.59% and 344 mg enriched to 20.9%. Data were collected for 99.1 days with the larger sample (151.9 mg ^{156}Dy) and 132.8 days with both samples in place (213.6 mg ^{156}Dy). The results presented here are the combined limits from both of these runs.

Each of these states has a distinct region of interest that was analyzed separately. Decays producing two coincident γ rays were the primary search criteria. The NaI annulus was used as a strict veto and energy cuts on the detectors were $\pm 2\sigma$, where σ is a Gaussian detector resolution. The 2^+ 2003.7 keV state has three separate two- γ -ray transitions with a significant branching ratio. The present results are the combined analysis of all three branches. For one of these branches, the background rate was found to be sufficiently high that a better limit could be obtained by only including external coincidences. In all other cases, both internal and external coincidences are included to provide the best possible limits.

No statistically significant counts were observed above background, so limits for resonant $0\nu ECEC$ were set and are given in Table 5.7. The limit-setting procedure is identical to that of Sect. 5.1.14. The 0_4^+ state suffers from a dearth of nuclear data. This state cannot decay directly to the 0^+ ground state, but no decay branching ratios have been measured for this decay. In calculating these limits, it was assumed that the 0_4^+ state decays entirely through the 2_0^+ state. Given the nuclear structure of ^{156}Gd , this is a reason-

able assumption. This limit may be easily updated, should the branching ratio be measured, by simply multiplying the limit by the measured branching ratio.

The limits produced by the current work represent a large improvement over the previous best limits measured by Ref. [Bel12]. The limit to the 1^- state is improved by a factor of 29, the 0^- state by a factor of 7.3, the 0_4^+ state by a factor of 26, and the 2^+ state by a factor of 220. This previous experiment used a single HPGe detector, so no coincidence technique could be applied. A natural Dy_2O_3 sample of 322 g, resulting in only 157 mg of ^{156}Dy , was measured for 104.7 days. The results are significantly limited by the spatial extent of this large sample and attenuation of the signal γ rays by the target itself. The improved limits presented here are due in large part to the higher efficiency of the two-clover apparatus and to the use of an isotopically enriched sample. A much larger sample mass is still necessary in order to test the theory of Majorana neutrinos using resonant $0\nu ECEC$. ^{156}Dy samples are of course limited by the small natural abundance of this isotope.

[Bel12] P. Belli *et al.*, J. Phys. Conf. Ser., **375**, 042024 (2012).

[Eli11] S. Eliseev *et al.*, Phys. Rev. C, **84**, 012501 (2011).

[Kri11] M. I. Krivoruchenko *et al.*, Nucl. Phys., **A859**, 140 (2011).

5.1.17 A Brief Exploration of Low-Threshold Detectors

K. MASOOD, *University of Florida, Gainesville, FL*; P.S. BARBEAU, G. RICH, *TUNL*

We are developing prototype low-noise, low-threshold, gas-filled detectors for use in modern particle-physics research and for exploring the use of alkane targets for reactor anti-neutrino experiments involving observation of inverse beta decay. We have successfully operated a prototype chamber using both isobutane and P-10 at pressures between 1 and 30 psi. A threshold of 150 eV is demonstrated with only preliminary noise- and threshold-reduction efforts. With very modest shielding, background count rates are below $1000 \text{ counts keV}^{-1} \text{ kg}^{-1} \text{ day}^{-1}$.

Low-threshold gas-filled detectors are a powerful tool in a variety of possible applications, including inverse beta-decay detection; exotic efforts such as direct-detection spin-dependent WIMP searches; and observations of never-before-observed interactions predicted by the standard model, such as coherent, elastic neutrino-nucleus scattering ($\text{CE}\nu\text{NS}$) [Col01]. Considering the usual scale and investment involved in such projects, success in just one of these goals would be a considerable innovation. With this in mind, the goal this summer was to develop and characterize prototype detectors with such experiments in mind.



Figure 5.32: An exterior view of our first prototype.

The initial design was a proportional counter with a roughly cylindrical geometry. A gold-tungsten anode wire was strung down the center of a series of Conflat flanges. The design allowed for a high voltage (for our interests, positive) to be applied on the wire, with the outer casing serving as ground. Gas was permitted to flow through two Conflat to Swagelok fittings. Figure 5.32 is a photograph of the detector. The ^{55}Fe source, when used, was secured to the back of a Conflat blank, as demonstrated in Fig. 5.33.

The detector was then connected to an Ortec 142 preamplifier, an Ortec 672 spectroscopic amplifier, an ADC, and a computer for data acquisition.

A variety of operating voltages and pressures were tested, with the goal of keeping at least one known peak in range for calibration. In addition, layers of aluminum, a copper collimator, and sometimes both, were used to reduce the count rate to prevent signal pile-up. The spectrum taken for each set of conditions had a run time of one hour, except in the cases where the collimator was used, due to the severely reduced rate.

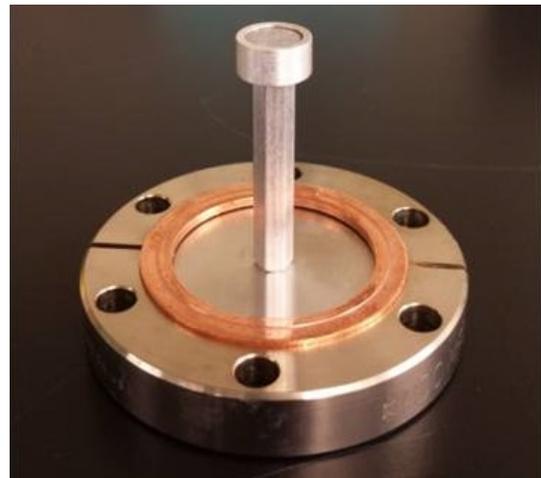


Figure 5.33: A view of the ^{55}Fe source, mounted on a standoff to be closer to the anode.

Both P-10 (a mixture of 90% argon, 10% methane), and isobutane were used as fill gases, with the operating voltages chosen with consideration of the range on the ADC being used. Then the source was removed and a series of back-

ground runs was taken using various amounts of shielding. Each background run was also taken for an hour. The shielding used is shown in Fig. 5.34.

When using P-10, with pressures of 1 psi, 14 psi, and 30 psi (gauge), adequate voltages were found that display the 5.9 keV X-ray peak associated with the decay of ^{55}Fe . Also present was a 3 keV peak resulting from a 5.9 keV γ ray ionizing a k-shell electron of Ar and then depositing the remaining energy in the detector. Furthermore, when the aluminum layers were used to reduce the rate, an additional peak was present. It arises when a ^{55}Fe γ ray ionizes a k-shell electron of Al, and an outer-shell electron de-excites to fill this vacancy, depositing the released photon of 1.48 keV in the detector.

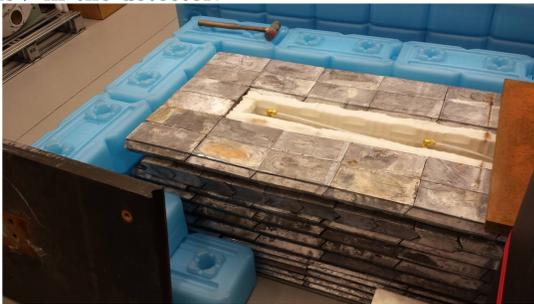


Figure 5.34: The background reduction methods included a lead castle, water bricks, and borated polyethylene.

An example of a spectrum taken using P-10 is provided in Fig. 5.35. Using the known peaks, a two-point, linear calibration of the x axis can be done. The sizeable peak near threshold is attributed to noise, since it is present in the background run as well. This gives an effective threshold of around 250 eV.

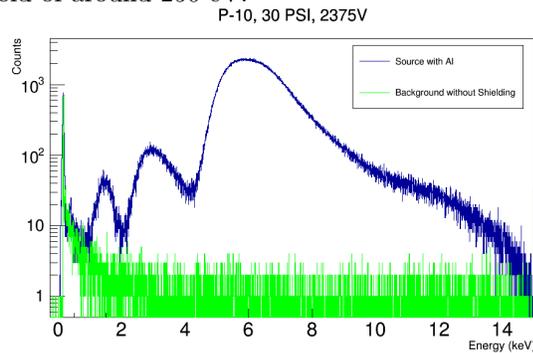


Figure 5.35: A sample spectrum taken using P-10 as a fill gas.

Figure 5.36 shows a spectrum taken with isobutane instead. Now, the Ar peak is ab-

sent. However, the high energy behavior makes it harder to perform a calibration, so the axis is set in ADC bins.

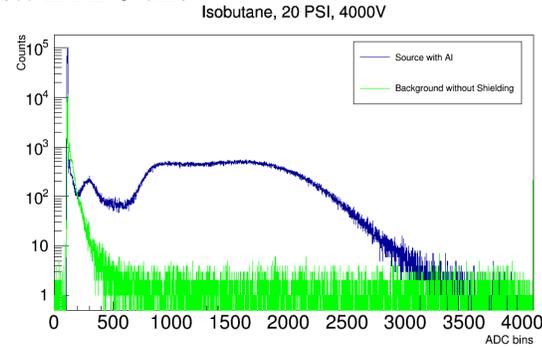


Figure 5.36: A sample spectrum taken using isobutane as a fill gas.

Figure 5.37 shows that the background is reduced as more shielding is applied. A rough estimate of the background index so far is $1000 \text{ counts kg}^{-1}\text{keV}^{-1} \text{ day}^{-1}$.

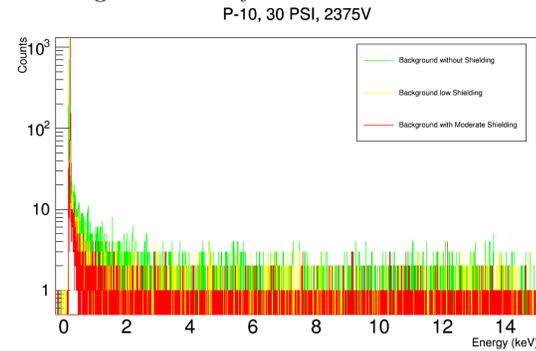


Figure 5.37: Spectra of background radiation at various levels of shielding.

While increasing the pressure allows for a greater density, it also reduces the avalanching that occurs. Furthermore, the detector bias cannot be increased arbitrarily in order to lower the threshold, due to the steady loss of energy resolution. A possible improvement would be to change to a point-contact design, which would detect the initial ions rather than relying on avalanching. The use of a CoolFET preamplifier in conjunction with a lower detector capacitance, could very well keep the signal above the noise. In that case, the fill gas could even be liquefied to yield a higher cross section. To further reduce background, muon-veto panels can be placed around the set up to reject unwanted events.

[Col01] J. Collar and Y. Giomataris, Nucl. Instrum. Methods, **471**, 254 (2001).

5.1.18 TUNL’s KamLAND Effort

H.J. KARWOWSKI, W. TORNOW, *TUNL*; D.M. MARKOFF, *North Carolina Central University, Durham, NC*

The KamLAND-Zen Phase 2 search for neutrinoless double-beta ($0\nu\beta\beta$) decay of ^{136}Xe continues to successfully collect data. In addition, the detection of terrestrial anti-neutrinos from the decay of uranium and thorium in the earth’s crust continues to benefit from a reduced reactor-neutrino background resulting from the shutdown of Japanese nuclear power plants. The same statement holds for other rare event searches of the KamLAND main detector, such as the search for the proton decay mode $p \rightarrow \bar{\nu} + K^+$

Our group has continued to provide KamLAND and KamLAND-Zen shift service, both on-site and remotely. Collaborators residing outside of Japan are required to perform at least eight days of on-site shift service per year. In addition, each of these members is responsible for remote monitoring shifts (eight hours per day) when it is nighttime in Japan. The TUNL members of the collaboration completed a total of 91 monitoring-shift days during the October 2014 through September 2015 shift-year. This is one quarter of all monitoring shifts and about 25% more than our quota. TUNL collaborator D. Markoff coordinates the monitoring shifts for the collaboration.

During the reporting period the KamLAND Collaboration prepared for the third phase of KamLAND-Zen. This involved the design and construction of a larger mini balloon to accommodate the increased loading of ^{136}Xe in the liquid scintillator from the current 383 kg (91% enriched in ^{136}Xe) to approximately 600 kg. Preparations are underway to refurbish the water Cherenkov veto (outer) detector, originally designed and built by the TUNL group. The refurbishment involves the replacement of all 225 photomultiplier tubes with 140 new 20-inch Hamamatsu R3600 photomultiplier tubes providing 0.9% phototube coverage and about 99.5% muon detection efficiency. The improvements will be performed during the expected six-month downtime of KamLAND starting at the end of calendar year 2015. The required inspection of the 20-m-diameter stainless-steel sphere of the main KamLAND detector is also scheduled to take place.

The KamLAND collaboration was also heavily involved in data analysis and the writing of

journal articles.

The following articles were published during the reporting period:

1. Laboratory studies on the removal of radon-born lead from KamLAND’s organic liquid scintillator [Kee15].
2. A compact ultra-clean system for deploying radioactive sources inside the KamLAND detector [Ban15].
3. Study of electron anti-neutrinos associated with gamma-ray bursts using KamLAND [Asa15d].
4. Search for the proton decay mode $p \rightarrow \bar{\nu} + K^+$ with KamLAND [Asa15c].

The following papers have been submitted for publication during the reporting period:

5. ^7Be solar neutrino measurements with KamLAND [Gan15].
6. KamLAND sensitivity to neutrinos from pre-supernova stars [Asa15a].
7. Search for double-beta decay of ^{136}Xe to excited states of ^{136}Ba with the KamLAND-Zen experiment [Asa15b].

The release of the KamLAND-Zen Phase 2 result for the $0\nu\beta\beta$ decay of ^{136}Xe is planned for the spring of 2016.

[Asa15a] K. Asakura *et al.*, submitted to *Astrophys. J.*, (2015).

[Asa15b] K. Asakura *et al.*, submitted to *Phys. Rev. C*, (2015).

- [Asa15c] K. Asakura *et al.*, Phys. Rev. D, **92**, 052006 (2015).
- [Asa15d] K. Asakura *et al.*, Astrophys. J., **80**, 87 (2015).
- [Ban15] T. Banks *et al.*, Nucl. Instrum. Methods A, **769**, 88 (2015).
- [Gan15] A. Gando *et al.*, submitted to Phys. Rev. C, (2015).
- [Kee15] G. Keefer *et al.*, Nucl. Instrum. Methods A, **769**, 79 (2015).

5.1.19 Effective Operators for Double-Beta Decay

R. NIAZI, *University of Oklahoma, Norman, OK*; J. ENGEL, *University of North Carolina at Chapel Hill, Chapel Hill, NC*

Neutrinoless double-beta decay is a theoretically predicted process that, if observed, would allow the neutrino mass to be calculated. However, due to a lack of experimentally determined parameters, the calculation of the necessary matrix elements does not have a clear and defined approach. We approximate the infinite shell model space, with that of a 2 shell system and calculate operators and matrix elements.

To approximate the matrix elements involving the decay operator for neutrinoless double-beta decay, we first must define our system. Since the decay of ^{76}Ge into ^{76}Se is a process likely to exhibit neutrinoless double-beta decay, we consider a truncated two-shell system for the nucleons of these species. We only consider systems where all nucleons are paired, so seniority ν is equal to 0. Considering a two-particle state within the two-shell system, the goal is to calculate the transition matrix elements of a two-body double-beta decay operator. The first step is to calculate the expectation values of the proton-creation and neutron-destruction operators.

We denote any state of Z protons and N neutrons within a j -shell of a certain $\Omega = j + 1/2$ as $|Z N \Omega\rangle$. After using the quasi-spin operator properties and commutation relations and two applications of the Wigner-Eckart theorem, it can be seen that, for a generalized transition from Z to $Z+2$ protons, the expectation value of the proton creation operators is

$$\langle Z+2 0 \Omega | \pi_{j_1 m_1}^\dagger \pi_{j_2 m_2}^\dagger | Z 0 \Omega \rangle = -A_{12} \frac{\sqrt{(Z+2)(2\Omega-Z)}}{2\Omega}, \quad (5.3)$$

where

$$A_{ab} = (-1)^{j_a+m_a} \delta_{j_a, j_b} \delta_{-m_a, m_b} \forall a, b \in \mathbb{N}. \quad (5.4)$$

Likewise, we can find the expectation value of neutron-destruction operators to be

$$\langle 0 N-2 \Omega | \tilde{\nu}_{j_1 m_1} \tilde{\nu}_{j_2 m_2} | 0 N \Omega \rangle = A_{12} \frac{\sqrt{N(2\Omega+2-N)}}{2\Omega}. \quad (5.5)$$

If we define the matrix element of the decay operator for certain total angular momentum values, as $M_{pqrs} \forall p, q, r, s \in \mathbb{N}$, such that

$$M_{pqrs} \equiv \langle Z+2 N-2 \Omega | \pi_{j_p m_p}^\dagger \pi_{j_q m_q}^\dagger \tilde{\nu}_{j_r m_r} \tilde{\nu}_{j_s m_s} | Z N \Omega \rangle, \quad (5.6)$$

then one can naturally see that the matrix element of our two-particle, seniority-zero beta-decay operator will be given by

$$M_{1234} = -A_{12} A_{34} \times \frac{\sqrt{(Z+2)(2\Omega-Z)N(2\Omega+2-N)}}{4\Omega^2}. \quad (5.7)$$

With these results in mind, we can find the general form of the decay operator, whose matrix elements we are interested in. Because the decay operator must be a scalar spherical-tensor operator in our formalism, the total system's angular momentum and its projection must be 0. So, the operator of interest, \hat{D} , will be given by

$$\hat{D} = \sum_{j_1, j_2, j_3, j_4} \sum_J D_{j_1 j_2 j_3 j_4}^J \times \left[(\pi_{j_1 m_1}^\dagger \pi_{j_2 m_2}^\dagger)^J (\tilde{\nu}_{j_3 m_3} \tilde{\nu}_{j_4 m_4})^J \right]_0^0. \quad (5.8)$$

Now, we can apply the results of Eq. (5.8) to see that the matrix elements of our generalized operator $D_{ZN} = \langle Z+2 N-2 \Omega | \hat{D} | Z N \Omega \rangle$ will be given by

$$D_{ZN} = - \sum_{j_1, j_3} K D_{j_1 j_1 j_3 j_3}^0 \sqrt{(2j_1 + 1)(2j_3 + 1)}, \quad (5.9)$$

where $K \equiv \frac{\sqrt{(Z+2)(2\Omega-Z)N(2\Omega+2-N)}}{4\Omega^2}$. Therefore, all that is needed to determine the matrix elements is to find the constants $D_{j_1 j_1 j_3 j_3}^0$.

Having established the form of our decay operator in our two-shell space, we consider the simplest configuration, the one with one pair of nucleons. The Hamiltonian for our two-shell system is given by

$$\hat{H} = \epsilon \hat{N}_2 - G \sum_{a,b=1}^2 (S_{pp}^{\dagger a} S_{pp}^b + S_{nn}^{\dagger a} S_{nn}^b). \quad (5.10)$$

Here ϵ is the energy difference between the two shells, \hat{N}_2 is the number operator acting on the second level, and G is just a constant. The creation operators are given by

$$S_{pp}^{\dagger a} = \frac{1}{2} \sum_{j \in a} \sum_m (-1)^{j-m} \pi_{jm}^{\dagger} \pi_{j-m}^{\dagger}, \quad (5.11)$$

$$S_{nn}^{\dagger a} = \frac{1}{2} \sum_{j \in a} \sum_m (-1)^{j-m} \nu_{jm}^{\dagger} \nu_{j-m}^{\dagger}, \quad (5.12)$$

where S_{pp}^a and S_{nn}^a are the adjoints of these terms. We can use what we know about the proton and neutron operators acting upon a state to determine what the operators in the Hamiltonian will do to these states. We can readily see that,

$$S_{pp}^{\dagger a} |Z 0 \Omega_a\rangle = \frac{\sqrt{(Z+2)(2\Omega_a - Z)}}{2} |Z+2 0 \Omega_a\rangle, \quad (5.13)$$

$$S_{pp}^a |Z 0 \Omega_a\rangle = \frac{\sqrt{Z(2\Omega_a + 2 - Z)}}{2} |Z-2 0 \Omega_a\rangle. \quad (5.14)$$

The neutron analogs to these operators have the same form except that Z would naturally be replaced by N .

With the results of Eqs. (5.13) and (5.14), we can construct the Hamiltonian for our two-particle state. We only have two possible initial states: one where the neutron pair is in the first level, which is represented as $|\phi_1\rangle = |0 2 \Omega_1\rangle |0 0 \Omega_2\rangle$, and one where the neutron pair is in the second level, represented as $|\phi_2\rangle = |0 0 \Omega_1\rangle |0 2 \Omega_2\rangle$. This results in a Hamiltonian given in matrix form as

$$\begin{pmatrix} -G\Omega_1 & -G\sqrt{\Omega_1\Omega_2} \\ -G\sqrt{\Omega_1\Omega_2} & 2\epsilon - G\Omega_2 \end{pmatrix}.$$

The simple form of this Hamiltonian allows us diagonalize it easily and find its eigenvalues and eigenvectors. If we define $O_{1,2} = \Omega_1 + \Omega_2$ and $O_{1,-2} = \Omega_1 - \Omega_2$, then the eigenvalues are given by

$$\lambda_{\pm} = \epsilon - \frac{G}{2} O_{1,2\pm} \frac{1}{2} \sqrt{4\epsilon(\epsilon + G O_{1,-2}) + G^2[2\Omega_1\Omega_2 + (\Omega_1^2 + \Omega_2^2)]}. \quad (5.15)$$

Likewise, the eigenvector normalizing factors, denoted by a_1 and a_2 , whose square will be used as the probability amplitudes in the linear combination of the two states $|\phi_1\rangle$ and $|\phi_2\rangle$ are given by

$$a_1^2 = \frac{G^2\Omega_1\Omega_2}{(\lambda_- + G\Omega_1)^2 + G^2\Omega_1\Omega_2}, \quad (5.16)$$

$$a_2^2 = \frac{(\lambda_- + G\Omega_1)^2}{(\lambda_- + G\Omega_1)^2 + G^2\Omega_1\Omega_2}. \quad (5.17)$$

For more complicated cases, we have constructed a program that computationally constructs the Hamiltonian and diagonalizes the matrix. This enabled us to construct eigenstates of our truncated 36-nucleon model space that was used to approximate the shells of ^{76}Ge and ^{76}Se . With these results in hand, one only has to determine the coefficients of the operator to be able to construct it and to describe the states that it connects. This future work will allow us to determine the full (36 nucleon) and effective (2 nucleon) double-beta decay operators and apply to the entire shell space. The goal would be to determine the disparity of the full and effective operators' matrix elements within the full space. If they are in good agreement—however that may be defined—then one can consider three- and four-body operators, so as to try and increase the coherence of the values. However, if these higher order corrections still cannot remedy a vast disparity in the matrix elements, then this approximation must be reconsidered.

Of course, the Hamiltonian does not take into account neutron-proton coupling and other important interactions. Unfortunately, including these effects would require generators that are not elements of the $\text{SU}(2)$ algebra. This would make our simplified analytic technique much more complex. Ultimately, there are many more considerations to be taken into account once a final result is achieved, and hopefully there will be a successful method that will allow the neutrino mass to be calculated, if neutrinoless double-beta decay is observed.

Applications of Nuclear Physics and Nuclear Data Evaluation

Chapter 6

- **Homeland and National Nuclear Security**
- **National Ignition Facility Activities**
- **Public Health Research**
- **Plant Physiology Research**
- **Nuclear Data Evaluation**

The research infrastructure at TUNL, developed for basic research in low-energy nuclear physics, is well suited for applied research in areas of national nuclear security, homeland security, nuclear energy, nuclear medicine, and nuclear data dissemination.

A new component of TUNL's research portfolio is cross-section measurements on reactions of interest for diagnostic purposes at the National Ignition Facility (NIF) at LLNL. Several (n, xn) reactions that are key to understanding neutron yields at NIF have been measured. Our most active applied nuclear physics research overlaps strongly with our basic research at TUNL. Examples include the nuclear structure research partially supported by the Domestic Nuclear Detection Office at the Department of Homeland Security (DNDO/DHS) and the National Nuclear Security Administration (NNSA) at DOE. Measurements in this area have been conducted both at the tandem lab and at HI γ S. They include studies of the $(n, 2n)$ reaction on ^{238}U , dipole transitions in ^{240}Pu , and sub-barrier photofission in ^{232}Th and ^{238}U . The plant physiology and water filtration membrane experiments continue to be an important service to the general public. Finally, TUNL's ongoing nuclear data activities provide key information to the nuclear engineering and nuclear physics communities.

6.1 Homeland and National Nuclear Security

6.1.1 Measurements of the $^{238}\text{U}(n,2n)^{237}\text{U}$ Cross Section of from 6 to 15 MeV

KRISHICHAYAN, M. BHIKE, W. TORNOW, *TUNL*

Precise $^{238}\text{U}(n,2n)^{237}\text{U}$ cross-section data have been measured for neutron energies between 6 and 15 MeV in small energy steps in order to resolve inconsistencies in the existing database. The activation technique was used to determine the cross section through the detection of the 208.01 keV γ -ray from the decay of ^{237}U .

The $(n,2n)$ reaction on ^{238}U is important for various applications, including nuclear reactors, especially advanced heavy water and fast breeder reactors. In addition, the activation product ^{237}U ($T_{1/2} = 6.75$ days) has the daughter nuclide ^{237}Np ($T_{1/2} = 2.144 \times 10^6$ years), which can be used to produce ^{238}Pu , via the $(n, \gamma \beta^-)$ process [Lan08], making it an ideal radioisotope for energy generation in spacecraft.

plms were used for the measurements. In order to determine the neutron fluence, the ^{238}U sample was sandwiched between gold/aluminum foils of same area, with known thicknesses and masses. The ^{238}U samples along with the monitor foils were irradiated for two to eight hours, depending on the beam energy and the $(n,2n)$ cross section.

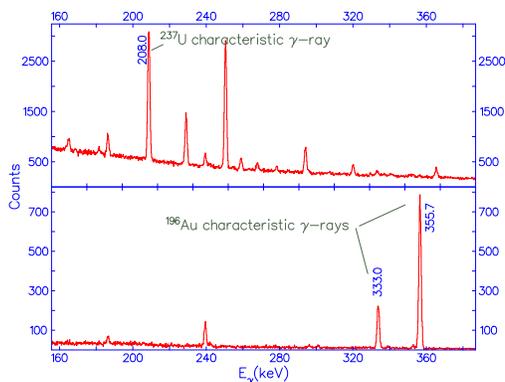


Figure 6.1: Spectra showing characteristic γ -ray lines for ^{237}U and ^{196}Au .

The $^{238}\text{U}(n,2n)^{237}\text{U}$ cross section was measured using the activation technique. Monoenergetic neutron beams were produced at sixteen energies from 6.5 to 12.5 MeV using the $^2\text{H}(d,n)^3\text{He}$ reaction and from 13.6 to 14.8 MeV using the $^3\text{H}(d,n)^4\text{He}$ reaction. Typical deuteron beam currents on target were $2 \mu\text{A}$. The deuterium gas pressure was adjusted to keep the neutron energy spread below ± 200 keV. Six depleted ^{238}U sam-

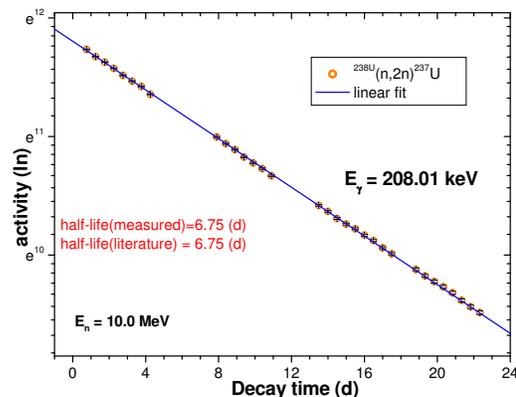


Figure 6.3: Decay curve for 208.01 keV γ -ray line of ^{237}U measured at $E_n = 10.0$ MeV.

The γ rays produced in the irradiated targets and monitor foils were measured in the low-background counting facility using clover and HPGe detectors and the GENIE2K data-acquisition platform. Off-line γ -ray analysis was done using the RADWARE analysis package [Rad95] to identify the reaction products and their respective peak areas.

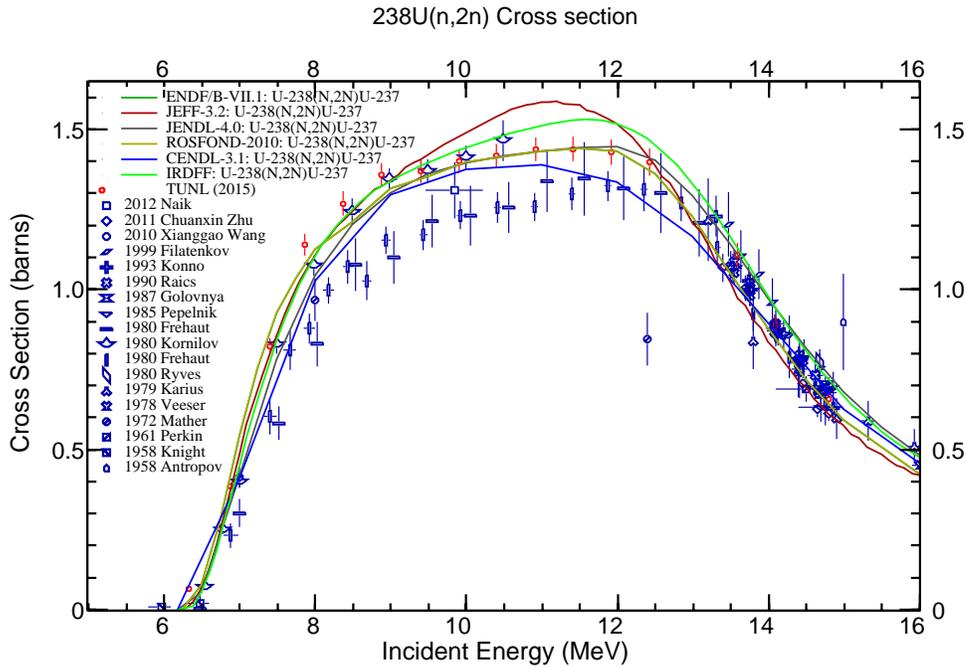


Figure 6.2: Our measured cross sections for the $^{238}\text{U}(n,2n)^{237}\text{U}$ reaction (small red symbols) compared with other available values.

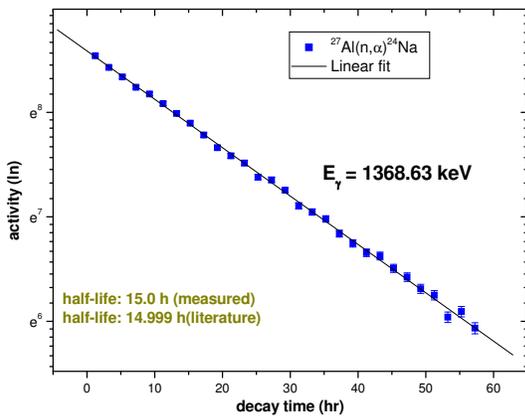


Figure 6.4: Decay curve for the 1368.63 keV γ -ray line of ^{24}Na measured at $E_n = 9.0$ MeV.

Typical γ -ray spectra for ^{237}U and ^{196}Au (from the $^{197}\text{Au}(n,2n)^{197}\text{Au}$ reaction) are shown in Fig. 6.1, where the characteristic γ -ray lines (208.01 keV in ^{237}U and 332.35 and 355.73 keV in ^{196}Au) are clearly seen. The decay curve for the 208.01 keV γ ray from ^{237}U and the 1368.63 keV γ ray from ^{24}Na are shown in Figs. 6.3 and 6.4, respectively. Fig. 6.2 shows the measured cross-section data between 6.5 and 14.8 MeV compared with other available data and evaluations. Table 6.1 shows the experimental results.

Table 6.1: Cross-section values for $^{238}\text{U}(n,2n)^{237}\text{U}$ measured in the present work

E_n (MeV)	Au (b)	Al (b)	$^{238}\text{U}(n,2n)$ (b)
6.34		0.005211	0.068 ± 0.003
6.89		0.015051	0.386 ± 0.012
7.40		0.025962	0.824 ± 0.024
7.87		0.038072	1.14 ± 0.034
8.38		0.052042	1.27 ± 0.037
8.89		0.066025	1.36 ± 0.036
9.40		0.078543	1.37 ± 0.035
9.91	0.9694		1.40 ± 0.039
10.41	1.2178		1.42 ± 0.037
10.92	1.4164		1.44 ± 0.037
11.42	1.5757		1.44 ± 0.038
11.93	1.7109		1.43 ± 0.038
12.43	1.8316		1.40 ± 0.043
13.60	2.087		1.11 ± 0.037
14.10	2.1415		0.893 ± 0.027
14.80	2.1622		0.66 ± 0.02

[Lan08] R. G. Lange and W. P. Carroll, Energy Conversion and Management, **49**, 393 (2008).

[Rad95] D. C. Radford, Nucl. Instrum. Methods A, **361**, 297 (1995).

6.1.2 Dipole Transitions in ^{240}Pu

B. FALLIN, C.R. HOWELL, W. TORNOW, M. BHIKE, KRISHICHAYAN, M.E. GOODEN, D. TICEHURST, *TUNL*; R.S. PEDRONI, *North Carolina A&T State University, Greensboro, NC*

During this reporting period we analyzed data from nuclear resonance fluorescence (NRF) measurements performed in January and May 2013 to determine the distribution of dipole transitions in ^{240}Pu over excitation energies from 1.9 to 3.0 MeV. The γ -ray transition energies, multiplicities, integrated cross-sections, branching ratios, widths, and reduced transition probabilities have been determined. Our results are in good agreement with the findings of Quiter et al. [Qui12].

Dipole transitions were excited using linearly-polarized, quasi-monoenergetic γ -rays at HI γ S, operated by the Triangle Universities Nuclear Laboratory. The γ -ray beam was delivered to target in the energy range from 1.95 to 2.95 MeV in 100 keV steps. The primary beam was collimated through a 0.75 in. diameter circular lead aperture, resulting in a FWHM energy spread of 3 to 4.5%. The incident γ -ray beam was linearly polarized in the horizontal plane. Four HPGe detectors with 60% efficient (relative to a 3 in. diameter x 3 in. thick NaI detector) were placed at scattering angles of 90° around the ^{240}Pu target, with the centers of one pair of the detectors lying in the horizontal plane and the other pair contained in a plane perpendicular to the plane of beam polarization. The detectors were positioned such that their front faces were an average of about 8 cm from the center of the ^{240}Pu target.

In this detector configuration, because ^{240}Pu has a 0^+ ground state, excited states that decay to the ground state via electric dipole (E1) transitions emit γ -rays in the direction of the 90° detectors in the vertical plane, but not the detectors in the horizontal plane. Likewise, states that decay to the ground state via magnetic dipole (M1) and electric quadrupole (E2) transitions emit γ -rays in the direction of the 90° detectors in the horizontal plane, but not the vertical plane. For most of the excited states, transitions indicating decay to the 2^+ first excited state in ^{240}Pu at 42.8 keV were also observed. The target was irradiated for between 3.5 and 5.5 hours at each incident γ -ray energy where dipole transitions were observed. A sample spectrum representing 5 hr 21 min of beam time is shown in Fig. 6.5.

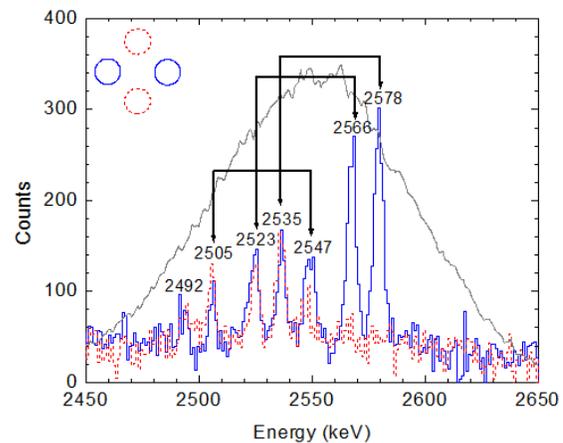


Figure 6.5: Measured energy spectra of NRF γ -rays emitted from ^{240}Pu . Transitions from the excited state to the ground or the first excited state in ^{240}Pu are indicated by the double arrows separated by 42.8 keV. The γ -ray beam envelope is overlaid for reference.

At incident γ -ray energies where ground state transitions were observed in the horizontal plane detectors, additional measurements were made with detectors at 90° and 135° in the plane of beam polarization for sufficient time to distinguish between M1 and E2 transitions. All detectors were passively shielded with 2.5 to 5 mm of lead and 2.5-mm-thick copper disks in front of the detector face. The target was placed in an evacuated plastic pipe to reduce the counting rate from scatter of the primary γ -ray beam and the intrinsic activity of the ^{240}Pu target.

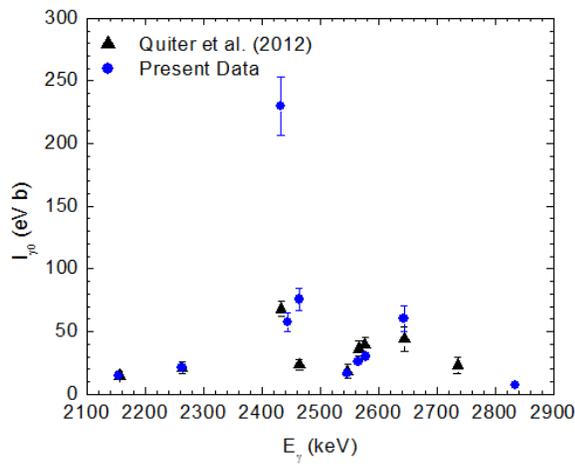


Figure 6.6: Integrated cross-section data for transitions to the ground-state in ^{240}Pu . The data are from the present work and from Quiter et al. [Qui12]. The error bars represent the total uncertainties (statistical + systematic).

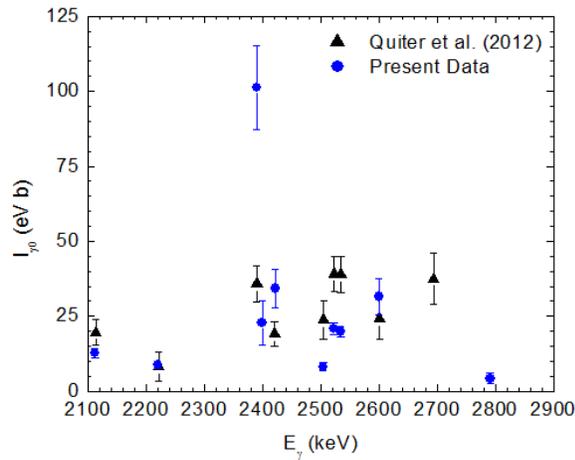


Figure 6.7: Integrated cross-section data for transitions to the first excited state in ^{240}Pu . The data are from the same experiments as in Fig. 6.6.

sisted of 4.65 g of ^{240}Pu in the form of a PuO_2 powder. The target contained minute quantities (milligrams) of ^{239}Pu , ^{241}Pu , and ^{241}Am . The PuO_2 powder was wrapped in 30 μm thick aluminum foil and placed inside a 2.8-cm-diameter aluminum canister. The walls of the canister were approximately 1 mm thick. To reduce the effects of γ -ray scattering off of air in the vicinity of the detectors, the target canister was placed inside an evacuated plastic tube, as previously mentioned.

The integrated cross sections determined for excited state transitions decaying to the ground and first excited states of ^{240}Pu , as well as the corresponding reduced transition probabilities (R_{sub}) are shown in Figs. 6.6, 6.7, and 6.8. Final analysis of the data is underway with final results scheduled to be published in the first quarter of 2016.

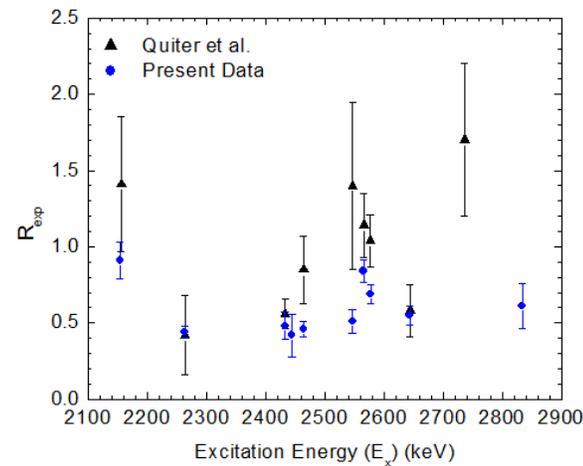


Figure 6.8: Ratio of the reduced transition probabilities for transitions to the ground and first excited states in ^{240}Pu . The data are from the same experiments as in Fig. 6.6.

The target was obtained on loan from Lawrence Berkeley National Laboratory and con-

[Qui12] B. J. Quiter *et al.*, Phys. Rev. C, **86**, 034307 (2012).

6.1.3 Sub-barrier Photofission of ^{232}Th and ^{238}U

J.A. SILANO, H.J. KARWOWSKI, *TUNL*; A. BANU, *James Madison University*; N. PARIKH, *The University of North Carolina at Chapel Hill*

An experiment to measure photofission in ^{232}Th and ^{238}U at sub-barrier energies was performed at HI γ S using linearly polarized γ -ray beams. Photofission neutrons were recorded with the newly upgraded INVS detector to determine the photofission cross section, prompt fission neutron multiplicities and asymmetries in the angular distribution.

The fission process may be better understood through improved knowledge of the structure of the fission barrier, the potential energy surface that an excited nucleus must overcome to split apart. For example, an inferred fission barrier of ^{238}U is shown in Fig. 6.9. For a given element, the fission barriers of the heavier isotopes typically include two local minima, while a deep third minimum has been observed in some lighter isotopes.

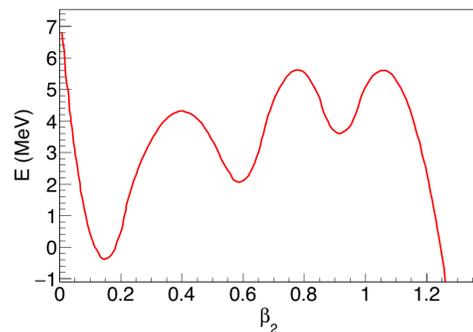


Figure 6.9: Inferred fission barrier of ^{238}U . Data from Ref. [Csi13]

In the case of ^{232}Th and ^{238}U , a variety of modern theoretical approaches to modeling the fission barrier predict shallow or nonexistent third minima including the self-consistent Skyrme-interaction-based functional employed by McDonnell *et al.* [Mcd13] and the microscopic-macroscopic model by Jachimowicz *et al.* [Jac13]. These predictions disagree with a recent measurement by Csige *et al.* [Csi13], which infers the existence of a 2-MeV-deep third minimum in ^{238}U by fitting a barrier structure to the measured fission cross section. As a consequence, they predict a low-energy resonance in the fission cross section. A direct measurement of this fission res-

onance would be clear evidence of a deep third minimum and would contribute to resolving differences between theory and experiment.

A measurement of the photofission cross sections of ^{232}Th and ^{238}U was performed at HI γ S in January 2015. Approximately 60 h of polarized γ -ray beam-time were used, with beam energies ranging from 4.3 to 6.3 MeV. Prompt neutrons emitted by the fission fragments were detected using the newly upgraded inventory-sample (INVS) neutron detector (see Sect. 6.1.4). The INVS detector consists of eighteen ^3He proportional counters, which are 2.54 cm in diameter and have an active length of 39.4 cm, embedded in a cylindrical shell of polyethylene moderator. They are arranged in two concentric rings with diameters of 15.28 and 12.22 cm. Neutrons are detected after first thermalizing in the moderator and then being captured on the ^3He in the proportional-counter tubes. The detector upgrade allows for each proportional counter to be read out independently by a digitizer. Offline pulse-shape discrimination selects only neutron-induced events.

The INVS detector was placed in the Upstream Target Room at HI γ S and was centered around the γ -ray beam axis, with a target placed in the center of the detector. The beam flux was measured with a D_2O target placed downstream of the INVS and viewed by two BC501A liquid-scintillator neutron detectors, one on either side, at 50 cm distance. A GEANT simulation will be used to determine the efficiency of this detector and target configuration, accounting for the effects of neutron scattering within both the target and the detectors and of the angular distribution of neutrons from the photodisintegration of deuterium with a linearly polarized γ -ray beam.

Due to the low count rate, background re-

duction and characterization is essential to the measurement. Shielding of about 1 m of borated polyethylene was placed around the INVS detector to reduce background neutrons produced by cosmic ray muons. The borated polyethylene further shielded against neutrons produced by the γ -ray beam in the collimator, air, D₂O flux-monitor target and beam dump. A natural lead target was used to measure the background from γ -rays scattering off the target and into the INVS moderator, producing neutrons through the $D(\gamma,n)$ reaction on the trace deuterium present in the polyethylene.

A high-energy bremsstrahlung contamination to the HI γ S γ -ray beam has been identified as one of the larger sources of background for this experiment. High-energy electrons in the free-electron-laser storage ring can scatter on residual gas or equipment near the beam line producing bremsstrahlung γ -rays with energies up to the ring energy, which, for this experiment, means between 350 and 450 MeV. To determine the background contribution from the high-energy bremsstrahlung, HI γ S was run in single-bunch mode. In this mode, only one electron bunch is present in the storage ring and no Compton scattered γ -ray beam is produced.

Extracting the absolute photofission cross section by detecting neutrons requires knowing the number of neutrons emitted per fission. Each fission event emits a variable number of prompt neutrons, with neutron multiplicity increasing with excitation energy. Because the existing multiplicity data does not extend down to the experimental energies, the prompt-neutron multiplicities will be measured. Simulations of the INVS detector with GEANT indicate that neutrons from a single fission event will produce detector signals within about a 200 μ s window. Since the neutrons fully thermalize in less than 1 μ s, the neutron detection timescale is primarily determined by the random walk of thermal neutrons in the moderator before they are absorbed and interact in one of the ³He proportional counters. Coincident neutrons will be grouped using time stamps from the digitized waveforms to generate neutron multiplicity distributions.

The asymmetries in the photofission neutron distributions will also be determined, using the individual tube readout of the INVS, which allows for sensitivity to asymmetries in the neutron distribution arising from the linear polarization of the γ -ray beam. A recent measurement at HI γ S by Mueller *et al.* [Mue13] determined the asymmetry of the photofission neutron angular distribution in a number of actinides, including ²³²Th and ²³⁸U. The present experiment will complement Mueller's work by extending the excitation energy range to lower sub-barrier energies. Figure 6.10 shows an example of the observed asymmetry in the inner ring of INVS counters for a ²³²Th target with a 5.5 MeV linearly polarized γ -ray beam.

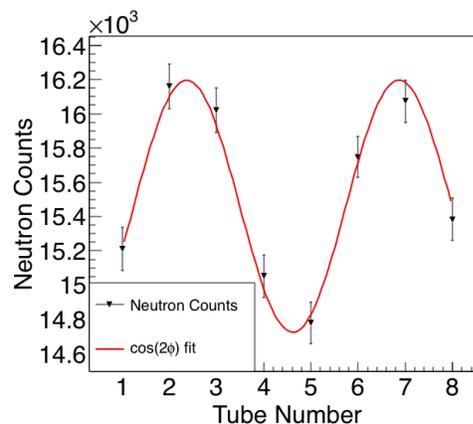


Figure 6.10: Neutron asymmetry for photofission of ²³²Th target induced by a 5.5 MeV linearly polarized γ -ray beam.

-
- [Csi13] L. Csige *et al.*, Phys. Rev. C, **87**, 044321 (2013).
- [Jac13] P. Jachimowicz *et al.*, Phys. Rev. C, **87**, 044308 (2013).
- [Mcd13] J. McDonnell *et al.*, Phys. Rev. C, **87**, 054327 (2013).
- [Mue13] J. Mueller *et al.*, Phys. Rev. C, **87**, 014605 (2013).

6.1.4 Upgrade to the Inventory-Sample Neutron Detector

J.A. SILANO, H.J. KARWOWSKI, K. WIERMAN, *TUNL*

The INVS neutron detector has been upgraded to enable independent channel readout of its eighteen ^3He proportional counters. Waveforms from a newly designed preamplifier array are digitized for offline analysis. Pulse-shape discrimination selects only neutron-induced pulses, excluding beam-induced γ -ray scattering events. With independent tube readout, the detector has sensitivity to asymmetries in the azimuthal angle of the neutron distribution.

The model IV inventory-sample neutron detector (INVS) has been used extensively for in-beam measurements at TUNL [Rau13, Arn12]. The INVS detector, shown in Fig. 6.11, consists of eighteen ^3He proportional counters 2.54 cm in diameter with an active length of 39.4 cm, embedded in a cylindrical shell of polyethylene moderator and arranged in two concentric rings with diameters of 15.28 and 12.22 cm. Incident neutrons are first thermalized in the moderator, and then captured in the ^3He in the proportional counters. The proton and triton emitted in the $^3\text{He}(n,p)^3\text{H}$ reaction produce Townsend avalanches in the biased proportional counters, and the resulting charge is collected on a central anode wire, creating a signal which is then sent to a preamplifier.

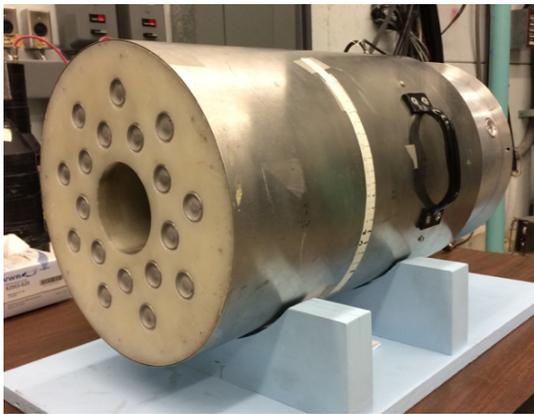


Figure 6.11: Photograph of the INVS detector.

In the original INVS configuration, the anode pins of the counters were wired together to create a single channel out for multiple proportional counters. The summed channels were then sent through a preamplifier and discriminators to output TTL signals for neutron detection. The

eighteen counters are divided into groups: two groups of inner ring counters and one for the outer ring. The inner ring groups have their TTL outputs summed together resulting in two output signals, one for each ring. This configuration provides only the total number of counts in the inner and outer rings, with no knowledge of which tube made a given detection and therefore no sensitivity to the neutron angular distribution. In addition, the discriminator threshold settings are not adjustable, making it difficult to determine if background signals due to scattered γ -rays and electrons are fully excluded. These limitations pose a significant problem for experiments with low neutron count rates, large γ -ray backgrounds, and asymmetrical neutron angular distributions, such as sub-barrier photofission measurements.

In response to these deficiencies, the INVS has been upgraded to allow readout of the individual proportional counters. The original, self-contained signal-processing electronics were replaced with SHV connectors which lead directly to the individual proportional-counter tubes. Two multi-channel preamplifier modules were built to replace the existing preamplifiers. The modules, shown in Fig.6.12, include 10 Cremat CR-110 preamplifiers isolated from one another with an aluminum housing to minimize interference. The outputs of the preamplifiers are recorded with a CAEN V1730 sixteen-channel 500 MHz digitizer and stored for offline analysis.

Scattered γ -rays and electrons represent a potential background sources for experiments at HI γ S. The γ -rays can Compton-scatter electrons into the gas volume, resulting in pulses which typically have lower height than neutron-induced events but are otherwise similar. A pulse height threshold was used in the original INVS configuration to reject γ -ray backgrounds. However,

with γ -ray beam energies much higher than available calibration sources and with fluxes of around 10^8 γ /s, it is unclear whether the γ -ray backgrounds are fully rejected.

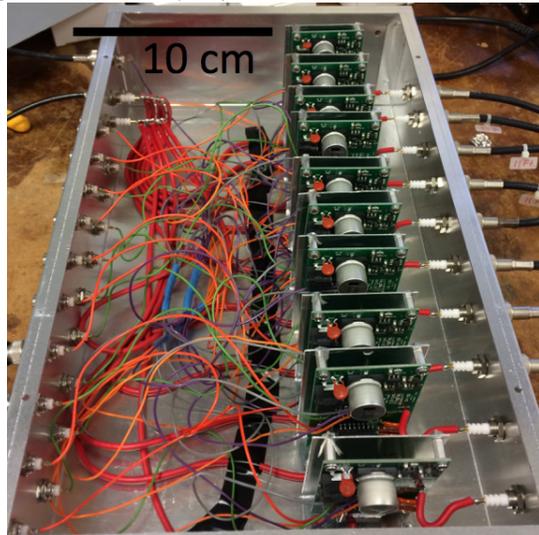


Figure 6.12: Preamplifier module.

In the upgraded INVS, offline pulse shape discrimination is used to reliably suppresses γ -ray background events through cuts in the pulse height and rise time [Lan13] extracted from the digitized waveforms. Data from a HI γ S run with a 6 MeV γ -ray beam and a lead scattering target, displayed in Fig. 6.13, show a clear separation between neutrons and γ -rays. A two-dimensional cut includes all neutron-induced events while completely excluding the γ -ray background.

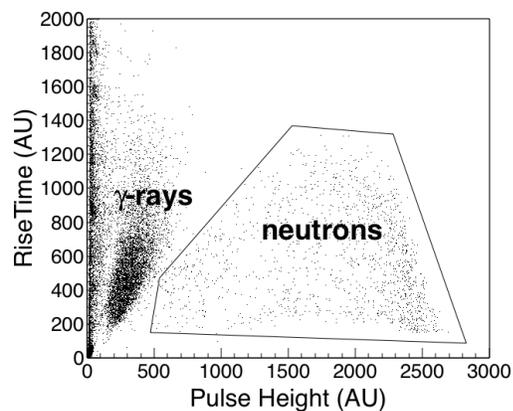


Figure 6.13: Pulse shape discrimination plot.

The INVS was simulated in GEANT to determine its sensitivity to asymmetries in the neutron angular distribution. The detection efficiency per proportional-counter tube is plotted in Fig. 6.14

for a beam of neutrons directed at $\phi = 200^\circ$. The detected distribution is inherently spread by the scattering of the neutrons in the moderator, but there is a clear correlation between the detector response and the initial neutron distribution. Thus with individual-tube readout, the INVS is sensitive to neutron angular distribution asymmetries produced by the linearly polarized γ -ray beams available at HI γ S.

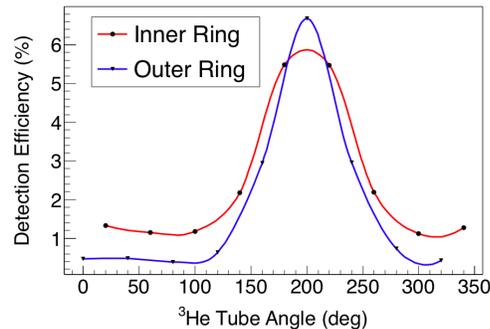


Figure 6.14: Simulated INVS individual tube efficiency.

To validate the GEANT simulation, $D(\gamma, n)$ reaction data were taken at HI γ S with a linearly polarized γ -ray beam with energies between 4.3 and 5 MeV. The beam was incident first on a D_2O cell placed in the center of the INVS and then on a second, downstream D_2O cell viewed by two BC501A scintillator neutron detectors to monitor the beam flux. The preliminary results show strong asymmetries about the beam polarization axis, with the maxima and minima consistent with the expected angular distribution from the $D(\gamma, n)$ reaction. Further work is being done to simulate the detector response to those neutron distributions and compare the result with the data. The goal is the ability to unfold the detector response from the measured data and to determine the initial neutron distribution. Progress has also been made in calibrating the flux-monitor apparatus so that the absolute beam flux, and therefore the INVS detection efficiency, can be extracted and compared with simulation.

[Arn12] C. Arnold *et al.*, Phys. Rev. C, **85**, 044605 (2012).

[Lan13] T. Langford *et al.*, Nucl. Instrum. Methods, **717**, 51 (2013).

[Rau13] R. Raut *et al.*, Phys. Rev. Lett., **111**, 112501 (2013).

6.2 National Ignition Facility Activities

6.2.1 Measurement of the $^{80}\text{Kr}(n,2n)^{79}\text{Kr}$ Cross Section at 14.8 MeV

M.E. GOODEN, M.M. FOWLER, J.B. WILHELMY, *Los Alamos National Laboratory, Los Alamos, NM*; W. TORNOW, *TUNL*; A.P. TONCHEV, *Lawrence Livermore National Laboratory, Livermore, CA*

A program has been initiated to measure the cross section of the $^{80}\text{Kr}(n,2n)^{79}\text{Kr}$ reaction at energies from 12 to 15 MeV using monoenergetic neutrons. The goal is to provide accurate cross-section information to the National Ignition Facility at Lawrence Livermore National Laboratory in its quest to measure the yield of 14 MeV neutrons obtained in inertial-confinement fusion experiments involving small deuterium-tritium capsules doped with ^{80}Kr . An exploratory measurement at $E_n = 14.8$ MeV has been performed.

Currently, the yield of 14 MeV neutrons obtained at the National Ignition Facility (NIF) in laser shots involving deuterium-tritium filled capsules is approximately three orders of magnitude lower than the design goal of a few 10^{19} neutrons per shot. Because the neutrons are produced within a few femtoseconds, it is difficult to measure their yield reliably using active detectors. Therefore, the activation technique provides an excellent tool for measuring the neutron yield.

Noble gases are the favorite isotopes for neutron yield measurements at NIF. The capsules can be doped with a precisely known amount of an isotope. After a laser shot, the noble gas is collected by the Radiochemical Analysis of Gaseous Samples (RAGS) apparatus [Sha12] and subsequently γ -ray counted to measure the induced activity. If the cross section for the neutron-induced reaction of interest and the collection efficiency of RAGS are known, the neutron fluence can be extracted.

the near future. The natural abundance of ^{80}Kr is only 2.28%, but the threshold for the $^{80}\text{Kr}(n,2n)^{79}\text{Kr}$ and the half-life of ^{79}Kr are suitable. The threshold is 11.17 MeV, and the half-life is 35.04 hours. The useful γ -ray lines of ^{79}Kr are given in Table 6.2.

As stated above, the cross section for the $^{80}\text{Kr}(n,2n)^{79}\text{Kr}$ must be known in order to extract valuable information on the neutron yield from the laser shots at NIF. Unfortunately, only evaluations and model calculations exist; there are only a few experimental data in the 14 MeV energy region to which the predictions can be compared. Therefore, we decided to measure this cross section over a broader energy range.

Table 6.2: Useful γ -ray decay lines in ^{79}Kr

E_γ (keV)	Intensity (%)
261.29	12.7
397.54	9.3
511.0	14.0
606.09	8.1

The krypton isotope ^{80}Kr has recently been selected as a dopant in deuterium-tritium filled capsules. Laser shots at NIF are planned for

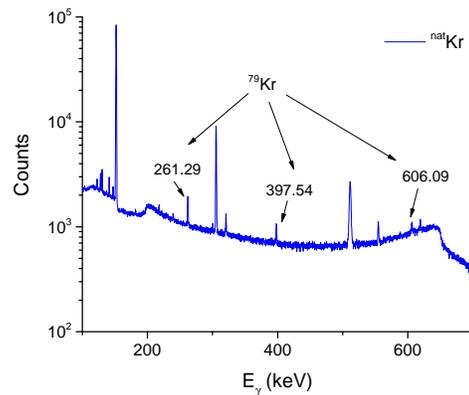


Figure 6.15: Partial γ -ray spectrum of a stainless steel sphere filled with natural krypton gas after irradiation with 14.8 MeV neutrons. The γ -ray lines of interest from the $^{80}\text{Kr}(n,2n)^{79}\text{Kr}$ reaction are labeled.

In Ref. [Bhi15], we used highly enriched ^{86}Kr , but isotopically enriched ^{80}Kr was not available for the present work. Therefore we filled a thin-walled stainless steel sphere [Rup09] with an inner diameter of 20 mm and wall thickness of 0.5 mm with 2.053 g of natural krypton gas, containing 46.8 mg of ^{80}Kr . The resulting pressure inside the sphere was approximately 130 atm.

The center of the sphere was positioned at a distance of 24 mm from the tritiated target described in Sect. 6.2.2. Gold foils were attached to the front and back face of the sphere for neutron fluence determination via the $^{197}\text{Au}(n,2n)^{196}\text{Au}$ reaction, with its well-known cross section in the energy region of interest. Monoenergetic neutrons of energy 14.8 MeV were produced via the $^3\text{H}(d,n)^4\text{He}$ reaction with an incident beam current of 2.8 μA . The krypton sphere was irradi-

ated for a total of eight hours. Subsequently, the sphere and the gold foils were γ -ray counted in separate HPGe detectors of known efficiency. Figure 6.15 shows a γ -ray spectrum with some of the ^{79}Kr lines of interest labeled by their energy. Clearly, our sensitivity is high enough to obtain very good peak-to-background ratios even with only 46.8 mg of target material. Data analysis is underway.

In the future, we will take data with the $^3\text{H}(d,n)^4\text{He}$ neutron-production reaction at neutron energies of 14.5, 14.1 and 13.7 MeV before switching to the $^2\text{H}(d,n)^3\text{He}$ reaction to cover the neutron-energy range between 11.5 and 13.5 MeV.

-
- [Bhi15] M. Bhide *et al.*, Phys. Rev. C, **92**, 014624 (2015).
- [Rup09] G. Rupp *et al.*, Nucl. Instrum. Methods A, **608**, 152 (2009).
- [Sha12] D. A. Shaughnessy *et al.*, Rev. Sci. Instrum., **83**, 10D917 (2012).

6.2.2 Exploratory Measurement of the $^{209}\text{Bi}(n,4n)^{206}\text{Bi}$ Cross Section at 28 MeV

M.E. GOODEN, M.M. FOWLER, J.B. WILHELMY, *Los Alamos National Laboratory, Los Alamos, NM*; W. TORNOW, *TUNL*; A.P. TONCHEV, *Lawrence Livermore National Laboratory, Livermore, CA*

A program has been initiated to measure the cross section of the $^{209}\text{Bi}(n,4n)^{206}\text{Bi}$ reaction in the 24 to 30 MeV energy range using monoenergetic neutrons produced via the $^3\text{H}(d,n)^4\text{He}$ reaction. The goal is to provide the National Ignition Facility at Lawrence Livermore National Laboratory with accurate cross-section data for determining the yield of the highest energy reaction-in-flight neutrons produced in laser shots on DT capsules used in inertial confinement fusion studies. An exploratory cross-section measurement at $E_n = 28$ MeV is described.

As was stated in Sect. 6.2.1, the 192 high-power laser beams at the National Ignition Facility (NIF) at Lawrence Livermore National Laboratory are directed onto a small capsule filled with an equimolar mixture of deuterium (D) and tritium (T) and positioned inside of a gold hohlraum to achieve ignition via inertial-confinement fusion of the DT plasma [Lin14]. Currently, ignition has not been achieved, and a broad experimental and theoretical effort is underway to better understand the complicated physics governing the plasma produced in inertial-confinement-fusion laser shots.

A good measure of the plasma density is the yield of high energy neutrons. The incident laser beams produce the primary 14.1 MeV neutrons via DT fusion at a temperature of approximately 8 keV. Higher energy neutrons are created when a primary neutron scatters elastically off a D or T ion, transferring some of its energy to the ions, which in turn initiate the DT reaction. These associated neutrons with energies up to 30 MeV are called “reaction-in-flight (RIF)” neutrons. They carry important information about the stopping power of the charged particles in the plasma. Currently, there is no solid experimental information available at NIF regarding the production of RIF neutrons with energies above 25 MeV.

The element bismuth is a very convenient candidate for measuring the highest energy RIF neutrons. It is mono-isotopic and the $^{209}\text{Bi}(n,4n)^{206}\text{Bi}$ reaction has a threshold of 22.6 MeV. The reaction product ^{206}Bi is expected to have a high production cross section. Furthermore, ^{206}Bi has convenient decay properties. Its

half-life is $T_{1/2} = 6.2$ days, with a strong γ -ray transition ($I_\gamma = 99\%$) at 803.1 keV. However, experimental data for this reaction do not exist.

The $^3\text{H}(d,n)^4\text{He}$ reaction was used to produce 28 MeV neutrons. An 11 MeV deuteron beam of 2 μA bombarded a tritiated titanium target consisting of 2 Ci of tritium loaded into a titanium layer, 2 mg/cm² thick and with a diameter of 16 mm, that had been evaporated onto a 0.4 mm thick copper disk of 18.9 mm diameter. This target was mounted at the end of a water-cooled target cell made of thin-walled copper. In addition, a special nozzle directed refrigerated and compressed air to the copper disk to help carry away the heat load deposited by the incident deuteron beam.

The ^{209}Bi foil of 9.53 mm diameter and 1 mm thickness was positioned at a distance of 15 mm from the copper disk. It was sandwiched between two 0.1-mm-thick ^{197}Au foils of the same diameter. The $^{197}\text{Au}(n,4n)^{194}\text{Au}$ reaction, with a threshold of 23.3 MeV, provided a measure of the neutron fluence. The isotope ^{194}Au has a half-life of 38.02 hours and is characterized by two strong γ -ray lines, one at 328.5 keV with $I_\gamma = 60.4\%$ and the other at 293.5 keV with $I_\gamma = 10.6\%$.

At a distance of 306 cm from the copper foil, our standard 3.9 cm \times 3.9 cm neutron monitor, which uses the liquid scintillator BC-501A, was positioned at 0° to monitor the stability of the neutron flux. Currently, the absolute detection efficiency of this neutron monitor has not been determined at energies above 20 MeV.

The $^{209}\text{Bi}/^{197}\text{Au}$ foil assembly was irradiated for eight hours. After irradiation, the foils

were γ -ray counted in TUNL's Low-Background Counting Facility to determine their initial activity. Figure 6.16 shows a γ -ray spectrum showing the peaks of interest from the decay of ^{206}Bi . Data analysis is underway.

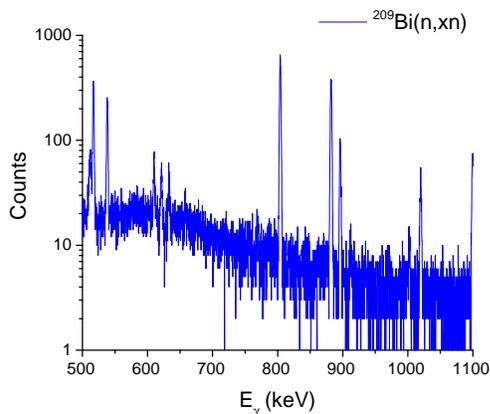


Figure 6.16: Partial γ -ray spectrum obtained from the decay of ^{206}Bi produced via the $^{209}\text{Bi}(n,4n)^{206}\text{Bi}$ reaction with 28 MeV neutrons.

Because the cross-section values predicted for the $^{197}\text{Au}(n,4n)^{194}\text{Au}$ reaction by the ENDF/B-VII.1 evaluation [Cha11] and the TALYS code [Kon05] are rather inconsistent, we plan to determine the detection efficiency of our neutron monitor detector in the 20 to 30 MeV energy range in the near future. Once this is accomplished, more accurate values for both the $^{197}\text{Au}(n,4n)^{194}\text{Au}$ and $^{209}\text{Bi}(n,4n)^{206}\text{Bi}$ cross sections will become available. Cross-section values will then be measured between 24 and 30 MeV in energy steps of 1 MeV.

[Cha11] M. B. Chadwick *et al.*, Nucl. Data Sheets, **112**, 2887 (2011).

[Kon05] A. J. Koning, S. Hilaire, and M. C. Duijvestijn, AIP Conf. Proc., **769**, 1154 (2005).

[Lin14] J. Lindl *et al.*, Phys. Plasmas, **21**, 020501 (2014).

6.2.3 Measurement of the $^{169}\text{Tm}(n,3n)^{167}\text{Tm}$ cross section

B. CHAMPINE, E.B. NORMAN, K.J. THOMAS, *University of California, Berkeley, CA*; M.E. GOODEN, *Los Alamos National Laboratory, Los Alamos, NM*; N.D. SCIELZO, M.A. STOYER, A.P. TONCHEV, *Lawrence Livermore National Laboratory, Livermore, CA*; KRISHICHAYAN, W. TORNOW, *TUNL*

The $^{169}\text{Tm}(n,3n)^{167}\text{Tm}$ reaction cross section was measured from 17.5 to 21.5 MeV using quasi-monoenergetic neutrons. The goal was to resolve the discrepancy between two previous measurements. Our results provide more accurate data for an important diagnostic that is used at the National Ignition Facility to measure the yield of reaction-in-flight neutrons produced during inertial confinement fusion.

The National Ignition Facility (NIF) at Lawrence Livermore National Laboratory is designed to drive deuterium-tritium (DT) inertial confinement fusion targets to ignition. As a result of DT fusion, primary neutrons are produced during the burn phase via the $^3\text{H}(d,n)^4\text{He}$ reaction with energies centered at $E_n = 14.1$ MeV. The width of the associated energy distribution is defined by the temperature of the DT burn, or about 8 keV. Higher energy neutrons are created when a primary neutron scatters elastically off a D or T ion, transferring some of its energy to the ions, which in turn initiate the DT reaction. The associated neutrons, with energies up to 30 MeV, are called reaction in-flight (RIF) neutrons. They carry important information about the stopping power of the charged particles in the plasma and may help researchers understand why the break-even goal has not been achieved yet at NIF. Currently the RIF neutrons represent less than 0.3% of the total neutron fluence, which is still about three orders of magnitude below the design goal.

The element thulium is a convenient candidate for measuring the RIF neutrons. It is monoisotopic, and the $^{169}\text{Tm}(n,3n)^{167}\text{Tm}$ reaction has a threshold of 14.963 MeV. The daughter ^{167}Tm has a high production cross section and convenient decay properties, with a half-life 9.2 days and a 42% abundant γ -ray transition at 207.8 keV. Activation of ^{169}Tm foils and subsequent off-line counting have been used successfully at NIF to determine the yield of RIF neutrons.

The production of ^{167}Tm at NIF is determined by the RIF neutron energy spectrum, which drops off above 15 MeV, and the $^{169}\text{Tm}(n,3n)^{167}\text{Tm}$ cross section, which in-

creases with energy up to approximately 25 MeV. Figure 6.17 shows the simulated energy distribution of NIF neutrons and the evaluated $^{169}\text{Tm}(n,3n)^{167}\text{Tm}$ cross section. The peak yield of ^{167}Tm for a typical NIF shot is at about 20 MeV. However, existing data for the $^{169}\text{Tm}(n,3n)$ cross section do not agree at energies above 19 MeV. To improve the accuracy of the RIF neutron yield measurements at NIF, the cross section for this reaction was measured at TUNL at five incident neutron energies between 17.5 and 21.5 MeV.

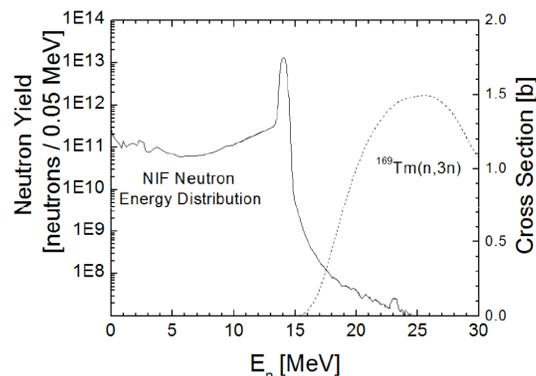


Figure 6.17: Overlay of a simulated NIF neutron-energy distribution (left y-axis) and the $^{169}\text{Tm}(n,3n)^{167}\text{Tm}$ cross section (right y-axis). Only reaction-in-flight neutrons have enough energy to produce ^{167}Tm .

Deuteron beams with energies between 17.5 and 19.2 MeV were used to produce the neutron

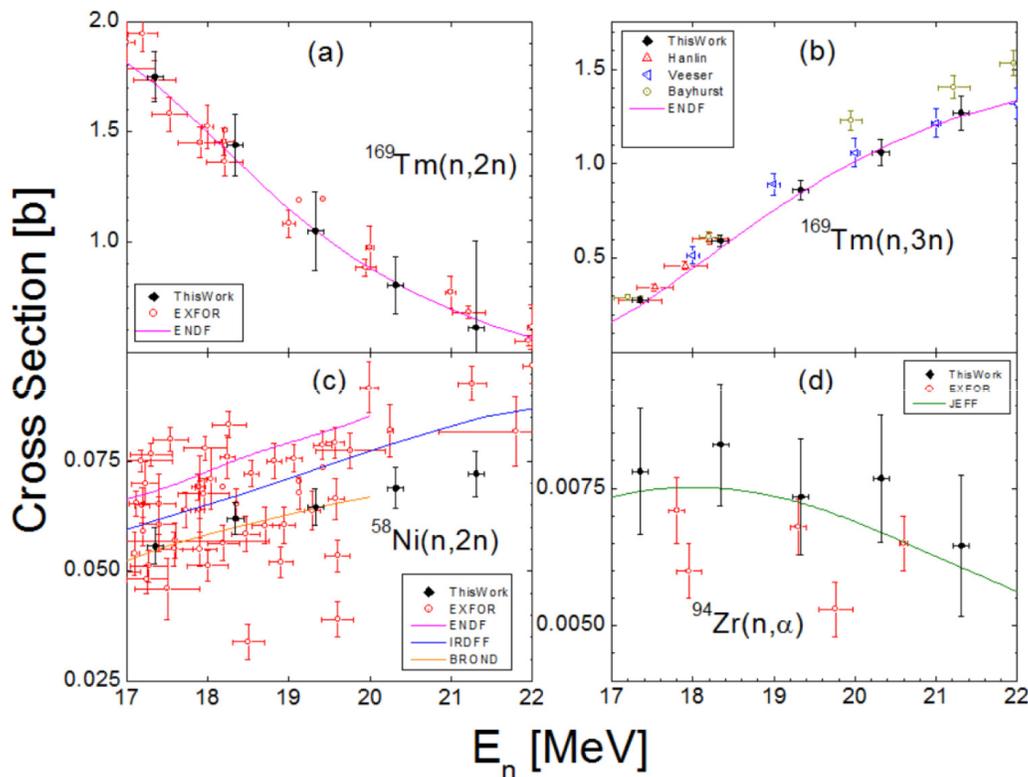


Figure 6.18: Results for the $^{169}\text{Tm}(n,3n)^{167}\text{Tm}$ reaction compared to previous data and the ENDF evaluation are shown in part (a). Byproduct results obtained for the $^{169}\text{Tm}(n,2n)^{168}\text{Tm}$, $^{58}\text{Ni}(n,2n)^{57}\text{Ni}$, and $^{94}\text{Zr}(n,\alpha)^{91}\text{Sr}$ reactions are shown in parts (a), (c), and (d), respectively.

energies of interest using the $^2\text{H}(d,n)^3\text{He}$ reaction. The deuterium gas cell was pressurized to 5 atm and separated from the accelerator vacuum by a $6.5\ \mu\text{m}$ Havar foil. Deuteron beam currents were typically $2\ \mu\text{A}$. The ^{169}Tm foil, 0.95 cm in diameter, was sandwiched between a ^{nat}Zr neutron fluence monitor foil and a ^{nat}Ni foil for additional, byproduct measurements. The foils were placed at a distance of 0.9 cm from the end of the deuterium gas cell.

In order to account for the influence of breakup neutrons produced on the entrance collimator, on the Havar foil, and on the tantalum beam stop of the deuterium gas cell, the deuteron beam was pulsed, and the neutron energy spectrum was measured via the time-of-flight technique using our standard 3.81-cm-diameter and 3.81-cm-long liquid scintillator (BC-501A) neutron detector. In principle, because the highest energy breakup neutrons have energies 5.5 MeV below those of the primary monoenergetic neutrons, the energy spectra are needed only to account for the breakup-

neutron sensitivity of the neutron monitor reactions, $^{58}\text{Ni}(n,2n)^{57}\text{Ni}$ (threshold 12.43 MeV) and $^{90}\text{Zr}(n,2n)^{89}\text{Zr}$ (threshold 12.1 MeV), but not for the $^{169}\text{Tm}(n,3n)^{167}\text{Tm}$ reaction itself. In addition, because the $^{169}\text{Tm}(n,2n)^{168}\text{Tm}$ (threshold 8.1 MeV) and $^{94}\text{Zr}(n,\alpha)^{91}\text{Sr}$ (Q value +2.03 MeV) cross sections were obtained as a byproduct, the breakup neutron determination is needed at lower energies as well.

After irradiation, γ -rays from the foils were counted, and the neutron fluence was determined from the monitor foils using published cross-section data. The measured neutron fluence was then used to convert measured γ -ray yields into the cross sections of interest.

Monte-Carlo simulations have been used to calculate the neutron energy distribution seen by the activation foils. Figure 6.18 shows the present results. Here, the $^{90}\text{Zr}(n,2n)^{89}\text{Zr}$ reaction was used as the neutron fluence monitor. In addition to the $^{169}\text{Tm}(n,3n)^{167}\text{Tm}$ cross section of interest, the $^{169}\text{Tm}(n,2n)^{168}\text{Tm}$ cross section measured, along with the $^{58}\text{Ni}(n,2n)^{57}\text{Ni}$ and $^{94}\text{Zr}(n,\alpha)^{91}\text{Sr}$ cross sections.

6.3 Public Health Research

6.3.1 Rutherford Backscattering Spectrometry of Small Molecules in Water Purification Membranes

A. ATKINSON, J. WANG, O. CORONELL, *University of North Carolina, Chapel Hill, NC*; T.B. CLEGG, *TUNL*

We evaluated the incorporation of small organic molecules into the polyamide active layer and polysulfone support of several commercial and hand-cast reverse osmosis membranes using Rutherford backscattering spectrometry (RBS). Results show that the method of incorporation and the materials used influence the amount and location of small organic molecules within the membrane, and whether the molecules remain in the membrane after use.

Reverse osmosis (RO) and nanofiltration (NF) membranes are widely used for the desalination of brackish and seawaters as well as for water reuse because they are able to remove a wide range of contaminants. Commercial RO and NF membranes have a thin-film composite structure consisting of three layers: the polyamide active layer (20 to 200 nm in thickness), a polysulfone porous support (20 to 50 μm), and a polyester fiber backing (40 to 150 μm).

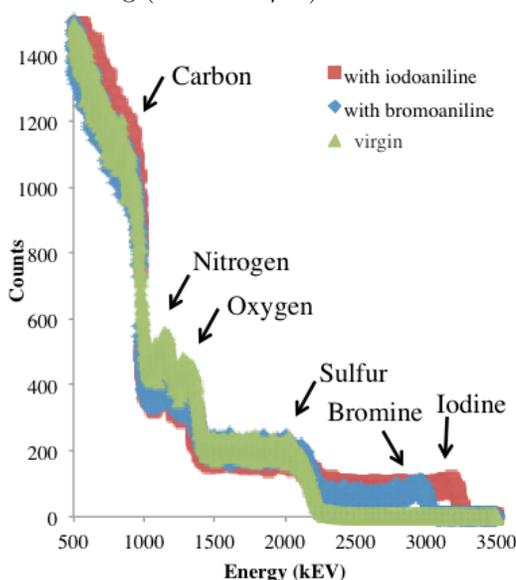


Figure 6.19: RBS spectra of a virgin membrane (green), with iodoaniline incorporated (red), and bromoaniline incorporated (blue).

There are numerous reasons to incorporate

small organic compounds into the structure of water purification RO and NF membranes: adding functional groups with specific purposes (e.g. antifouling), changing physical properties (e.g. surface charge, hydrophilicity), and increasing performance (e.g. water permeability, contaminant rejection). One specific group of molecules of interest is 2-aminoimidazoles (2AIs) which are believed to have the potential of providing antibiofouling properties if successfully incorporated into the polyamide active layer. Having the ability to assess the quantity and location of 2AIs within the membrane is essential to ascertain that the desired modifications have been achieved. Due to its sensitivity, resolution, and depth of analysis, RBS was chosen to analyze the incorporation of iodoaniline and bromoaniline into polyamide active layers. These compounds serve as surrogates of 2AIs because of their similarities with polyamides in structure and reaction chemistry.

RO and NF membranes typically are composed of hydrogen, carbon, nitrogen, oxygen, and sulfur. In Fig. 6.19, distinctive peaks in the RBS spectrum of a virgin commercial membrane corresponded to these elements, except for hydrogen, which cannot be detected in RBS. Iodine in iodoaniline and bromine in bromoaniline are elements that are not typically present in membranes, and so the presence of additional spectral peaks corresponding to those elements confirmed the incorporation of iodoaniline and bromoaniline in prepared membrane samples. The RBS spectra were analyzed with the simulation software SIMNRA [MM99] to quantify the concentra-

tion of each element in the polyamide and polysulfone layers.

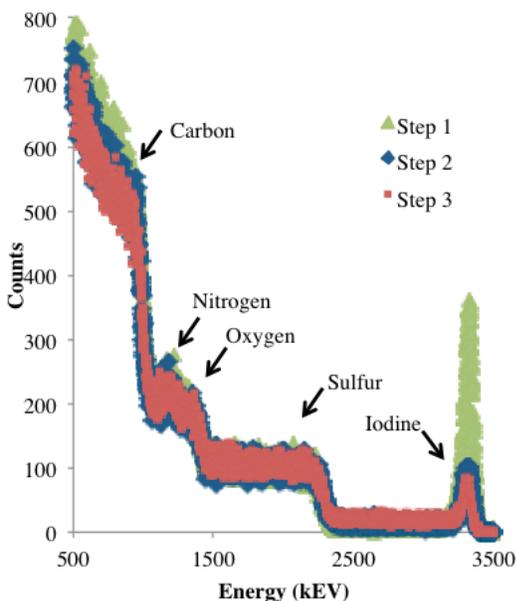


Figure 6.20: RBS spectra of samples in which iodoaniline was added at different steps during polyamide fabrication.

The incorporation methods used could potentially impact the quantity and location of the bromoaniline/iodoaniline within the membrane. The two approaches are to add the compound during different steps of the polyamide layer casting process or to incorporate the compound into a pre-fabricated commercial membrane. For each approach we were able (i) to confirm that the iodoaniline/bromoaniline had been successfully incorporated and (ii) to quantify the concentration of each compound. As shown in Fig. 6.20, the quantity of iodoaniline incorporated varied with the step during which it was incorporated in the polyamide-layer casting process, as indicated by the size of the iodine peak. When iodoaniline/bromoaniline was incorporated into pre-fabricated commercial membranes, the iodine/bromine peaks had longer shoulders, indicating incorporation of the compounds also in the polysulfone support layer.

It is important to know whether the incorporated compounds are tightly bound to the membrane and so will remain in it after typical use. Figure 6.21 shows that the bromine peak associated with the incorporated bromoaniline decreased after the membrane was used for six hours to purify water. The level to which the

bromoaniline content decreased after membrane use depended on the membrane sample and was no higher than 74% in any case. The extent of the decrease depended on the materials used (i.e., the commercial membrane chosen) and the method of bromoaniline incorporation.

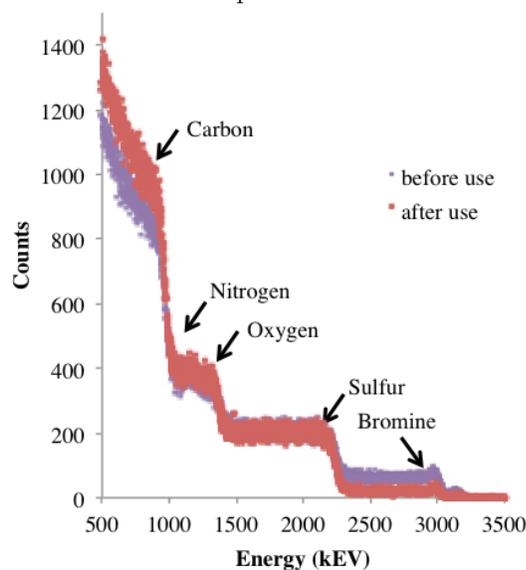


Figure 6.21: RBS spectra of a membrane with bromoaniline incorporated. Spectra were taken before (purple) and after (red) use to purify water. The level of bromoaniline reduction after membrane use was 72%.

In summary, the results of this study demonstrate that RBS can be used to detect iodine- and bromine-containing organic compounds in RO/NF membranes. It can also quantify their concentration and identify their location within the membrane. Specifically, iodoaniline and bromoaniline, which serve as surrogates of 2-aminoimidazoles, were successfully detected and quantified after incorporation into RO/NF membranes. Various membrane incorporation methods were evaluated with RBS, and the results obtained can be used to determine the best method(s) to incorporate small organic molecules, similar to iodoaniline/bromoaniline, into RO/NF membranes based on the desired compound concentration and location within the membrane.

[MM99] J. D. M. Mayer and I. Morgan, AIP Conference Proceedings, **475**, 541 (1999), 15th Int'l Conf. Application of Accelerators in Research and Industry.

6.3.2 Nuclear Resonance Fluorescence Measurements on Light Nuclei

B. FALLIN, C.R. HOWELL, W. TORNOW, M. BHIKE, KRISHICHAYAN, D. TICEHURST, *TUNL*; R.S. PEDRONI, *North Carolina A&T State University, Greensboro, NC*

During this reporting period, the strength of dipole and quadrupole excited states in several light nuclei of biological significance were investigated using nuclear resonance fluorescence (NRF). This was accomplished during four different NRF measurements conducted at HI γ S. Dipole states in isotopes of carbon, nitrogen, oxygen, sodium, magnesium, sulfur, chlorine, and potassium were probed at γ -ray beam energies between 1.748 and 15.685 MeV. These data are expected to yield cross sections and branching ratios for observed γ -ray transitions with improved accuracy over published values.

Early diagnosis and treatment of cancer is critical for maximizing long-term survival rates. Later stage / more advanced cancer generally requires more aggressive treatment, such as extensive surgery and high dose radiation therapy. This may result in short- and long-term negative health effects. Traditional radiographic imaging techniques, such as planar x-ray and CT, that are most frequently used to screen for cancer can only be used to discern gross differences in density between tissues in the body, resulting in a significant number of false positive diagnoses (i.e., suspicious lesions that upon biopsy are proven to be benign) as well as false negative results (i.e., early stage, subclinical disease that may be missed).

Recent studies have shown that significant elemental and isotopic asymmetries of trace elements can exist between healthy and cancerous tissue [Lak14]. Traditional radiographic imaging is insensitive to these differences, but the presence and relative abundances of targeted isotopes in a sample can be determined using nuclear resonance fluorescence (NRF). Every isotope has its own nuclear “fingerprint” in the form of a unique set of nuclear energy levels. Nuclear resonance fluorescence can be used to detect these isotopes by exciting dipole states with high energy photons in the keV to MeV range. These subsequently decay back to the ground state purely by photon emission, provided the excitation energies are below the particle separation threshold. By preferentially exciting dipole states with energies of several MeV and short lifetimes (attoseconds to a few femtoseconds) with high resolution γ -ray beams and by using high efficiency γ -ray detectors, the signal to tissue dose

ratio can be maximized. Preliminary simulation studies using GEANT4 conducted by Lakshmanan et al. [Lak14] and Belley et al. [Bel14] have demonstrated promise for using NRF-based gamma-stimulated emission computer tomography (GSECT) for diagnosis of breast cancer. Their research was built on the findings of prior studies that found substantial differences in the elemental percentages of potassium and calcium in healthy vs. malignant breast tissue.

The principal roadblocks to clinical use of the NRF technique presently are: (1) the large size of current electron accelerators needed to produce tunable γ -ray beams with energy spreads of only a few percent and (2) the high dose rates compared to x-ray CT that are necessary to obtain full field-of-view tomographic images. Portable electron accelerators for use in NRF applications are currently under active development, driven by the need to detect special nuclear materials for Homeland Security applications. Also, next-generation tunable x-ray sources using laser-Compton scattering provide the possibility of higher fluxes coupled with energy spreads of less than 1%. These energy spreads are smaller than achievable with current FEL based γ -sources and have the potential to reduce scan doses by a factor of ten [Hab12, Gib10].

In the current reporting period, excited states in isotopes of carbon, nitrogen, oxygen, sodium, magnesium, sulfur, chlorine, and potassium were investigated at γ -ray beam energies ranging from 1.748 to 15.685 MeV. The carbon, magnesium, and sulfur targets were pure elemental samples. The nitrogen, potassium, sodium, and chlorine targets were in the form of salts: ammonium

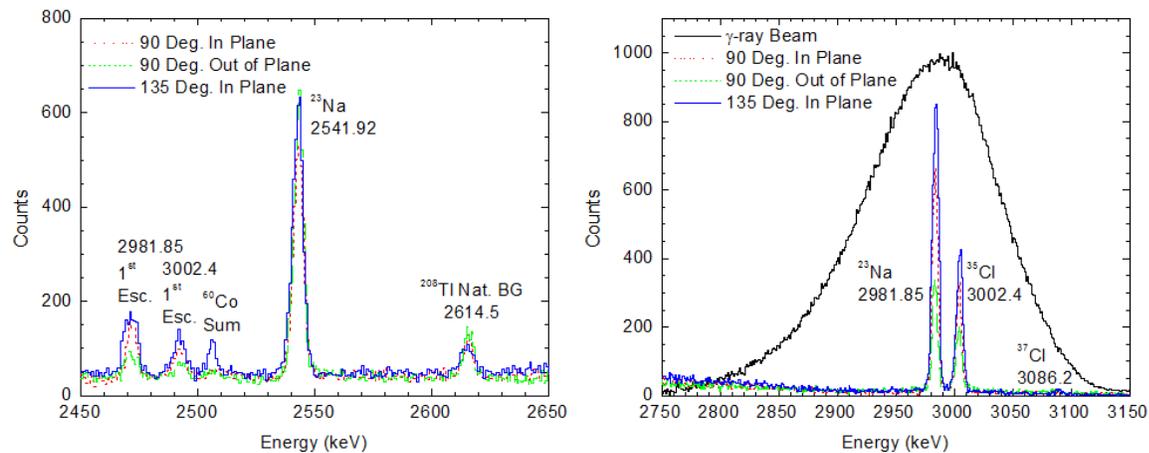


Figure 6.22: Right Panel: Portion of the measured energy spectrum of NRF γ -rays emitted from the NaCl target at a mean excitation energy of 2.99 MeV. Transitions from the excited state to the ground state are observed in all isotopes. The γ -ray beam envelope is overlaid for reference. Left panel: A lower energy portion of the same spectrum. The 2542-keV γ -ray is emitted by a transition in ^{23}Na from the excited state at 2982 keV to the first excited state located at 439.99 keV. Also shown are the first escape γ -rays from the ground state transitions in ^{23}Na and ^{35}Cl , a natural background line, and the sum peak from ^{60}Co (which was used as a dead-time and pileup monitor during the experiment).

chloride (NH_4Cl), potassium nitrate (KNO_3), and sodium chloride (NaCl), respectively. A water target enriched to 98% in ^{18}O was used to probe the excited state levels in oxygen. With the exception of the water target, all targets contained elements with natural isotopic abundances.

Dipole and quadrupole transitions were excited using quasi-monoenergetic γ -rays at HI γ S, operated by the Triangle Universities Nuclear Laboratory. Incident γ -rays were linearly polarized in the horizontal plane. HPGe detectors (60% efficient relative to a 3 in. diameter and 3 in. thick NaI detector) were placed at scattering angles of 90° and 135° in the plane of beam polarization, and 90° in a plane perpendicular to the polarization plane of the beam. Detectors were positioned between 8 and 10 cm from the center of the target. All detectors were passively shielded with lead and copper disks in front of the detector face. The disks had sufficient thickness to reduce the detector counting rates to a few kHz. The targets were placed in an evacuated plastic pipe to reduce the counting rate

from scattering of the primary γ -ray beam by air. This improves the signal-to-background ratio of the measured spectra. Portions of the measured NRF spectrum from transitions in ^{23}Na , ^{35}Cl , and ^{37}Cl around 2.99 MeV are shown in Fig. 6.22 and are the result of 8.4 hours of beam time. Also shown are a transition in ^{23}Na to the first excited state, a background line, two escape peaks, and a ^{60}Co sum peak used to monitor dead-time and pileup.

Analysis of the data is underway with final results expected in the last quarter of 2016.

-
- [Bel14] M. D. Belley *et al.*, *Med. Phys.*, **41**, 063902 (2014).
- [Gib10] D. Gibson *et al.*, *Phys. Rev. Spec. Top. Accel. Beams*, **13** (2010).
- [Hab12] D. Habs *et al.*, *AIP Conf. Proc.*, **1462**, 177 (2012).
- [Lak14] M. N. Lakshmanan *et al.*, *IEEE Trans. Med. Imag.*, **33** (2014).

6.4 Plant Physiology Research

6.4.1 Development of a Modular Plant Imaging PET System and Its Use in Evaluating Corn Plant Root Systems

L.C. CUMBERBATCH, A.S. CROWELL, C.R. HOWELL, B.A. FALLIN *TUNL*; C.D. REID, G. BONITO, C. TOPP, *Duke University Department of Biology, Durham, NC*; A.G. WEISENBERGER, S.J. LEE, J.E. MCKISSON, C. ZORN *Thomas Jefferson National Accelerator Facility, Newport News, VA*; M.F. SMITH, *University of Maryland, Baltimore, MD*

A modular high-resolution positron emission tomography system has been developed at Thomas Jefferson National Accelerator Facility for studies of the physiological processes in live plants that influence the biodistribution of substances tagged with positron-emitting radiotracers. The radiotracer ^{11}C is used to investigate sugar transport under varying environmental conditions. Initial evaluation of the PhytoPET system to image the biodistribution of ^{11}C in corn plants is underway, and preliminary results are presented.

Positron emission tomography (PET) is a useful imaging modality for plant eco-physiological studies. The ^{11}C radiotracer is a common positron emitter used in plant biology research due to its ease of incorporation in live plants through the photosynthesis of radio-tagged carbon dioxide gas. Production of $^{11}\text{CO}_2$ gas occurs in the tandem accelerator laboratory at TUNL using the $^{14}\text{N}(p,\alpha)^{11}\text{C}$ reaction. The standard method is to bombard a cell pressured to about 8 atm of research-grade nitrogen gas with a 10 MeV proton beam. The $^{11}\text{CO}_2$ gas that is produced is then transferred about 100 meters via underground tubing from the tandem lab to the Phytotron facility where the labeling measurements are performed. Approximately 10-20 millicuries of ^{11}C activity are typically produced.

PhytoPET, a live-plant imaging PET system targeted for plant eco-physiology research, is being developed at Thomas Jefferson National Accelerator Facility in collaboration with Duke University and the University of Maryland at Baltimore. The new plant-imaging PET system geometry is both versatile and scalable. The goal is to enable the system to meet imaging requirements over a wide range of research conditions, including visualizing and analyzing dynamic carbohydrate transport throughout leaves, roots, and stems. The PhytoPET imager consists of flexible arrangements of PET detectors based on individual stand-alone detector modules built from single 5 cm x 5 cm Hamamatsu H8500 position sen-

sitive photomultiplier tubes. Each H8500 is coupled to a LYSO:Ce scintillator array composed of 48 x 48 elements that are 10 mm thick arranged with a 1.0 mm pitch. The detector modules can be arranged and stacked to adjust for individual plant size or structure.

Preliminary imaging studies of corn plant root systems are currently underway at Duke University. Radiotracer production and transfer occurs at TUNL, while plant growth, labeling, and imaging occurs at the nearby Phytotron facility. The $^{11}\text{CO}_2$ produced at TUNL is loaded into early-stage corn plants via photosynthesis, and subsequent translocation of ^{11}C in the form of sugars is imaged by arranging PhytoPET modules on each side of the plant.

Initial measurements were made using the PhytoPET system for dynamic studies of ^{11}C -sugar translocation from a leaf to the roots in a corn plant. One of the problems associated with root imaging is that the root structure is not visible since it is hidden inside the soil. To overcome this problem, we used a clear growth media gel rather than regular soil for an unobstructed view of the root area. This clear media provides for easy registration of optical and PET root images and facilitates image analysis [Lee13]. During data acquisition, a total of four or eight detector modules were used to image either the stalk or the root area or both. Detector modules were arranged so as to have the best imaging field-of-view, depending on the root shape. PET imag-

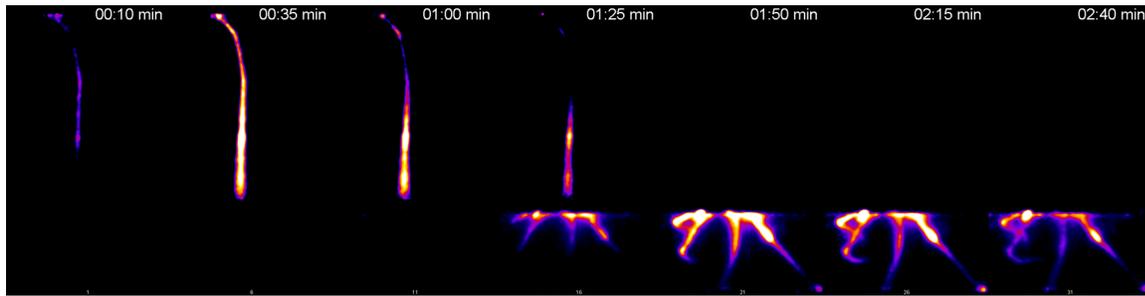


Figure 6.23: Reconstructed images (without decay correction) from a corn scan. The time that has elapsed from the application of the radio-tagged $^{11}\text{C}\text{O}_2$ to the tip of the leaf is shown at the top of each image. Images clearly show the distribution of ^{11}C -sugar in the stalk (left three images) and the root (right four images).

ing scans were acquired for three to four hours for each plant, and image reconstruction was performed using the maximum-likelihood estimation method.

Figure 6.23 depicts the reconstructed images of a labeled corn plant. The ^{11}C -sugar distribution is clearly shown in the images. The images show a different distribution pattern between the crown root and primary root. Most of sugar appears to be deposited in the end tip of the crown root since the crown root grows at the end tip. However, an even distribution was observed for the primary root since there are many root hairs along with the primary root for exchanging water and nutrients with the surrounding media/soil [Lee13]. Data analysis indicates that the sugar transit time from leaf to the end tip of roots is approximately an hour.

We have developed a unique PET system for plant biology and have demonstrated its ability to image ^{11}C transport using corn plants. The PhytoPET system successfully traces ^{11}C -sugar transport from the leaf to the root and has sufficient system spatial resolution to clearly image corn root structures. The next radiotracer study will focus on plant response to root fungal infections on carbon transport using the split-root

cuvette shown in Fig. 6.24.

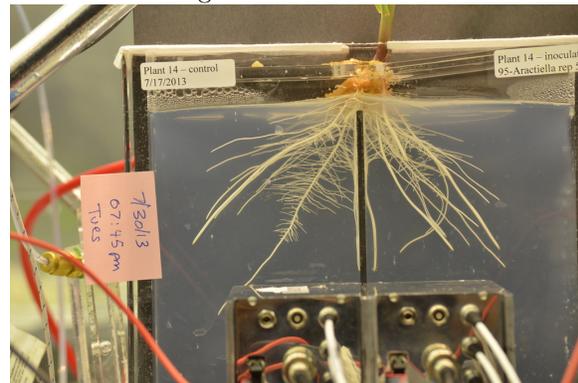


Figure 6.24: PhytoPET setup for future corn imaging. Four detector modules will be placed on each side of the root cuvette. (The upper two modules were removed for this photograph.) The corn is planted in a split-root cuvette for separation of control and fungal-infected root regions.

[Lee13] S. J. Lee *et al.*, 2013, Poster presented at the 2013 IEEE Nuclear Science Symposium and Medical Imaging Conference (NSS/MIC 2013).

6.5 Nuclear Data Evaluation

6.5.1 Nuclear Data Evaluation Activities

J.H. KELLEY, K. LEUNG, C.G. SHEU, H.R. WELLER, *TUNL*; J.E. PURCELL, *Georgia State University, Atlanta, GA*

The Nuclear Data Evaluation Group at TUNL is part of the United States Nuclear Data Program and the International Nuclear Structure and Decay Data network. After the retirement of Fay Ajzenberg-Selove in 1990, TUNL assumed responsibility for evaluation of nuclides in the mass range $A = 3$ to 20. The status of the published evaluations and preliminary reviews is presented.

The Nuclear Data Evaluation Group is charged with producing evaluations of the $A = 3$ to 20 nuclei and providing the reviews to the Evaluated Nuclear Structure Data Files (ENSDF) database that is maintained at the National Nuclear Data Center (NNDC) at Brookhaven National Laboratory. We also provide a web-based service for the nuclear science and applications communities at <http://www.tunl.duke.edu/nucldata/>.

Publications

Table 6.5.1 displays the status of our most recent published evaluations and preliminary reviews.

Table 6.3: Current publication status.

Nuclear Mass	Publication	Institution
Published:		
$A = 3$	Nucl. Phys. A848 (2010) 1	TUNL
$A = 4$	Nucl. Phys. A541 (1992) 1	TUNL ^a
$A = 5$ to 7	Nucl. Phys. A708 (2002) 3	TUNL ^{a,b}
$A = 8$ to 10	Nucl. Phys. A745 (2004) 155	TUNL ^c
$A = 11$	Nucl. Phys. A880 (2012) 88	TUNL
$A = 12$	Nucl. Phys. A506 (1990) 1	Penn ^d
$A = 13$ to 15	Nucl. Phys. A523 (1991) 1	Penn ^d
$A = 16, 17$	Nucl. Phys. A564 (1993) 1	TUNL
$A = 18, 19$	Nucl. Phys. A595 (1995) 1	TUNL
$A = 20$	Nucl. Phys. A636 (1998) 247	TUNL ^e
Reviews in Progress:		
$A = 3$	Submitted to NDS	TUNL
$A = 12$	Expected 2016	TUNL

^a Co-authored with G.M. Hale, LANL.

^b Co-authored with H.M. Hofmann, Universität Erlangen-Nürnberg, Germany.

^c Co-authored with D.J. Millener, BNL.

^d F. Ajzenberg-Selove, University of Pennsylvania.

^e Co-authored with S. Raman, ORNL.

Evaluated Nuclear Structure Data Files

The ENSDF files contain concise nuclear structure information such as tables of adopted level energies and tables of properties for levels that have been observed in various nuclear reactions and decays. The ENSDF files have been updated concurrently with the last published reviews in the “Energy Levels of Light Nuclei” series. In the future we will publish articles in Nuclear Data Sheets (NDS), which utilizes the ENSDF format.

The $A = 3$ ENSDF file was submitted to NDS in August, 2015. ENSDF files for thirteen near-dripline nuclides have been submitted since 2014. Work on the $A = 2$ and 12 ENSDF files is presently underway.

Experimental Unevaluated Nuclear Data List

TUNL has taken responsibility for creating the $A = 2$ to 20 data sets for the Experimental Unevaluated Nuclear Data List (XUNDL) beginning in April 2009. This activity was developed at McMaster University by Dr. Balraj Singh, who aimed to quickly provide the most current data to users in the high-spin community. The nuclear structure data in recent references is compiled in XUNDL with minimal evaluation effort. Since becoming involved, TUNL has prepared roughly 400 data sets, an average rate of 5 per month. The data sets are reviewed by Dr. Singh and then added to the database at NNDC.

World Wide Web Services

Our group continues to develop web-based services for the nuclear science and applications

communities. The website layout and contents are constantly revised and kept up to date, to ensure high-quality service and accurate information. Figure 6.25 displays the usage of our website since April 2002.

The following items are currently available:

- Ground-State Decay Data. This provides evaluated data from work on ground-state β decays and charged-particle decays. It has been completed for nuclides with $A = 3$ to 20.

We continue to review and evaluate β -delayed-particle-emission data and have added roughly 30 relevant data sets to the ENSDF database since 2012. We carried out a horizontal evaluation of life-times for nuclei in the $A = 3$ to 20 region that β decay with a 2015 REU (Research Experience for Undergraduates) student.

- Thermal Neutron Capture Data on $A = 2$ to 20 nuclei, based on compiled data.
- Excitation Function Data. This page provides compiled data related to the level parameters for $A = 3$ to 20 nuclei populated in proton- and α -particle-induced reactions.
- PDF and HTML documents for TUNL's and Fay Ajzenberg-Selove's reviews from 1959 to the present. The PDF versions include hyperlinks for references, Tables of Recommended Level Energies, Electromagnetic Transitions Tables, General Tables, Energy Level Diagrams, and Erratum to the Publications. The HTML documents are more comprehensive than the PDF documents, as they include hyperlinks to tables in the PDF and PS formats, reactions and reaction discussions, TUNL and NNDC references, Energy Level Diagrams, and General Tables.

We have essentially completed the re-creation of PDF files for our publications, in order to provide the most current NNDC reference keys and to correct all errors found since the articles went to press. We will continue to work on the corresponding HTML and table/PS/PDF files for publications prior to 1976.

- Energy Level Diagrams for publication years from 1959 to the present. These are provided in GIF, PDF and EPS/PS formats.
- Tables of Energy Levels. A brief listing of the tables of recommended energy levels (in PDF and PS formats) from the most recent publications for nuclides with $A = 4$ to 20. Twenty-five Tables of Energy Levels (in PDF format) of near dripline nuclides have been added since 2014.
- ENSDF information for $A = 3$ to 20 nuclides available through the NNDC site.
- A link to NuDat (Nuclear Structure and Decay Data). The link allows users to search and plot nuclear-structure and nuclear-decay data interactively through the NNDC site.
- Links to the NNDC and other useful sites, as well as to the online journals that the nuclear science communities use most often. There is also a sitemap with a complete listing and links to everything on the website.
- A link with access to TUNL Ph.D. Dissertations from 1949 to the present. About 210 theses have been scanned by our group. This activity is 93% completed and includes all presently available documents.

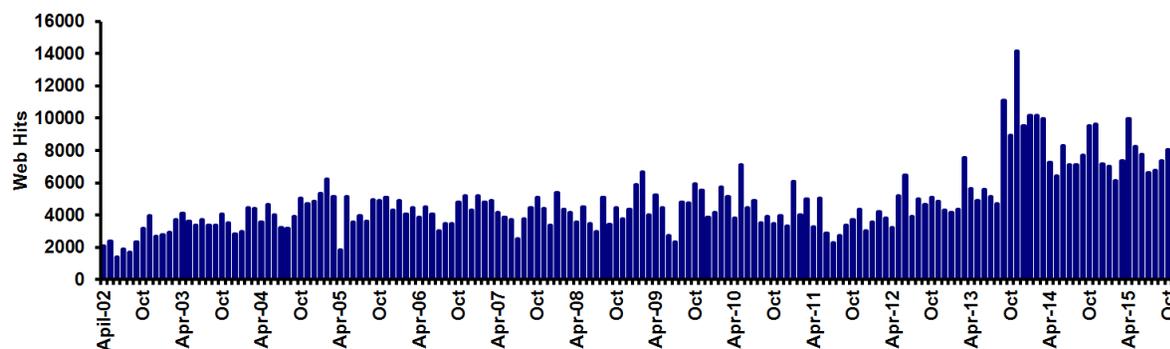


Figure 6.25: (Color online) Overview of web usage deduced from the Analog Web Analysis Package

6.5.2 A Systematic Evaluation of β -Decay Half-Life Values in the Light Nuclei

J.H. KELLEY, *TUNL*; S. OLMSTEAD, *East Tennessee State University, Johnson City, TN*; C.G. SHEU, *TUNL*

A systematic literature search for articles reporting experimentally measured lifetimes of $A = 3$ -20 nuclei that decay by β emission has been carried out resulting in a compilation of β -decay lifetime values and a systematic horizontal evaluation of lifetimes that produced a set of recommended values.

Systematic evaluation of lifetime values based on a complete compilation of existing measurements provides information useful for basic and applied science applications. Within the light nuclei, isotopes such as ^{14}C , ^{10}C , ^{14}O , and ^{18}Ne are simple examples of such cases, where the lifetimes are important for applications such as determining the age of historical artifacts or testing the Standard Model.

In this light, we have utilized the Nuclear Science Reference (NSR) database [Pri11] at the National Nuclear Data Center (NNDC) and other search methods to obtain a complete set of references reporting experimentally determined lifetime values. The articles have been reviewed and the lifetimes have been compiled in a section of our online website that is dedicated to information related to ground-state decays of $A = 3$ -20 nuclides.

Much of the effort centered on identifying sets of independent lifetime values. In some cases successive reports on a single experimental value are reported in the literature resulting in interrelated values. For example, the results of several experimental runs, sometimes separated by years, are combined into a single article reporting a result. Instances such as these are isolated, and the interdependencies are identified within our list of compiled values. Inclusion of multiple reports on the same data would result in an improper weighting of a given result.

The analysis of lifetime values was carried out by using a program, “Visual Averaging Library,” [Bir14] that was written by Michael Birch as a tool for U.S. Nuclear Data Program (USNDP) evaluators to perform analysis of data. The program reads in a set of values with uncertainties and determines average values by following a

wide range of analysis prescriptions. The methods included in the analysis are:

- The Unweighted Average
- The Weighted Average (WA)
- The Limitation of Relative Statistical Weights Method (LWM)
- The Normalized Residuals Methods (NRM)
- The Rajeval Technique (RT)
- The Method of Best Representation (MBR)
- The Bootstrap Method (BM)
- The Mandel-Paule Method (MP).

Analysis of data using this program permits a comparison of recommended values from each of these techniques, as well as, useful visualizations of the data in both data-point plotting on a grid and a plot of the overall probability density distribution. Much of the effort here was carried out by a TUNL REU (Research Experience for Undergraduates) student who describes her experience elsewhere in this report.

Throughout the analysis process, there were clear examples of reported results where the authors had not identified or underestimated the systematic errors present in their data. In most cases such data was excluded from further consideration. For some cases, such as ^{16}N , there is evidence that contaminant species were included in decay curve analyses resulting in erroneous values. In other cases, precisely reported values are discrepant from average values that have emerged from the full collection of results; such values were typically excluded when they significantly

impacted the average. We highlight that we assume that the lifetime values reported are dominated by systematic uncertainty, and therefore as a matter of policy the uncertainty we report cannot be smaller than the uncertainty of the most precisely reported result.

In summary, we have compiled and evaluated the β -decay lifetimes associated with nuclei in the $A = 3$ -20 nuclei. We provide tables of the lifetimes for nuclei that β^+ decay in Table 6.4 and for those that β^- decay in Table 6.5.

Table 6.4: Lifetime values deduced for nuclei that β^+ /(electron capture) decay.

Nuclide	Recommended Lifetime
^7Be	in progress
^8B	770.3 ± 0.4 msec
^9C	126.5 ± 1.0 msec
^{10}C	19.305 ± 0.005 sec
^{11}C	20.360 ± 0.022 min
^{12}N	11.000 ± 0.016 msec
^{13}N	9.967 ± 0.005 min
^{13}O	8.58 ± 0.07 msec
^{14}O	70.617 ± 0.020 sec
^{15}O	122.22 ± 0.32 sec
^{17}F	64.73 ± 0.33 sec
^{17}Ne	109.2 ± 0.6 msec
^{18}F	109.733 ± 0.011 min
^{18}Ne	1.66428 ± 0.00060 sec
^{19}Ne	17.260 ± 0.014 sec
^{20}Na	447.9 ± 2.3 msec
^{20}Mg	91 ± 4 msec

Table 6.5: Lifetime values deduced for nuclei that β^- decay.

Nuclide	Recommended Lifetime
^3H	12.323 ± 0.020 years
^6He	$806.89^{+0.25}_{-0.22}$ msec
^8He	119.0 ± 1.6 msec
^8Li	838.79 ± 0.36 msec
^9Li	177.7 ± 0.6 msec
^{10}Be	$(1.51 \pm 0.06) \times 10^6$ years
^{11}Li	8.74 ± 0.15 msec
^{11}Be	13.77 ± 0.08 sec
^{12}Be	21.46 ± 0.05 msec
^{12}B	20.22 ± 0.04 msec
^{13}B	17.30 ± 0.17 msec
^{14}Be	4.65 ± 0.20 msec
^{14}B	12.6 ± 0.6 msec
^{14}C	5686 ± 40 years
^{15}B	10.00 ± 0.11 msec
^{15}C	2.450 ± 0.005 sec
^{16}C	750 ± 8 msec
^{16}N	7.13 ± 0.02 sec
^{17}B	5.07 ± 0.05 msec
^{17}C	193 ± 6 msec
^{17}N	4.173 ± 0.004 sec
^{18}C	92 ± 2 msec
^{18}N	619 ± 2 msec
^{19}B	2.92 ± 0.13 msec
^{19}C	46.3 ± 4.0 msec
^{19}N	336 ± 3 msec
^{19}O	26.470 ± 0.018 sec
^{20}C	$16.3^{+4.0}_{-3.5}$ msec
^{20}N	134.4 ± 3.7 msec
^{20}O	13.51 ± 0.05 sec
^{20}F	11.150 ± 0.021 sec

[Bir14] M. Birch and B. Singh, Nucl. Data Sheets, **120**, 106 (2014).

[Pri11] B. Pritychenko *et al.*, Nucl. Instrum. Methods Phys. Res., **640**, 213 (2011).

6.5.3 Nuclear Data Compilation for Beta Decay Isotopes

S.C. OLMSTED, *East Tennessee State University, Johnson City, TN*; J.H. KELLEY, G.C. SHEU, *TUNL*

We have reviewed all available literature to determine the most accurate experimental half-life values for beta-unstable isotopes in the $A = 3$ to 20 range and found recommended half-life values for most of these isotopes. This analysis will be folded into the Evaluated Nuclear Structure Data File. Meanwhile, our findings have been used to update information given on the TUNL Nuclear Data Evaluation group website.

The TUNL nuclear data group works with the Nuclear Structure and Decay Data network to compile and evaluate data for use in nuclear physics research and applied technologies. Data evaluation is necessary to deriving meaning from existing data, as well as to establish context for contradicting data. Our project focused on compiling half-life values for use in nuclear research and nuclear physics applications, such as nuclear spectroscopy and the measurement of nuclear reaction cross sections [Bie64]. Therefore, it is important to know half-life values as accurately as possible.

Our goal was to determine half-life values for beta-decay isotopes within the $A = 3$ to 20 range and to include these values in an online database at TUNL. Ultimately, we hoped to have a central location that contains not just the recommended half lives, but also a list of the compiled articles and raw data that led to that conclusion. Eventually, the results would be transferred to the Evaluated Nuclear Structure Data File (ENSDF) database at the National Nuclear Data Center (NNDC) at Brookhaven National Laboratory.

To accomplish this, we reviewed half-life literature, using the NNDC database to collect an assortment of half-life values for each isotope. The articles were carefully examined to make sure that the half life was actually measured, not compiled from other sources, and that the value was reliable. An example will be given of a case in which a careful literature review was essential.

The data averaging software used was the Visual Averaging Library. We used it to compare eight different averaging techniques: Unweighted Average, Weighted Average, Limitation of Statistical Weights, Normalization Residuals, Rejal Technique, Method of Best Representation, Bootstrap, and Mandel-Paule. The unweighted

average is fairly intuitive: all values are weighed equally before averaging. However, this method does not make a lot of sense when the values have different uncertainties.

Giving some values more weight based on their relative credibility and accuracy is recommended. Therefore, the weighted average is the preferred method for data evaluation. The weighted average gives the most precise values more weight before averaging. This technique works very well if the data are consistent, as was the case for a little over half of the isotopes we studied.

Sometimes, however, values do not agree as well, and other methods must be used. The next-most-reliable method is the Limitation of Statistical Weights, which manipulates the weights such that no single value carries more than fifty percent of the weight. The reasoning behind this is that, if any one value is that much more precise than the others, then it is possible that the uncertainty has been greatly underestimated, so that the weight should be limited.

The rest of the averaging methods above have similar methods of increasing the values' uncertainties, or otherwise working with the assumption that, if the values have poor agreement, the values must be inaccurate. However, the Weighted Average and the Limitation of Statistical Weights are the most commonly used, since they avoid changing the data to force agreement. Additionally, averaging methods can be compared using a chi-square test.

Note that these methods often produce very low uncertainty values that can be lower than the lowest uncertainty from the individual measurements. Thus we had to be careful to choose the higher uncertainty between the compiled value and the lowest individual one.

As is often the case with data sets, the half-life values sometimes included outliers. The averaging software picks out outliers (values that deviate from the mean) using Chauvenet's Criterion, without taking uncertainties into account. This means that it is as possible for inaccurate values to be targeted, as for the most-reliable ones. Therefore, it was important to take the outliers into account, but to use caution before dismissing anything.

The example of the half-life values of ^{17}C is shown in Fig. 6.26. This is a fairly intuitive example, in which all of the values agree well. As you can see, the weighted average overlaps with all of the values. As one would expect, the chi-square value of the weighted average is 0.24, much lower than the critical chi-square of 2.37. Therefore, we adopted the weighted average and adjusted the uncertainty to match that of the measurement with the lowest uncertainty.

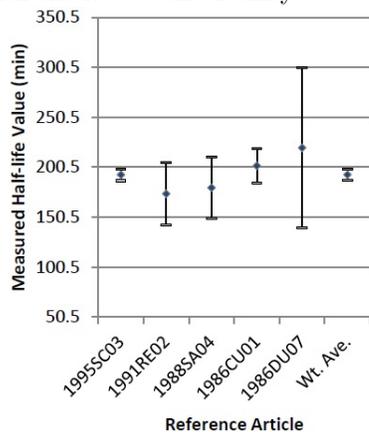


Figure 6.26: Half-life values for ^{17}C plotted alongside their weighted average.

A very different example is the half-life values of ^{16}N shown in Fig. 6.27. Here the source articles are arranged chronologically. You can see that these values disagree significantly, the weighted average does not align with many of the values, and the chi-square value is 21.77, compared to a critical chi-square of 1.88.

Before considering different averaging methods, however, it is important to review the articles. Note that the half-life values seem to drop significantly with the fifth article. Upon reviewing this article, we found that, according to Bienlein *et al.*, the first four measurements likely suffered from systematic errors. Bienlein explained that they had found that the background radia-

tion for those measurements was not determined accurately, causing the researchers to underestimate the background and therefore overestimate the half life [Bie64]. The first four half-life values, then, had to be excluded from the sample. Once the data were recompiled, they agreed nicely, and the new weighted average had a very acceptable chi-square value of 0.48.

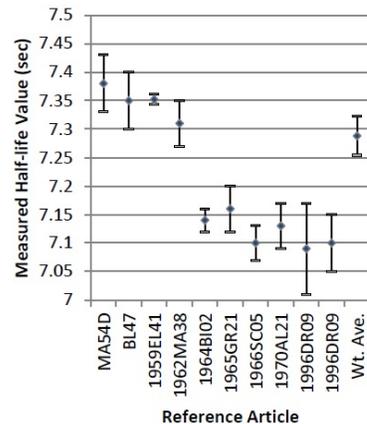


Figure 6.27: Half-life values for ^{16}N arranged chronologically by year published, plotted alongside their weighted average.

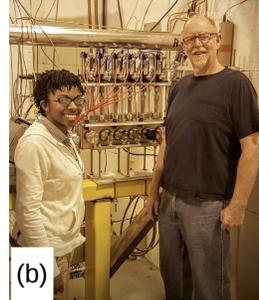
Ultimately, we found half-life values for most of the isotopes. Additionally, we began updating the nuclear-data website at TUNL with recommended half-life values. We also included tables with averaging information for each isotope. These tables list each averaging method, the half-life value produced by the method, either a chi-square value or a percent confidence value (depending on the method), a list of potential outliers, and a recommended value (if a recommended value could be determined). Using these tables, researchers can see the reasoning behind our recommendations.

Future work will include determining half-life values for the isotopes that have poor agreement or outliers. This will require a closer review of the articles, as well as a closer examination of the averaging methods. The averaging method tables that we created will greatly aid in this examination. Additionally, the website will soon be fully activated, and the data will eventually be added to the ENSDF database.

[Bie64] J. Bienlein and E. Kalsch, Nucl. Phys., **50**, 202 (1964).



(a)



(b)



(c)



(d)



(e)

AT LENA, (A) ANDREW COOPER, BRIAN WALSH, AND MARK EMAMIAN ARE INSTALLING THE NEW ACCELERATION COLUMN ON THE HIGH-VOLTAGE PLATFORM. ACCELERATOR DEVELOPMENT ACTIVITIES AT HI γ S: (B) BROGAN THOMAS IS INSPECTING THE γ -RAY BEAMLINE GUIDED BY GARY SWIFT; (C) JOE FAIRCLOTH AND PAT WALLACE ARE EXAMINING AN RF TUBE BEFORE INSTALLATION; (D) GARY SWIFT AND MARTY JOHNSON ARE WORKING ON A NEW γ -RAY ATTENUATOR ASSEMBLY; AND (E) MAURICE PENTICO IS WORKING WITH GRADUATE STUDENT JUN YAN TO PREPARE TESTING THE PERSONNEL PROTECTION SYSTEM (PPS).

Accelerator Physics

- **The High Intensity γ -Ray Source (HI γ S)**
- **The FN Tandem Accelerator and Ion Sources**
- **The LENA Accelerator and Ion Sources**

At the HI γ S facility, significant progress has been made in four key areas. (1) With regard to improving the reliability and availability of the accelerators and FEL, we continue to operate the HI γ S accelerators with an extremely high reliability, exceeding 98% (July 2014–June 2015) (Section 7.1.2). Further, by tracking the failures of various subsystems and equipment, we continue to develop strategies to build an inventory of critical replacement parts (Sections 7.1.1 and 7.1.2). (2) In order to increase the electron injection rate into the storage ring, we have generated a higher-charge electron beam with 100-ns pulses from the linac gun and have used it in a radiation survey. This is a key step toward increasing the electron injection rate (Section 7.1.3). (3) In order to develop stable and high-intensity γ -ray beam operation at higher energies, we have tested the high current OK-5 wiggler operation up to 4 kA with an artificially lowered cooling-water temperature (Section 7.1.4). We have also carried out accelerator research on the magnetic optics of the storage ring in order to extend its operation to higher energies with good performance (Sections 7.1.5 and 7.1.6). (4) Finally, we have developed several new γ -ray capabilities, including both a new pulsed-mode FEL and γ -ray operation that can be extended to the entire energy range (Section 7.1.7) and a demonstration of the first two-color γ -ray beam as the result of on-going research with the two-color FEL (Section 7.1.8).

During this reporting period, we operated the Tandem accelerator and ion sources extensively to deliver several species of ion beams in a wide range of energies while carrying out several accelerator development projects (Section 7.2.1). Additionally, a ^3He recirculation system for the helium ion source has been completed and evaluated under normal operating conditions with a recovery rate of over 85% (Section 7.2.2).

At the LENA facility, we have devoted substantial effort to the development, commissioning, and optimization of the new electron-cyclotron-resonance ion source (ECRIS). The new ECRIS will allow stable production of high-intensity pulsed proton beams for the study of important nuclear reactions in stellar nucleosynthesis. The new ECRIS accelerator column is designed to realize a higher current while overcoming many shortcomings of the older system (Section 7.3.1). It has a superb electrostatic design (Section 7.3.2) and a highly effective scheme to suppress secondary electrons (Section 7.3.3). We have also made important progress in upgrading the related plasma extraction system (Section 7.3.4) and in developing the pulsed-mode operation of the LENA ECR (Section 7.3.5).

7.1 The High-Intensity γ -Ray Source (HI γ S)

7.1.1 Operation of the HI γ S Facility—FY 2014

Y.K. WU, P. WALLACE, S.F. MIKHAILOV, *TUNL*

This HI γ S beam-time report covers the time period from July 1, 2013 through June 30, 2014. During this period, the HI γ S accelerator facility was operated for about 3055 hours for a variety of research programs and accelerator-related activities with a reliability of about 98.5%. A total of 1763 hours of on-target γ -ray beam time was delivered to the HI γ S user research program.

HI γ S Operations

This report summarizes the operation of the HI γ S Cost Center accelerators for fiscal year 2014, from July 1, 2013 to June 30, 2014. During this period, the HI γ S accelerator facility operated 222 days out of 251 university workdays, providing 3054.5 hours of beam time for a variety of research programs and accelerator-related activities. The operation of the accelerators and HI γ S was carried out mostly with a two-shift, five-day operation schedule. However, we were able to increase the number of overnight shifts—forty overnight shifts in nine different months (18% of days operated)—in order to accommodate experiments requiring continuous data-taking. This was possible without sacrificing overall operation reliability because of the high-quality operation support provided by two postdoctoral fellows who were trained as accelerator operators.

In this period, the overall reliability of the operation of the HI γ S accelerators and light sources was about 98.5%, exceeding the typical performance goal of 95% set for national synchrotron light sources. This very high level of reliability was realized in spite of the complex and challenging operation of the free-electron lasers and Compton γ source, and the challenges associated with a very intense run schedule in certain months with 24-hour operation. A detailed break-down of accelerator operation hours is summarized in Fig. 7.1 and Table 7.1.

This was a highly productive year for HI γ S operation. From July 1, 2013 to June 30, 2014, we delivered 1763 hours of HI γ S γ -ray beam time (15 hours more than in the previous fiscal year) to basic and applied nuclear physics research pro-

grams. We also provided 933 hours for accelerator research and development projects. This allowed us to complete several delayed accelerator development projects, including the upgrade and test of accelerator control software and the development of magnetic field compensation schemes for the OK-5 wigglers in the reverse helicity. We also spent time in developing new FEL and γ -ray capabilities, including the commissioning of dual-band FEL mirrors, and the development of fast helicity-switch capabilities and a novel method to rotate the FEL and γ -ray linear polarization using two helical OK-5 wigglers.

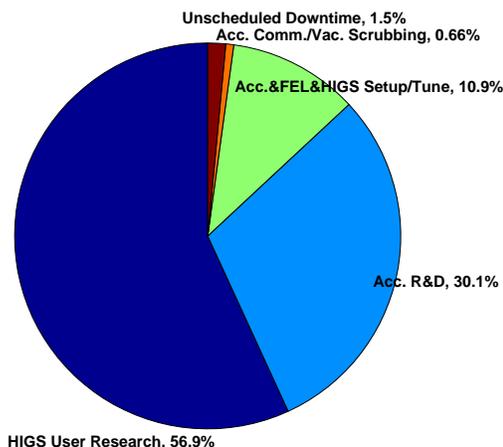


Figure 7.1: Accelerator beam time distribution from July 1, 2013 to June 30, 2014.

A total of 338 hours was used for setting up and tuning the accelerators, FELs, the Compton γ -ray source, along with related activities. The machine setup time was reduced significantly compared to the 563 hours in FY 2013, as we carefully planned the accelerator R&D projects

to use the same accelerator setups as the upcoming user experiments. During this reporting period, the wiggler switchyard was used once to change the wiggler configuration from OK-4 to OK-5, and the subsequent vacuum scrubbing was completed in 21 hours.

Table 7.1: Summary of the accelerator beam time from July 1, 2013 to June 30, 2014.

Activities	Beam time (hrs)	%
HI γ S user research	1763	56.9%
Acc. R&D	933	30.1%
Acc./FEL/HI γ S setup and tune	338	10.9%
Acc. commissioning/ Vac. scrubbing	20.5	0.66%
Unscheduled downtime	46.5	1.5%
Total scheduled beam time	3101	100%

The monthly HI γ S user beam time is shown in Fig. 7.2. The delivered average γ -ray beam time is about 147 hours per month. Careful run planning allowed us to more than double the number of HI γ S beam-time hours in two peak months of operation. In August 2013 and May 2014, 352.5 and 329 hours of γ -ray beam time were delivered to the nuclear physics program with fourteen and nine overnight shifts scheduled, respectively.

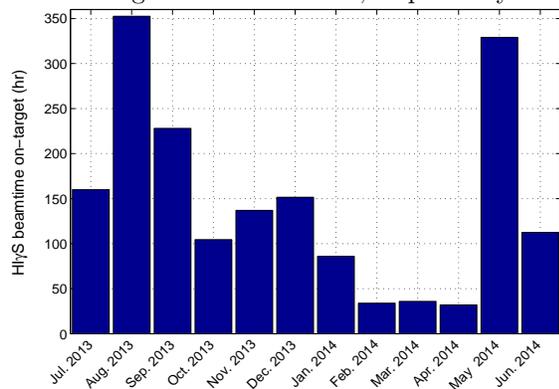


Figure 7.2: Monthly distribution of γ -ray beam-time hours delivered to the HI γ S experimental program (July 1, 2013 – June 30, 2014). The total HI γ S beam time on-target is 1763 hr.

Reliability Issues of Accelerators

The total unscheduled downtime (UD) was 46.5 hours or about 1.5% of the total scheduled operation time. This was significantly lower than many previous years (typically 3 to 7%). The causes are summarized in Fig. 7.3. Two-thirds of the UD hours were from four causes: (1) AC power losses, 9.5 hr (20% of UD); (2) two linac modulators, 12 hr (26%); (3) the storage-ring RF

system, 5.5 hr (12%); and (4) the linac gun nitrogen laser, 4 hr (9%). One power loss resulted in multiple equipment problems, which required more than eight hours to recover machine operation. The linac modulator faults were from high voltage arcing inside and outside the pulse-forming network (PFN) tank. The storage ring RF problems were generally trips of the RF generator or cavity controls, which could be reset after a short time. However, these caused complete beam loss, and time had to be taken to refill the storage ring. The linac-gun nitrogen-laser fault occurred on two consecutive days (October 9 and 10, 2013). The failed laser was replaced by a spare, and then needed startup, aligning, power optimization and testing. UD hours from faults of the kicker systems accounted for only 3.5 hours, a marked reduction from past years. This was the result of implementing a steady and careful maintenance and diagnostic-testing program for the kicker systems.

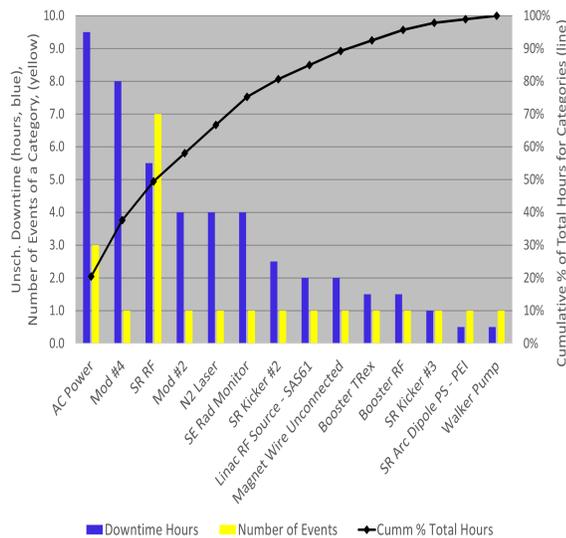


Figure 7.3: Chart of the various categories of events (horizontal axis) showing the unscheduled downtime hours (blue bars), number of failure events in a category (yellow bars), and the cumulative total hours lost in % (black line).

While the reliability of the HI γ S accelerators has been high, we recognize that the HI γ S scientific program in the coming years will require a significant increase in higher energy beams, which will in turn demand a higher level of reliability of all accelerator systems. We have made and will continue to make strategic purchases to stock critical components for spares, and build up redundancy for frequently failed subsystems, as allowed by the available budget.

7.1.2 Operation of the HI γ S Facility—FY 2015

Y.K.WU, P.WALLACE, S.F.MIKHAILOV, *TUNL*

This HI γ S beam-time report covers the time period from July 1, 2014 through June 30, 2015. During this period, the HI γ S accelerator facility was operated for 2324 hours for a variety of research programs and accelerator-related activities with a reliability of about 98.3%. A total of 1052 hours of on-target γ -ray beam time were delivered to the HI γ S user research program.

HI γ S Operation

This report summarizes the operation of the HI γ S Cost Center accelerators for fiscal year 2015, from July 1, 2014 to June 30, 2015. During this period, the HI γ S accelerator facility operated 207 days out of 251 university workdays, providing 2324 hours of beam time for a variety of research programs and accelerator-related activities. The operation of the accelerators and HI γ S was carried out mostly with a two-shift, five-day operation schedule. However, we were able to operate 23 overnight shifts in three different months (11% of days operated) in order to accommodate experiments requiring continuous data-taking.

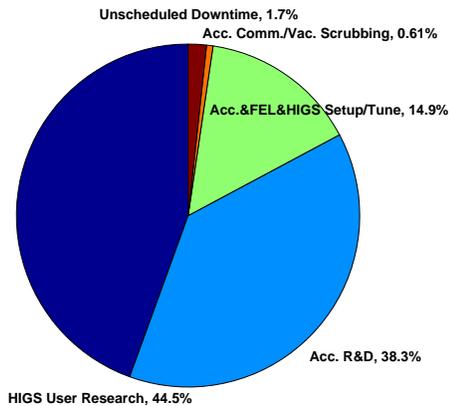


Figure 7.4: Accelerator beam time distribution from July 1, 2014 to June 30, 2015.

In this period, the overall reliability of the operation of HI γ S accelerators and light sources was about 98.3%, exceeding the typical performance goal of 95% set for national synchrotron light sources. This very high level of reliability was realized in spite of the complex and challenging

operation of the free-electron lasers and Compton γ source, and the challenges associated with a very intense run schedule in certain months with 24-hour operation. A break-down of accelerator operation hours is summarized in Fig. 7.4 and Table 7.2.

Table 7.2: Summary of the accelerator beam time from July 1, 2014 to June 30, 2015.

Activities	Beam time	
	(hrs)	%
HI γ S user research	1051.5	44.5%
Acc. R&D	906.5	38.3%
Acc./FEL/HI γ S setup and tune	351.5	14.9%
Acc. commissioning/ Vac. scrubbing	14.5	0.6%
Unscheduled downtime	40.5	1.7%
Total scheduled beam time	2364.5	100%

From July 1, 2014 to June 30, 2015, we delivered 1052 hours of HI γ S γ -ray beam time to basic and applied nuclear physics research programs. Compared to a typical year, fewer user hours were delivered during this period, as all user experiments had to be scheduled to use the smaller, upstream target room. The larger gamma-vault target room, was devoted to the development and testing of the HIFROST target, including building the necessary infrastructure to provide cryogenic cooling to the target.

In this period, we provided a total of 907 of beam-time hours for accelerator research and development projects. This allowed work on multiple accelerator projects, including (1) improving the linac reliability by upgrading the linac RF source and the high-voltage power supplies for the modulators; (2) developing a scheme to compensate for the orbit changes in the storage ring due to the leakage magnetic field from the ad-

jacent energy-ramping booster-injector; and (3) developing new methods to characterize the magnetic optics of the storage ring. In addition, we continued to develop new FEL and γ -ray capabilities, including two-color FEL lasing and the first production of a two-color γ -ray beam, plus a novel method to rotate the γ -ray linear polarization using two helical OK-5 wigglers.

A total of 352 hours was used for setting up and tuning the accelerators, FELs, the Compton γ -ray source, along with related activities. In addition, about fifteen hours were used to perform vacuum scrubbing after the wiggler configuration was changed using the switchyard system.

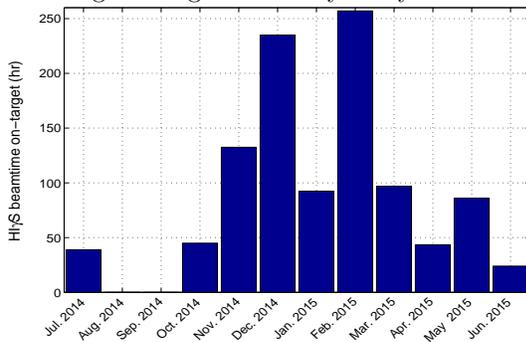


Figure 7.5: Monthly distribution of γ -ray beamtime hours delivered to the HI γ S experimental program (July 1, 2014 to June 30, 2015). The total HI γ S beamtime on-target is 1052 hr.

The monthly HI γ S user beam time is shown in Fig. 7.5. The delivered average γ -ray beam time is about 88 hours per month, with two peak months of operation with some overnight shifts in Dec. 2014 and Feb. 2015, delivering 235 and 257 hours of beam time, respectively.

Reliability Issues of Accelerators

The total unscheduled downtime (UD) was 40.5 hours, or about 1.7% of the total scheduled operation time, significantly lower than in many previous years (typically 4 to 7%). The causes are summarized in Fig. 7.6. Two-thirds of the UD hours were from three causes: (1) the storage-ring RF system, 20.0 hr, (49% of UD), (2) failure of a CAMAC crate, 5.5 hr (14%), and (3) a server failure in the EPICS control system hardware, 2.5 hr (6%).

The RF problems were generally trips of the RF-generator controls, which could be reset after 10 to 15 minutes. However, these cause complete beam loss, and time is needed to refill the electrons in the storage ring. Two cases required

conditioning of the main RF amplifier tube with high voltage to burn a recurring short between the filament and grid screens inside the tube. We have allocated funds for the purchase and installation of a new main RF tube from a different supplier in the coming year to replace our aging tube, which has over seventeen thousand hours of operation time. This is expected to greatly reduce RF-related downtime. The CAMAC crates (typically over forty years old) suffer from failures of their power supplies and fans. We have positioned refurbished CAMAC crates in the storage ring to speed up recovery from future failures. There were no failures of the kickers in the booster or ring that interfered with scheduled operations. Steady and careful maintenance and diagnostic testing of the kicker systems continues to be effective in keeping them in reliable operation.

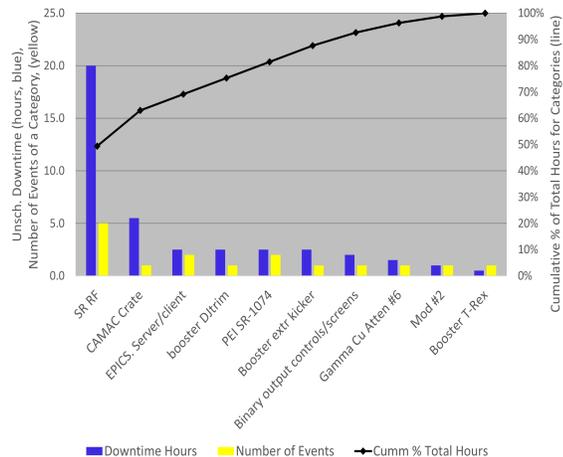


Figure 7.6: Chart of the various categories of events (horizontal axis) showing unscheduled downtime hours (blue bars), the number of events of a category (yellow bars), and the cumulative total hours lost in % (black line).

While the reliability of the HI γ S accelerators has been high, we recognize that we will move into operations at high energies with hundreds of user operation hours for each run. The high energies will require almost continuous top-off injection, which will put all linac, booster and kicker systems under great stress, leading to more frequent failures and likely more catastrophic failures. We are working to develop strategies to meet this challenge by improved forecasting of the need for hardware replacement and by acquiring critical hardware components in a timely manner.

7.1.3 Developing an Injection Mode with 100 ns Electron Beam Pulses

Y.K. WU, V.G. POPOV, P. WALLACE, S.F. MIKHAILOV, *TUNL*

To increase the electron beam injection rate into the storage ring, a new injection mode with 100 ns electron beam pulses is being developed. We report the successful operation of a new high-voltage electron beam chopper, as well as the results from the first round of radiation surveys to test this new operation mode.

Introduction

The HI γ S γ -ray flux in the higher energy range, especially above 20 MeV, is limited by the electron injection rate into the storage ring to replace the electrons lost after Compton scattering. Increasing the electron injection rate is a long-term development project initiated in 2012. The injector system of the HI γ S facility is comprised of two accelerators, a 0.16 GeV linac pre-injector and a 0.16 to 1.2 GeV booster injector. The electron source is a single-cell RF gun that can be operated either in thermionic mode to produce long, microsecond, pulses or in photocathode mode with a nitrogen laser to produce 1 to 2 ns pulses. Currently, we operate the electron gun in photocathode mode to minimize the radiation background, with the maximum injection rate into the storage ring about 13 mA/min, or 5×10^8 e⁻/s. To further increase the charge injection rate, we are developing a new mode of thermionic operation while maintaining a low radiation background.

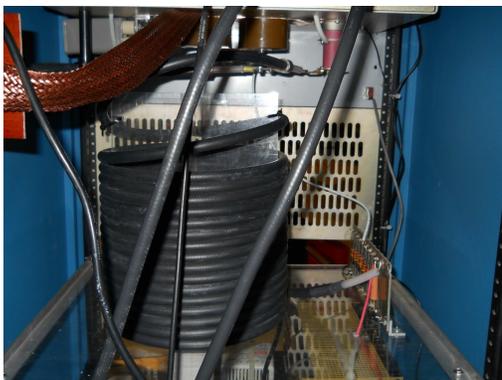


Figure 7.7: Photo showing the pulse forming line, high voltage divider and the thyatron switch.

To reduce the radiation caused by the electrons in long pulses that are not accepted into the booster, the microsecond beam pulses in thermionic mode will need to be chopped to short pulses of about 100 ns to match the revolution time of the booster synchrotron. With this mode of operation, the injection rate can be further increased by about a factor of three, to 1.2 to 1.6×10^9 e⁻/s, or 32 to 43 mA/min). At this level, the γ -ray flux at all energies will likely no longer be limited by the injection rate, but by other factors such as FEL mirror instabilities caused by thermal loading from a high intra-cavity FEL power.

Electron Beam Chopper

A built-in high-voltage (HV) kicker located immediately downstream from the electron gun was designed to be used as a beam chopper. It takes advantage of the low energy (about 1 MeV or less) of the electrons as they exit from the gun but before the momentum-selecting alpha-magnet. The kicker plate is held at 5 kV for most of the time, in order to stop the electrons from passing through the alpha-magnet. The voltage is then momentarily dropped to zero to allow a 100 ns electron beam pulse to pass through.

To produce 100 ns beam pulses, a HV pulsed chopper-driver has been successfully developed using a single cable delay line as a pulse-forming line (PFL) and a cold cathode thyatron as a switch (see Figs. 7.7 and 7.8). The PFL voltage and positive bias voltage are used to control the chopper pulse width. Due to a simple design, the gun kicker has a non-standard impedance which is difficult to match. To produce a properly shaped high-voltage pulse on the kicker plate, a 50 Ohm impedance is chosen for the PFL and for

the transfer line, which is also terminated with a 50 Ohm resistor (see Fig. 7.8).

The HV chopper drive was successfully tested in 2014. Figure 7.9 shows a measured HV pulse on the linac gun kicker plate. In May 2015, the chopper was used to produce the first 100 ns electron beams for two days of radiation surveys.

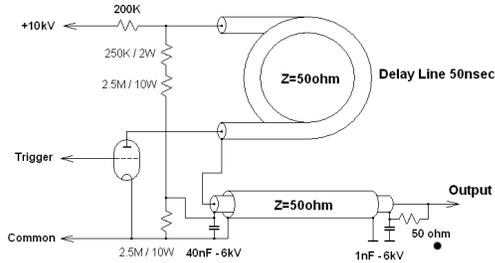


Figure 7.8: Schematic of the 100 ns HV driver for the electron beam chopper.

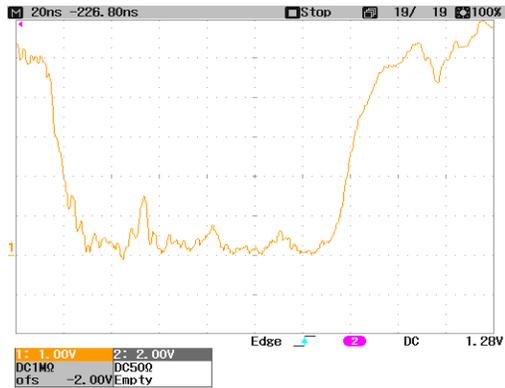


Figure 7.9: A measured 120 ns pulse on the linac gun kicker plate (the voltage scale is 1 kV/division).

Radiation Surveys with a 100 ns e-Beam

Radiation surveys were done under various conditions. With the booster injector configured to accept nanosecond, short pulses for user operation, it did not accept most of the charge from 100 ns beam pulses. This created a worst-case scenario of electron spill-over, an ideal condition for radiation survey. The first important result was measured with the injection charge pulses of 2 nC, with no screen inserted, and the booster injection kicker not operating. The reading on the NW maze area monitor was about 1 mR/hr. In normal operation, injection into the booster typically causes this monitor to read 15 to 20 mR/hr from the 0.35 nC combined photo-electrons in the few nanosecond pulse and thermionic electrons in the microsecond-long pulse. This reduction of

the radiation level is due to the reduced energy spread of the chopped 100 ns pulse beam compared with the normal pulse.

Radiation surveys were also performed with various screens inserted. With the L01 screen along the linac-to-booster (LTB) beamline inserted, the NW maze monitor reading was about 22 mR/hr, and with the L02 LTB screen inserted, the reading was 9 mR/hr. Because of these results, we plan to disable the L01 screen, and to enlarge the local shielding downstream of the L02 screen.

Inserting the S03 screen in the booster, a portable survey meter read 15 mR/hr outside the door of the NW maze. Typical readings are only about 0.5 mR/hr in normal operations. In addition, a reading of 4 mR/hr was found on the booster roof above the S03 screen (through the concrete roof). Inserting the N03 screen caused readings up to 20 mR/hr at booster roof penetrations, and a reading of 4 mR/hr in the mechanical room behind the FEL building (which is a public area). Because of these results, we plan to add circuitry to the controls of the booster screen insertions that will limit the amount of time a booster screen can remain inserted, possibly to 30 seconds in any 5 minute period.

The timing trigger for the 100 ns pulse was scanned across the 1000 ns wide thermionic pulse, and at some settings, high levels of radiation were produced, with readings up to 180 mR/hr on the NW maze monitor.

Further Development

In addition to the modified screen controls and additional local shielding listed above, several other aspects of the new injection mode must be developed before the next test with 100 ns beam pulses. The operation of the HV power supply in the linac chopper must be assured and must provide a switch-closure output for inclusion in the Personnel Protection System (PPS) to prevent linac operation when the HV is not present. The NW maze monitor acts as a final point of control to prevent linac operation if readings go above 30 mR/hr. Because an inadvertent setting of the 100 ns pulse-trigger can produce much higher radiation levels, a second instrument to monitor radiation at this location will be needed for redundancy. We will also test locations inside the booster enclosure to determine if placing additional radiation monitors closer to the location of lost electrons will provide a more sensitive or more reliable signal to the PPS.

7.1.4 Extending OK-5 Wiggler Operations at the Duke Storage Ring

P. WALLACE, M. EMAMIAN, H. HAO, S.F. MIKHAILOV, V. POPOV, Y.K. WU, *TUNL*; J.Y. LI, *University of Science and Technology of China, Hefei, China*

Important physics experiments, such as proton spin-polarizability studies, require γ -ray beam energies of 110 to 120 MeV, which are above the 100-MeV maximum currently available at HI γ S. We are developing methods to operate the wigglers at higher currents in order to achieve these higher energies.

The maximum γ -ray energy currently available at HI γ S is 100 MeV, using 190 nm mirrors and operating with 1.05 GeV electrons and a current of 3.5 kA in the OK-5 wigglers. However, there are important experiments, such as proton spin-polarizability studies, that need γ -ray energies of 110 to 120 MeV. Having no expectation in the short-term of obtaining robust and highly reflective mirrors for shorter wavelengths, nor of a significant increase of the electron beam energy in the storage ring, we need to identify ways to operate the wigglers at higher currents if we are to achieve these energies.

The main design and operational parameters of the OK-5 wigglers are given in Table 7.3.

Table 7.3: Parameters for OK-5 Wigglers

Parameters	Values
Polarization	Circular
No. of wigglers	4
No. of regular periods	30
Wiggler period [cm]	12
Maximum current [kA]	3.5
Maximum magnetic field [kG]	3.17
Maximum K_w	3.53
FEL wavelength [nm]	190 – 1064

A significant issue is the cooling water. Each wiggler contains eight coils of hollow, square copper tubing which wind through the 120 poles in the magnet, with cooling water flowing through each of these coils (see Fig. 7.10). The cooling water supply has been controlled at 29° C, and the temperatures of the return flow range from 40 to 59° C with 3.5 kA of wiggler current. Raising the wiggler currents from 3.5 to 4.0 kA will increase resistive heating by 30%, and could raise the return flow maximum temperature another 10° C or more.

OK-5 wiggler operation with currents over 3.5 kA requires that one T-Rex power supply drives

current through only one wiggler, due to the T-Rex voltage limitation. To keep the wiggler return flow temperature well under 100° C, as well as under the 90° C klixon temperature trip point, we ran the first test by reducing the cooling water control point (the supply temperature) to 21° C, or 8° C below the routine operational value.

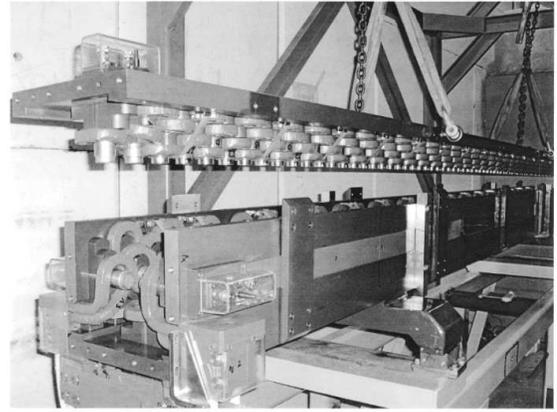


Figure 7.10: OK-5 wiggler coils

Data were collected on cooling water supply and return temperatures, plus the temperatures of all return flows in two OK-5 wigglers and in the two T-Rex power supplies. Fig. 7.11 shows a graph of the temperatures of the eight wiggler coil-cooling water return flows in one wiggler. In the left half, the cooling-water control point is set to 21° C, and the wiggler current was set first to 3.5 kA and then to 4.0 kA. In the right half, the control point is set to 29° C, and the wiggler current is set to 3.5 kA. With a wiggler current of 3.5 kA, the return temperature for a supply temperature of 29° C is higher by an average of 6.2° C (range from 5.0 to 7.7°C) than with a supply temperature of 21° C. At the lower 21°C supply tem-

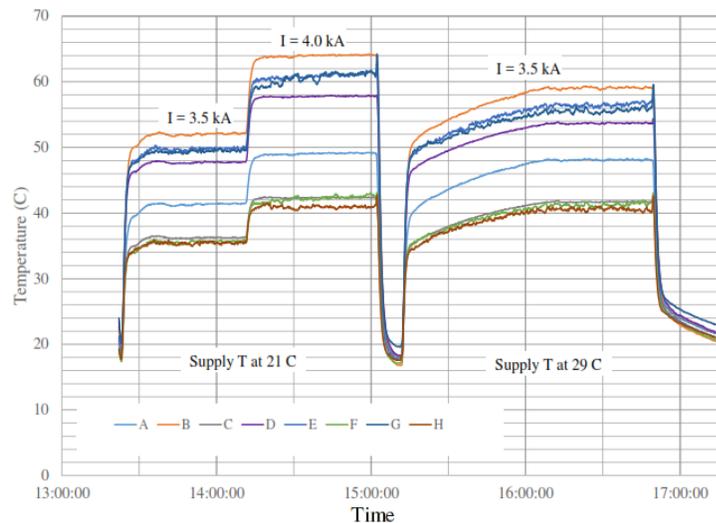


Figure 7.11: Return temperatures of eight wiggler coils (A–H) in one wiggler. In the left half, the supply temperature was set at 21° C and the wiggler currents were set to 3.5 and 4.0 kA respectively. In the right half, the supply temperature was set at 29° C and the wiggler current was set at 3.5 kA.

perature, a wiggler current of 4.0 kA produces a return water temperature that is an average of 8.9° C higher (range from 5.5 to 12.2° C) than with a current of 3.5 kA. There were no magnet over-temperature interlock trips during the hour of operation at 4.0 kA.

The results of the first test are encouraging, holding promise that the goal of operating the OK-5 wigglers with currents up to 4.0 kA can be achieved with a reset of the cooling water temperature setpoint. However, this significant lowering of the cooling water temperature will have wide repercussions in many aspects of accelerator operations, and thus will need significant planning and preparation.

There will need to be further tests conducted at 4.0 kA before we can provide routine operation

at this setting. These tests will have durations of over four hours and simultaneous operation of the storage ring at energies above 1.0 GeV, while studying potential difficulties with the electron beam orbit and achieving lasing of the FEL. Also, since lowering the cooling water temperature will change the temperature in all magnets, power supplies and accelerator vacuum chambers, there will need to be a major re-tuning of the storage ring and injection booster.

For long-term operation with the control point set to 21°C, we must also upgrade the cooling water system, switching from a conventional evaporative cooling tower to the campus-wide Duke University chilled water system. Implementation of the cooling system change is expected in the latter part of 2015.

7.1.5 Characterizing the Betatron Tune Knobs at the Duke Storage Ring

H. HAO, S. MIKHAILOV, V. POPOV, Y.K. WU, *TUNL*; J. LI, *University of Science and Technology of China, Hefei, China*

As the driver for the Duke free-electron lasers (FELs) and HI γ S, the Duke storage ring is operated in a wide energy range with several different FEL configurations. This creates the challenge of producing a systematic and uniform control of the betatron tunes of the electron beam in the storage ring. We have designed a set of feed-forward tune-knob schemes having a minimal impact on the electron beam dynamics (the injection and lifetime). The tune measurements show good agreement with calculations.

In the operation of a storage-ring-based light source, it is necessary to have full control of the transverse oscillation frequencies of the electron beam (the betatron tunes). This is usually accomplished using a tune knob which allows a set of quadrupoles to be varied simultaneously in a way that changes the tunes as needed. At HI γ S, the wide operation energy range of the storage ring and the use of different free-electron-laser (FEL) wigglers create the challenge of designing and developing a set of betatron tune knobs to work with different magnetic optics. In 2012, a set of tune knobs was designed, together with the needed wiggler-focusing compensations [Hao12]. In this work, we report the quantitative investigation of the effectiveness of these tune knobs, and we document a set of calibrations to improve their usefulness.

A tune knob is realized by changing the strength of a set of quadrupoles in the storage ring. To minimize the impact on the beam dynamics, e.g. the injection efficiency and the beam life time, the β -function changes introduced by the quadrupole variations are constrained within the 34-meter-long FEL straight section. The lattice parameters (Twiss parameters) at the two ends of the straight section are required to match with those of the arc lattices when the quadrupoles are varied. To preserve the beam dynamics, the symmetry of the straight section lattice also should be preserved whenever possible. At the Duke storage ring, the horizontal (or vertical) tune knob is designed to control the tune in only one direction. Simultaneous tune changes are realized by simply adjusting the two independent knobs.

Calibration of the tune knobs requires a large number of tune measurements. A tune measurement technique based on transverse feedback (TFB) was used to reduce the measurement time. In the measurement, the electron beam is excited by a radio-frequency drive signal with a finite bandwidth that covers the frequency range of the betatron oscillations. The turn-by-turn signal of the electron beam's transverse motion from the beam position monitor is recorded using the TFB [WXu13]. Using the fast-Fourier-transform technique, the betatron tunes can be identified. In the operation of the Duke storage ring, the maximum tune changes allowed are smaller than the designed maximum tune knob ranges of ± 0.1 , due to betatron tune resonances. One of the resonances is the horizontal integer resonance $\nu_x = 9$; the other one is the difference resonance $\nu_x - \nu_y = 5$. In our measurements, the tune knob variations are limited within ± 0.05 , which is more than adequate to cover the lattice tuning ranges needed for HI γ S operation.

The tune knobs are calibrated for the nominal storage ring lattice with all wigglers turned off. Figure 7.12 shows the measured horizontal tune changes as a function of tune-knob settings. It can be seen that the relationship between measured tune changes $\Delta\nu_{x,\text{meas}}$ and the corresponding tune-knob settings $\Delta\nu_{x,\text{knob}}$ is close to linear. The fitting result is $\Delta\nu_{x,\text{meas}} = 0.939 \Delta\nu_{x,\text{knob}}$, so the measured horizontal tune change is 6.1% less than the knob setting. The horizontal tune knob has a very small effect on the vertical tune, changing it by about 2% ($\Delta\nu_{y,\text{meas}} \approx 0.02 \Delta\nu_{x,\text{knob}}$). One main reason that the fitting coefficients are not unity is that the real lattice

is different from the designed one. According to Ref. [WLi15], the measured rms beta-beating in the horizontal direction is about 5%. Another source of discrepancy is the hysteresis effect of the quadrupole magnets. The relationship between the driving current and the magnetic field of the quadrupoles in the storage ring is determined using the up-branch of the hysteresis curve. For the quadrupoles where strengths are decreased in the tune knob, the magnetic field does not change exactly as expected, introducing a discrepancy in the focusing-strength change, which leads to a small inconsistency in the tune change.

Based on the above measurement results, the horizontal-tune-knob calibration can be realized using the fitted slope: $\Delta\nu_{x,\text{knob,calib}} = \Delta\nu_{x,\text{knob}}/0.939$. Figure 7.13 shows the horizontal tune differences between the measured tune variations and the calibrated tune knobs. We can see that the maximum residual horizontal tune variations using the calibrated tune knobs are reduced to the level of a few 10^{-4} , which corresponds to a maximum relative difference of about 2%. This amount of discrepancy is comparable with the tune reproducibility of the same lattice operated at different times.

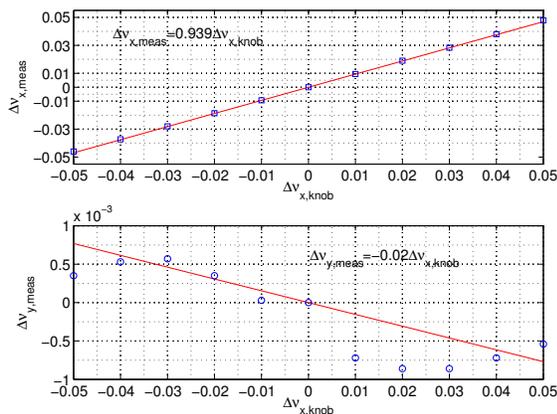


Figure 7.12: Measured horizontal and vertical tune variations by varying the horizontal tune knobs.

In addition to measuring the tunes in one direction, two-dimensional tune-scan measurements in both the x and y directions were conducted. As an example, Fig. 7.14 shows the differences between the measured tune variations and the calibrated tune knobs in two dimensions. In the blank area at the bottom-right corner of the plot, the tunes cannot be measured due to the

resonance $\nu_x - \nu_y = 5$. The residual tune variations with the calibrated tune knobs are smaller than 3×10^{-3} in the entire plane, showing good agreement between the measured and calibrated tune knobs.

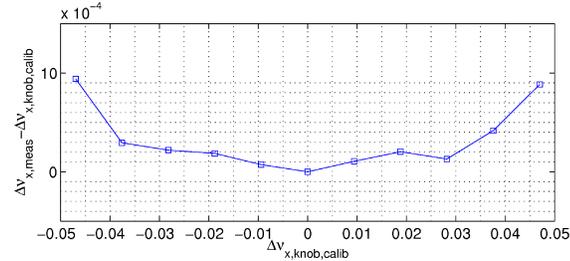


Figure 7.13: The residual tune variations after applying the tune-knob-calibration relation $\Delta\nu_{x,\text{knob,calib}} = \Delta\nu_{x,\text{knob}}/0.939$.

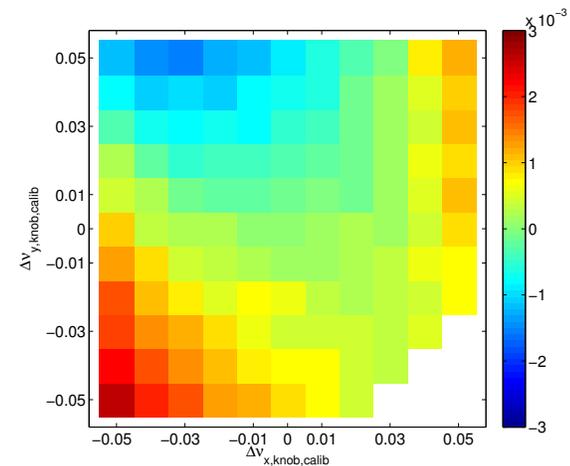


Figure 7.14: Residual horizontal tune variations by varying the horizontal and vertical tune knobs simultaneously.

In this report, the Duke storage ring tune knobs are measured for the nominal lattice with all wigglers turned off. The results show that the calibrated tune knobs agree well with the designed one within a few times of 10^{-4} for tune changes of up to ± 0.05 .

[Hao12] H. Hao *et al.*, In *International Particle Accelerator Conference*, 2012.

[WLi15] W. Li *et al.*, In *International Particle Accelerator Conference*, 2015.

[WXu13] W. Xu *et al.*, *Chin. Phys. C*, **37**, 077006 (2013).

7.1.6 Measuring the Storage Ring Lattice Using a Tune-Based Technique

W. LI, J.Y. LI, *University of Science and Technology of China, Hefei, China*; H. HAO, S.F. MIKHAILOV, V. POPOV, Y.K. WU, *TUNL*

Since 2012, the Duke storage ring has demonstrated all of its design characteristics for lattice flexibility and tuning. The present work seeks a better understanding of the real storage-ring lattice through measurements of the beta-functions along the storage ring. The beta-functions in the quadrupoles are measured directly with good accuracy using a tune-measurement system.

Introduction

The Duke electron storage ring (DSR) is a dedicated driver for oscillator free-electron lasers (FELs) and has demonstrated all its design characteristics for lattice flexibility and tuning [Hao12]. One of the greatest challenges in characterizing and calibrating the DSR lattice is the use of combined function quadru-sextupoles in the arcs. With these complex magnets, the closed beam orbit in the arc is not known. However, the electron beam orbit is directly coupled to the focusing strength of the quadrupoles. This has been a major difficulty in using the LOCO method [Saf02] to calibrate the DSR. Unlike the LOCO method, the present method does not depend on the beam orbit. Instead, it measures the beta-function in the quadrupoles directly with good accuracy using the transverse-feedback system [WXu12]. We describe the measurement method and system; the tune change related to the beam current decay; the influence of quadrupole hysteresis on the beta-function measurement; and finally our experimental design and preliminary results for the lattice characterization.

Measurement method and system

In a storage ring with quadrupoles whose strengths can be controlled independently, beta-functions at the locations of the quadrupoles can be measured directly. A change in the quadrupole strength will cause a tune change proportional to the beta-function at the quadrupole, where the relation between the beta-function and the change in tune is given by:

$$\langle\beta\rangle = \frac{4\pi\Delta\nu}{\Delta K_1 L_{eff}}, \quad (7.1)$$

where $\Delta\nu$ is the measured tune change, ΔK_1 is the change in the quadrupole strength, L_{eff} is the effective length of the quadrupole, and the measured $\langle\beta\rangle$ is the average beta-function over the quadrupole.

This beta-function measurement method is based on the tune measurement. The basic approach to determine the betatron tune of the electron beam is to excite the beam and measure its response. Two tune-measurement systems are available in the Duke storage ring. The slow one uses a network analyzer, and a tune measurement with a resolution of 10^{-4} in the tune scan range of [0.1, 0.2] takes about 30 seconds. The faster one is based on the transverse feedback (TFB) technique, and a tune measurement with a resolution of 3.5×10^{-5} in the range [-0.072, 0.215] takes about 12 seconds.

Beam current decay and hysteresis

During the process of measuring the beta-function, the electron beam current decays due to electron loss through electron-electron and electron-residual-gas scattering. As the current decays, the wake field of the electron beam is reduced, resulting in an increase of the betatron tunes. To find out how much this influences the beta-function measurements, we measured the betatron tune as the beam current decayed from 4.4 to 1.3 mA. The measured tunes and linear fits are shown in Fig. 7.15. The fitted slope is about -1.75×10^{-4} in the horizontal direction and -4.95×10^{-4} mA in the vertical. In our beta-function measurements with the TFB system, beam-current decay between two subsequent tune measurements is typically about 0.01 mA.

Like many storage rings, the nominal operation of the DSR is along the up-branch of the magnetic field hysteresis curve, and the quadrupole field was measured and calibrated for this branch. Therefore, a reliable beta-function measurement should also be carried out along the up-branch. However, it is important to investigate the impact of hysteresis for the beta-function measurement when field changes are made in both directions along the up- and down-branches of the hysteresis curve.

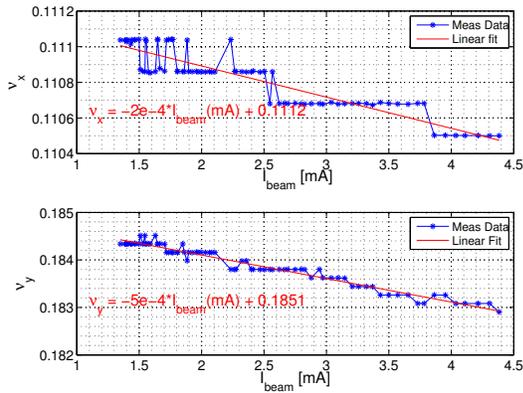


Figure 7.15: Tune shift with beam current decay.

To study this effect, betatron tunes were measured by changing the quadrupole strength in a closed loop of $[0, +\Delta K_1, 0, -\Delta K_1, 0]$. This local loop is repeated 4 times. The average beta-function can be calculated with each two subsequently measured tunes. The measured beta-functions at different segments of the loop are compared to the first measurement, considered to be the true beta-function. We find that the beta-functions in the later measurements are always smaller than the first measurement.

Sources of measurement errors

In this measurement, ΔK_1 for each quadrupole is optimized with a typical value of 1% of the quadrupole strength. To reduce the residual field, the quadrupole setting is returned by completing a local normalization loop. To minimize the influence on the tune change, beta-functions are measured at focusing and defocusing quadrupoles alternately. To improve consistency, the storage ring magnets are normalized so that the magnet optics are restored after a certain number of mea-

surements.

The beta-functions were measured for 78 quadrupoles on the Duke storage ring, with a 638 MeV electron beam. All the measurements were taken with a single-bunch beam and a beam current of 3 to 4.5 mA. The designed, measured and simulated vertical beta-functions are shown in Fig. 7.16. The simulated values are for an ideal designed lattice. The rms difference between the measured and simulated beta-function is 16% in the vertical direction.

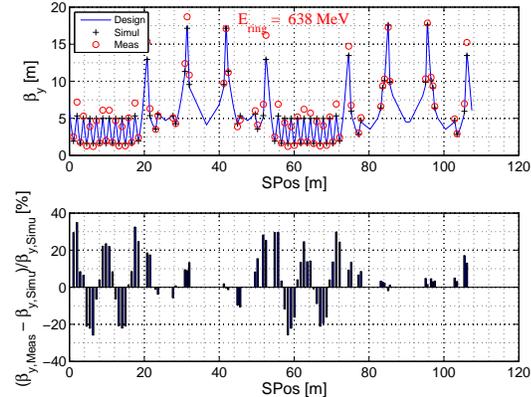


Figure 7.16: Measured β_y and relative difference around the ring.

Summary

We have developed a fast beta-function measurement technique using the TFB system. The effects of beam current decay and magnet hysteresis are discussed. Other factors that can influence the beta function measurement include the quality of the quadrupole magnet calibration, temperature changes during the measurement, and changes in power supplies. With directly measured beta-functions, we will develop a lattice-compensation technique using the single value decomposition algorithm.

-
- [Hao12] H. Hao *et al.*, In *Proceedings of IPAC2012, New Orleans, USA*, 2012.
- [Saf02] J. Safranek, G. Portmann, and A. Terebilo, In *EPAC*, pp. 1184–1186, 2002.
- [WXu12] W. Xu *et al.*, In *Proceedings of IPAC2012, New Orleans, USA*, 2012.

7.1.7 Improved Pulsed Mode Operation for the Duke Storage-Ring-Based FEL

S.F. MIKHAILOV, H. HAO, V.G. POPOV, Y.K. WU, *TUNL*

While the Duke FEL and HI γ S are typically operated in quasi-CW mode, some HI γ S user experiments can benefit tremendously from a pulsed mode of FEL operation. Therefore, we developed and successfully tested a radio-frequency frequency modulation technique to pulse the FEL beam. We report our results of this pulsed FEL operation.

The Duke storage ring is designed as a dedicated FEL driver and as a host for several FEL wigglers in a thirty-four-meter long straight section. One of the main FEL configurations is the OK-4 FEL, which is an optical-klystron FEL consisting of two planar wigglers sandwiching a buncher magnet. A second commonly used FEL configuration is the OK-5 FEL, which employs up to four OK-5 helical wigglers. Two OK-5 wigglers in the middle of the straight section are mechanically switchable with the two OK-4 wigglers using a switchyard system [YWu13]. The Duke FEL can also be operated using either one OK-4, or one OK-5 wiggler alone, when new FEL mirrors are available with very high reflectivity.

Typically, in all wiggler configurations and polarizations, the Duke FEL is operated in a quasi-CW mode, but for some experiments, a pulsed FEL beam, and therefore γ -ray beam, can be highly beneficial, allowing users to reduce the background noise by two to three orders of magnitude by using time discrimination synchronized with the FEL macro-pulses.

Development of RF Frequency Switch

To enable pulsed mode FEL operation, a fast-steering magnet, the FEL gain modulator, was developed [Pin01]. It decouples the electron beam from the FEL beam in the interaction region for most of time, but periodically allows a brief overlap of the two beams. This enables a pulsed mode of FEL operation with a high peak power in the FEL macro-pulses.

The low-energy range for γ rays is the most commonly demanded for nuclear physics experiments which use a pulsed beam. Production of γ -ray beams of high intensity also requires high

electron beam currents. The use of the FEL gain modulator in such a regime is constrained due to beam instability and poor injection. To facilitate high intensity γ -ray production in a pulsed mode, especially at low electron-beam and γ -ray energies, we developed a radio-frequency (RF) frequency modulation of the FEL gain (an RF frequency switch) to pulse the FEL.

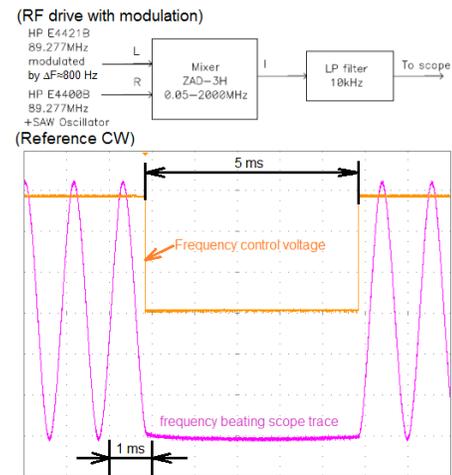


Figure 7.17: Fast switch of the RF frequency as demonstrated by the transition in time of the beating between the RF drive signal and a CW reference signal.

The Duke storage ring RF system utilizes a high-stability commercial synthesizer, HP 4400B, as the master oscillator [Kur05a, Kur05b]. An additional SAW oscillator filter is used to eliminate digital phase and frequency noise of the master oscillator. However, to enable a fast RF frequency jump, the SAW filter has to be bypassed. Under that condition, the RF system allows a

fast frequency jump, within tens of microseconds (Fig. 7.17). Detuning the RF frequency by $\Delta f/f \approx 10^{-5}$ is sufficient to fully stop lasing in low-gain FEL configurations.

Pulsed FEL operation using the RF frequency switch

For the practical use of pulsed FEL operation at HI γ S, we need to achieve a reasonable degree of reproducibility of the magnitude and length of the FEL macro-pulses. To provide this reproducibility, we can force the FEL to operate in the pulsed mode.

The period of the forced pulsing, and therefore of the forcing drive, has to be at least twice as long as the period of the “natural” FEL relaxation pulsing so that $T_{\text{forced}} \geq 2T_{\text{natural}}$. If $T_{\text{forced}} < 2T_{\text{natural}}$, the electron beam is not damped sufficiently to build up every FEL macro-pulse. As a result, we have a macro-temporal structure where alternate macro-pulses are fully developed, while those in between the full-strength pulses are under-developed, as shown in Fig. 7.18.

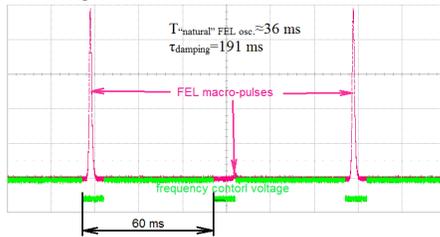


Figure 7.18: Pulsed FEL operation with a drive period too short to provide reproducible FEL macro-pulses. The data were taken with an OK-5A FEL at 705 nm, $E_e = 350$ MeV, and mirror round-trip losses of about 0.16%.

To insure a reasonable stability of pulsed FEL operation, it is better to set the period of pulsing so that $T_{\text{forced}} \geq 2.5T_{\text{natural}}$. With the condition that $T_{\text{forced}} \approx 2.5T_{\text{natural}}$, the average FEL power is practically the same as that in a quasi-CW regime, with a very high peak power in the FEL micro-pulses. Figure 7.19 shows the dependence of the shape of the FEL macro-pulses on the pulsing period for a fully periodic macro-temporal structure ($T_{\text{forced}} \geq 2T_{\text{natural}}$). With a longer period of pulsing, the reproducibility of the FEL macro-pulses is also much better, and jitter is much lower. The RF frequency drive signal has to switch periodically to a frequency which allows full synchronization of the electron and FEL beams. The duration of that synchro-

nization has to be long enough to allow the FEL pulse to build up fully. This duration depends on the period of the pulsing, as shown in Fig. 7.19.

The pulsing period cannot be arbitrarily long for high-current, low-energy operation of the storage ring. The limiting factor to increasing the pulsing period is loss of the electron beam, if we allow it to fully damp due to synchrotron damping. For typical HI γ S γ -ray production, we operate with the electron beam currents far above the two-bunch current threshold without lasing. The electron beam is stable only due to a significant FEL-induced beam stretch. If this stretch is reduced substantially, electron beam loss occurs.

For synchronization of HI γ S data-acquisition equipment, users are provided with a trigger by the relative amplitude of FEL macro-pulses. The trigger can be set at 10 to 70% of the level of a typical maximum.

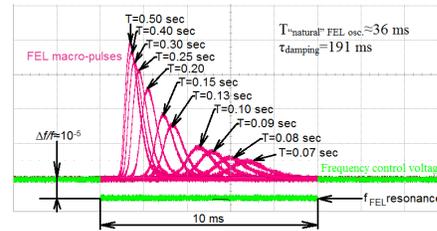


Figure 7.19: FEL pulsed operation with “stable,” fully periodical FEL macro-pulses for different periods of drive. The data were taken with an OK-5A FEL at 705 nm, $E_e = 350$ MeV, and mirror round trip losses of around 0.16%.

Conclusion

An RF frequency detune drive has been developed at DFELL and is ready to be used in pulsed FEL and HI γ S operation. It can provide high γ -ray beam intensity, with an average intensity close to the level of quasi-CW operation and, therefore, with a very high peak intensity during the pulses.

- [Kur05a] G. Kurkin and P. Wang, In *Particle Accelerator Conference*, pp. 1494–1495, 2005.
- [Kur05b] G. Kurkin *et al.*, In *Particle Accelerator Conference*, pp. 3159–3160, 2005.
- [Pin01] I. Pinaev *et al.*, Nucl. Instrum. Methods A, **475**, 222 (2001).
- [YWu13] Y. Wu *et al.*, In *International Particle Accelerator Conference*, pp. 267–269, 2013.

7.1.8 A Two-Color Storage Ring FEL

J. YAN, Y.K. WU, H. HAO, S. MIKHAILOV, V. POPOV, *TUNL*; J.Y. LI, *University of Science and Technology of China, Hefei, China*; N.A. VINOKUROV, *Budker Institute of Nuclear Physics, Novosibirsk, Russia*; S. HUANG, *Peking University, Beijing, China*; J. WU, *SLAC National Accelerator Laboratory, Menlo Park, CA*

Using three-undulator and four-undulator configurations on the Duke storage ring, we have successfully achieved lasing with a novel two-color storage-ring FEL. Simultaneous lasing was realized in the IR, around 720 nm, and in the UV, around 360 nm. With this two-color FEL, we have demonstrated independent wavelength tuning, including the tuning of harmonic lasing with the UV lasing wavelength being the second harmonic of the IR lasing. We have also demonstrated good control of FEL power-sharing between the two colors.

Introduction

Multi-color lasers have found many important applications in scientific research. Simultaneous multi-color lasing on conventional lasers is typically realized by using a dispersive or diffractive wavelength filter such as a prism or grating, either intracavity or in an external feedback cavity. However, the wavelength tunability of these lasers is limited by the bandwidth of the gain medium. The natural advantages of an FEL, such as its broadband gain medium (an electron beam), make the FEL an excellent device for multi-color lasing with good wavelength tunability. Since the early 1990s, multi-color FEL operations have been developed with several linac-based FELs. The first experimental demonstration of a widely tunable two-color storage-ring FEL was at the Duke FEL and was reported in Ref. [YWu15]. Here we present an experimental study of two-color lasing using a different undulator configuration. The experimental results show good performance of this two-color operation in terms of wavelength tunability, power tunability and power stability. Furthermore, this two-color FEL can serve as a photon source for two-energy γ -ray production via Compton backscattering at HI γ S.

Experimental Setup

The Duke FEL system can use a variety of undulator configurations, with four available electromagnetic undulator magnets: two planar OK-4 undulators and two helical OK-5 undulators (see Fig. 7.20). This provides the possibility

of operating a multi-color FEL using the same electron beam and a shared optical cavity. We have achieved two-color lasing with both three-undulator and four-undulator configurations. In the four-undulator configuration, all the undulators are powered up so that the OK-4 and OK-5 undulators form two sets of optical klystrons.

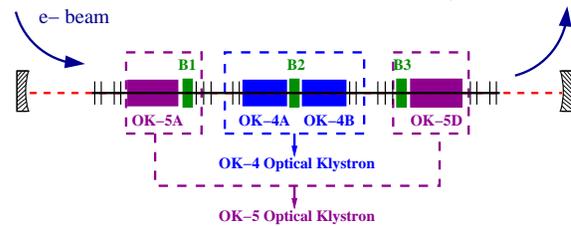


Figure 7.20: A four-undulator configuration for two-color FEL operation. The two OK-4 undulators and two OK-5 undulators form two sets of interleaved optical klystrons.

The two-color FEL lasing is tuned to the IR wavelength around 720 nm (λ_1) and the UV wavelength around 360 nm (λ_2). The setup also allows for harmonic lasing with λ_1 about twice λ_2 . To enable two-color lasing, a pair of dual-band FEL mirrors have been developed with two highly reflective wavelength bands centered around 720 nm and 360 nm, respectively. The measured round-trip losses in the IR and UV bands show that the minimum cavity loss in the UV is roughly four times larger than that in the IR. To balance the gain of two-color lasing, the OK-5 FEL is operated in the IR since its relatively low gain can be compensated by the lower loss of the optical cavity. With a higher gain,

the OK-4 FEL is operated in UV where the cavity loss is also higher. The wavelength tuning is mainly done by changing the magnetic field strength in the OK-4 and OK-5 undulators. Several other tuning knobs are found to be useful for fine wavelength tuning and adjustments of the relative gains at the two wavelengths. These include the RF frequency detune df_{RF} , which controls the synchronization between the FEL and the electron beams, and the settings of bunchers B1, B2, and B3.

Experimental Results

For many important research applications that use a two-color laser, it is critical to have the ability to tune one of the lasing wavelengths while fixing the other. Figure 7.21 shows a tuning setup using the four-undulator configuration in which λ_1 was fixed at 720.06 ± 0.07 nm, while λ_2 was tuned from 374.06 nm to 360.19 nm, demonstrating a wavelength tuning range of $\Delta\lambda_2 \approx 14$ nm. Such wavelength tuning was achieved by varying the magnetic field strength of the OK-4 undulators as the primary tuning knob, and using buncher B2 as an auxiliary knob for fine wavelength adjustment.

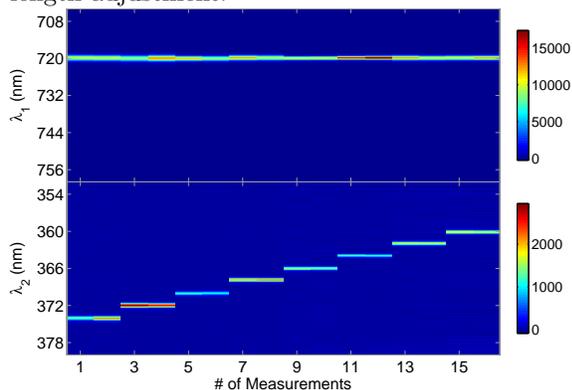


Figure 7.21: Single-wavelength tuning. The UV wavelength λ_2 is tuned while the IR wavelength λ_1 is fixed. The beam current is maintained between 12.2 and 12.7 mA.

The two lasing processes at two different wavelengths share the same gain medium, the electron beam. The wavelength tuning experiments have clearly demonstrated the capability of providing effective gain balance for the two

lasing processes. A precise control of the partitioning of the FEL power for two different wavelengths was realized by adjusting N_{B3} , the relative optical phase slippage between the laser and electron beams produced by buncher B3. As shown in Fig. 7.22, power modulation close to 100% for IR and UV was achieved while the total FEL power was maintained constant to within 6.8% (rms). The periodic power modulation in this measurement can be attributed to the gain modulation mechanism of an optical klystron, where, by tuning N_{B3} , the IR beams emitted in OK-5A and OK-5D produce constructive and destructive interference alternately for electrons of a certain energy.

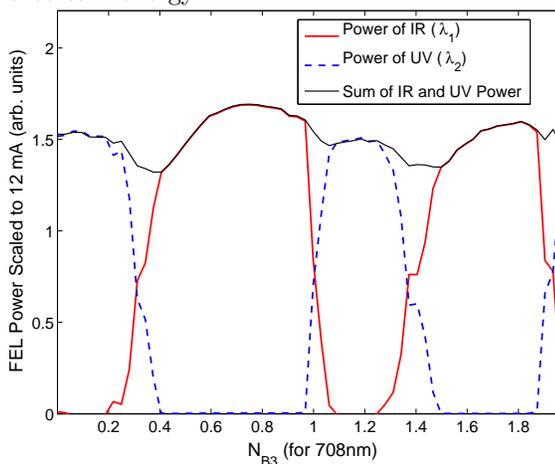


Figure 7.22: (Color online) Two-color FEL power control using N_{B3} . The beam current was maintained between 12.2 and 12.5 mA with top-off injection. The settings of other bunchers: $N_{\text{B1}} = 0$, $N_{\text{B2}} = 0.68$ for 367 nm.

Summary

We report the successful operation of a two-color FEL using a four-undulator configuration. We have demonstrated wavelength tunability in a wide range by changing one of the two lasing wavelengths. Furthermore, we have demonstrated full control of the FEL power in two colors while maintaining the total FEL power at a steady level.

[YWu15] Y. Wu *et al.*, submitted for publication, (2015).

7.2 The FN Tandem Accelerator and Ion Sources

7.2.1 Tandem Accelerator Operation

C.R. WESTERFELDT, J.D. DUNHAM, R. O'QUINN, B. WALSH, *TUNL*

The operation, maintenance, and improvements at the TUNL FN tandem accelerator over the last year are summarized.

Tandem Operation

During the period September 1, 2014 to August 31, 2015, the TUNL FN tandem accelerator was operated on 234 days for 2585 hours at terminal potentials ranging from 0.6 MV to 10.4 MV. Beams accelerated during this period include unpolarized protons and deuterons (DC and pulsed) as well as both ^3He and ^4He . The terminal operating potential as a function of date during the reporting period is shown graphically in Fig. 7.23, along with the number of days the terminal was used at different potentials.

The tandem was opened on May 4, 2015 for routine maintenance. One bad column resistor was found at this opening. The foil stripper box was opened and cleaned. A new set of 75 ACF “Classic Carbon” collodian-coated stripper foils was installed. The thicknesses of the foils are primarily in the range from 1.5 to 2.0 $\mu\text{g}/\text{cm}^2$. The Pelletron charging system was inspected and all idlers were replaced. The chains were removed and cleaned. Five links were replaced in the low-energy chain because of obvious fret corrosion. The corona needles were cleaned and the corona shield was cleaned and buffed. We also replaced one man-door delta gasket due to a crack that was found. The tandem was closed on May 12, 2015 and operations resumed the next day. Unfortunately, about a week later, a high voltage spark apparently damaged the high-energy chain, producing very unstable operation, so we have disabled that motor and will make another tank entry in September to make repairs.

Laboratory Projects

The TUNL helium exchange source has operated for a significant number of hours this past year, producing beams of $^3,^4\text{He}$ of 1 to 2 microamperes to the tandem low-energy cup via its sodium charge-exchange canal. An NEC BPM-

80 beam scanner was installed at the exit of the charge-exchange box to permit the properties of the exit beam to be observed. A parallel-plate radio-frequency chopper has been fabricated and installed at the exit of the helium source, permitting us to chop and bunch the ^3He beams for ($^3\text{He},n$) experiments. A TUNL-designed ^3He recirculation system was also constructed and is in use to recover close to 90% of the ^3He fed to the helium charge-exchange negative-ion source (see Sect. 7.2.2). DC beam currents approaching 2 μA are transported to the tandem low-energy cup. A diagram of this system is shown in Fig. 7.24.

The 20°-R port of our analyzing magnet has been redesigned and reconstructed to provide greatly improved shielding and collimation for neutrons produced in a deuterium gas cell. The cell is enclosed in a massive copper, tungsten, lead, concrete, and borated polyethylene shield. Access to the cell is simplified by the addition of shielding on a linear bearing that permits the shielding to be moved by hand to expose the cell for replacement as needed. New pumping and interlocks protect the tandem in case of window failure in the gas cell.

A newly constructed 70°-R port on our analyzing magnet delivers pulsed ^3He beams to targets in a chamber in the tandem high-energy bay. We have opened up the shielding wall between the high-energy bay and target room one to permit a 10-meter flight-path for time-of-flight measurements using an array of neutron detectors located in the target room and covering an angular spread from 0 to 30°.

Another beamline is under design to be installed in target room four for producing low-energy neutrons for detector tests. It is anticipated that this will be finished in early spring 2016. This will bring our total number of active beamlines to eight. The current tandem layout is shown in the diagram at the back of the progress report.

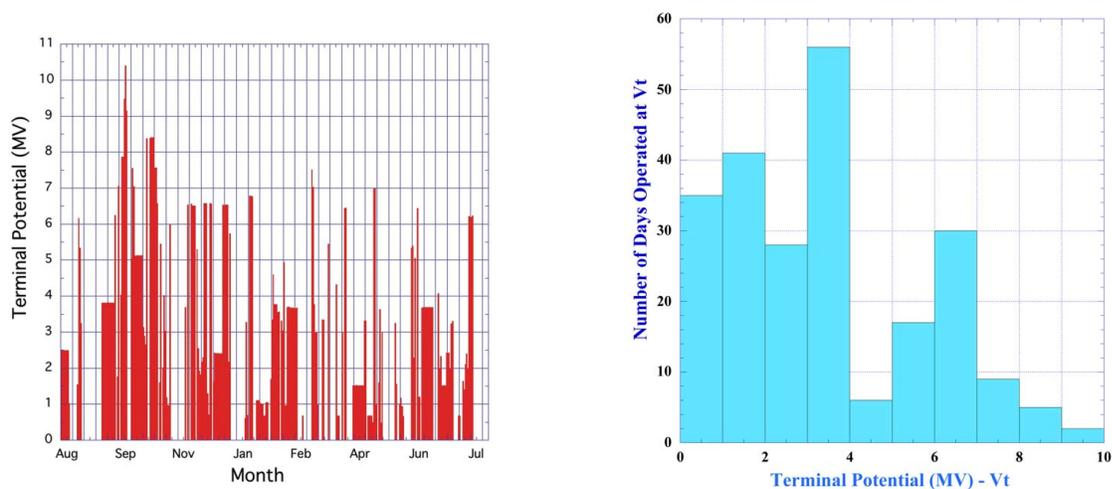


Figure 7.23: The TUNL FN tandem operating potential during the present reporting period.

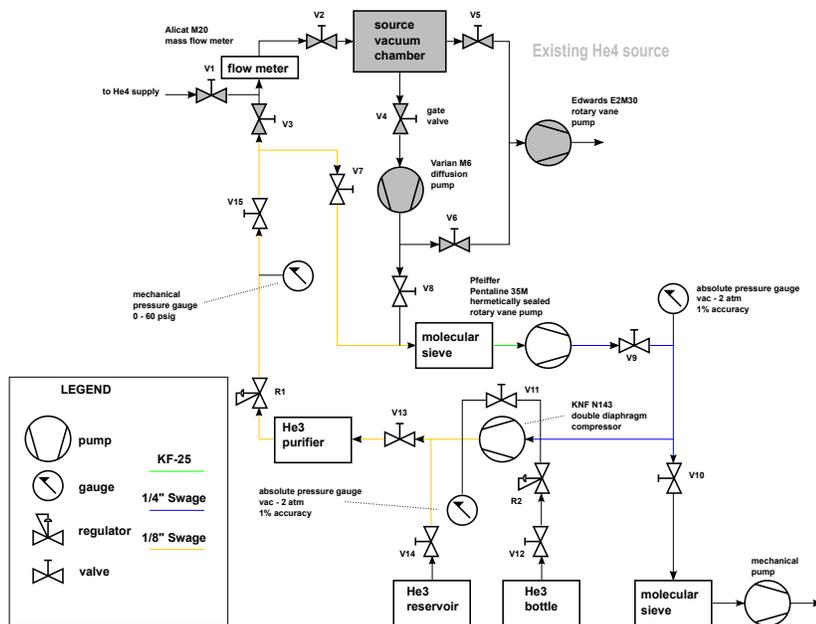


Figure 7.24: The ³He recirculation system.

7.2.2 A ^3He Gas-Recirculation System for the Helium Ion Source

D.C. COMBS, J. DUNHAM, C.R. HOWELL, D.R. TICEHURST, C.R. WESTERFELDT, A.R. YOUNG, TUNL;

A system for recirculating ^3He gas has been installed on the helium ion source in the tandem accelerator laboratory. This system allows the ^3He gas to be recovered and stored after the source has been operated to produce ^3He ion beams. The average gas recovery fraction after a 12 hour operating period is 0.86 ± 0.07 . Beam currents of greater than $2\ \mu\text{A}$ have been measured at the low-energy cup. During this reporting period the performance of the gas recirculation and recovery system was evaluated under normal operating conditions.

Neutrinoless double-beta-decay ($0\nu\beta\beta$) experiments have the potential to probe the absolute mass scale of the neutrino, but doing so requires accurate knowledge of the nuclear matrix elements used to calculate the decay rate. The calculated values of the $0\nu\beta\beta$ nuclear matrix elements for a specific isotope vary considerably depending on the model used [Eli04]. To constrain the calculated values of the ^{76}Ge $0\nu\beta\beta$ -decay nuclear matrix element, cross section measurements of the two-nucleon-transfer reaction ($^3\text{He},n$) on isotopes used in $0\nu\beta\beta$ experiments are being carried out at TUNL. Given the scarcity and high cost of ^3He gas [Ade10], a system to recirculate and recover the gas in the helium ion source has been constructed and installed.

The helium ion source uses a diffusion pump backed by a mechanical pump to evacuate the source chamber. In the original system the mechanical pump exhausted to atmosphere. Gas flow at the source intake has been measured to be approximately 1 standard cubic centimeter per minute under normal operating conditions.

The new recirculation system and the original source are shown in Fig. 7.25. Gas from the reservoir is fed to the source chamber through a flow meter. The reservoir can be refilled from a ^3He gas cylinder. To reduce contamination of the gas recirculation system by pump oil, a hermetically sealed rotary vane pump is used to back the diffusion pump. A molecular sieve is in the line between the diffusion pump exhaust and the rotary vane pump input to prevent diffusion pump oil from entering the recirculation system. A diaphragm compressor pump is used to refill and pressurize the helium reservoir.

The rotary vane pump is a Pfeiffer PentaLine 35M. The helium compressor is a KNF N143 double-diaphragm pump. The mass flow meter is an Alicat M20 mass flow meter. The valves in the recirculation system (V7-V17 in Fig. 7.25) are stainless steel bellows-sealed valves with Swagelok connections. The gas lines are constructed from stainless steel tubing.

The output from a residual gas analyzer (RGA) connected at the source box is shown in Fig. 7.26. Scans were taken before filling the system with ^3He , immediately after filling and after recirculating for 8 hours. The dominant source of contamination in the gas at the source chamber is water vapor followed by hydrogen and nitrogen. No hydrocarbons from pump oil are seen in the spectra.

The performance of the helium source when running ^3He is comparable to its performance when running ^4He . Beam current on the low-energy cup has been between 1.5 and 2.5 μA when using ^3He .

The average recovery rate using this system has been measured at 0.86 ± 0.07 per twelve hours. This recovery rate is taken to be the final pressure in the manifold divided by the pressure at the beginning of the run. The quoted number is the result of averaging over six runs with durations from 6 hours to 17 hours. The quoted uncertainty is the standard deviation in the measurements.

[Ade10] S. Ade, IEEE Spectrum, **47**, 16 (2010).

[Eli04] S. R. Elliott and J. Engel, J. Phys. G, **30**, R183 (2004).

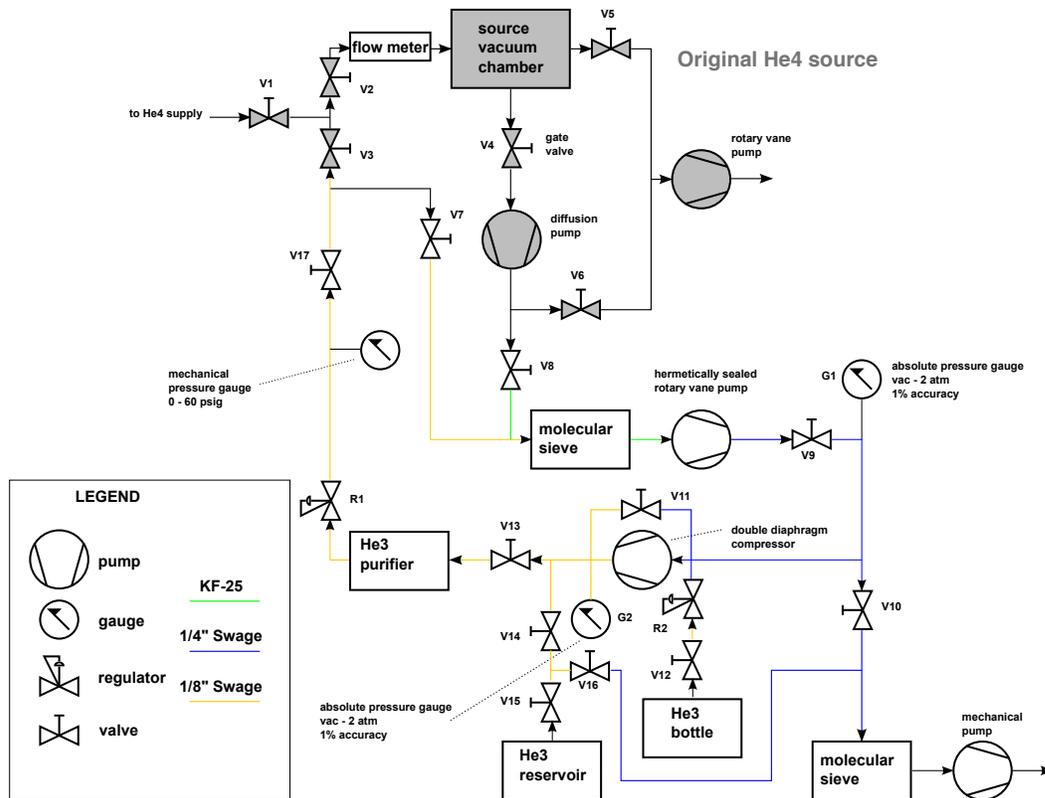


Figure 7.25: Schematic diagram of the ^3He recirculation system. The shaded components are the original source parts.

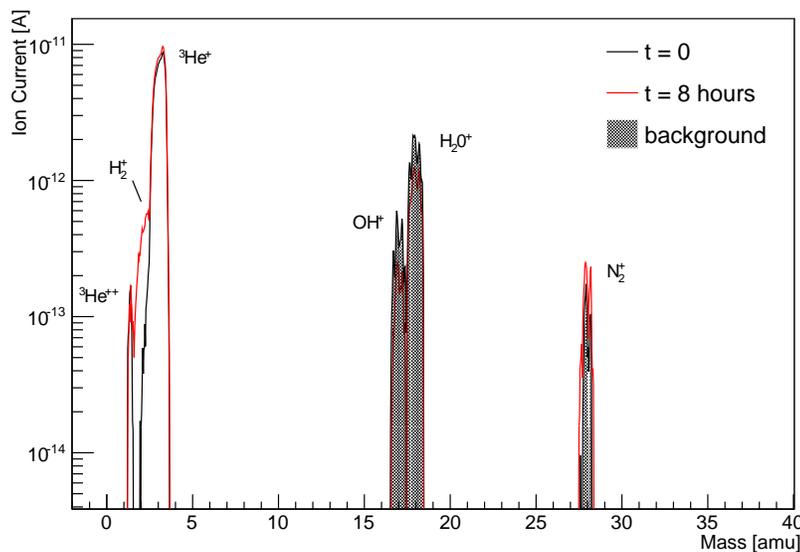


Figure 7.26: RGA scans taken at the source box at the time of initial fill and after 8 hours of recirculation.

7.3 The LENA Accelerator and Ion Sources

7.3.1 LENA's New ECRIS Acceleration Column: Overview

A.L. COOPER, K.J. KELLY, E. MACHADO, J. SURBROOK, J.R. DERMIGNY, C. CALDORADO, J. MARTIN, A.E. CHAMPAGNE, T.B. CLEGG, I. POGREBNIYAK, C. TYSOR, P. THOMPSON, M. EMAMIAN, B. WALSH, B. CARLIN, *TUNL*;

The electron cyclotron resonance ion source at LENA underwent a complete upgrade of its acceleration column and microwave system. This allows the stable production of the high-intensity pulsed proton beams needed for the study of nuclear reactions important in understanding stellar nucleosynthesis. The various aspects of the project are summarized here, along with the initial performance results.

Background

The science objective of the Laboratory for Experimental Nuclear Astrophysics (LENA) is the characterization of nuclear reaction rates central to the stellar life cycle. Nuclear cross sections at stellar core fusion energies—tens to hundreds of keV—are pivotal for calculating nuclear reaction rates but can be vanishingly small because of the dominant Coulomb repulsion between reacting nuclei. Hence we employ intense proton beams and multiple background suppression techniques to raise our signal-to-noise ratio.

In order to cover the energy range from 110 to 1000 keV, we use two accelerators: a modified 1 MV electrostatic accelerator and an electron cyclotron resonance ion source (ECRIS). ECRIS is used primarily for the production of highly intense beams of hydrogen ions, with currents of around 2 mA, for use in studying low-energy reactions.

ECRIS's previous acceleration tube was built by High Voltage Engineering Corporation to withstand our maximum operating voltage of 200 kV. An extraction system designed at LENA optically mated the source to this acceleration tube [Ces10]. However, inefficient pumping capability, a high flux of secondary electrons, and column heating combined in a cascade to weaken the PVA seals bonding the aluminum electrodes to the glass insulators in the tube, thus creating vacuum leaks. The resulting gas discharges eventually caused permanent damage to several of the insulators.

We therefore decided to design a new tube that would overcome these difficulties. Our goals

were a satisfactory electrode geometry for focusing and accelerating intense H^+ beams to energies between 110 and 230 keV; a better vacuum through a more open geometry and less out-gassing; and magnetic fields to suppress secondary electrons created by beam ionization of any residual gas.

Here we present an overview of the major project components. Details are given in the following contributions.

Project Components

Our starting point in designing the new acceleration column was a column developed by GT Advanced Technologies [Ryd12]. This afforded a more open electrode geometry than in the original ECRIS design, thus allowing for more efficient pumping and less residual gas for the beam to ionize. Simulations of the electrostatic effects were modeled using the software package KASPER, which is described further in Sect. 7.3.2. Simulation calculations eventually led to the geometry and voltage configuration shown in Fig. 7.27. To accomplish effective focusing over the desired beam energy range of 110 to 230 keV, we limited the maximum energy of the beam extracted from ECR plasma chamber to around 40 keV. After extraction from the plasma chamber, the beam is allowed to expand rapidly in diameter to minimize space charge effects. The energy limit on the extracted beam means that it can be strongly focused by two narrow electrode gaps as it leaves the expansion region and begins its acceleration down the column to ground potential through a series of eight wider gaps.

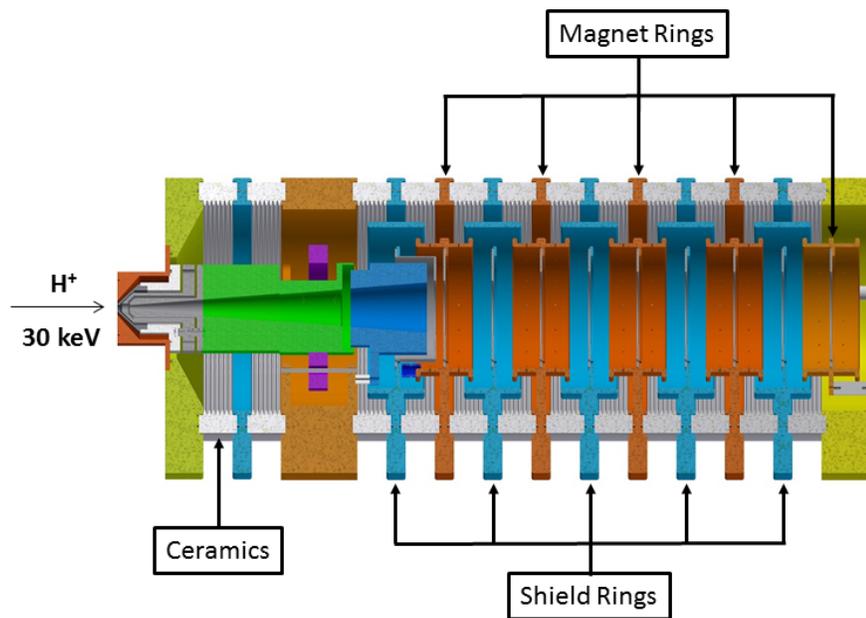


Figure 7.27: A cut-away drawing of the new acceleration column. Protons from the ECR plasma enter from the left. They then undergo a rapid radial expansion before being focused into a parallel beam for acceleration to ground potential.

Transverse magnetic fields were used to suppress any secondary electrons created by beam interactions with residual gas in our new column. They steer the secondary electrons into column electrodes before they can gain any appreciable kinetic energy. The optical effects of magnetic suppression on the beam are not dependent on the beam's velocity profile [How67], so that for any proton injection energy, the magnetic fields will always have the net effect of preserving the beam's dynamics.

The overall structural and high-vacuum support of ECRIS's new column comes from a self-aligning, compression design [Ryd12]. Compression is facilitated by three G10 fiberglass rods, on which all of our electrode and ceramic sections are supported. The use of O-rings to provide high-vacuum seals at the interfaces of the metal and ceramic components avoids the use of volatile adhesives, with their associated out-gassing issues. Similarly, our high-density Al_2O_3 ceramics were chosen to have superior high-vacuum properties and thicknesses great enough to withstand voltage differences well above 20 kV across a section.

Finally, a new extraction system was needed to mate the new acceleration column with the plasma chamber. This too is a modified version of a GT Advanced Technologies design [Ryd12].

Initial Beam Tests and Summary

The new extraction system and acceleration column have been constructed and put into operation at ECRIS. The newfound stability and robustness is exemplified by the absence of sparks and intense x-ray radiation from its regular operation. When high-voltage breakdown occurred during testing, our spark gap system performed as designed. Our magnetic suppression system has decreased the bremsstrahlung x-ray radiation from over 1 R/hr to background levels, or about 0.007 mR/hr. At beam energies of around 160 keV, repeatable beam currents of 12 mA were measured at the unsuppressed beam-stop located about 1.7 m beyond the acceleration column exit. Of this amount, 1.1 mA can be momentum-analyzed and focused to our suppressed target. These currents are roughly 2.4 and 0.85 times those produced by the prior system at these respective positions and at around 165 keV. The aperture of our analyzing magnet is too constricted to transport a larger portion of the beam to target. We are continuing tests and modifications to overcome this issue.

[Ces10] J. M. Cesaratto *et al.*, Nucl. Instrum. Methods A, **623**, 888 (2010).

[How67] F. A. Howe, IEEE Trans. Nucl. Sci., **14**, 122 (1967).

[Ryd12] G. Ryding, Private Communication, 2012.

7.3.2 New ECRIS Acceleration Column: Electrostatic Design

A.L. COOPER, K.J. KELLY, E. MACHADO, J. SURBROOK, J.R. DERMIGNY, C. CALDORADO, J. MARTIN, A.E. CHAMPAGNE, T.B. CLEGG, I. POGREBNIYAK C. TYSOR, P. THOMPSON, M. EMAMIAN, B. WALSH, B. CARLIN, *TUNL*;

Using the software package *sc kasper*, we have modeled the electrostatics and beam-transport properties of a new high-current acceleration column for LENA’s electron cyclotron resonance ion source. Through this effort, we have achieved our goal of a more open geometry for better vacuum pumping while preserving the excellent beam properties necessary for our low-energy nuclear astrophysics experiments over the full range of energies from 110 to 230 keV.

A crucial design goal for a new high-current acceleration column for LENA’s electron cyclotron resonance ion source (ECRIS) is a more open geometry than its predecessor to facilitate better vacuum pumping while preserving excellent beam transport and focusing for over the desired range of final beam energies, from 110 to 230 keV. This required extensive computer simulations of the electrostatic properties and effects.

We used an acceleration-column geometry similar to that developed at GT Advanced Technologies [Ryd12]. The simulations were carried out using a software package known as KASPER, supplied to us by the KATRIN (KARlsruhe TRitium Neutrino) group at UNC. KASPER is a charged-particle propagation and tracking software suite with two main subpackages: KEMFIELD and KASSIOPEIA [Cor14, Fur].

KEMFIELD is an electrostatic field solver that solves Laplace’s equation within charge-free regions using two different methods: the indirect boundary element method (BEM) and, in axially symmetric regions far from charge distributions, a zonal harmonic expansion [Cor14]. With the aid of boundary conditions, zonal harmonic coefficients of a quickly converging expansion are solved in terms of charge densities provided by the initial BEM calculations. The output from KEMFIELD is then passed to the particle-tracking code KASSIOPEIA [Fur]. Using an eighth-order Runge-Kutta integrator to compute particle trajectories, KASSIOPEIA obtains a complete description of the kinematics of charged particles in the user-defined region.

KASPER does not account for space charge effects, so it cannot reliably simulate trajectories within our extraction region, where they are most

significant. Also, any particles that were generated on collisional trajectories with our electrodes were removed from the simulation.

These simulations led to the geometry and associated voltage configuration shown in Fig. 7.28. After initial extraction from the ECR plasma chamber, the beam is allowed to expand radially to minimize space-charge effects before further acceleration. To effectively focus the beam over the desired energy range of 110 to 230 keV, we limited the maximum beam energy from the plasma to around 40 keV. This facilitates additional strong focusing over our entire energy range by the initial electrode gaps, labeled d' in the figure, as the beam emerges from the expansion cone. The electrode spacing of 2 cm for these gaps was chosen to facilitate this strong focusing. The beam then encounters eight successive 5-cm electrode gaps of up to 20 kV each (depending on the final beam energy), which continue to step the voltage to ground. This configuration yields a nearly parallel beam upon exit from the column, so that the beam can be propagated effectively by solenoid lenses further down the beamline.

We assumed that our ECR plasma provided a maximum current density of about 200 mA/cm², comparable to that at LANL and GT Advanced Technologies [She02, Ryd12]. Our 200 kV, 36 mA Glassman power supply used for acceleration provided a maximum current limit and therefore determined the plasma aperture size from which we extracted the beam. Further details of beam extraction from the ECR plasma are discussed in Sect. 7.3.3.

Our aluminum electrode design is based on the one in GT Advanced Technologies’ Hyperion accelerator [Ryd12]. Two principal elec-

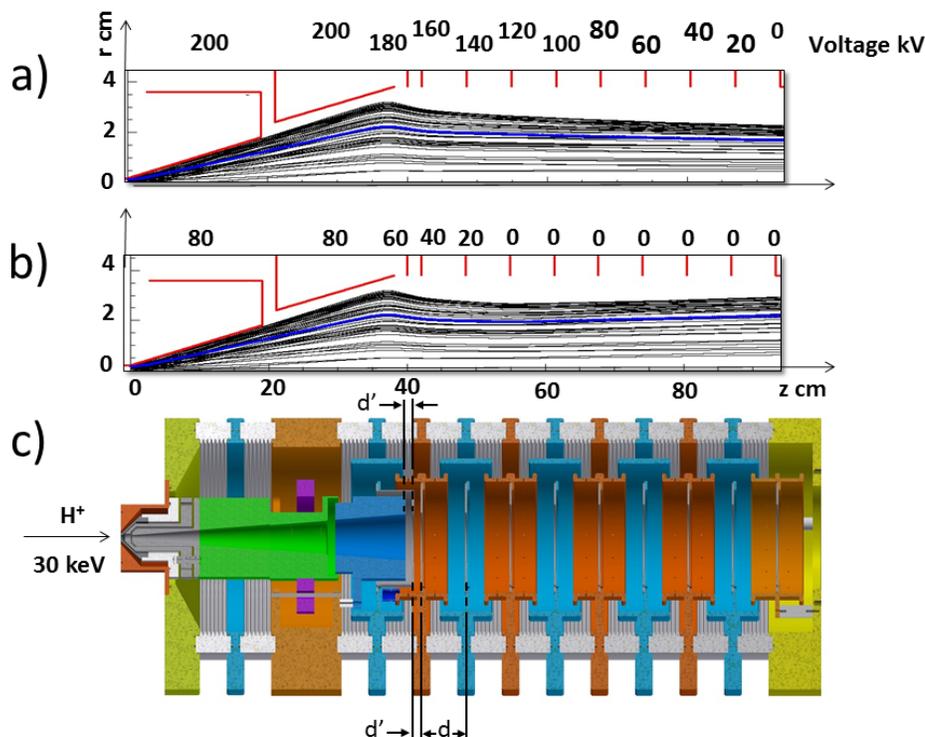


Figure 7.28: Beam profiles from KASPER at our maximum (230 keV) (a) and minimum (110 keV) (b) operating energies. Average radii are illustrated by thick blue lines. A scaled drawing of the column (c) is included.

trode geometries compose the main part of the column: *shield-ring* and *magnet-ring* electrodes. (The function of the magnets is discussed in Sect. 7.3.3.) These electrodes have cylindrical ends which extend axially in both directions and together block any line-of-sight trajectory for stray beam charge to reach our ceramic insulators. Twenty-eight neodymium magnets are mounted on the outside circumference of the magnet-ring electrodes and are not exposed to beam or secondary electrons.

Our high density Al_2O_3 ceramics were chosen to have superior high-vacuum properties and enough thickness to withstand voltages well over 20 kV per section. Undulations on the high vacuum side extend the surface spark length; the atmospheric side is glazed for cleanliness. We rely on spark gaps to prevent damage to the column. The gap size of 17.5 mm was calibrated at atmosphere to fire at 30 kV.

The voltage gradient of ECRIS's new acceleration column, and hence its allowed leakage current, is supported by the resistance of parallel flowing, chilled, de-ionized water channels. We determined their length, cross-sectional area, and

radii to yield 4 to 5 mA of leakage current at a maximum operating voltage of 200 kV. We have the ability to control both the conductivity and the temperature of the de-ionized water supplied to these channels. This allows some adjustment of our leakage current to suit the needs dictated by beam-loading or the limits of the Glassman power supply.

Figure 7.28 shows the final geometry and the resulting beam profiles at our maximum and minimum final beam energies. The beams profiles at both energies are similar and show the production of a parallel nearly beam.

[Cor14] T. J. Corona, Ph.D. thesis, University of North Carolina, Chapel Hill, NC, 2014.

[Fur] D. Furse, Ph.D. thesis, Massachusetts Institute of Technology, Cambridge, MA, In preparation.

[Ryd12] G. Ryding, Private Communication, 2012.

[She02] J. Sherman *et al.*, Rev. Sci. Instrum., **73**, 917 (2002).

7.3.3 New ECRIS Acceleration Column: Secondary Electron Issues

A.L. COOPER, K.J. KELLY, E. MACHADO, J. SURBROOK, J.R. DERMIGNY, C. CALDORADO, J. MARTIN, A.E. CHAMPAGNE, T.B. CLEGG, I. POGREBNIYAK, C. TYSOR, P. THOMPSON, M. EMAMIAN, B. WALSH, B. CARLIN, *TUNL*;

We discuss features of the new ECRIS acceleration column that are designed to reduce residual gas in the tube and suppress any secondary electrons. A compression structure uses O-ring seals instead of volatile adhesives, to support its high vacuum environment. Electron suppression is achieved through alternating transverse magnetic fields

In performing low-energy nuclear astrophysics reaction-rate measurements, it is not enough to have a high-current, well focused beam. In replacing the old acceleration column of the electron cyclotron resonance ion source (ECRIS), we wanted to reduce the amount of residual gas in the acceleration tube to minimize the production of secondary electrons, and we wanted an effective means to suppress any such electrons before they could create bremsstrahlung x-rays or damage parts of the column structure. To accomplish this, we chose compressional support for our column structure, thus avoiding the use of volatile adhesives, and magnetic fields for secondary-electron suppression.

Compression Design

The overall structural and high vacuum support of the new ECRIS column comes from a self-aligning, compression design [Ryd12]. Such compression is facilitated by three G10 fiberglass rods on which all of our electrode and ceramic sections are supported. As large hex nuts on the ends of these rods are tightened, all of the electrodes and ceramics are squeezed together, and the O-rings that provide high vacuum seals at their interfaces are compressed.

The leading benefit of this design is that we no longer rely on volatile adhesives to obtain a high vacuum seal, avoiding the out-gassing issues associated with adhesive joints [Hyd05]. The materials used in the electrodes and ceramic components are discussed in Sect. 7.3.2. The use of O-rings, coupled with the more open electrode geometry of the new column, results in improved vacuum inside the acceleration tube and thus less production of secondary electrons.

Transverse Magnetic Field Effects

When secondary electrons are produced by beam interactions with residual gas in our new column, transverse magnetic fields are an effective means for suppressing them. The magnetic fields steer any secondary electrons into the column electrodes before they gain any appreciable kinetic energy, thereby limiting the maximum intensity of bremsstrahlung X-rays produced upon collision and offering a solution to the radiation problems of our prior system.

In addition, the optical effects of magnetic suppression on the beam are not dependent on the beam's velocity profile [How67], and the suppression system is electrostatically decoupled from the column electrodes, along with all of their vulnerabilities to electron and beam loading effects [Hyd05]. This means that for any proton injection energy, the magnetic fields will always have the net effect of preserving the beam's dynamics. Inclined electric field suppression systems, on the other hand, can produce divergent beam profiles [How67].

As discussed in Sect. 7.3.2, two principal electrode geometries compose the main part of the column: shield-ring electrodes (bright blue in Fig. 7.29) and magnet-ring electrodes (rust color in the figure). Twenty-eight neodymium magnets are mounted on the outside circumference of the magnet-ring electrodes and are not exposed to the beam or to secondary electrons. These magnets create the transverse fields that rapidly steer any secondary electrons into the electrodes.

We used a simplified kinematic model to estimate the resultant transverse displacement of our proton beam centroid as it passes through regions of transverse magnetic fields in the ECRIS

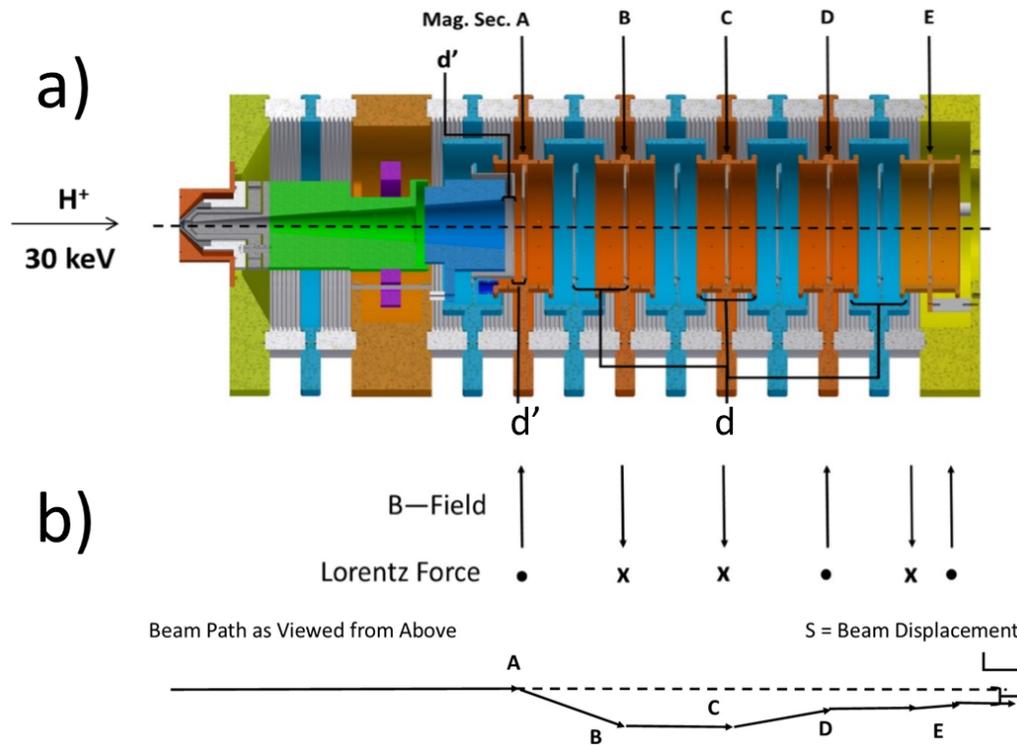


Figure 7.29: A scaled cut-away drawing of the column, along with the associated magnetic field orientations, the directions of the Lorentz forces, and the axial beam displacements caused by our transverse magnetic suppression system.

column. The Lorentz forces that act on an axial proton on its journey down the acceleration column were considered and are illustrated in part (b) of Fig. 7.29). Since the injection energy of the proton, the electrode axial spacings, and the voltage differences across each gap were all known from our electrostatic design, the proton's axial acceleration and transit time across any region of the column were calculable. By alternating the direction of the magnetic field sections along the length of the column, an initially axial proton experiences equal and opposite impulses at each

section and takes the path shown in the figure.

[How67] F. A. Howe, *IEEE Trans. Nucl. Sci.*, **14**, 122 (1967).

[Hyd05] H. R. M. Hyder, In R. Hellborg, editor, *Electrostatic Accelerators*, Particle Acceleration and Detection, pp. 123–146. Springer Berlin Heidelberg, 2005.

[Ryd12] G. Ryding, Private Communication, 2012.

7.3.4 ECRIS Upgrade: The Plasma Extraction System

A.L. COOPER, K.J. KELLY, E. MACHADO, J. SURBROOK, J.R. DERMIGNY, C. CALDORADO, J. MARTIN, A.E. CHAMPAGNE, T.B. CLEGG, I. POGREBNIYAK C. TYSOR, P. THOMPSON, M. EMAMIAN, B. WALSH, B. CARLIN, *TUNL*;

As part of the complete upgrade of the electron cyclotron resonance ion source at LENA, we designed a new extraction system to mate the existing plasma chamber to the new acceleration column. The design is self-aligning and consists of five main elements. It has larger apertures than its predecessor, to allow for the higher beam currents needed for our low-energy nuclear astrophysics experiments.

The electron cyclotron resonance ion source (ECRIS) at LENA has recently undergone a complete upgrade with the construction and installation of a new acceleration column to allow for the production of higher beam currents. Our previous extraction system was designed to smoothly mate the electron cyclotron resonance plasma chamber to the old acceleration column. With the advent of the new column, it was necessary to design and construct a new extraction system with larger apertures to accommodate the higher beam currents. The final design is shown in Fig. 7.30. The plasma chamber is at the left of the figure. Beam extracted from the plasma undergoes a rapid radial expansion in the expansion cone, and then encounters two narrow strong-focusing electrode gaps (shown at the extreme right of the figure), located at the beginning of the acceleration column.

As noted in Sects. 7.3.1 and 7.3.2, in order to accomplish effective focusing over the desired beam energy range of 110 to 230 keV, we chose to limit the maximum extracted beam energy to around 40 keV. This facilitates additional strong focusing over our entire energy range by the two narrow electrode gaps the beam encounters as it emerges from the expansion cone and starts down the acceleration column. We assumed that our ECR plasma provided a maximum current density of around 200 mA/cm², comparable to that at LANL and GT Advanced Technologies [She02, Ryd12]. Our 200 kV, 36 mA Glassman power supply, used for acceleration, provided a maximum current limit and therefore determined the plasma aperture size from which we extracted beam. Extraction and focusing of this beam is optimized by varying the gap between

the plasma aperture and the extraction electrode seen in Fig. 7.30. A suitable range of extraction gap sizes (see Table 7.4) was estimated using the Child-Langmuir Law [Chi11, Lan13].

The new extraction system for LENA's ECRIS is a modified version of the one used in the Hyperion accelerator [Ryd12]. Positive hydrogen ions created in the plasma chamber leave through its aperture toward the first grounded extraction electrode of the movable extraction system. "Ground" here is the potential of the high voltage table. The following suppression electrode, biased up to -2 kV, impedes backstreaming electrons from reaching the plasma chamber. The second ground electrode defines the conical region to guide the expanding beam into the variable-voltage electrode. It also provides further drift length for the expanding beam. The variable-voltage electrode can be biased to positive potentials from 0 to $+10$ kV.

Concerning materials, the removable apertures of the plasma, suppression, and both ground electrodes are all molybdenum, while the variable voltage electrode is aluminum. Present aperture diameters are given in Table 7.4 but are subject to change.

The extraction, suppression, and ground electrodes depicted in the figure form a self-aligning system that is movable axially [Ryd12]. They are held together by compression and are insulated from each other with Vespel washers, which also provide the necessary vacuum-tight connections for the circulation of chilled deionized water. This system of cooled electrodes is mounted on an axially adjustable platform [Alt04], which is gear-driven by a stepper motor outside the vacuum system. The average gap size and range

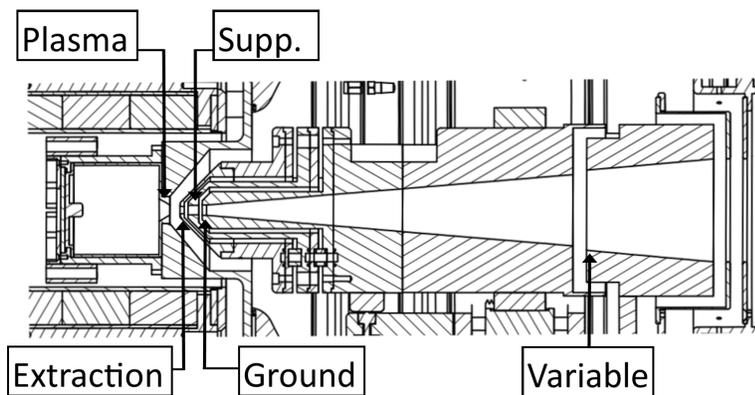


Figure 7.30: Detailed drawing of the plasma chamber, shown at the left, and the axially adjustable extraction system with its electrodes labeled. The strong focusing gaps at the start of the acceleration column are shown at the far right, after the expansion cone. Column five of Table 7.4 gives the aperture diameters and extraction gap range.

Table 7.4: Comparison of Extraction System Aperture Diameters (mm)

Parameter	LANL	GT	LENA (Prior)	LENA (New)
Plasma Aperture	8.6	8.0	5.0	6.50
Extraction Aperture	6.6	7.0		5.00
Suppressor Aperture	8.8	11.0	4.5	8.25
Ground Aperture	9.0	10.0	5.0	7.60
Extraction Gap	12.9	7.52	6.83	12.5 (± 6)

between the plasma aperture and the extraction aperture is given in Table 7.4. Our apertures are smaller than those used at LANL and GT Advanced Technologies but larger than those in the prior ECRIS extraction system.

The new extraction system, coupled with the new acceleration column successfully combined in initial beam tests to produce significantly higher beam currents emerging from the column than was the case with the previous ECRIS design.

[Alt04] G. D. Alton and H. Bilheux, *Rev. Sci. Instrum.*, **75**, 1431 (2004).

[Chi11] C. D. Child, *Phys. Rev. (Series I)*, **32**, 492 (1911).

[Lan13] I. Langmuir, *Phys. Rev.*, **2**, 450 (1913).

[Ryd12] G. Ryding, Private Communication, 2012.

[She02] J. Sherman *et al.*, *Rev. Sci. Instrum.*, **73**, 917 (2002).

7.3.5 The LENA ECR Ion Source: Beam Pulsing

K.J. KELLY, A.L. COOPER, J.R. DERMIGNY, T.B. CLEGG, B.P. CARLIN, A.E. CHAMPAGNE, E. MACHADO, C. CALDERADO, C. ILIADIS *TUNL*

We report on progress with regard to pulsing the ECR ion source at LENA. Pulsed data acquisition has been established and tested through measurements of the $^{18}\text{O}(p,\gamma)^{19}\text{F}$ resonance at $E_r^{\text{cm}} = 151$ keV using the ECR source prior to its recent upgrade. The newly upgraded ion source has also been tested with proton energies up to $E_p = 110$ keV yielding maximum pulsed beam currents of about 5 mA prior to mass and energy selection via an analyzing magnet.

The electron cyclotron resonance (ECR) ion source at LENA holds the world record for the highest intensity proton beams on target for research in nuclear astrophysics. Presently, the maximum observed beam current on target is 2.05 mA, averaged over 1 C of integrated beam charge [Buc15]. The target heating that occurs as a result of direct current (DC) beams of this intensity can be mitigated using direct water cooling of the target.

The ECR source is currently being upgraded with the goal of increasing the output beam intensity by an order of magnitude, reaching approximately an unprecedented 20 mA proton beam current on target. The target heating resulting from this beam intensity is enough to melt the target backings used at LENA, even with direct target water cooling. Therefore, it is necessary to pulse the ECR beam on target when these large beam currents are used.

Successful beam pulsing has recently been achieved by pulsing the microwave input power used in the creation of an ECR plasma. No adjustments of the high voltages applied to the plasma chamber or high voltage table are required with this pulsing method. Instead, the plasma is fully extinguished between beam pulses and subsequently reignited during each pulse.

This repeated cycle of extinguishing and striking a plasma presented a significant challenge with regard to the impedance matching for microwave transfer between the waveguide and plasma chamber. The waveguide impedance is adjusted via a three-stub tuner and is typically optimized prior to striking a plasma by introducing microwave power and minimizing the amount of power reflected back towards the magnetron.

However, when a plasma is created within the plasma chamber the impedance of the plasma chamber changes drastically. This results in a significant increase in microwave power reflected back towards the magnetron. During DC beam extraction this change is accounted for by simply optimizing the waveguide impedance once more until nearly all microwave power is transferred to the plasma chamber. If the microwave power is switched off while the waveguide impedance is matched to that of the plasma chamber with a plasma present, then the plasma is extinguished and the plasma chamber impedance is no longer matched by the waveguide. Thus, when microwaves are reintroduced to the plasma chamber, the majority of the microwave power is reflected away from the source and it is difficult to re-strike the plasma without adjusting the three-stub tuner.

It was discovered that the key to maintaining a long-lasting and reliable pulsed plasma is to intentionally introduce an impedance mismatch between the plasma chamber and waveguide. If this is done properly, there will be a significant amount of microwave power transferred into the plasma chamber both with and without a plasma present. Therefore, an intense plasma can exist while microwave power is on and a plasma can be easily re-struck after the plasma has been extinguished.

An example of the observed beam pulses from the previous ECR source is shown in Fig.7.31. The blue and yellow traces are measured from DC and pulsed ECR beams, respectively. Note that the maximum current achieved during a pulse is approximately equivalent to the DC beam current. This implies that little to no beam current

decrease is experienced going from DC to pulsed operation modes. The rise time of the measured current signal is about 500 ns.

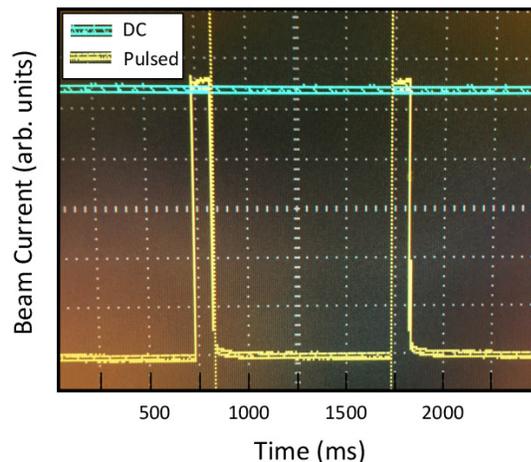


Figure 7.31: Waveform of measured beam current with ECR beam pulsing for 100 ms on, 900 ms off.

In Fig.7.31 pulsing was carried out with the microwave supply on for 100 ms of every second and off the other 900 ms. Given that the proposed maximum ECR beam current on target after the upgrade is a factor of 10 greater than the present observed maximum, this ratio of time with beam-on to time with beam-off would achieve a 10% duty cycle with respect to the current maximum observed beam current on target. In other words, we could potentially provide beam on target with ten times the original beam intensity, but only for one tenth of the time. Pulsing beam on target in this way provides the same net power deposition on the target as was previously obtained.

The data acquisition system at LENA was updated to allow discrimination between beam-on and beam-off data. As a test of this method and of the beam pulsing method described above, data were taken on the $^{18}\text{O}(p,\gamma)^{19}\text{F}$ resonance at $E_r^{\text{cm}} = 151$ keV. Data were acquired with both DC and pulsed beams on target using beam currents of 37 and 370 μA , respectively. No target degradation occurred between data sets. This choice of DC and pulsed beam currents simulated the data acquisition improvements that would be obtained by increasing the present maximum ECR beam current on target by the proposed amount.

Data obtained on this resonance using DC and pulsed ECR beams are shown in Fig. 7.32 as

the red and black histograms, respectively. The pulsed spectrum contains only the data taken when beam was on target. The peak shown at channel 918 is from the ^{19}F decay initiated by proton capture onto ^{18}O , while the peak labeled ^{208}Tl is a common environmental background line. Note that since the net beam charge accumulated on target is nearly identical between DC and pulsed data sets, the resonance peak at channel 918 is nearly unchanged. However, the total time during which pulsed data were taken is one tenth that of the DC data set. Thus, the intensity of the environmental background line from ^{208}Tl decreased by the same factor in the pulsed data set. This makes clear the ability of pulsed beams to drastically reduce environmental background and is a major advantage of a pulsed ECR beam.

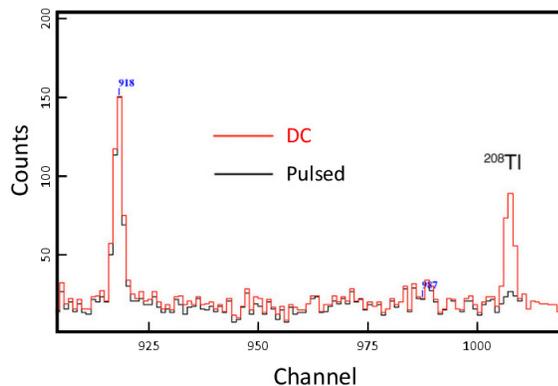
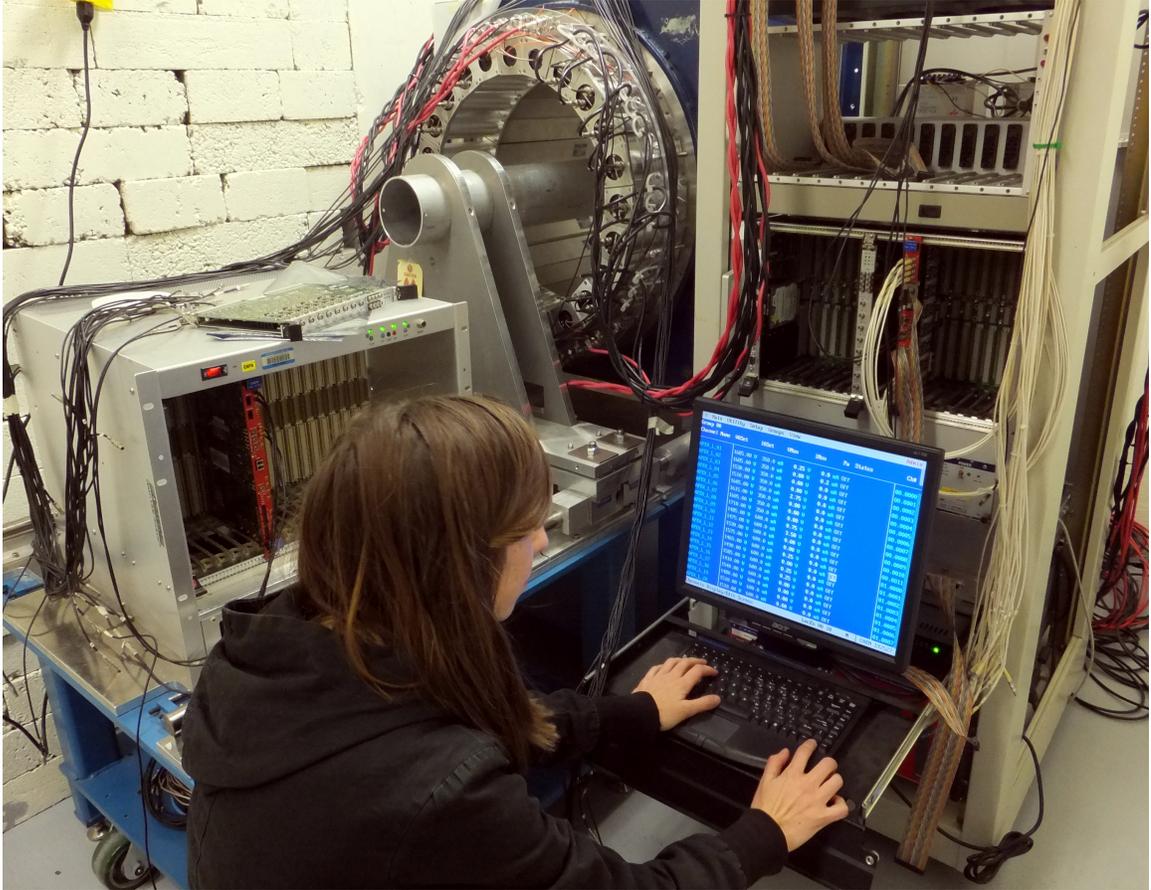


Figure 7.32: Data taken on the 151-keV resonance in $^{18}\text{O}(p,\gamma)^{19}\text{F}$ using DC (red) and pulsed (black) ECR beams.

The upgraded ECR source, in its present state, has also been tested using beam pulsing despite issues with its current operation. A maximum pulsed beam current before the analyzing magnet of 5 mA was observed using a total beam energy of up to 110 keV. This beam current was obtained with beam optics that are not ideal for beam transport but had to be employed due to limitations at the present stage of the upgrade. Considering that the maximum observed DC ECR beam current before the analyzing magnet prior to the upgrade and with near perfect optical conditions was only about 4.5 mA, this is a promising sign that the upgraded ECR source will significantly outperform its previous iteration.

[Buc15] M. Q. Buckner *et al.*, Phys. Rev. C, **91**, 015812 (2015).



GRADUATE STUDENT CHELSEA BARTRAM FROM UNC IS SHOWN WORKING WITH THE APEX NAI DETECTOR ARRAY. THIS DETECTOR ARRAY IS BEING USED BY TUNL FACULTY MEMBER REYCO HENNING AND HIS RESEARCH GROUP TO SEARCH FOR CP VIOLATION IN ORTHOPOSITRONIUM.

Nuclear Instrumentation and Methods

- **Detector Development and Characterization**
- **Data Acquisition Hardware and Software Development**

The diverse experimental research program at TUNL requires continual improvement to the lab's accelerator systems, along with the design and acquisition of improved detectors and data collection electronics. This is especially critical for the nuclear astrophysics and fundamental symmetries groups, where very low counting rates relative to the environmental backgrounds are the norm.

In the age of digital-electronics for data acquisition, researchers at TUNL are modernizing their detector systems and analysis methods. These efforts are coming to fruition now, paving the way for unique experiments with unprecedented sensitivity.

The current reporting period produced a number of nuclear instrumentation and methods accomplishments that will enable forefront research to be realized in the coming years.

At the LENA accelerator facility, a novel, borated liquid scintillator for fast neutron detection was characterized using fast digitization of the detector's anode signals and rigorously-tested pulse-shape algorithms. This achievement will allow sensitive neutron detection from neutron-producing reactions important for astrophysics. Fast digitization was also used for event-position reconstruction. By collecting timing signals from two ends of a long NaI(Tl) scintillator bar, the position of a γ -ray interaction can be determined. Algorithms were developed to extract these timing signals, which will be essential in the effort to investigate CP violation in positronium decay. Additionally, simulation of a new HPGe clover geometry has been performed to explore what new measurements would be possible with an upgrade to the current LENA γ -ray detection system.

A number of efforts are underway to upgrade the Enge Split-Pole Spectrograph, following an operational hiatus. The focal plane detector has been refurbished and tested with radioactive sources. For data acquisition, a VME-based system is under active development. Because a flexible and expandable system is required for upgrades in the future, new software systems are being investigated. To ensure a common interface between those systems and to allow an easy-to-use interface, a fast data transfer library was developed and tested. This library uses existing technology to transfer data over a network interface at 95% of the available bandwidth with very little overhead.

In addition, new controls for the Enge split-pole sub-system are being developed. In the past year, an advanced, distributed control system based on Raspberry Pi hardware and the EPICS (Experimental Physics and Industrial Control System) tools was developed for the magnet controls. It will be extended to stepper motors and vacuum control hardware in the coming year. This technology requires significantly less overhead than previous systems, and allows us to tie alarm systems into the data acquisition system for more robust data analysis.

Data analysis has seen some revolutionary developments at TUNL over the reporting period. The astrophysics group designed a new method to analyze singles and coincidence γ -ray pulse-height spectra using spectrum-wide fitting. This method was enabled by past success in accurately modeling detector response at LENA, and will provide robust, sensitive cross-section analysis in the future.

8.1 Detector Development and Characterization

8.1.1 Characterizing TUNL’s Surface Barrier Silicon Detectors

F.E. PORTILLO, R. LONGLAND, *TUNL*; K. KOWAL, *Lewis and Clark College, Portland, OR*.

A large selection of TUNL’s surface barrier silicon detectors was tested to determine their condition and performance. Tests involved measurements of the leakage current present in the detectors, their resolution, and, in many cases, of their bias voltage. After testing, each detector was placed in a box with a label indicating its condition and information relevant for its usage.

Due to their small size, high resolution and efficiency, as well as their relatively low cost, surface barrier silicon detectors are useful tools in many nuclear physics laboratories. They can be used for particle spectroscopy or in E - ΔE detector arrays to identify particle species in low-energy nuclear reactions. A large inventory of these detectors exists at TUNL. However, their operating characteristics are poorly documented. One convenient method for determining the health of a silicon detector is to measure its leakage current, which results from the motion of charge carriers created within the detector without the incidence of a particle.

Detectors were tested under high-vacuum conditions in a dedicated Si-detector testing station. The voltage applied to the detectors was provided by an Ortec 710 Quad Bias Supply. The detector’s output was connected to an MSI-8 device (an eight-channel preamplifier + shaper + time-filter amplifier), and then to an Ortec EASY-MCA-8K multi-channel analyzer connected to a computer to generate the spectra using the software MAESTRO.

The source used was a ^{241}Am spot painted on the center of a circular metallic disc. It had an activity of $1.34 \times 10^{-2} \mu\text{Ci}$. ^{241}Am decays via α -particle emission into ^{237}Np in five different energy states, with energies and approximate branching ratios of 5.546 MeV (< 1%); 5.503 MeV (< 1%) 5.486 MeV (85%); 5.443 MeV (12%); 5.387 MeV (2%). Two other ^{241}Am sources were found to contain contamination that degraded their alpha-particle energy spectra.

Before testing, the serial number etched in each detector was checked with the one written on its box. The detectors were then grouped by manufacturer and by active area size. There were

several detectors without a box, so no information was available for them. This necessitated an extra procedure to determine their parameters.

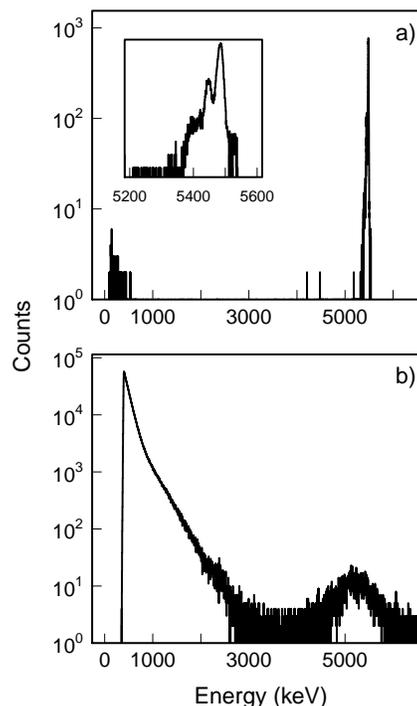


Figure 8.1: Energy spectra measured in (a) the reference detector and (b) a bad detector. The inset in (a) expands the region around 5.4 MeV, showing peaks at 5.443 MeV and 5.486 MeV.

To determine the condition of each detector three main parameters were tested: 1) resolution, 2) leakage current, and 3) noise in the signal. Resolution was obtained by measuring the full width at half maximum (FWHM) of the most intense peak in the spectrum, which is due to de-

cay to the 5.486-MeV state in ^{237}Np . Leakage current values were recorded directly from the bias supply used, and signal noise values were measured using an oscilloscope. To determine the condition of a detector, another detector (Ortec BU-014-050-100) known to be good was used as a reference. This allowed us to check that the source used, the electronics, and the software were working correctly.

A detector was considered to be in good condition if: a) its resolution was within 20 keV of that specified by the manufacturer and b) if its leakage current represented a drop in the applied voltage of no more than 15%. The first parameter tested was the noise in the detector's signal with no voltage applied. In almost all cases, detectors with high noise signals generated spectra with a high amount of noise and poor resolution as shown in the lower portion of Fig. 1. The wide peak in the low-channel region is due to the high noise of the detector. The peak just above 5 MeV seen in the spectrum from the reference detector is also present but is appreciably broadened by noise.

The applied voltage in the detector was determined by multiplying the measured leakage current by $20\text{ M}\Omega$, the resistance of the MSI-8, and then subtracting the result from the applied voltage. This process was done for four different applied voltages, up to the manufacturer's specification. The final stage was to measure the FWHM of the 5.486-MeV peak in the spectra. Since the activity of the source was low, these measurements were done only for the bias voltage and for the voltage that produced the smallest signal noise. The value obtained for each FWHM was compared with the resolution specified by the manufacturer.

The detectors that had no box required special treatment because there was information about their resolution, depletion-region depth, effective area, and bias voltage. The first procedure was to measure an approximate bias voltage. This was done by carefully increasing the applied voltage on the detector until the smallest noise signal was observed on the oscilloscope. Knowing the bias voltage we could estimate the depletion region's depth by using a nomogram in the manufacturer's manual [Ort12]. The active area was obtained by comparing the detector with other detectors whose geometric characteristics were known. Finally, by measuring the FWHM of the 5.486-MeV peak in the spectrum generated at the bias voltage obtained previously, we could determine its resolution.

A total of fifty detectors were tested; twenty-one were found to be bad and were discarded. Every good detector was placed in a box with new labels indicating its condition and relevant information. Its bias voltage, resolution, and leakage current were written on the labels. As a result of this project, a spreadsheet containing information about each detector, the parameters tested, and the results obtained was created. Finally, the ultimate purpose of this project was to create an on-line database with information and spectra for each detector. This will allow TUNL researchers to find easily the appropriate silicon surface barrier detectors for their experiments.

[Ort12] Ortec, *Introduction to Charged-Particle Detectors.*, <http://www.ortec-online.com/introduction-charged-particle-detectors>, 2012, [Accessed June 7, 2015].

8.1.2 Commissioning the Enge Focal Plane Detector

K.M. KOWAL, *Lewis and Clark College, Portland, OR*; C.A. MARSHALL, R.L. LONGLAND, *TUNL*

The Enge Split-Pole Magnetic Spectrometer is used to measure the energy of charged particles in nuclear reactions by recording their positions in a focal plane detector. We constructed the detector, improved its vacuum system, and integrated the detector's signals with a data acquisition system. Position measurements were recorded using a collimated ^{241}Am source. Further development is required to improve the stability and performance of the detector.

The precise measurement of nuclear reactions provides the foundation for nuclear astrophysics and the predictions of stellar models, where key reactions provide constraints on nucleosynthesis and energy production in stars [Wie12]. The building blocks for understanding these reactions are nuclear cross sections, and particle spectroscopy makes it possible to determine them, particularly when direct laboratory measurements are not feasible.

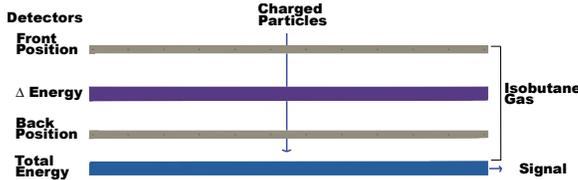


Figure 8.2: The focal plane detector is comprised of four separate detectors, enabling it to identify particles and capture their spread in position

The energy of charged particles exiting nuclear reactions can be precisely measured using the Enge split-pole spectrometer [Spe67], which bends charged particles through a magnetic field. Their orbital radii can then be related to their initial energy. The energy resolution of the split-pole spectrograph is limited by energy straggling in the target and the resolution of the detection system placed at the focal plane. Energy straggling in the target typically amounts to less than 10 parts per million, so the challenge arises in designing a detector capable of the same resolution as the Enge. The focal plane detector was developed to achieve this goal [Hal99]. It also allows us to determine particle type, energy, and trajectory.

The focal plane detector, shown in Fig. 8.2, is comprised of four main elements: front and back

position sensors, separated by an energy loss section and followed by a total energy section. The position and energy loss sections are filled with isobutane gas, which is easy to ionize and relatively noncorrosive to the inside of the detector.

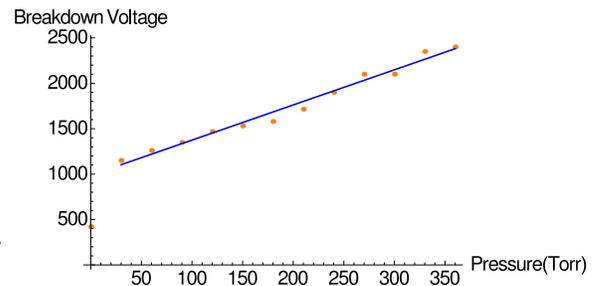


Figure 8.3: Breakdown voltage in the position section's high voltage wires as a function of detector pressure.

From the two position detectors, we capture the location and trajectory of the charged particles. Signals generated in the position sections travel to both ends of a delay line, resulting in a time difference in signal arrival times that depends on the position an event occurred. Using a time-to-amplitude converter, we reconstruct the time difference between the two signals in the front detector and identify where the particle entered the detector. From the additional use of the back position detector, we measure the angle at which the particle travels. This allows us to correct for aberrations in the focal plane and imprecise positioning of the detector. By capturing the particles' trajectories, the detector enables us to ray-trace this plane in the computer after the data measurement and thus obtain higher energy resolution.

The energy loss detector uses a proportional counter. Its purpose is to aid in particle iden-

tification. In some cases, two charged particle species entering the detector can carry the same total energy, but, as is the case with an alpha particle and a proton, they differ in their rate of energy loss in the proportional counter. This enables us to separate the events for the particle type of interest.

In the final section a scintillator stops the particles and measures their total energy. Our design incorporates aluminum foil surrounding the scintillator. The foil serves both to protect the detector from external light and to internally reflect the emitted photons created by the incoming charged particles.

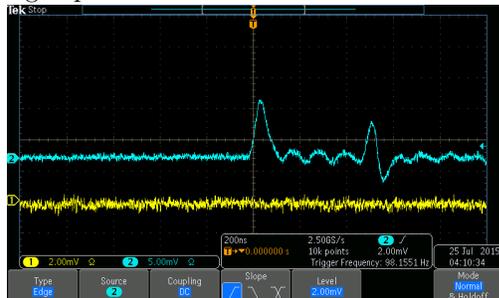


Figure 8.4: Front left position signal. The existence of multiple peaks is problematic.

One challenge in operating this detector is that it is pressurized equipment placed inside a vacuum chamber. O-rings are used between sections to create a vacuum seal. To prevent the cracking or breaking of the o-rings due to overstretching, custom o-rings were spliced and their joints sanded down. A combination of sand paper and Baretex was used to ensure a smooth sealing surface on the aluminum pieces where the o-rings sit. In addition, any wrinkles in the aluminum foil surrounding the scintillator in the total energy detector pose the potential for vacuum leaks. Liberal application of vacuum grease was found to lessen their impact. Imprecise machining of the feed-through fittings was also repaired using Torr seal. Ultimately, our largest problem was that the machined o-ring grooves in our metal pieces were too deep. Replacements are being constructed.

Another concern with this detector is sparking. Any crease in the aluminized mylar foil used as a ground plane in both the position and energy loss sections can result in a spark. To maximize signal quality, 2000 V must be applied to the anode wires in our position sections. We were able

to apply up to 1500 V sporadically before sparking occurred. This could indicate either dust or a fray in one of the wires. Figure 8.3 shows a potential correlation between the pressure inside the detector and the voltage we were able to reach before sparking occurred. However, these data were taken over a couple of hours, and time may have influenced the detector's performance.

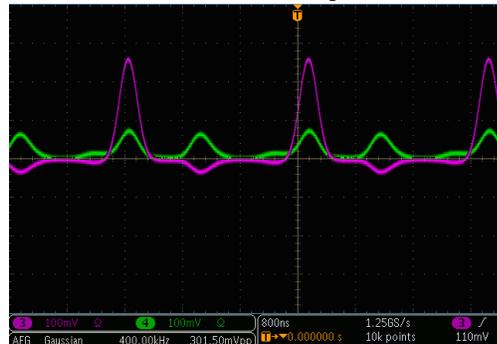


Figure 8.5: Top panel: ungrounded delay line test with the signal (green) and signal generator (purple). Bottom panel: grounded delay test.

Despite these challenges, we were able to collect signals from the position sensitive sections. However, as Fig. 8.4 demonstrates, the signal has two positive peaks instead of the single peak expected. The larger peak on the left will be referred to as the prompt peak. The delay peak is also followed by a negative signal. To investigate the cause of these additional signals, we tested the delay line using a signal generator and found a grounding issue. Figure 8.5 shows that the negative signal as well as the prompt signal disappear when the apparatus is properly grounded.

Future work on this detector will focus on the sparking issues we have found. While we have managed to create vacuum in this device to an acceptable level for obtaining valid signals, sparking will be the next challenge to overcome.

-
- [Hal99] S. E. Hale, Jr., Ph.D. thesis, The University of North Carolina at Chapel Hill, 1999.
 - [Spe67] J. E. Spencer and H. A. Enge, *Nucl. Instrum. Methods*, **49**, 181 (1967).
 - [Wie12] M. Wiescher, F. Käppeler, and K. Langanke, *Ann. Rev. Astro. Astrophys.*, **50**, 165 (2012).

8.1.3 The Characterization of a ^{10}B -Doped Capture-Gated Liquid Scintillator

S. HUNT, C. ILIADIS, R. LONGLAND, *TUNL*

We use a 250 MHz digitizer to characterize the pulse shape discrimination of a BC-523A ^{10}B -doped liquid scintillator with capture-gating capabilities. The time-of-flight method was utilized to measure the intrinsic neutron detection efficiency for fast neutrons with capture-gating and to compare the results with Monte Carlo simulations.

Capture-gated liquid scintillators are an attractive choice for portable neutron spectrometers used to monitor special nuclear materials outside of a nuclear laboratory. Standard liquid scintillators do not determine neutron energies because of their inability to differentiate between fully and partially moderated neutrons. Capture-gating uses standard organic liquid-scintillator fluid doped with materials that have a high absorption cross section for thermal neutrons. A fast neutron striking the detector will lose energy, producing a standard scintillation signal. If the neutron thermalizes, it may capture onto the doping agent (e.g., ^{10}B). The reaction products ($\alpha + ^7\text{Li} + \gamma$ -ray in the case of ^{10}B doping) will lose their energy in the active volume, which will give rise to a characteristic double-peaked signal, allowing for differentiation between fully and partially moderated neutrons. The detector used in this work is a BC-523A scintillator doped with ^{10}B .

Some groups claim it is possible to differentiate the breakup products from incident particles using pulse shape discrimination [Fla09]. To test this, a 19.7 μCi americium-beryllium (AmBe) source was placed about 0.3 m from the detector. The scintillator cell has a diameter of 8.89 cm, and a length of 10.76 cm. A 12-bit 250 MHz (4 ns sampling step) digitizer was used to collect waveforms for a total digitization time of 1.04 μs each. For the pulse shape discrimination (PSD) method, we chose the tail-to-total charge ratio. Figure 8.6(a) shows the PSD for every pulse arriving in the detector, regardless of arrival time. The figure exhibits good discrimination between fast neutrons and γ -rays, and it also shows a separate structure, which we will refer to as the *third branch*. Figure 8.6b shows only those events obtained when a moderation pulse

triggered the digitizer but PSD was only applied to a peak that arrived more than 150 ns after the triggering pulse (long after the moderation pulse has decayed). The lower left oval is due to capture events with no breakup- γ -ray energy deposition, and the branch off of it has γ -ray energy deposition. The events in these two regions will be collectively referred to as the *afterpulse region* events.

Much of the current literature identifies the third branch as the capture events [Fla09]. We analyzed the arrival time of the third branch and afterpulse events, along with the triggering pulse for a waveform containing the events. We discovered that the third branch is not associated with arrival times or triggering pulses that would be consistent with the current understanding of a capture event [Jas04]. However, the afterpulse events match known values for capture-pulse timing and match the current understanding of triggering events.

A second experiment was used to investigate the intrinsic neutron detection efficiency with capture-gating, which is a value rarely reported in the literature. A weak (0.185 μCi) ^{252}Cf source inside an argon gas scintillator was placed 1 m away from the BC-523A detector. When a ^{252}Cf fission event occurred, it created a scintillation signal. This allowed for the time-of-flight method to be used to measure the energy of each detected neutron. During the run, about 3×10^5 neutrons were detected. We measured the detector efficiency at several incident neutron energies, with and without capture-gating. The intrinsic efficiency was calculated according to $\epsilon = \frac{N_d}{N_i} \times 100\%$, where N_d is the total number of neutrons detected, and N_i is the number of neutrons incident on the detector; N_i was calculated from the known intensity of the ^{252}Cf source, the

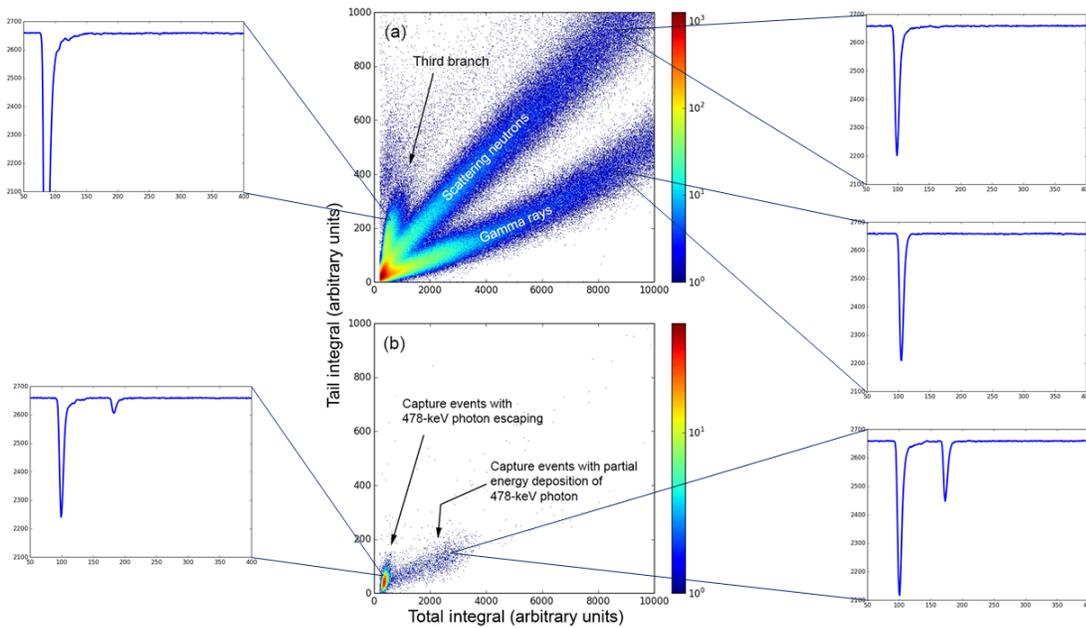


Figure 8.6: Pulse tail integrated charge (PSD number) vs. pulse total integrated charge (energy). (a) All pulses recorded by the digitizer. (b) All pulses arriving at least 150 ns after the digitizer triggered. Each structure is associated with an oscilloscope view (voltage vs. time) of a typical waveform within that structure. Units for the oscilloscope views are arbitrary.

known neutron energy distribution of the source, and the geometry of the setup.

Without capture gating, the measured intrinsic efficiency for fast neutrons with energies between 1 MeV and 4 MeV was approximately 35% and showed little energy resolution. After capture-gating was applied, the resulting efficiency, shown in Fig. 8.7, was about 1%, and the detector had an energy resolution of around 150% (defined as $R = \frac{FWHM}{\theta} \times 100\%$ where θ is the centroid of the pulse height spectrum). The efficiency also decreases with increasing neutron energy, because higher-energy neutrons have a lower chance of fully moderating within the detector, thereby decreasing the likelihood of a capture event.

We also used the GEANT4 toolkit to perform Monte Carlo simulations for efficiencies at energies below the measured data points. Fast neutron detection efficiencies were extracted from the simulations, and were adjusted by a common scaling factor to account for the uncertain light collection in the scintillator, so that the simulations are matched closely to the measured values at the higher neutron energies.

This work was recently submitted for publi-

cation.

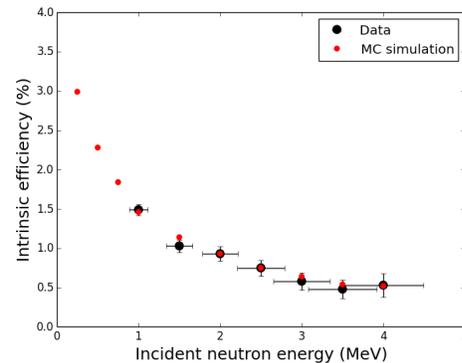


Figure 8.7: Efficiency for incident fast neutrons. The black points are measured data, and the smaller red points are simulated with GEANT4.

[Fla09] M. Flaska and S. A. Pozzi, Nucl. Instrum. Methods A, **599**, 221 (2009).

[Jas04] S. Jastaniah and P. Sellin, Nucl. Instrum. Methods A, **517**, 202 (2004).

8.1.4 Simulation of Proposed New HPGe Clover Detector for LENA

D. LITTLE, A.E. CHAMPAGNE, R. LONGLAND, K.J. KELLY, *TUNL*

Using GEANT4, a new HPGe detector geometry was simulated as a possible future upgrade to the LENA detector system. Efficiency measurements of this new clover geometry were simulated and compared to the efficiency of the current LENA detector setup. Both the peak and total efficiencies were found to be significantly higher.

While the present HPGe detector at LENA has been thoroughly characterized and is very well understood, there are a number of experiments that cannot be feasibly performed with the current setup. These include the $^{20}\text{Ne}(p,\gamma)^{21}\text{Na}$ and $^{25}\text{Mg}(p,\gamma)^{26}\text{Al}$ reactions at low energy. However, with an increase in the efficiency of the current detector apparatus, some of these measurements would become possible.

There are several different ways to improve detector efficiency, with one of the most obvious choices being a switch to a more favorable geometry. While the coaxial geometry for HPGe detectors has been standard for many years, recent improvements on germanium crystal growth have produced larger detectors of increasingly complex design. One particular type of detector geometry that has become more prominent in recent years is referred to as a clover. The majority of clover detectors consist of four nearly cylindrical HPGe crystals tightly packed together in a square.

There are two important advantages that a typical clover detector will have over a comparable coaxial geometry in the detection of γ rays. The first advantage is that, because of the multiple crystals, a clover simply tends to have a larger cross-sectional area than a regular coaxial detector. The large surface area of the four crystals significantly increases the probability of γ -ray detection, especially at energies around a few hundred keV. This is because, at such low energies, the single-site photoelectric effect is the dominating energy-loss process [Kno10], so in those cases the peak efficiency of the detector is directly proportional to its cross-sectional area. However, this effect decreases at mid-range to high γ -ray energies, where Compton scattering and pair-production dominate.

The second major advantage of a clover detector is the γ -ray add-back feature. While having

four detectors working separately still tends to be an improvement on a single detector, by allowing all four of the clover crystals to work together, the detector obtains an appreciably larger peak efficiency. Using the combination of the four detectors, we can sum up the energy depositions from each γ -ray interaction throughout each of the four crystals, thus effectively using the clover as a single detector with four times the volume of a single crystal [Hu98]. Although this may seem elementary, it plays a significant role in the detection of higher energy γ rays, where the effect of the increased cross-sectional area tends to fall off. As the energy increases, the increase in effective volume becomes more and more advantageous relative to a generic coaxial detector, where a comparable volume may be too costly to produce or is altogether too large to manufacture.

However, it is important to quantitatively characterize these advantages before upgrading the LENA detector system to the clover geometry. In order to optimize the gain-to-cost ratio and justify the upgrade, version 9.6 of the GEANT4 nuclear and particle physics software was used to simulate the total and peak efficiencies of both the current LENA setup and the proposed clover detector [Ago03]. The current detector consists of a p-type HPGe crystal surrounded by sixteen NaI scintillation detectors for background rejection. Since the NaI scintillators will still be included with the clover setup, only the HPGe detectors were monitored in the simulation. The current germanium crystal is of a coaxial geometry with a depth of 91.6 mm, a diameter of 89 mm and a dead layer thickness of 1.2 mm. The proposed clover detector consists of four semi-cylindrical crystals, each with a 70 mm by 70 mm front face and a depth of 70 mm (see Fig. 8.8). Additionally, the estimate for the clover dead layer thickness given by Canberra is

approximately 0.5 mm, which would already be a significant improvement over the current detector in terms of the photoelectric peak efficiency.

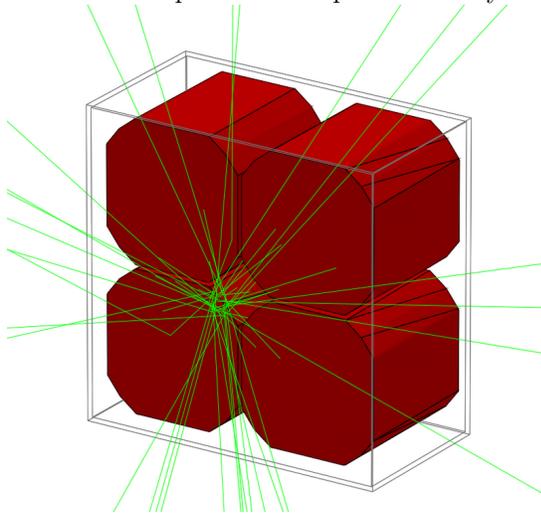


Figure 8.8: A GEANT4 visual simulation of an HPGe clover detector with an isotropic γ -ray distribution.

In both simulations, the distance from the γ -ray origin to the crystal face was set at 15.9 mm [How13]. Efficiencies were simulated for both the LENA detector and the clover using an isotropic distribution of mono-energetic γ -rays running at 1 million events per energy simulated. This process was repeated for energies ranging between 100 keV and 12.4 MeV.

When comparing the simulated efficiencies of the clover and current LENA detector, the peak efficiency of the clover detector is 1.8 times that of LENA at its lowest point and it increases linearly to about 2.6 times the LENA efficiency at the highest simulated beam energy of 12.4 MeV, as shown in Fig. 8.9. In terms of total efficiency, the clover detector remains steady at about 1.5 times the LENA efficiency throughout most of the energies measured, as seen in Fig. 8.10). Both efficiency comparisons show a sharp increase in the clover-to-LENA ratio at low energies, due to the reduced dead layer and large cross-sectional area of the clover. These improvements upon the present HPGe detector make the clover an important logical next step for LENA. Further on-

going research is aimed at incorporating in the simulations a new NaI annulus that is capable of encompassing the larger HPGe geometry.

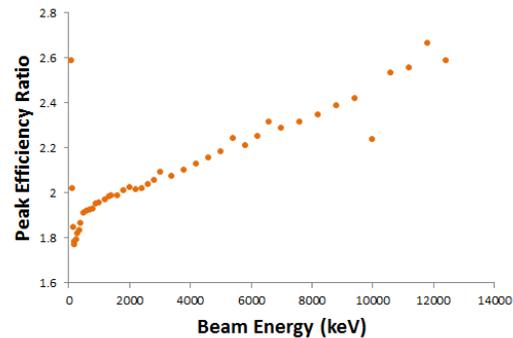


Figure 8.9: Peak efficiency ratio of the clover to the present LENA HPGe detector.

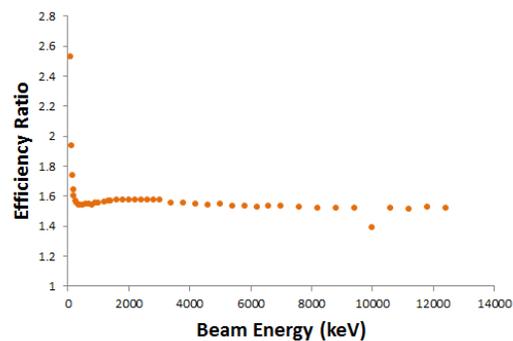


Figure 8.10: Total efficiency ratio of the clover to the present LENA HPGe detector.

-
- [Ago03] S. Agostinelli *et al.*, Nucl. Instrum. Methods A, **506**, 250 (2003).
- [How13] C. Howard, C. Iliadis, and A. E. Champagne, Nucl. Instrum. Methods A, **729**, 254 (2013).
- [Hu98] Z. Hu *et al.*, Nucl. Instrum. Methods A, **419**, 121 (1998).
- [Kno10] G. F. Knoll, *Radiation Detection and Measurement, 4th edition*, John Wiley & Sons, 2010.

8.2 Data Acquisition Hardware and Software Development

8.2.1 Development of the DAQLINK Package for Live DAQ Monitoring

D. J. UNDERWOOD, *TUNL*

A data-acquisition communication system, DAQLINK, is being developed to use alongside data acquisition systems that do not have the built-in capability to view live data. It uses high-performance networking code based on the ZeroMQ networking library to transfer live events between data acquisition computers at rates exceeding 1 GHz.

Data acquisition systems for nuclear physics experiments have been developed for high throughput of data and high configurability. Examples of these are Maximum Integration Data Acquisition System (MIDAS), developed at TRIUMF and the Paul Scherrer Institut; ORCA, developed at UNC and used primarily by the neutrino groups at TUNL; and CODA, developed at Jefferson Laboratory and used extensively at TUNL. However, many of these systems do not include convenient ways to view live data. Here, we present a networking library, DAQLink, that is designed to transfer data to a remote display client written in PYTHON.

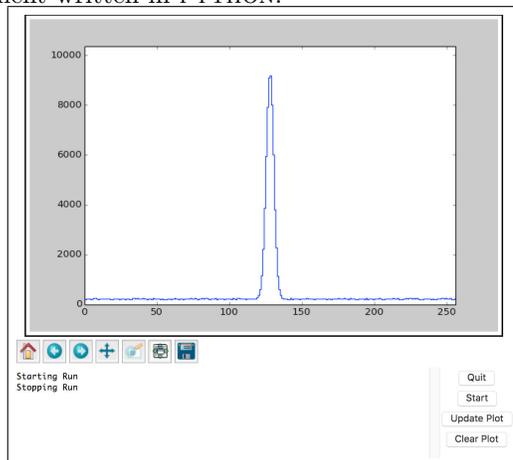


Figure 8.11: Screenshot of the DAQLINK interface

DAQLINK was originally written as a companion to the MIDAS data acquisition code. However, it should be compatible with any data acquisition that provides a way to access events as they are generated. Adding it to a new data acquisition system is trivial, requiring only function calls to setup and shutdown DAQLINK, a call

to publish events, and a callback function written to allow control of the data acquisition software. Furthermore, it manages its own threading and should not block execution in the data acquisition system. This results in no loss of data when using the library for live event viewing. DAQLINK consists of two components: a server and a client. The server provides an interface to which the client connects without any dependency on the data acquisition system being used with the server. This server component of the software was written in C to provide an interface compatible with data acquisition systems written in various languages.

In addition to the server component of DAQLINK, there is the client component. The client is written in PYTHON using TKINTER for the interface and MATPLOTLIB for plotting. A screenshot of the interface is shown in Fig. 8.11.

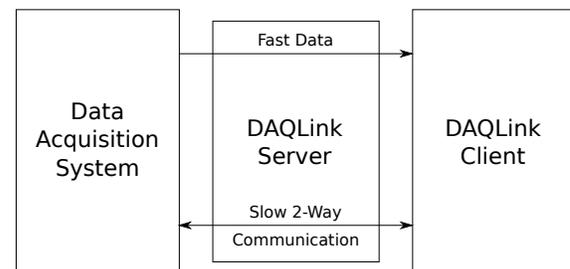


Figure 8.12: Networking Setup

The client and server components are connected via networking code using the ZEROMQ (ZMQ) [iC] library. The usage of ZMQ allows high-performance networking without having to maintain code for different platforms. The networking architecture consists of two pairs of sockets as shown in Fig. 8.12. Using network com-

Table 8.1: Benchmark Bandwidth Results.

Interface	DAQLINK Bandwidth (Mb/s)	Network Bandwidth (Mb/s)
localhost	10900	38600
Gigabit	788	939
10/100 Megabit	87.5	93.9

munications for transferring data—rather than other methods such as monitoring a file—allows the client to work on both the same machine as the server and on remote machines. In addition, it does not have a coupling with the type of file produced by the data acquisition system in use.

One pair of sockets follows a Request/Reply pattern in which the client sends a request to the server and the server responds with a suitable reply. These sockets are used for controlling the data acquisition system and requesting status information such as server-side event rate. The second pair of sockets follows a Publisher/Subscriber pattern and allows data to be transmitted at high rates. Current benchmarks indicate that the event-rate limitation is based on processor frequency and network bandwidth. Table 8.2.1 shows the network bandwidth as measured from DAQLINK and compares it with the real network bandwidth measured by IPERF

[ESn]. The results in the table come from running the client on the same machine as the DAQLINK server (localhost), as well as running the server on remote machines with Gigabit and 10/100 Megabit LAN connections.

Along with viewing live data, DAQLINK allows the facilitation of other DAQ-related tasks, such as live analysis. Incorporating live event analysis, such as peak fitting and spectrum integration, is currently in development, along with mathematical manipulation of incoming data via PYTHON scripting.

[ESn] ESnet and Lawrence Berkeley National Laboratory, *iPerf*, <https://iperf.fr/>, Accessed: 2015-09-17.

[iC] iMatix Corporation, *ZeroMQ*, <http://www.zeromq.org>, Accessed: 2015-08-06.

8.2.2 Toward an EPICS Slow Control System for the Enge Spectrograph

R. LONGLAND, C. MARSHALL, *TUNL*

An EPICS control system for the Enge split-pole spectrograph is being investigated as a means to achieve robust remote control over stepper motors, vacuum systems, and power supplies. Successful operation of the Enge’s field-regulation system has been achieved using a low-cost Raspberry Pi control system that takes advantage of the existing TUNL DAQ network.

Previous operation of the Enge split-pole spectrograph consisted of a mixture of local vacuum-gauge controls, DC drive motors for target and detector positioning, and magnetic-field regulation via a hand held microcomputer. These systems, while adequate in the past, have a number of shortcomings as we move toward an upgraded, more flexible research program with the spectrograph.

The vacuum interlock system is robustly designed but has no remote monitoring capabilities. During operation of the accelerator, no personnel can be present in the target room, so diagnosing in-run vacuum-related problems requires time-consuming interruption in beam production. A remote monitoring system similar to the one used elsewhere in the laboratory will be advantageous.

Currently, the DC motor-drives have remote operation capabilities, but they are not easy to control, either remotely or locally, owing to their push-button operation. As we move towards an upgraded research program, it will be useful to use computer-controlled stepper motors to precisely control aspects of the spectrometer.

Finally, the magnetic field is regulated in a feedback loop with the NMR probe and a Metrolab precision teslameter PT 2025. Previously, this was controlled via a hand-held microcomputer that is no longer operational. This final aspect of the control system is essential to successful research with the Enge spectrograph—a fact which prompted us to investigate new, low-cost control systems. The EPICS [Dal94] control system is used extensively at nuclear physics laboratories worldwide, including at HI γ S, but has not received much attention elsewhere at TUNL. For that reason, we have investigated the implementation of EPICS for controlling the Enge split-pole spectrograph.

Our initial test case for creating a low-cost

control system with EPICS was to implement the NMR feedback control. The Metrolab teslameter contains a module, the RG2024 field-regulation module, that connects with an external Danfysik 8000 power supply via a serial connection. The RG2024 contains all necessary field-correction algorithms, so no custom regulation software is required. However, commands must be sent to the module in order to calibrate, start, and stop field regulation. This is typically performed by transmitting command strings over a serial connection.

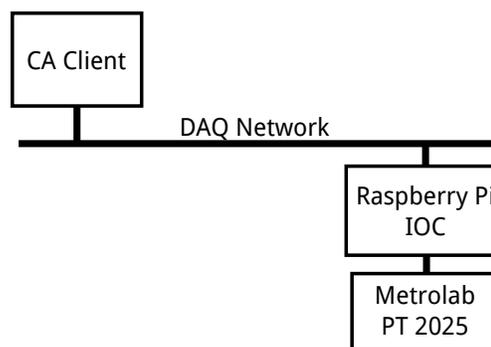


Figure 8.13: Architecture of the EPICS magnet-control system. Clients are typically shown above the line, with servers below. Here, we define a single client and server. The Raspberry Pi server communicates through a serial connection with the Metrolab PT 2025.

Building an EPICS application consists of two steps: (i) creation of the input-output controller (IOC) that is directly connected to the controlled hardware, and (ii) development of an EPICS channel-access (CA) client. The latter communicates with the former over the DAQ network, allowing us to separate control over many distributed devices. Figure 8.13 shows a schematic of this architecture. In our case, the CA client

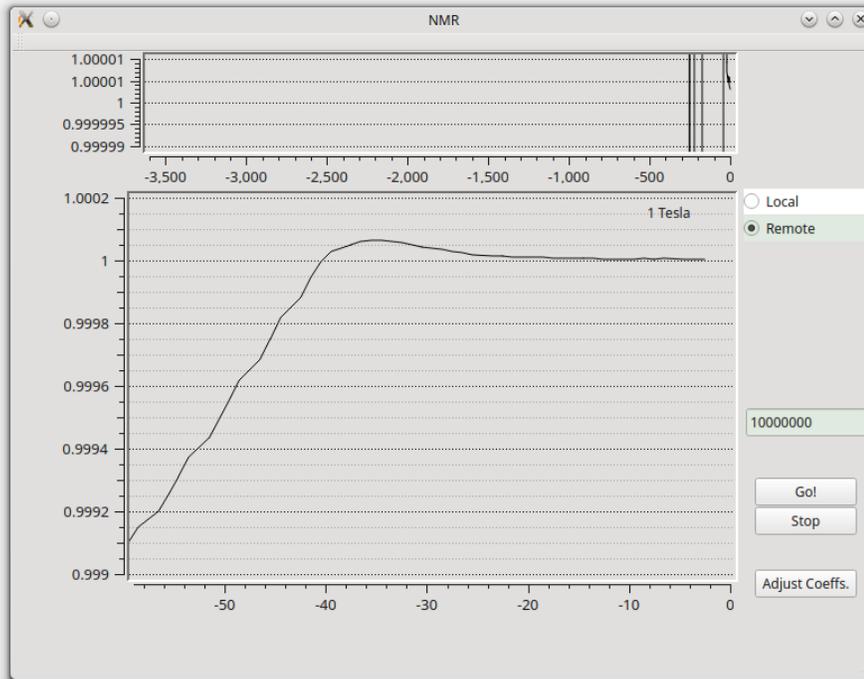


Figure 8.14: The field regulation control GUI developed for the Enge split-pole spectrograph, showing active regulation of the field shortly after initialization.

was developed as a graphical user interface (GUI) for ease of use with the drag-and-drop tools provided by the software Qt Creator [QT]. EPICS-aware plugins from the EPICSQT project [EPI] were also installed to aid in this development. This CA client runs on a standard Linux PC.

In the interest of cost savings, a \$35 Raspberry Pi computer was used for the IOC component. Its role is to communicate with the Metrolab over a serial connection and report values (defined as “process variables” in EPICS) to the CA client when requested. As such, high performance is not required of the IOC.

The IOC software was written using the STREAMDEVICE support in EPICS. This allows us to define a set of protocols to interpret commands into serial control commands, as well as interpret strings received from the Metrolab into meaningful measurements of the field, lock states,

etc. Development of IOCs using this support allows us to rapidly implement serial-device control systems, with the EPICS backbone handling communications automatically with little to no development cost.

Our finished control GUI on the CA client is shown in Fig. 8.14. This exercise has shown great promise for developing an EPICS control system for the Enge split-pole spectrograph at TUNL. Development is now ongoing to implement stepper motor controls, which is expected to be completed in the next few months.

[Dal94] L. R. Dalesio *et al.*, Nucl. Instrum. Methods A, **352**, 179 (1994).

[EPI] <http://www.epicsqt.org>.

[QT] <http://www.qt.io/ide>.

8.2.3 γ -Ray Spectroscopy Using the Binned Likelihood Method

J.R. DERMIGNY, C. ILIADIS, K.J. KELLY, *TUNL*; M.Q. BUCKNER, *Lawrence Livermore National Laboratory, Livermore, CA*

Common spectroscopic techniques can be of limited use in the presence of complex γ -ray cascades, where photopeaks are frequently obscured by secondary photopeaks, escape peaks, or environmental background. We report on a method of analysis that was developed at LENA and disentangles these spectral features, providing reaction intensities and that branching ratios without cumbersome corrections or background subtraction.

Two main areas of interest in the study of nuclear reactions are (i) the fraction of primary decays from the composite state to lower-lying levels, i.e., the primary branching ratios, and (ii) the total number of nuclear reactions that took place. These are frequently obtained using pulse-height spectra collected through γ -ray spectroscopy. The traditional method for analysis is to measure the net-area of all the full-energy primary-transition photopeaks. Careful correction for the detector efficiency yields the desired intensities.

While this is an attractive option for simple spectra, γ -ray cascades are often sufficiently complex that “peak-by-peak” analysis is quite limited. This can be the case, for instance, when photopeaks are affected by coincidence summing, by angular correlations, or by the need to do background subtraction. The situation worsens for $\gamma\gamma$ -coincidence spectroscopy, where the net-area of a photopeak is dependent not only on its own detection efficiency, but on the detection efficiencies for all γ -rays present in its cascade. This effect, compounded with the challenges described above, makes precision measurements with coincidence spectra difficult.

A methodology to mitigate these complications has been developed at LENA and is reported on in an upcoming paper in *Nuclear Instruments and Methods*. Used properly, it is an elegant solution to these problems. A summary is presented here.

The method, known informally as “fraction fitting” (after the ROOT class, “TFractionFitter”), utilizes the high fidelity simulation of our $\gamma\gamma$ -coincidence spectrometer to create Monte-Carlo-generated templates, which are simulated pulse height spectra imitating the detector’s re-

sponse to constituent γ -ray cascades. For illustrative purposes, a sample decay is provided below in Fig. 8.15.

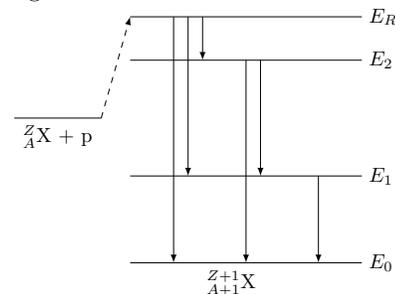


Figure 8.15: A generic proton capture with decay scheme.

Templates are prepared for each observed primary transition (i.e., $E_R \rightarrow E_n$) by simulating the transition to the secondary state, E_n , plus the succeeding γ -ray cascade. This is accomplished by executing a GEANT program, where all known excited states and their branching ratios are loaded prior to simulation. An event begins with the simulated nucleus in the composite state, E_R . The program then computes the next decay by sampling a random number generator. This process continues until the simulated nucleus has deexcited to the ground state, E_0 . All γ rays are tracked as they interact with the environment through photoelectric absorption, Compton scattering, and pair production. Energy deposition in the detectors is evaluated for each event and used to construct reaction templates. For environmental radionuclides, such as ^{40}K and ^{208}Tl , a template is created by measuring the room background.

The contribution of each template to an experimentally measured pulse height spectrum

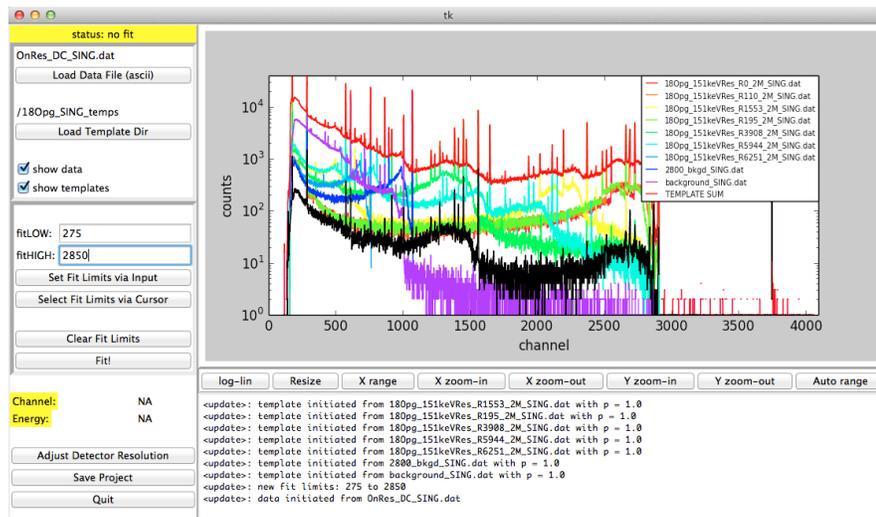


Figure 8.16: The LENAfracfit interface. Users can load the experimental spectrum and templates, apply resolution adjustments, and perform the fitting. Pictured, $^{18}\text{O}(p,\gamma)^{19}\text{F}$ templates (colors) are plotted against the experimental spectrum (black).

is determined by minimizing the log-likelihood function [Bar93]. The results of the minimization can be used to calculate primary transition branching ratios as well as the total number of decay events. This is a marked departure from traditional analysis. Here, instead of relying solely on corrected full-energy photopeak intensities, our results derive from all primary and secondary transition photopeaks, escape peaks, and Compton continua present in the experimental spectrum. Further, complications due to angular correlations and coincidence summing are virtually eliminated as these effects are included in the template spectra.

To facilitate more rapid data analysis and provide an intuitive user interface, a cross-platform app, LENAfracfit, was written. LENAfracfit uses the MINUIT2 library for minimization, while graphics and user-interface tools are provided by MATPLOTLIB and TKINTER. Users are able to visualize and fine-tune templates to better match experimental data by adjusting the resolution of entire spectra or confined regions. The user interface is shown in Fig. 8.16.

The use of this method is not limited to reaction-specific measurements, but can be extended to background radiation studies. The LENA ECR ion source has undergone extensive upgrades recently with the goal of delivering up to 20 mA of protons pulsed at a 10% duty cycle. This promises to significantly diminish the presence of environmental radionuclides in an experimental pulse height spectrum. To

benchmark the performances of the pulsed beam, the spectra obtained in Sect. 2.2.1 were analyzed by applying the fraction-fitting formalism to the $^{18}\text{O}(p,\gamma)^{19}\text{F}$ reaction. For each of the seven primary transitions reported in Ref. [Til95], templates were generated via the method outlined above. An environmental radionuclides template was created using measured background accumulated for twenty hours. A fit was performed on direct current and pulsed beam spectra using the LENAfracfit program; the measured levels of environmental background in each are shown in Table 8.2.3.

Table 8.2: Environmental Background Count Rate

mode	observed counts	count rate (cps)
DC beam	14500(200)	13.8(2)
Pulsed beam	2000(200)	1.9(2)

We find that beam pulsing reduces the presence of environmental background by $86.3 \pm 1.3\%$. This affords an increase in detector sensitivity, which, coupled with these new analysis techniques, further pushes the limits of surface-based nuclear astrophysics research.

[Bar93] R. Barlow, *Comp. Phys. Commun.*, **77**, 219 (1993).

[Til95] D. R. Tilley, *Nucl. Phys.*, **A595**, 1 (1995).

8.2.4 Timing Reconstruction Algorithm for γ -Ray Detections

K. NIBBS, *Vassar College, Poughkeepsie, NY*; R. HENNING, C. BARTRAM, G. OTHMAN, *TUNL*

An algorithm has been developed to find the time that scintillation light entered a photomultiplier tube by analyzing the tube's output voltage. The algorithm will hopefully be used to reconstruct ortho-positronium decays and the momentum vectors of the emitted γ rays. An observed angular correlation between the spin axis of the ortho-positronium and the directions of the emitted γ rays will be evidence of CP violation. Though the algorithm has not yet been rigorously tested, it has shown consistency and promise in preliminary trials.

Positronium is a bound state of an electron and a positron. Its triplet state, ortho-positronium or o-Ps, decays into three γ rays. If CP violation occurs in o-Ps decay, it will manifest itself in an angular correlation between the spin axis of the o-Ps and the direction of the three emitted γ rays. The relevant vectors and angles are shown in Fig. 8.17

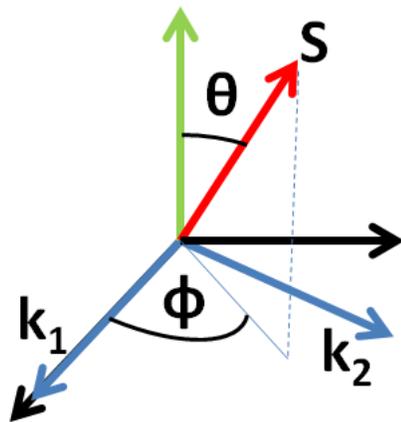


Figure 8.17: Vectors and angles associated with o-Ps decay. The vector S is the spin axis of the o-Ps, k_1 and k_2 are the momenta of the first and second most energetic γ rays. The green, vertical arrow is the normal to the decay plane.

An asymmetry between positive and negative values of $2 \cos \theta \cos \phi$, observed over numerous trials, would suggest such an angular correlation, and therefore CP violation as well. Our APEX detector array is an annular array of sodium iodide (NaI) bars for detecting emitted γ rays. Used in conjunction with our photomultiplier

tubes (PMTs), PMT bases, digitizer, and signal processing techniques, it allows us to calculate and rank their energies as needed.

A more challenging problem, however, has been reconstructing the emitted γ rays' angles of emission. Former graduate student Stephen Daigle found that because of light's attenuation as it moves through a medium, the ratio of the charge amplitudes from the PMTs at opposite ends of the NaI bar gives us the position at which the γ ray struck the bar as shown in Fig. 8.18.

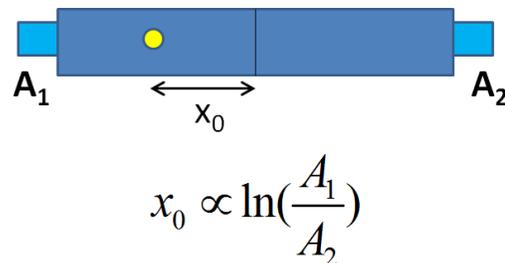


Figure 8.18: Schematic drawing of a NaI test bar and its PMTs. A_1 and A_2 are the charge amplitudes from the first and second PMTs respectively. The yellow circle indicates the event site.

There are, however, a few scenarios where this method will fail. The most readily conceptualized example is an unfortunately placed γ -ray strike at the corner of a NaI bar and against the frame of a PMT. In this scenario, some of the scintillation light will be reflected or absorbed by the PMT, the charge amplitude ratio will be skewed to favor the PMT at the opposite end of the bar, and a faulty position reconstruction will result.

In order to identify, and possibly discard, these problematic o-Ps decays, we devised a second method to complement the first, so that a significant disagreement between the two would indicate an issue. Implementing this method hinged on our ability to identify the time at which light started to enter the PMTs. From the time difference, we would deduce the difference in distances that the light traveled to reach the PMTs and thus, using simple arithmetic, the position in the NaI bar. My main task this summer was to formulate a reliable computer program to determine the γ -ray detection times.

Our team prepared data to test my program by placing a ^{22}Na source in the center of the APEX array and leaving one NaI bar, along with the signal-processing complex, active. The data were stored in a ROOT file that contained two TTrees, corresponding to the two active PMTs. Each TTree contained numerous waveforms, each containing a digital pulse generated by a γ -ray detection. The waveforms were composed of 4096 digitized voltages sampled at regular time intervals of roughly 10 ns. The waveforms held a steady baseline voltage value in the absence of activity, and then the voltage dropped precipitously when scintillation light entered the PMT before slowly returning to the baseline value. I endeavored to fit the rising edge of the pulse with a linear regression, and then find the best-fit line's intersection with the baseline. The x-coordinate of this intersection would give the time at which light entered the PMT, offset by a constant due to our electronic setup.

To find the pulse in each waveform, I set a reasonable threshold value below the digitizer's

baseline that would rarely be reached without scintillation light being present. I then identified the longest chain of consecutive values below the threshold as the pulse. After finding the pulse's location, I used one function to find the index of the lowest recorded voltage (the peak location), which corresponded to the fastest influx of scintillation light to the PMT, and another function to return the average of the indices between the pulse's peak and its start where the voltage was halfway between the baseline and its peak value (half-peak location). I performed the linear regression fit using all points on the waveform between the pulse's rising half-peak and its start for which the voltage's decrease was linear. The choice to use the early part of the waveform was important, because the waveform was noisier and less linear near the peak location. The x-coordinate of the best-fit line's intersection with the digitizer's baseline was the time at which the scintillation light began entering the PMT.

Although the REU program ended before I could use delay lines to rigorously test the accuracy of my timing-reconstruction algorithm, I found that its calculated detection time consistently fell near the last waveform indices with voltage values at or near the baseline. A few dramatic failures occurred where the x-intersection of the best-fit line and the baseline was outside of the bounds of the waveform. However, upon closer examination, we determined that these resulted from false triggers of the digitizer, which created waveforms without pulses. Future changes, such as selecting different points to perform the linear regression fit, may improve the accuracy of the timing reconstruction.

8.2.5 Status of the ORCA Data Acquisition Software

M.A. HOWE, S. MEIJER, J.F. WILKERSON, *TUNL*;

ORCA is an object-oriented real-time control and acquisition system that is being used in a number of laboratories in the US, Canada, and Germany and is under continuous development. Over the last year, new VME and USB devices were added to the list of supported hardware, and new features were added to some of ORCA's subsystems to support the KATRIN, HALO, and MAJORANA experiments.

The ORCA (object-oriented real-time control and acquisition) software system [How09] is designed for dynamically building flexible and robust data acquisition systems. ORCA is being used at UNC, TUNL, KURF, Sanford Underground Research Facility (SURF), University of Washington's Center for Experimental Nuclear Physics and Astrophysics, SNOLAB, LANL, LBNL, MIT, ORNL, and Karlsruhe Institute of Technology (KIT). It is being used in the MAJORANA DEMONSTRATOR (MJD), SNO+, HALO, KATRIN, and Edelweiss experiments, among others. Slow control systems based on ORCA are monitoring the environmental conditions for MAJORANA and the e-forming lab at SURF. At KIT the ORCA slow control sub-system is used to provide communication between ORCA and the KATRIN main slow control system.

ORCA is under continuous development. The release of a new compiler, XCode 6, and MacOS operating system 10.10 required a large sweep of the ORCA code base to eliminate new compiler warnings and to remove deprecated methods. The new version of the XCode static analysis tools helped to clear a number of long-standing bugs. New features and supported objects continue to be added to ORCA as needed.

The new VME cards that were added are the SIS 3305, a 5GS/s 10-bit digitizer; the CAEN V1730, a 16-channel 14-bit 500 MS/s digitizer; support for a variant of GRETINA's digitized firmware developed at Argonne National Laboratory; the GRETINA Master Trigger Card used by MJD; the GRETINA Trigger Router Card, used in conjunction with the Master Trigger Card to pass the master clock signal to the digitizers.

The USB devices that were added or updated are the CAEN DT5720, a USB-controlled 4-channel 12-bit 250MS/s digitizer, and the MotionNode Accelerometer's Version 10. Work on

the second object to add long-term tracking of the data is continuing

A few objects specific to individual experiments were also added or improved. One was a new version of the KATRIN Power and Control Board object that talks directly to the KATRIN slow control system via a field point. In addition, an interlock system was added to the MJD main controller object to monitor the MJD vacuum system. In the event that the cryostat vacuum reports an increase in cryostat pressure or if the vacuum computer cannot be reached, the detector high voltage is automatically ramped down. In addition, the HV dialogs are locked out if the vacuum system reports unsafe vacuum conditions. The MJD calibration-source hardware that is attached to the vacuum system computer can now be deployed or retracted and monitored from the DAQ computer. Scripts were developed to do 'one-click' calibration runs where sources are deployed, data is taken, and the source is retracted. Finally, scripts were developed to put the entire MAJORANA experiment in a safe state in the event of a power failure that lasts long enough to run down the UPS batteries.

Some objects and ORCA subsystems had major improvements. The run control system was expanded to execute specific scripts at the start of a run to set up different run-types. The ORCA scripting language was expanded to include ObjectiveC 2.0 syntax for creating arrays and dictionaries. In addition, syntax was added that allows native Cocoa objects to be directly created within a script. The RAD7 communication software was re-written to fully comply with the correct protocol. The Remote Socket object now uses a command queue that allows multiple ORCA objects to share the same socket object when talking to a remote system.

We also made improvements to the CouchDB

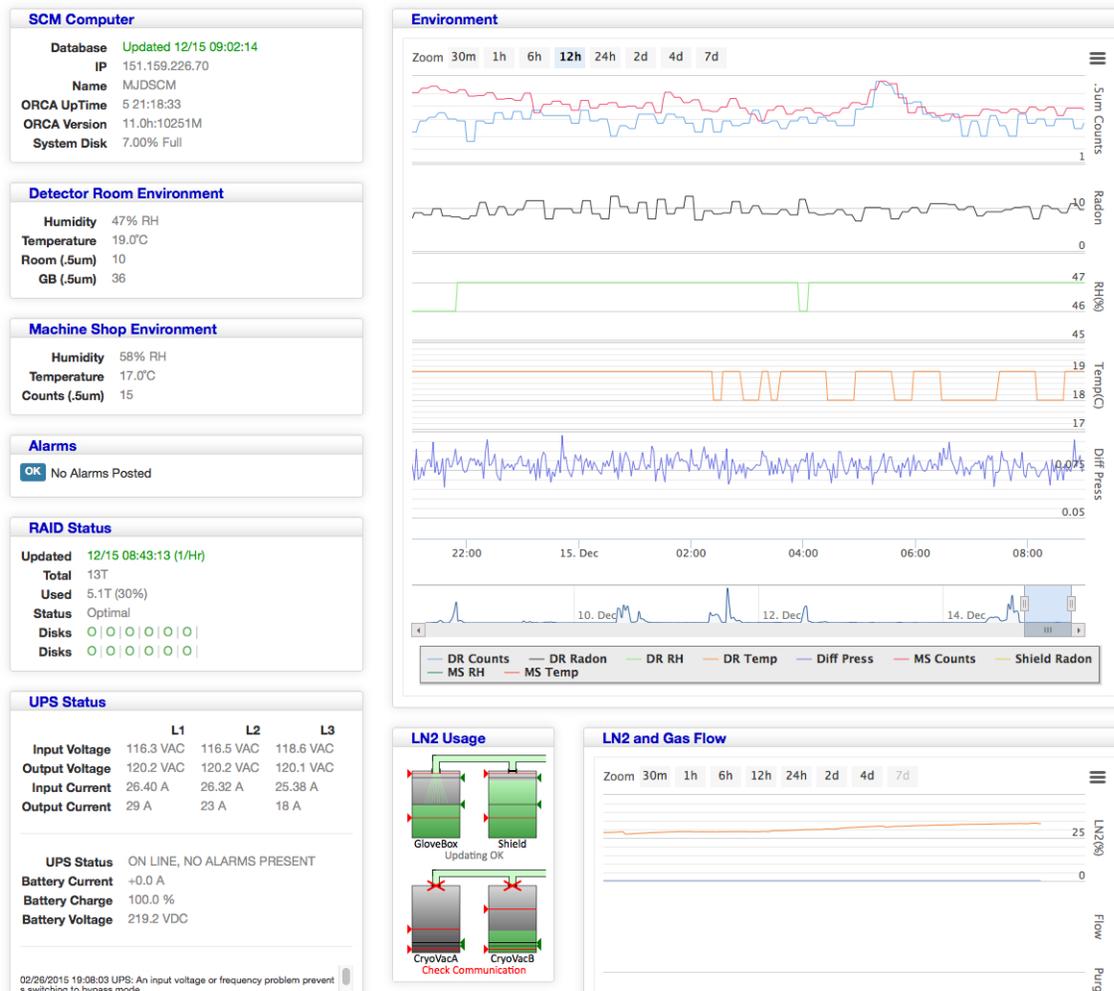


Figure 8.19: A screen shot of the web tool for monitoring MAJORANA. At the left are panels showing snapshot information about the environment. At the right are charts showing the history of various parameters. Note the nitrogen fill status.

data base. It now has two queues, one for high priority records and one for low priority records. Low priority records are discarded if the queue is filling faster than it is being emptied. In addition, more objects in ORCA are now CouchDB-aware, which means that they can be remotely monitored. Certain types of events, such as run starts and stops and ORCA restarts and crashes, can now be logged into a CouchDB.

For MAJORANA, the web-based monitoring tools have been expanded for displaying experiment-specific information. Rates are monitored and are now displayed for the entire system as well as for each detector and veto channel. The total event-count is displayed for each digitizer channel. Detector baseline values for individual detectors are displayed in strip charts showing the previous few day's worth of data, and graphics show the layout of the detectors in each string. The names of the detectors, the elec-

tronics and high voltage connections and status are also displayed, and the entire hardware map is shown in table form. All digitizer histograms from each crate and the veto system can now be displayed on one page to give a quick overview of the system status. The experiment's live time is also calculated and displayed. Finally, there is now more detailed information about the state of the nitrogen purge system. (See Fig. 8.19.)

ORCAROOT, a support application for ORCA, is a tool kit that can be used to build analysis programs that can decode raw ORCA data streams. A recent addition is code that can produce ROOT trees for generic digitizers. New decoders continue to be added to ORCAROOT to support new objects added to ORCA.

[How09] Howe, M. A. *et al.*, TUNL Progress Report, **XLVIII**, 171 (2009).



UNDERGRADUATE STUDENTS AFFILIATED WITH THE 2015 TUNL RESEARCH EXPERIENCE FOR UNDERGRADUATES (REU) PROGRAM ARE SHOWN IN FRONT OF THE FRENCH FAMILY SCIENCE CENTER. IN ADDITION TO WORKING ON THEIR FOCUSED PROJECTS, THE STUDENTS TAKE PART IN A NUMBER OF SOCIAL AND PROFESSIONAL DEVELOPMENT ACTIVITIES AS A GROUP. SHOWN IN THE PHOTOGRAPH FROM LEFT TO RIGHT ARE: (FRONT ROW) ADRYANNA SMITH (BAYLOR UNIVERSITY), SUSAN OLMSTED (EAST TENNESSEE STATE UNIVERSITY), KATIE KOWAL (LEWIS AND CLARK COLLEGE), RAY NIAZI (UNIVERSITY OF OKLAHOMA), CHLOE LINDEMAN (HAVERFORD COLLEGE), DANIELLE RIGGIN (DUKE UNIVERSITY), ISABEL BRAY (CLARKSON UNIVERSITY); (BACK ROW) JOHN MARTIN (UNIVERSITY OF NORTH CAROLINA AT CHAPEL HILL), KIROLLOS MASOOD (UNIVERSITY OF FLORIDA), OZ AMRAM (CARNEGIE MELLON UNIVERSITY), NATHAN PERREAU (UNIVERSITY OF NORTH CAROLINA AT CHAPEL HILL), KADEEM NIBBS (VASSAR COLLEGE), DAVE ELOFSON (BRIDGEWATER STATE UNIVERSITY), AND CHRIS CALDERADO (UNIVERSITY OF NORTH CAROLINA AT CHAPEL HILL).

Appendices

- Graduate Degrees Awarded
- Publications
- Invited Talks, Seminars, and Colloquia
- Professional Service Activities

A.1 Graduate Degrees Awarded

Ph.D. Degrees

1. Thomas J. Corona, *Methodology and Application of High Performance Electrostatic Field Simulation in the KATRIN Experiment*,
University of North Carolina at Chapel Hill, September 2014
Supervisor: J. F. Wilkerson
2. Matthew Q. Buckner, *Hydrogen Burning of the Rare Oxygen Isotopes*,
University of North Carolina at Chapel Hill, October 2014
Supervisor: C. Iliadis
3. Brittney M. VornDick, *Guide Fabrication for UCN Transport*,
North Carolina State University, January 2015
Supervisor: A. R. Young
4. Sean W. Finch, *Double-Beta Decay of ^{96}Zr and Double-Electron Capture of ^{156}Dy to Excited Final States*,
Duke University, March 2015
Supervisor: W. Tornow
5. Georgios Laskaris, *Photodisintegration of ^3He with Double Polarizations*,
Duke University, April 2015
Supervisor: H. Gao
6. Graham K. Giovanetti, *P-Type Point Contact Germanium Detectors and their Application in Rare-Event Searches*,
University of North Carolina at Chapel Hill, May 2015
Supervisor: J. F. Wilkerson
7. Jacqueline Strain MacMullin, *Validation of the Background Model for the MAJORANA DEMONSTRATOR*,
University of North Carolina at Chapel Hill, October 2015
Supervisor: J. F. Wilkerson
8. Pooyan Sahbaee Bagherzadeh, *Patient-specific Image Quality and Dose Estimation for Contrast Enhanced CT*,
North Carolina State University, November 2015
Supervisors: P. R. Huffman and E. Samei

M.S. and M.A. Degrees

1. Weizheng Zhou, *Flux Limitations of a Compton Light Source Driven by Storage Ring*,
Duke University, December 2014
Supervisor: Y. K. Wu
2. Zhonglin Han, *Monte-Carlo Simulation for $^3\text{H}(\gamma, pn)n$ Experiment with High Intensity Gamma-ray Source (HI γ S)*,
Duke University, November 2015
Supervisor: C. R. Howell

A.2 Publications

The publications co-authored by members of TUNL research groups between September 2014 and November 2015 are tabulated in Table A.1. The papers in refereed journals by TUNL research groups are listed below in chronological order.

Type	No.
Refereed Journal Articles	62
Conference Proceeding Papers	35

Table A.1: Summary of TUNL publications from September 2014 through November 2015. Among the 62 refereed journal papers, 11 were letters or published in other similar high-impact journals.

Journal Articles Published

1. *Two-neutrino double- β decay of ^{150}Nd to excited final states in ^{150}Sm* , M. F. Kidd, J. H. Esterline, S. W. Finch and W. Tornow, Phys. Rev. C **90**, 055501 (2014).
2. *Measurement of double-polarization asymmetries in the quasi-elastic $^3\bar{\text{H}}\text{e}(\bar{\text{e}}, \text{e}'\text{d})$ process*, M. Mihovilović *et al.* (including H. Gao), Phys. Rev. Lett. **113**, 232505 (2014).
3. *Measurement of “pretzelosity” asymmetry of charged pion production in semi-inclusive deep inelastic scattering on a polarized ^3He target*, Y. Zhang *et al.* (including H. Gao), Phys. Rev. C **90**, 055209 (2014).
4. *Single spin asymmetries in charged kaon production from semi-inclusive deep inelastic scattering on a transversely polarized ^3He target*, Y.X. Zhao *et al.* (including H. Gao), Phys. Rev. C **90**, 055201 (2014).
5. *Neutron-Deuteron Analyzing Power Data at $E_n = 22.5$ MeV*, G. J. Weisel, W. Tornow, A. S. Crowell, J. H. Esterline, G. M. Hale, C. R. Howell, P. D. O'Malley, J. R. Tompkins, and H. Witała, Phys. Rev. C **89**, 054001 (2014).
6. *Measurement of the Half-Life of the $T=1/2$ Mirror Decay of ^{19}Ne and its Implication on Physics Beyond the Standard Model*, L.J. Broussard *et al.* (including A. S. Crowell, C. R. Howell, and A. R. Young), Phys. Rev. Lett. **112**, 212301 (2014).
7. *Dual-Fission Chamber and Neutron Beam Characterization for Fission Product Yields Using Monoenergetic Beam*, C. Bhatia *et al.* (including C. R. Howell, J. H. Kelley, and W. Tornow), Nucl. Instrum. Methods A **757**, 7 (2014).
8. *A novel method to assay special nuclear materials by measuring prompt neutrons from polarized photofission*, J. M. Mueller, M. W. Ahmed, and H. R. Weller, Nucl. Instrum. Methods A **754**, 57 (2014).
9. *Conditioning of BPM pickup signals for operations of the Duke storage ring with a wide range of single-bunch current*, X. Wei, L. Jing-Yi, H. Sen-Lin, W. Z. Wu, H. Hao, P. Wang, and Y. K. Wu, Chin. Phys. C, **38**, 107003 (2014).
10. *Ultracold neutron source at the PULSTAR reactor: Engineering design and cryogenic testing*, E. Korobkina, G. Medlin, B. Wehring, A. I. Hawari, P. R. Huffman, A. R. Young, B. Beaumont, and G. Palmquist, Nucl. Instrum. Methods A, **767**, 169 (2014).
11. *The MAJORANA DEMONSTRATOR Neutrinoless Double-Beta Decay Experiment*, N. Abgrall *et al.* (the MAJORANA Collaboration including M. P. Green, R. Henning, W. Tornow, J. F. Wilkerson, and A. R. Young), Adv. High Energy Phys., 365432 (2014).

12. *Design and performance of a cryogenic apparatus for magnetically trapping ultracold neutrons*, P. R. Huffman, K. J. Coakley, J. M. Doyle, C. R. Huffer, H. P. Mumm, C. M. O’Shaughnessy, K. W. Schelhammer, P-N. Seo, L. Yang, *Cryogenics* **64**, 40 (2014).
13. *Thermonuclear reaction rate of $^{18}\text{Ne}(\alpha,p)^{21}\text{Na}$ from Monte Carlo calculations*, P. Mohr, R. Longland, and C. Iliadis, *Phys. Rev. C* **90**, 065806 (2014).
14. *High Statistics Measurement of the Positron Fraction in Primary Cosmic Rays of 0.5500 GeV with the Alpha Magnetic Spectrometer on the International Space Station*, The AMS Collaboration (including R. Henning), *Phys. Rev. Lett.* **113**, 121101 (2014).
15. *Validating resonance properties using nuclear resonance fluorescence*, C. T. Angell, R. Hajima, T. Hayakawa, T. Shizuma, H. J. Karwowski, and J. Silano, *Phys. Rev. C* **90**, 054315 (2014).
16. *Search for Majoron-emitting modes of double-beta decay of ^{136}Xe with EXO-200*, J. B. Albert *et al.* (the EXO-200 Collaboration including P. S. Barbeau), *Phys. Rev. D* **90**, 092004 (2014).
17. *Comment on “Fitting the annual modulation in DAMA with neutrons from muons and neutrinos”*, P. S. Barbeau, J. I. Collar, Y. Efremenko and K. Scholberg, *Phys. Rev. Lett.* **113**, 229001 (2014).
18. *Measurements of the $^{40}\text{Ar}(n,\gamma)^{41}\text{Ar}$ radiative-capture cross section between 0.4 and 14.8 MeV*, M. Bhike, B. A. Fallin, and W. Tornow, *Phys. Lett.* **B736**, 361 (2014).
19. *Magnetic Dipole Strength in ^{124}Xe and ^{134}Xe in the spin-flip resonance region*, R. Massarczyk, G. Rusev, R. Schwengner, F. Dönau, C. Bhatia, M. E. Gooden, J. H. Kelley, A. P. Tonchev, and W. Tornow, *Phys. Rev. C* **90**, 054310 (2014).
20. *Measurement of the neutron-capture cross section of ^{76}Ge and ^{74}Ge below 15 MeV and its relevance to $0\nu\beta\beta$ decay searches of ^{76}Ge* , M. Bhike, B. Fallin, Krishichayan, and W. Tornow, *Phys. Lett. B* **741**, 150 (2015).
21. *The MAJORANA Parts Tracking Database*, N. Abgrall *et al.* (the MAJORANA Collaboration including M. P. Green, R. Henning, W. Tornow, J. F. Wilkerson, and A. R. Young), *Nucl. Instrum. Methods A* **779**, 52 (2015).
22. *Status of the MAJORANA DEMONSTRATOR: A search for neutrinoless double-beta decay*, Y. Efremenko *et al.* (the MAJORANA Collaboration including M. P. Green, R. Henning, W. Tornow, J. F. Wilkerson, and A. R. Young), *Int. J. Mod. Phys. A* **30**, 1530032 (2015).
23. *Study of electron anti-neutrinos associated with gamma-ray bursts using KamLAND*, K. Asakura *et al.* (the KamLAND Collaboration including H. J. Karwowski, D. M. Markoff, and W. Tornow), *Astrophys. J.* **806**, 87 (2015).
24. *Search for the proton decay mode $p \rightarrow \bar{\nu}K^+$ with KamLAND*, K. Asakura *et al.* (the KamLAND Collaboration including H. J. Karwowski, D. M. Markoff, and W. Tornow) *Phys. Rev. D* **92**, 052006 (2015).
25. *Separation of the $1^+/1^-$ parity doublet in ^{20}Ne* , J. Beller *et al.* (including J. H. Kelley, A. P. Tonchev, W. Tornow, and H. R. Weller), *Phys. Lett.* **B741**, 128 (2015).
26. *Comprehensive Sets of $^{124}\text{Xe}(n,\gamma)^{125}\text{Xe}$ and $^{124}\text{Xe}(n,2n)^{123}\text{Xe}$ Cross-Section Data for Assessment of Inertial Confinement Deuterium-Tritium Fusion Plasma*, M. Bhike, B. A. Fallin, M. E. Gooden, N. Ludin, and W. Tornow, *Phys. Rev. C* **91**, 011601(R) (2015).
27. *Polarized photon scattering off ^{52}Cr : Determining the parity of $J=1$ states*, Krishichayan, M. Bhike, W. Tornow, G. Rusev, A. P. Tonchev, N. Tsoneva, and H. Lenske, *Phys. Rev. C* **91**, 044328 (2015).
28. *Measurements of the $^{86}\text{Kr}(n,\gamma)^{87}\text{Kr}$ and $^{86}\text{Kr}(n,2n)^{85}\text{Kr}^m$ reaction cross sections below $E_n=15$ MeV*, M. Bhike, E. Rubino, M. E. Gooden, Krishichayan, and W. Tornow, *Phys. Rev. C* **92**, 014624 (2015).

29. *Search for two-neutrino double- β decay of ^{96}Zr to excited states of ^{96}Mo* , S. W. Finch and W. Tornow, *Phys. Rev. C* **92**, 045501 (2015).
30. *^7Be Solar Neutrino Measurement with KamLAND*, A. Gando *et al.* (the KamLAND Collaboration including H. J. Karwowski, D. M. Markoff, and W. Tornow), *Phys. Rev. C* **92**, 055808 (2015).
31. *Precision Measurements of A_1^n in the Deep Inelastic Regime*, D.S. Parno *et al.* (including H. Gao), *Phys. Lett.* **B744**, 309 (2015).
32. *Moments of the neutron g_2 structure function at intermediate Q^2* , P. Solvignon *et al.* (including H. Gao), *Phys. Rev. C* **92**, 015208 (2015).
33. *Double spin asymmetries of inclusive hadron electroproduction from a transversely polarized ^3He target*, Y. X. Zhao *et al.* (including H. Gao), *Phys. Rev. C* **92**, 015207 (2015).
34. *Radiative corrections beyond the ultra relativistic limit in unpolarized ep elastic and Moller scatterings for the PRad experiment at Jefferson Laboratory*, I. Akushevich, H. Gao, A. Ilyichev, and M. Meziane, *Euro. Phys. J. A* **51**, 1 (2015).
35. *Exploratory study of fission product yields of neutron-induced fission of ^{235}U , ^{238}U , and ^{239}Pu at 8.9 MeV*, C. Bhatia *et al.* (including C. R. Howell, J. H. Kelley, and W. Tornow), *Phys. Rev. C* **91**, 064604 (2015).
36. *Nuclear Physics Research at HI γ S*, H. R. Weller, M. W. Ahmed, and Y. K. Wu, *Nucl. Phys. News*, **25**, No. 3, 19 (2015).
37. *Tests of a novel method to assay SNM using polarized photofission and its sensitivity in the presence of shielding*, J. M. Mueller, M. W. Ahmed, A. Kafkarkou, D. P. Kendellen, M. H. Sikora, M. C. Spraker, H. R. Weller, and W. R. Zimmerman, *Nucl. Instrum. Methods A* **776**, 107 (2015).
38. *Polarization asymmetries in the $^9\text{Be}(\gamma, n_0)$ reaction*, J. M. Mueller *et al.* (including M. W. Ahmed, H. J. Karwowski, D. M. Markoff, and H. R. Weller), *Phys. Rev. C* **92**, 034604 (2015).
39. *Photodisintegration of ^7Li with progeny nuclei in excited states*, W. A. Wurtz, R. E. Pywell, B. E. Norum, S. Kucuker, B. D. Sawatzky, H. R. Weller, S. Stave, and M. W. Ahmed, *Phys. Rev. C* **92**, 044603 (2015).
40. *A Widely Tunable Two-Color Free-Electron Laser on a Storage Ring*, Y. K. Wu, J. Yan, H. Hao, J. Y. Li, S. F. Mikhailov, V. G. Popov, N. A. Vinokurov, S. Huang, and J. Wu, *Phys. Rev. Lett.* **115**, 184801 (2015).
41. *Measurement of the Doubly-Polarized $^3\vec{H}e(\vec{\gamma}, n)pp$ Reaction at 16.5 MeV and Its Implications for the GDH Sum Rule*, G. Laskaris *et al.* (including M. W. Ahmed, H. Gao, H. J. Karwowski, H. R. Weller, and Y. K. Wu), *Phys. Lett.* **B750**, 547 (2015).
42. *Measurements of the ion fraction and mobility of α - and β -decay products in liquid xenon using the EXO-200 detector*, J. B. Albert *et al.* (the EXO-200 Collaboration including P. S. Barbeau), *Phys. Rev. C* **92**, 045504 (2015).
43. *An RF-only ion-funnel for extraction from high-pressure gases*, T. Brunner *et al.* (including P. S. Barbeau), *Int. J. Mass Spectrom.* **379**, 110 (2015).
44. *Spectroscopy of Ba and Ba $^+$ deposits in solid xenon for barium tagging in nEXO*, B. Mong *et al.* (the nEXO Collaboration including P. S. Barbeau), *Phys. Rev. A* **91**, 022505 (2015).
45. *A multilayer surface detector for ultracold neutrons*, Z. Wang *et al.*, (including A. R. Young), *Nucl. Instrum. Methods A* **798**, 30 (2015).
46. *Radial Distribution of Charged Particles in a Magnetic Field*, S. K. L. Sjue, L. J. Broussard, M. Makela, P. L. McGaughey, A. R. Young, and B. A. Zeck, *Rev. Sci. Instrum.* **86**, 023102 (2015).

47. *Fundamental neutron physics beamline at the spallation neutron source at ORNL*, N. Fomin, G. L. Greene, R. R. Allen, V. Cianciolo, C. Crawford, T. M. Tito, P. R. Huffman, E. B. Iverson, R. Mahurin, and W. M. Snow, *Nucl. Instrum. Methods A*, **773**, 45, (2015).
48. *Corrigendum to “Fundamental neutron physics beamline at the spallation neutron source at ORNL” [Nucl. Instrum. Methods A, 773 (2015) 45-51]*, N. Fomin, G. L. Greene, R. R. Allen, V. Cianciolo, C. Crawford, T. M. Ito, P. R. Huffman, E. B. Iverson, R. Mahurin, W. M. Snow, *Nucl. Instrum. Methods A*, **788**, 203 (2015).
49. *Ultracold neutron accumulation in a superfluid-helium converter with magnetic multipole reflector*, O. Zimmer and R. Golub, *Phys. Rev. C* **92**, 015501 (2015).
50. *Frequency shifts and relaxation rates for spin-1/2 particles moving in electromagnetic fields*, G. Pignol, M. Guigue, A. Petukhov, and R. Golub, *Phys. Rev. A* **92**, 053407 (2015).
51. *Measurement of the $^{97}\text{Mo}(n, \gamma)$ reaction with the DANCE γ calorimeter array*, C. L. Walker *et al.* (including G. E. Mitchell), *Phys. Rev. C* **92**, 014324 (2015).
52. *Statistical Methods for Thermonuclear Reaction Rates and Nucleosynthesis Simulations*, C. Iliadis, A. Coc, R. Longland, F. Timmes, and A. E. Champagne, *J. Phys. G*, **42**, 034007 (2015).
53. *High-intensity-beam study of $^{17}\text{O}(p, \gamma)^{18}\text{F}$ and thermonuclear reaction rates for $^{17}\text{O}+p$* , M. Q. Buckner, C. Iliadis, K. J. Kelly, L. N. Downen, A. E. Champagne, J. M. Cesaratto, C. Howard, and R. Longland, *Phys. Rev. C* **91**, 015812 (2015).
54. *Laboratory studies on the removal of radon-born lead from KamLAND’s organic liquid scintillator*, G. Keefer *et al.* (the KamLAND Collaboration including H. J. Karwowski, D. M. Markoff, and W. Tornow), *Nucl. Instrum. Methods A* **769** 79 (2015).
55. *A compact ultra-clean system for deploying radioactive sources inside the KamLAND detector*, T. I. Banks *et al.* (the KamLAND Collaboration including H. J. Karwowski, D. M. Markoff, and W. Tornow), *Nucl. Instrum. Methods A* **769** 88 (2015).
56. *Demonstration of a transmission nuclear resonance fluorescence measurement for a realistic radioactive waste canister scenario*, C. T. Angell *et al.* (including H. J. Karwowski), *Nucl. Instrum. Methods B* **347**, 11 (2015).
57. *Compact source of narrowband and tunable x-rays for radiography*, S. Banerjee *et al.* (including H.J. Karwowski), *Nucl. Instrum. Methods B* **350**, 106 (2015).
58. *Performance of A Compact Multi-crystal High-purity Germanium Detector Array for Measuring Coincident Gamma-ray Emissions*, C. Howard *et al.* (including A. E. Champagne), *Nucl. Instrum. Methods A* **783**, 85 (2015).
59. *Low Energy Scattering Cross Section Ratios of $^{14}\text{N}(p, p)^{14}\text{N}$* , R. J. deBoer *et al.* (including A. E. Champagne), *Phys. Rev. C* **91**, 045804 (2015).
60. *New recommended $\omega\gamma$ for the $E_r^{\text{c.m.}} = 458 \text{ keV}$ resonance in $^{22}\text{Ne}(p, \gamma)^{23}\text{Na}$* , K. J. Kelly, A. E. Champagne, R. Longland, *Phys. Rev. C* **92**, 035805 (2015).
61. *Focal-plane detector system for the KATRIN experiment*, J. F. Amsbaugh *et al.* (including J. F. Wilkerson), *Nucl. Instrum. Methods A* **778**, 40 (2015).
62. *Current Status of new SAGE Project with ^{51}Cr Neutrino Source*, V. Gavrin *et al.* (including J. F. Wilkerson), *Phys. Part. Nuclei* **46**, no. 2, 131 (2015).

Journal Articles Accepted

1. *Up-scattering of Ultracold Neutron from Gases*, S. J. Seestrom *et al.* (including A. R. Young), accepted for publication in Phys. Rev. C.
2. *Neutron-Antineutron Oscillations: Theoretical Status, Experimental Prospects*, D. G. Phillips II *et al.* (including A. R. Young), accepted for publication in Phys. Rep., arXiv:1410.1100.
3. *Characterization of a ^{10}B -doped liquid scintillator as a capture-gated neutron spectrometer*, S. Hunt, C. Iliadis, and R. Longland, accepted for publication in Nucl. Instrum. Methods A.
4. *New reaction rates for improved primordial D/H calculation and the cosmic evolution of deuterium*, A. Coc, P. Petitjean, J-P. Uzan, E. Vangioni, P. Descouvemont, C. Iliadis, and R. Longland, accepted for publication in Phys. Rev. D.
5. *Search for the β decay of ^{96}Zr* , S. W. Finch and W. Tornow, to be published in Nucl. Instrum. Methods A **806**, 70 (2016).
6. *Search for double-beta decay of ^{136}Xe to excited states of ^{136}Ba with the KamLAND-Zen Experiment*, K. Asakura *et al.*, (the KamLAND Collaboration, including H. J. Karwowski, D. M. Markoff, and W. Tornow), to be published in Nucl. Phys. **A946**, 171 (2016).
7. *Energy Dependence of Fission Product Yields from ^{235}U , ^{238}U and ^{239}Pu for Incident Neutron Energies between 0.5 and 14.8 MeV*, M. E. Gooden *et al.* (including C. R. Howell, J. H. Kelley, A. P. Tonchev, and W. Tornow), accepted for publication in Nucl. Data Sheets.

Journal Articles Submitted

1. *Survival analysis approach to account for non-exponential decay rate effects in lifetime experiments*, K. J. Coakley, M. S. Dewey, M. G. Huber, P. R. Huffman, C. R. Huffer, D. E. Marley, H. P. Mumm, C. M. O'Shaughnessy, K. W. Schelhammer, A. K. Thompson, A. T. Yue, submitted to Nucl. Instrum. Methods A.
2. *On potassium and other abundance anomalies of red giants in NGC 2419*, C. Iliadis, A. Karakas, N. Prantzos, J. Lattanzio, C. Doherty, submitted to Astrophys. J.
3. *The Thermonuclear Runaway and the Classical Nova Outburst (Topical Review)*, S. Starrfield, C. Iliadis, and R. Hix, submitted to Publ. Astron. Soc. Pac.
4. *Search for neutrinoless double-electron capture of ^{156}Dy* , S.W. Finch and W. Tornow, submitted to Phys. Rev. C.
5. *Fast neutron-induced potential background near the Q-value of neutrinoless double-beta decay of ^{76}Ge* , W. Tornow, M. Bhike, B. A. Fallin, and Krishichayan, submitted to Phys. Rev. C.
6. *Measurement of the $^{169}\text{Tm}(n,3n)^{167}\text{Tm}$ cross section and the branching ratios in the decay of ^{167}Tm* , B. Champine, M. Bhike, M. E. Gooden, Krishichayan, E. B. Norman, N. D. Scielzo, M. A. Stoyer, K. J. Thomas, A. P. Tonchev, and W. Tornow, submitted to Phys. Rev. C.
7. *KamLAND Sensitivity to Neutrinos from Pre-Supernova Stars*, K. Asakura *et al.* (the KamLAND Collaboration, including H. J. Karwowski, D. M. Markoff, and W. Tornow), submitted to Phys. Rev. D.
8. *Magnetic dipole excitations of ^{50}Cr* , H. Pai *et al.* (including W. Tornow), submitted to Phys. Rev. C.
9. *The decay pattern of the Pygmy Dipole Resonance of ^{140}Ce* , B. Löher *et al.* (including J. H. Kelley, A. P. Tonchev, W. Tornow, and H. R. Weller), submitted to Phys. Rev. Lett.
10. *Low-lying Dipole Strength in the Odd-Proton Nucleus ^{205}Tl up to the Neutron-Separation Threshold*, N. Benouaret *et al.* (including J. H. Kelley, A. P. Tonchev, W. Tornow, and H. R. Weller), submitted to J. Phys. G: Nucl. Phys.

Special Reports and Books

1. *Nuclear Physics of Stars*, 2nd Edition, enlarged and revised, C. Iliadis, (Wiley-VCH, Weinheim, 2015) 653 pages.
2. *Stellar Explosions: Hydrodynamics and Nucleosynthesis*, J. Jose, Foreword by C. Iliadis (Taylor & Francis, 2015) 431 pages.

Conference Reports and Articles in Conference Proceedings

1. *Partial Cross Sections of Neutron-Induced Reactions on ^{nat}Cu at $E_n = 6, 8, 10, 12, 14,$ and 16 MeV for $0\nu\beta\beta$ Background Studies*, M. E. Gooden, B. A. Fallin, S. W. Finch, J. H. Kelley, C. R. Howell, G. Rusev, A. P. Tonchev, W. Tornow, and V. Stanislav, Int. Nucl. Data Conf., New York, 2013, Nucl. Data Sheets **119**, 121 (2014).
2. *Measurements of the $(n,2n)$ Reaction Cross Section of ^{181}Ta from 8 to 15 MeV*, C. Bhatia, M. E. Gooden, W. Tornow, and A. P. Tonchev, Int. Nucl. Data Conf., New York, 2013, Nucl. Data Sheets **119**, 176 (2014).
3. *Fission Product Yield Study of ^{235}U , ^{238}U , and ^{239}Pu Using Dual Fission Chambers*, C. Bhatia *et al.* (including J. H. Kelley, C. R. Howell, and W. Tornow), Int. Nucl. Data Conf., New York, 2013, Nucl. Data Sheets **119**, 324 (2014).
4. *Rate and uncertainty of the $^{18}\text{Ne}(\alpha,p)^{21}\text{Na}$ reaction from the Monte-Carlo simulation*, P. Mohr, R. Longland, and C. Iliadis, Proceedings of the International Symposium on Nuclear Astrophysics Nuclei in the Cosmos XIII, Debrecen, Hungary, 2014, Proc. Sci. (PoS) **NIC-XIII**, 036 (2014).
5. *Measuring Duke Storage Ring Lattice Using Tune Based Technique*, W. Li, J. Y. Li, H. Hao, W. Li, S. F. Mikhailov, V. Popov, and Y. K. Wu, Proceedings of the 2015 International Particle Accelerator Conference (IPAC'15), Richmond, VA, May 3–8, 2015, pp. 293–295 (2015).
6. *Characterizing Betatron Tune Knobs on Duke Storage Ring*, H. Hao, S. F. Mikhailov, V. Popov, Y. K. Wu, and J. Y. Li, Proceedings of the 2015 International Particle Accelerator Conference (IPAC'15), Richmond, VA, May 3–8, 2015, pp. 672–674 (2015).
7. *Experimental Study of a Two-Color Storage Ring FEL*, J. Yan, H. Hao, S. F. Mikhailov, V. Popov, Y. K. Wu, S. Huang, J. Y. Li, N. Vinokurov, and J. Wu, Proceedings of the 2015 International Particle Accelerator Conference (IPAC'15), Richmond, VA, May 3–8, 2015, pp. 1198–1200 (2015).
8. *Developing an Improved Pulsed Mode Operation for Duke Storage Ring Based FEL*, S. F. Mikhailov, H. Hao, V. Popov, and Y. K. Wu, Proceedings of the 2015 International Particle Accelerator Conference (IPAC'15), Richmond, VA, May 3–8, 2015, pp. 1860–1862 (2015).
9. *Extending OK5 Wiggler Operational Limit at Duke FEL/HIGS Facility*, P. W. Wallace, M. Emamian, H. Hao, J. Y. Li, S. F. Mikhailov, V. Popov, Y. K. Wu, and J. Y. Li, Proceedings of the 2015 International Particle Accelerator Conference (IPAC'15), Richmond, VA, May 3–8, 2015, pp. 1863–1865 (2015).
10. *Light Source and Accelerator Physics Research Program at Duke University*, Y. K. Wu, Proceedings of the 2015 International Particle Accelerator Conference (IPAC'15), Richmond, VA, May 3–8, 2015, pp. 1866–1868 (2015).
11. *A Dark Matter Search with MALBEK*, G. K. Giovanetti *et al.* (the MAJORANA Collaboration including M. P. Green, R. Henning, W. Tornow, J. F. Wilkerson, and A. R. Young), 13th International Conference on Topics in Astroparticle and Underground Physics (TAUP 2013), Asilomar, CA, September 8 - 13, 2013, Phys. Procedia **61**, 77 (2015).
12. *The MAJORANA DEMONSTRATOR for $0\nu\beta\beta$: Current Status and Future Plans*, M. P. Green *et al.* (the MAJORANA Collaboration including R. Henning, W. Tornow, J. F. Wilkerson, and A. R. Young), 13th International Conference on Topics in Astroparticle and Underground Physics (TAUP 2013), Asilomar, CA, September 8 - 13, 2013, Phys. Procedia **61**, 232 (2015).

13. *The MAJORANA Low-noise Low-background Front-end Electronics*, N. Abgrall *et al.* (the MAJORANA Collaboration including M. P. Green, R. Henning, W. Tornow, J. F. Wilkerson, and A. R. Young), 13th International Conference on Topics in Astroparticle and Underground Physics (TAUP 2013), Asilomar, CA, September 8 - 13, 2013, Phys. Procedia **61**, 654 (2015).
14. *Testing the Ge detectors for the MAJORANA DEMONSTRATOR*, W. Xu *et al.* (the MAJORANA Collaboration including M. P. Green, R. Henning, W. Tornow, J. F. Wilkerson, and A. R. Young), 13th International Conference on Topics in Astroparticle and Underground Physics (TAUP 2013), Asilomar, CA, September 8 - 13, 2013, Phys. Procedia **61**, 807 (2015).
15. *Background Model for the MAJORANA DEMONSTRATOR*, C. Cuesta *et al.* (the MAJORANA Collaboration including M. P. Green, R. Henning, W. Tornow, J. F. Wilkerson, and A. R. Young), 13th International Conference on Topics in Astroparticle and Underground Physics (TAUP 2013), Asilomar, CA, September 8 - 13, 2013, Phys. Procedia **61**, 821 (2015).
16. *Status of the MAJORANA DEMONSTRATOR*, C. Cuesta *et al.* (the MAJORANA Collaboration including M. P. Green, R. Henning, W. Tornow, J. F. Wilkerson, and A. R. Young), Neutrino Oscillation Workshop (NOW 2014), Conca Specchiulla, Otranto, Lecce, Italy, September 7 - 14, 2014, Nucl. Part. Phys. Proc. **265-266**, 70 (2015).
17. *COHERENT Neutrino Scattering*, P. S. Barbeau for the COHERENT Collaboration, Neutrino Oscillation Workshop (NOW 2014), Conca Specchiulla, Otranto, Lecce, Italy, September 7 - 14, 2014, Nucl. Part. Phys. Proc. **265-266**, 117 (2015).
18. *The MAJORANA DEMONSTRATOR: A Search for Neutrinoless Double-beta Decay of ^{76}Ge* , W. Xu *et al.* (the MAJORANA Collaboration including M. P. Green, R. Henning, W. Tornow, J. F. Wilkerson, and A. R. Young), 2nd Workshop on Germanium-Based Detectors and Technologies, Vermillion, SD, September 14 - 17, 2014, J. Phys. Conf. Ser. **606**, 012004 (2015).
19. *MAJORANA Collaboration's Experience with Germanium Detectors*, S. Mertens *et al.* (the MAJORANA Collaboration including M. P. Green, R. Henning, W. Tornow, J. F. Wilkerson, and A. R. Young), 2nd Workshop on Germanium-Based Detectors and Technologies, Vermillion, SD, September 14 - 17, 2014, J. Phys. Conf. Ser. **606**, 012005 (2015).
20. *Low Background Signal Readout Electronics for the MAJORANA DEMONSTRATOR*, I. Guinn *et al.* (the MAJORANA Collaboration including M. P. Green, R. Henning, W. Tornow, J. F. Wilkerson, and A. R. Young), 2nd Workshop on Germanium-Based Detectors and Technologies, Vermillion, SD, September 14 - 17, 2014, J. Phys. Conf. Ser. **606**, 012009 (2015).
21. *Low Background Signal Readout Electronics for the MAJORANA DEMONSTRATOR*, I. Guinn *et al.* (the MAJORANA Collaboration including M. P. Green, R. Henning, W. Tornow, J. F. Wilkerson, and A. R. Young), 5th Topical Workshop on Low Radioactivity Techniques (LRT 2015), Seattle, WA, March 18 - 20, 2015, AIP Conf. Proc. **1672**, 030001 (2015).
22. *Analysis techniques for background rejection at the MAJORANA DEMONSTRATOR*, C. Cuesta *et al.* (the MAJORANA Collaboration including M. P. Green, R. Henning, W. Tornow, J. F. Wilkerson, and A. R. Young), 5th Topical Workshop on Low Radioactivity Techniques (LRT 2015), Seattle, WA, March 18 - 20, 2015, AIP Conf. Proc. **1672**, 140006 (2015).
23. *Status of the MAJORANA DEMONSTRATOR*, C. Cuesta *et al.* (the MAJORANA Collaboration including M. P. Green, R. Henning, W. Tornow, J. F. Wilkerson, and A. R. Young), Matrix Elements for the Double-beta-decay EXperiments (MEDEX'15) Conference, Prague, Czech Republic, June 9 - 12, 2015, AIP Conf. Proc. **1686**, 020005 (2015).
24. *A sensitive search for dark energy through chameleon scalar fields using neutron interferometry*, W. M. Snow, M. Arif, B. Heacock, M. Huber, K. Li, D. Pushin, V. Skayvish, and A. R. Young, XXXVII Symposium on Nuclear Physics, Cocoyoc, Mexico, January 6 - 9, 2014, J. Phys. Conf. Ser., **578**, 012009 (2015).

25. *Nuclear Structure Studies with Gamma-Ray Beams*, A. P. Tonchev, C. Bhatia, J. H. Kelley, R. Raut, G. Rusev, W. Tornow, and N. Tsoneva, 15th International Symposium on Capture Gamma-Ray Spectroscopy and Related Topics (CGS15), Dresden, Germany, August 25 - 29, 2014, EPJ Web Conf. **93**, 01030 (2015).
26. *Dipole strength distributions from HIGS Experiments*, V. Werner *et al.* (including J. H. Kelley and W. Tornow), 15th International Symposium on Capture Gamma-Ray Spectroscopy and Related Topics (CGS15), Dresden, Germany, August 25 - 29, 2014, EPJ Web Conf. **93**, 01031 (2015)
27. *Photon Strength Functions from Two-Step gamma Cascades Experiment on $^{155,157}\text{Gd}$* , J. Kroll, S. Valenta, M. Kr̄tička, F. Bečvář, I. Tomandl, and G. E. Mitchell, 15th International Symposium on Capture Gamma-Ray Spectroscopy and Related Topics (CGS15), Dresden, Germany, August 25 - 29, 2014, EPJ Web Conf. **93**, 01036 (2015).
28. *Scissors Mode of ^{162}Dy Studied from Resonance Neutron Capture*, B. Baramsai *et al.* (including G. E. Mitchell), 15th International Symposium on Capture Gamma-Ray Spectroscopy and Related Topics (CGS15), Dresden, Germany, August 25 - 29, 2014, EPJ Web Conf. **93**, 01037 (2015).
29. *QPM Analysis of ^{205}Tl Nuclear Excitations below the Giant Dipole Resonance*, N. Benouaret *et al.* (including J. H. Kelley, A. P. Tonchev, W. Tornow, and H. R. Weller), 15th International Symposium on Capture Gamma-Ray Spectroscopy and Related Topics (CGS15), Dresden, Germany, August 25 - 29, 2014, EPJ Web Conf. **93**, 01044 (2015).
30. *Decay pattern of the Pygmy Dipole Resonance in ^{140}Ce* , J. Isaak *et al.* (including J. H. Kelley, A. P. Tonchev, W. Tornow, and H. R. Weller), 15th International Symposium on Capture Gamma-Ray Spectroscopy and Related Topics (CGS15), Dresden, Germany, August 25 - 29, 2014, EPJ Web Conf. **93**, 01048 (2015).
31. *$^{124}\text{Xe}(n,\gamma)^{125}\text{Xe}$ and $^{124}\text{Xe}(n,2n)^{123}\text{Xe}$ measurements for National Ignition Facility*, M. Bhike, N. Ludin, and W. Tornow, 15th International Symposium on Capture Gamma-Ray Spectroscopy and Related Topics (CGS15), Dresden, Germany, August 25 - 29, 2014, EPJ Web Conf. **93**, 02003 (2015).
32. *Neutron radiative capture reactions on nuclei of relevance to $0\nu\beta\beta$, dark matter and neutrino / antineutrino searches*, W. Tornow and M. Bhike, 15th International Symposium on Capture Gamma-Ray Spectroscopy and Related Topics (CGS15), Dresden, Germany, August 25 - 29, 2014, EPJ Web Conf. **93**, 03001 (2015).
33. *Review and experiments on nuclear astrophysics*, C. Iliadis and A. E. Champagne, Proceedings of the Gran Sasso Summer Institute 2014 on Hands-On Experimental Underground Physics at LNGS, Laboratori Nazionali del Gran Sasso, Assergi, Italy, 2014, Proc. Sci. (PoS) **GSSI14**, 009 (2015).
34. *Demonstrating the integral resonance transmission method; Conceptual and experimental studies*, C. Angell, T. Hayakawa, T. Shizuma, R. Hajima, B. J. Quiter, B. L. Ludewigt, H. J. Karwowski, G. Rich, and J. Silano, Proceedings of the Institute of Nuclear Materials Management (INMM) 56th Annual Meeting, Indian Wells, CA, July 12 - 16, 2015, 9 pages
35. *Improving the Assay of ^{239}Pu in Spent and Melted Fuel Using the Nuclear Resonance Fluorescence Integral Resonance Transmission Method*, C. T. Angell, T. Hayakawa, T. Shizuma, R. Hajima, B. J. Quiter, B. A. Ludewigt, H. J. Karwowski, and G. Rich, Nuclear Physics and Gamma-Ray Sources for Nuclear Security and Nonproliferation - Proceedings of the International Symposium, Ed. H. Takehito *et al.* World Scientific Publishing Co. Ltd., pp. 133-141, 2015.

Conference Proceedings and Meeting Articles Accepted

1. *MEIC detector and interaction at JLab*, Z. W. Zhao *et al.* (including H. Gao), 23rd International Workshop on Deep-Inelastic Scattering and Related Subjects (DIS 2015), Dallas, Texas, April 27 - May 1, 2015, to be published by Proceedings of Science.
2. *SoLID-SIDIS: Future Measurements of Transversity, TMDs and more*, Z. Ye *et al.* (including H. Gao), 23rd International Workshop on Deep-Inelastic Scattering and Related Subjects (DIS 2015), Dallas, Texas, April 27 - May 1, 2015, to be published by Proceedings of Science.
3. *Experimental progress and status on nucleon electromagnetic form factors*, H. Gao, C. Peng, and Z. W. Zhao, 21st International Conference on Few-Body Problems in Physics, Chicago, Illinois, May 18-22, 2015, to be published by EPJ Web of Conferences.
4. *Proton Charge Radius Experiment (PRad) in Hall B, JLab*, C. Peng and H. Gao, 21st International Conference on Few-Body Problems in Physics, Chicago, Illinois, May 18-22, 2015, to be published by EPJ Web of Conferences.
5. *Photodisintegration of ^3He with double polarizations*, G. Laskaris and H. Gao, 21st International Conference on Few-Body Problems in Physics, Chicago, Illinois, May 18-22, 2015, to be published by EPJ Web of Conferences.
6. *Few-Nucleon Research at TUNL: Probing Two- and Three-Nucleon Interactions with Neutrons*, C. R. Howell, W. Tornow, H. Witała, 21st International Conference on Few-Body Problems in Physics, Chicago, Illinois, May 18-22, 2015, to be published by EPJ Web of Conferences.
7. *Photon-Induced Reaction Studies at the High Intensity Gamma Ray Source (HIGS) for $A = 3$ to 16*, M. W. Ahmed, H. Gao, C. R. Howell, W. Tornow, H. R. Weller, 21st International Conference on Few-Body Problems in Physics, Chicago, Illinois, May 18-22, 2015, to be published by EPJ Web of Conferences.
8. *Neutron-neutron quasifree scattering in nd breakup at 10 MeV*, R. C. Malone, B. J. Crowe, A. S. Crowell, L. C. Cumberbatch, B. A. Fallin, F. Q. L. Friesen, Z. Han, C. R. Howell, D. Markoff, W. Tornow, H. Witała, 21st International Conference on Few-Body Problems in Physics, Chicago, Illinois, May 18-22, 2015, to be published by EPJ Web of Conferences.
9. *Progress Toward Monte-Carlo Simulation of $^3\text{H}(\gamma,p)nn$ and $^3\text{He}(\gamma,p)pn$ Experiments*, Z. Han, M. W. Ahmed, B. J. Crowe, A. S. Crowell, L. C. Cumberbatch, B. A. Fallin, F. Q. L. Friesen, C. R. Howell, D. Ticehurst, W. Tornow, H. Witała, 21st International Conference on Few-Body Problems in Physics, Chicago, Illinois, May 18-22, 2015, to be published by EPJ Web of Conferences.
10. *Progress Toward Measurement of a_{nn} Using $^3\text{H}(\gamma,p)nn$ at the Triangle Universities Nuclear Laboratory*, F. Q. L. Friesen, M. W. Ahmed, B. J. Crowe, A. S. Crowell, L. C. Cumberbatch, B. A. Fallin, Z. Han, C. R. Howell, D. Markoff, W. Tornow, H. Witała, 21st International Conference on Few-Body Problems in Physics, Chicago, Illinois, May 18-22, 2015, to be published by EPJ Web of Conferences.

Abstracts to Meetings and Conferences

1. *A Cryogenic Target for Compton Scattering Experiments at HI γ S*, D. Kendellen, M. Ahmed, H. Weller, and G. Feldman,
<http://meetings.aps.org/Meeting/APR15/Session/E4.7>
2. *Search for strongly coupled Chameleon scalar field with neutron interferometry*, K. Li *et al.* (including A. Young),
<http://meetings.aps.org/Meeting/APR15/Session/H2.6>
3. *Neutron interferometry in a temperature controlled vacuum environment for the search of dark energy and other precision experiments*, P. Saggi *et al.* (including A. Young),
<http://meetings.aps.org/Meeting/APR15/Session/R6.8>
4. *COHERENT First Steps for an Experimental Neutrino Program at the Spallation Neutron Source*, G. Rich,
<http://meetings.aps.org/Meeting/APR15/Session/S4.5>
5. *Precision Optics Optimization for GMp Experiment*, Y. Wang, K. Allada, T. Averett, E. Christy, C. Gu, M. Huang, and B. Wojtsekhowski,
<http://meetings.aps.org/Meeting/APR15/Session/C15.3>
6. *Search for CP Violation in Positronium*, C. Bartram,
<http://meetings.aps.org/Meeting/APR15/Session/C6.5>
7. *Electromagnet Design for an Experimental Search for CP Violation in Positronium Decay*, R. Petersburg, R. Henning, and C. Bartram,
<http://meetings.aps.org/Meeting/APR15/Session/D1.12>
8. *Status Update of the MAJORANA DEMONSTRATOR Neutrinoless Double-Beta Decay Experiment*, K. Vorren
<http://meetings.aps.org/Meeting/APR15/Session/D1.12>
9. *Data Acquisition and Environmental Monitoring of the MAJORANA DEMONSTRATOR*, S. Meijer,
<http://meetings.aps.org/Meeting/APR15/Session/R5.3>
10. *Validation of Pulse Shape Simulation for Ge Detectors in the MAJORANA DEMONSTRATOR*, B. Shanks,
<http://meetings.aps.org/Meeting/APR15/Session/S4.2>
11. *Detector Characterization for the MAJORANA DEMONSTRATOR*, T. Gilliss,
<http://meetings.aps.org/Meeting/APR15/Session/S4.3>
12. *Optimization of Geometries for Experimental Searches of Chameleon Scalar Fields*, V. Skavysh, M. Arif, C. Shahi, R. Haun, M. Snow, K. Li, B. Heacock, and A. Young,
<http://meetings.aps.org/Meeting/APR15/Session/H2.5>
13. *Energy Dependence of Fission Product Yields from ^{235}U , ^{238}U and ^{239}Pu for Incident Neutron Energies Between 0.5 and 14.8 MeV* M. Gooden *et al.* (including A. Tonchev and W. Tornow),
<http://meetings.aps.org/Meeting/DNP15/Session/DF.4>
14. *Cross-Section Measurement of the $^{169}\text{Tm}(n, 3n)^{167}\text{Tm}$ Reaction and Constraining the Branching Ratio of ^{167}Tm* , B. Champine, M. Gooden, K. Thomas, F. Krishichayan, E. Norman, N. Scielzo, A. Tonchev, and W. Tornow,
<http://meetings.aps.org/Meeting/DNP15/Session/NE.8>

15. *Assembly and Test for the Large GEM detector for pRad experiment at JLab Hall B*, X. Bai, K. Gnanvo, H. Nguyen, V. Nelyubin, Y. Huang, A. Katzenstein, Y. Zhang, and N. Liyanage, <http://meetings.aps.org/Meeting/DNP15/Session/CD.2>
16. *New limits for the $2\nu\beta\beta$ decay of ^{96}Zr to excited nuclear states of ^{96}Mo* , S. Finch and W. Tornow, <http://meetings.aps.org/Meeting/DNP15/Session/DD.6>
17. *Measurement of unpolarized differential cross section of semi-inclusive deep-inelastic scattering on a ^3He target*, X. Yan, <http://meetings.aps.org/Meeting/DNP15/Session/DG.7>
18. *Nuclear Data Compilation for Beta Decay Isotope*, S. Olmstead, J. Kelley, and G. Sheu, <http://meetings.aps.org/Meeting/DNP15/Session/EA.144>
19. *Neutron Interactions with ^7Be and the Primordial ^7Li Problem*, E. E. Kading *et al.* (including C. R. Howell), <http://meetings.aps.org/Meeting/DNP15/Session/HC.3>
20. *Measurement of the Response Function of a BC501A Neutron Detector*, J. Miller, D. Alexander, A. Daniel, E. V. Hungerford, M. W. Ahmed, and M. Sikora, <http://meetings.aps.org/Meeting/DNP15/Session/HG.6>
21. *The $^{76}\text{Ge}(n,p)^{76}\text{Ga}$ reaction and its relevance to searches for the neutrino-less double-beta decay of ^{76}Ge* , W. Tornow, M. Bhike, B. Fallin, and F. Krishichayan, <http://meetings.aps.org/Meeting/DNP15/Session/JD.3>
22. *Practical Experience of Signals Processing Using Digitizers*, M. Sikora and M. Ahmed <http://meetings.aps.org/Meeting/DNP15/Session/JJ.5>
23. *Photo-Induced depopulation of the ^{180m}Ta isomer*, M. Bhike, F. Krishichayan, and W. Tornow, <http://meetings.aps.org/Meeting/DNP15/Session/KC.9>
24. *Photo-induced Fission Product Yield Measurements on ^{235}U , ^{238}U , and ^{239}Pu* , F. Krishichayan, M. Bhike, A. P. Tonchev, and W. Tornow, <http://meetings.aps.org/Meeting/DNP15/Session/NE.9>
25. *Measurement of the Neutral Pion Lifetime*, Y. Zhang, <http://meetings.aps.org/Meeting/DNP15/Session/NH.6>
26. *COHERENT at the Spallation Neutron Source*, J. Raybern and K. Scholberg, <http://meetings.aps.org/Meeting/DNP15/Session/NH.6>
27. *Testing new designs for the MAJORANA DEMONSTRATOR's low-mass front-end board*, C. Salemi, <http://meetings.aps.org/Meeting/DNP15/Session/EA.67>
28. *Bayesian signal processing of pulse shapes for background rejection in the MAJORANA DEMONSTRATOR*, B. Shanks, <http://meetings.aps.org/Meeting/DNP15/Session/JJ.6>
29. *Searching for Solar Axions using the MAJORANA DEMONSTRATOR*, C. O'Shaughnessy, <http://meetings.aps.org/Meeting/DNP15/Session/KD.5>
30. *Penning Trap Searches in the KATRIN Main Spectrometer*, K. Wierman, <http://meetings.aps.org/Meeting/DNP15/Session/PD.6>
31. *Uncertainty and Systematic Corrections for the Neutron Polarization in the UCNA Experiments*, E. Dees, <http://meetings.aps.org/Meeting/DNP15/Session/FJ.7>
32. *Measurement of the ^{242}Pu neutron capture cross section*, M. Q. Buckner *et al.* (including A. Chyzh), <http://meetings.aps.org/Meeting/DNP15/Session/JH.1>

33. *Gamma-Ray Emission Spectra as a Constraint on Calculations of $^{234,236,238}\text{U}$ Neutron-Capture Cross Sections*, J. L. Ullmann *et al.* (including A. Chyzh),
<http://meetings.aps.org/Meeting/DNP15/Session/JH.2>
34. *Neutron Interferometric Search for Chameleon Dark Energy*, B. Heacock,
<http://meetings.aps.org/Meeting/DNP15/Session/ND.4>
35. *Measurement of spin flip probabilities for ultracold neutrons on guide materials*, Z. Tang *et al.* (including A. Young),
<http://meetings.aps.org/Meeting/DNP15/Session/PJ.3>
36. *The Charged Particle Spectroscopy Program at TUNL*, R. Longland,
<http://meetings.aps.org/Meeting/SES15/Session/A1.1>
37. *Neutron-neutron quasifree scattering in nd breakup at 10 MeV*, R. C. Malone,
<http://meetings.aps.org/Meeting/SES15/Session/A1.2>
38. *Research activities using High Intensity Gamma-ray Source facility at TUNL*, Krishichayan,
<http://meetings.aps.org/Meeting/SES15/Session/A1.3>
39. *Development of an Experiment to Measure a_{nn} Using $^3\text{H}(\gamma,p)nn$ at the Triangle Universities Nuclear Laboratory*, F. Friesen,
<http://meetings.aps.org/Meeting/SES15/Session/G1.2>
40. *Sub-barrier Photofission and Beam Diagnostics at HI γ S* J. Silano,
<http://meetings.aps.org/Meeting/SES15/Session/G1.1>
41. *Neutron-neutron quasifree scattering in nd breakup at 10 MeV*, R. C. Malone, B. Crowe, A. S. Crowell, L. C. Cumberbatch, B. A. Fallin, F. Q. L. Friesen, Z. Han, C. R. Howell, D. Markoff, W. Tornow, and H. Witała, 21st International Conference on Few-Body Problems in Physics, Chicago, IL, May 2015.
42. *Progress Toward Monte-Carlo Simulation of $^3\text{H}(\gamma,p)nn$ and $^3\text{He}(\gamma,p)pn$ Experiments*, Z. Han, M. W. Ahmed, B. J. Crowe, A. S. Crowell, L. C. Cumberbatch, B. Fallin, F. Q. L. Friesen, C. R. Howell, D. Ticehurst, W. Tornow, and H. Witała, 21st International Conference on Few-Body Problems in Physics, Chicago, IL, May 2015.
43. *Progress Toward Measurement of a_{nn} Using $^3\text{H}(\gamma,p)nn$ at the Triangle Universities Nuclear Laboratory*, F. Q. L. Friesen, M. W. Ahmed, B. J. Crowe, A. S. Crowell, L. C. Cumberbatch, B. Fallin, Z. Han, C. R. Howell, D. Markoff, W. Tornow, and H. Witała, 21st International Conference on Few-Body Problems in Physics, Chicago, IL, May 2015.
44. *Photodisintegration of ^3He with double polarizations*, G. Laskaris and H. Gao, 21st International Conference on Few-Body Problems in Physics, Chicago, IL, May 2015.
45. *Proton Charge Radius Experiment (PRad) in Hall B, JLab*, C. Peng and H. Gao, 21st International Conference on Few-Body Problems in Physics, Chicago, IL, May 2015.
46. *Measuring Duke Storage Ring Lattice Using Tune Based Technique*, W. Li, J. Y. Li, H. Hao, W. Li, S. F. Mikhailov, V. Popov, and Y. K. Wu, 2015 International Particle Accelerator Conference (IPAC'15), Richmond, VA, May 3-8 2015.
47. *Characterizing Betatron Tune Knobs on Duke Storage Ring*, H. Hao, S. F. Mikhailov, V. Popov, Y. K. Wu, and J. Y. Li, 2015 International Particle Accelerator Conference (IPAC'15), Richmond, VA, May 3-8 2015.
48. *Experimental Study of a Two-Color Storage Ring FEL*, J. Yan, H. Hao, S. F. Mikhailov, V. Popov, Y. K. Wu, S. Huang, J. Y. Li, N. Vinokurov, and J. Wu, 2015 International Particle Accelerator Conference (IPAC'15), Richmond, VA, May 3-8 2015.

49. *Developing an Improved Pulsed Mode Operation for Duke Storage Ring Based FEL*, S. F. Mikhailov, H. Hao, V. Popov, and Y. K. Wu, 2015 International Particle Accelerator Conference (IPAC'15), Richmond, VA, May 3-8 2015.
50. *Extending OK5 Wiggler Operational Limit at Duke FEL/HIGS Facility*, P. W. Wallace, M. Emamian, H. Hao, J. Y. Li, S. F. Mikhailov, V. Popov, Y. K. Wu, and J. Y. Li, 2015 International Particle Accelerator Conference (IPAC'15), Richmond, VA, May 3-8 2015.
51. *Light Source and Accelerator Physics Research Program at Duke University*, Y. K. Wu, 2015 International Particle Accelerator Conference (IPAC'15), Richmond, VA, May 3-8 2015.
52. *Low Background Signal Readout Electronics for the MAJORANA DEMONSTRATOR*, I. Guinn *et al.* (the MAJORANACollaboration including M. P. Green, R. Henning, W. Tornow, J. F. Wilkerson, and A. R. Young), 5th Topical Workshop on Low Radioactivity Techniques (LRT 2015), Seattle, WA, March 18 - 20, 2015.
53. *Analysis techniques for background rejection at the MAJORANA DEMONSTRATOR*, C. Cuesta *et al.* (the MAJORANACollaboration including M. P. Green, R. Henning, W. Tornow, J. F. Wilkerson, and A. R. Young), 5th Topical Workshop on Low Radioactivity Techniques (LRT 2015), Seattle, WA, March 18 - 20, 2015.
54. *Status of the MAJORANA DEMONSTRATOR*, C. Cuesta *et al.* (the MAJORANACollaboration including M. P. Green, R. Henning, W. Tornow, J. F. Wilkerson, and A. R. Young), Matrix Elements for the Double-beta-decay EXperiments (MEDEX'15) Conference, Prague, Czech Republic, June 9 - 12, 2015.
55. *Choosing your partner: Trade-offs in dynamic carbon and nitrogen exchange between plants and their fungal symbionts*, C. D. Reid, C. R. Howell, A. S. Crowell, A. Weisenberger, S. Lee, G. Bonito, L. C. Cumberbatch, and R. Vilgalys, Ecological Society of America Annual Meeting, Baltimore, MD, August 11, 2015.

A.3 Invited Talks, Seminars, and Colloquia

Invited Talks, Seminars, and Colloquia

1. *Low-Energy Description of the Hadron Structure With Few-Body Systems*, M. W. Ahmed, 21st International Conference on Few-Body Problems in Physics, Chicago, IL, May 18 - 22, 2015.
2. *QCD at HIGS*, M. W. Ahmed, Triangle Universities Nuclear Laboratory's 50th Anniversary Celebration, Durham, NC, November 7, 2015.
3. *Neutrinos*, P. S. Barbeau, Triangle Universities Nuclear Laboratory's 50th Anniversary Celebration, Durham, NC, November 7, 2015.
4. *Nuclear Astrophysics*, A. E. Champagne, Triangle Universities Nuclear Laboratory's 50th Anniversary Celebration, Durham, NC, November 7, 2015.
5. *A Brief TUNL History - How a Small Accelerator Lab Became Today's DOE Center of Excellence*, T. B. Clegg, Triangle Universities Nuclear Laboratory's 50th Anniversary Celebration, Durham, NC, November 7, 2015.
6. *Summary of the joint town meetings on QCD*, H. Gao, invited presentation at the JSA Science Council Meeting, JLab, September 18, 2014.
7. *Spin Physics and Nucleon Structure*, H. Gao, invited talk at the 11th ICFA Seminar on Future Perspective in High Energy Physics, Beijing, Oct 27 - 30, 2014.
8. *Summary of the town meeting on QCD and Hadron Physics*, H. Gao, invited talk at the Long Range Plan working group meeting, Rockville, MD, November 16, 2014.
9. *Searches for T- and P-symmetry violating quantities and new forces*, H. Gao, invited talk at the Workshop on Major Research Initiatives on Precision Measurements, National Natural science Foundation of China, Changping, Beijing, China, January 25 - 27, 2015.
10. *Proton - a fascinating relativistic many-body system - remains puzzling*, H. Gao, invited plenary talk at the American Physical Society April Meeting, Baltimore, MD, April 11-14, 2015.
11. *The Overview of the SoLID Physics Program*, H. Gao, invited talk at the Long Range Plan working group resolution meeting, Kitty Hawk, NC, April 16-20, 2015.
12. *Experimental progress and status on nucleon electromagnetic form factors*, H. Gao, invited plenary talk at the 21st International Conference on Few-Body Problems in Physics, Chicago, IL, May 18 - 22, 2015.
13. *Latest results on few-body physics from $HI\gamma S$* , H. Gao, invited plenary talk at the 8th International Workshop on Chiral Dynamics, Pisa, Italy, June 29 - July 3, 2015.
14. *Facility at JLab for hadron physics*, H. Gao, invited talk at the International Workshop on e^+e^- collisions from Phi to PSi 2015, USTC, Heifei, China, September 23-26, 2015.
15. *New JLab experiment (PRad) on proton charge radius*, H. Gao, invited talk at the International Workshop on e^+e^- collisions from Phi to PSi 2015, USTC, Heifei, China, September 23 - 26, 2015.
16. *Proton remains puzzling*, H. Gao, Invited talk at the 10th Circum-Pan-Pacific Symposium on High Energy Spin Physics, Taipei, R.O.C., October 5-8, 2015.
17. *Fundamental Symmetries*, C. R. Gould, Triangle Universities Nuclear Laboratory's 50th Anniversary Celebration, Durham, NC, November 7, 2015.

18. MAJORANA *Research at NCSU*, M. P. Green, Triangle Universities Nuclear Laboratory's 50th Anniversary Celebration, Durham, NC, November 7, 2015.
19. *Update on The MAJORANA Neutrinoless Double-beta Decay Experiment*, R. Henning, Invited Talk at the 2015 International Workshop on Baryon and Lepton Number Violation, Amherst, MA, April 27, 2015.
20. *My Research Program at TUNL*, R. Henning, Triangle Universities Nuclear Laboratory's 50th Anniversary Celebration, Durham, NC, November 7, 2015.
21. *Plant Physiology Studies Using Radioisotope Tracing*, C. R. Howell, 2014 DNP/LRP Town Meeting on Education and Innovation, East Lansing, MI, August 2014.
22. *Nuclear Physics Research at HI γ S: A Decadal Vision*, C. R. Howell, Duke University Physics Faculty Lunch Talk, Durham, NC, Sept. 2014.
23. *Probing Hadron Structure with Photons*, C. R. Howell, APS Division of Nuclear Physics: 2014 Long-range plan Joint Town Meetings on Hadron and Heavy Ion QCD, Philadelphia, PA, Sept. 2014.
24. *Laying the Scientific Foundation for Nuclear Security and Non-proliferation Technologies with Gamma-ray Induced Reaction Studies*, C. R. Howell, 2015 Conference of the National Society of Black Physicists, Baltimore, MD, Feb. 2015.
25. *Photo-Induced Precision Cross-Section Measurements on Actinide Nuclei using Monoenergetic and Polarized Photon Beams*, C. R. Howell, Stewardship Science Academic Alliances Symposium 2015, Santa Fe, NM, March 2015.
26. *Few-Nucleon Research at TUNL: Probing Two- and Three-Nucleon Interactions with Neutrons*, C. R. Howell, 21st International Conference on Few-Body Problems in Physics, Chicago, IL, May 18 - 22, 2015.
27. *Nuclear Data Measurements Using Gamma Rays and Radiation Detector Development*, C. R. Howell, Annual DNDO Academic Research Initiative Grantees Conference, Dallas, TX, July 2015.
28. *Applications and Interdisciplinary Research at TUNL*, C. R. Howell, Triangle Universities Nuclear Laboratory's 50th Anniversary Celebration, Durham, NC, November 7, 2015.
29. *Fundamental Symmetries at TUNL*, P. R. Huffman, Triangle Universities Nuclear Laboratory's 50th Anniversary Celebration, Durham, NC, November 7, 2015.
30. *Cosmic Furnaces and the Origin of the Elements*, C. Iliadis, Monash Centre for Astrophysics (MoCA) Public Lecture. Monash University, Melbourne, Australia, February 2015.
31. *Nuclear Astrophysics*, C. Iliadis, Lectures (6 hours) given at Monash University, Melbourne, Australia, March 2015.
32. *Origin of the Elements*, C. Iliadis, Colloquium, University of Guelph, Guelph, Ontario, Canada, October 2015.
33. *The Future of Nuclear Astrophysics at TUNL*, C. Iliadis, Triangle Universities Nuclear Laboratory's 50th Anniversary Celebration, Durham, NC, November 7, 2015.
34. *Geoneutrino measurements with KamLAND*, H. J. Karwowski, Colloquium, Tel Aviv University, Tel Aviv, Israel, December 4, 2014.
35. *Nuclear Astrophysics with the ENGE Spectrometer*, R. Longland, Triangle Universities Nuclear Laboratory's 50th Anniversary Celebration, Durham, NC, November 7, 2015.
36. *Statistical Properties of Nuclei*, G. E. Mitchell, Triangle Universities Nuclear Laboratory's 50th Anniversary Celebration, Durham, NC, November 7, 2015.

37. *The High-Intensity Gamma-Ray Source (HI γ S) at TUNL: A New Tool for Nuclear Physics*, W. Tornow, Physics Department Colloquium, The University of Connecticut, Storrs, CT, February 27, 2015.
38. *From Photon-Induced Reactions at HI γ S to Double-Beta Decay*, W. Tornow, CRC634 Concluding Conference, Darmstadt, Germany, June 8 - 12, 2015.
39. *Nuclear Potentials and Few-Body Interactions*, W. Tornow, Triangle Universities Nuclear Laboratory's 50th Anniversary Celebration, Durham, NC, November 7, 2015.
40. *Gamma Beam Delivery and Diagnostics*, H. R. Weller, Technical Design Report Meeting, ELI-NP, Bucharest, Romania February, 2015.
41. *Nuclear Physics Research at the HI γ S Facility*, H. R. Weller, University of York, UK, July, 2015.
42. *Developing Beam Diagnostics for ELI-NP*, H. R. Weller, Final Technical Design Report Meeting, ELI-NP, Bucharest, Romania, October, 2015.
43. *Photonuclear Reactions*, H. R. Weller, Triangle Universities Nuclear Laboratory's 50th Anniversary Celebration, Durham, NC, November 7, 2015.
44. *Experiments and detection methods for $0\nu\beta\beta$ -decay searches*, J. F. Wilkerson, invited lecture, Gran Sasso Summer Institute, Assergi, Italy, September 23, 2014.
45. *The MAJORANA DEMONSTRATOR⁷⁶Ge $0\nu\beta\beta$ Experiment*, J. F. Wilkerson, invited seminar, National Laboratory Gran Sasso, Assergi, Italy, September 23, 2014.
46. *Neutrinoless Double Beta Decay*, J. F. Wilkerson, invited talk, NSAC Long Range Plan Working Group Resolution Meeting, Kitty Hawk, NC, April 18, 2015.
47. *A Next Generation ⁷⁶Ge $0\nu\beta\beta$ Experiment*, J. F. Wilkerson, NSAC Neutrinoless Double Beta Decay Sub-committee, August 2015.
48. *Ray Davis, his science and legacy*, J. F. Wilkerson, invited address, Raymond Davis Jr., Memorial Dedication, Lead, SD, August 26, 2015.
49. *Future Physics with Germanium: Where are we now and what do we need for $0\nu\beta\beta$ and dark matter*, J. F. Wilkerson, invited talk, Sino-German Germanium Detector Technologies Symposium, Ringberg, Germany, October 23, 2015.
50. *An Overview of the Institute for Cosmology, Subatomic Matter, and Symmetries*, J. F. Wilkerson, invited talk, Physics and Astronomy Advisory Committee, University of North Carolina at Chapel Hill, Chapel Hill, NC, November 6, 2015.
51. *Neutrinos*, J. F. Wilkerson, Triangle Universities Nuclear Laboratory's 50th Anniversary Celebration, Durham, NC, November 7, 2015.
52. *A Two-Color Storage Ring FEL*, J. Yan, an invited talk at 37th International Free-Electron Laser Conference (FEL2015), Daejeon, Korea, August 26, 2015.
53. *Some New Developments in High Precision Beta Spectroscopy in Measurements of Nuclear Beta Decay*, A. R. Young, ILL Invited Seminar, Institut Laue Langevin, Grenoble, August 2015.
54. *Fundamental Neutron Physics Drivers for a New High Power Spallation Neutron Source*, A. R. Young, CoNS Workshop, Mito, Japan, October 12, 2015.
55. *Neutron physics with a high intensity spallation neutron source*, A. R. Young, HINT2015 Workshop, Mito Japan, October 13 - 14, 2015.

Seminars at TUNL

1. Richard deBoer, University of Notre Dame, (September 25, 2014)
Precision Cross Sections for Nuclear Astrophysics
2. Jeff Blackmon, Louisiana State University, (October 2, 2014)
Nuclear Physics of X-ray Bursts
3. Rashi Talwar, University of Notre Dame, (October 23, 2014)
Stellar Neutron Sources and s-Process in Massive Stars
4. Kiana Setoodehnia, University of Notre Dame, (November 6, 2014)
Recent Research Facility Upgrades for Nuclear Physics Studies at Notre Dame
5. Sherry Yennello, Texas A&M University, (November 18, 2014)
How Much Cooler Would It Be With Some More Neutrons? Exploring the Asymmetry Dependence of the Nuclear Caloric Curve and the Liquid-Gas Phase Transition
6. Patrick Huber, Virginia Tech, (November 20, 2014)
Reactor Neutrino Fluxes and Nuclear Data
7. Zhiwen Zhao, Jefferson Lab/Old Dominion University, (November 25, 2014)
J/Psi at Jefferson Lab
8. Gleb Fedotov, University of South Carolina, (December 3, 2014)
Nucleon Resonances Studies With CLAS Detectors
9. Toshiyuki Kubo, RIKEN Nishina Center, (February 5, 2015)
Search for New Isotopes and New Isomers at RIKEN RI Beam Factory
10. Tom Ward, U.S. DOE/Office of Nuclear Energy, (February 12, 2015)
The QCD Nucleon and the Spin-Statistics Theorem
11. Tom Caldwell, University of Pennsylvania, (February 13, 2015)
Searching for Dark Matter with Single-Phase Liquid Argon in MiniCLEAN
12. Jordi Jose, Universitat Politcnica de Catalunya, (May 21, 2015)
Stellar Explosions and the Quest for the Origin of the Elements
13. Henryk Witała, Jagiellonian University, (September 22, 2015)
Ab initio calculations of $3N$ reactions with modern forces
14. Libby McCutchan, National Nuclear Data Center, (September 24, 2015)
Following Fission Fragments: A nuclear data-base approach to decay heat and Daya Bay antineutrinos
15. Sara Pozzi, University of Michigan, (November 19, 2015)
Applied Nuclear Physics for Nuclear Nonproliferation

Advances in Physics Lectures and Seminars

1. Mohammad Ahmed, North Carolina Central University and Duke University, (June 1, 2015)
Building Blocks of the Cosmos
2. Mohammad Ahmed, North Carolina Central University and Duke University, (June 2, 2015)
NN Interactions and Local Accelerators
3. Mohammad Ahmed, North Carolina Central University and Duke University, (June 3, 2015)
Nuclear Detectors and Instrumentation
4. Calvin Howell, Duke University, (June 4, 2015)
Introduction to Nuclear Scattering
5. Eric Schreiber, University of North Carolina at Chapel Hill School of Medicine, (June 25, 2015)
Physicians and Physicists: Working in Medical Physics
6. David Haase, North Carolina State University, (July 2, 2015)
Nuclear Physics at Ultralow Temperatures
7. Diane Markoff, North Carolina Central University, (July 9, 2015)
Neutrinos: Much Ado About (Nearly) Nothing
8. Hugon Karwowski, University of North Carolina at Chapel Hill, (July 16, 2015)
Fundamentals of Nuclear Models: Part I
9. Hugon Karwowski, University of North Carolina at Chapel Hill, (July 20, 2015)
Fundamentals of Nuclear Models: Part II
10. Christian Iliadis, University of North Carolina at Chapel Hill, (July 23, 2015)
Cosmic Furnaces and the Origin of the Elements

A.4 Professional Service Activities

Advisory/Fellowship/Review Committees

1. Secretary, Southeastern Section of the American Physical Society, 2015 - present, *M. W. Ahmed*
2. Fellowship Committee, American Physical Society, 2015 - present, *A.E. Champagne*
3. SURA Board of Trustees, 2014, *A.E. Champagne*
4. Fellowship Committee, Division of Nuclear Physics, APS, 2014 - 2015, *A.E. Champagne*
5. Member, NSAC Long Range Plan Working Group, 2014 - 2015, *H. Gao*
6. Member, Program Advisory Committee, BNL, April 2013 - December, 2015, *H. Gao*
7. Member, Dean's Laboratory for Nuclear Science Advisory Committee, MIT, 07/01/2013-06/30/2016, *H. Gao*
8. Chair, Jefferson Lab Users Group Board of Directors, 2015 - 2016, *H. Gao*
9. Member, European Research Council COG PE2 Review Panel, 2015 - present, *H. Gao*
10. Review panel, SFB 1044, Deutsche Forschungsgemeinschaft, September 3 -4, 2015, *H. Gao*
11. Member, Fellowship Committee, Topical Group on Hadronic Physics, American Physical Society, 2014, *H. Gao*
12. General Councillor, American Physical Society, 2011 - present, *H. Gao*
13. Vice Chair, APS Pipkin award selection committee, 2014 - present, *H. Gao*
14. Vice Chair, Jefferson Lab Users Group Board of Directors, 2014 - 2015, *H. Gao*
15. Trustee, Southeastern Universities Research Association (SURA), 2014 - 2016, *H. Gao*
16. Executive Committee, Division of Nuclear Physics, American Physical Society, April 2013 - April 2015, *H. Gao*
17. Chair Elect, International Spin Physics Committee, January 1, 2015 - present, *H. Gao*
18. Editorial Board of Physical Review C, January 1, 2014 - December 31, 2016, *H. Gao*
19. Associate Editor, Frontiers in Physics, 2011 - present, *H. Gao*
20. Member, Executive Committee, Neutron Electric Dipole Moment Experiment, *R. Golub*
21. Co-PI for NCSU PhysTEC grant (American Physical Society and NSF), *D. G. Haase*
22. Member, Site Visit Committee for PhysTEC program at Georgia State University, *D. G. Haase*
23. Selection Committee for TUNL REU program, *D. G. Haase*
24. Member, Program Committee, American Physical Society Division of Nuclear Physics, *R. Henning*
25. Chair, APS/DNP Tom W. Bonner Prize Selection Committee (2015), *C. R. Howell*
26. Member, DOE/NSF Nuclear Science Advisory Committee, The Long Range Plan Working Group (2014 - 2015), *C. R. Howell*
27. Member, International Scientific Advisory Board ELI-NP, 2014-present, *C. R. Howell*

28. Member, Majorana Senior Advisory Committee, 2007 - present, *C. R. Howell*
29. Member, Selection Committee for the Mellon Mays Dissertation Grant, 2000-present, *C. R. Howell*
30. Member, APS Hadronic Physics Topical Group, Nominating Committee (2014), *C. R. Howell*
31. Member of the PRC Editorial Board (2011 - 2014), *C. R. Howell*
32. Member, Executive Committee, Neutron Electric Dipole Moment Experiment, *P. R. Huffman*
33. Reviewer, SuperCDMS CD1 project review, *P. R. Huffman*
34. Member, Scientific Advisory Committee, Russbach School on Nuclear Astrophysics, March 8 - 14, 2015, Russbach, Austria, *C. Iliadis*
35. Member, Merit Review Panel organized by PNNL for NA-22: *Study of neutron angular correlations in spontaneous and neutron induced fission*, LLNL, Livermore, CA, December, 2014, *H. R. Weller*
36. Member, Merit Review Panel organized by PNNL for NA-22: *Two neutron correlations in photofission*, Idaho State University, Pocatello, Idaho, May, 2015, *H. R. Weller*
37. Member, Merit Review Panel organized by PNNL for NA-22: *Monoenergetic photon sources*, LBNL, Berkely, CA, October, 2015, *H. R. Weller*
38. Outside PhD examiner for Cristina Collicott, Dalhousie University, Halifax, NS, April 2015, *H. R. Weller*
39. Member, NSAC Nuclear Physics Long Range Plan Working Group and Writing Committee, 2014-present, *J. F. Wilkerson*
40. Chair-Elect, American Physical Society Division of Nuclear Physics, 2014, *J.F. Wilkerson*
41. Chair, American Physical Society Division of Nuclear Physics, 2015, *J.F. Wilkerson*
42. Chair, Program Committee, American Physical Society Division of Nuclear Physics, 2014, *J.F. Wilkerson*
43. Past-Chair, Program Committee, American Physical Society Division of Nuclear Physics, 2015, *J.F. Wilkerson*
44. Chair, Dissertation Award Committee, American Physical Society Division of Nuclear Physics, 2015, *J.F. Wilkerson*
45. Co-spokesman, UCNA experiment, *A. R. Young*

Conferences, APS Meetings and Workshops

1. Member, Organizing Committee, Triangle Universities Nuclear Laboratory's 50th Anniversary Celebration, Durham, NC, Nov. 2015, *M. W. Ahmed*
2. Member, Organizing Committee, Triangle Universities Nuclear Laboratory's 50th Anniversary Celebration, Durham, NC, Nov. 2015, *T. B. Clegg*
3. Member, International Advisory Committee, The 21st International Conference on Few-Body Physics, Chicago, U.S.A., May 18-22, 2015, *H. Gao*
4. Member, International Advisory Committee, The 8th International Workshop on Chiral Dynamics (CD15), University of Pisa, Pisa, Italy, 2015, *H. Gao*
5. Member, International Advisory Committee, Circum-Pan-Pacific Symposium on High Energy Spin Physics (Pacific Spin 2015), Oct 5 - 8, 2015, *H. Gao*
6. Member, International Advisory Committee, Conferences series on Electromagnetic Interactions with Nucleons and Nuclei (EINN2015), Nov. 2-7, 2015, *H. Gao*
7. Convener, QCD town meeting, DNP long range plan, Temple University, September 13-15, 2014, *H. Gao*
8. Co-Chair, 7th Workshop on Hadron Physics in China and Opportunities Worldwide, Kunshan, China, August 3-7, 2015, *H. Gao*
9. Member, Organizing Committee, Triangle Universities Nuclear Laboratory's 50th Anniversary Celebration, Durham, NC, Nov. 2015, *C. R. Gould*
10. Member, Organizing Committee, Triangle Universities Nuclear Laboratory's 50th Anniversary Celebration, Durham, NC, Nov. 2015, *C. R. Howell*
11. Co-chair, Organizing Committee, Workshop on Applications of Nuclear Reactions with Gamma-rays and Surrogates for Neutrons, 4th Joint Meeting of the APS Division of Nuclear Physics and the Physical Society of Japan, Waikoloa, HI, Oct. 2014, *C. R. Howell*
12. Member, International Advisory Committee, 21th International Conference on Few-Body Problems in Physics, Chicago, Ill, May 2015, *C. R. Howell*
13. Member, Organizing Committee, Triangle Universities Nuclear Laboratory's 50th Anniversary Celebration, Durham, NC, Nov. 2015, *P. R. Huffman*
14. Member, Organizing Committee, Triangle Universities Nuclear Laboratory's 50th Anniversary Celebration, Durham, NC, Nov. 2015, *W. Tornow*
15. Member, Organizing Committee, Triangle Universities Nuclear Laboratory's 50th Anniversary Celebration, Durham, NC, Nov. 2015, *J. F. Willkerson*
16. Member, Scientific Program Committee, The 37th International Free-Electron Laser Conference (FEL2015), August 2015, Daejeon, Korea, *Y.K. Wu*
17. Organizer for LUG2015, the 2015 LANSCE User Group Meeting: LANSCE Futures, Nov. 2 - 3, 2015, Santa Fe, NM, *A. R. Young*

Glossary of Acronyms

Laboratories, Facilities, Experiments and Programs

ANL	Argonne National Laboratory
BNL	Brookhaven National Laboratory
DFELL	Duke Free-Electron Laser Laboratory
DNDO	Domestic Nuclear Detection Office
GV	Gamma-Vault at HI γ S
HI γ S	High Intensity Gamma-Ray Source
JLAB	Thomas Jefferson Lab National Accelerator Facility
KURF	Kimballton Underground Research Facility
LANL	Los Alamos National Laboratory
LENA	Laboratory for Experimental Nuclear Astrophysics
LLNL	Lawrence Livermore National Laboratory
MJD	MAJORANA DEMONSTRATOR
nEDM	Neutron Electric Dipole Moment
NNSA	National Nuclear Security Administration
ORNL	Oak Ridge National Laboratory
PNNL	Pacific Northwest National Laboratory
UTR	Upstream Target Room at HI γ S

Detectors, Material, Particles, Electronics, Acquisition and Software

DAQ	Data Acquisition
HPGe	High Purity Ge Detector
MCNP	Monte Carlo N-Particle
NaI	Sodium Iodide
ORCA	Object-oriented Real-time Control and Acquisition
PSD	Pulse Shape Discrimination
VME	VERSA module Eurocard

Calculations, Reactions, and Techniques

FWHM	Full Width at Half Maximum
GDR	Giant Dipole Resonance
NRF	Nuclear Resonance Fluorescence
QCD	Quantum Chromodynamics
QRPA	Quasiparticle Random Phase Approximation

Index

(Listed by corresponding author)

- Bartram, C.L., 85, 87
Bhike, M., 36, 50, 103, 105, 115
Busch, M., 91
- Clegg, T.B., 146
Combs, D.C., 79, 178
Cooper, A.L., 180, 182, 184, 186
Cumberbatch, L.C., 150
- Davis, E.D., 83
Dermigny, J.R., 204
Downen, L.N., 34
- Esterline, J.H., 109
- Fallin, B., 134, 148
Finch, S.W., 117, 119, 121
Friesen, F.Q.L., 16, 18, 20, 22
- Gao, H., 14
Gilliss, T., 97
- Haase, D.G., 65, 67, 71
Han, Z., 24
Hao, H., 168
Heacock, B.J., 81
Howe, M.A., 208
Huffman, P.R., 57, 59
Hunt, S., 196
- Iliadis, C., 30, 40
- Kelley, J.H., 152, 154
Kelly, K.J., 28, 38, 188
Kendellen, D.P., 4
Kowal, K.M., 194
Krishichayan, 44, 48, 52, 132, 144
- Leung, K.K.H., 61, 63, 69
Li, W., 170
Little, D., 198
Longland, R., 32, 202
- Malone, R.C., 10, 12
Masood, K., 123
Medlin, G.L., 73
Mikhailov, S.F., 172
Mitchell, G.E., 53
- Niazi, R., 127
Nibbs, K., 206
- Olmsted, S.C., 156
- Portillo, F.E., 192
Pywell, R.E., 8
- Rager, J., 95
- Seo, P.-N., 6
Shanks, B., 93
Sikora, M.H., 2
Silano, J.A., 136, 138
- Ticehurst, D.R., 101
Tornow, W., 46, 107, 111, 125, 140, 142
Trimble, J., 99
- Underwood, D.J., 200
- Wallace, P., 166
Westerfeldt, C.R., 176
Wu, Y.K., 160, 162, 164
- Yan, J., 174
Young, A.R., 75, 77

Triangle Universities Nuclear Laboratory

